



TECHNISCHE
UNIVERSITÄT
WIEN
Vienna University of Technology

Dissertation

Effect of Manufacturing Parameters and Chemical Composition on Sintering and Properties of Powder Metallurgy Steels

durchgeführt zum Zwecke der Erlangung des akademischen Grades eines Doktors der
technischen Wissenschaften unter der Leitung von

Univ. Prof. i.R. Dr. Dr.h.c. mult. Herbert Danninger
und
Assoc. Prof. Dr. Christian Gierl-Mayer

E 164
Institut für chemische Technologie und Analytik

Eingereicht an der Technischen Universität Wien
Fakultät für Technische Chemie

Durch
Milad Hojati MSc.
Matrikel-Nr. 11736441

Wien, June 2022

Kurzfassung

Die Pulvermetallurgie ist eine material- und energiesparende Fertigungstechnologie, die sich besonders gut für die Herstellung komplex geformter Präzisionsteile in hohen Stückzahlen eignet. Bisher war die Anwendung von Sinterstahlbauteilen jedoch durch die mechanischen Eigenschaften von Sinterstählen begrenzt, die aufgrund der inhärenten Porosität denen von Kompaktstählen unterlegen sind. Andererseits führt die Porosität zu geringerem Gewicht und verbessertem Geräuschdämpfungsvermögen der Bauteile. In der vorliegenden Studie werden optimale mechanische Eigenschaften durch geeignete Auswahl von Zusammensetzung, Legierungsvariante und Herstellungsparametern angestrebt. Diese Doktorarbeit besteht aus zwei Hauptteilen.

Im ersten Teil der Studie wurde der Einfluss verschiedener Parameter wie Pressdruck, Sintertemperatur und -atmosphäre sowie chemische Zusammensetzung auf die Eigenschaften von PM-Stählen systematisch untersucht.

Die Auswirkung des Preßdrucks und der Sintertemperatur wurde an gesinterten Stählen mit mittlerem Kohlenstoffgehalt untersucht, die aus reinem Eisenpulver bzw. Mo-vorlegierten Stahlpulvern durch Verdichten bei unterschiedlichen Drücken (300, 500 und 700 MPa) und Sintern in Ar hergestellt wurden. Die Kohlenstoffauflösung wurde durch Metallographie und durch Messung der elektrischen Leitfähigkeit untersucht, wobei sich für diese Eigenschaft zeigte, dass dem Einfluß der Bildung und des Wachstums von Sinterhälsen durch die Kohlenstoffaufnahme der Matrix entgegengewirkt wird. Der letztere Vorgang kann auch untersucht werden, indem die Koerzitivkraft H_c als Funktion der Sintertemperatur gemessen wird, wobei H_c jedoch viel weniger vom Pressdruck beeinflusst wird als die Leitfähigkeit. Die Messung der Schwingungsdämpfung zeigte, dass eine Erhöhung der Dichte diesen Parameter in PM-Stählen reduziert. Die Wirkung einer reduzierenden (H_2) gegenüber einer inerten (Ar) Atmosphäre wurde an unlegiertem Eisen und Kohlenstoffstahl bei verschiedenen Sintertemperaturen untersucht. Es zeigte sich, dass sowohl die Reduktion von Oxiden als auch die Kohlenstoffauflösung während des Sinterns durch die Atmosphäre beeinflusst wird. Die mechanischen Eigenschaften im Sinterzustand werden bei Kohlenstoffstählen weniger von der Atmosphäre beeinflusst als bei reinem Eisen, bei dem Sintern in Ar zu starkem Kornwachstum und zu Korngrenzenbruch führte. Die Aktivierung des Sinterns durch Verwendung einer Fe-Fe₃C-Vorlegierung als Kohlenstoffträger wurde sowohl an unlegiertem Kohlenstoffstahl als auch an Cr-Mo-Stahl untersucht. Die Experimente, durchgeführt in inerte Atmosphäre (Ar), zeigten, dass die Zugabe dieser Vorlegierung selbst in kleinen Mengen Prozesse wie die Reduktion von Oxiden und die Kohlenstoffauflösung in den frühen Stadien des Sinterns fördert, was das Sintern in beiden Qualitäten aktivierte und die Eigenschaften verbesserte. Abschließend wurde das Sinterverhalten von fünf pulvermetallurgischen Stahlsorten, die bei unterschiedlichen Temperaturen gesintert wurden, anhand der resultierenden Eigenschaften verglichen. Dazu gehörten drei Sorten von Pulver auf Basis von Reineisenpulver mit Graphit, davon eine Sorte, die auch mit elementarem Kupfer legiert wurde, und eine andere mit Fe-Mn-Si-Masteralloy. Zwei weitere Qualitäten wurden aus vorlegierten Cr-Mo- und Mo-Stahlpulvern mit beigemischtem Graphit hergestellt. Beim legierten Chromstahl verzögert das Vorhandensein der stabilen Chromoxide die Sinterprozesse bis zu höheren Temperaturen, während diese Prozesse bei den anderen Stählen in der Aufheizphase bereits früher, bei

niedrigeren Temperaturen, stattfinden. Im Vergleich zu den Standardgütern Fe-C, Fe-Cu-C und Fe-Mo-C erfordert der Cr-Mo-Stahl eine aufwändigere Sinterung, insbesondere ausreichend hohe Temperatur, um die Sauerstoffentfernung zu gewährleisten, bietet aber andererseits in diesem Fall die besten Eigenschaften. Die Masteralloy-Variante zeigte schließlich einen äußerst attraktiven Kompromiss zwischen Herstellungsanforderungen, Legierungselementgehalt und Produkteigenschaften.

Im zweiten Teil der Arbeit war das Ziel die Herstellung von PM-Stählen für hochbelastete Anwendungen. Dazu wurden hybridlegierte Sinterstähle auf der Basis von vorlegiertem Stahlpulver Fe-1,8%Cr hergestellt, denen Mn, Ni bzw. die Mn-Si-Masteralloy zugesetzt wurden. Das Verdichten erfolgte gleichmäßig bei 700 MPa und das Sintern bei 1250°C. Es zeigte sich, dass die Zugabe von Legierungselementen zum System zu attraktiven Sintereigenschaften und einem guten Potenzial für die Sinterhärtung führt, was für hochbelastete pulvermetallurgische Bauteile relevant ist. Bei manganlegierten Stählen wurde jedoch beobachtet, dass der Weg, über den Mn in die Legierung eingebracht wird, einen signifikanten Einfluss auf die endgültigen Sintereigenschaften des Materials hat, wobei elementares Mn tendenziell zu Korngrenzenversprödung führt. Da viele PM-Eisenbasisformteile bei hohen Zyklenzahlen ermüdungsbelastet sind, wurden 3 ausgewählte Stahlsorten durch Ultraschallresonanz-Ermüdungsprüfung bis zu Lastspielzahlen von $10E10$ untersucht. Die Ni-Legierung erwies sich sowohl für die Schlagenergie als auch für die Gigazyklen-Ermüdungsfestigkeit als positiv, während Mn weniger effektiv war, teilweise wegen interkristalliner Versprödung. Die Mn-Si Vorlegierung zeigte ebenfalls etwas interkristallines Versagen, aber insbesondere bei $N > 10E8$ war die Ermüdungsfestigkeit ähnlich der des Ni-legierten Typs, jedoch mit deutlich geringerer Streuung.

چکیده

متالورژی پودر یک فناوری مقرون بصره - در مواد بری و انرژی- بمنظور تولید قطعات دقیق با اشکال هندسی پیچیده می باشد. با این وجود، تا به امروز، استفاده از اجزا و قطعات فولادی تف جوشی شده بدلیل خواص مکانیکی ضعیف تر ناشی از تخلخل ذاتی - نسبت به فولاد های آهنگری شده، محدود شده است. از سوی دیگر، وجود تخلخل در قطعات متالورژی پودر باعث کاهش وزن و بهبود ظرفیت میرایی صوتی قطعات می شود. در مطالعه حاضر، خواص مکانیکی بهینه با انتخاب مناسب ترکیب آلیاژی، پارامترهای ساخت، و روابط خواص-ریزساختار مورد بررسی قرار گرفته است. این پایان نامه دکتری شامل دو بخش اصلی می باشد.

در بخش اول این مطالعه، تأثیر پارامترهای مختلف مانند فشار کامپکت، دما و اتمسفر تف جوشی و همچنین ترکیب شیمیایی بر خواص فولادهای PM به طور سیستماتیک بررسی شده است.

تأثیر دمای تف جوشی و فشار کامپکت بر روی فولادهای تف جوشی شده با محتوای کربن متوسط، تهیه شده از پودرهای آهن و فولاد پیش آلیاژی مولیبدن دار به ترتیب با کامپکت در فشارهای مختلف (300، 500 و 700 مگاپاسکال) و تف جوشی در اتمسفر آرگون مورد بررسی قرار گرفت. انحلال کربن از طریق متالوگرافی و با اندازه گیری رسانایی الکتریکی مورد مطالعه قرار گرفت، که برای این ویژگی نشان داده شد که اثر تشکیل و رشد گلوبی های تف جوشی با جذب کربن در زمینه خنثی می شود. فرآیند دوم (انحلال کربن در شبکه آهن) را می توان با اندازه گیری کورسیویتی Hc به عنوان تابعی از دمای تف جوشی نیز مطالعه کرد، اگرچه این پارامتر نسبت به رسانایی الکتریکی کمتر تحت تأثیر فشار تراکم قرار می گیرد. اندازه گیری ظرفیت میرایی ارتعاشات صوت نشان داد که افزایش چگالی این ویژگی را در فولادهای PM کاهش می دهد. اثر احیای هیدروژن در مقابل اتمسفر خنثی آرگون بر روی آهن ساده و فولاد کربنی، نیز در بازه گسترده ای از دماهای زینترینگ مورد بررسی قرار گرفت. نتایج این بررسی نشان داد که هم احیای اکسیدها و هم انحلال کربن در حین تف جوشی تحت تأثیر اتمسفر تف جوشی قرار دارند. مشخص شد که خواص مکانیکی نهایی در مورد فولادهای ساده کربنی در مقایسه با آهن خالص کمتر تحت تأثیر اتمسفر قرار می گیرد، که در مورد اخیر (آهن خالص) تف جوشی در آرگون منجر به رشد چشمگیر دانه و شکنندگی مرز دانه ها می شود. فعال سازی تف جوشی با استفاده از مسترالوی Fe-Fe₃C به عنوان حامل کربن بر روی فولاد کربنی ساده و همچنین فولاد کروم-مولیبدنی مورد مطالعه قرار گرفت. آزمایشات انجام شده در اتمسفر بی اثر (آرگون)، نشان داد که افزودن این مسترابوی حتی در مقادیر کم، فرآیندهایی مانند احیای اکسیدها و انحلال کربن در مراحل اولیه تف جوشی را بهبود می بخشد که باعث افزایش درجه تف جوشی و بهبود خواص در هر دو گرید اصلی می شود و به عنوان فعال کننده تف جوشی عمل می کند. در نهایت، رفتار تف جوشی پنج گرید فولاد متالورژی پودر در دماهای مختلف بر اساس خواص نهایی مقایسه گردید. این پنج گرید از سه گرید تهیه شده از پودر پایه آهن با مخلوط با گرافیت، یک گرید آلیاژ شده با مس عنصری و دیگری با مسترالوی Fe-Mn-Si و همچنین دو گرید دیگر از پودرهای فولادی پیش آلیاژی Cr-Mo و Mo با گرافیت افزوده تهیه شدند. بر اساس نتایج، در فولاد آلیاژی کروم دار، وجود اکسیدهای پایدار کروم، فرآیند تف جوشی را تا دماهای بالاتر به تأخیر می اندازد، در حالی که در سایر فولادها، این فرآیندها زودتر و در مراحل اولیه گرمایش و در دماهای پایین تر انجام می شود. در خصوص تف جوشی فولاد Cr-Mo، در مقایسه با گریدهای استاندارد Fe-C، Fe-Cu-C و Fe-Mo-C چالش بیشتری وجود دارد. اگرچه از طرف دیگر، این فولاد در صورت اعمال دمای تف جوشی به اندازه کافی بالا، به جهت اطمینان از حذف اکسیژن، بهترین خواص را ارائه می دهد. در نهایت، با توجه به سازگاری با تجهیزات ساخت و همچنین ارایه خواص نهایی مطلوب می توان فولاد آلیاژی شده بوسیله مسترالوی را به عنوان یک گزینه مناسب رقابتی جدید با گرید تجاری موجود در نظر گرفت.

در بخش دوم پایان نامه، هدف تولید فولادهای PM برای کاربردهای استحکام بالا بود. برای این منظور، فولادهای متخلخل آلیاژی هیبریدی بر پایه پودر فولاد پیش آلیاژ شده Fe-1.8% Cr تهیه شد و به ترتیب منگنز و نیکل و همچنین مسترالوی Mn-Si، به ترکیب های پودری اضافه شدند. کامپکت به طور یکنواخت در 700 مگاپاسکال و تف جوشی در دمای 1250 درجه سانتیگراد انجام شد. نتایج آزمایشات نشان داد که افزودن عناصر آلیاژی به سیستم منجر به خواص تف جوشی بسیار مطلوب و قابلیت خوبی برای سختکاری حین تف جوشی می شود که برای تولید اجزای متالورژی پودر با استحکام بالا مطلوب می باشد. با این حال، در فولادهای آلیاژی شده با منگنز مشاهده شد که شیوه آلیاژ سازی، تأثیر قابل توجهی بر ویژگی های نهایی ماده دارد، و آلیاژ سازی با منگنز عنصری تمایل به تردی در مرزی دانه ها را افزایش می دهد. از آنجایی که بسیاری از قطعات آهنی PM تا اعداد سیکل بالا بارگذاری می شوند، در این بخش 3 گرید انتخاب شده از فولاد

با آزمایش خستگی اولتراسونیک تا سیکل $10E10$ مورد بررسی قرار گرفتند. نتایج بررسی تاثیر مثبت عنصر نیکل را هم برای انرژی ضربه و هم برای استحکام خستگی گیگاسیکل نشان داد در حالی که منگنز به دلیل شکنندگی بین دانه‌ای، کمتر مؤثر واقع شد. در فولاد آلیاژی شده با مسترالوی Mn-Si نیز مقادیری شکست بین دانه ای مشاهده شد، هرچند استحکام خستگی به ویژه در $N > 10E8$ مشابه با نوع آلیاژ نیکل دار اما با پراکنندگی بمراتب کمتر، حاصل شد.

Abstract

Powder metallurgy is a material- and energy-saving manufacturing technology particularly well suited for production of complex-shaped precision parts in large quantities. So far, application of sintered steel components has however been limited by the mechanical properties of sintered steels, which are inferior to those of wrought steels, as a consequence of the inherent porosity. On the other hand, the porosity results in lower weight and improved noise damping capacity of the components. In the present study, optimum mechanical properties are aimed at by suitable selection of composition, alloying variant and manufacturing parameters, and structure-property relationships have been studied. This PhD thesis contains two main parts.

In the first part of the study the effect of different parameters such as compacting pressure, sintering temperature and atmosphere as well as chemical composition on properties of PM steels was systematically investigated.

The effect of sintering temperature and compacting pressure was studied on sintered steels with medium carbon content prepared from plain iron and Mo prealloyed steel powders, respectively, by compacting at different pressures (300, 500 and 700 MPa) and sintering in Ar. Carbon dissolution was studied through metallography and by measuring the electrical conductivity, for which property it showed that the effect of formation and growth of sintering necks is counteracted by carbon uptake of the matrix. The latter process can also be studied by measuring the coercive force H_c as a function of the sintering temperature, H_c however being affected much less by the compacting pressure than is the conductivity. Measuring the vibration damping capacity showed that increasing the density lowers this property in PM steels. The effect of reducing (H_2) vs. inert (Ar) atmosphere was investigated on plain iron and on carbon steel, also here the sintering temperature being widely varied. It showed that both reduction of oxides and carbon dissolution during sintering are affected by the atmosphere. The final mechanical properties were found to be less affected by the atmosphere in case of carbon steels compared with plain iron, in which case sintering in Ar resulted in enormous grain growth and grain boundary embrittlement. Activation of sintering by using an Fe-Fe₃C masteralloy as a carbon carrier was studied on plain carbon steel as well as Cr-Mo steel. The experiments, done in inert atmosphere (Ar), showed that adding this masteralloy even in small quantity promotes processes such as reduction of oxides and carbon dissolution in the early stages of sintering, which enhanced sintering and improved the properties in both grades, the masteralloy acting as sintering activator. Finally, the sintering behavior of five powder metallurgy steel grades at varying temperatures was compared, based on the resulting properties. This included three grades prepared from plain iron base powder with admixed graphite, one grade alloyed also with elemental copper and another with Fe-Mn-Si masteralloy. Two further grades were prepared from Cr-Mo and Mo pre-alloyed steel powders with admixed graphite. In the chromium alloy steel, the presence of the stable chromium oxides delays the sintering processes up to higher temperatures, while in the other steels, these processes take place earlier in the heating stage, at lower temperatures. Compared to the standard Fe-C, Fe-Cu-C and Fe-Mo-C grades, the Cr-Mo steel requires more sophisticated sintering, esp. sufficiently high temperature, to ensure oxygen removal, but on the other hand it offers the best properties. The masteralloy variant, finally, can be regarded as a highly attractive compromise between manufacturing requirements, alloy element content, and product properties.

In the second part of the thesis, the aim was production of PM steels for highly loaded applications. For this purpose, hybrid alloyed sintered steels were prepared based on prealloyed steel powder Fe-1.8%Cr, and Mn and Ni, respectively, were admixed as well as the Mn-Si masteralloy. Compaction was done uniformly at 700 MPa and sintering at 1250°C. It showed that addition of alloying elements to the system results in attractive sintered properties and a good potential for sinter hardening, which is of relevance for highly loaded powder metallurgy components. However, in the manganese-alloyed steels it was observed that the route through which Mn is introduced to the alloy has a significant effect on the final sintered properties of the material, elemental Mn resulting in a tendency to grain boundary embrittlement. Since many PM ferrous parts are fatigue loaded up to very loading high cycle numbers, 3 selected grades of steels were examined by ultrasonic resonance fatigue testing up to 10E10 cycles. Ni alloying proved to be positive both for the impact energy and the gigacycle fatigue strength while Mn was less effective, in part because of intergranular embrittlement. The Mn-Si masteralloy also showed some intergranular failure, but in particular at $N > 10E8$ the fatigue endurance strength was similar to that of the Ni alloyed type, however with significantly lower scatter.

Acknowledgement

First and foremost I am extremely grateful to my supervisor, Prof. Dr. Herbert Danninger for his invaluable advice, continuous support, and patience during my PhD study. His immense knowledge and plentiful experience have encouraged me in all the time of my academic research and daily life.

This thesis would not be possible without the support of Prof. Dr. Christian Gierl-Mayer who has given me a lot of valuable information and also his prompt helping especially during practical work.

I owe my deepest gratitude to Dr. Abolghasem Arvand since without his support I could not have started my PhD studies.

I would also like to thank Prof. Dr. Golta Khatibi and Dr. Agnieska Betzwar-Kotas for their technical assistance with the fatigue tests, and many thanks to Mr. Johannes Frank for the support and help with preparation of the fatigue test samples.

I would like to offer my special thanks to Dr. Maryam Jalilizyaeian, who helped me and provided a lot of useful information for working in the labs.

Furthermore, I am grateful to Dipl.-Ing Ahmad Hashemi for his technical support and useful advices for SEM investigations.

I thank the whole PM group for being such good friends even beside work which made the time during this project very joyful and entertaining for me. I enjoyed almost every day of work due to the great working atmosphere.

I would like to express my appreciations to Dr. Johannes Zbiral for his cooperation in XRF analysis.

Many thanks go to Stefan Geroldinger for his support with some practical parts of the work, especially quenching dilatometry.

Finally, I would like to express my gratitude to my mother and family in Iran and the Arvand Family in Austria. Without their tremendous understanding and encouragement in the past few years, it would be impossible for me to complete my study.

Table of Contents

1. Background and fundamentals.....	13
1.1. Ferrous powder metallurgy	13
1.2. Raw materials and alloying methods	15
1.3. Compaction and compactibility	17
1.4. Sintering	19
1.4.1. General aspects of sintering and mechanisms	19
1.4.1.1. Solid state sintering	19
1.4.1.2. Liquid phase sintering	20
1.4.2. Chemical aspects of sintering	23
1.4.2.1. Reduction of oxides	23
1.4.2.2. Carbon dissolution	26
1.5. Alloying elements	28
1.5.1. Copper	28
1.5.2. Molybdenum	30
1.5.3. Nickel	30
1.5.4. Chromium.....	31
1.5.5. Manganese.....	32
1.6. Properties of PM steels.....	34
1.6.1. Mechanical properties	34
1.6.2. Fatigue behaviour of PM steels	36
1.6.3. Electrical conductivity.....	38
1.6.4. Magnetic properties.....	40
2. Experimental procedures	42
2.1. Starting powders.....	42
2.2. Specimen preparation	49
2.2.1. Mixing and compaction.....	49
2.2.2. Sintering	49
2.3. Characterization techniques	50
2.3.1. Green density.....	50
2.3.2. Sintered density	50
2.3.3. Dimensional change	51
2.3.4. Electrical and magnetic properties	51

2.3.4.1.	Specific electrical conductivity.....	51
2.3.4.2.	Coercivity.....	52
2.3.4.3.	Magnetic saturation.....	52
2.3.5.	Chemical and thermal analysis.....	53
2.3.5.1.	Carbon analysis	53
2.3.5.2.	Oxygen analysis	53
2.3.5.3.	XRF.....	53
2.3.6.	Thermal analysis	54
2.3.6.1.	DTA/TG/MS studies	54
2.3.6.2.	Dilatometric studies	54
2.3.6.3.	Quenching dilatometry (CCT diagram)	54
2.3.7.	Mechanical properties	54
2.3.7.1.	Dynamic Young's modulus and damping	54
2.3.7.2.	Specific Damping (Q^{-1}).....	55
2.3.7.3.	Hardness test	56
2.3.7.4.	Charpy impact test	56
2.3.8.	Metallographic investigations	57
2.3.9.	Fractography.....	57
2.3.10.	Fatigue test.....	57

3. Results and discussion Part 1: Sintering of ferrous powder compacts: Processes in the early stages of sintering60

3.1.	Part 1a: Effect of density on mechanical and physical properties of carbon and Mo alloyed steels	60
3.1.1.	Green density.....	64
3.1.2.	Metallographic investigations (pore morphology and matrix microstructure) ...	64
3.1.3.	Fractography.....	83
3.1.4.	Sintered density and dimensional change	87
3.1.5.	Mechanical properties	90
3.1.5.1.	Charpy impact energy	90
3.1.5.2.	Hardness.....	93
3.1.5.3.	Dynamic Young's modulus	97
3.1.5.4.	Damping.....	100
3.1.6.	Physical properties	104
3.1.6.1.	Electrical conductivity	104

3.1.6.2.	Coercive force	106
3.2.	Part 1b: Effect of the sintering atmosphere on physical and chemical processes during sintering of ferrous PM components	108
3.2.1.	Green density.....	111
3.2.2.	Thermal analysis and degassing behaviour	111
3.2.3.	Chemical analysis (carbon and oxygen content):.....	117
3.2.4.	Metallographic investigations (pore morphology and matrix microstructure) .	120
3.2.5.	Fractography.....	138
3.2.6.	Dimensional change and sintered density	143
3.2.7.	Mechanical properties	145
3.2.7.1.	Hardness.....	145
3.2.7.2.	Charpy impact energy	146
3.2.7.3.	Dynamic Young's modulus	148
3.2.8.	Physical properties	150
3.2.8.1.	Electrical conductivity	150
3.2.8.2.	Coercivity.....	152
3.3.	Part 1c: Sintering process and properties of PM steels alloyed with atomized Fe-C Masteralloy.....	155
3.3.1.	Green density.....	159
3.3.2.	Thermal analysis and degassing behaviour	159
3.3.3.	Chemical analysis (carbon and oxygen content).....	165
3.3.4.	Metallographic investigations (pore morphology and matrix microstructure) .	169
3.3.5.	Fractography.....	174
3.3.6.	Dimensional change and sintered density	177
3.3.7.	Mechanical properties	180
3.3.7.1.	Hardness.....	180
3.3.7.2.	Charpy impact energy	182
3.3.7.3.	Dynamic Young's modulus	183
3.3.8.	Physical properties	185
3.3.8.1.	Electrical conductivity	185
3.3.8.2.	Coercivity.....	186
3.4.	Part 1d: Mechanical and physical properties of differently alloyed sintered steels as a function of the sintering temperature	188
3.4.1.	Green density.....	195

3.4.2.	Thermal analysis and degassing behaviour	195
3.4.3.	Chemical analysis (carbon and oxygen content)	203
3.4.4.	Metallographic investigations (pore morphology and matrix microstructure)	205
3.4.5.	Fractography	224
3.4.6.	Dimensional change and sintered density	230
3.4.7.	Mechanical properties	232
3.4.7.1.	Hardness	232
3.4.7.2.	Charpy impact energy	233
3.4.7.3.	Dynamic Young's modulus	234
3.4.7.4.	Damping	235
3.4.8.	Physical properties	236
3.4.8.1.	Electrical conductivity	236
3.4.8.2.	Coercivity	237

4. Results and discussion Part 2: Hybrid (Cr-X) alloyed sintered steels for highly loaded PM parts.....239

4.1.	Green density	241
4.2.	Chemical analysis	242
4.2.1.	Oxygen and carbon content	242
4.2.2.	XRF analysis (manganese containing steels)	243
4.3.	Metallographic investigations (pore morphology and matrix microstructure)	248
4.4.	Fractography	267
4.5.	Dimensional change and sintered density	272
4.6.	Mechanical properties	275
4.6.1.	Hardness	275
4.6.2.	Charpy impact energy	277
4.6.3.	Dynamic Young's modulus	279
4.7.	Physical properties	282
4.7.1.	Electrical conductivity	282
4.7.2.	Coercivity	284
4.7.3.	Magnetic saturation	287
4.8.	Hardenability and CCT diagrams	290
4.9.	Gigacycle fatigue of hybrid (Cr-X) alloyed steels	295
4.9.1.	Chemical analysis (carbon and oxygen content)	295

4.9.2. Metallographic investigations (pore morphology and matrix microstructure and singularities).....	297
4.9.3. Fractography (broken by Charpy impact test at RT).....	306
4.9.4. Mechanical properties	308
4.9.5. Fatigue S/N curves	311
4.9.6. Fractography of fatigue specimens	314
5. Summary	324
5.1. Part 1	324
5.1.1. Part 1a.....	324
5.1.2. Part 1b	325
5.1.3. Part 1c.....	327
5.1.4. Part 1d	328
5.2. Part 2	329
6. References	333

1. Background and fundamentals

1.1. Ferrous powder metallurgy

In conventional metallurgy the processing steps generally consist at least of melting and casting, often hot and cold working with a large number of secondary operations, while Powder Metallurgy (PM) deals with metallic powders, which involves powder production (for which numerous routes are available), subsequent treatment and conditioning of the powders, one or more consolidation steps involving application of pressure and temperature (either jointly or in separated stages), and a multitude of secondary treatments which can be similar to those applied to wrought metallic products or specific for powder metallurgy [5]. In reality, powder metallurgy comprises a variety of different technologies for fabricating semi-dense and fully dense components. The conventional powder metallurgy process, referred to as press-and-sinter route, is shown in Figure 1.1 [6].

The basic procedure in the manufacture of PM ferrous parts is [7] :

- Mixing, which is blending a base powder- plain iron or steel powder- with the other additives including e.g. graphite, lubricant, alloying elements, etc.
- Compacting, which is pressing the mixture into a die with pressure up to 800 MPa being applied in order to obtain a defined shape and enable it to be handled safely and transferred to the next stage.
- Sintering, which is heating the compacts, usually in a protective atmosphere, at a temperature below the melting point of the main constituent so that the powder particles weld together and gain sufficient strength to the object for the target usage.

Most conventional PM steel parts weigh less than 5 pounds (2.27 kg). While many of the early PM parts, such as bushings and bearings, were very simple shapes, today's sophisticated PM process produces components with complex shapes and multiple levels [6].

The advantages of the Powder Metallurgy process are as listed below:

- Eliminates or minimizes machining by producing parts at, or close to, final dimensions
- Eliminates or minimizes scrap losses and waste by typically using more than 97% of the starting raw material in the finished part
- Permits a wide variety of alloy systems
- Produces good surface finish
- Provides controlled porosity for self-lubrication or filtration
- Facilitates manufacturing of complex or unique shapes which would be impractical or impossible with other metalworking processes, at least in high production lots.
- Enables obtaining microstructures inaccessible by ingot metallurgy.

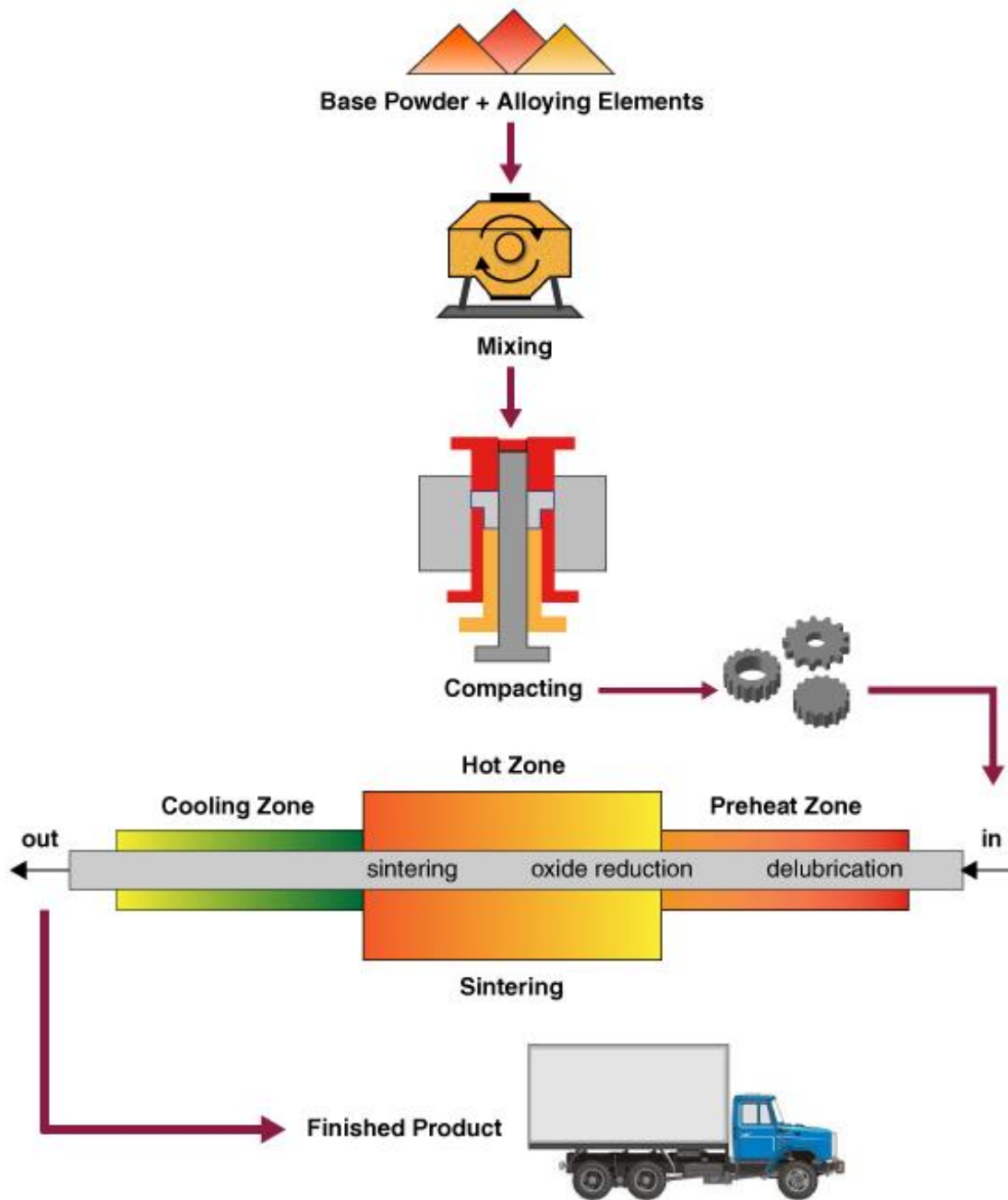


Figure 1.1: Basic conventional powder metallurgy (press-and-sinter route) [6].

PM parts are typically used in two main fields of automotive applications, which are transmission and engine applications, respectively (Figure 1.2). These parts are produced by powder metallurgy because of the cost advantage the sintering route offers for these components. The most important requirements for such parts are [8, 9]:

- ability to transmit the full torque resulting from engine torque and gear rotation
- ability to withstand the usually acting heavy synchronizer loads
- good resistance against wear
- extremely good dimensional accuracy needed for smooth performance and shift quality

Further requirements for such parts are low weight, noise damping, and cost reduction compared to cast iron or machined steel, however there should not be any compromises in terms of fatigue strength and machinability. This is possible through good material choice, good heat treatment and sophisticated compacting technologies.



Figure 1.2: PM components for engine and transmission systems [10].

1.2. Raw materials and alloying methods

The raw materials in PM are metallic powders and also powders of the other additives (graphite, lubricant, MnS, etc.). Depending on the targeted mechanical and physical properties of the PM product, the alloying method can vary significantly, PM offering a much wider variety than e.g. ingot metallurgy. It cannot be stated that one given alloying method will be the best one with respect to the technical and economic aspects. Therefore, advantages and disadvantages of the alloying method used must be carefully taken into consideration for each individual case. While carbon is normally admixed to the iron powder in the form of graphite [11], metallic alloying elements can be introduced by other methods [5, 12]. Five main alloying methods for production of PM steels are listed here:

- A- manufacture of a fully prealloyed powder, e.g. by atomizing
- B- admixing of elemental powders to a plain iron base powder
- C- admixing of masteralloy powders to a plain iron powder
- D- using diffusion alloyed powder (e.g. “Distaloy” grades)
- E- coating the base particles with an alloying metal by electrochemical or other metal deposition methods

The various alloying options are schematically demonstrated in Fig. 1.3.

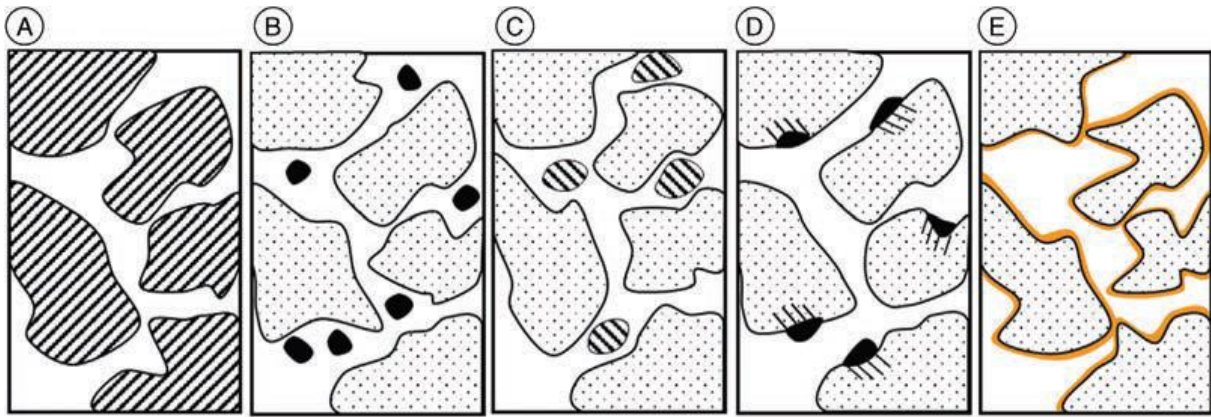


Figure 1.3: Alloy variants for sintered steels A) Prealloyed; B) Powder mixture; C) Masteralloy; D) Diffusion bonded; E) Coated [5].

The **Prealloyed powders** are obtained when alloying elements such as e.g. molybdenum, manganese, and chromium are added to molten iron prior to the atomization process. In the prealloyed powders the alloying elements do not segregate when the powder is handled, therefore it brings advantages in homogeneity but suffers from lower compactibility due to solid solution strengthening (See Figure 1.4), and the available compositions are limited, while **Admixed** grades have better compactibility and compositional flexibility, however the risk of segregation should be considered. The needs for good compactibility and homogeneity had led to the development of the **Diffusion Bonded** alloy powders such as the Distalloy grades [1], which combine high compactibility (see Figure 1.5) with consistency of alloy composition. In this case the mostly fine alloy metal particles are sintered to the iron particles by careful heat treatment that avoids formation of solid solution. Also here, the compositions available in the market are limited and include nickel, copper and molybdenum alloyed variants.

The **Masteralloy** (MA) route could also be another option for alloying the mixture when the compressibility of the prealloyed variant would suffer too much or the costs of elemental powders are extremely high. Another reason for using this method is controlling the metallurgical reactions by tailoring new alloying systems [13-15]. This method applied to sintered steels consists of mixing a base powder with an MA powder that contains all alloying elements in a combined form. The introduction of oxygen sensitive elements such as Si, Mn and Cr would be possible with this method as shown by De Oro Calderon et al. [13, 16], which can significantly improve the mechanical properties of the low alloy steels. The chemical composition of the MA can be designed such as to promote the formation of a transient liquid phase for enhancing the sintering process, effectively distributing the alloy elements and resulting in better mechanical properties [14, 17, 18]. The earlier approaches on development of masteralloys for PM steels were abandoned in the 90's because of the excessive tool wear resulting from the very hard and angular MA powder particles, which at that time were produced by casting and milling [19-23]. In the last two decades the use of gas atomization techniques has enhanced the research in MA's because it allows obtaining powder particles with adequate, rounded, morphology and low oxygen contents [13].

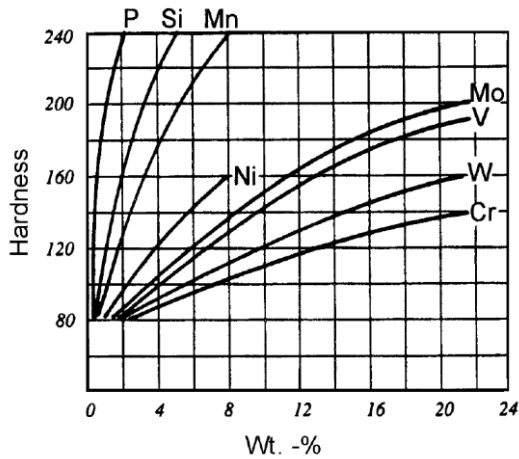


Figure 1.4: Influence of some alloying elements on the hardness of ferrite [1].

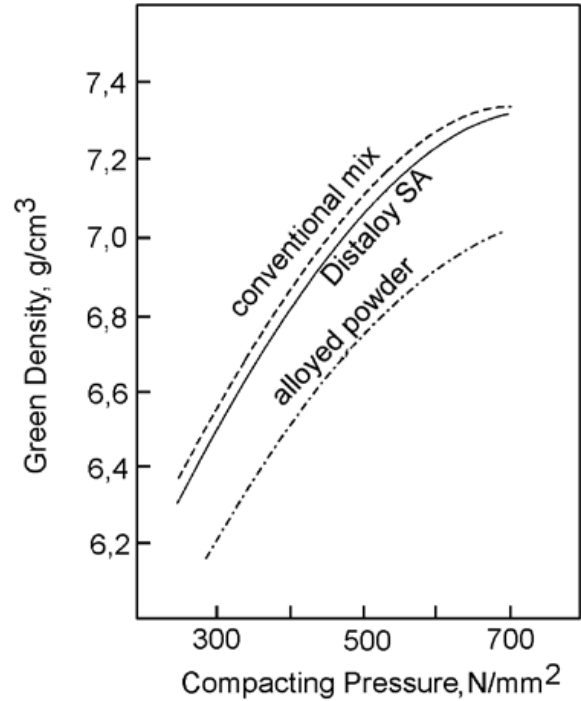


Figure 1.5: Compactibility of Fe-1.75Ni-1.5Cu-0.5Mo, alloyed through different methods [1].

1.3. Compaction and compactibility

The uniaxial compaction in rigid dies (die compaction) is the most common method for shaping PM precision parts, a cost-effective technique very suitable for the production of large series. In this process, densification and shaping occur simultaneously. In general, uniaxial die compaction technology is employed for large series of not too large parts (Figure 1.6).

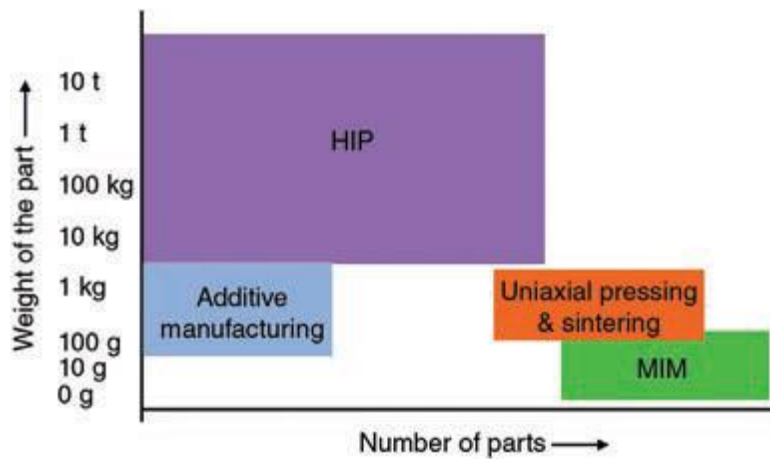


Figure 1.6: Positioning of different PM shaping technologies. Based on information from Olle Gröner [24].

Density has a very pronounced impact on mechanical properties. An increase of the density improves the strength, ductility, and toughness (Figure 1.7) as well as fatigue endurance of PM steels [25, 26]. In addition to the mechanical properties, degassing and de-oxidation of sintered steels can be affected by the green density, as Danninger showed [27, 28]; lowering the green density improves the de-oxidation process.

The measurement of compactibility (compressibility) is described in ISO 3927 [ISO 3927]. It is characterized by the uniaxial compression of powder in a steel or hard metal die (cylindrical or rectangular) at different pressures (200–800 MPa) and subsequent measurement of the density of the resulting compact. Compact density is the weight of a powder compact divided by its bulk volume. The main factors that affect the compactibility are:

- Compacting pressure
- Particle shape/size
- Particle porosity
- Lubricants/organics content
- Type and powder composition (hardness, work hardening capacity)

As an example, the effect of compaction condition (lubrication) of ASC100.29 is shown in Figure 1.8. Increased density can be achieved by increasing the compacting pressure. Compacting pressures are normally around 150–900 MPa (for ferrous parts usually 400–600 MPa) [29]. However, Haynes [3] has already shown that at very high pressures the compressibility curves for iron powders become almost parallel to the abscissa (Figure 1.9), and cold pressing cannot result in full density, some porosity being always left as a consequence of work hardening.

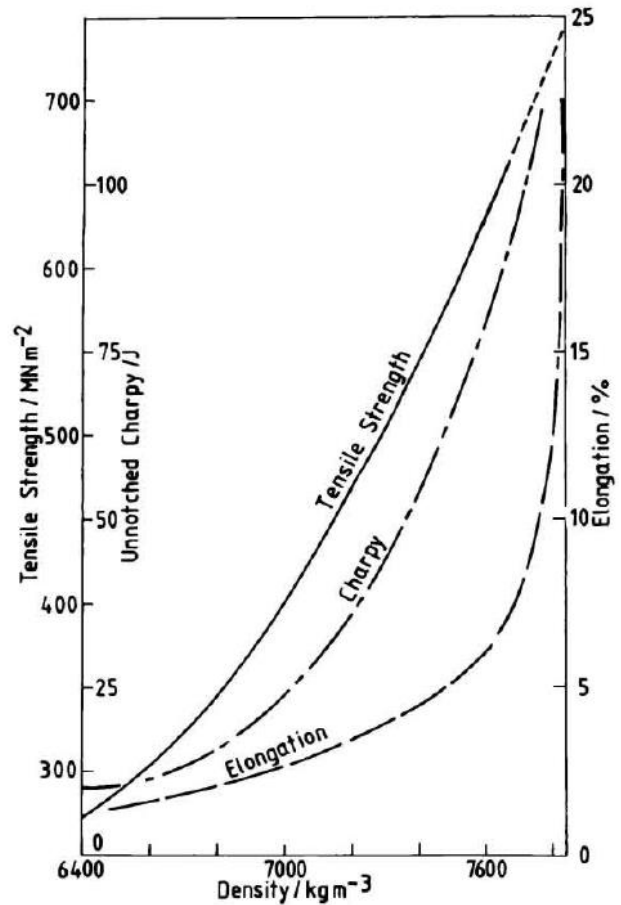


Figure 1.7: Effect of density on mechanical properties of sintered Fe-0.4C-4Ni steel, sintered at 1120 °C [3].

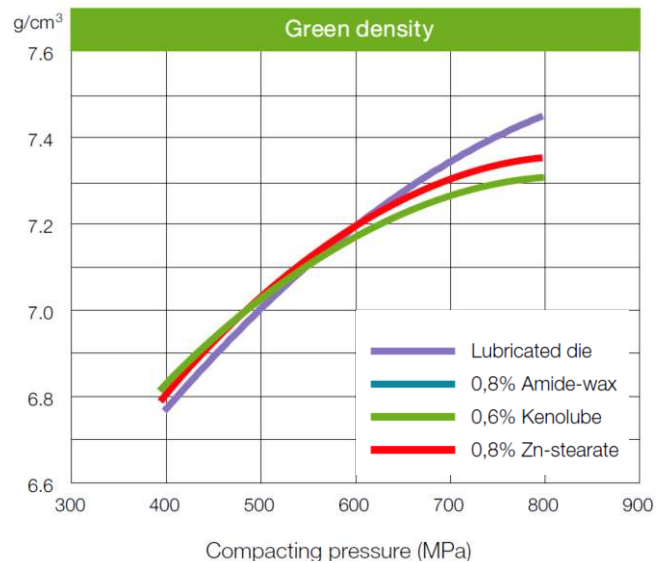


Figure 1.8: Compactibility (compressibility) of ASC100.29 at different lubricating conditions [2].

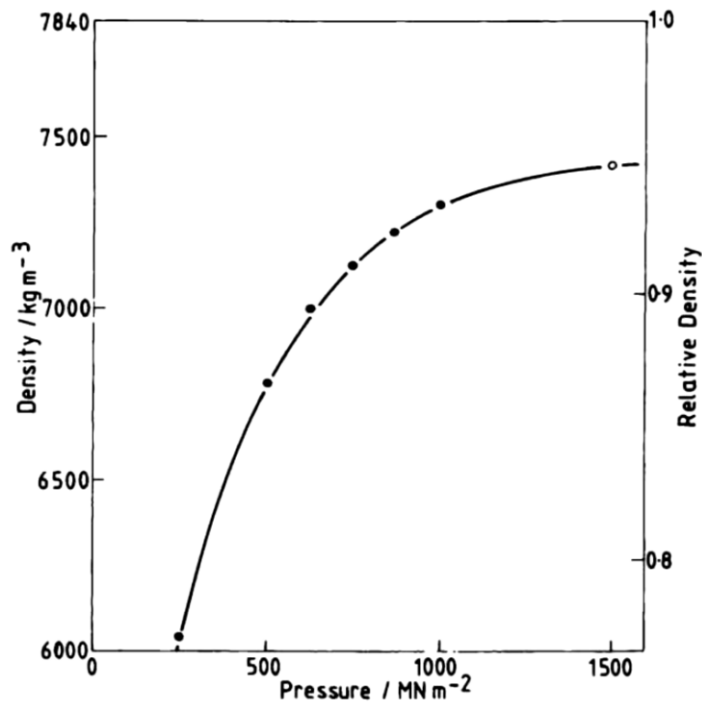


Figure 1.9: Compressibility curve for single pressed diffusion bonded Distaloy SA powder [3].

1.4. Sintering

The ISO definition of sintering is: “The thermal treatment of a powder or compact at a temperature below the melting point of the main constituent, for the purpose of increasing its strength by bonding together of the particles [30].

Sintering of metals in air would result in considerable oxidation due to the large specific surface and thus high chemical reactivity of powder-based systems. Therefore, sintering of metallic systems needs protective atmosphere, which has a pronounced impact both on mechanism of sintering and on the industrial sintering process.

1.4.1. General aspects of sintering and mechanisms

1.4.1.1. Solid state sintering

Sintering can be performed in different variants, depending on the phases present and the components of which the respective systems consists: solid state, activated, liquid phase (persistent or transient), reactive [31]. The most common mechanism of sintering of single component systems is *solid state sintering*.

During solid state sintering the powder particles are bonded together by diffusion processes in the solid state which gives the sintered part a certain mechanical strength.

Here, the driving force is elimination of defects, among which the surface is dominant; i.e., the disperse system lowers its energy primarily by reducing its surface. Additional inherent structural defects which were formed during pressing are eliminated [32]. In the presence of chemical concentration gradients (heterogeneous powders) the Gibbs free energy of the system

must be minimized by homogenization [33]. This requires that a large amount of material must be transported during sintering, which is achieved by the different material transport mechanisms as shown in Figure 1.10 [34]. In most PM materials, more than one component is present, and particularly if starting from powder mixes, hetero-diffusion and homogenization processes have to be considered. In the case of alloy formation, the driving forces, especially the mixing entropy, are much higher than those caused by the surface energy, and, therefore, the formation of new pores during mutual diffusion can occur (“Kirkendall effect”) [5].

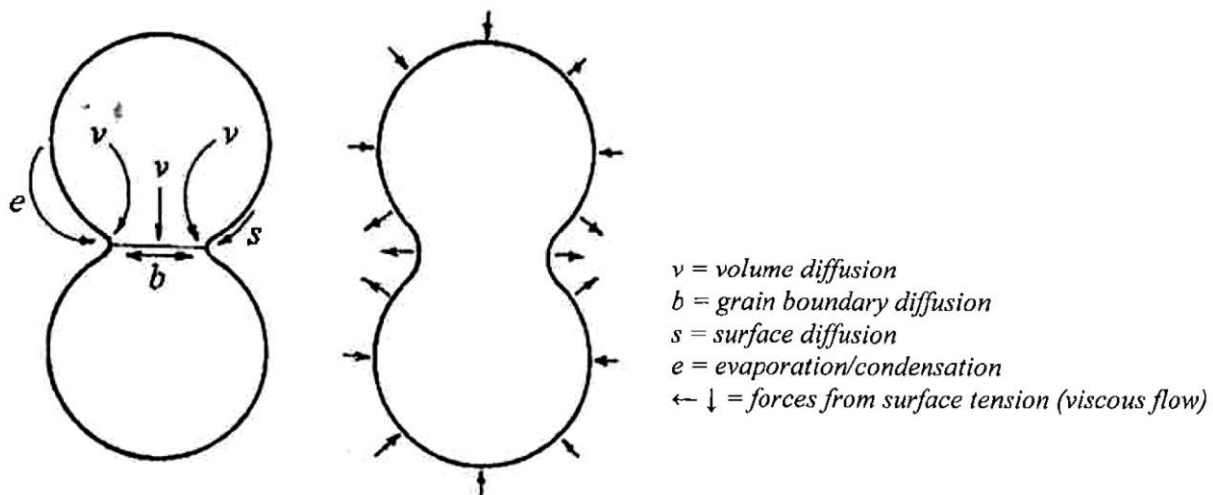


Figure 1.10: Neck enlargement between metallic particles during sintering [34].

1.4.1.2. Liquid phase sintering

Another sintering mechanism which is offering mass transport not through a solid layer but a liquid is *liquid phase sintering* (LPS). Important technical advances in LPS came in the 1920s and 1930s with the development of several materials; cemented carbides (WC–Co, patented in 1923), porous bronze (Cu–Sn), tungsten heavy alloys (W–Ni–Cu), copper steels (Fe–Cu–C), and cermets (TiC–Fe). Over the next 70 years, LPS processing spread to a diverse range of applications. Oil well drilling tips, porcelain jacketed dental crowns, automotive valve seats, wire drawing dies, high-temperature bearings, electrical contacts, electronic capacitors, radiation shields, diesel engine turbochargers, electronic insulator substrates, golf clubs balance weights, ultrasonic transducers, electronic solders, and grinding abrasives, can be mentioned as examples [4].

Through activated and liquid-phase techniques, lower sintering temperatures or enhanced densification are possible. Metal powders treated with selected chemical additives can experience enhanced sintering through increased transport rates [35].

Two types of liquid phase are possible when mixed particles are heated above the solidus temperature (Figure 1.11). The first type is **Persistent Liquid Phase**, and it forms if at sintering temperature the liquid phase is in chemical equilibrium with the solid phase. The liquid phase enhances material transport and typically also densification; therefore, persistent liquid phase sintering is the process applied if full density is required, such as for hard metals or tungsten heavy alloys. Solubility of the main constituent in the liquid phase usually promotes densification [4, 5].

The second type is **Transient Liquid Phase**, in this case, during sintering, also homogenization must take place, which may occur through solid state sintering. If, however, the melting point of the minor constituent is below the sintering temperature or if a low melting eutectic is formed [36, 37], a liquid phase is formed that is not thermodynamically stable and rapidly disappears into solid solution. Transient liquid phase sintering is a common process in sintering of iron base PM components, for example sintering occurs in such a way in Fe-Cu-C which is widely used in production of PM precision parts, [38, 39]. This type of sintering does not lead to densification but, in contrast, results in “Cu swelling”, which is used in industrial practice to compensate for the natural shrinkage of pressed compacts; thus, net dimensional change +/- 0 can be adjusted [40]. This phenomenon can be observed very well through dilatometry, as shown by Dautzenberg (see Figure 1.12) [41].

In addition to enhancing the sintering process, another benefit of the transient liquid phase is enhanced distribution and homogenization of the alloy elements, which improves the mechanical properties, as shown not only for Fe-Cu-C but also for steels alloyed with other elements such as Mo and Cr [42-46].

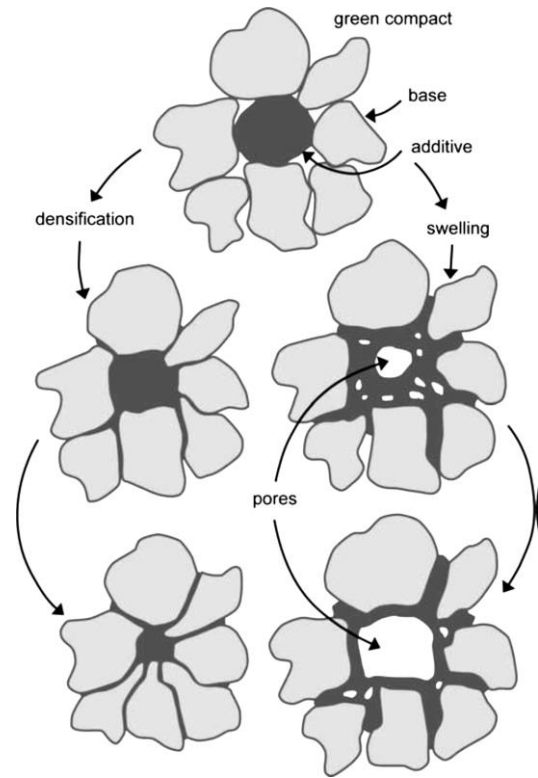


Figure 11: liquid phase sintering mechanism, swelling when transient melt forms and densification when persistent liquid phase forms [4].

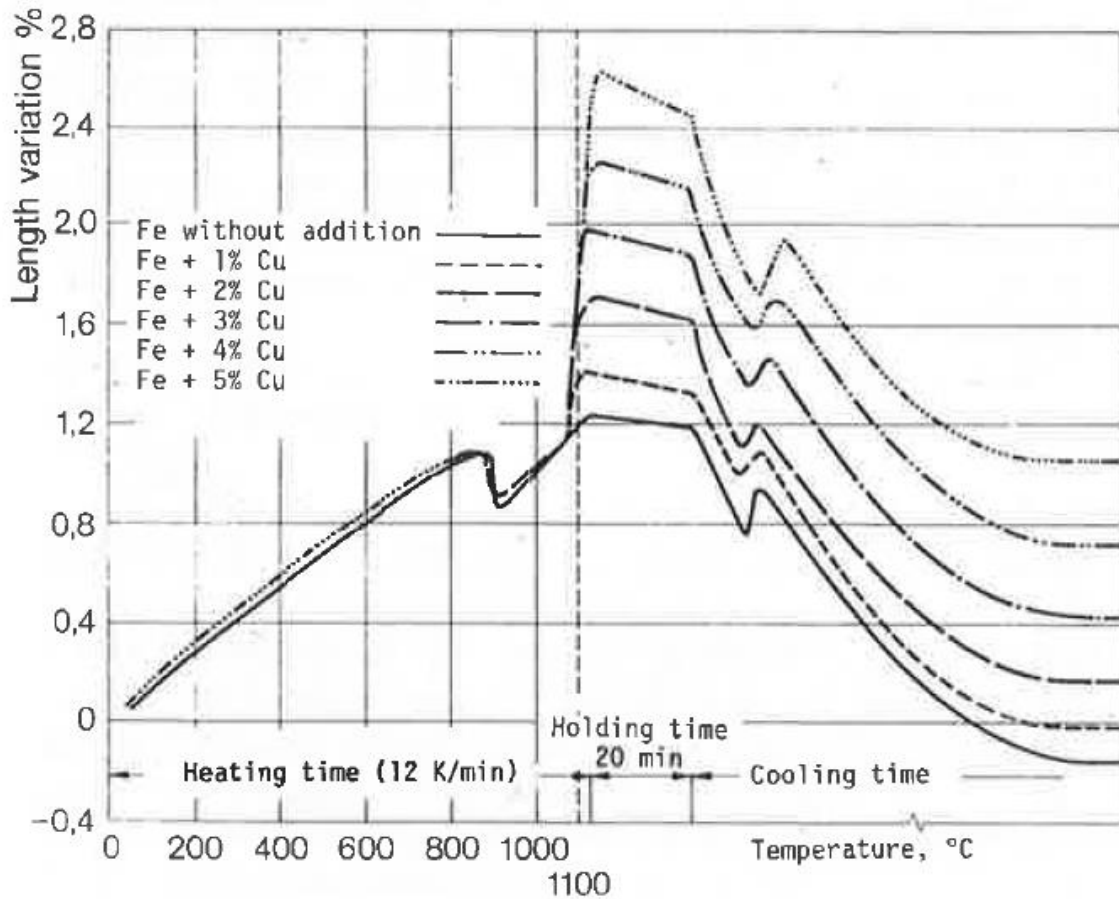


Figure 1.12: Dilatometry of Fe-Cu sintered steels [41].

This type of sintering usually also leads to formation of “Secondary pores” which results from the rapid distribution of the liquid phase in the pores of the matrix [37, 47]. These “secondary” pores may be of the same size as the original particles, as for Fe–Cu, or considerably larger, such as for Fe–Mo–C, and have to be considered especially with regard to fatigue properties because larger secondary pores may act as crack initiation sites [48]. Danninger [47] already showed that using Cu powder with coarser particles would lead to formation of larger secondary pores (Figure 1.13) which has negative effects on the mechanical properties, larger pores lowering tensile strength, elongation and especially impact and fatigue strength. Therefore, using fine alloy powders is recommended, and agglomeration of alloy element particles must be avoided.

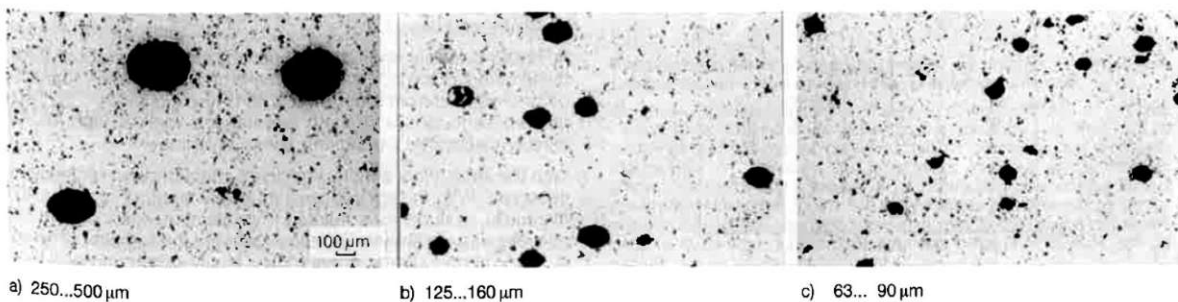
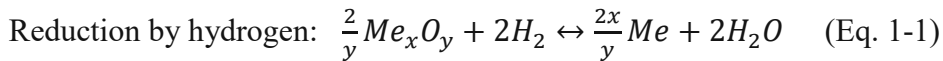


Figure 1.13: Effect of Cu particle fraction on secondary pore size [47].

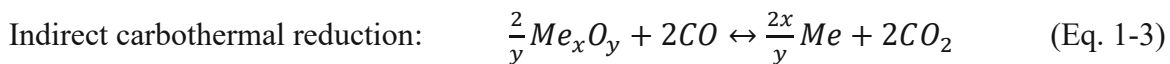
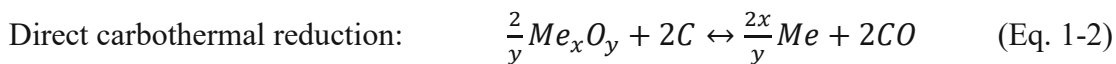
1.4.2. Chemical aspects of sintering

1.4.2.1. Reduction of oxides

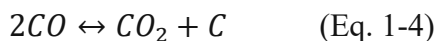
The surfaces of all metal powders that have been exposed to air are covered by layers consisting of oxides, hydroxides, and adsorbed gases. These layers usually inhibit the sintering process and contact formation because they lower the surface energy and thus the driving force and also slow down transport processes. Therefore, removal of the layers in the early stages of sintering is necessary to ensure successful sintering. Most oxide layers covering powder particles can be reduced by different agents. In powder metallurgy the most common reducing agents are components of the sintering atmosphere and carbon. Suitable sintering atmospheres contain reducing agents such as hydrogen and carbon monoxide which is produced by the carbothermal reaction due to the presence of admixed graphite. The respective oxide reduction reactions are given below:



Where Me and Me_xO_y are the metal and its oxide, respectively. Carbon participates in the oxide reduction in two stages. The first is reaction between carbon and metal oxide which is called *direct carbothermal reduction*, for example, the reaction between graphite and surface oxides which produces carbon monoxide (Eq. 1-2). The produced carbon monoxide then can react with the existing oxides, which produces carbon dioxide (Eq. 1-3). This reaction is called *indirect carbothermal reduction*. However, at sintering temperature CO_2 is not stable and any CO_2 present is rapidly converted to CO by reaction with C, according to Boudouard's equilibrium.



At higher temperature the Boudouard reaction (Eq. 1-4) is shifted toward the formation of carbon monoxide which is more stable at higher temperatures.



Equilibrium between oxidation and reduction in hydrogen and carbon monoxide containing atmospheres is given respectively by:

$$\frac{p(\text{H}_2\text{O})}{p(\text{H}_2)} = \exp\left(\frac{\Delta G_1^0}{2RT}\right) \quad (\text{Eq. 1-5})$$

$$\frac{p(\text{CO}_2)}{p(\text{CO})} = \exp\left(\frac{\Delta G_2^0}{2RT}\right) \quad (\text{Eq. 1-6})$$

Where ΔG_1^0 and ΔG_2^0 are the standard Gibbs free energy changes for the oxide reduction by hydrogen and carbon monoxide respectively.

All the above reactions are summarized in an Ellingham-Richardson diagram (Figure 1.14) where the equilibrium conditions in terms of oxygen partial pressure, $\text{H}_2/\text{H}_2\text{O}$ and CO_2/CO , as well as possibility reduction of oxides can be defined.

Dry hydrogen gas can easily reduce the Fe-oxides on the powder at temperatures 350-550 °C [49], the findings by Gierl-Mayer [50] also confirm this. Generally, from a thermodynamic point of view, at lower temperature, H₂ is the stronger reducing agent than C or CO, and at high temperatures, C is the strongest reducing agent because the Gibbs free energy of CO formation becomes more negative with increasing temperature whereas that of H₂O becomes less negative and that of CO₂ is constant.

Mass spectrometry (MS) is a well-known method for studying and monitoring the degassing and deoxidation behaviour of the material during the thermal process [42, 51-53]. In Figure 1.15, examples of MS graphs for Fe-C sintered in different atmosphere (Ar and H₂) are given.

Sintering in H₂ results in an m18 = H₂O degassing peak at about 400°C while in Ar, the first peak (m28 = CO) is at about 800°C related to carbothermal reduction of oxides, which confirms that at lower temperature, H₂O is the stronger reducing agent while at higher temperature carbothermal reduction is the dominant mechanism for reduction of oxides also when sintering in H₂.

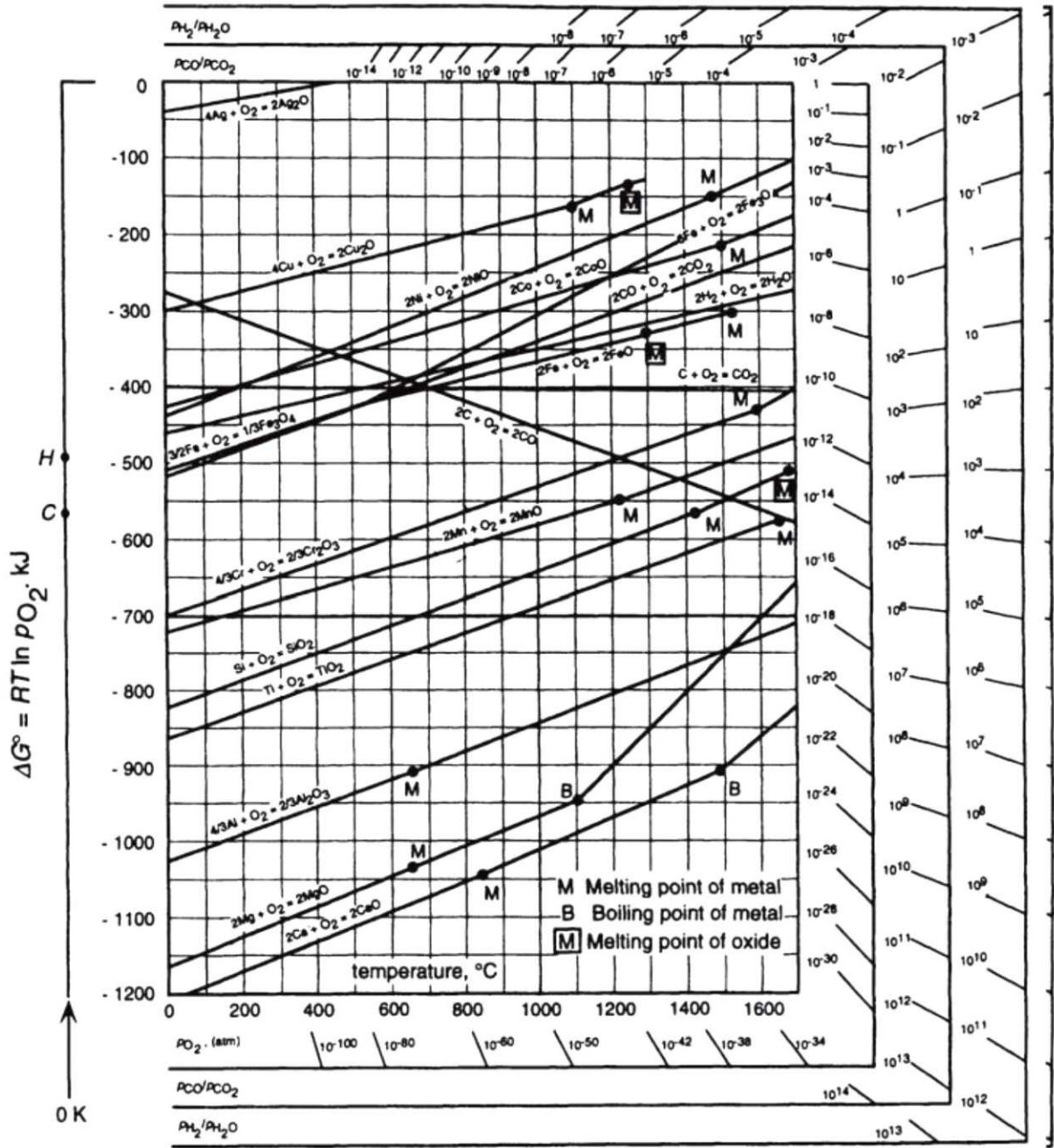


Figure 1.14: The Ellingham-Richardson diagram for selected oxides [54].

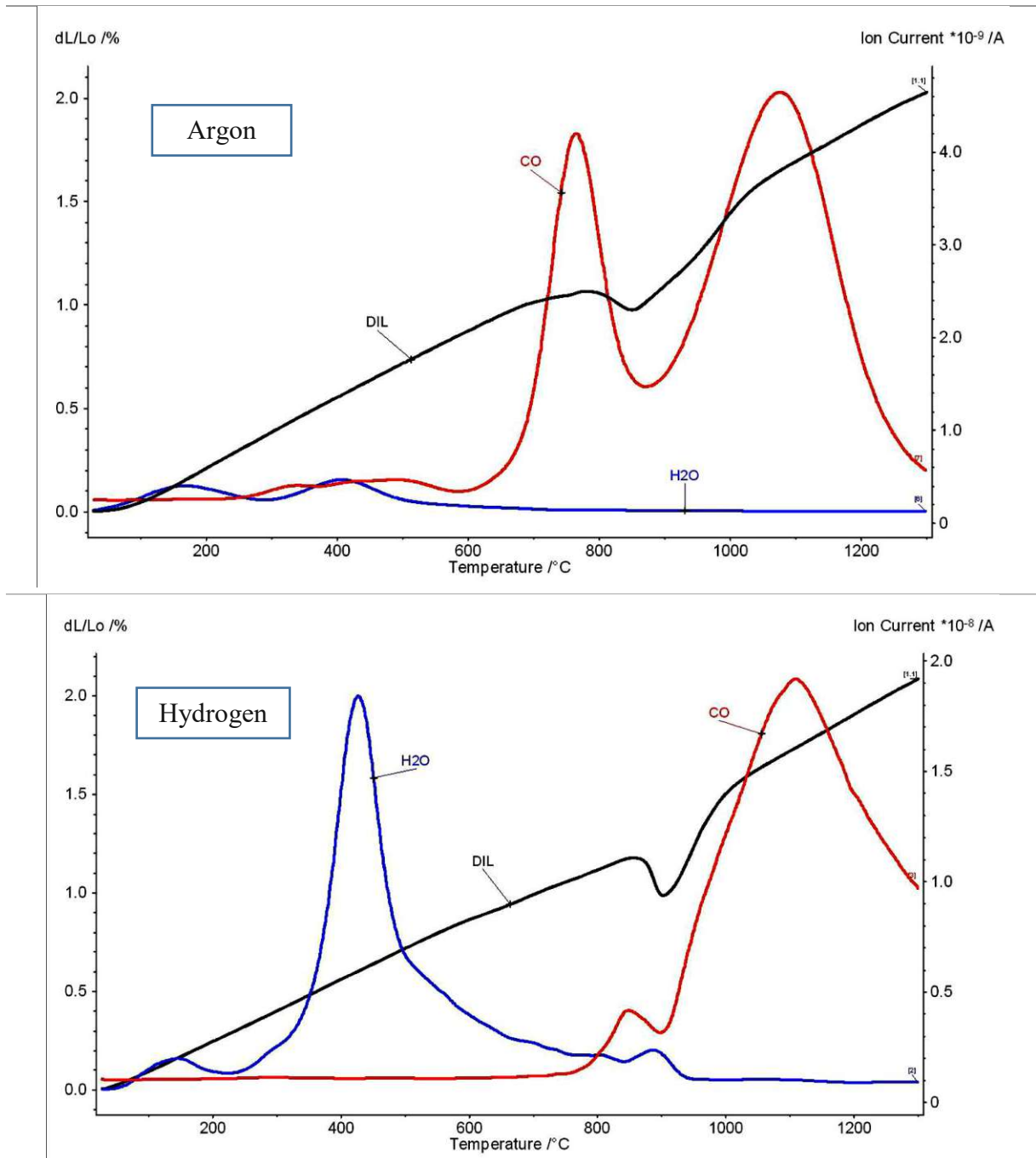


Figure 1.15: DIL/MS runs of Fe-0.5C. 10 K/min, 1300°C 60 min isothermal, 10 K/min: heating section [50].

1.4.2.2. Carbon dissolution

Most ferrous PM precision parts, especially those with higher strength and hardness, need carbon in their chemical composition. Since carbon present within the powder particles increases the hardness and thus severely lowers the compactibility, addition of this carbon is usually done through admixing fine graphite grades that are expected to completely dissolve during sintering.

The process of graphite dissolution has been studied rather infrequently, despite its practical importance. Dautzenberg et al. [55] stated that the solution of carbon into premixed sintered steel during sintering is not depending – as usually assumed - on a conversion of the graphite into CO but appears to be a direct solid state diffusion, while Tanaka and Lund [56, 57] concluded that gas phase transport is of major importance. Oxide layers are not only barriers for the formation of sintering contacts but also for the dissolution of the graphite in the metallic matrix. Apparently diffusion of carbon through an oxide layer is almost as difficult as is that of the metallic elements [58]. In this connection, Banerjee [59, 60] states that reduction of the oxide films covering the metal particle surfaces has to occur before significant carbon dissolution can take place. As discussed above, a major deoxidation process in Fe–C occurs at about 700°C, well below the temperatures at which carbon dissolution is even thermodynamically possible.

It has also been claimed that dissolution of carbon in the iron matrix is started at around 800°C by different mechanisms, i.e. there are solid state and / or gasification theories [61].

From metallographic sections of unalloyed Fe-C steels the percentage of pearlite can be estimated, which has been used as an indicator for the percentage of dissolved C. This method is preferred to other analytical methods, the chemical measurements of free carbon, which is done e.g. for cemented carbides, at least for PM steels being somewhat tricky and sensitive to experimental errors [62]. Compared to other alloying elements, carbon diffuses much more rapidly into the cores of the iron particles. Figure 1.16 shows the growth of the area fraction of pearlite in the investigated Fe-0.8%C steel. Especially important is the significant increase of the pearlite content between the temperatures of 950 and 1000°C, indicating fast carbon dissolution in this narrow temperature band. These results are in good agreement with those given by Danninger et al for Fe-0.8%C [11] who also observed fairly slow carbon dissolution up to about 900-950°C and also showed that dissolution of the graphite can be affected by the graphite grades used (artificial and natural).

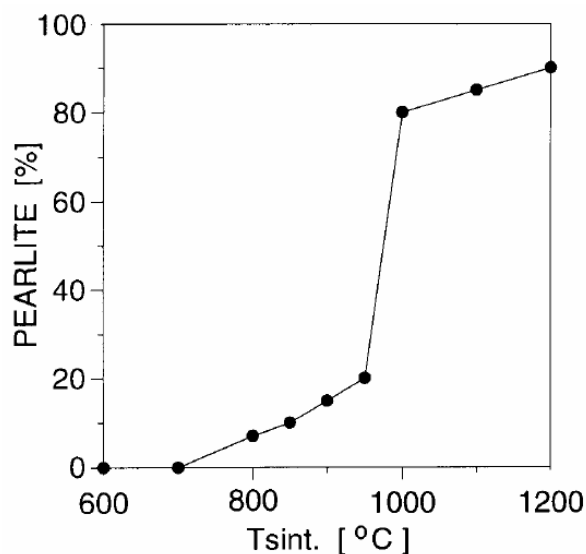


Figure 1.16: Dependence of pearlite content in the microstructure on sintering temperature for ASC100.29-0.8%C compacted at 600 MPa, sintered in N₂ for 1 h [63].

1.5. Alloying elements

Ferrous powder metallurgy has continued to displace competing cast or wrought technologies in automotive applications. This required the development of material systems with higher, more consistent performance than those available previously. However, competing technologies are not static, therefore development of PM steels has to be continued. The nature of the PM process leads to a choice of alloying elements and alloying techniques which deviate considerably from those in wrought steel technology. Alloying additions in order to improve the mechanical properties must be of such a kind and made in such a manner that the dimensional precision is not lost. Some of the most common requirements of the end users are [64]:

- Closer Tolerances
- Higher Tensile Strength
- Higher Yield Strength
- Improved Ductility
- Higher Fatigue Strength
- Lower Cost

These requirements can be met by adding alloying elements through any of the routes shown in Fig.1.3. The alloying elements are dissolved in the base metal, give rise to the formation of various microstructures and increase the material's resistance to deformation. Alloying elements are indispensable with respect to the hardenability of conventional as well as sintered steels. See Fig. 1.17.

Today, the most frequently used alloying elements in sintered alloy steels are Nickel, Copper, Molybdenum, all of which have low affinity for oxygen [3].

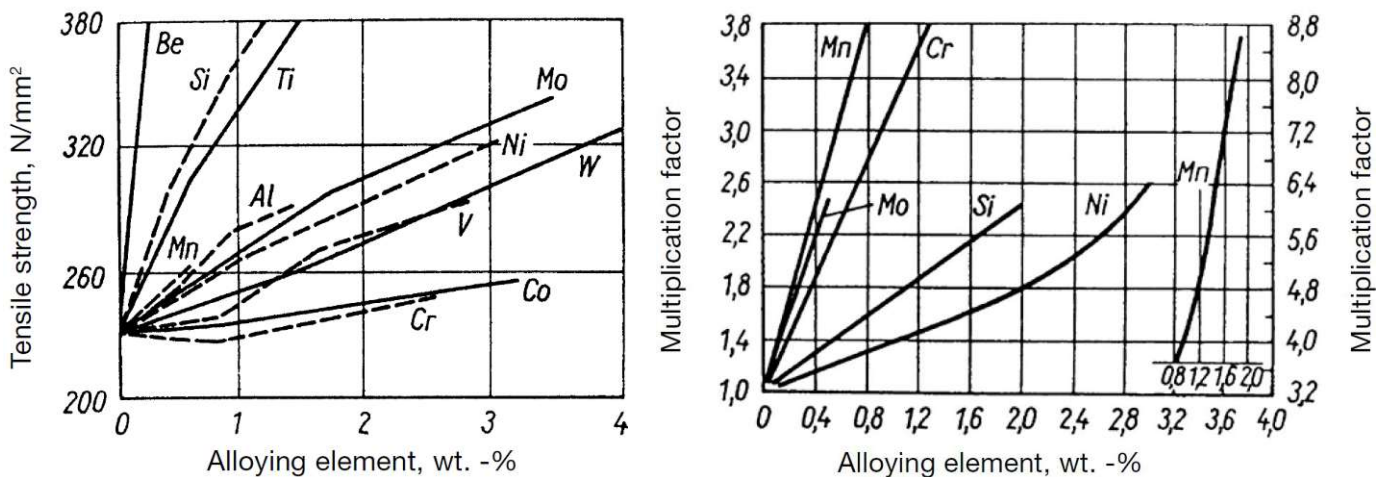


Figure 1.17: Influence of alloying elements upon tensile strength (a) and hardenability (b) [65].

1.5.1. Copper

A common alloying metal in powder metallurgy is Cu, which is not sensitive to oxidation and improves mechanical properties such as hardness and strength [66]. Copper also forms a

transient liquid phase in sintered steels. Upon melting, the Cu particles leave behind small, rounded “**Secondary Pores**” (in the order of the original Cu particle size). As discussed above, these pores could affect the mechanical properties such as the impact energy, therefore very fine alloying powder should be used for obtaining optimum mechanical properties [47]. Copper melts at 1083°C (i.e. below the usual sintering temperature) and rapidly infiltrates the pore system of a powder compact, from where it diffuses relatively easily into the iron particles. “**Copper Swelling**” (or expanding) is the other important phenomenon which happens due to Cu melting and resulting transient liquid phase formation [39, 67]. In this connection Kaysser [40] concluded that careful control of the powders, with respect to particle and grain size, and of the compacting condition can be used to control the different contributions to swelling. Figure 1.18 shows the copper swelling in Fe-Cu-C system for different amounts of Cu.

Results of a research by Wanibe et al [68] showed that up to 10%Cu the expansion increased with higher Cu content, but above 10%Cu, which is above the solubility limit of Cu in iron (9%), with further increasing Cu, persistent liquid phase is formed which supports densification. It was also shown that in the Fe-Cu-C system the graphite reduces the degree of expansion, and this effect is associated with increasing equilibrium dihedral angle [69].

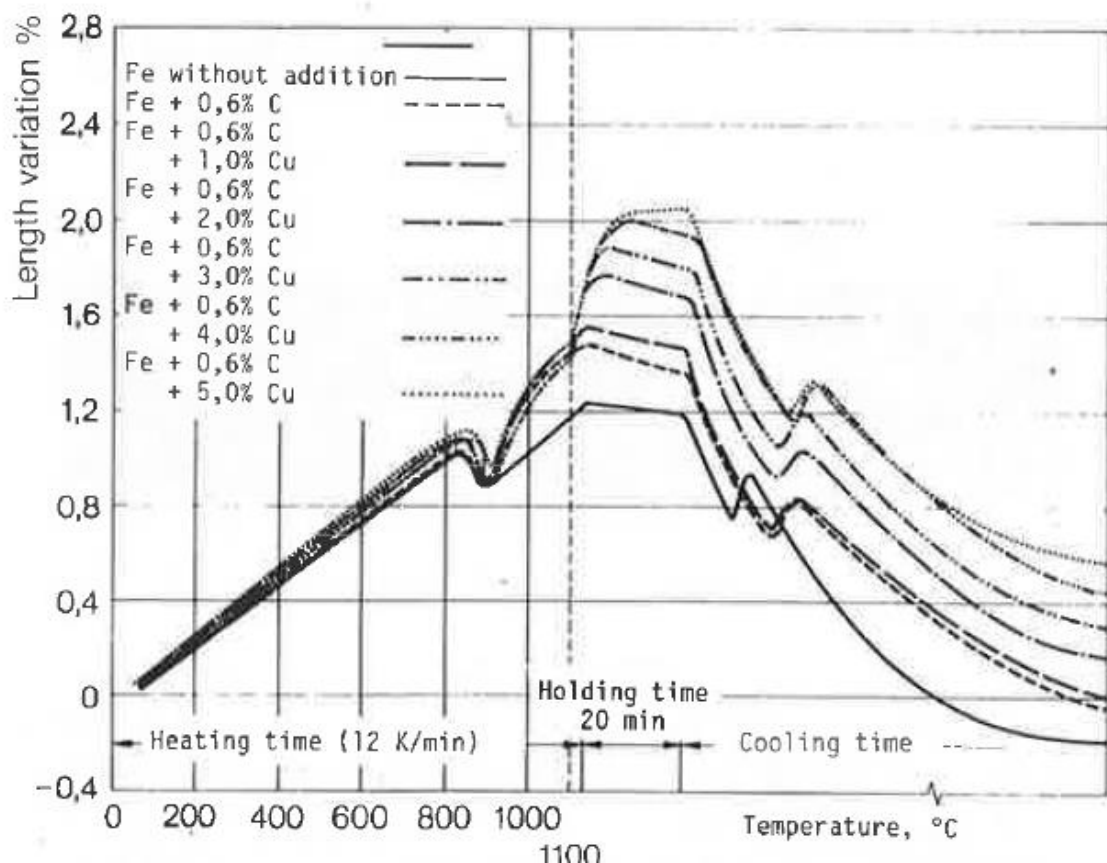


Figure 1.18: Dimensional behaviour of Fe-Cu-0.6 C during sintering in the Dilatometer [41].

1.5.2. Molybdenum

Molybdenum is widely used for alloying in powder metallurgy because of its low affinity for oxygen and solid solution strengthening of iron. Using Mo in PM steels can enhance mechanical properties [45, 70]. Danninger [45] showed that addition of Mo as elemental powder to Fe-C systems leads to formation of transient liquid phase and “copper swelling” above about 1240°C (for 0.7%C, see Figure 1.19). Improvement in Mo distribution and impact behaviour of the material is another result of the formation of transient liquid phase.

Mo stabilises ferrite [71], thus this could promote the sintering in the ferrite range if carbon is absent. Molybdenum is, as Cr, an alloying element that increases the hardenability significantly [72]. Therefore, it is often present in sinter hardening grade steels.

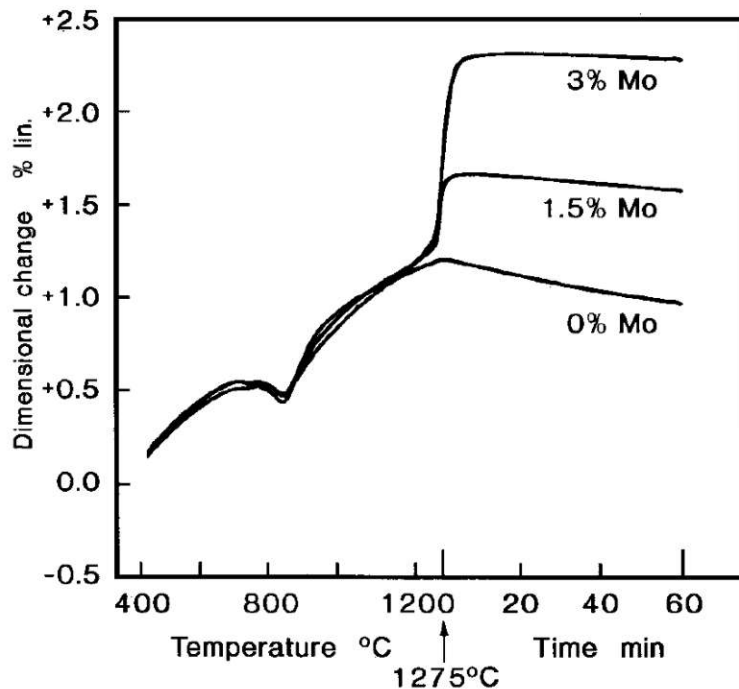


Figure 1.19: Dilatometric graphs for Fe-x%Mo-0.7%C shows swelling above about 1240°C (Mo added elementally) [46].

1.5.3. Nickel

Nickel is an austenite-stabilizing element and one of the few alloying elements that can increase the toughness and the fatigue properties of a material without compromising the hardness [73]. Nickel increases densification and impact energy of PM carbon steels (Figure 1.20) [74]. The microstructures of Ni alloyed PM steels are not homogenized even after high temperature sintering. The inhomogeneous Ni distribution causes large amounts of Ni-rich areas to be present in the microstructures, The reason why the distribution of Ni is inhomogeneous has generally been attributed to the slow diffusion rate of Ni in Fe as compared to that of other main alloying elements, such as C, Cu and Mo [74]. Nickel remains in the solid state during sintering and diffuses only partially into iron, contributing to a heterogeneous microstructure where

nickel is present predominantly at the periphery of the pores [75]. Anyway, there are some big drawbacks when working with Ni. One is the high price, the other one is the health hazard.

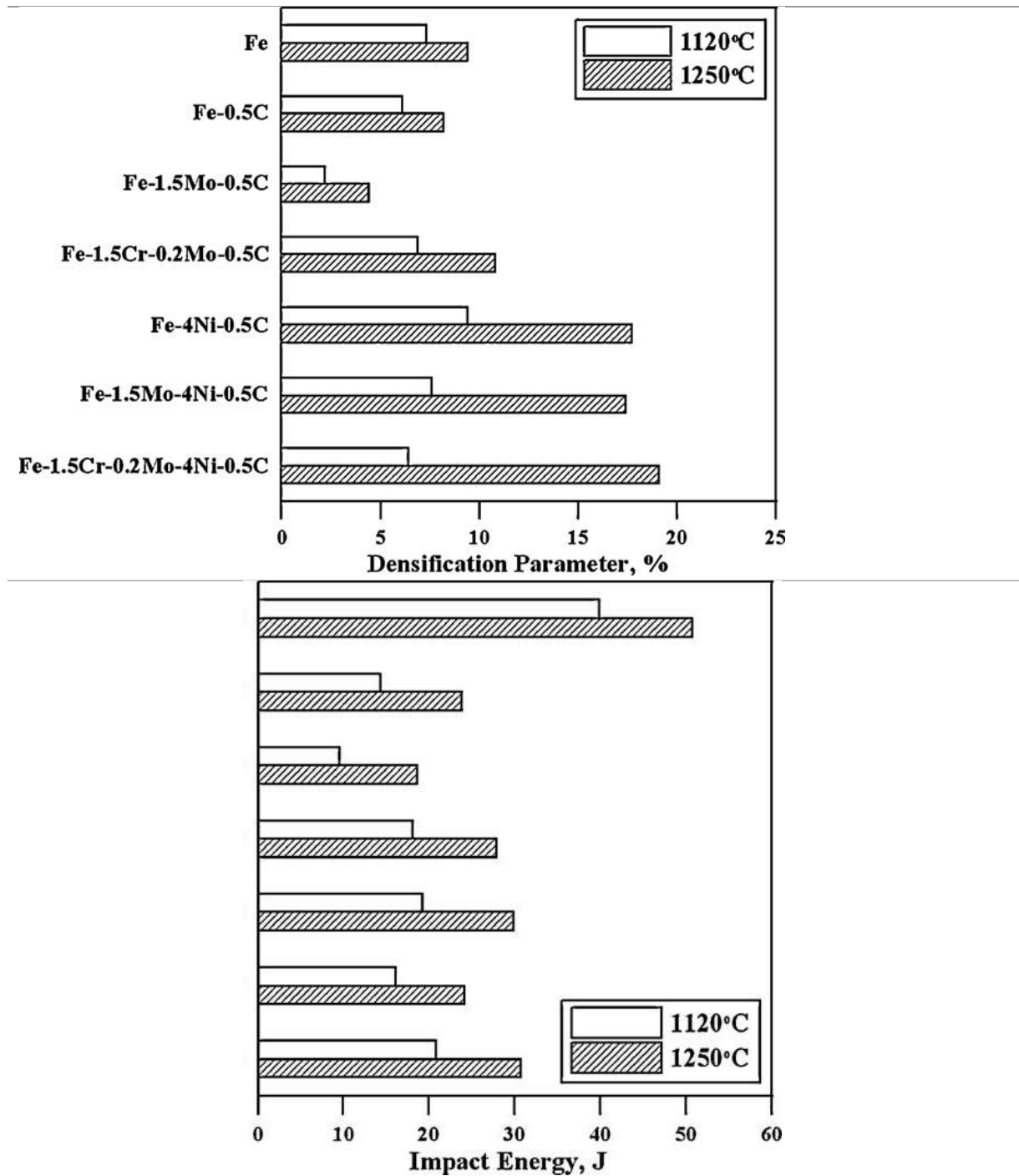


Figure 1.20: Densification and impact energy of different PM steels, compacted at 550 MPa [74].

1.5.4. Chromium

Chromium is a ferrite stabilizing element and a very important alloying element in PM steels. It increases strength, hardness and hardenability and forms hard carbides, which makes it suitable for sinter-hardening applications [76-78]. Chromium, which has a somewhat stronger carbide-

forming tendency than iron, partitions between the ferrite and carbide phases. In steels, these carbides are typically $(\text{Fe,Cr})_7\text{C}_3$ and $(\text{Fe,Cr})_{23}\text{C}_6$ as well as Cr cementite $((\text{Fe,Cr})_3\text{C}$ [79]. It can also increase the toughness of steel and the wear resistance [80]. As shown in Figure 1.4, chromium increases the hardness of the ferrite only slightly, therefore has little effect on compactibility, but its use as an alloying addition in water atomized powders is restricted because of the stable oxides it forms. The advantages of using chromium containing PM steels have been hindered by the necessity to reduce oxides at high sintering temperatures. This element can also retard transformation during tempering of steel [79].

With Cr alloy steels, de-oxidation is shifted to markedly higher temperatures, taking place above 1000 °C [51, 52, 81]. CO formation is observed even at $T > 1250$ °C, indicating the necessity of high temperature sintering to ensure oxygen removal. Numerous studies showed that the full potential of chromium containing steels can be used when sintering at temperatures of ~1250 °C minimum. The reason is the incomplete reduction of Cr oxides at lower sintering temperatures [79, 82-84]. Furthermore, these steels have a particularly high sintering activity at higher temperatures.

1.5.5. Manganese

Manganese is a very attractive and cost-effective alloy element in steels in conventional metallurgy, it is an austenite stabilizer element and enhances strength and hardenability in wrought low alloy steels [85]. A special grade is Hadfield manganese steel which is essentially a high-carbon high-manganese steel where the carbon content is around 1.1–1.4% with 11-14% manganese. The alloy is principally made for high-wear resistance application and its high work hardening ability and good toughness makes it applicable for various applications [86], however this property (high work hardening) of manganese as well as its hardening effect on ferrite (see Fig.1.17) limits the usage of this element in PM prealloyed powder grades. Therefore, in most cases the easiest way to introduce manganese is by admixing elemental powder or ferromanganese [87]. In powder metallurgy, due to some peculiar properties of manganese such as oxygen affinity, high vapour pressure, ferrite strengthening, etc., attempts to develop Mn sintered steels are still ongoing. One of these properties is the manganese vapour pressure, which is much higher than that of other alloying elements (See table 1.1).

Table 1.1: Vapour pressure of manganese and of some alloying elements used in powder metallurgy in dependence on temperature in the temperature range 900– 1300°C [88].

Element	Temperature [°C]				
	900	1000	1100	1200	1300
	Vapour pressure [Pa]				
Mo	$2.03 \cdot 10^{-17}$	$4.07 \cdot 10^{-15}$	$3.73 \cdot 10^{-13}$	$1.85 \cdot 10^{-11}$	$5.66 \cdot 10^{-10}$
Si	$2.25 \cdot 10^{-17}$	$5.40 \cdot 10^{-6}$	$8.13 \cdot 10^{-5}$	$8.44 \cdot 10^{-4}$	$6.49 \cdot 10^{-3}$
Ni	$3.95 \cdot 10^{-6}$	$1.17 \cdot 10^{-15}$	$2.11 \cdot 10^{-4}$	$2.68 \cdot 10^{-3}$	$2.25 \cdot 10^{-2}$
Fe	$2.99 \cdot 10^{-6}$	$6.47 \cdot 10^{-15}$	$8.85 \cdot 10^{-4}$	$8.40 \cdot 10^{-3}$	$5.93 \cdot 10^{-2}$
Cr	$1.08 \cdot 10^{-5}$	$2.36 \cdot 10^{-4}$	$3.26 \cdot 10^{-3}$	$3.13 \cdot 10^{-2}$	$2.24 \cdot 10^{-1}$
Cu	$4.23 \cdot 10^{-4}$	$6.10 \cdot 10^{-3}$	$5.94 \cdot 10^{-2}$	$4.23 \cdot 10^{-1}$	$2.33 \cdot 10^0$
Mn	0.38	3.23	20.0	95.0	367.0

Another property of this alloying element that has to be considered when sintering Mn alloyed steels is the high oxygen affinity, which leads to formation of very stable manganese oxides. However it was shown that sintering of such alloys is possible due to the so-called “self – cleaning” effect [89, 90]. This effect uses the unique property of manganese to sublime at rather low temperature, the Mn vapour shell thus generated around the powder compact protecting the specimens against further oxidation during the heating stage of sintering. Another benefit of admixed manganese is manganese homogenization in Fe-Mn systems through the gas phase (Mn vapour) during the heating stage. It is also shown that formation of transient liquid phase is possible when using high-carbon ferromanganese as Mn carrier at certain circumstances at sintering temperatures [91], however such liquid phase formation was not registered in Fe-Mn-C steel when using high purity electrolytic manganese.

As mentioned above, this element has a much higher vapour pressure than all other metallic alloy elements used in ferrous PM and therefore is homogenized preferentially through Mn evaporation and condensation at the Fe particle surfaces, forming solid solution [92]. This, however, is a one-way process since the vapour pressure of Fe is negligible. The volume of the iron particles is thus increased, and at the sites of the Mn particles pores remain, and the net effect is once more expansion which is shown in Figure 1.21 [42, 81]. The high vapour pressure of manganese results in manganese loss during sintering, primarily at the surfaces where the positive effect of Mn is needed [93]. Results of a study by Danninger showed that introducing Mn through suitable masteralloys (or ferromanganese) results in significantly less Mn evaporation [24].

Another concern regarding using elemental Mn in PM steels is inter-granular decohesion failure which results in material embrittlement. Hryha et al [94] showed that this embrittlement is due to condensation of Mn vapour on the surrounding iron particles and reaction with the iron oxide layers there, which suppresses inter-particles neck development in the areas around the manganese source and results in extended defect areas. He also showed that using a medium carbon ferromanganese powder (80%Mn, 1.5%C) can reduce the brittleness of the specimens.

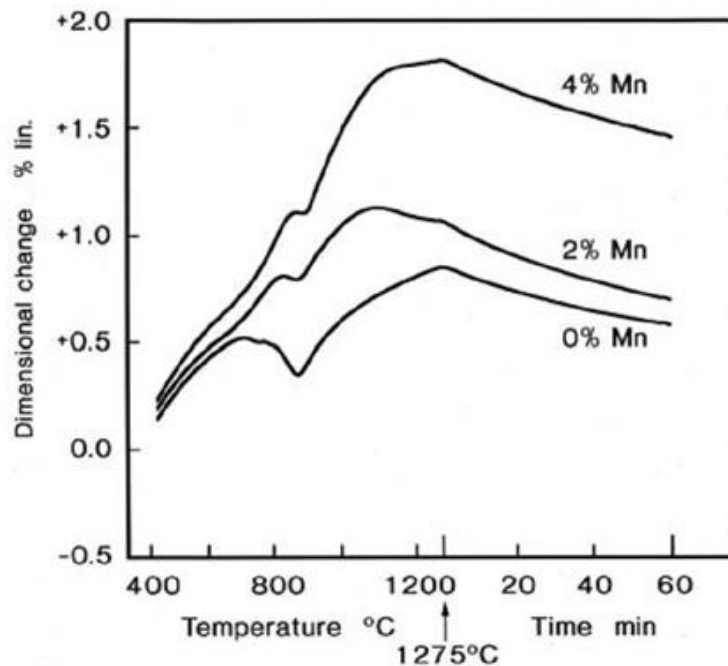


Figure 1.21: Dilatometric graphs for Mn alloyed steels (alloyed with elemental Mn powder) shows expansion during heating stage. $10 \text{ K} \cdot \text{min}^{-1}$, vacuum [81].

1.6. Properties of PM steels

1.6.1. Mechanical properties

Mechanical properties of PM steels can be influenced by different parameters. For example, impact resistance is particularly sensitive to density and microhardness. Results of a study by Stoyanova on Cr and Mo low alloyed sintered steels showed that increasing the density improves the load bearing cross section and also increases all the characteristic parameters of the impact curve, and in particular deflection and impact energy, while the increase in matrix microhardness decreases the impact energy and causes transition from a ductile behaviour to a brittle one [95]. Impact energy is sensitive to interparticle bonding, the increase of this property is mainly influenced by the neck growth, which is enhanced with higher sintering temperatures [58]. Sintering for adequate time is necessary to ensure the formation of the desired microstructure. For example, sintering for 10 min already might result in high hardness, but the mechanical properties would still be insufficient [96]. This can be explained by the better diffusion after longer times. Furthermore, the interparticle bonding is improved, and higher shrinkage and densification are reached. Higher sintering temperature results in more homogeneous microstructure. Furthermore, it results in better impact properties by better interparticle bonding and rounding of the pores (Figure 1.22) [97]. Temperature has a much higher effect on diffusion than time, therefore sintering at higher temperatures is more effective than sintering for longer times. Also for sintering, as for creep, the Larson-Miller parameter $LM = T \cdot (k + \ln t)$ can be used to describe the intensity of the effects.

For carbon steels [98], reduction of surface oxides on the powder particles occurs in a fairly early stage of sintering, and this enables the formation of sintering necks and improvement of the impact energy. Removal of oxygen in Cr-Mo pre-alloyed powder is more critical, as is attaining the mechanical properties compared to carbon steels, and as shown in [58], the superior impact properties of a 3% Cr alloyed steel can only be obtained when combining high density with sufficiently intense sintering, therefore specimens should be appropriately sintered (See Fig. 1.23).

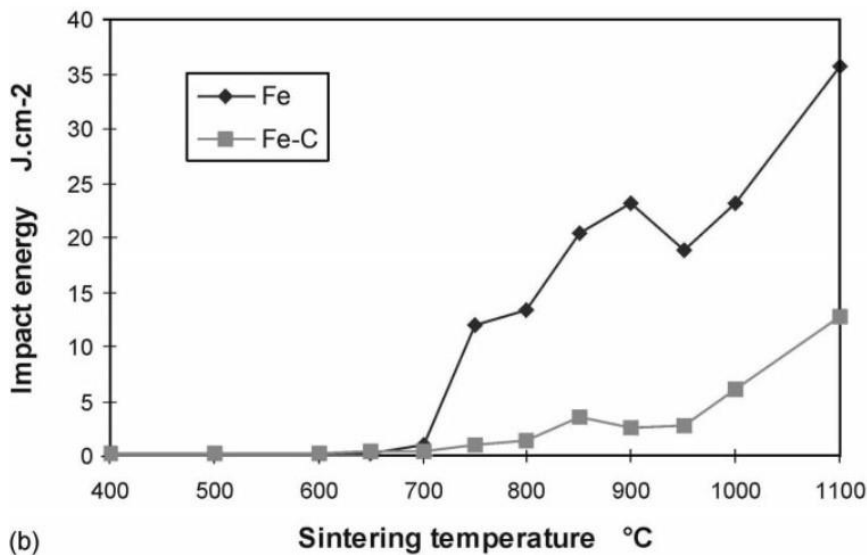


Figure 1.22: Impact energy (room temperature) of Fe and Fe-0.8%C (water atomized powder) sintered for 1 h at different temperatures in H₂ [42].

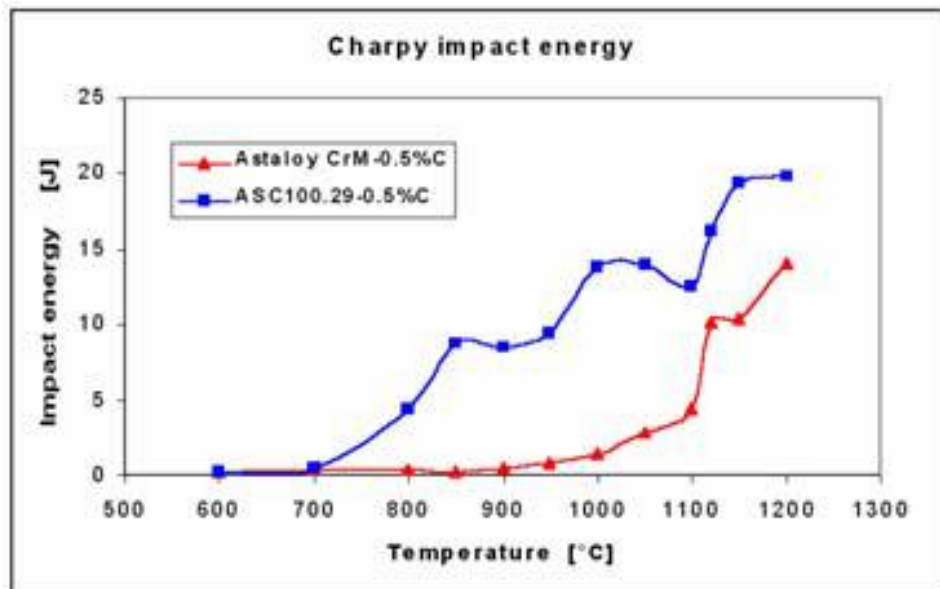


Figure 1.23: Properties of AstaloyCrM-0.5%C and ASC100.29-0.5%C, compacted at 700 MPa and sintered 60 min at varying temperatures in N₂ (99.999%) [58].

1.6.2. Fatigue behaviour of PM steels

Mechanical properties of sintered PM steels have been studied mainly by tensile and impact testing, but the information obtained by these methods is not sufficient for the design of sintered parts which are subjected to cyclic loading. Therefore, knowledge of the fatigue behaviour is necessary in order to enable a safe design [99]. PM steel parts, especially components used in engines or transmissions, are fatigue loaded to high cycle numbers, e.g. a connecting rod can easily exceed 10^8 cycles during service lifetime [100]. The Ultrasonic Fatigue Testing - cyclic stressing of material at a frequency typically in the range of 15 to 25 kHz - could be used for assessing fatigue behaviour of such components in the ultra-high cycle regimes. The major advantage of using ultrasonic fatigue is its ability to provide fatigue limit and near-threshold data within a reasonable length of time (see Figure 1.24).

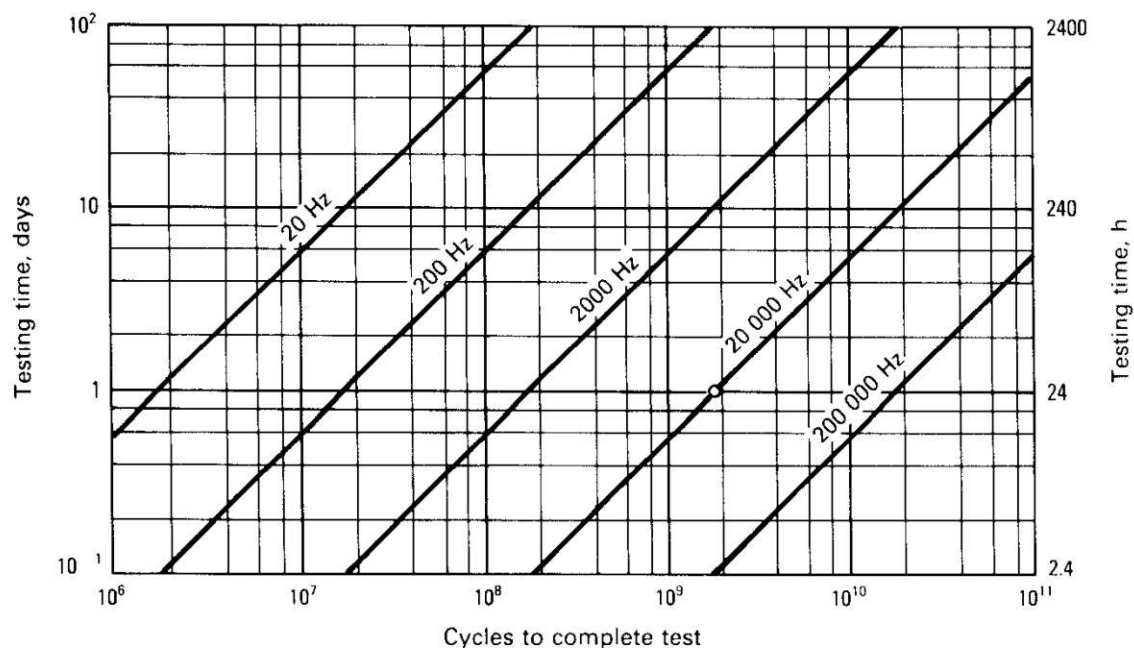


Figure 1.24: Testing time vs number of cycles to complete test as a function of frequency [101].

Influence of porosity

The fatigue behaviour of PM steels is mainly influenced by the porosity, Danninger et al. [25], showed that the dependence of the fatigue strength on total porosity and sintering intensity is comparable to that of the tensile strength and the Young's modulus (Figure 1.25). He also showed that the cyclic properties, fatigue strength and threshold stress intensity, show a generally linear correlation with A_c which is the load bearing section of the material and is obtained by quantitative fractography [102, 103].

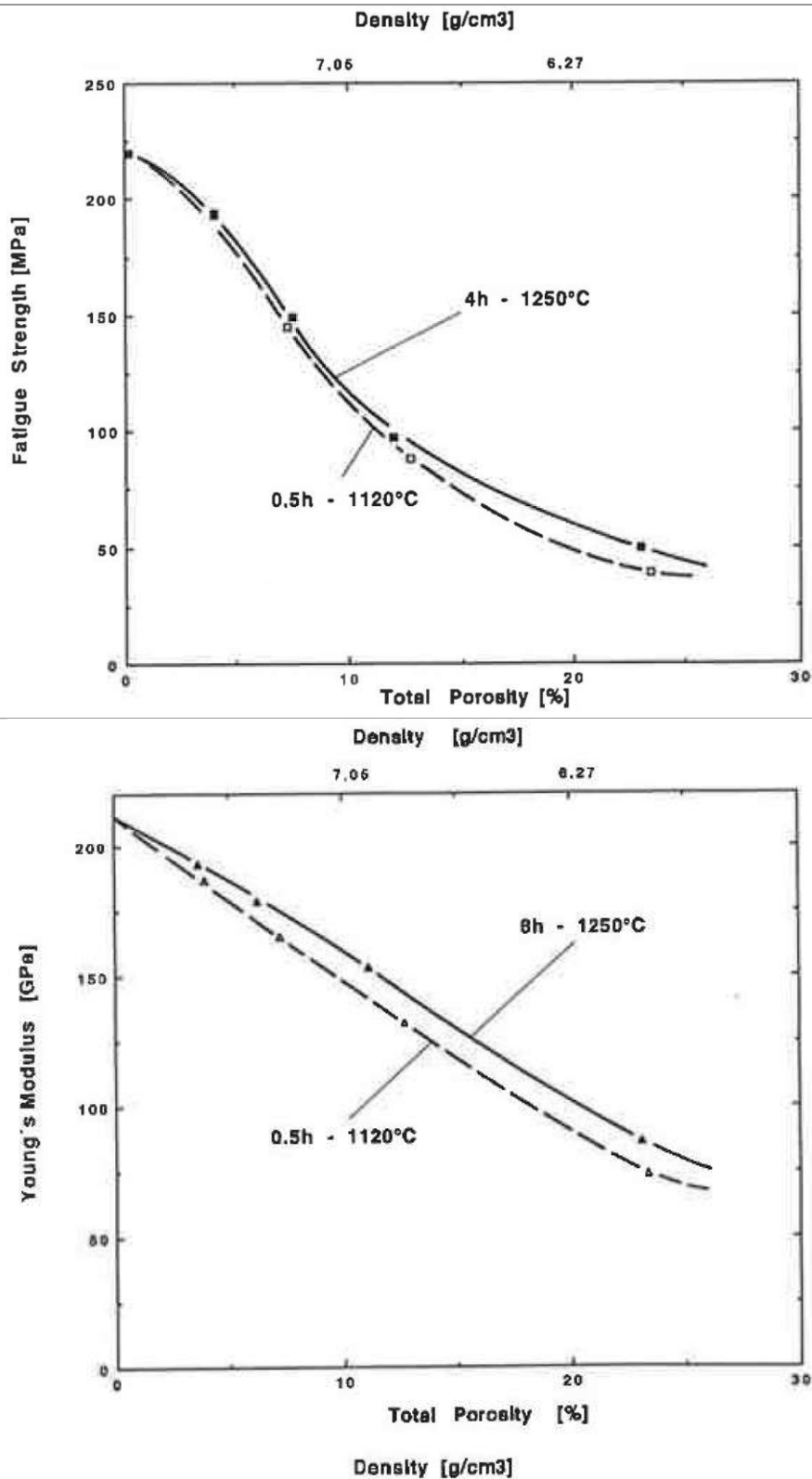


Figure 1.25: Fatigue strength (20 kHz, $N_{\max} = 2 \cdot 10^8$) and Young's modulus of plain iron as a function of total porosity for different sintering treatments

Beside the total amount of porosity, the pore shape could be a matter of interest. Sharp, angular pores are reportedly acting as notches which can affect adversely the fatigue strength [104]. Sintering at higher temperatures results in rounder pores and therefore in much better fatigue properties [105], of course also due to higher load bearing cross section. It is also shown that secondary pores generated in an Fe-3%Cu steel by transient liquid phase affect strongly the fatigue strength of sintered steels, and steels made of larger Cu powder particles showed lower fatigue strength compared to those with finer particles [106].

Influence of the element distribution and homogeneity of the alloying elements

As mentioned above, with sintered steels the inherent porosity lowers the fatigue endurance strength, thus lowering the sensitivity to singular defects and favouring microstructure-controlled failure [107]. It is still an open discussion if chemically heterogeneous steels offer better mechanical, especially fatigue, performance compared to homogeneous (prealloyed) steels with the same composition. Results of a study done by Bergmark [108] showed that fully prealloyed powder grades have better fatigue strength compared to the diffusion alloyed grades. He explained this by the existence of soft Ni rich austenitic areas in the microstructure in diffusion alloyed steels, which make the nucleation of cracks easily possible. However, there are also opposite ideas stating that heterogeneous microstructures of steels from diffusion alloyed powders result in better fatigue strength compared to prealloyed grades due to slower crack growth in materials with Ni rich austenitic phases. For these materials also higher sintering temperature did not improve the fatigue strength, due to a better homogenization and therefore higher amounts of martensitic phases instead of austenitic Ni rich areas [109].

Influence of the other parameters

The influence of the testing frequency was studied by Spoljaric et al. [110], who tested Astaloy 1.5Mo and Distaloy AE, and they could show that the testing frequency does not markedly influence the high cycle fatigue behaviour, at least with these low alloy steels.

In a further work on the fatigue behaviour of porous steels in the ultra-high cycle regime at 20 kHz, it was shown that the fatigue behaviour of Fe-1.5%Mo-0.7%C is better for heat treated material than for as sintered ones [111], which is in good agreement with the results of a study done by Saritaş et al. [112]. Similar results were also obtained by Khorsand et al. [113] after sintering and heat treating of Fe-1.5Mo-3Mn-0.7C. The positive influence of the surface quality on fatigue properties was shown by Spoljaric et al. [114], they also showed that the endurance limit of sintered specimens was improved by 70% by plasma nitriding treatment due to formation of a dense 20 µm thick boundary layer and resulting compressive residual stresses.

1.6.3. Electrical conductivity

Electrical conductivity measurement could be an interesting method for evaluating possible variations in material structure occurring during processing of sintered parts. In comparison to some destructive measurement methods, it is possible to use this method continuously,

precisely, and in a non-destructive manner [115]. The technique may be used to monitor powder surface oxidation, as long as the effect of the oxide on the electrical resistivity has been previously evaluated [116]. Generally the electrical conductivity of PM components increases when the compacting pressure is increased [116, 117]. Many empirical and theoretical models have been proposed to determine the correlation between the total porosity and the properties of PM materials; however these formulae are not very beneficial and are unreliable because of the pore geometry effect [118]. Simchi et al. [61] showed that there is a linear relationship between the effective load bearing area (A_c) and the relative conductivity of Fe-0.8C compacts, and the electrical conductivity could be used for predicting the mechanical strength of sintered materials with homogeneous matrix microstructure [119]. However, it should be noted that besides the A_c , total porosity and the pore morphology, the electrical conductivity is very sensitive to other factors such as grain size, impurities, internal structure of each particle and microstructural heterogeneity. Therefore, even slight changes in the microstructure during processing of metal compacts lead to a resistivity change. This measurement could be very useful for studying the carbon dissolution process during sintering (Figure 1.26), and it also could be used to estimate the thermal conductivity through Wiedemann-Franz's law (Fig. 1.27) [117, 120].

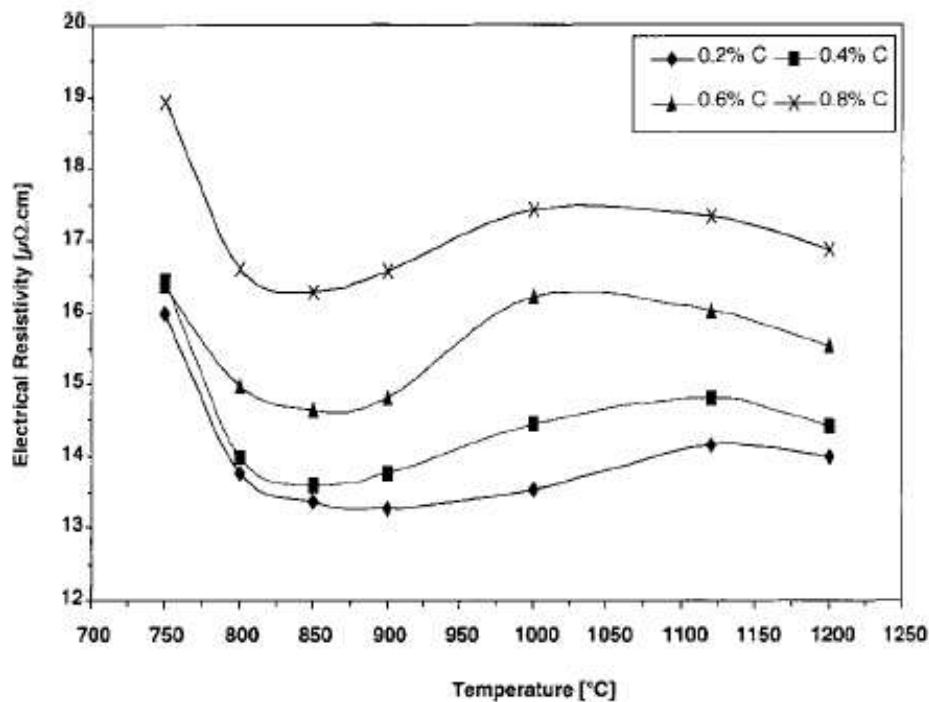


Figure 1.26: Electrical resistivity of Fe-C powder compacts versus sintering temperature for different graphite (UF4) contents added, compacted at 600 MPa and sintered for 60 min in dry nitrogen [115].

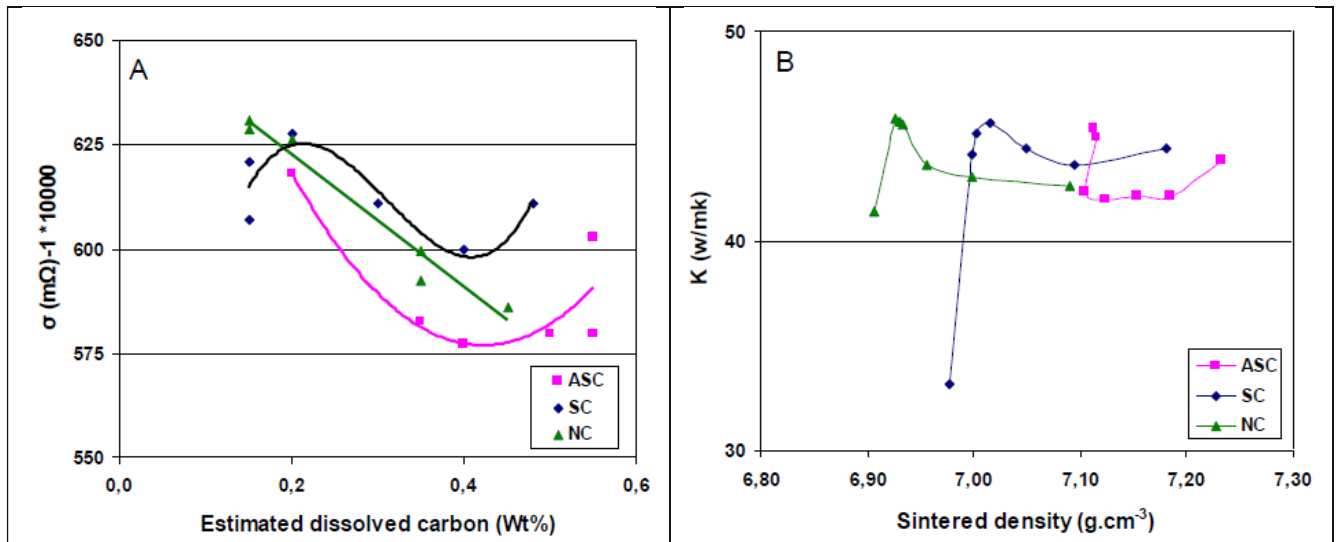


Figure 1.27: A- Electrical conductivity as a function of estimated dissolved carbon, B- Calculated thermal conductivity using Wiedemann Franz's law at room temperature as a function of sintered density, compacted at 600 MPa and sintered 60 min in N_2 [120].

1.6.4. Magnetic properties

Magnetic measurements are fast and frequently non-destructive methods for characterizing ferrous materials, which holds also for PM steels. Microstructural features such as grain size, dislocations and precipitates influence the magnetic and mechanical properties of ferromagnetic materials [121]. In materials such as steel the most important compositional factor is the amount of carbon, which is present principally as Fe_3C precipitates, and its distribution [122]. For instance, results of a study by Rangan [123] showed that the increased grain size and reduced number of Fe_3C precipitates has allowed the domain walls to move further between pinning sites, thereby generating larger changes in the magnetization and reducing the coercivity of carbon steels (Figure 1.28).

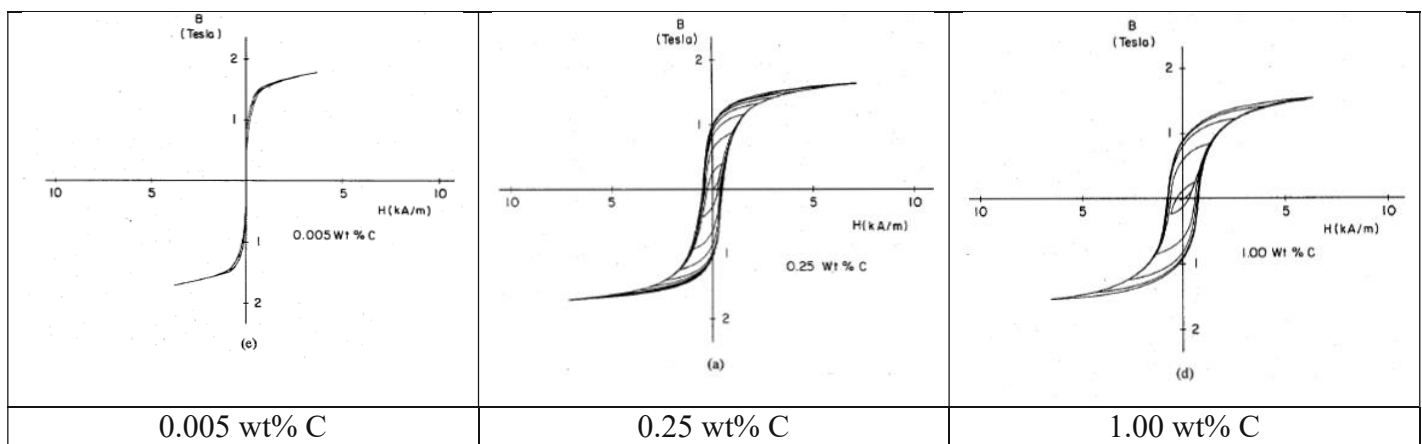


Figure 1.28: magnetization curves for carbon steels with various carbon content [123].

Analysing the influence of various parameters on the coercive force of sintered Fe parts showed that the density is rather insignificant. H_c is influenced mainly by the grain size of the Fe matrix and by pore size and shape, the latter parameters being predominant, for instance the low H_c of irons prepared from coarse powders may be deduced from their larger pores [121, 124]. In PM soft magnetic alloys (Ancorsteel 45P), the soft magnetic properties improve (decrease in H_c) with increasing temperature since grain growth and pore coalescence are enhanced at the higher temperature. It is also shown that secondary operations such as sizing and steam treatment could increase the coercivity of PM soft magnetic materials, however the effect on magnetic saturation of the steel was less pronounced [125]. Another study on the magnetic properties of different grades of PM steels showed that increasing the retained austenite content reduces the coercivity of the material, and prediction of retained austenite in the microstructure based on magnetic properties would be possible when the proper model for calculation was chosen [126].

2. Experimental procedures

2.1. Starting powders

ASC 100.29

ASC100.29 supplied by Höganäs AB, is a water atomized iron powder with very high compactibility, which makes it possible to single press compacts with densities of up to 7.2 g/cm^3 . ASC100.29 is particularly suited for high density structural parts and also as a base material for soft magnetic applications [2]. SEM micrographs of ASC 100.29 are shown in Figure 2.1.

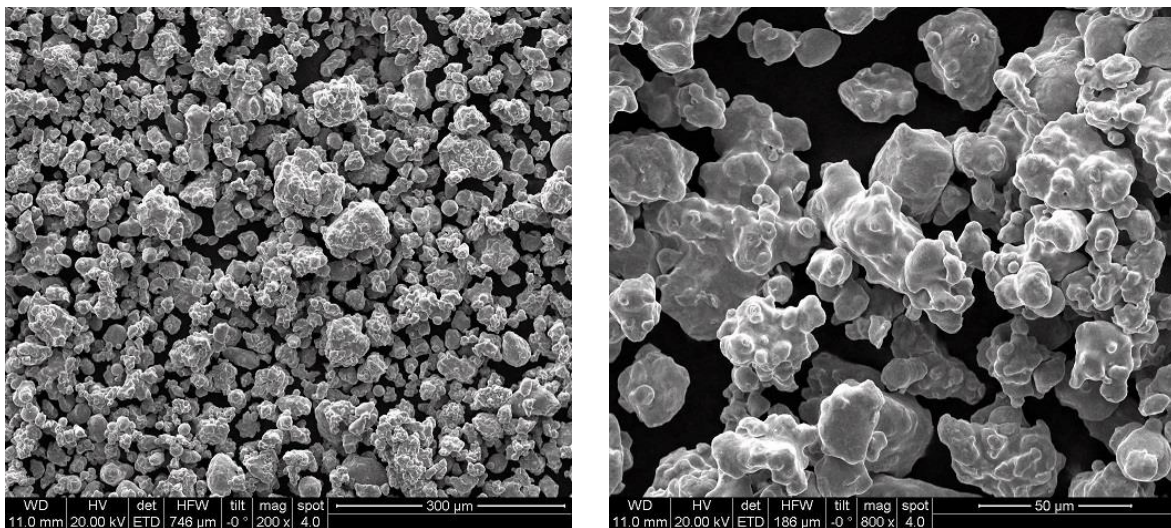


Figure 2.1: SEM micrographs of ASC100.29 at two different magnifications.

Astaloy Mo

Astaloy Mo is a water atomized steel powder pre-alloyed with 1.5% Mo. This grade exhibits high compactibility and a homogeneous microstructure after sintering. This, in combination with its optimal hardenability, makes this powder an excellent choice for parts requiring surface hardening. The result is high surface hardness and good core toughness. Astaloy Mo is often used as-sintered with additions of copper and/or nickel, typically diffusion bonded [2]. SEM micrographs of Astaloy Mo are shown in Figure 2.2.

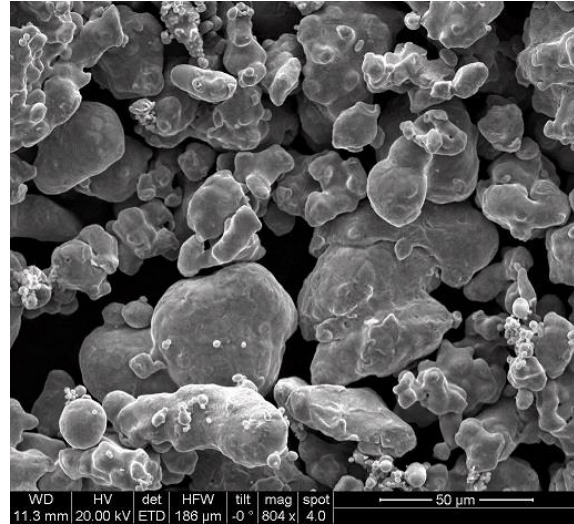
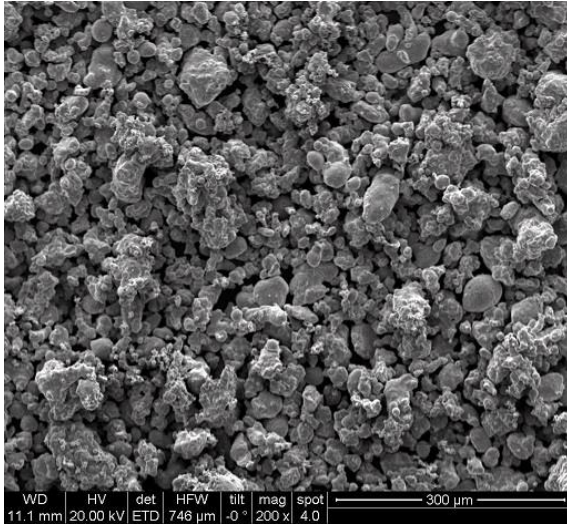


Figure 2.2: SEM micrographs of Astaloy Mo at two different magnifications.

Astaloy CrM

Astaloy CrM is a water atomized iron powder pre-alloyed with 3% Cr and 0.5% Mo, exhibiting excellent hardenability at suitable carbon content. The low oxygen content gives good compactibility. Very high strength and hardness can be achieved after sintering. Astaloy CrM is also suitable for high temperature sintering, sinter hardening and plasma nitriding. The fully pre-alloyed composition results in a homogeneous microstructure with very good properties [2]. SEM micrographs of Astaloy CrM are shown in Figure 2.3.

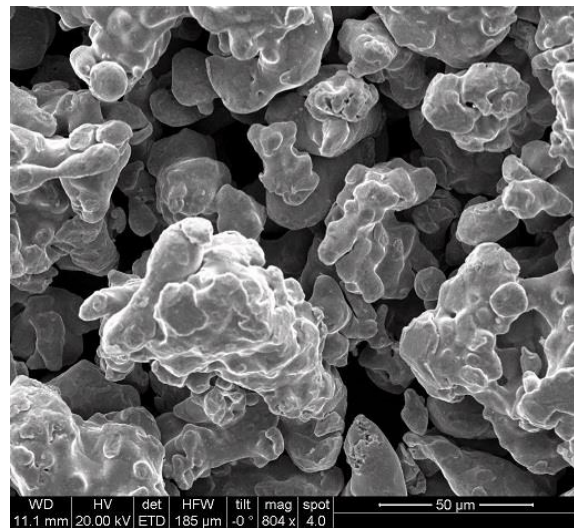
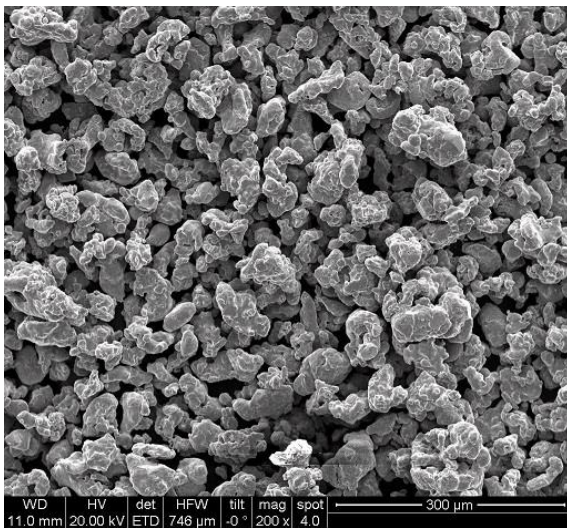


Figure 2.3: SEM micrographs of Astaloy CrM at two different magnifications.

Astaloy CrA

Astaloy CrA is a pure pre-alloyed chromium (1.8% Cr) steel for metal powder component production. In medium to high-strength applications, alloyed only with carbon, it exhibits a fine pearlitic structure, which is robust and offers improved machinability. It is a cost-effective pre-

alloyed Cr grade suitable for sinter hardening with Cu or Ni addition and for nitriding, giving excellent wear resistance [2]. SEM micrographs of Astaloy CrA are shown in Figure 2.4.

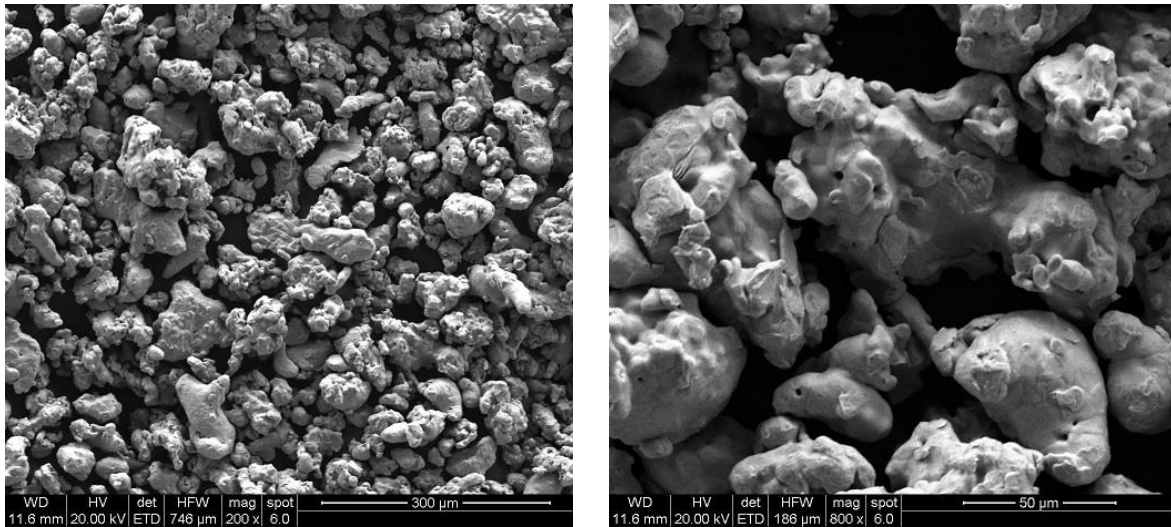


Figure 2.4: SEM micrographs of Astaloy CrA at two different magnifications.

The physical properties and chemical compositions of the base powders used in this research are presented in Table 2.1. Table 2.2 shows the sieve analysis of the base powders.

Table 2.1: Physical properties and chemical composition of the base powders used [2].

Powder	Apparent density (g/cm ³)	Flow (sec/50g)	Compactibility at 600 MPa, lubricated die (g/cm ³)	Chemical composition (wt%)			
				Cr	Mo	O*	C
ASC100.29	2.98	25	7.20	0.09	<0.01
Astaloy Mo	3.00	25	7.10	...	1.5	0.09	<0.01
Astaloy CrM	2.80	27	6.98	3.0	0.5	0.18	<0.01
Astaloy CrA	2.85	26	7.05	1.8	...	0.14	<0.01

* O content obtained by LECO

Table 2.2: Sieve analysis of the base powders (%) [2].

Sieve	ASC100.29	Astaloy Mo	Astaloy CrM	Astaloy CrA
+ 212 µm	0	0	0	0
+ 150 µm	7	12	8	8
- 45 µm	23	20	16	16

Graphite powder

The graphite grade used in this research is Kropfmühl UF4 96/97. SEM micrographs of UF4 natural graphite are shown in Figure 2.5 at two magnifications. The characteristics of the graphite are given in Table 2.3.

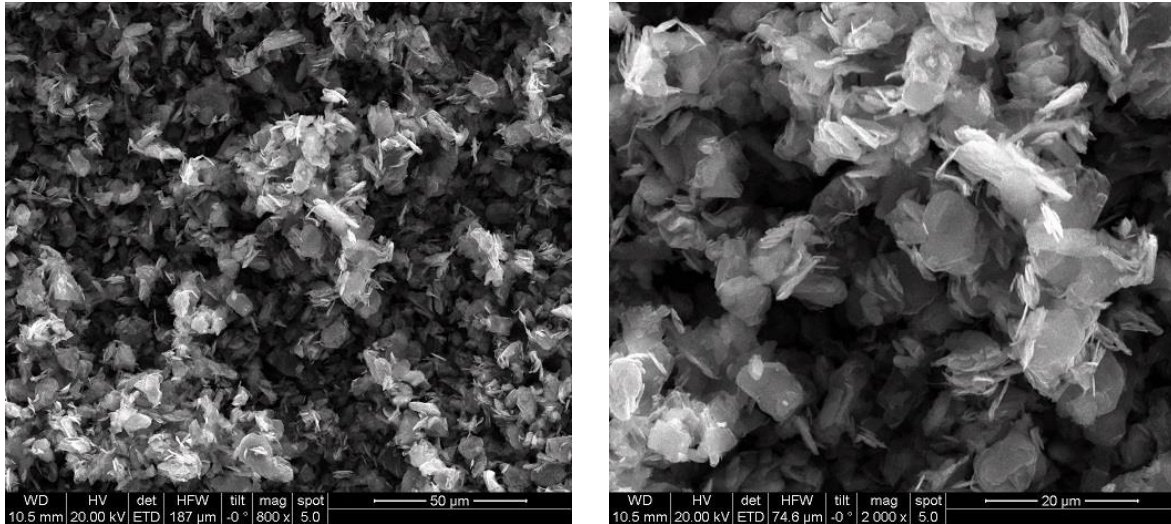


Figure 2.5: SEM micrographs of graphite (UF4) at two different magnifications.

Table 2.3: Characteristics of the graphite grade used in the research.

Graphite type	Ash content (wt%)	Xylene density (g/cm ³)	BET surface (m ² /g)	Al (ppm)	Mg (ppm)	Ca (ppm)	Si (ppm)	Ti (ppm)	K (ppm)	Fe (ppm)	S (ppm)
UF4	3.587	2.271	13.3	4910	577	631	12700	114	496	2410	519

Copper powder

The copper used in this research was of electrolytic type, which was sieved to the dimensional size <25 µm. SEM micrographs of the copper powder are shown in Figure 2.6 at two magnifications.

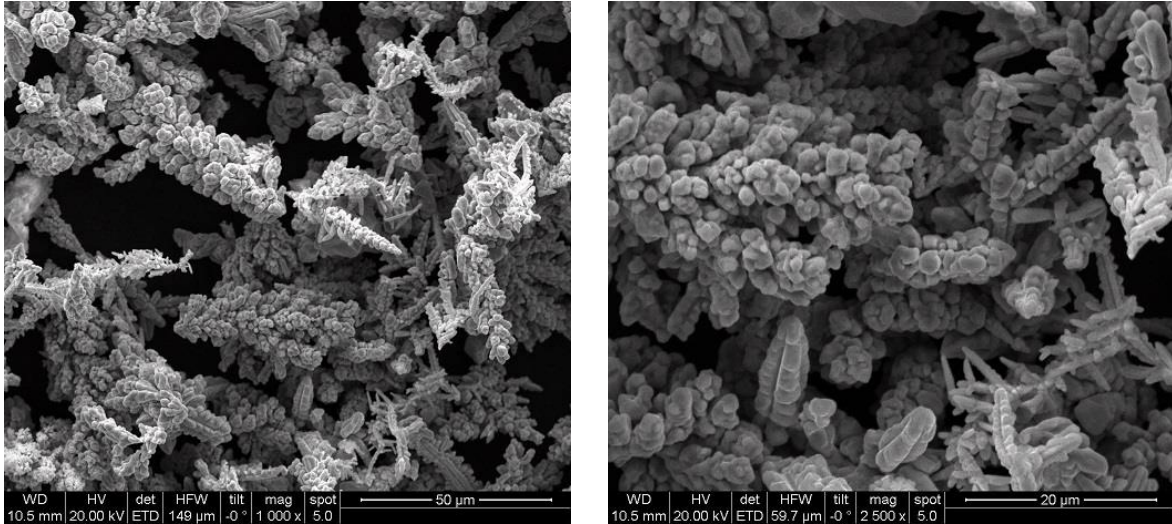


Figure 2.6: SEM micrographs of copper powder at two different magnifications.

Iron-Manganese-Silicon masteralloy powder

The Fe-Mn-Si masteralloy used in this research was H46 produced by Ultra High-Pressure Water Atomization, sieved below 25 µm. The powder was supplied by Atomising Systems Ltd., Sheffield, UK; SEM micrographs of H46 are shown in Figure 2.7 at two magnifications. The chemical composition is given in Table 2.4, and the particle size distribution as well as the melting range of the material in Table 2.5.

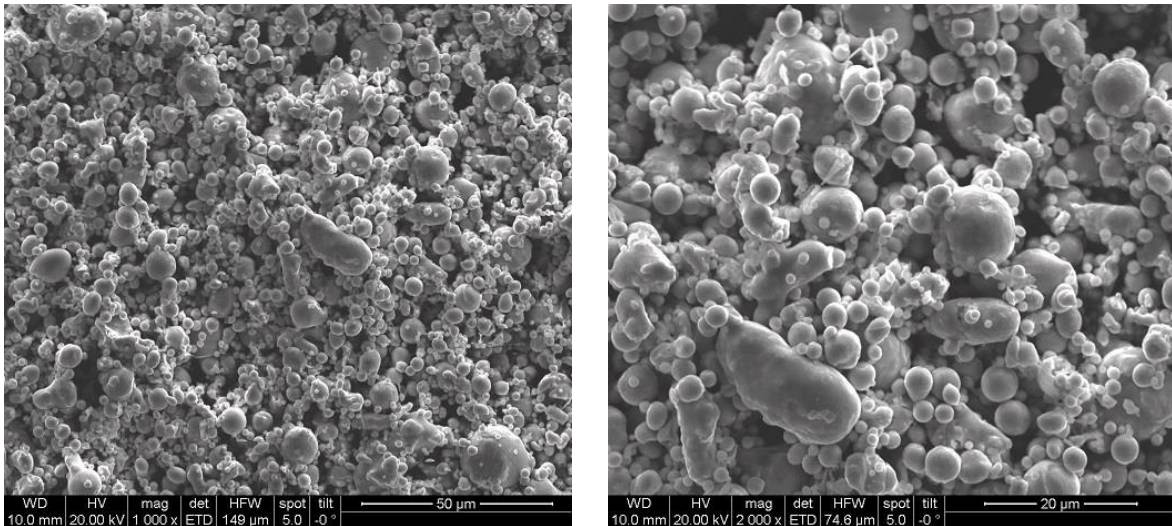


Figure 2.7: SEM micrographs of H46 masteralloy at two different magnifications.

Table 2.4: Chemical composition of the masteralloy used (wt %).

Name	Fe	Mn	Si	Cr	Cu	Ni	C	O
H46	balance	39.9	7.6	0.7	0.2	0.1	0.48	2.18

(Data obtained by XRF, C and O by LECO).

Table 2.5: Particle size and melting range of the masteralloy used [13].

Name	d ₁₀	d ₅₀	d ₉₀	Melting range
H46	2.33	6.7	16.1	1120 – 1200 °C

Iron-Carbon masteralloy powder

The iron-carbon masteralloy used in this research was also manufactured by Atomizing Systems Ltd., UK, through ultra-high pressure water pressure atomization (UHPWA). The experimental grade had particle sizes of about 10 μm, with almost spherical shapes. SEM micrographs of Fe-C masteralloy are shown in Figure 2.8 at two magnifications. Results of the carbon and oxygen measurements of this powder are presented in Table 2.6.

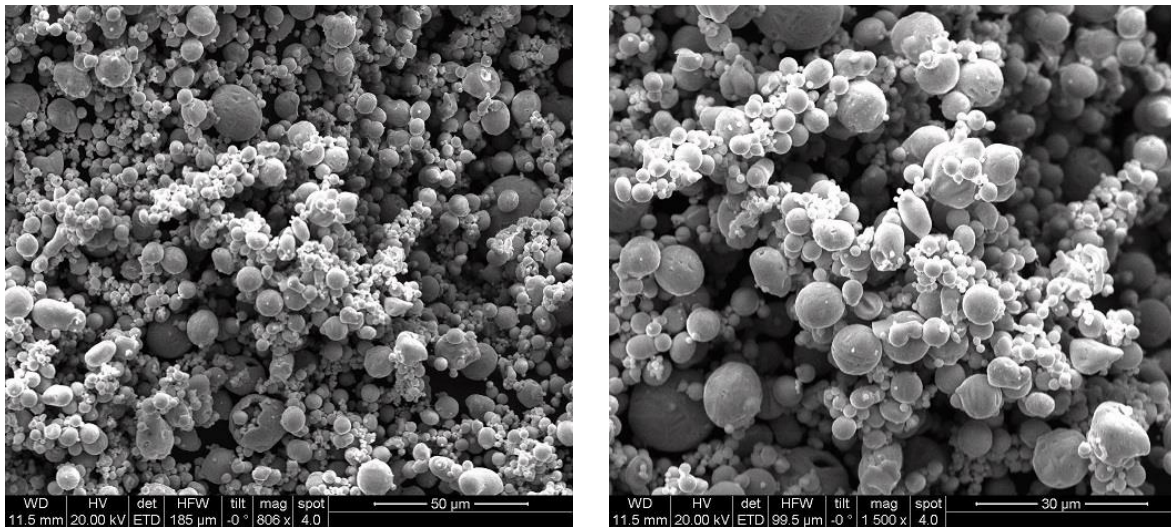


Figure 2.8: SEM micrographs of Fe-C masteralloy at two different magnifications.

Table 2.6: Oxygen and carbon content of Fe-C masteralloy (wt %).

Name	Oxygen	Carbon
Fe-C masteralloy	0.29 ± 0.04	4.54 ± 0.06

(Data obtained by LECO).

Manganese powder

The elemental Mn used in this research was an electrolytic grade supplied by Poudmet, which was sieved to the dimensional size < 25 μm. SEM micrographs of the manganese powder are shown in Figure 2.9 at two magnifications. The chemical composition is given in Table 2.7.

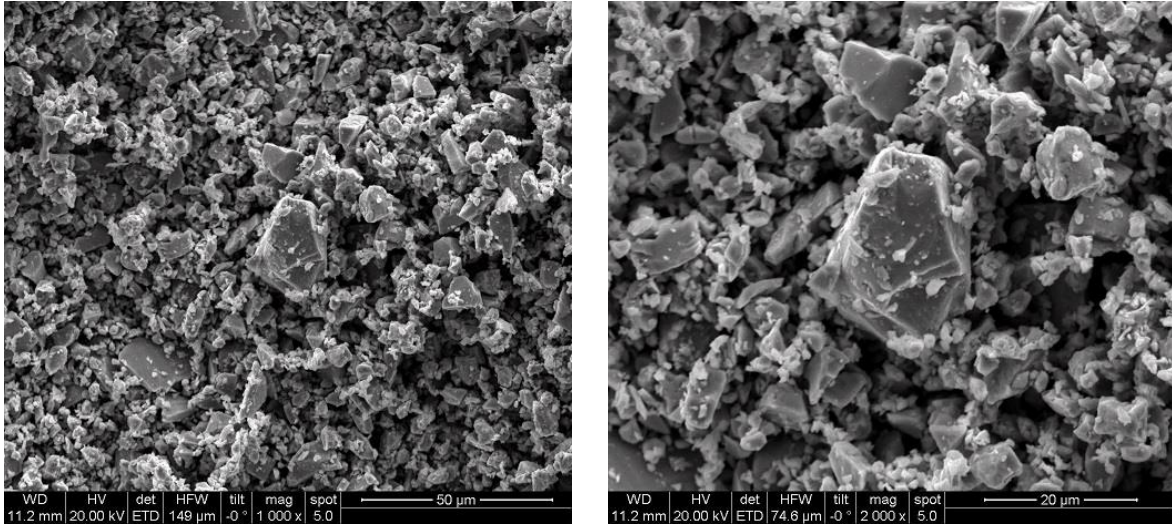


Figure 2.9: SEM micrographs of electrolytic manganese powder at two different magnifications.

Table 2.7: Chemical composition of manganese powder used in this research (wt %).

Name	Mn	Fe	Si	Mo	P	Cu	Ni	C	O
Manganese powder	balance	0.85	0.08	0.01	0.02	0.06	0.13	<0.01	0.74

(Data obtained by XRF, C and O by LECO).

Nickel powder

The elemental nickel powder used in this research was carbonyl grade (Ni 287), which was sieved to the dimensional size < 25 µm. SEM micrographs of the nickel powder are shown in Figure 2.10 at two magnifications. The chemical composition is presented in Table 2.8.

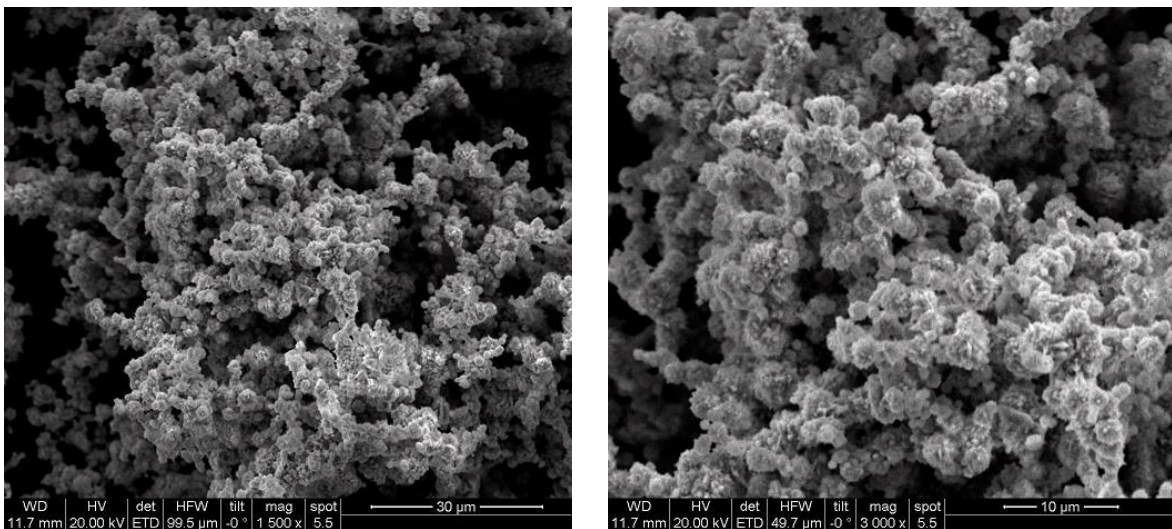


Figure 2.10: SEM micrographs of nickel powder at two different magnifications.

Table 2.8: Chemical composition of nickel powder used in this research (wt.%).

Name	Ni	Fe	Mo	Cu	Mn	C	O
Ni 287	balance	0.12	0.02	0.25	0.1	<0.01	0.21

(Data obtained by XRF, C and O by LECO).

2.2. Specimen preparation

2.2.1. Mixing and compaction

The addition of the graphite and the other additives (elemental powder and masteralloy) to the base powders was done in one step. The powder batches were weighed into polymer vessels and dry blended in a tumbling mixer for 60 min. Charpy impact test bars (ISO 5754, 55 x 10 x approx.. 6 mm) were pressed in a tool with floating die at the desired compaction loads, with die wall lubrication being afforded (using Multical sizing fluid). Figure 2.11 shows a typical specimen compacted for this study.



Figure 2.11: Charpy impact bar prepared for this research

2.2.2. Sintering

Sintering of the samples was performed in an SiC rod heated electrical laboratory furnace equipped with a gas-tight Kanthal APM superalloy muffle at the desired temperatures for 1 hr (dwell time in the high temperature zone, i.e. push-in-push-out) under the desired atmosphere (Figure 2.12). The samples were placed in a boat made of mild steel and were covered with fused alumina granulate. After the isothermal holding period at the desired temperature, the boats with the samples were pushed into a water-jacketed exit zone and cooled under the same protective atmosphere that was used for the sintering.



Figure 2.12: Electrical sintering furnace

2.3. Characterization techniques

2.3.1. Green density

Green densities were calculated from the mass divided by dimensional volume of each sample as shown in Eq. 2-1. The mass was measured using a balance with precision of 0.0001 g, and the dimensions were measured using a calliper with precision of 0.01 mm.

$$\rho(\text{GD}) = \frac{m \cdot 1000}{l \cdot h \cdot w} \quad (\text{Eq. 2-1})$$

ρ (GD): Green density (g/cm^3)

m: Mass of the green part (g)

l: Length of the green part (mm)

h: Height of the green part (mm)

w: Width of the green part (mm)

2.3.2. Sintered density

The sintered density was determined by the water displacement method (Archimedes principle). The mass of the sintered Charpy bars was measured in air and in water. In order to prevent penetration of water into the pores, a water-stop solution was employed to prevent penetration of water into the pores, and then the densities were calculated according to the below equation (Eq. 2-2); the displacement in air being ignored and the density of water taken as $1.00 \text{ g}\cdot\text{cm}^{-3}$:

$$\rho(\text{SD}) = \frac{m_1}{m_1 - m_2} \times d(\text{water}) \quad (\text{Eq. 2-2})$$

ρ (SD): Sintered density (g/cm^3)

m_1 : Mass of sintered sample in air (g)

m_2 : Mass of sintered sample in water (g)

2.3.3. Dimensional change

Sintered dimensional change of the samples was calculated by comparing the length of the compacted and the sintered Charpy bars (these dimensions were measured with precision 0.01 mm using a calliper) and was calculated according to Eq. 2-3.

$$\Delta l = \frac{l_s - l_g}{l_g} \times 100 \quad (\text{Eq. 2-3})$$

Δl : Dimensional change (%)

l_s : Length of sintered part (mm)

l_g : Length of compacted part (mm)

2.3.4. Electrical and magnetic properties

2.3.4.1. Specific electrical conductivity

The electrical conductivity σ is defined as the inverse of the resistivity. The electrical resistivity of the sintered Charpy bars (R) was examined at RT by a 4-point method with the instrument shown in Fig 2.13 via Ohm's law, and then the specific electrical conductivity was calculated by the following Equation:

$$\sigma = \frac{L}{R \cdot A} \quad (\text{Eq. 2-4})$$

Where σ is the specific conductivity of sample in SI unit Siemens per meter [S/m], L is the distance of the pins [m], R is the resistance of the samples [ohms] and A is the cross section of the Charpy bar [m²].

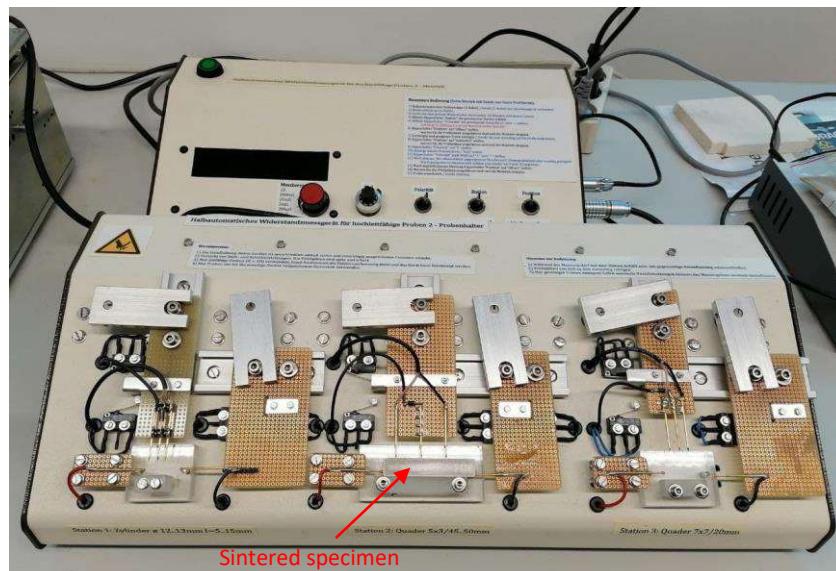


Figure 2.13: The instrument used for measuring the electrical resistivity

2.3.4.2. Coercivity

Coercive field strength (coercivity, coercive force H_c) is determined according to DIN IEC 404-7 and is the (opposite) magnetic field strength which must be applied in order to cause a disappearance of the magnetic flux density, the polarization or the magnetization of a magnetized material (Fig. 2.14). For measurement of the coercive force H_{cJ} of the sintered materials, a 'Foerster-Koerzimat CS 1.096 was used [127], and the measurements were performed on the samples cut to cuboid shape (approx. $10 \times 6 \times 3$ mm) with the magnetizing field of 200 kA/m. For each condition, one sample was measured.

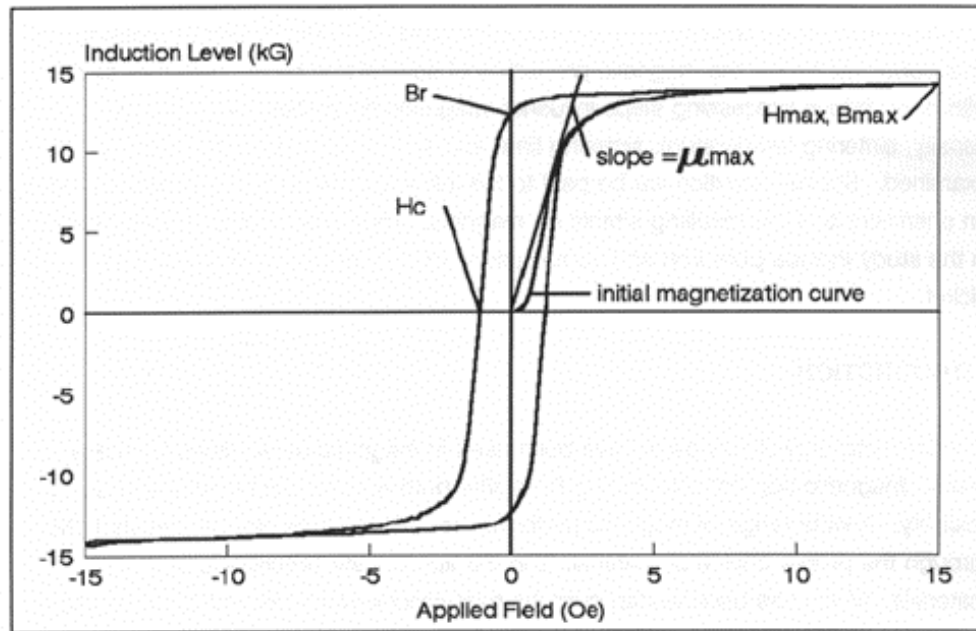


Figure 2.14: Typical Hysteresis Loop [128].

2.3.4.3. Magnetic saturation

The maximum magnetization attainable in a material, achieved when an increase in an external magnetic field does not affect the material's magnetization any more, is called saturation magnetization (M_s). Weight-specific saturation magnetization measurements were performed with a permanent saturation magnet (part of a Foerster-Koerzimat CS 1.096 instrument) by placing the sample in the air gap of the magnet, magnetizing it and then swiftly pulling it out of the air gap ("pull method" according to DIN IEC 60404-14). The magnetic moment during pull-out is measured with a Helmholtz measuring coil and a fluxmeter, from which the weight-specific saturation magnetization is then calculated. The applied external field was 1.10 T (875 kA/m).

2.3.5. Chemical and thermal analysis

2.3.5.1. Carbon analysis

Carbon contents of the powders and the sintered specimens (“combined carbon”) were measured using a LECO CS230 machine. In this method, steel burning is necessary to measure the carbon content. The carbon in the sample is oxidized in plain O₂ to carbon dioxide (CO₂). CO₂ can then be measured by infrared (IR) detectors. Often, combustion of inorganic materials can be enhanced through the use of an accelerator. Therefore, tungsten powder has been used as an accelerator, providing excellent combustion characteristics in this measurement. In an induction furnace, induced electrical currents heat the sample and accelerator; this transfer of power is commonly referred to as coupling with the electric field. Certain metals such as copper and iron, as well as their oxides, will couple in an HF furnace, thereby maintaining sufficient temperature to permit complete oxidation of the carbon and sulfur present in a sample. For these purposes, the samples were cut into small pieces of 0.3–0.6 g, and each value given for the C content is a mean of 4 measurements.

2.3.5.2. Oxygen analysis

Oxygen contents of the specimens were measured after sintering using a LECO TC400 machine. The TC400 is a microprocessor-based, software-controlled instrument that can measure oxygen (and nitrogen) in a wide variety of metals, refractories, and other inorganic materials. The inert gas fusion principle is employed. A weighed sample (0.3 – 0.6 g), placed in a high purity graphite crucible, is fused under a flowing helium gas stream at temperatures sufficient to release oxygen. The oxygen in the sample combines with the carbon from the crucible forming primarily carbon monoxide (CO). In some instances, depending upon sample type and furnace temperature, some oxygen can be released directly as carbon dioxide (CO₂). These oxygen compounds are measured by infrared absorption. Sample gases first enter the IR module and pass through CO and CO₂ detectors. Oxygen present as either CO or CO₂ is detected. Following this, the sample gas is passed through a heated rare earth copper oxide catalyst to convert CO to CO₂. The gases then re-enter the IR module and pass through a separate CO₂ detector for total oxygen measurement. This configuration maximizes performance and accuracy for both low and high range. Each value given in this thesis is a mean of four oxygen measurements.

2.3.5.3. XRF

X-ray fluorescence is a non-destructive method for measuring the elemental composition by irradiating a sample with X-rays and analysing the photons subsequently emitted from the material through fluorescence processes with an X-ray detector. For analysis performed in the course of this thesis, a wavelength-dispersive X-ray fluorescence instrument Panalytical Axios Advanced was used with Rh K_a irradiation. Analysis was performed on the hot embedded section of the samples after fine grinding.

2.3.6. Thermal analysis

2.3.6.1. DTA/TG/MS studies

For DTA/TG/MS investigations, small pieces were cut from the green compacts and crushed to form a granulate of 0.5-1 mm particle size. Approx. 500 mg of the granulates each were filled into small alumina crucibles which were placed into a simultaneous thermal analyser Netzsch STA 449C Jupiter, equipped with capillary coupled mass spectrometer Netzsch Aeolos. The runs were performed by heating at 20 K/min up to 1300°C, soaking for 15 min, and then cooling down at -20 K/min. DTA and thermo-balance signals were continuously recorded, as were the signals of various mass numbers on the mass spectrometer. The respective signals of an empty run were subtracted in order to eliminate the influence of the apparatus characteristics. As atmospheres, gases of high purity were used, Ar (99.999%) with flow rates of 20 ml/min as protective gas (only running through the balance) and 50 ml/min as working atmosphere. The masses recorded by mass spectrometry were as follows: m12 (black thin line), m16 (light blue), m18 (dark blue), m28 (red) and m44 (pink).

2.3.6.2. Dilatometric studies

In this research, dilatometric runs have been conducted in a horizontal pushrod dilatometer Netzsch STA 402C equipped with alumina measuring system and linked to a capillary coupled mass spectrometer Netzsch Aeolos, to analyze the gaseous reaction products formed during sintering [129]. The runs were performed by heating at 10 K/min up to 1300°C, 60 min isothermal hold, and then cooling down at -10 K/min. The test runs were done in high purity Ar or H₂ (grade 5.0 = 99.999% purity). The measurements were performed on 10 mm long specimens cut from Charpy bars, the dimensional change being measured perpendicular to the pressing direction (i.e. between die surfaces). The masses recorded by mass spectrometry were as follows: 12 (black thin line), 16 (light blue), 18 (dark blue), 28 (red), 44 (pink).

2.3.6.3. Quenching dilatometry (CCT diagram)

For plotting the CCT diagrams, a quenching dilatometer (Linseis L78Q) was used. Pieces 10.4 × 4 × 4 (mm) were cut from the sintered Charpy specimens. 13 measurements were successively carried out with the same sample in N₂ atmosphere. The specimen was inductively heated from RT to 1100 °C with the heating rate of 11 K/s, held for 300 s and then quenched at the following cooling rates: 45; 22.5; 15; 11.25; 9; 6.4; 5; 4.5; 3; 1.5; 1; 0.75 and 0.5 K/s. In the 14th run the sample was finally quenched once more at 3 K/s for metallographic examination.

2.3.7. Mechanical properties

2.3.7.1. Dynamic Young's modulus and damping

Since determining the static Young's modulus from tensile tests is a destructive and potentially imprecise method, fast and non-destructive measurements of the dynamic Young's modulus were performed using the impulse excitation technique with a resonance frequency detection system (RFDA Professional, IMCE). A sample with a well-defined geometry (e.g. rectangular bars or cylindrical rods) is excited by mechanical impact. Sound waves resulting from the

vibration of the sample after impact are recorded by a microphone and electronically processed to obtain the fundamental flexural resonance frequency f_f . For rectangular bars with known mass and dimensions, Young's modulus can then be calculated according to ASTM E1876 from Eq 2-5 [130]:

$$E = 0.9465 \left(\frac{m \cdot f_f^2}{b} \right) \cdot \left(\frac{L}{t} \right)^3 \cdot T \quad (\text{Eq 2-5})$$

E = Young's modulus, Pa,

m = Mass of the bar, g

b = Width of the bar, mm

L = Length of the bar, mm

t = Thickness of the bar, mm

f_f = Fundamental flexural resonant frequency of bar, Hz

T = correction factor for fundamental flexural mode to account for finite thickness of bar, Poisson's ratio, etc.

For the Young's modulus measurements performed in this thesis, one sintered Charpy bar was measured for each condition.

2.3.7.2. Specific Damping (Q^{-1})

Damping capacity is a measure of a material's ability to dissipate elastic strain energy during mechanical vibration or wave propagation. When a vibration is induced by a small mechanical impulse, the energy is dissipated by the material into a vibration with a resonant frequency. Each frequency will damp according to the energy absorption of the material [131] (Figure 2.15).

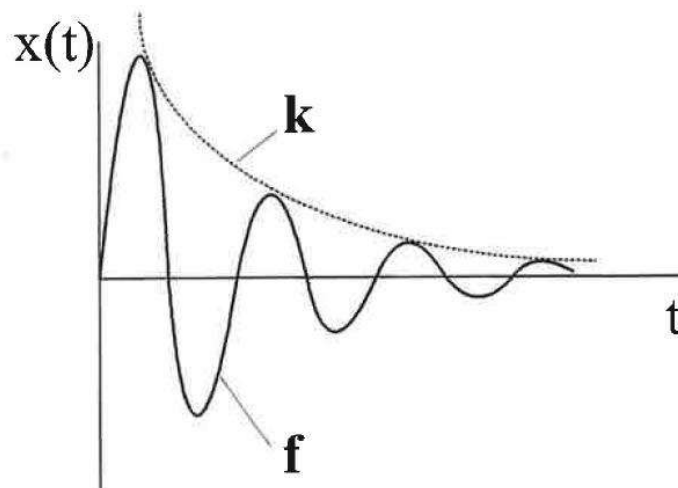


Figure 2.15: Sinusoidal damped vibration [132].

$$x(t) = A e^{-kt} \sin(\omega t + \phi) \quad (\text{Eq 2-6})$$

For each ω the corresponding frequency is calculated as:

$$f = \omega / 2\pi \quad (\text{Eq 2-7})$$

The specific damping of the material which is the ratio of the dissipated energy defined as:

$$Q^{-1} = \Delta W / 2\pi W \quad (\text{Eq 2-8})$$

The mechanical loss is reflected in the measured vibration of the specimen and can be seen as the relative decrease of the signal

$$Q^{-1} = \frac{1}{\pi} \ln \left(\frac{x_1}{x_2} \right) = \delta / \pi \quad (\text{Eq 2-9})$$

Where,

x_1/x_2 = ratio of the amplitude of the signal in one period T

δ = the logarithmic decrement

From Eq 2-8 and Eq 2-6 equation Eq 2-10 can be derived:

$$Q^{-1} = \frac{kT}{\pi} = k / \pi f \quad (\text{Eq 2-10})$$

In this research in order to measure the damping parameter of the specimens the Resonant Frequency and Damping Analyser (RFDA Professional, IMCE), which is a non-destructive testing device, was used to determine the resonant frequencies of the materials by measuring the decay of the amplitude. A vibration is induced by a small mechanical impulse. The energy is dissipated by the material into a vibration. The vibration is detected by a transducer of the device. After computerizing the data, the capacity of damping k (dependent on the dimensions of the specimen) and the corresponding frequency f is calculated, then the specific damping, which is a material property, can be calculated from Eq 2-10

2.3.7.3. Hardness test

Hardness tests were conducted on a hardness tester EMCO M4U-025 with Vickers indenter and 30 kg load, i.e. HV30. The hardness measurements were carried out on cut and polished samples on the cross section; each value is a mean of at least 3 hardness measurements.

2.3.7.4. Charpy impact test

The Charpy impact energy was determined on un-notched specimens using a Charpy impact Tester Wolpert PW5 with 50 J initial energy at room temperature. The impact energy is calculated according to the following equation (Eq. 2-11):

$$\alpha_k = \frac{A_v}{w.h} \times 100 \quad (\text{Eq. 2-11})$$

α_k : impact energy (J/cm²)

A_v : impact work (J)

w : width of the sample (mm)

h : height of the sample (mm)

2.3.8. Metallographic investigations

Small pieces of the Charpy bars were cut with a water cooled SiC disc at low cutting speed, to avoid thermal effects, and then the samples were hot embedded to investigate the cut surface. In order to avoid any change in the microstructure during curing process, only the sinter hardened specimens in Chapter 4, were cold embedded. Grinding was done with a Struers Piano grinding disk (1 min), the polishing with an Allegro polishing disk with 9 μm (3 min), a Dac polishing disk with 3 μm diamond suspension (9 min) and a 1 μm DP-suspension on a softer cloth (3 min) were done, respectively. For examination of the microstructures before and after etching, an optical microscope (Olympus GX51) was used. The samples were etched with Nital (3%) at RT to achieve suitable microstructure.

2.3.9. Fractography

For the fractographic investigations, the fracture surfaces were cut off using a water cooled SiC disc, the cut-off pieces being ultrasonically cleaned in isopropanol. The investigation of the fractured surfaces was performed with a FEI Quanta 200 electron microscope in secondary electron mode with an acceleration voltage of 20 kHz.

2.3.10. Fatigue test

For the high cycle fatigue testing, sintered rectangular bars with dimension of 90*12*12 were prepared. The steel powders were compacted uniaxially in a tool with floating lubricated die at 700 MPa and then sintered at 1250°C in N₂-10% H₂ for 60 min. Then they were cooled in the water-jacketed exit zone. Before shaping (turning) the samples were soft annealed at 650°C for 1 hr in N₂. From these bars, dumbbell-shaped specimens were machined (Figure 2-16). The length of the fatigue test specimen, which is extremely crucial to ensure proper vibration (see below) was calculated according to Eq. 2-12. This was possible after measuring the dynamic Young's modulus.

$$L = \frac{1}{2f} \cdot \sqrt{\frac{E}{\rho}} \quad (\text{Eq. 2-12})$$

L: specimen length [m]

f : measured frequency [Hz]

E: dynamic Young's Modulus [Pa]

ρ: sintered density [kg/m³]

It is well known that the quality of the surface affects the fatigue properties of the PM steel [114], therefore after turning, in order to obtain proper surface finish and to remove any surface scratches, the samples were ground up to 2400 mesh grinding paper, then, in order to simulate a sinter hardening process, the samples were again heated to 1000°C in N₂ and held for 30 min, then they were fast cooled with pressurized nitrogen at a cooling rate of 3 K/ sec (linearized)[133]. Heat treatment of samples was completed by tempering at 150°C for 1 hr.

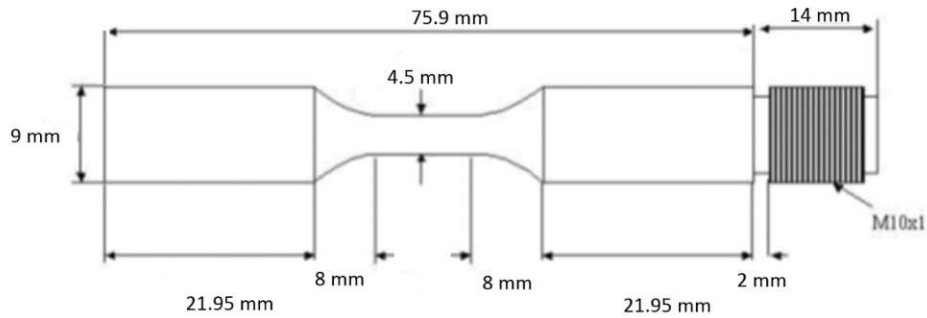


Figure 2-16: Final geometry (machined) of the fatigue test samples for Astaloy CrA + 0.6%C + 3%Ni sinter hardened at 1250 °C

The fatigue tests were performed in fully reversed ($R = -1$) push-pull mode at ~ 20 kHz in continuous mode (no interrupts for cooling). The testing system consists of an ultrasonic generator with a control unit, followed by a transducer. The transducer is connected to an acoustic horn and a coupling piece. On the coupling piece the sample was fixed. A strain gauge was fixed on the coupling piece controlling the actual strains. A circulating cooling system (3 % solution of inhibitor Multrol PWZ 200 (Aral) in water) was used for keeping the specimen and the coupling piece at room temperature and inhibiting corrosion at the same time (Figure 2-17), otherwise, at this high frequency damping effects would result in rapid heating of the specimens, with resulting uncontrollable change of the mechanical properties (other ultrasonic test systems operate with sequences of 100 ms loading and 900 ms break for air cooling [134, 135], but the effect of the interrupts on the results are still unknown; furthermore, the tests take 10x the time of the continuous run for the same loading cycle number).

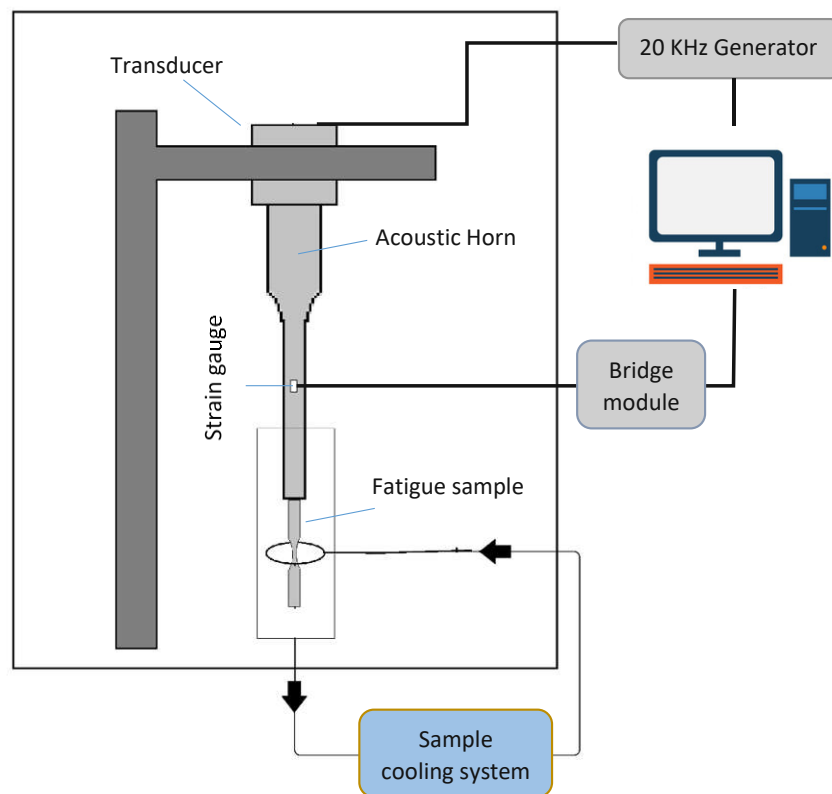


Figure 2-17: Equipment for the ultrasonic fatigue testing

In this method, acoustic vibration is developed in the converter by application of the electrical excitation provided by the power supply. The converter generates a standing acoustic wave that produces a cyclic displacement at the end of the converter. The acoustic wave proceeds down the rest of the resonant wave train to the specimen. Variation of the displacement and strain amplitude along the wave train is shown in Figure 2-18. By properly adjusting the length of the specimen, the standing acoustic wave is established, with displacement maximum at the end of the specimen, and displacement node (= strain maximum) in the gauge section.

In this type of gigacycle fatigue test, the load or displacement cannot be recorded directly on the specimen during testing (the water cooling jacket is an obstacle here). The tester thus has to be calibrated for each material. For this purpose one strain gauge was fixed on the sample and one on the acoustic horn.

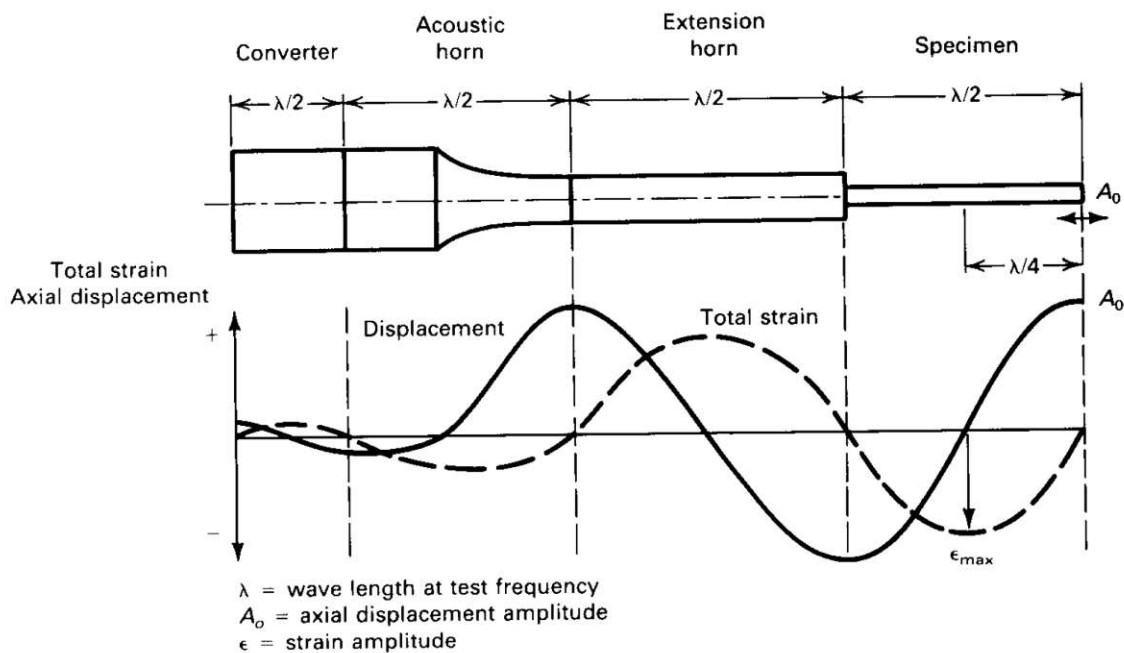


Figure 2-18: Variation of the displacement and strain amplitude along the acoustic wave train [101].

The resulting strain values in correlation with the applied excitation amplitude were recorded. During the real fatigue tests, the signals from the strain gage at the acoustic horn were continuously recorded, and the actual strain value of the sample could be calculated. Under the assumption of elastic behaviour, the stress amplitude of the specimens is calculated according to:

$$\frac{\Delta\epsilon}{2} = \frac{\Delta\sigma}{2} \cdot E \quad (\text{Eq. 2-13})$$

The dynamic Young's moduli (E) were measured on specimens with 90*12*12 mm as described in 2.3.7.1. For fractography, the fatigue fracture surfaces were investigated with a Stereomicroscope (Zeiss Discovery.V20) and SEM (Quanta 200).

3. Results and discussion Part 1: Sintering of ferrous powder compacts: Processes in the early stages of sintering

3.1. Part 1a: Effect of density on mechanical and physical properties of carbon and Mo alloyed steels

It is well known that the physical properties of PM parts are closely related to the microstructure, the alloying elements and the density [136]. For instance, the relationship between microstructure and electrical conductivity is shown very well in Simchi's work [118]. Measuring these properties is important because they can replace destructive methods for prediction of mechanical properties of such parts, at least for such with homogeneous microstructure. In recent years, demand for production of PM steel parts with improved mechanical properties has increased because of cost efficiency and dimensional accuracy of this technique of metal part manufacturing. In this connection, several methods for improving the properties of sintered materials are being investigated. The majority of these studies include developing alloying system or modification of the manufacturing process. Molybdenum is one of these alloying elements that showed significant effects on hardenability and strength of ferrous PM parts [46]. Carbon is another element that has a major usage in steel technology in general [137], and in the manufacturing of sintered steels parts, in particular those with higher strength, it plays the main role and is the most effective alloying element. For technological and economic reasons, addition of this element is usually done through admixing fine graphite. Therefore, knowledge of the mechanism of carbon dissolution in the iron matrix during sintering could be necessary for quality assurance. Despite the importance of the topic the mechanism has not been definitely clarified so far. As mentioned in Chapter 1.4.2.2, two different mechanisms, solid state diffusion and gas phase transport [56, 57] have been claimed to be the relevant process. The first mechanism assumes that carbon diffuses into the iron matrix directly at the point of contact during sintering, while according to the gasification theory, carbon reacts with oxide surfaces of the iron powder, forming CO. Then, carbon is formed at the iron surface from the resulting gas by adsorption and decomposition steps, e.g. through the Boudouard reaction. Therefore, studying the mechanism of carbon dissolution and the influence of manufacturing conditions can be still interesting.

In this part of work, the influence of two manufacturing parameters, the sintering temperature and the compacting pressure, on the microstructural changes and mechanical properties as well as the physical properties were assessed. Sintering runs were performed at widely varying temperatures to obtain a reasonable comparison between the results.

For this purpose, two PM steel grades were prepared, one a carbon steel with the plain iron base powder ASC100.29 and the other a prealloyed powder Astaloy Mo (Fe-1.5%Mo), both supplied by Höganäs AB, Sweden. Carbon was introduced as natural graphite (grade UF4, Kropfmühl). Table 3.1 shows the composition of the prepared mixtures. Here it should be noted that the carbon content given indicates the content of admixed graphite, i.e. the *nominal* content; the C content of the sintered specimens (the "*combined* carbon") is typically lower and has to be determined by LECO, as described in 2.3.5.1.

Charpy impact test bars were produced for this study in a tool with floating lubricated die at three different pressures of 300, 500 and 700 MPa. As described above, sintering of the samples was performed in a laboratory furnace equipped with Kanthal APM superalloy muffle at different temperatures of 700-1300°C (interval 100°C) for 1 hr under plain Ar (99.999 quality). After the holding period at temperature, the samples were cooled in the water-jacketed exit zone under the same protective atmosphere as was used for sintering. The results of the characterization are listed in Table 3.2 and 3.3.

Table 3.1: Material composition of mixes.

	Designation	Mix Composition
1	Fe-0.8C	ASC100.29 + 0.8%C
2	Fe-1.5Mo-0.8C	Astaloy Mo + 0.8%C

Table 3.2: Sintered properties of carbon steel (Fe-0.8% C_{admixed}); compacted differently in lubricated die, sintered 60 min at 700-1300°C in argon.

<i>Sintering Temperature</i> (°C)	<i>Compacting Pressure</i> (MPa)	<i>Sintered density</i> (g/cm ³)	<i>Total porosity</i> (%)	<i>Dimensional Change</i> (%)	<i>Impact energy</i> (J/cm ²)	<i>Hardness</i> (HV30)	<i>Electrical conductivity</i> (S.m ⁻¹)10 ⁴	<i>Coercivity</i> (kA/m)	<i>Dyn. Young's modulus</i> (GPa)	<i>Damping</i> (Q ⁻¹)10 ⁻⁹
700	300	6.40 ± 0.03	17.94	-0.02 ± 0.00	1.2 ± 0.3	41.7 ± 0.6	511	0.27	82.9	18.1
	500	7.00 ± 0.00	10.27	-0.02 ± 0.00	1.7 ± 0.2	62.3 ± 1.2	629	0.25	112.2	17.8
	700	7.28 ± 0.00	6.61	-0.02 ± 0.00	1.4 ± 0.2	68.0 ± 2.0	651	0.26	126.6	33.3
800	300	6.41 ± 0.01	17.82	-0.02 ± 0.01	3.0 ± 0.5	42.3 ± 3.2	529	0.35	98.7	10.2
	500	7.00 ± 0.00	10.20	-0.04 ± 0.00	6.1 ± 0.5	65.0 ± 2.0	674	0.33	135.4	7.9
	700	7.30 ± 0.01	6.47	-0.02 ± 0.01	7.0 ± 0.2	77.0 ± 1.0	734	0.35	157.1	8.0
900	300	6.39 ± 0.01	18.02	0.04 ± 0.00	3.6 ± 0.3	47.0 ± 1.0	506	0.52	99.9	8.1
	500	6.99 ± 0.02	10.36	0.01 ± 0.02	8.3 ± 0.1	64.0 ± 2.6	658	0.51	140.8	7.2
	700	7.30 ± 0.01	6.43	-0.04 ± 0.01	14.8 ± 0.4	76.7 ± 1.5	743	0.42	163.0	6.3
1000	300	6.36 ± 0.05	18.52	0.12 ± 0.01	4.8 ± 0.4	67.0 ± 2.6	458	0.71	102.6	7.9
	500	6.97 ± 0.01	10.62	0.10 ± 0.01	11.7 ± 1.4	84.0 ± 2.6	584	0.74	145.1	7.7
	700	7.28 ± 0.01	6.64	0.06 ± 0.01	17.4 ± 0.6	107.7 ± 1.5	652	0.66	164.2	6.5
1100	300	6.42 ± 0.01	17.73	-0.04 ± 0.00	6.3 ± 0.3	73.0 ± 4.2	462	0.70	108.6	8.3
	500	7.00 ± 0.02	10.28	-0.03 ± 0.02	15.4 ± 1.1	101.3 ± 4.0	575	0.69	150.1	7.0
	700	7.30 ± 0.00	6.40	-0.04 ± 0.00	26.9 ± 0.4	122.7 ± 3.5	624	0.76	171.0	6.2
1200	300	6.45 ± 0.01	17.35	-0.20 ± 0.02	7.6 ± 0.4	84.0 ± 1.7	471	0.79	112.4	8.1
	500	7.03 ± 0.01	9.89	-0.14 ± 0.01	17.1 ± 1.8	115.0 ± 1.0	575	0.72	152.4	6.6
	700	7.31 ± 0.00	6.23	-0.10 ± 0.01	27.9 ± 0.9	128.3 ± 3.1	624	0.74	173.9	5.1
1300	300	6.51 ± 0.01	16.54	-0.49 ± 0.02	9.3 ± 1.0	82.0 ± 3.6	484	0.74	120.0	8.4
	500	7.08 ± 0.02	9.25	-0.34 ± 0.02	22.1 ± 1.2	113.3 ± 2.3	590	0.78	157.8	6.5
	700	7.35 ± 0.00	5.78	-0.28 ± 0.01	33.1 ± 3.1	130.3 ± 1.2	635	0.73	176.6	5.4

Table 3.3: Sintered properties of Mo steel (Fe-1.5%Mo-0.8% C_{admixed}); compacted differently in lubricated die, sintered 60 min at 700-1300°C in Ar.

<i>Sintering Temperature</i> (°C)	<i>Compacting Pressure</i> (MPa)	<i>Sintered density</i> (g/cm ³)	<i>Total porosity</i> (%)	<i>Dimensional Change</i> (%)	<i>Impact energy</i> (J/cm ²)	<i>Hardness</i> (HV30)	<i>Electrical conductivity</i> (S.m ⁻¹)10 ⁴	<i>Coercivity</i> (kA/m)	<i>Dyn. Young's modulus</i> (GPa)	<i>Damping</i> (Q ⁻¹) 10 ⁻⁹
700	300	6.31 ± 0.10	19.13	0.04 ± 0.00	0.3 ± 0.0	52.3 ± 3.1	189	0.37	42.5	217.6
	500	6.92 ± 0.01	11.33	0.04 ± 0.00	0.3 ± 0.1	83.7 ± 2.5	130	0.36	40.1	243.1
	700	7.22 ± 0.00	7.40	0.04 ± 0.00	0.4 ± 0.1	98.7 ± 2.9	140	0.35	52.6	332.1
800	300	6.30 ± 0.00	19.28	0.09 ± 0.00	1.1 ± 0.0	71.0 ± 5.2	368	0.92	81.9	12.8
	500	6.92 ± 0.01	11.31	0.09 ± 0.09	1.2 ± 0.3	90.7 ± 2.1	482	0.75	117.2	11.3
	700	7.21 ± 0.00	7.52	0.05 ± 0.00	1.9 ± 0.2	104.3 ± 1.5	541	0.72	137.5	11.6
900	300	6.23 ± 0.08	20.15	0.22 ± 0.01	2.1 ± 0.1	92.0 ± 1.0	328	1.67	89.7	8.3
	500	6.89 ± 0.01	11.62	0.18 ± 0.00	5.2 ± 0.4	143.7 ± 2.3	422	1.64	132.6	7.5
	700	7.22 ± 0.02	7.45	0.09 ± 0.02	7.2 ± 0.8	163.3 ± 7.6	486	1.44	153.4	5.7
1000	300	6.27 ± 0.01	19.56	0.26 ± 0.01	3.0 ± 0.5	99.3 ± 4.7	322	1.86	94.8	8.3
	500	6.89 ± 0.01	11.65	0.20 ± 0.02	6.8 ± 0.4	155.0 ± 1.7	405	1.81	136.3	6.7
	700	7.22 ± 0.01	7.49	0.14 ± 0.03	9.7 ± 1.5	195.0 ± 9.5	453	1.75	157.6	5.5
1100	300	6.29 ± 0.01	19.35	0.13 ± 0.02	4.6 ± 0.2	103.7 ± 5.0	326	1.90	98.7	8.6
	500	6.91 ± 0.01	11.46	0.13 ± 0.03	9.7 ± 0.3	155.7 ± 2.1	407	1.81	138.7	7.1
	700	7.23 ± 0.03	7.26	0.08 ± 0.02	16.1 ± 0.9	205.3 ± 2.3	450	1.77	164.0	5.1
1200	300	6.33 ± 0.01	18.86	-0.06 ± 0.02	5.6 ± 0.4	116.0 ± 4.0	331	1.90	103.9	8.2
	500	6.94 ± 0.01	10.97	-0.02 ± 0.03	11.8 ± 1.4	166.3 ± 3.5	420	1.86	146.3	6.3
	700	7.26 ± 0.02	6.98	-0.05 ± 0.02	19.6 ± 2.3	205.3 ± 1.5	466	1.75	169.6	4.8
1300	300	6.43 ± 0.09	17.61	-0.36 ± 0.03	7.4 ± 0.9	117.3 ± 5.7	344	1.88	110.6	8.8
	500	6.98 ± 0.01	10.49	-0.22 ± 0.03	15.5 ± 1.2	164.3 ± 1.2	420	1.75	149.0	6.3
	700	7.27 ± 0.04	6.75	-0.13 ± 0.04	24.2 ± 1.1	213.3 ± 2.3	460	1.69	169.7	4.9

3.1.1. Green density

Compactibility is always a main property for pressed and sintered ferrous PM parts because almost all mechanical properties of the sintered part depend on the density, and since the parts hardly densify during sintering, “sintered density” usually means the green density [138]. In addition, there are evidences which show that the green density plays a major role in the deoxidation process and resulting carbon dissolution during sintering of PM steels [28].

The green density of the two steel grades compacted at different pressures is shown in Figure 3.1. It is evident that, as expected, increasing the compacting pressure leads to higher green density. In fact, higher compacting pressure in uniaxial pressing causes higher plastic deformation. It is obvious that the higher hardness and yield strength of the Mo alloyed powder compared to plain iron resulted in higher resistance against densification during the compacting process, which is in good agreement with previous findings [139, 140]. In fact, in this case work hardening is an important parameter that limits the densification and compactibility of the specimens at higher compacting pressures [5, 141].

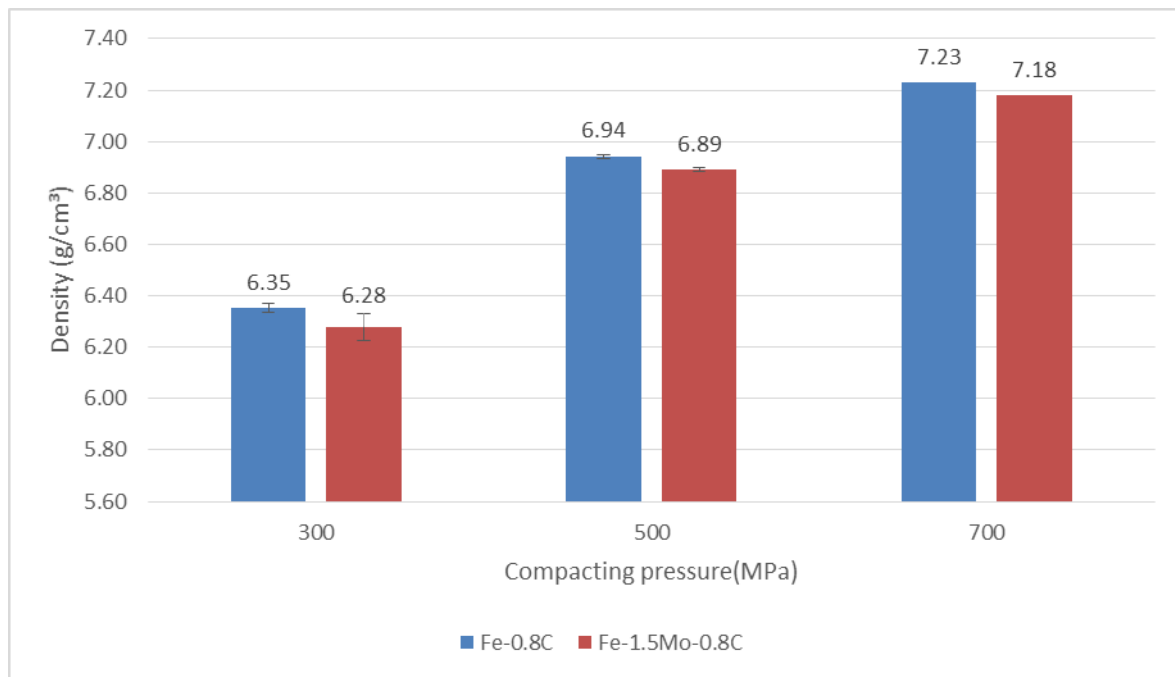


Figure 3.1: Green density of samples, compacted to Charpy impact bars (ISO 5754) in lubricated die at different pressures.

3.1.2. Metallographic investigations (pore morphology and matrix microstructure)

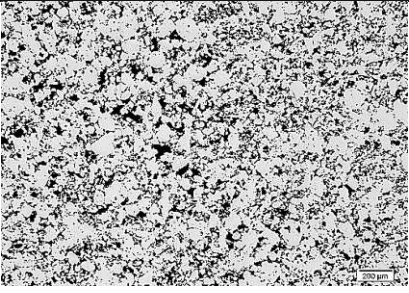
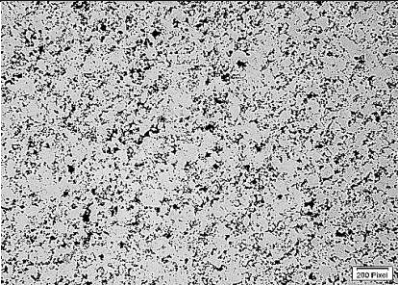
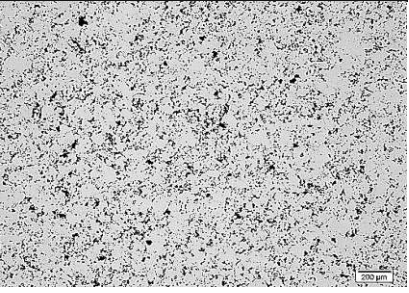
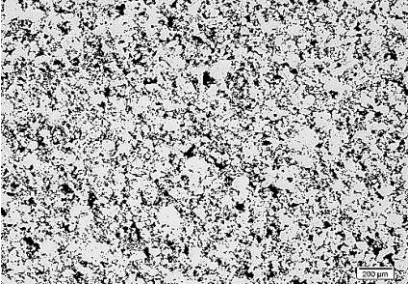
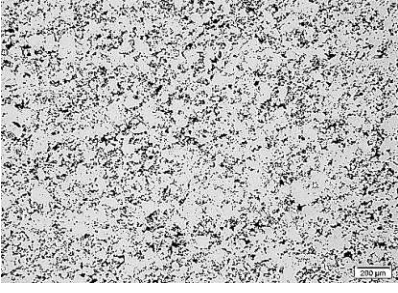
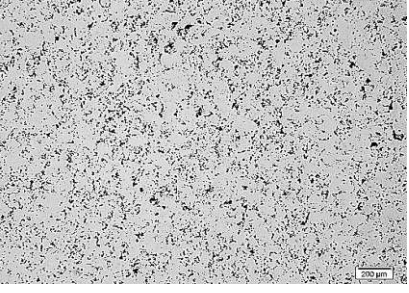

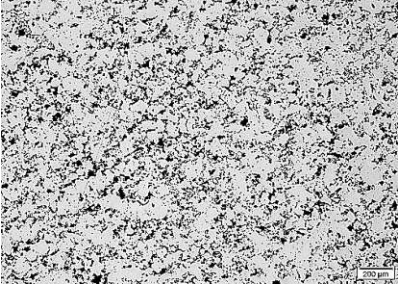

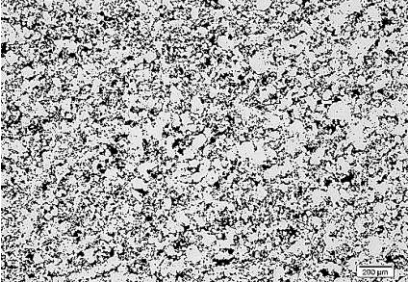
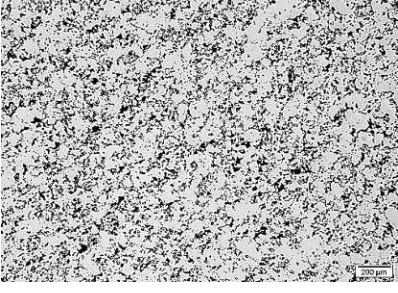
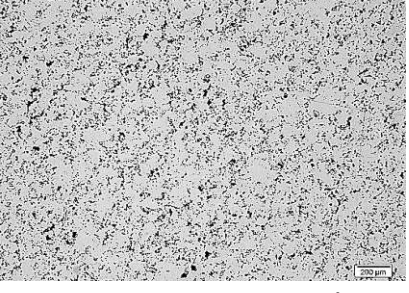


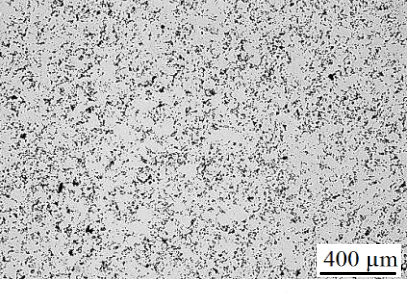
A useful method for characterizing sintering of PM steels is metallographic examination both un-etched and etched. Investigation of the sintering phenomena such as the disappearance of boundaries between the individual particles, dissolution of carbon, distribution and diffusion of alloy elements as well as the morphology of pores is possible with this method [142, 143].

Un-etched optical microscopy cross section of the steels compacted at different pressures are presented at two magnifications of 50 and 200 x in Figure 3.2 through Figure 3.5. The total

porosity data calculated from the theoretical and sintered density are presented on each micrograph for better comparison.

In Figure 3.2 and 3.4, the sections at the lower magnification of 50x show – as expected - that raising the compacting pressure led to denser structure and lower the amount of porosity. Visually evaluating the images shows that the pore size in the samples is reduced by increasing the compacting pressure.

In Figure 3.3 and 3.5, depicting specimens sintered at 700°C, the boundaries between the individual powder particles are visible in both steel grades. The sections of both steels compacted at 700 MPa at this temperature clearly indicate that the shape of each particle is influenced by surrounding particles which is the consequence of strong plastic deformation of particles. The micrographs at 800°C show elimination of the boundaries between particles; it seems that increasing the compacting pressure enhanced this process by providing more physical surface contacts between the particles. At moderate and high sintering temperatures, samples with higher density show stronger contacts which resulted in larger surface contact that causes more material transport between particles. High temperature sintering for both steel grades resulted in more rounded pores and stronger sintering necks.

	300 MPa	500 MPa	700 MPa
700°C	 <p>Total porosity: 17.94%, $\rho = 6.40 \text{ g/cm}^3$</p>	 <p>Total porosity: 10.27%, $\rho = 7.00 \text{ g/cm}^3$</p>	 <p>Total porosity: 6.61 %, $\rho = 7.28 \text{ g/cm}^3$</p>
800°C	 <p>Total porosity: 17.82%, $\rho = 6.41 \text{ g/cm}^3$</p>	 <p>Total porosity: 10.20 %, $\rho = 7.00 \text{ g/cm}^3$</p>	 <p>Total porosity: 6.47 %, $\rho = 7.30 \text{ g/cm}^3$</p>
900°C	 <p>Total porosity: 18.02%, $\rho = 6.39 \text{ g/cm}^3$</p>	 <p>Total porosity: 10.36%, $\rho = 6.99 \text{ g/cm}^3$</p>	 <p>Total porosity: 6.43%, $\rho = 7.30 \text{ g/cm}^3$</p>
1000°C	 <p>Total porosity: 18.52%, $\rho = 6.36 \text{ g/cm}^3$</p>	 <p>Total porosity: 10.62 %, $\rho = 6.97 \text{ g/cm}^3$</p>	 <p>Total porosity: 6.64 %, $\rho = 7.28 \text{ g/cm}^3$</p>
1100°C	 <p>Total porosity: 17.73%, $\rho = 6.42 \text{ g/cm}^3$</p>	 <p>Total porosity: 10.28%, $\rho = 7.00 \text{ g/cm}^3$</p>	 <p>Total porosity: 6.4%, $\rho = 7.30 \text{ g/cm}^3$</p>

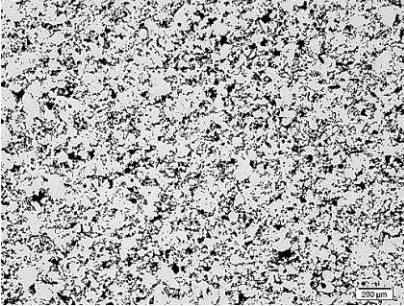
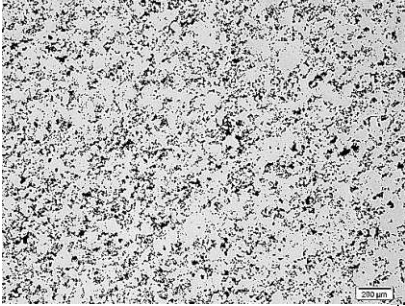
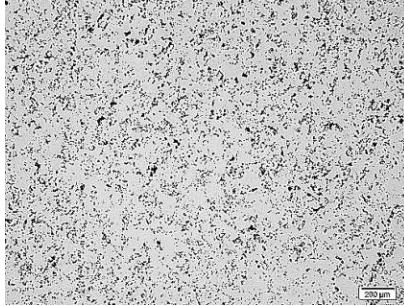
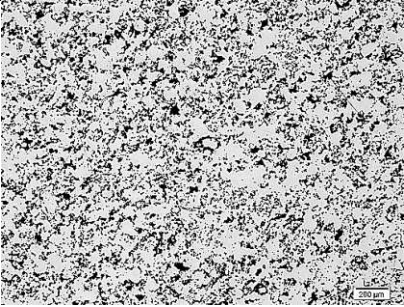
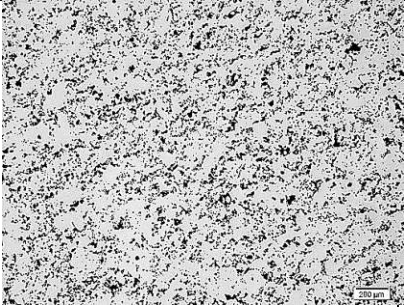
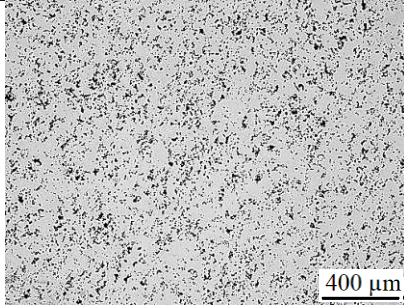
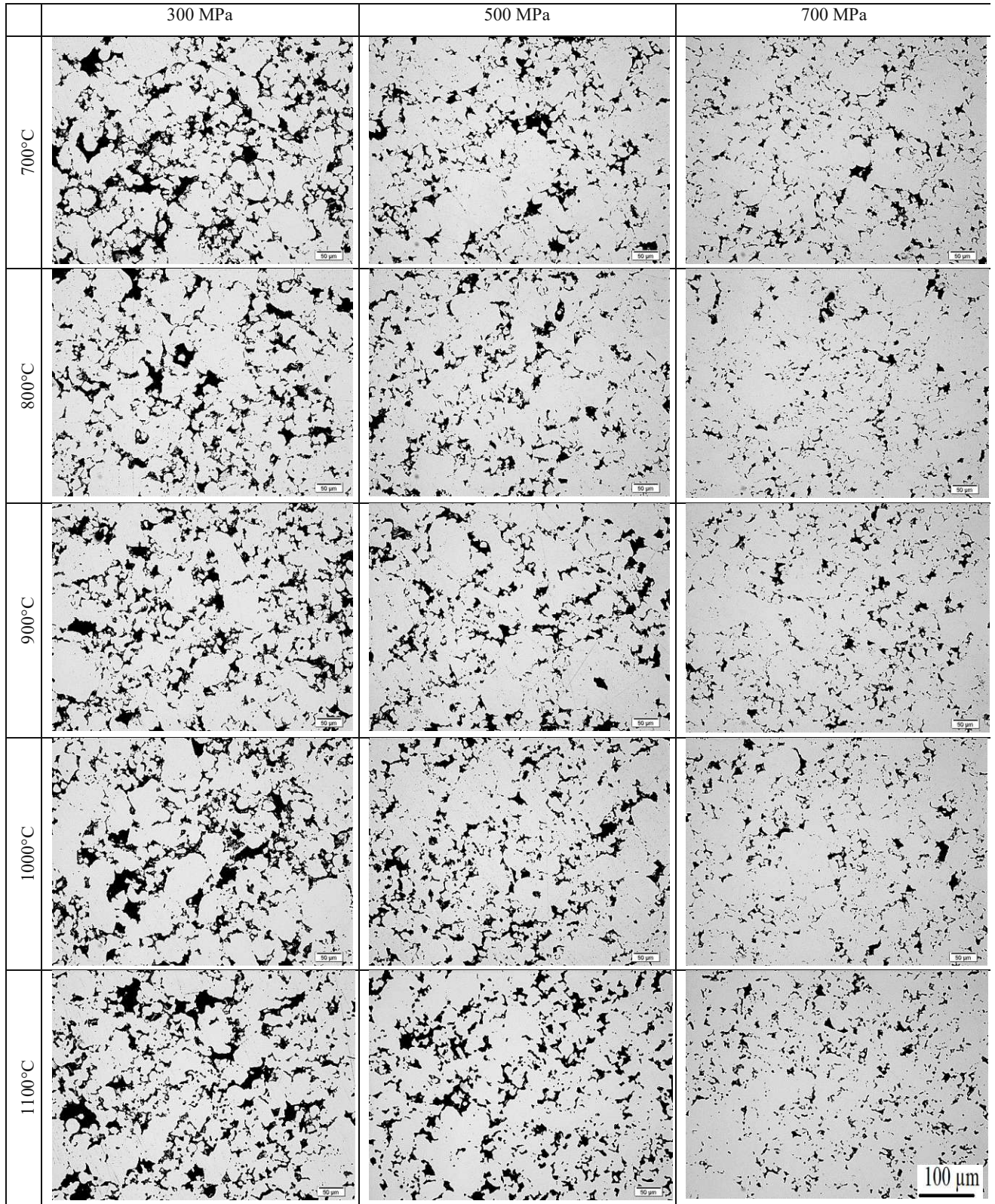
	300 MPa	500 MPa	700 MPa
1200°C	 <p>Total porosity: 17.35%, $\rho = 6.45 \text{ g/cm}^3$</p>	 <p>Total porosity: 9.89 %, $\rho = 7.03 \text{ g/cm}^3$</p>	 <p>Total porosity: 6.23 %, $\rho = 7.31 \text{ g/cm}^3$</p>
1300°C	 <p>Total porosity: 16.54%, $\rho = 6.51 \text{ g/cm}^3$</p>	 <p>Total porosity: 9.25 %, $\rho = 7.08 \text{ g/cm}^3$</p>	 <p>Total porosity: 5.78 %, $\rho = 7.35 \text{ g/cm}^3$</p>

Figure 3.2: Un-etched OM micrograph and pore morphology of Fe-0.8% C_{admixed} , compacted at different pressures, sintered 60 min between 700 and 1300°C in Ar, 50x. (the scale bar 400 μm holds for all images)



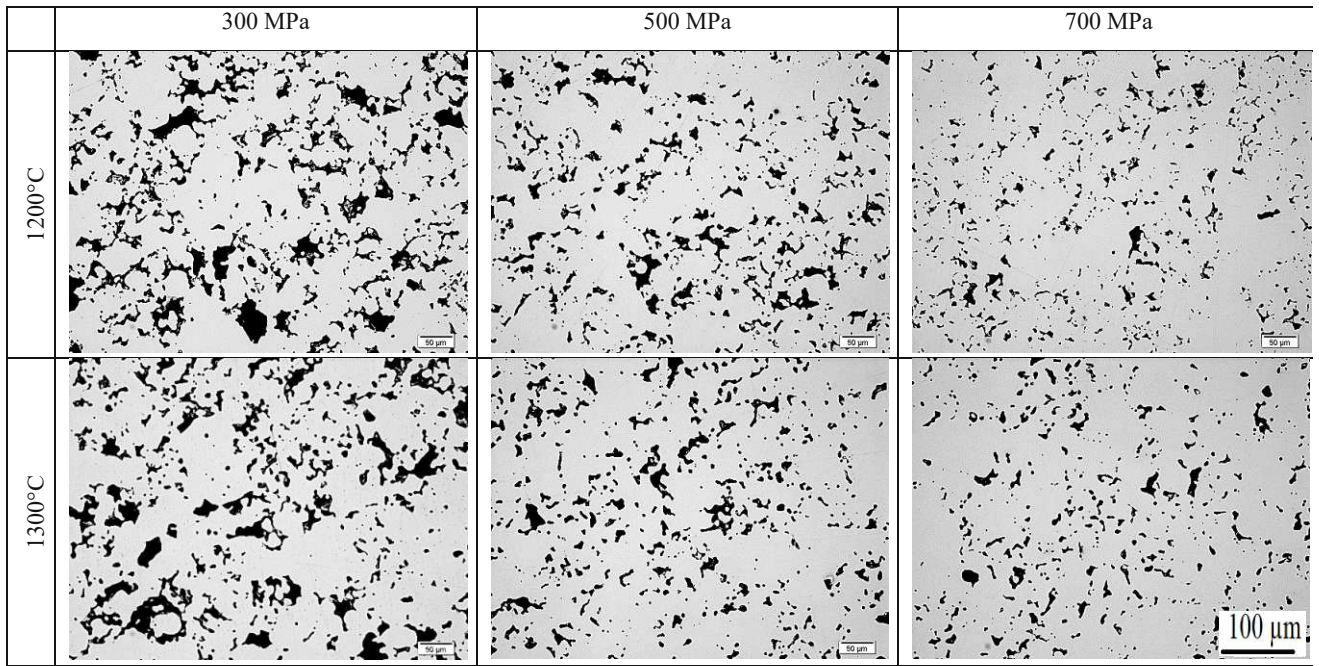
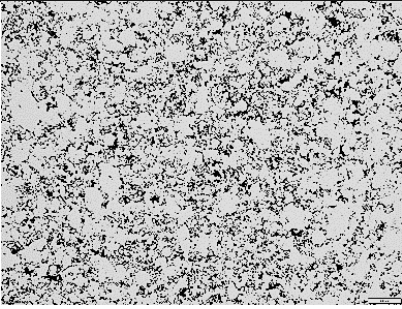
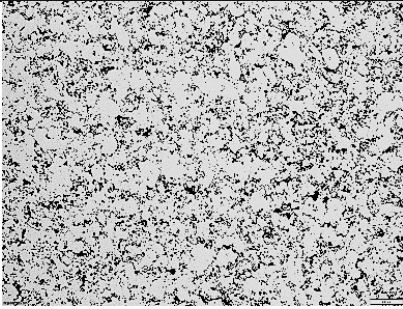
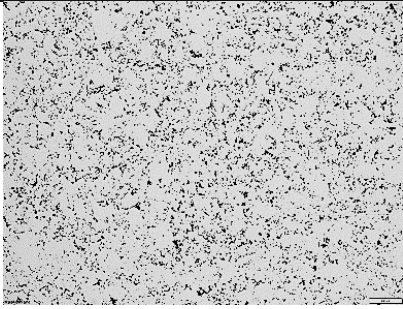
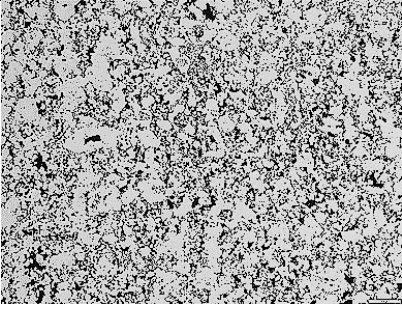
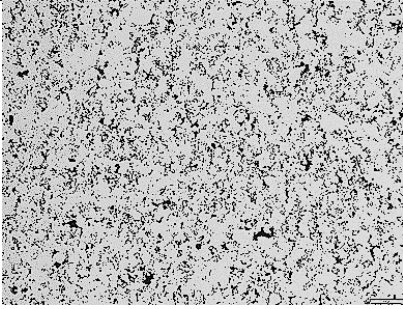
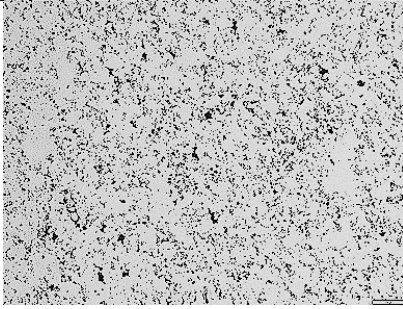
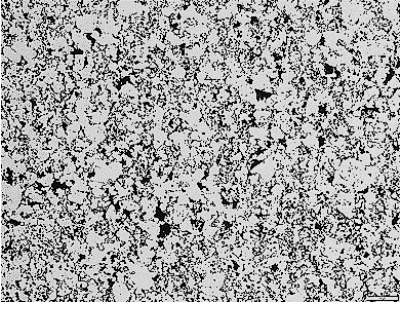

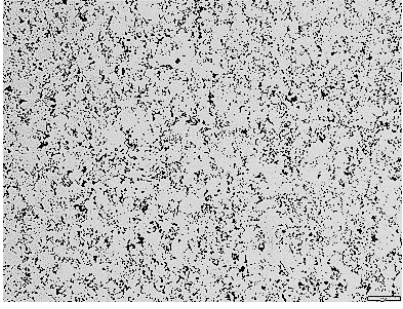
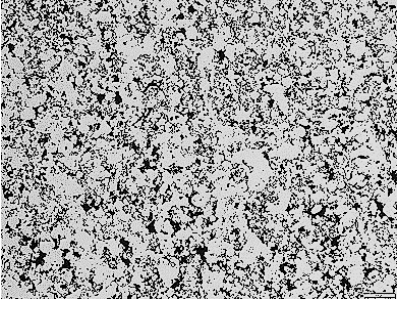
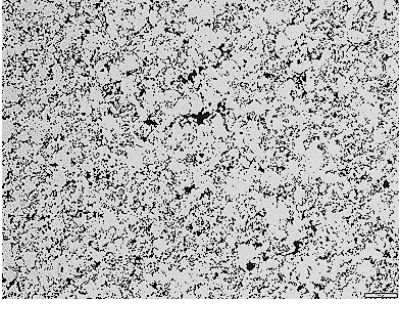

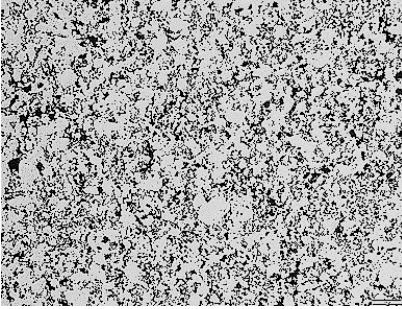
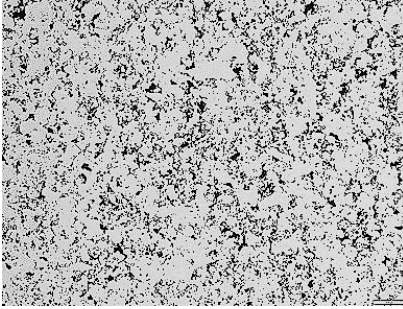
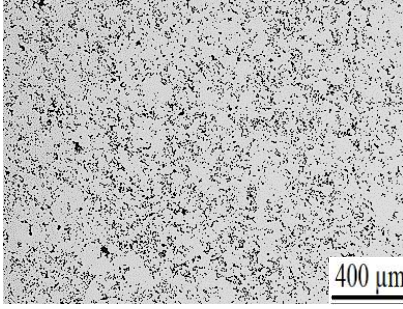


Figure 3.3: Un-etched OM micrograph and pore morphology of Fe-0.8% C_{admixed} , compacted at different pressures, sintered 60 min between 700 and 1300°C in Ar, 200x. (scale bar 100 μm holds for all images)

	300 MPa	500 MPa	700 MPa
700°C	 <p>Total porosity: 19.13 %, $\rho = 6.31 \text{ g/cm}^3$</p>	 <p>Total porosity: 11.33 %, $\rho = 6.92 \text{ g/cm}^3$</p>	 <p>Total porosity: 7.40 %, $\rho = 7.22 \text{ g/cm}^3$</p>
800°C	 <p>Total porosity: 19.28 %, $\rho = 6.30 \text{ g/cm}^3$</p>	 <p>Total porosity: 11.31 %, $\rho = 6.92 \text{ g/cm}^3$</p>	 <p>Total porosity: 7.52 %, $\rho = 7.21 \text{ g/cm}^3$</p>
900°C	 <p>Total porosity: 20.15 %, $\rho = 6.23 \text{ g/cm}^3$</p>	 <p>Total porosity: 11.62 %, $\rho = 6.89 \text{ g/cm}^3$</p>	 <p>Total porosity: 7.45 %, $\rho = 7.22 \text{ g/cm}^3$</p>
1000°C	 <p>Total porosity: 19.56 %, $\rho = 6.27 \text{ g/cm}^3$</p>	 <p>Total porosity: 11.65 %, $\rho = 6.89 \text{ g/cm}^3$</p>	 <p>Total porosity: 7.49 %, $\rho = 7.22 \text{ g/cm}^3$</p>
1100°C	 <p>Total porosity: 19.35 %, $\rho = 6.91 \text{ g/cm}^3$</p>	 <p>Total porosity: 11.46 %, $\rho = 6.91 \text{ g/cm}^3$</p>	 <p>Total porosity: 7.26 %, $\rho = 7.23 \text{ g/cm}^3$</p>

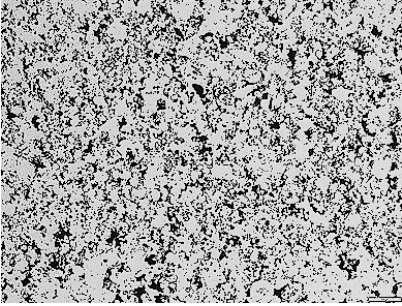
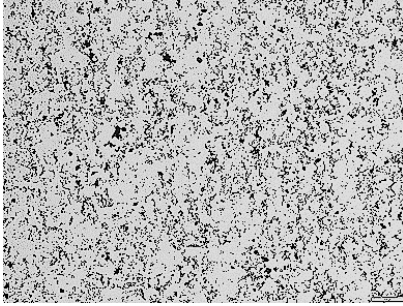
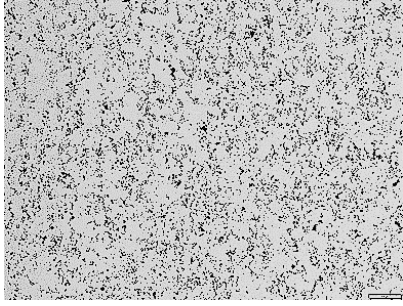
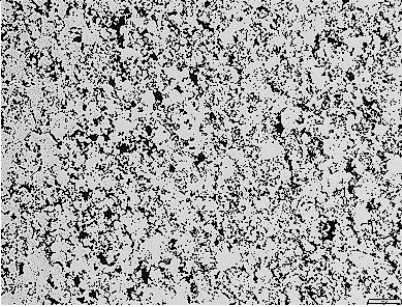
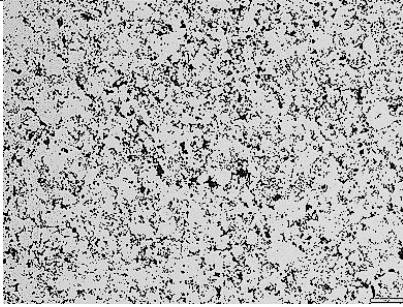
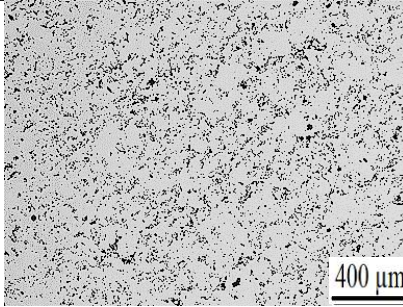
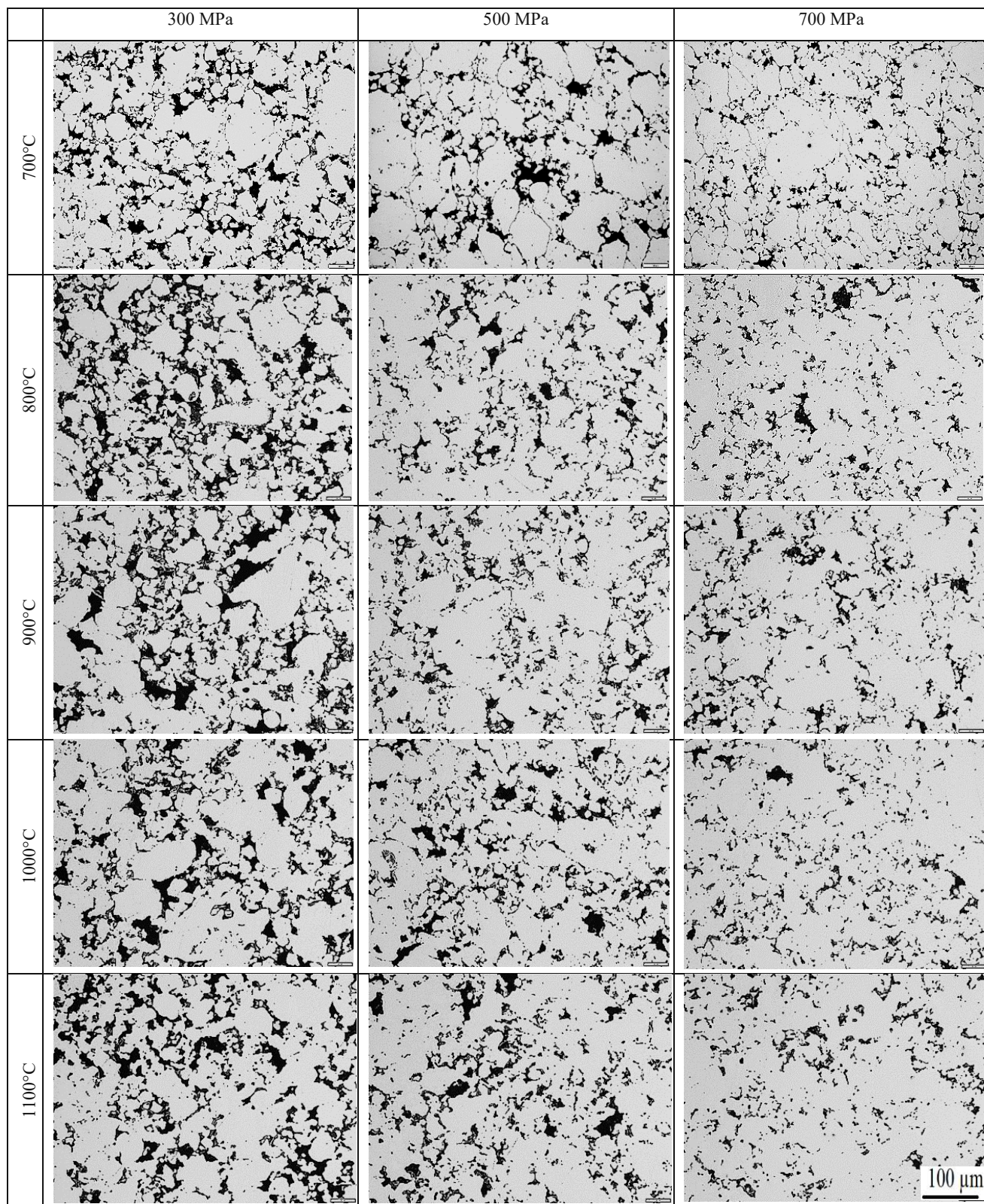
	300 MPa	500 MPa	700 MPa
1200°C	 <p>Total porosity: 18.86 %, $\rho = 6.33 \text{ g/cm}^3$</p>	 <p>Total porosity: 10.97 %, $\rho = 6.94 \text{ g/cm}^3$</p>	 <p>Total porosity: 6.98 %, $\rho = 7.26 \text{ g/cm}^3$</p>
1300°C	 <p>Total porosity: 17.61 %, $\rho = 6.43 \text{ g/cm}^3$</p>	 <p>Total porosity: 10.49 %, $\rho = 6.98 \text{ g/cm}^3$</p>	 <p>Total porosity: 6.75 %, $\rho = 7.27 \text{ g/cm}^3$</p>

Figure 3.4: Un-etched OM micrograph and pore morphology of Fe-1.5%Mo-0.8%C_{admixed}, compacted at different pressures, sintered 60 min between 700 and 1300°C in Ar, 50x. (scale bar 400µm holds for all images)



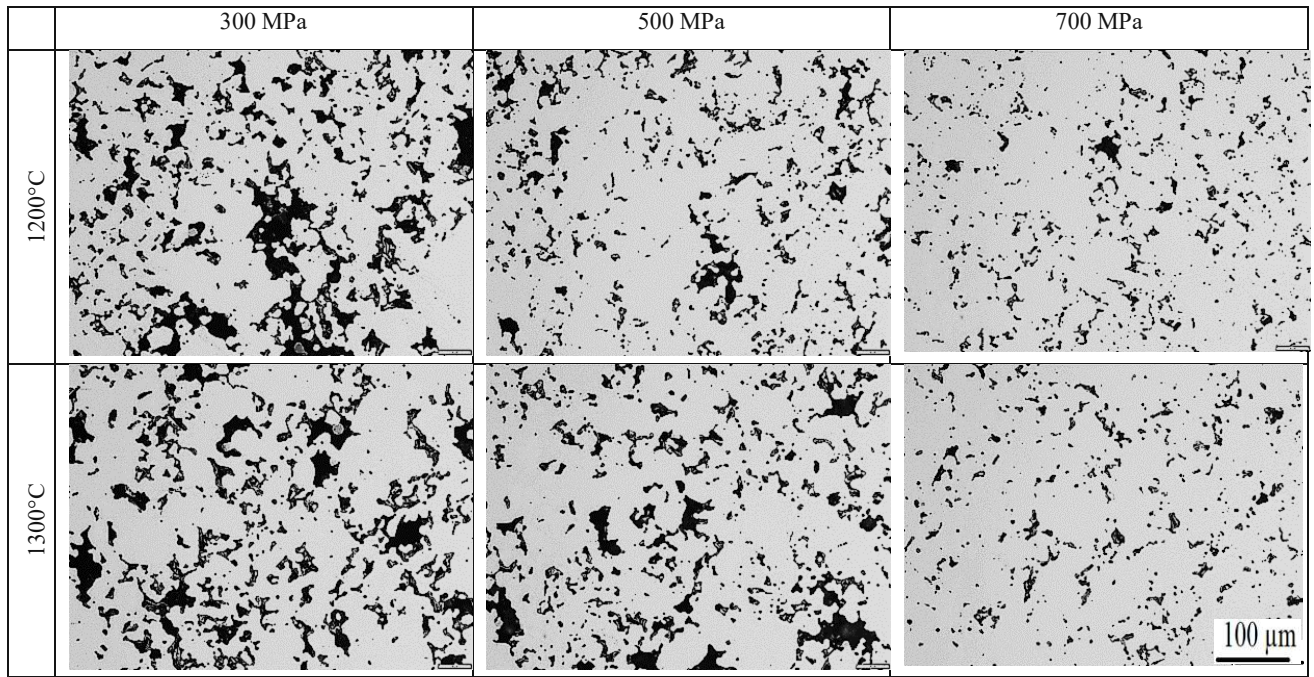

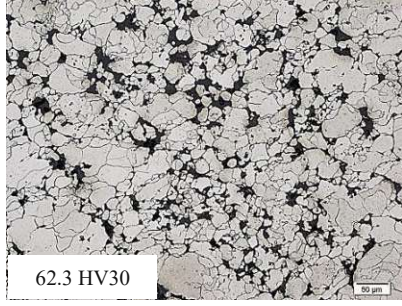




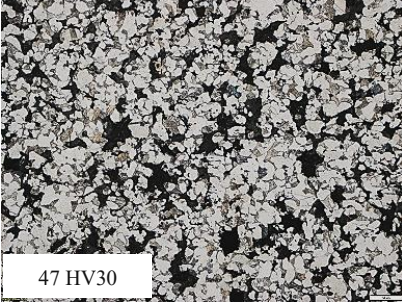







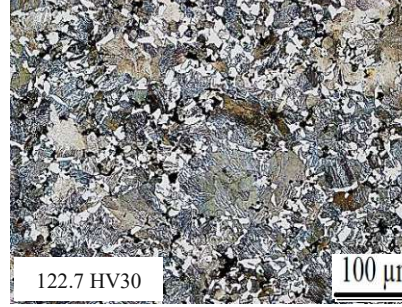


Figure 3.5: Un-etched OM micrograph and pore morphology of Fe-1.5%Mo-0.8%C_{admixed}, compacted at different pressures, sintered 60 min between 700 and 1300°C in Ar, 200x. (scale bar 100μm holds for all images)

Etched micrographs of both steel grades compacted at different pressures and sintered between 700 and 1300°C are presented in Figure 3.6 through Figure 3.9 at two different magnifications, i.e., 200 and 500 x. Figures 3.6 and 3.7 show microstructures of the carbon steel (Fe-0.8C). After sintering at 700°C, the boundaries between powder particles and also the sub-grain boundaries in the cores of the ferrite grains are discernible. The micrographs show that the nucleation of the pearlite, which is an indicator of carbon dissolution into the iron lattice, started from 800°C at all three compacting pressures. The microstructure of the sections at 900°C shows that dissolution of carbon in the iron resulted in finer microstructure. However, it seems that these ferrite grains that have been formed during cooling are smaller in the samples prepared with higher compacting pressure, which was caused by more cold working. From the evidences it is clearly visible that raising the sintering temperature enhanced the carbon dissolution process and raised the fraction of the formed pearlite. Comparing the sections at 1000°C shows that the pearlite fraction is slightly lower at the higher densities (see Figure 3.7-b). This might be an indicator that C dissolution occurs rather through gas phase transport than through solid state reaction, which would agree with the Tanaka and Lund studies [56, 57]. In the temperature range of 1100 to 1300°C, the fraction of the pearlite in all the microstructures remains constant almost without change, which shows that carbon dissolution is virtually complete at this temperature, and sintering is followed by microstructure homogenizing and pore rounding at the higher temperatures. Despite using 0.8% carbon in the mixes, microstructures after sintering at 1300°C do not show 100 % pearlite, and some grains of proeutectoid ferrite are discernible in the microstructures. An explanation for this is the carbon loss during sintering caused by carbothermal reduction of the oxides of the iron powders, which means that a sintered steel with nominally 0.8% admixed graphite after sintering rather contains less than this amount and thus is no more fully pearlitic unless cooled faster.

Microstructures of the prealloyed steel, Fe-1.5Mo-0.8C compacted at different pressures are presented through Figure 3.8 and 3.9. At 700°C, similar to Fe-0.8C, boundaries between the individual powder particles as well as ferrite grain boundaries in the core of the Mo alloyed steel particles are discernible. At 800°C, nucleation of bainite at the surfaces of powder particles is a consequence of the carbon dissolution into the alloy crystal at this temperature, however sub-grain boundaries are still discernible at this temperature. Formation of upper bainite is clearly visible at 900°C, which covers almost all of the microstructure. Unlike with Fe-C, which provides a ferrite-pearlite microstructure, estimation of the dissolved carbon in bainitic microstructures is not very easy, but the further increase of the hardness values at higher temperatures (see below) indicates that carbon dissolution is not complete at 900°C and proceeds at higher temperatures. It is evident that increasing the temperature resulted in a more homogeneous microstructure in the temperature range of 1000 to 1300°C.

	300 MPa	500 MPa	700 MPa
700°C	 41.7 HV30	 62.3 HV30	 68 HV30
800°C	 42.3 HV30	 65 HV30	 77 HV30
900°C	 47 HV30	 41.7 HV30	 41.7 HV30
1000°C	 41.7 HV30	 64 HV30	 76.7 HV30
1100°C	 73 HV30	 101.3 HV30	 122.7 HV30

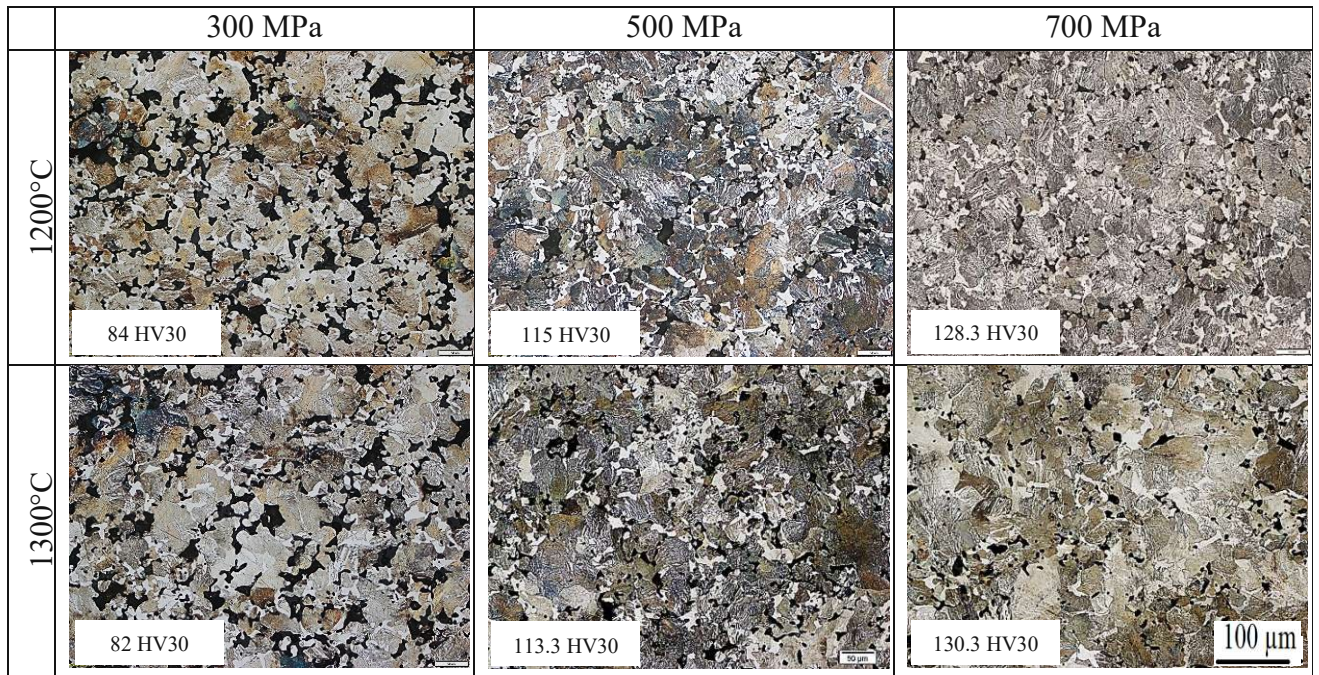
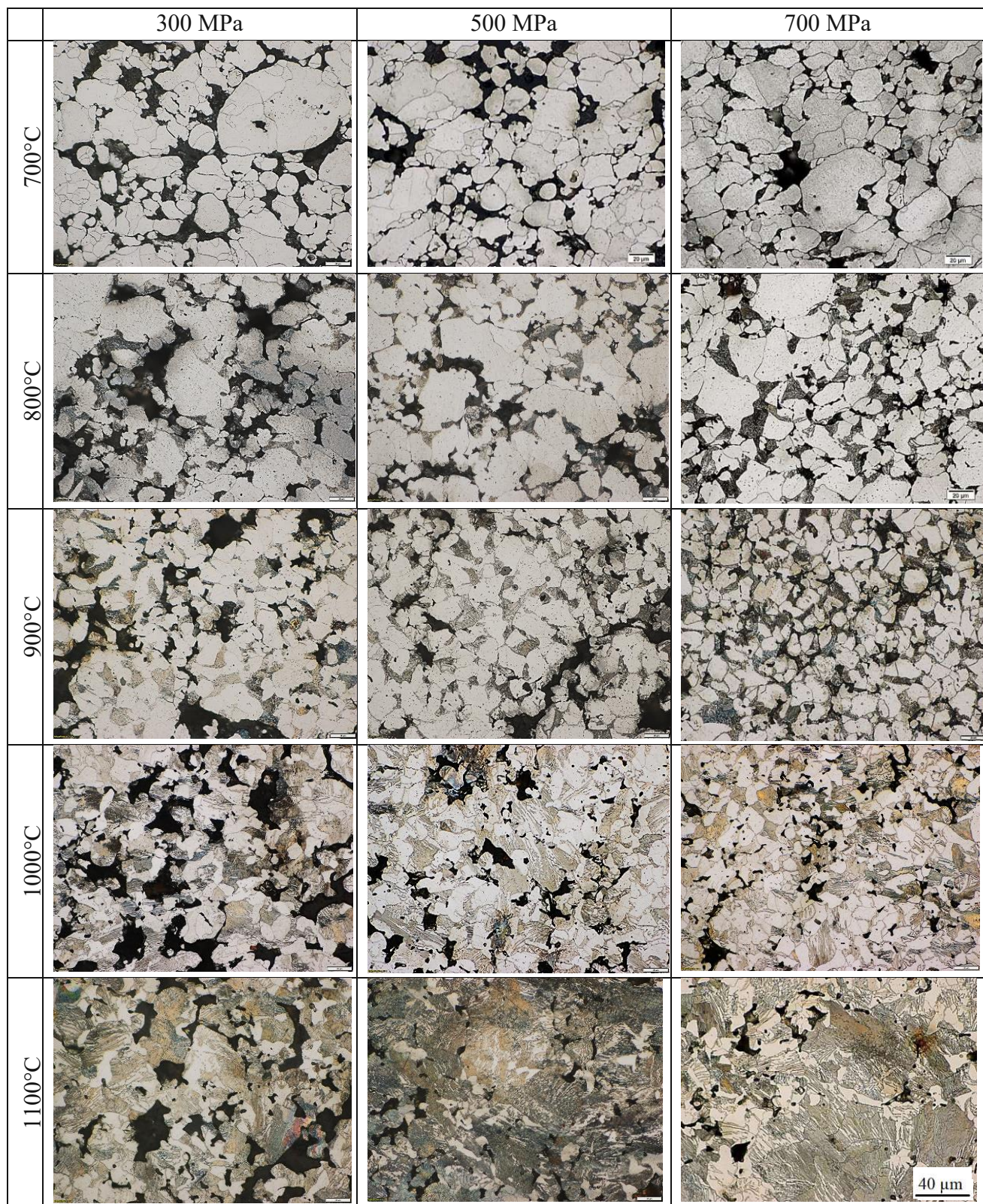


Figure 3.6: Etched microstructure of Fe-0.8% $C_{admixed}$, compacted at different pressures, sintered 60 min between 700 to 1300°C in Ar, Nital, 200 x. (scale bar 100µm holds for all images)



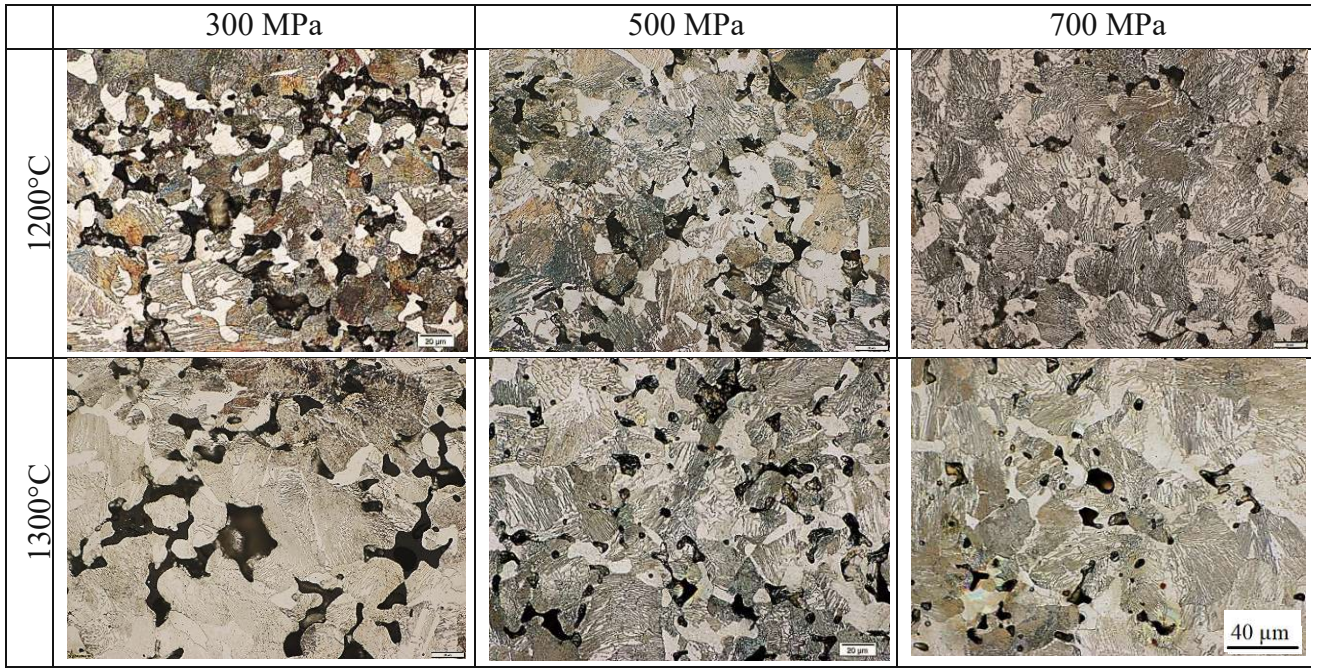


Figure 3.7: Etched microstructure of Fe-0.8%C_{admixed}, compacted at different pressures, sintered 60 min between 700 to 1300°C in Ar, Nital, 500 x. (scale bar 40µm holds for all images)

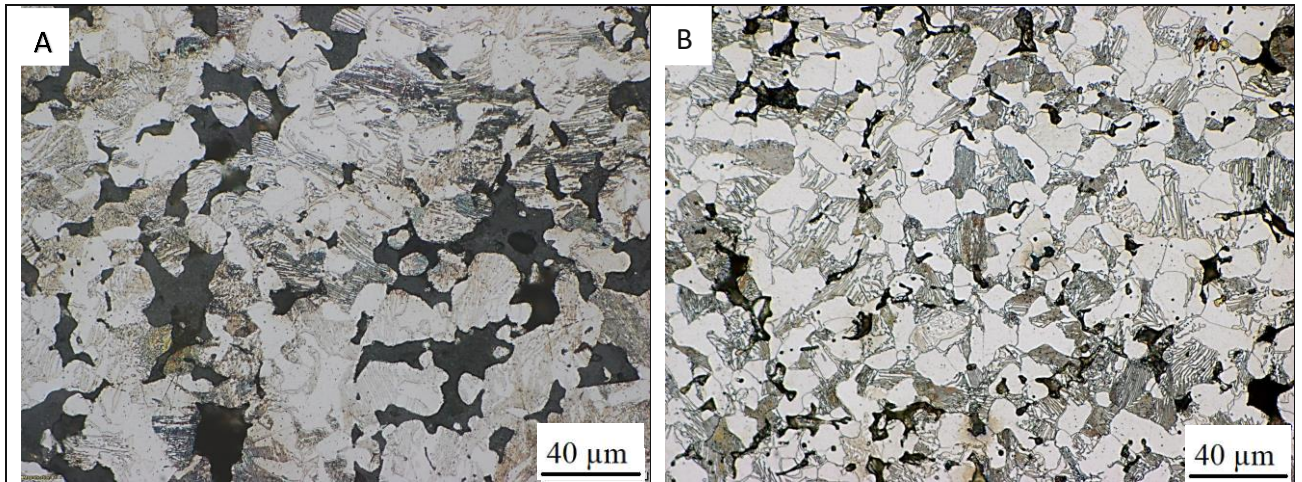
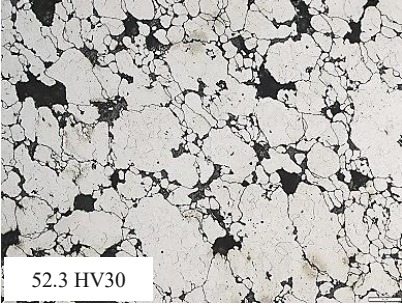
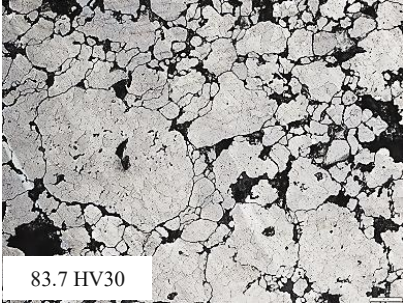
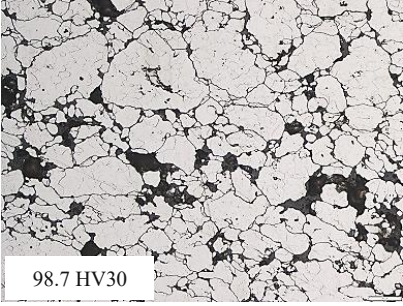
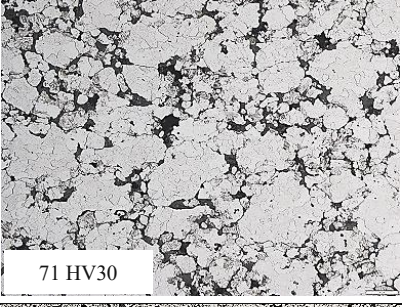

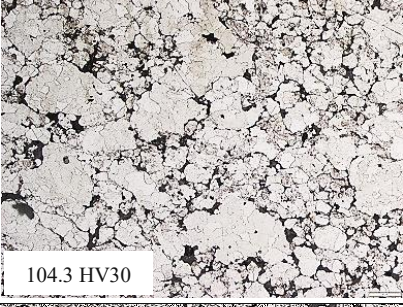
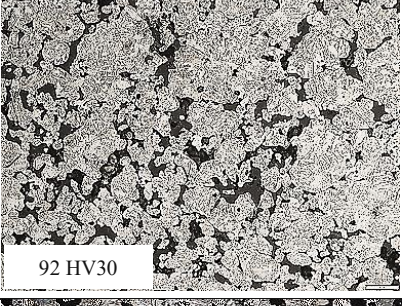
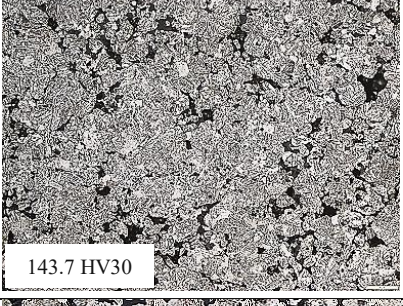
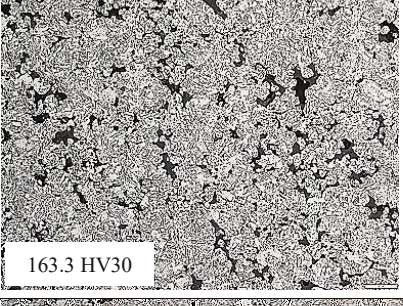
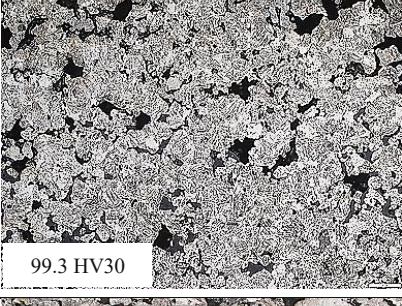
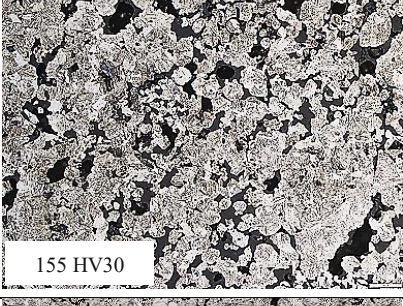


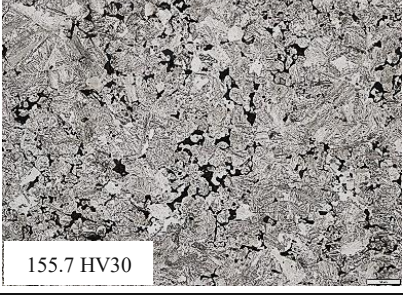
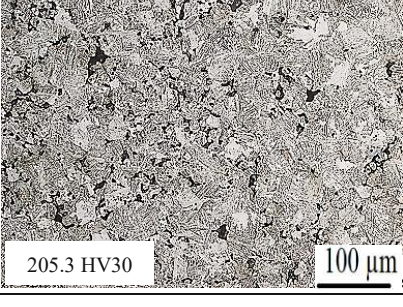


Figure 3.7-b: Pearlite formation in carbon steels (Fe-0.8%C_{admixed}), sintered 60 min at 1000 °C in Ar, compacted at 300 MPa (A) and 700 MPa (B).

	300 MPa	500 MPa	700 MPa
700°C	 52.3 HV30	 83.7 HV30	 98.7 HV30
800°C	 71 HV30	 90.7 HV30	 104.3 HV30
900°C	 92 HV30	 143.7 HV30	 163.3 HV30
1000°C	 99.3 HV30	 155 HV30	 195 HV30
1100°C	 103.7 HV30	 155.7 HV30	 205.3 HV30

100 μm

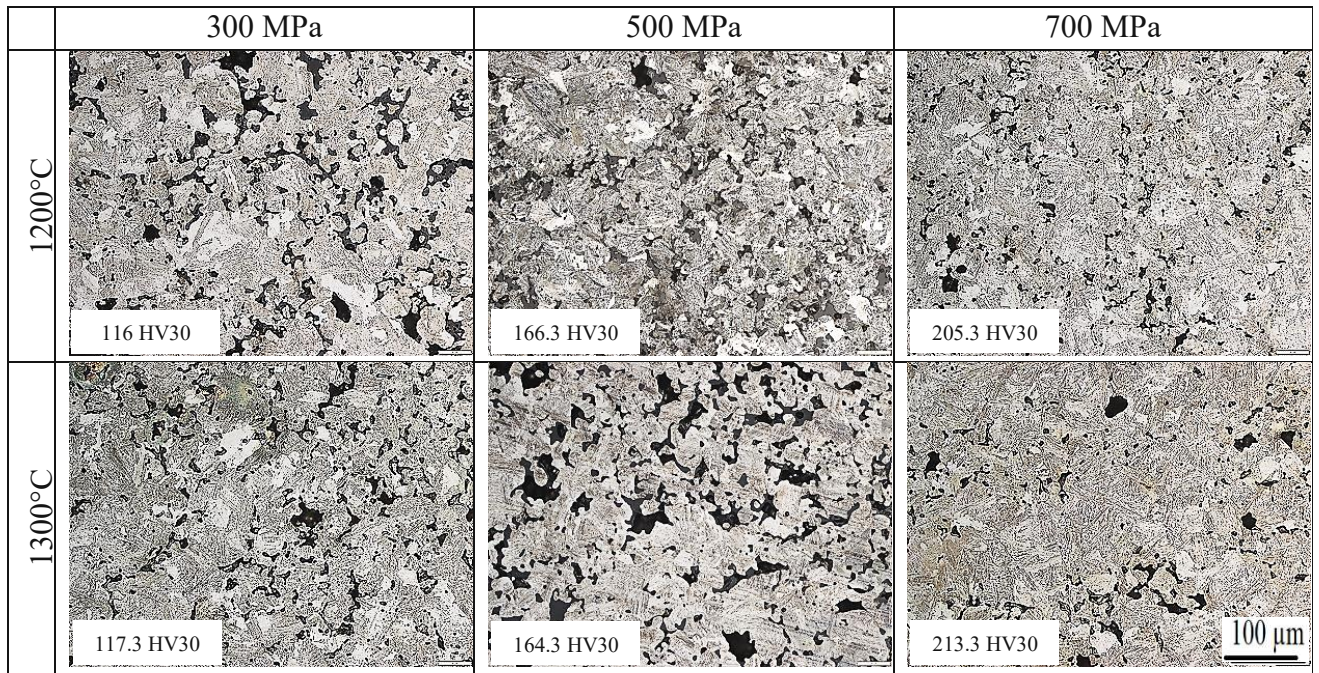
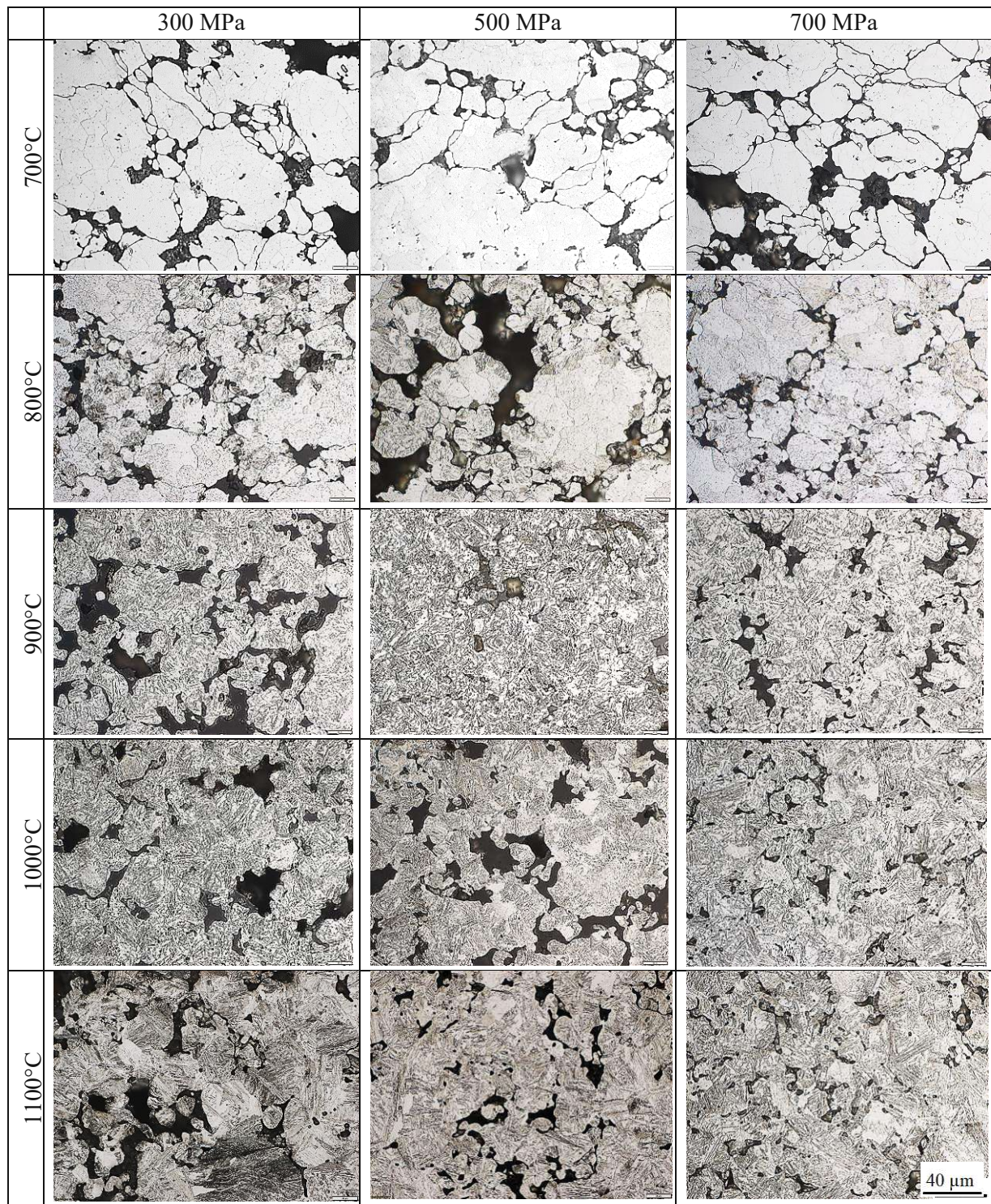


Figure 3.8: Etched microstructure of Fe-1.5%Mo-0.8% $C_{admixed}$, compacted at different pressures, sintered 60 min between 700 to 1300°C in Ar, Nital, 200 x. (scale bar 100µm holds for all images)



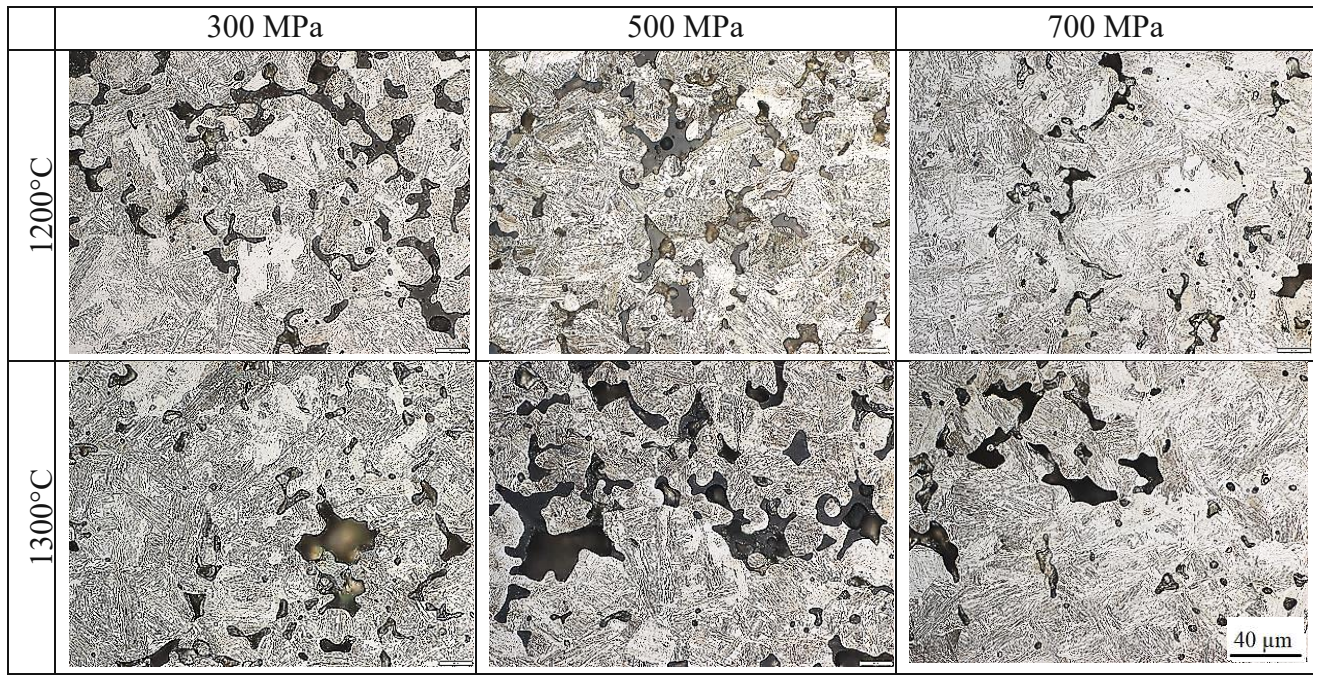


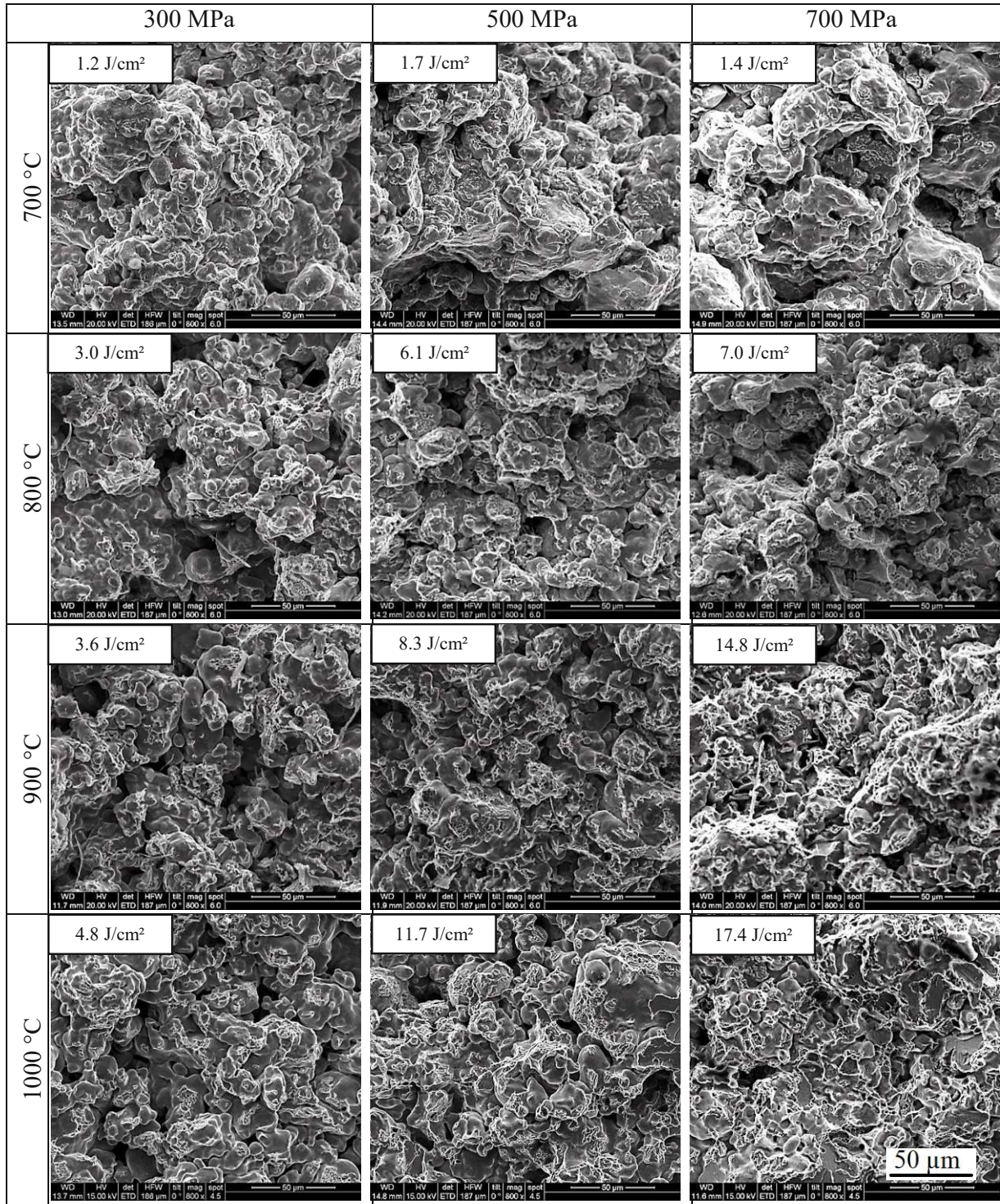
Figure 3.9: Etched microstructure of Fe-1.5%Mo-0.8%C_{admixed}, compacted at different pressure, Sintered 60 min between 700 to 1300°C in Ar, Nital, 500 x. (scale bar 40μm holds for all images)

3.1.3. Fractography

Formation of bonds or contacts between the particles during sintering is the main mechanism for mechanical strength of PM materials. A well-known method to observe the formation and development of these interparticle bridges is the fractographic investigation of the sintered components [144]. Therefore, this method was used in the present study for evaluating the sintering progress as well.

Fracture surfaces of the steels broken by Charpy impact test at room temperature are presented in Figure 3.10 and 3.11. Fracture surfaces of the carbon steels sintered at 700°C are presented in Figure 3.10. They show no sign of sintering and contact formation at this temperature. At 800°C, presence of some short lines and spots on the fracture surface is an indicator of formation of the first sintering contacts at this temperature. At 900°C, by increasing the sintering temperature more contacts between the particles are formed. The fracture mode at this temperature is mostly interparticle ductile dimple. At 1000°C, the main difference to 900°C is formation of cleavage facets with river pattern which is the result of formation of stronger sintering bonds. It is evident that the amount of these fracture facets is higher in the samples compacted at 700 MPa than at 500 MPa, while almost no cleavage facets are visible in the fracture surface of the samples compacted at 300 MPa. The fractographs also show that at the higher temperatures and above 1000°C, sintering led to increased transgranular cleavage fracture in the samples with higher density compacted at 500 and 700 MPa, while the samples compacted at low pressure (300 MPa) which are more loosely packed, show interparticle dimple fracture even at the high sintering temperature of 1300°C.

Figure 3.11 shows the fracture surfaces of Fe-1.5Mo-0.8C after the Charpy impact test. Similar to carbon steel, no sintering bridges are visible at 700°C. According to the fractographs, formation of the initial sintering contacts has started from 800°C, however compared to the Fe-C system, weaker sintering bonds are visible in the Mo alloyed steels at this sintering temperature. Similar to carbon steel, in this case as well, larger surface contacts between the original powder particles, resulting from compacting at higher pressure, led to formation of stronger sintering contacts. Visual evaluation of the images shows that sintering at higher temperatures leads to higher fraction of cleavage facets for samples compacted at 500 and 700 MPa, while the smaller and thus weaker sintering bonds between the particles in samples compacted at 300 MPa resulted in an interparticle dimple pattern in the entire range of sintering temperatures. Similar to carbon steel, it explains that more loose packing of powder resulting from lower compacting pressure will limit material transfer and development of larger sintering contacts even at the higher sintering temperatures.



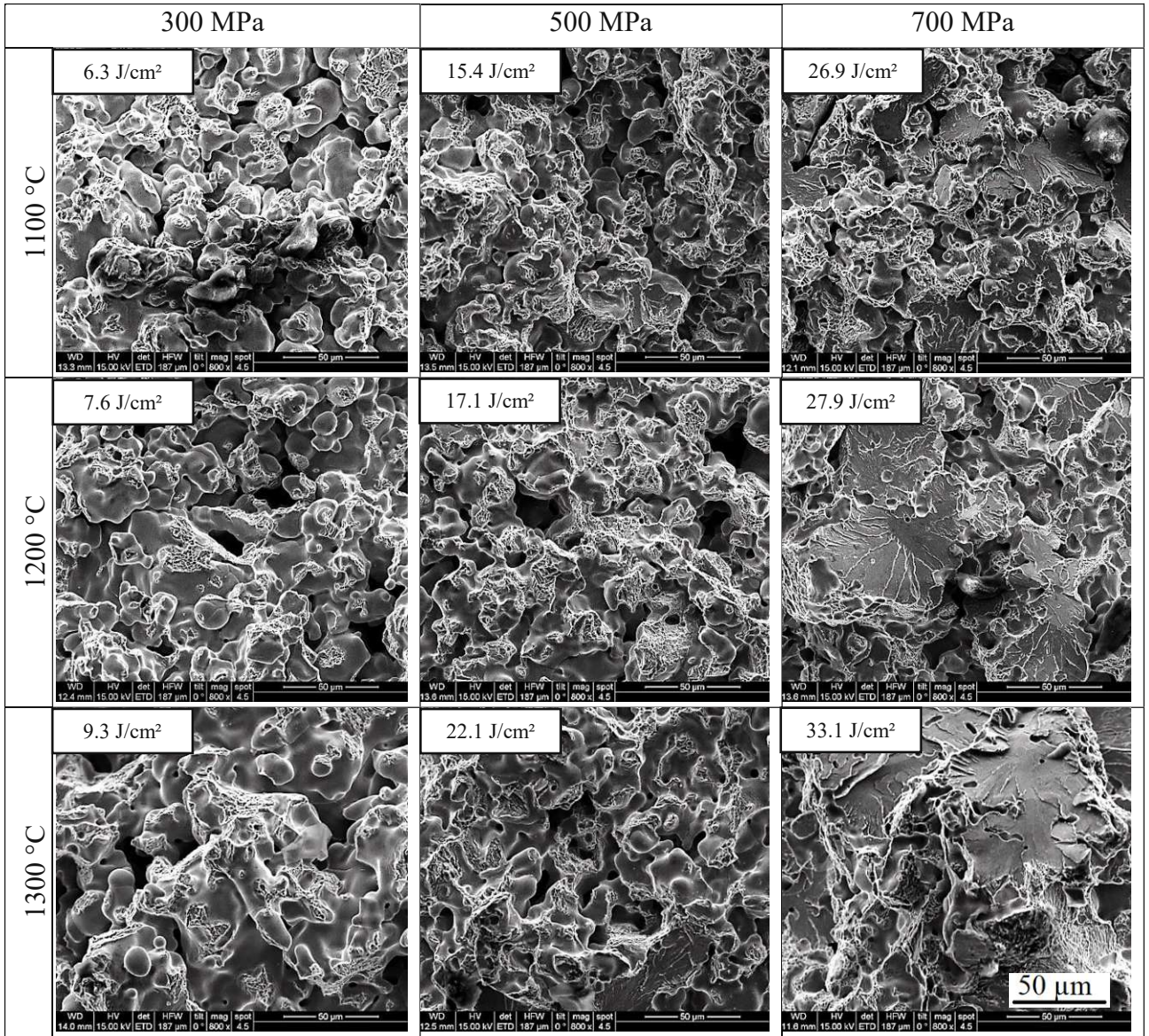
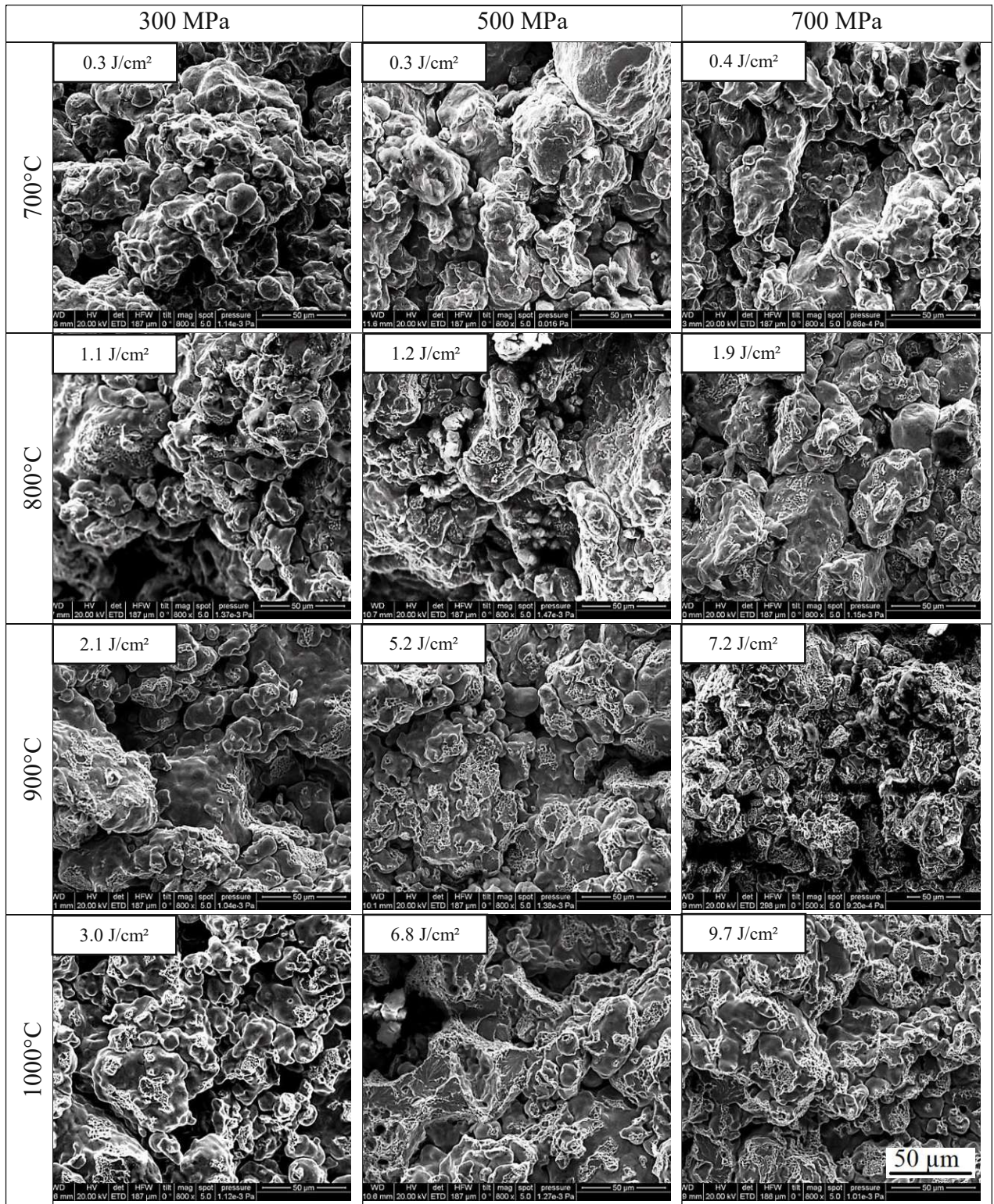


Figure 3.10: Fracture surfaces of Fe-0.8%C_{admixed} (broken at room temperature by Charpy impact test), compacted at different pressures, Sintered 60 min in Ar, 800x. (scale bar 50µm holds for all images)



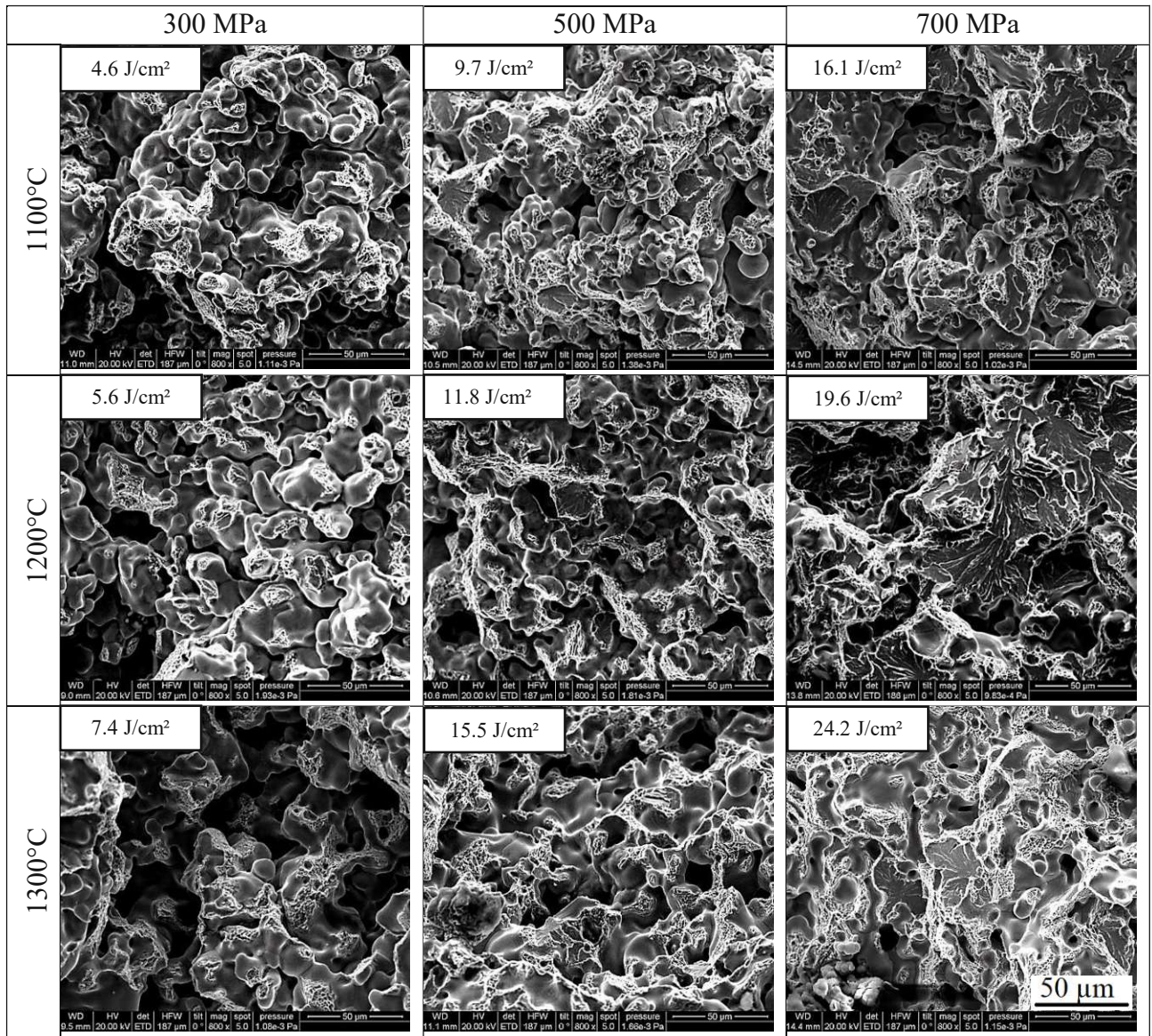


Figure 3.11: Fracture surface of Fe-1.5%Mo-0.8%C_{admixed} (broken at room temperature by Charpy impact test), compacted at different pressures, Sintered 60 min in Ar, 800x. (scale bar 50µm holds for all images)

3.1.4. Sintered density and dimensional change

The dimensional change during sintering of PM steels is affected by different phenomena. For instance, incorporation of the carbon atoms into the iron lattice results in a growth in volume [11, 41] while some phenomena such as pore elimination and transport of material from the cores of sintering necks to the surface could lead to shrinkage = negative dimensional change.

The effect of compacting pressure and sintering temperature on the sintered density for both steel grades is shown in Figure 3.12. It is obvious that the density mainly depends on the compacting pressure, with a slightly positive effect of the higher sintering temperatures, however the temperature effect is less visible in the samples compacted at higher pressure, while samples compacted at 300 MPa showed more change of the density after sintering at different temperatures. In Figure 3.13, the dimensional change of the steels is plotted vs the

sintering temperature. From 700 to 1000°C, dimensional behaviour in both steels seems to be similar, a progressive expansion, caused by uptake of carbon atoms by the iron lattice, is visible in all the samples. It is obvious that in this temperature range, the samples with lower densities showed higher expansion compared to the high density parts. A possible reason for this could be related to the higher carbon dissolution in the low density parts which was discussed in the metallography results. Above 1000°C and after carbon dissolution is finished, there follows a shrinkage during sintering at higher temperatures. Both groups of material show almost the same behaviour, after an expansion at the initial stage of sintering the samples then started to shrink continuously from 1000 to 1300°C, and those with higher densities showed less shrinkage in this temperature range.

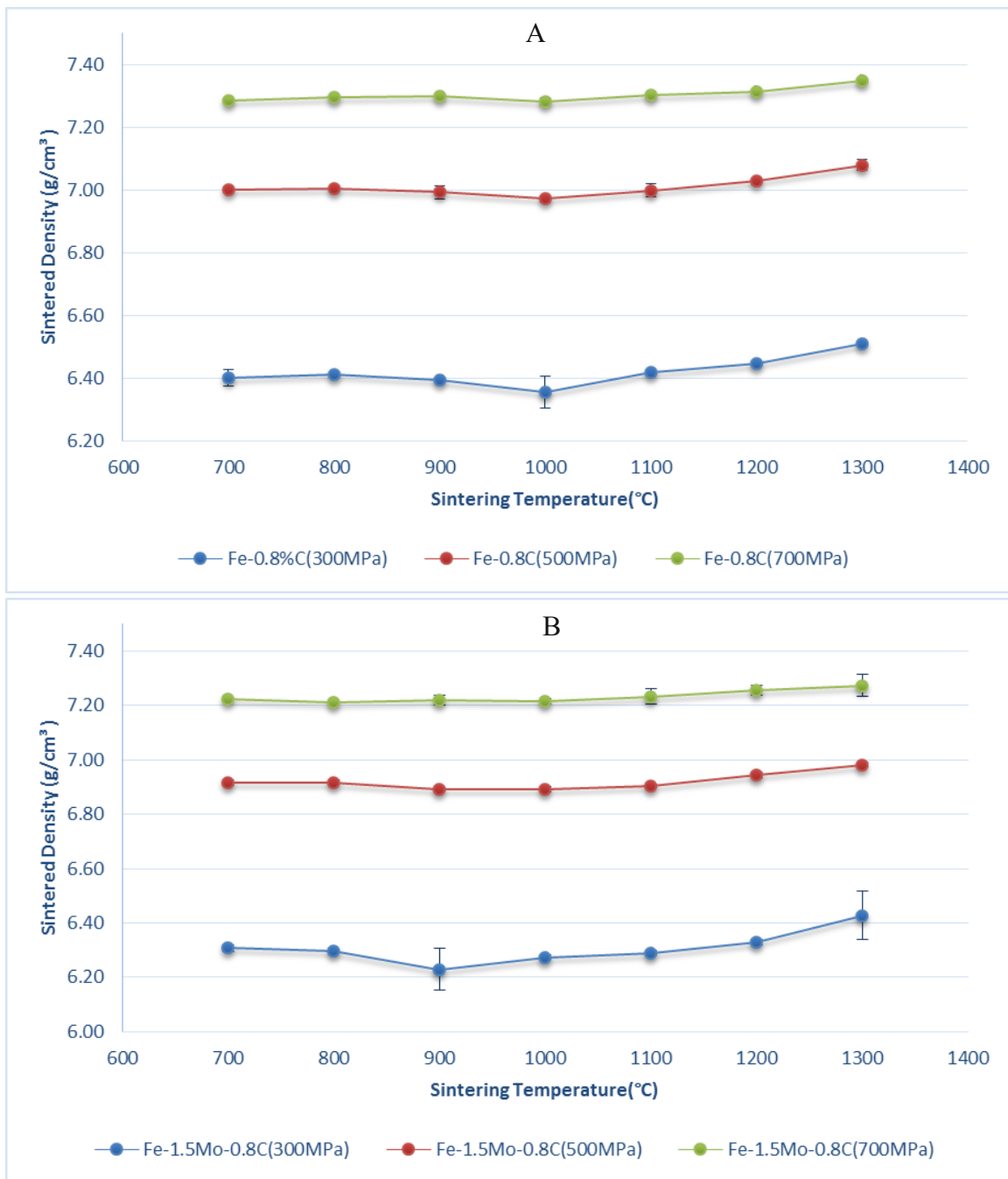


Figure 3.12: Sintered density of samples compacted at different pressures versus sintering temperature (sintered 60 min in Ar); A: Fe-0.8%C_{admixed}, B: Fe-1.5%Mo-0.8%C_{admixed}.

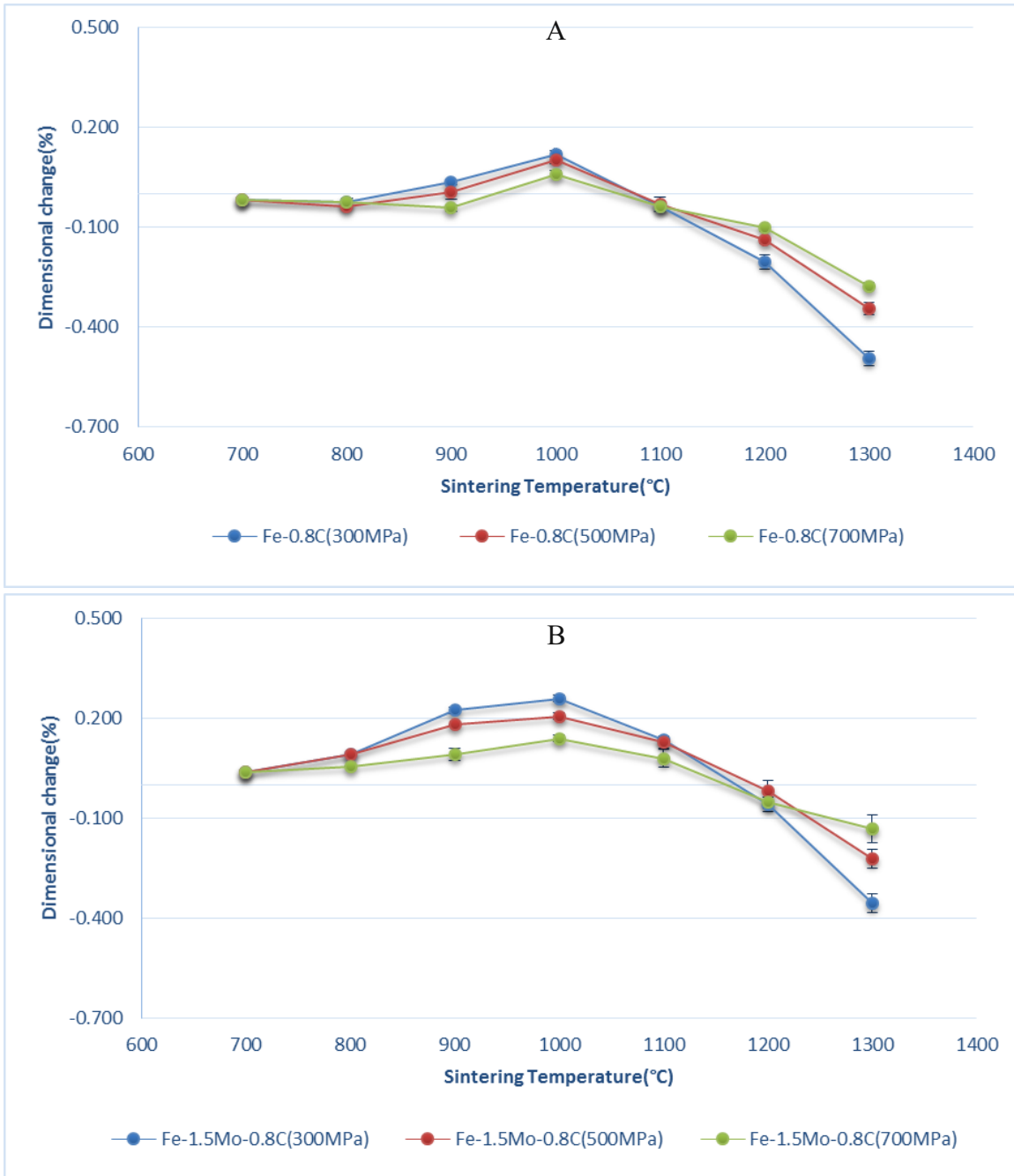


Figure 3.13: Dimensional change of samples compacted at different pressures versus sintering temperature (sintered 60 min in Ar); A: Fe-0.8%C_{admixed}, B: Fe-1.5%Mo-0.8%C_{admixed}.

3.1.5. Mechanical properties

3.1.5.1. Charpy impact energy

It is well known that mechanical properties of sintered materials are strongly influenced by the sintering temperature [63]. Processes such as development of the sintering contacts and pore rounding at higher temperatures as well as distribution of alloying elements play a key role in increasing the impact energy of the PM steels. The data for the impact energy consumed to break the Charpy specimen at room temperature are given in Figure 3.14. The upward trend of the impact energy versus the sintering temperature indicates a direct relationship between these two parameters. However, according to the equation of the trend lines the rate of the raise is not the same at different compacting pressures, and increasing the compacting pressure raised the slope of the trend line in both grades of steels. The results show that at the higher compacting pressures (higher green densities), the sintering temperature has a more pronounced effect on the raise of the impact energy, which is a consequence of the stronger sintering bonds and is in agreement with previous studies [25, 58]. The graphs also show that at the same sintering temperature, carbon steel (Fe-0.8C) with ferrite-pearlite microstructure which has lower hardness has higher impact energy compared to Mo alloyed steel (Fe-1.5Mo-0.8C) which showed bainitic microstructure and higher hardness. However, in this case the sintered density could also play a role, and in addition to the higher hardness of bainitic microstructure, the slightly lower density of Mo alloyed steels could be another reason for the lower impact energy. Figure 3.15 presents the relationship between the sintered density and the impact energy. It is clearly obvious that increasing compacting pressure and resulting green density as well as the sintering temperature play a significant role on the impact energy.

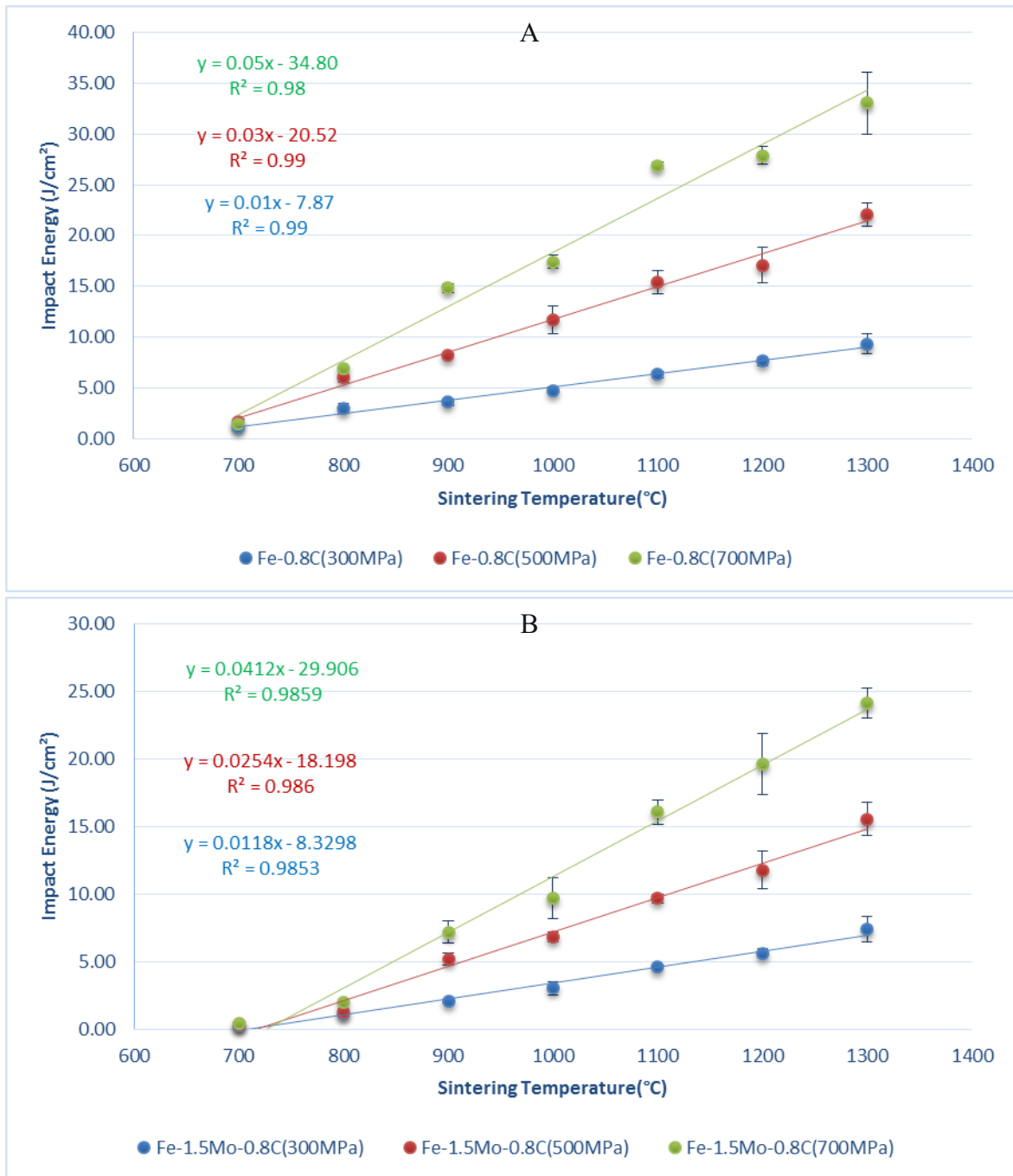


Figure 3.14: Impact energy as a function of the sintering temperature, compacted at different pressures. Sintered 60 min in Ar; A: Fe-0.8%C_{admixed}, B: Fe-1.5%Mo-0.8%C_{admixed}.

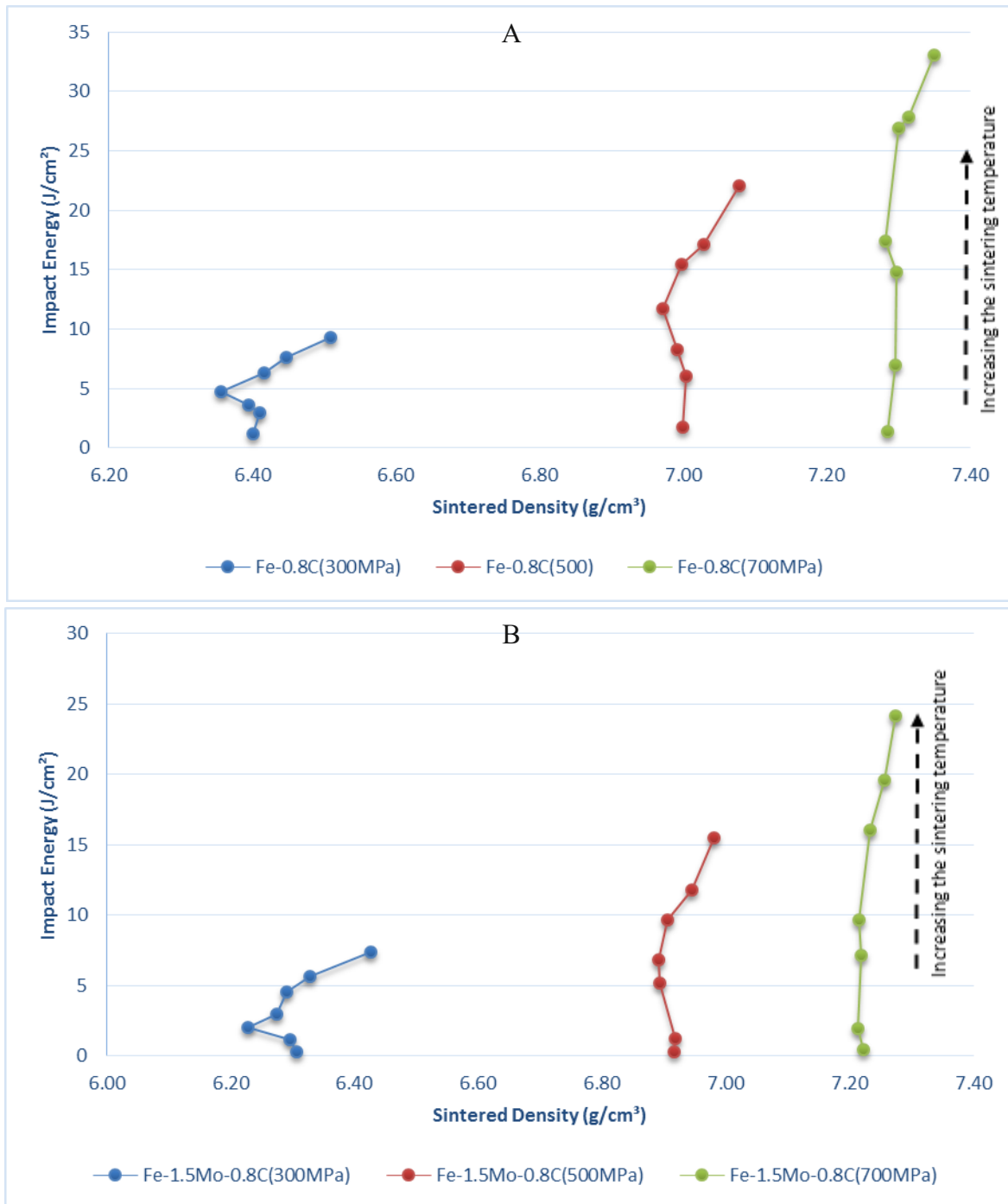


Figure 3.15: Relationship between impact energy and sintered density of steels compacted at different pressures; sintered between 700 and 1300°C, 60 min in argon; A: Fe-0.8%C_{admixed}, B: Fe-1.5%Mo-0.8%C_{admixed}.

3.1.5.2. Hardness

The results of the hardness measurement of Fe-0.8C and Fe-1.5Mo-0.8C are presented in Figure 3.16. According to these results, increasing the compacting pressure and resulting higher density of the steels led to higher hardness (See also Figure 3.17). Dissolution of carbon into the iron lattice at the initial stages of the sintering and below 1100°C, as shown in the metallography sections, is the main reason for increased hardness. However, above 1100°C, formation of stronger sintering contacts can influence the hardness as well. In the carbon steel, pearlite formation increases the hardness while for the Mo steel, presence of molybdenum in the solid solution of Mo prealloyed steel and formation of the bainitic microstructure as a consequence of carbon dissolution is the reason of this raise. As can be seen, in the carbon steels the main increase in the hardness was achieved after sintering at 1000°C. It shows that most of the carbon dissolution occurred at this temperature which is in good agreement with the results of dimensional change and metallography (Figure 3.7 and 3.13). Increasing the temperature to 1100 and 1200°C increased the hardness as well, however this raise at higher temperature is less significant. As mentioned before, a reason for the raise in this temperature ranges could be related to the formation of stronger sintering contacts which increases the resistance of the material against indentation. At 1300°C, the values for hardness saw less change compared to 1200 °C.

One point that should not be neglected here is carbothermal reduction and the resulting carbon loss, which can compensate the positive effect of densification on hardness, especially after sintering at higher temperatures which results in higher carbon loss (see the results of carbon measurement of Fe-C sintered in Ar in the module b of this part). Similar to Fe-C, an upward trend of the hardness with higher sintering temperature is also discernible for Fe-Mo-C steels. In this steel a pronounced increase of the hardness was attained after sintering at 900°C which is a lower temperature compared to the Fe-C system. Formation of bainitic microstructure due to carbon dissolution at 900°C is the main reason of this raise (see also the microstructures in Figure 3.9). Completion of the carbon dissolution as well as sintering neck enlargement are two processes which have positive effects on the hardness at the moderate and high sintering temperature, respectively. The relationship between the impact energy and the hardness of the steels is presented in Figure 3.18. It is obvious that increasing the compacting pressure resulted in both higher hardness and impact energy of the steels, which at least for a first assessment are the main mechanical properties of the materials.

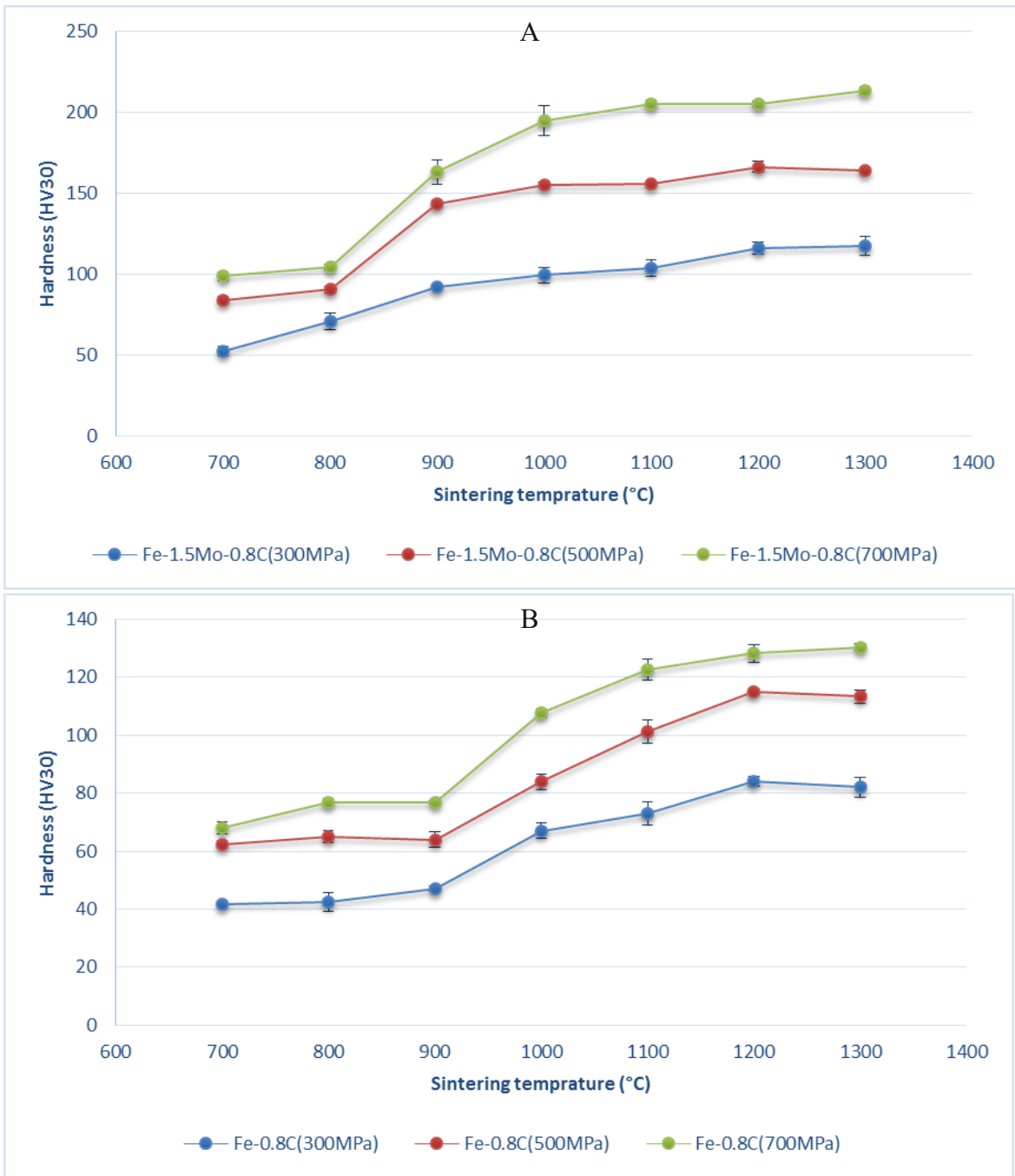


Figure 3.16: Hardness HV30 as a function of the sintering temperature, compacted at different pressures, Sintered 60 min in Ar; A: Fe-0.8%C_{admixed}, B: Fe-1.5%Mo-0.8%C_{admixed}.

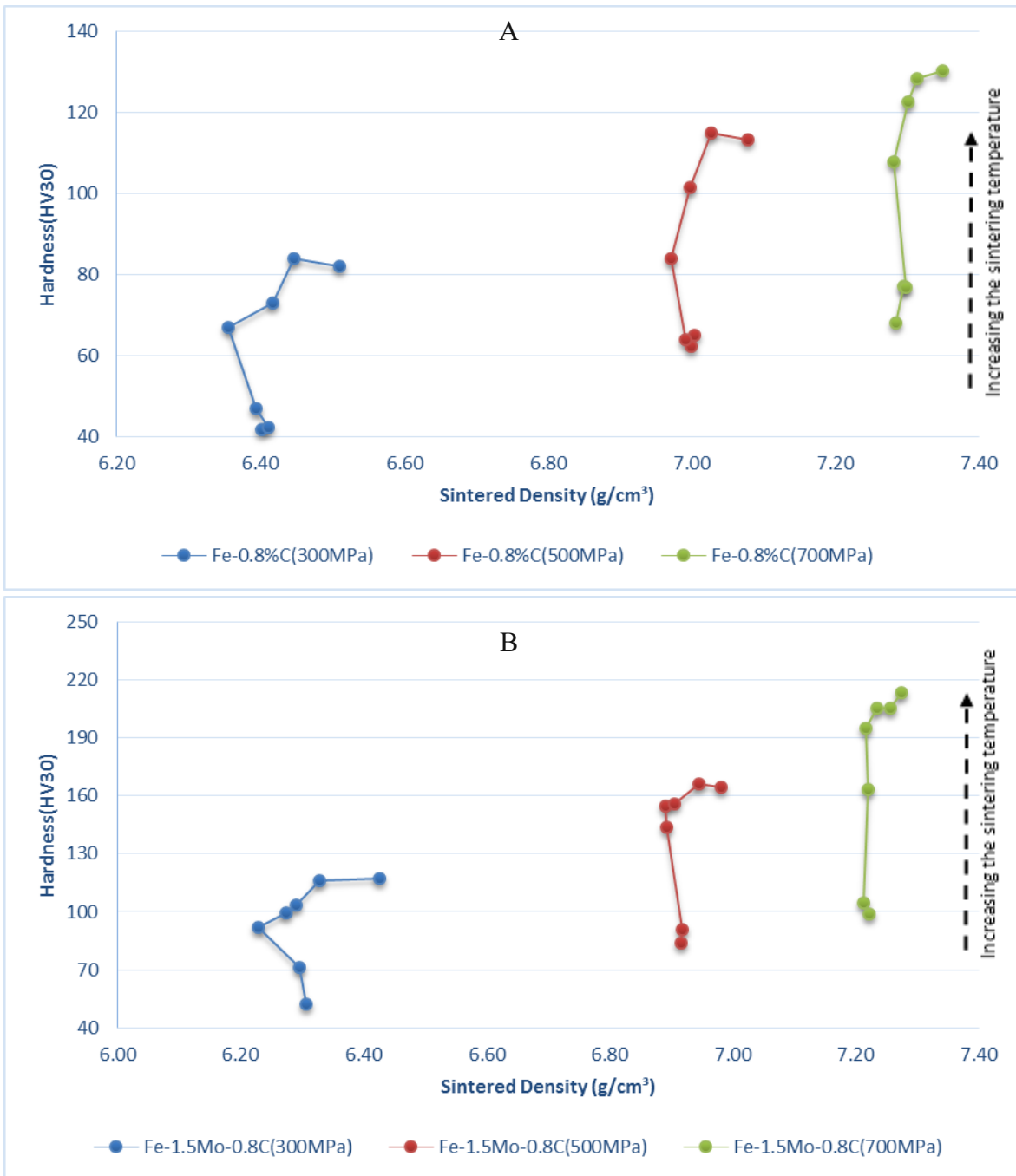


Figure 3.17: Relationship between hardness and sintered density of steels compacted at different pressures; sintered between 700 and 1300°C, 60 min in argon; A: Fe-0.8%C_{admixed}, B: Fe-1.5%Mo-0.8%C_{admixed}.

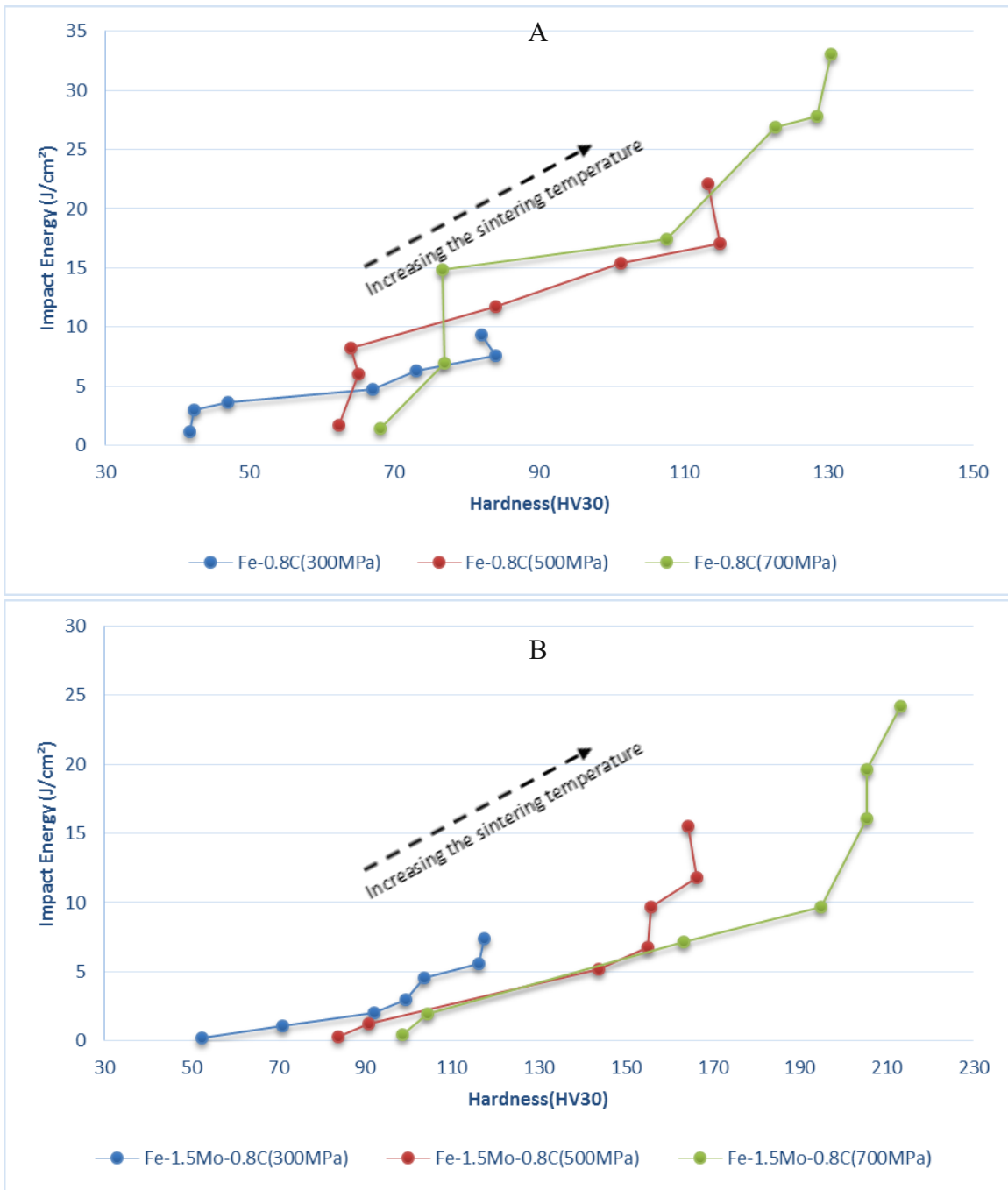


Figure 3.18: Relationship between impact energy and hardness of steels compacted at different pressures; sintered between 700 and 1300°C, 60 min in argon; A: Fe-0.8%C_{admixed}, B: Fe-1.5%Mo-0.8%C_{admixed}.

3.1.5.3. Dynamic Young's modulus

In order to describe the effect of the compacting pressure and the green density on the dynamic Young's modulus (dyn. E) of PM steels during sintering, the dynamic Young's modulus of the steels Fe-0.8C and Fe-1.5Mo-0.8C has been plotted as a function of the sintering temperature at three different compacting pressures of 300, 500 and 700 MPa (Figure 3.19). It is evident from the results that increasing the compacting pressure and the density affected the Young's modulus significantly and increased it. The graphs show that for both steel grades and at all densities, the Young's modulus showed a sharp raise between 700 and 800°C, indicating formation of the first sintering contacts. This is then followed by a gradual upward trend with higher sintering temperature up to 1300°C, which is in good agreement with the results of some previous studies [145, 146]. In Figure 3.19, the slopes of the trend lines above 800°C show that unlike the impact energy, in this case, the rate of increase with the sintering temperature is almost identical at different compacting pressures and is thus independent of the green density. The relationships between the dynamic Young's modulus and the sintered density of steels are presented in Figure 3.20. These graphs show that increasing the temperature always increased the dyn. Young's modulus even when there is expansion and density reduction. Linear relationships between dynamic Young's modulus and impact energy are presented in Figure 3.21.

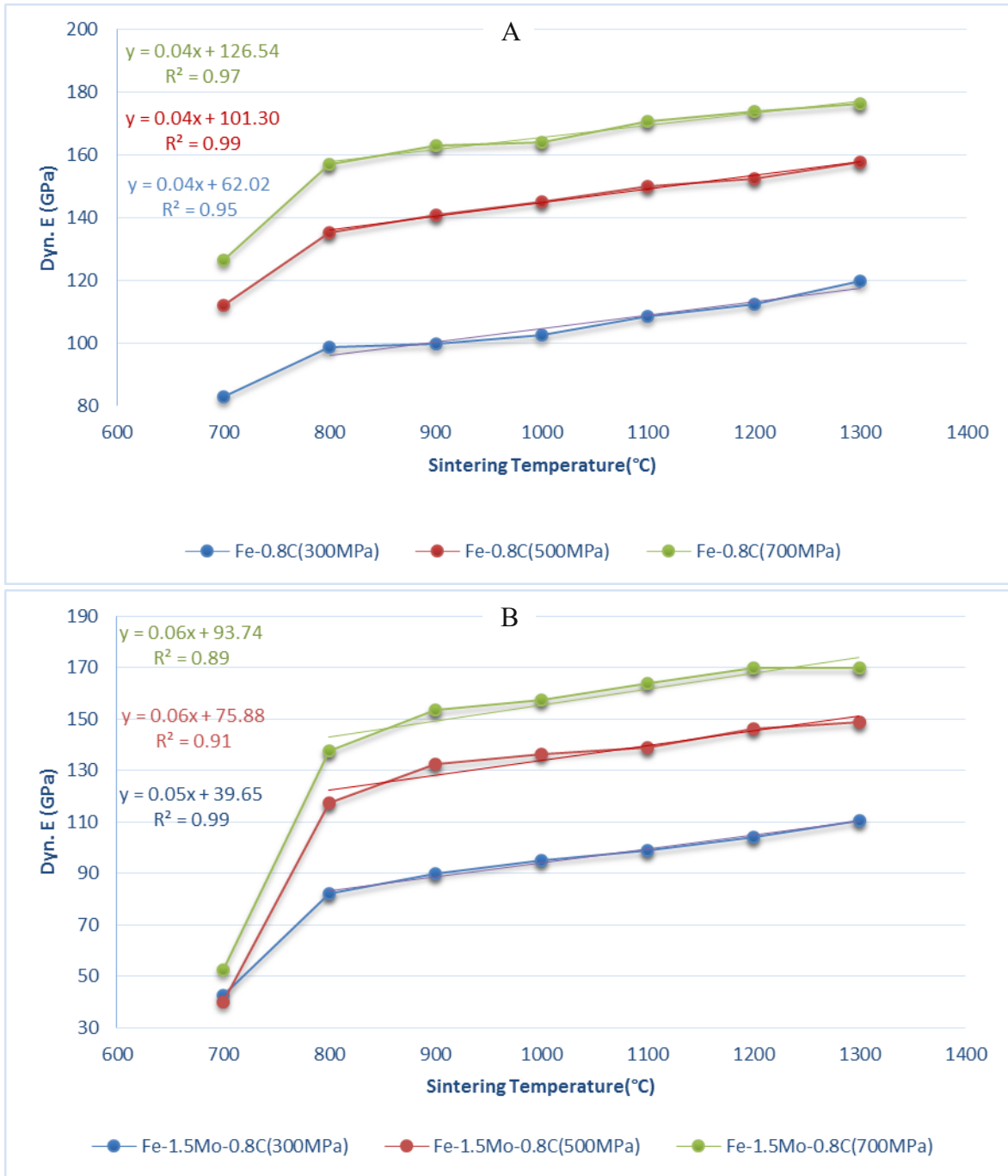


Figure 3.19: Dynamic Young's modulus as a function of the sintering temperature, compacted at different pressures, Sintered 60 min in Ar; A: Fe-0.8% C_{admixed} , B: Fe-1.5%Mo-0.8% C_{admixed} .

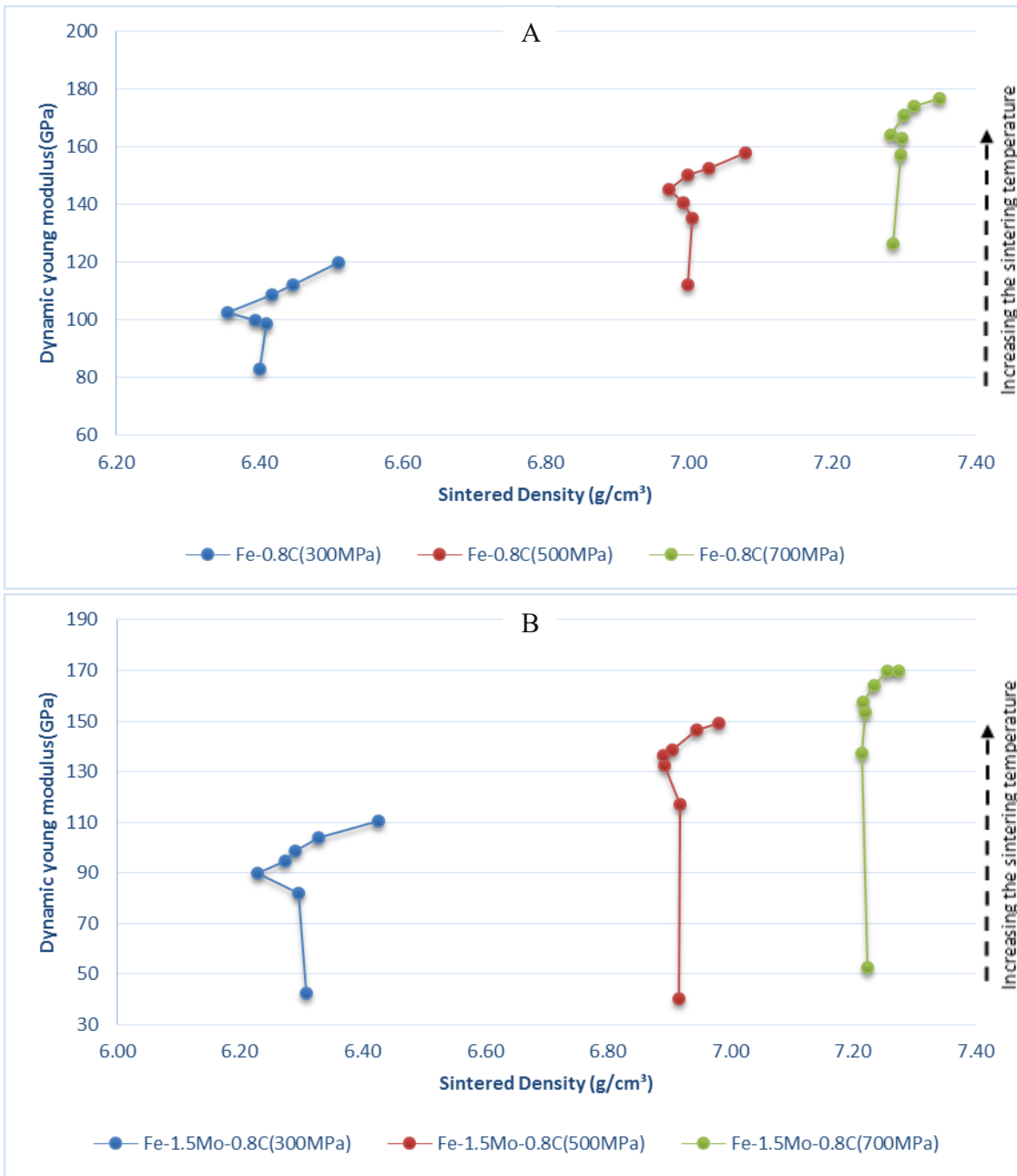


Figure 3.20: Relationship between dynamic Young's modulus and sintered density of steels compacted at different pressures; sintered between 700 and 1300°C, 60 min in argon; A: Fe-0.8%Cadmixed, B: Fe-1.5%Mo-0.8%Cadmixed.

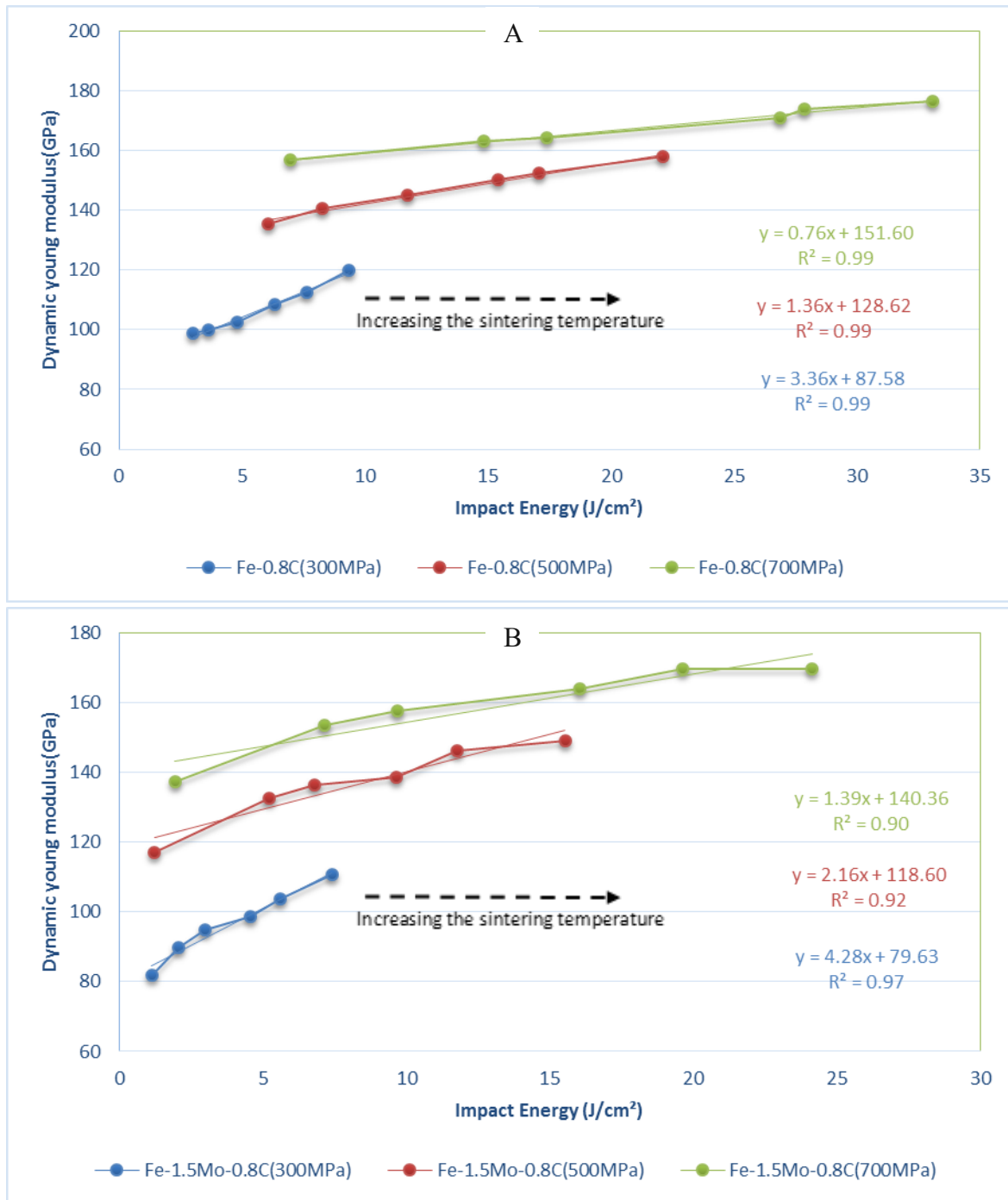


Figure 3.21: Relationship between dynamic Young's modulus and impact energy of steels compacted at different pressures; sintered between 800 and 1300°C, 60 min in argon; A: Fe-0.8%C_{admixed}, B: Fe-1.5%Mo-0.8%C_{admixed}.

3.1.5.4. Damping

Damping of the materials as a function of the sintering temperature is presented in Figure 3.22. The damping or Q-factor represents the energy absorption by the material. Results of damping, measured through amplitude decay, show the highest values for the steels sintered at 700°C, while the parameter dropped significantly at 800°C as soon as the first sintering bridges between

the particles are formed, although during subsequent sintering at higher temperature, less effect on this parameter has been observed. The results of this figure as well as the results presented in Figure 3.23 also indicate that, above 800°C, steels with lower densities (compacted at lower pressure) have higher damping ability compared to those with higher densities. The relationship between the damping parameter and dynamic Young's modulus is presented in Figure 3.24.

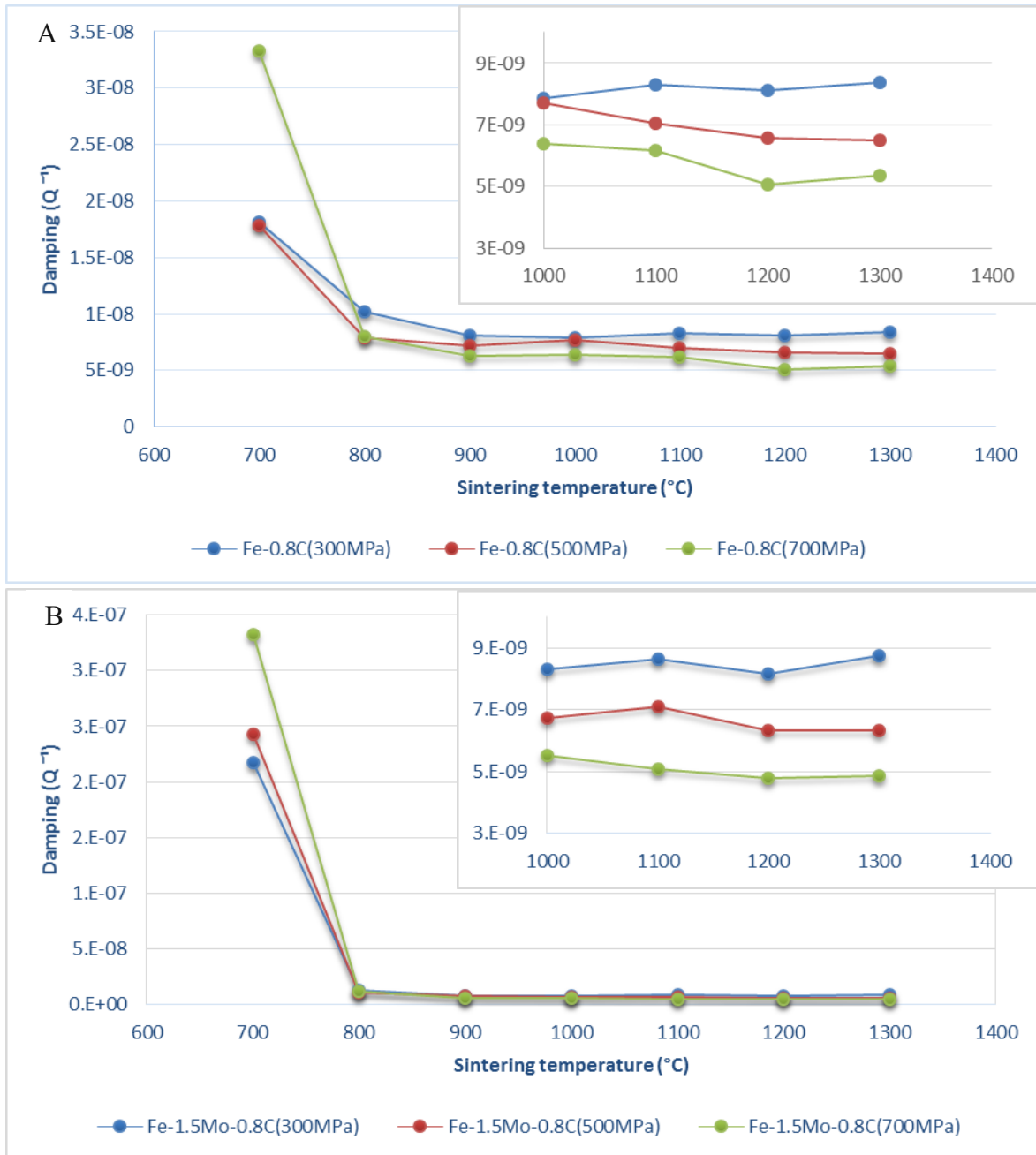


Figure 3.22: Damping parameter Q^{-1} of steels as a function of the sintering temperature, compacted at different pressures, Sintered 60 min in Ar, A: Fe-0.8%C_{admixed}, B Fe-1.5%Mo-0.8%C_{admixed}.

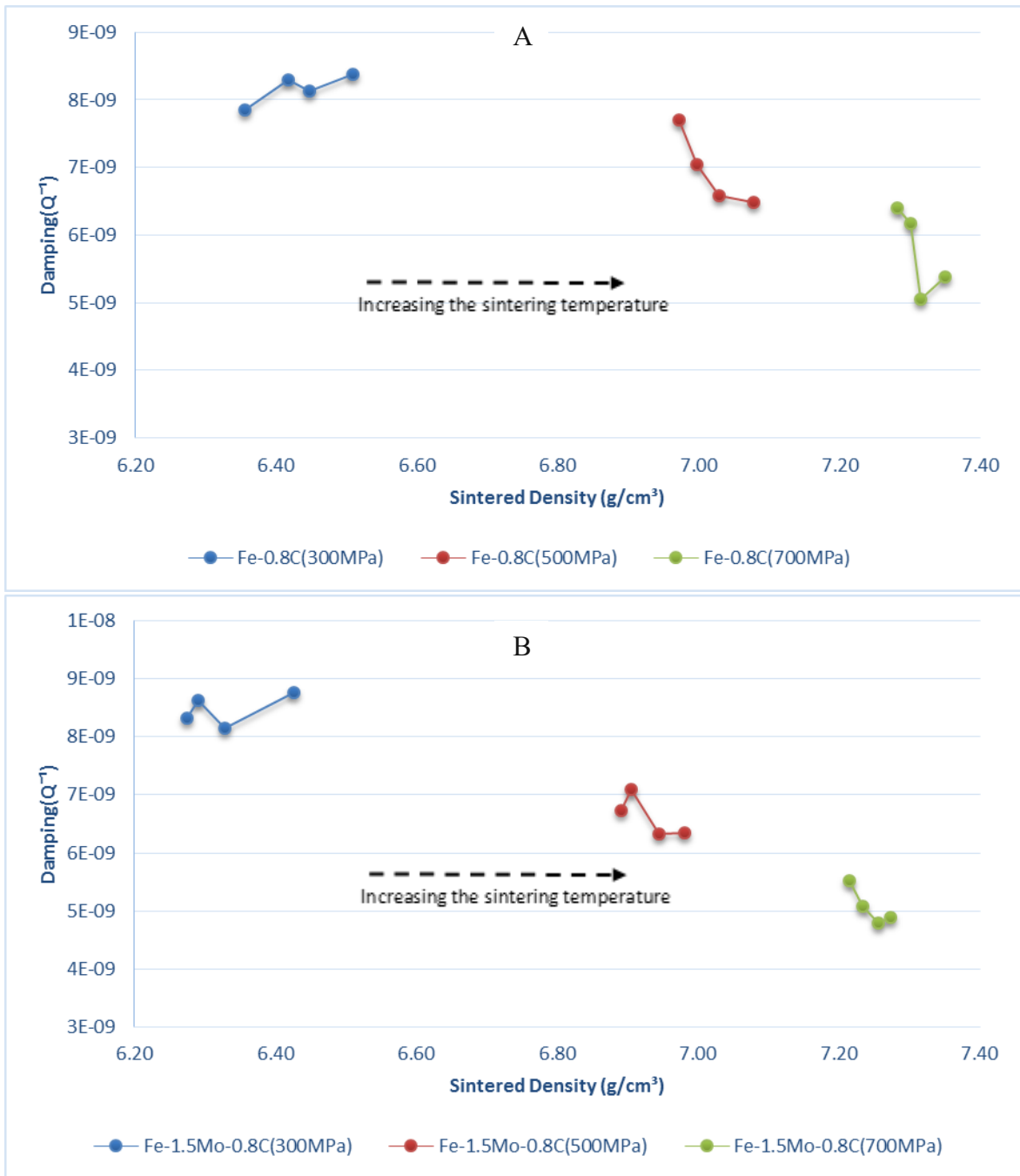


Figure 3.23: Relationship between sintered density and damping parameter of steels compacted at different pressures; sintered between 1000 and 1300°C, 60 min in argon; A: Fe-0.8%C_{admixed}, B: Fe-1.5%Mo-0.8%C_{admixed}.

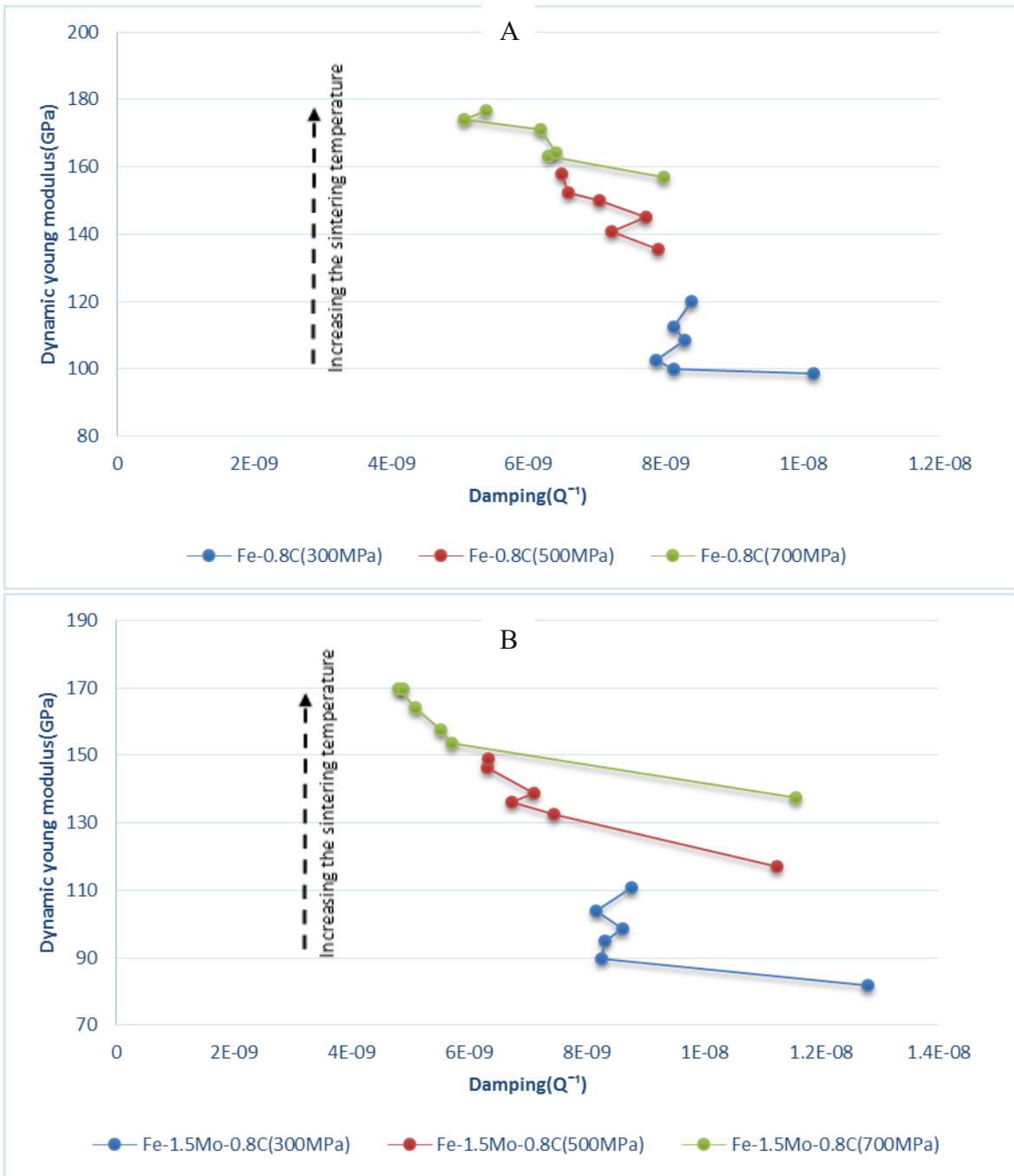


Figure 3.24: Relationship between dynamic Young's modulus and damping parameter of steels compacted at different pressures; sintered between 800 and 1300°C, 60 min in argon; A: Fe-0.8%Cadmixed, B: Fe-1.5%Mo-0.8%Cadmixed.

3.1.6. Physical properties

3.1.6.1. Electrical conductivity

The electrical conductivity of the steels is presented in Figure 3.25. Both groups of steels showed a rapid increase of the conductivity at 800°C, attributed to oxygen removal from the surface of the powder particles and stress relaxation in the grains [115, 118]. It is well known that above 800°C, the electrical conductivity of the compacts is influenced by different processes, carbon dissolution in the iron lattice and resulting pearlite formation which reduces the electrical conductivity. On the other hand, reduction of surface oxides, neck formation, developing sintering contacts can increase the conductivity of PM parts during sintering at higher temperatures [115, 118, 120]. For both groups of steels, Fe-C and Fe-Mo-C, a major decline in the electrical conductivity occurred at 1000 and 900°C, respectively. As described before, these are the temperatures in which most of the carbon is dissolved, which is in good agreement with the results of dimensional change and metallography as presented in Figs. 3.7, 3.9 and 3.13. Above these temperatures and after completion of carbon dissolution, sintering results in slight shrinkage, growth of sintering contacts and thus neck enlargement (between 1100 and 1300°C). In this range of the temperature, the steels showed less change of the electrical conductivity, which agrees with Simchi's results [115] who states that the most pronounced effects of sintering contact formation and growth occur in the medium temperature range. For the estimation of electrical properties of the material, plotting the electrical conductivity vs. the sintered density in this temperature range and after completion of the carbon dissolution is useful (Figure 3.26). Good fitting of the data with trend lines in Figure 3.26 allows to use the presented linear equations to estimate or predict the electrical conductivity according to the measured sintered density for each steel.

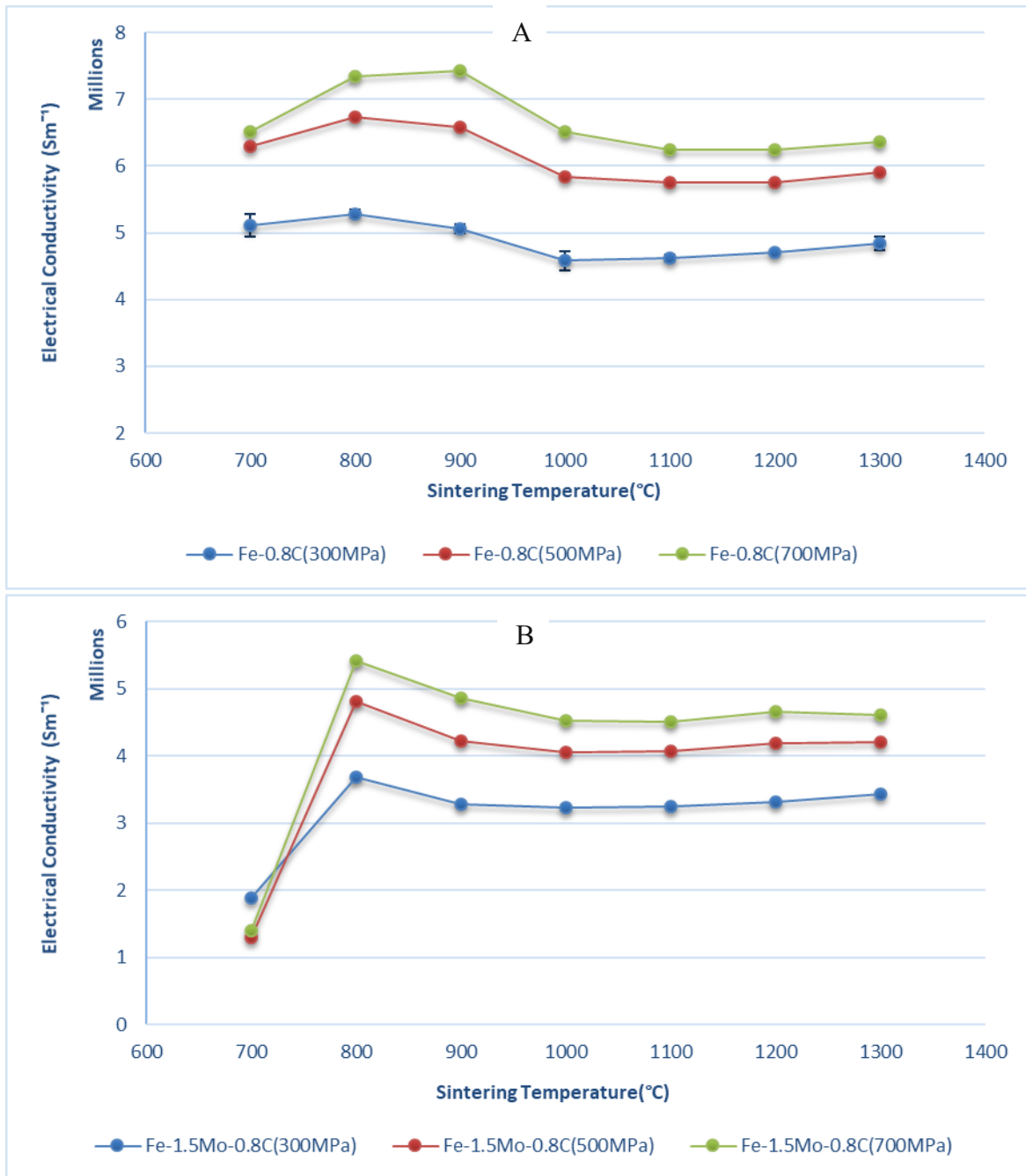


Figure 3.25: Electrical conductivity of steels as a function of the sintering temperature, compacted at different pressures, Sintered 60 min in Ar, A: Fe-0.8%C_{admixed}, B: Fe-1.5%Mo-0.8%C_{admixed}.

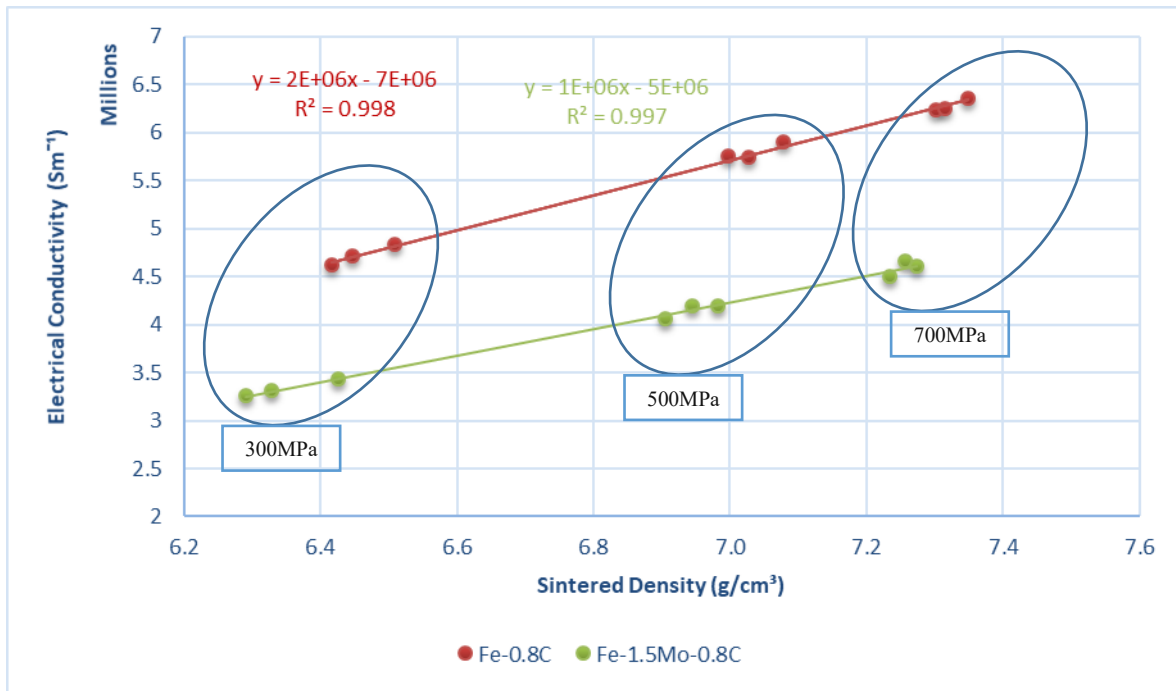


Figure 3.26: Electrical conductivity vs. sintered density for samples sintered between 1100 and 1300°C.

3.1.6.2. Coercive force

The coercive force data are shown in Figure 3.27. An upward trend between 700 and 1000°C is discernible for all groups of the steels. It shows that the carbon dissolution in both steel grades increases the coercive force of the material. However, it is evident that this raise is more pronounced in the Mo steels compared to the carbon steels. In the Mo steels we can also see a reasonable relationship between the density and coercivity, and it is evident that in this steel increasing the compacting pressure decreased the coercivity values, however such relationship is less visible in the carbon steel grade. Above 1000°C, the changes in the magnetic property of the materials are less significant, which shows that the effect of carbon dissolution is more pronounced compared with pore coarsening or rounding. The results also show that unlike the electrical conductivity, the coercivity is less affected by the sintered density or the amount of porosity.

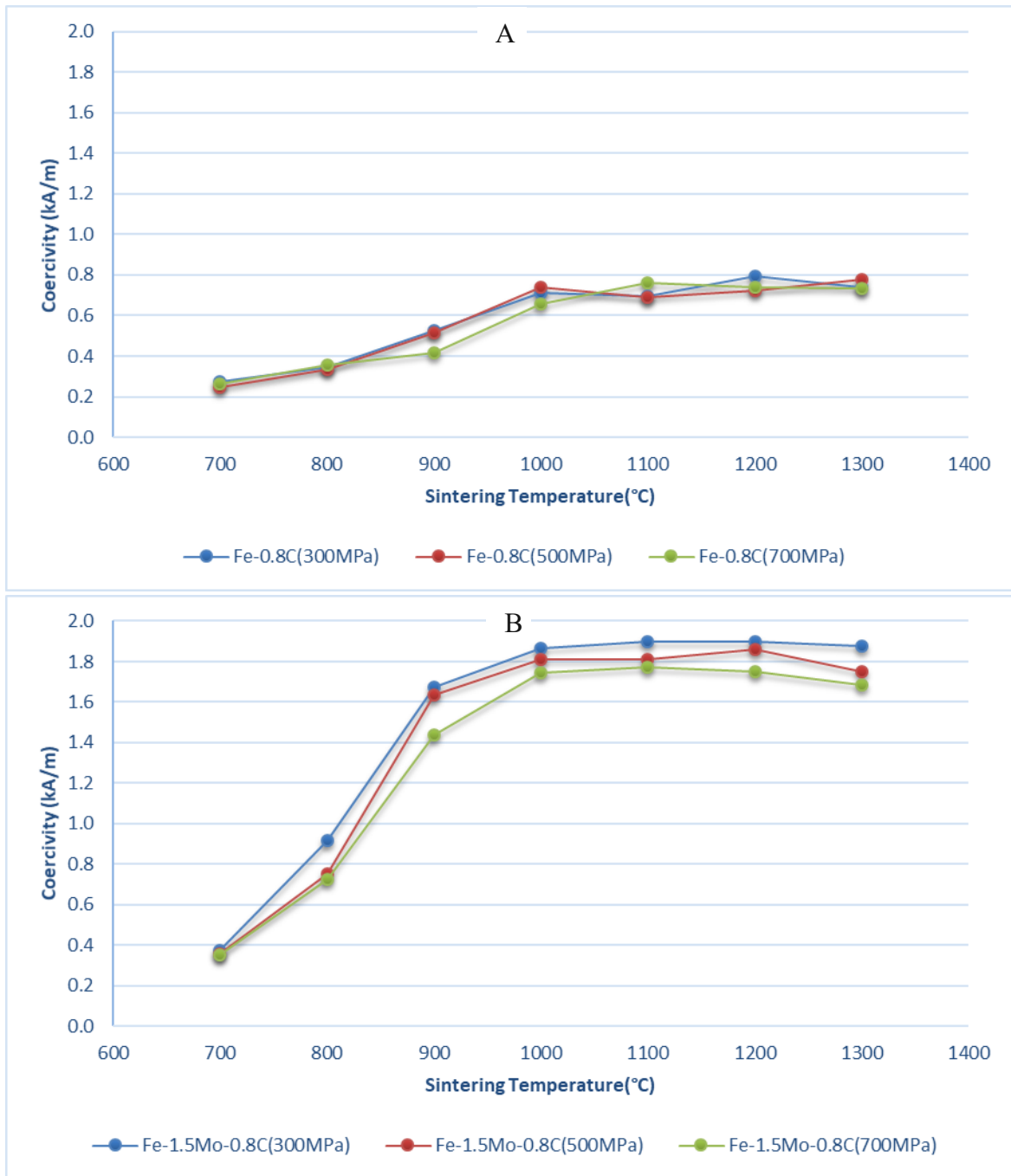


Figure 3.27: Coercivity of steels as a function of sintering temperature, compacted at different pressures, Sintered 60 min in Ar, A: Fe-0.8% C_{admixed}, B: Fe-1.5%Mo-0.8% C_{admixed}.

3.2. Part 1b: Effect of the sintering atmosphere on physical and chemical processes during sintering of ferrous PM components

Reactions with the atmosphere during heat treatment of steels can be significantly more intense with PM compacts than with ingot metallurgy parts, due to the dramatically larger specific surface in the porous PM parts. Thus, using a protective atmosphere during each thermal cycle is necessary to avoid oxidation of parts or other unwelcome reactions and also remove the oxide layers which cover the powder particles. Well selected pure sintering atmospheres not only prevent undesirable reactions but also remove impurities such as oxygen or carbon, resulting in products with desired mechanical, electrical or magnetic properties [147]. Using an inert atmosphere like argon would be useful when no chemical reactions with iron particles are expected while an atmosphere like H₂ can perform as a reducing agent and it can impact the other sintering processes [51]. As mentioned in Chapter 1, in addition to the removal of oxides through a reducing atmosphere, another possible mechanism for this process is carbothermal reduction, carbon acting as reducing agent both as element and in carbon monoxide [98]. Therefore, carbon in PM steels can also be used as a reducing agent in addition to being an alloying element. As explained above, another important phenomenon during sintering of PM steels is carbon dissolution, the added graphite is expected to rapidly and completely dissolve during sintering [11] and as stated in chapter 1.4.2.2, two different mechanisms, solid state diffusion and gas phase transport, have been claimed to be the relevant processes. The present chapter describes an investigation on the effect of two different sintering atmospheres – inert and reducing - on processes like deoxidation, dissolution of carbon in the iron lattice and also formation of sintering contacts during the initial stages of sintering. This study was performed in both presence (Fe-C) and absence (Fe) of the carbothermal reactions. Water atomized iron (ASC 100.29, Höganäs AB Sweden) was used as base powder, and 0.8% carbon was introduced as natural graphite (grade UF4, Kropfmühl). Two grades of materials, plain Fe and Fe-0.8C (admixed), were prepared for this study (Table 3.4).

Table 3.4: Material composition of mixes.

	Designation	Mix Composition
1	Fe	ASC100.29
2	Fe-0.8C	ASC100.29 + 0.8% C _{admixed}

Charpy bars (ISO 5754) were pressed for this study at 600 MPa, die wall lubrication being afforded (Multical sizing fluid). Sintering of the samples was performed in the SiC rod heated electrical laboratory furnace at temperatures varying in the range 700-1300°C (interval 100°C) for 1 hr under plain Ar and H₂ (99.999 quality each). After the holding period at temperature, the samples were cooled in the water-jacketed exit zone. Cooling and sintering atmosphere was the same in case of argon, while the samples sintered in hydrogen were cooled in nitrogen. Dilatometry in combination with mass spectrometry (MS) offers the possibility of in-situ studying dimensional and chemical sintering effects in PM materials [98, 148]. In this work, also the DIL/MS experiments were performed in Ar and H₂, both gases in 5.0 grade (99.999% purity). Heating and cooling were done at 10 K/min. The results of the measurements are listed in Tables 3.5 and 3.6. The carbon content given in Table 3.6. is the combined carbon content, i.e. the content measured by LECO on the sintered samples.

Table 3.5: Sintered properties of plain iron (Fe); compacted at 600 MPa, sintered 60 min at 700-1300°C in hydrogen and argon.

<i>Sintering Temperature</i> (°C)	<i>Sintering atmosphere</i> (°C)	<i>Sintered density</i> (g/cm ³)	<i>Dimensional change</i> (%)	<i>Impact energy</i> (J/cm ²)	<i>Hardness (HV30)</i>	<i>Dyn. Young's modulus (GPa)</i>	<i>Oxygen content (wt %)</i>	<i>Electrical conductivity (S.m⁻¹)10⁴</i>	<i>Coercivity (kA/m)</i>
700	H ₂	7.23 ± 0.00	-0.07 ± 0.01	11.0 ± 3.6	71.7 ± 8.5	161.1	0.076 ± 0.004	792	0.22
	Ar	7.21 ± 0.01	-0.04 ± 0.00	0.5 ± 0.1	75.5 ± 1.7	154.0	0.110 ± 0.076	772	0.24
800	H ₂	7.25 ± 0.00	-0.08 ± 0.01	21.6 ± 6.2	64.7 ± 4.0	159.1	0.059 ± 0.002	783	0.20
	Ar	7.20 ± 0.01	-0.04 ± 0.00	0.7 ± 0.2	67.7 ± 1.5	156.2	0.134 ± 0.028	791	0.21
900	H ₂	7.24 ± 0.00	-0.17 ± 0.02	32.7 ± 3.0	58.0 ± 1.0	164.6	0.051 ± 0.021	777	0.17
	Ar	7.20 ± 0.1	-0.07 ± 0.00	0.5 ± 0.1	61.0 ± 1.0	169.9	0.149 ± 0.034	803	0.20
1000	H ₂	7.21 ± 0.01	-0.08 ± 0.01	46.6 ± 7.5	62.3 ± 1.2	165.8	0.033 ± 0.001	760	0.17
	Ar	7.22 ± 0.01	-0.18 ± 0.04	1.8 ± 0.3	54.7 ± 2.5	163.4	0.105 ± 0.011	815	0.19
1100	H ₂	7.21 ± 0.01	-0.11 ± 0.05	45.3 ± 3.4	59.3 ± 0.6	165.6	0.008 ± 0.001	740	0.17
	Ar	7.20 ± 0.01	-0.14 ± 0.06	1.9 ± 0.3	59.3 ± 1.5	165.8	0.095 ± 0.003	823	0.19
1200	H ₂	7.21 ± 0.01	-0.07 ± 0.02	44.0 ± 9.8	66.7 ± 0.6	163.2	0.007 ± 0.002	729	0.14
	Ar	7.18 ± 0.02	-0.14 ± 0.13	2.0 ± 0.6	59.0 ± 2.6	165.1	0.104 ± 0.015	815	0.16
1300	H ₂	7.19 ± 0.00	-0.09 ± 0.03	50.4 ± 3.4	66.0 ± 0.0	167.3	0.006 ± 0.001	729	0.15
	Ar	7.20 ± 0.00	-0.16 ± 0.04	2.3 ± 0.2	63.7 ± 5.1	165.1	0.077 ± 0.001	814	0.15

Table 3.6: Sintered properties of carbon steel (Fe-0.8% C_{admixed}); compacted at 600 MPa, sintered 60 min at 700-1300°C in hydrogen and argon.

<i>Sintering temp. (°C)</i>	<i>Sintering atm. (°C)</i>	<i>Sintered density (g/cm³)</i>	<i>Dimensional Change (%)</i>	<i>Impact energy (J/cm²)</i>	<i>Hardness (HV30)</i>	<i>Dyn. Young's modulus (GPa)</i>	<i>Oxygen content (wt %)</i>	<i>Comb. carbon content (wt %)</i>	<i>Electrical conductivity (S.m⁻¹)10⁴</i>	<i>Coercivity (kA/m)</i>
700	H ₂	7.17 ± 0.01	0.00 ± 0.00	0.3 ± 0.1	65.7 ± 1.2	98.5	0.112 ± 0.007	0.779 ± 0.008	545	0.26
	Ar	7.18 ± 0.00	-0.02 ± 0.00	0.5 ± 0.5	64.0 ± 3.0	117.2	0.107 ± 0.004	0.786 ± 0.012	641	0.25
800	H ₂	7.18 ± 0.01	-0.04 ± 0.00	10.6 ± 0.5	71.3 ± 3.1	154.6	0.104 ± 0.027	0.753 ± 0.013	711	0.30
	Ar	7.19 ± 0.01	0.00 ± 0.00	5.3 ± 1.2	76.0 ± 2.6	148.1	0.094 ± 0.004	0.786 ± 0.005	706	0.36
900	H ₂	7.17 ± 0.00	0.00 ± 0.00	12.6 ± 1.1	98.7 ± 5.8	159.9	0.061 ± 0.001	0.742 ± 0.002	666	0.55
	Ar	7.18 ± 0.01	0.00 ± 0.00	9.7 ± 1.2	79.0 ± 2.0	154.6	0.081 ± 0.002	0.776 ± 0.006	712	0.40
1000	H ₂	7.16 ± 0.00	-0.02 ± 0.02	16.1 ± 1.5	120.7 ± 3.2	159.3	0.033 ± 0.002	0.705 ± 0.003	611	0.66
	Ar	7.17 ± 0.01	0.07 ± 0.00	14.5 ± 1.3	102.7 ± 3.8	158.2	0.041 ± 0.001	0.752 ± 0.004	638	0.64
1100	H ₂	7.16 ± 0.00	0.03 ± 0.01	16.4 ± 2.5	132.0 ± 3.6	163.6	0.012 ± 0.001	0.646 ± 0.019	602	0.66
	Ar	7.18 ± 0.00	0.05 ± 0.02	17.2 ± 1.6	119.0 ± 5.2	163.5	0.023 ± 0.003	0.744 ± 0.004	618	0.67
1200	H ₂	7.19 ± 0.01	-0.18 ± 0.04	24.2 ± 1.7	144.3 ± 3.8	165.4	0.007 ± 0.002	0.638 ± 0.019	606	0.65
	Ar	7.19 ± 0.00	-0.04 ± 0.00	19.5 ± 1.0	130.7 ± 3.5	164.1	0.011 ± 0.001	0.728 ± 0.004	612	0.66
1300	H ₂	7.24 ± 0.01	-0.36 ± 0.00	38.1 ± 4.5	110.7 ± 3.5	172.9	0.007 ± 0.006	0.576 ± 0.054	625	0.52
	Ar	7.23 ± 0.00	-0.22 ± 0.00	26.0 ± 1.1	134.3 ± 3.2	168.3	0.004 ± 0.001	0.733 ± 0.006	615	0.66

3.2.1. Green density

Green density of both grades, Fe and Fe-0.8C, is presented in Figure 3.28. The results show that the maximum attainable density of the mixes is lowered only slightly by adding 0.8% graphite. In fact, it shows that presence of the graphite particles with the density of 2.3 g/cm^3 in the spaces between the iron powder particles has a negligible effect on the green density, at least at the compacting pressures applied here.

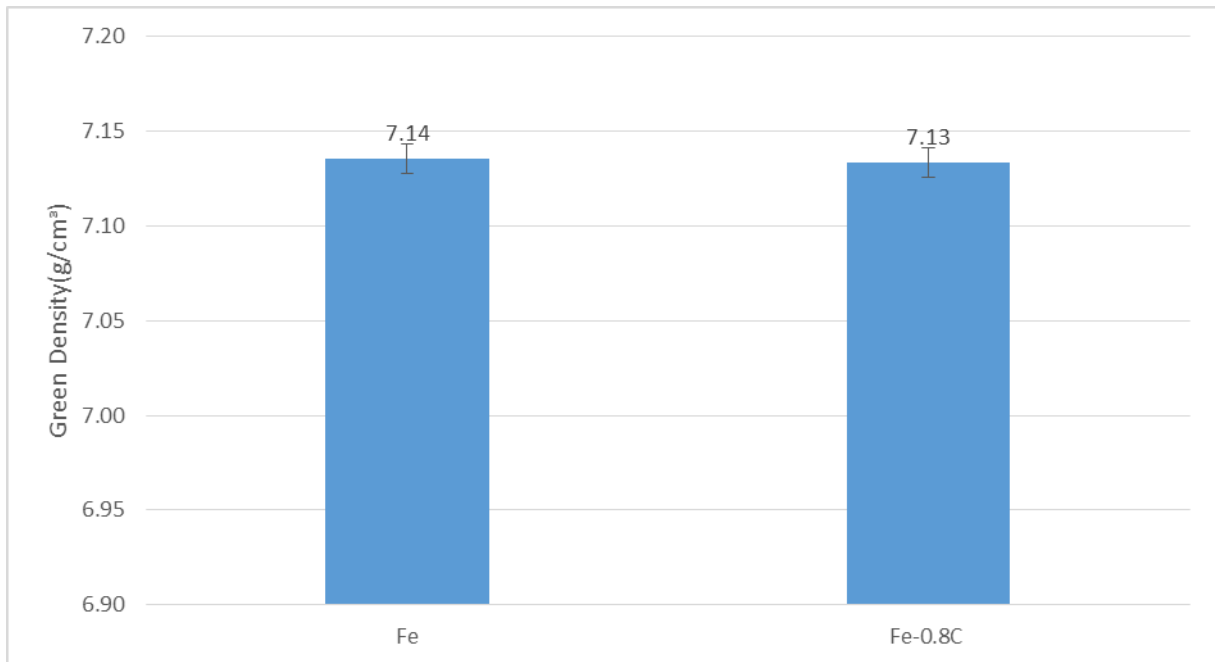


Figure 3.28: Green density of mixes, compacted at 600 MPa (lubricated die, Charpy bar geometry ISO 5754).

3.2.2. Thermal analysis and degassing behaviour

In order to study the oxide reduction processes, heating sections of dilatometric/MS runs in hydrogen and argon for plain iron (Fe) with gas intensities are shown in Figure 3.29. Five MS graphs for m12 (carbon), m16 (oxygen), mass 18 (water), mass 28 (CO) and mass 44 (CO₂) are presented for each atmosphere. In Fig.3.29-A there is an active reducing environment in H₂ atmosphere. According to the MS graph in hydrogen, a reduction peak is formed by m18 (H₂O) at about 380°C, indicating removal of the oxygen present on the powder surfaces as H₂O, which can escape easily through the open pores. The graph also shows a significant gradual emission of H₂O above 700°C. This latter reduction of oxides is known as reduction of internal oxides, which needs higher temperatures and longer times than the reduction of surface oxides [52]. According to the results, in contrast to hydrogen, in argon atmosphere (Fig.3.29-B), there are no pronounced degassing peaks related to reduction processes (please note the different MS intensity scales). Only a gradual trend with very slight slope is visible for m28 (CO) that shows a weak reducing condition for this virtually carbon-free material in Ar during heating.

Dilatometric runs of plain iron (Fe) in hydrogen and argon atmosphere are shown in Figure 3.30. According to the dilatometry graphs, the α - γ transformation occurred at almost the same temperature during both heating and cooling processes in both atmospheres. It shows that in this case, the type of atmosphere does not have a pronounced effect on the temperature of this transformation of plain iron. However, in the argon atmosphere (3.30-B) the reported dimensions during heating up and cooling down show a strongly asymmetrical dimensional change during α to γ and γ to α transformations insofar as the latter is more pronounced than the former, while the dimensional change in hydrogen showed a rather symmetrical behaviour. These results are in good agreement with the findings presented in [149]. It has been assumed that the asymmetrical dimensional change comes from very slight temperature gradients, which more or less guide the growth of large grains within a narrow temperature interval. The most probable gradient is in the longitudinal direction of the furnace, therefore the grains grow in that direction [150, 151].

In Figure 3.31, the typical MS signals are shown for the carbon steels. In H_2 atmosphere (Fig 3.31-A) the first reduction peak (similar to plain iron) is formed by m18 (H_2O) and occurs at lower temperature, at about $370^\circ C$, while the second, broader peak starting at higher temperature is formed by m28, indicating carbothermal reduction. It shows that, as stated in Chapter 1.4.2, at lower temperatures H_2 is the stronger reducing agent, while at higher temperature only the carbothermal reduction occurs by releasing CO. As discussed already, the H_2O peak (or, in inert atmosphere, the first CO peak) is attributed to reduction of surface oxides, while the reduction process at higher temperature is related to reduction of internal oxides of the powder particles and of the oxides trapped in the pressing contacts and is controlled by the diffusion rate of the oxygen atoms in the iron lattice to the surface. The section B of this figure shows the degassing behaviour of the carbon steel in Ar. Here, it is clear that during sintering in inert atmosphere - argon -, the main reduction processes are characterized by MS peaks of mass 28 (CO) at temperatures of about $700-800^\circ C$ and $900-1150^\circ C$, respectively.

Results of dilatometry of the carbon steels are presented in Figure 3.32. It is obvious that α to γ transformations started from lower temperature and in a broader interval in Ar compared with H_2 . This indicates that despite the faster reduction of surface oxides (at $370^\circ C$) in hydrogen, which provides a favorable condition for solid state carbon dissolution, the carbon started to be dissolved at higher temperature in this atmosphere. Considering the gas phase transport as the main mechanism of carbon dissolution and CO as the main player, it can be stated that the reason for carbon dissolution at lower temperature in Ar is formation of CO at about $730^\circ C$, while in H_2 , CO formation is delayed (occurs at higher temperature) because the surface oxides have already (at $370^\circ C$) been reduced by water formation and as a result, the carburizing started at higher temperature. However, the DIL/MS of carbon steel in hydrogen (Fig. 3.31-A), shows that as soon as CO is formed, the phase transformation occurred within a much smaller temperature interval compared to that for argon (Fig. 3.31-B). This shows a rather fast carbon dissolution in hydrogen after CO formation has started, which of course agrees with the gasification theory of carbon dissolution considered above as an assumption.

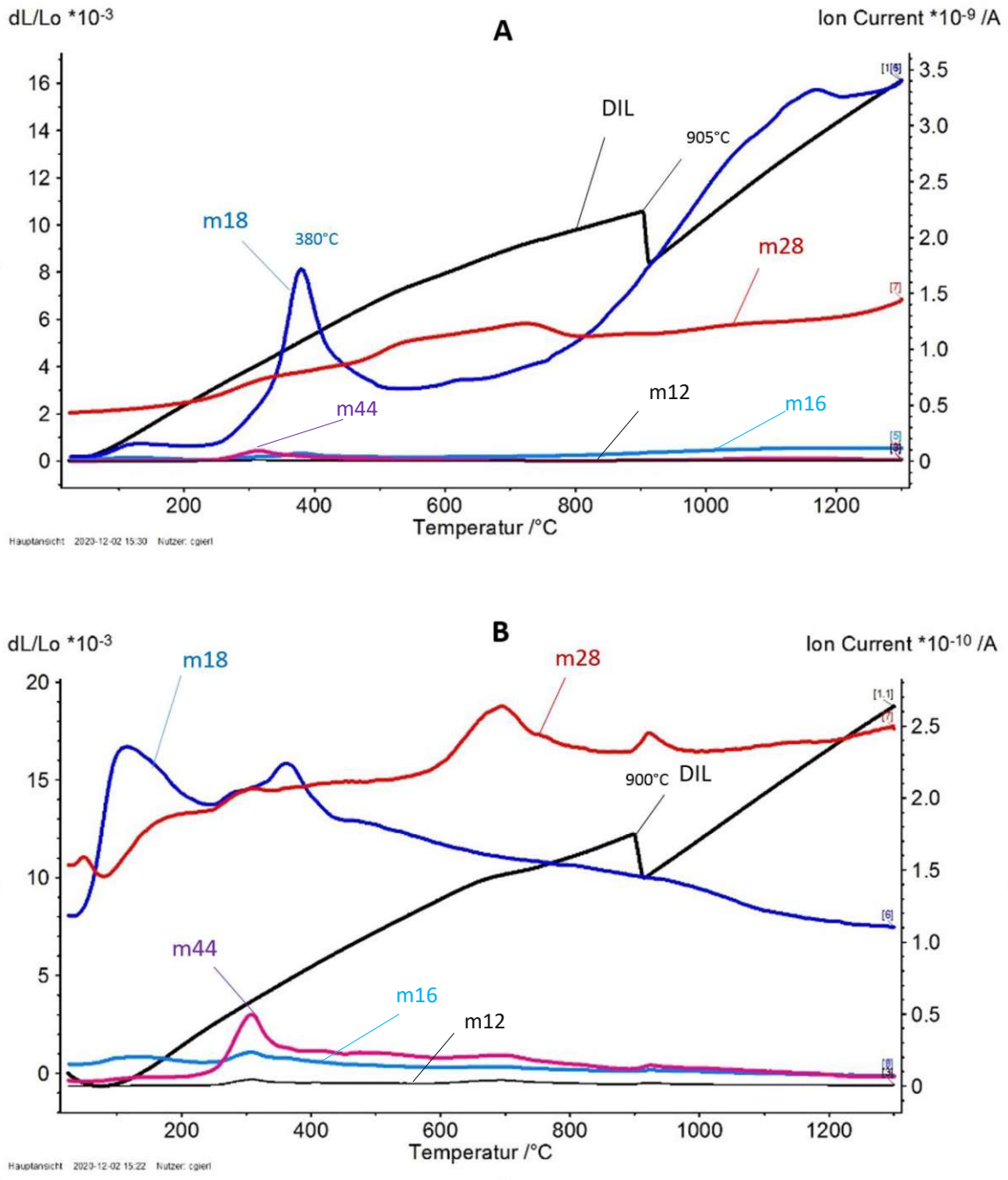


Figure 3.29: Dilatometry/MS graphs (heating section) of plain iron (Fe), compacted at 600 MPa, sintered 60 min at 1300°C in hydrogen (A) and argon (B), heating-cooling rate ± 10 K/min.

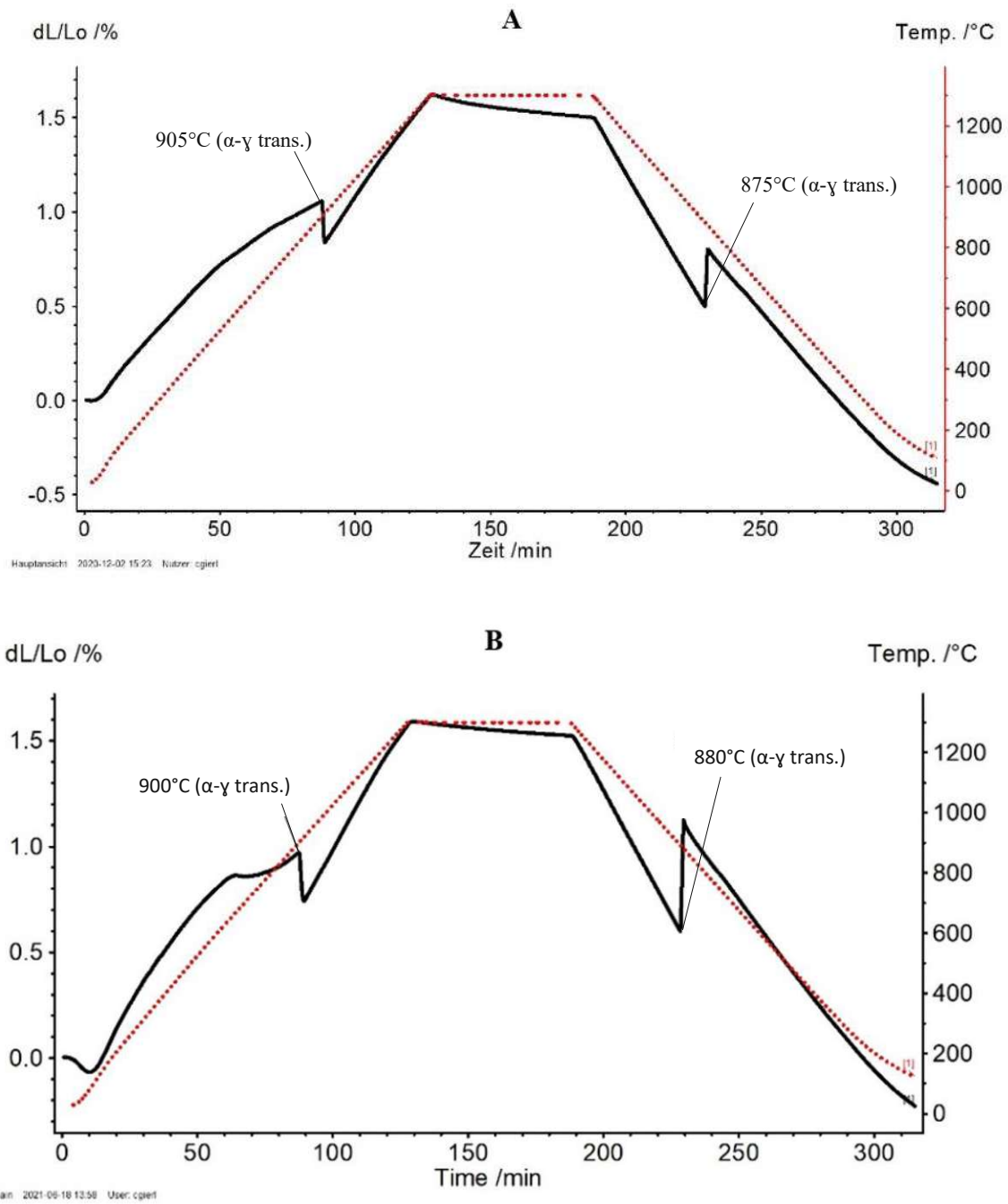
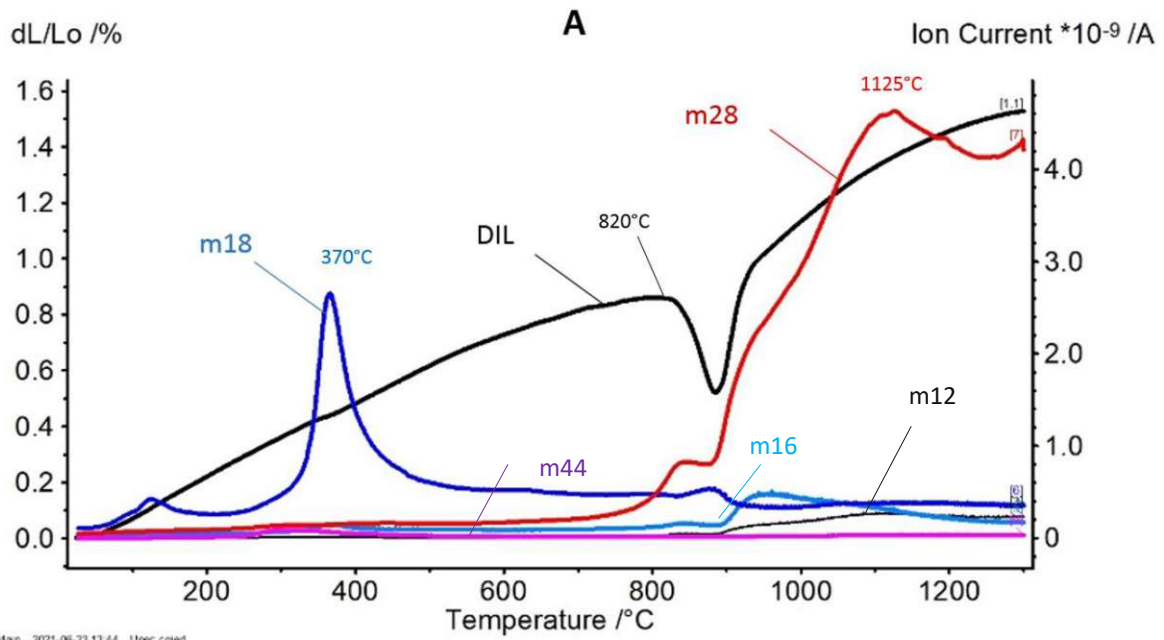
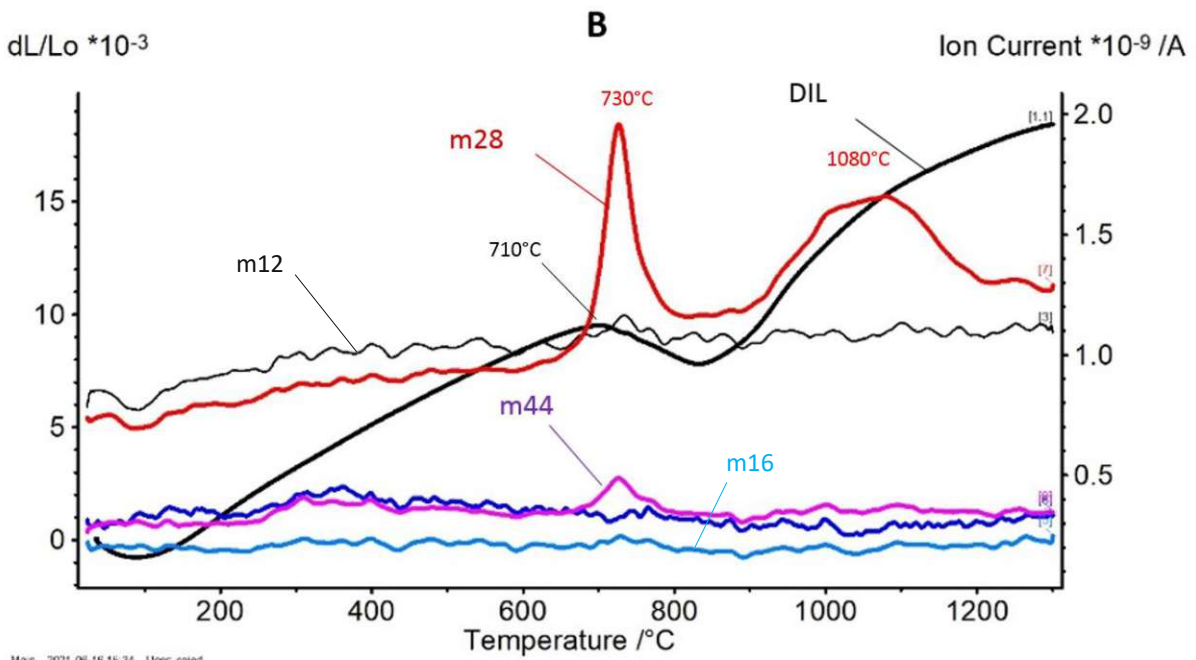


Figure 3.30: Dilatometry runs of plain iron (Fe), compacted at 600 MPa, sintered 60 min at 1300°C in hydrogen (A) and argon (B), heating-cooling rate ± 10 K/min.



Main: 2021-06-23 13:44 User: cglert



Main: 2021-06-16 15:34 User: cglert

Figure 3.31: Dilatometry/MS graphs (heating section) of carbon steel (Fe-0.8% C_{admixed}), compacted at 600 MPa, sintered 60 min at 1300°C in hydrogen (A) and argon (B), heating-cooling rate ± 10 K/min.

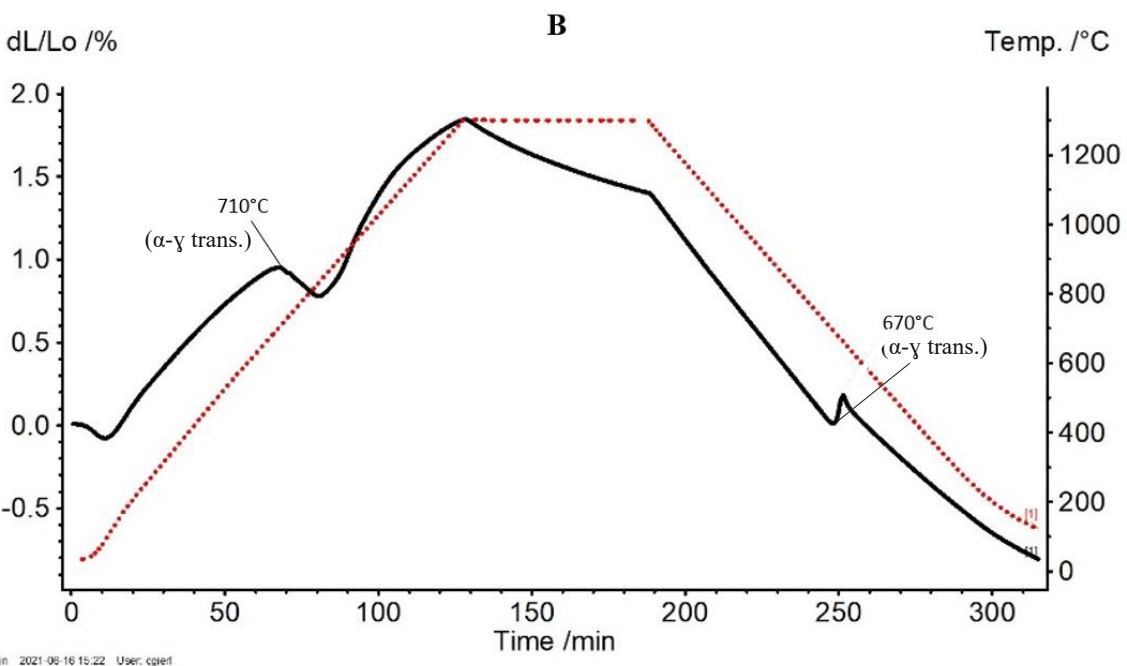
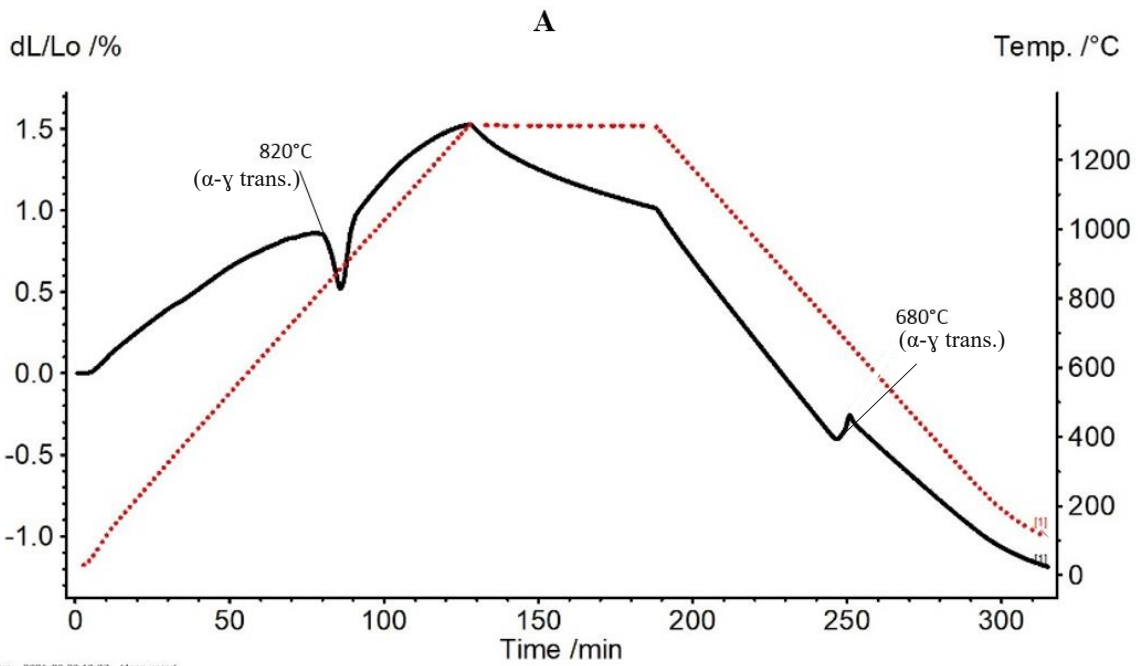


Figure 3.32: Dilatometry runs of carbon steel (Fe-0.8C_{admixed}), compacted at 600 MPa, sintered 60 min at 1300°C in hydrogen (A) and argon (B), heating-cooling rate ±10 K/min.

3.2.3. Chemical analysis (carbon and oxygen content):

The oxygen content of the plain iron specimens sintered at different temperatures in Ar and H₂ is presented in Figure 3.33. In H₂, a progressive trend towards lowering of the oxygen content is discernible, whereas the oxygen content of samples sintered in Ar does not change significantly even at high sintering temperatures. These results are in good agreement with the MS results and – not surprisingly - confirm the non-reducing property of the Ar atmosphere but also its high purity, since there is virtually no O pickup. The oxygen content of the carbon steel (Fe-0.8C) sintered at different temperatures in Ar and H₂ is presented in Figure 3.34. It is clear that in both atmospheres higher sintering temperature results in better oxygen removal. The results in argon show a significant oxygen removal at 1000°C, while in hydrogen atmosphere a considerable drop of the oxygen content is discernible at lower temperature, at 900°C, which shows that reduction of the oxides through water formation is more active than carbothermal reduction at lower temperatures.

Figure 3.35 presents the carbon contents of the carbon steels after sintering in argon and hydrogen. In argon atmosphere it seems that the main carbon consumption is started after sintering at 1000°C, at the same temperature with the pronounced oxygen removal, which indicates that the carbon consumption is mainly due to carbothermal reduction of oxides.

The results also show that sintering in hydrogen led to higher amount and rate of carbon consumption compared to Ar atmosphere, however theoretically the carbon loss in H₂ should be even lower than in Ar since in H₂ some oxide can be reduced by this atmosphere in place of carbon. Figure 3.36 shows the carbon loss as a function of oxygen removal. According to the graph, the relationship between carbon and oxygen consumption in argon atmosphere follows a linear equation, as expected for carbothermal reduction forming CO, while for hydrogen atmosphere an exponential equation is fitting. From the evidences, it could be stated that in the hydrogen atmosphere the carbothermal reduction of oxides could not be the only reason of this decarburization. The cross section of the samples in Figure 3.37 shows a significant surface decarburization after sintering at 1300°C in hydrogen, while no surface decarburization is visible after sintering in Ar. Here the reason of this decarburization might be explained by the chemical reaction $C + H_2O \rightarrow CO + H_2$, which has much stronger decarburization effect than oxygen. It is an indication that some traces of air have entered the furnace, the oxygen contained having reacted with H₂ to form H₂O, which, as stated, is highly decarburizing, much more than O₂ traces in Ar.

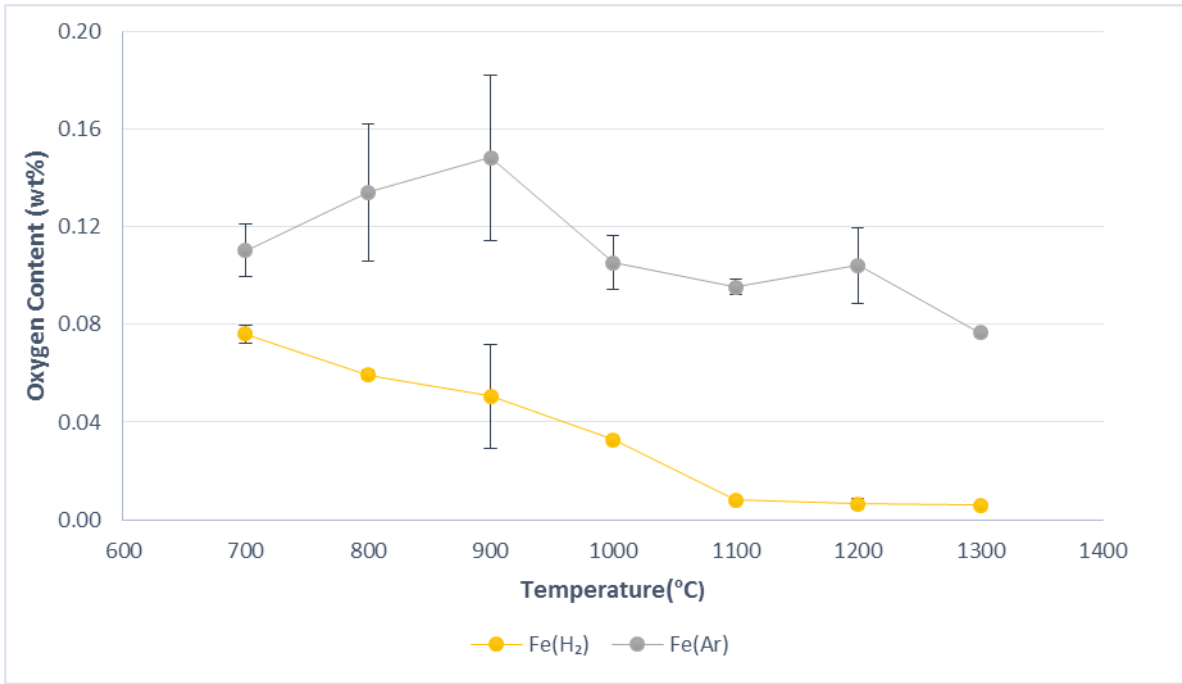


Figure 3.33: Oxygen content versus sintering temperature of plain iron sintered in argon and hydrogen.

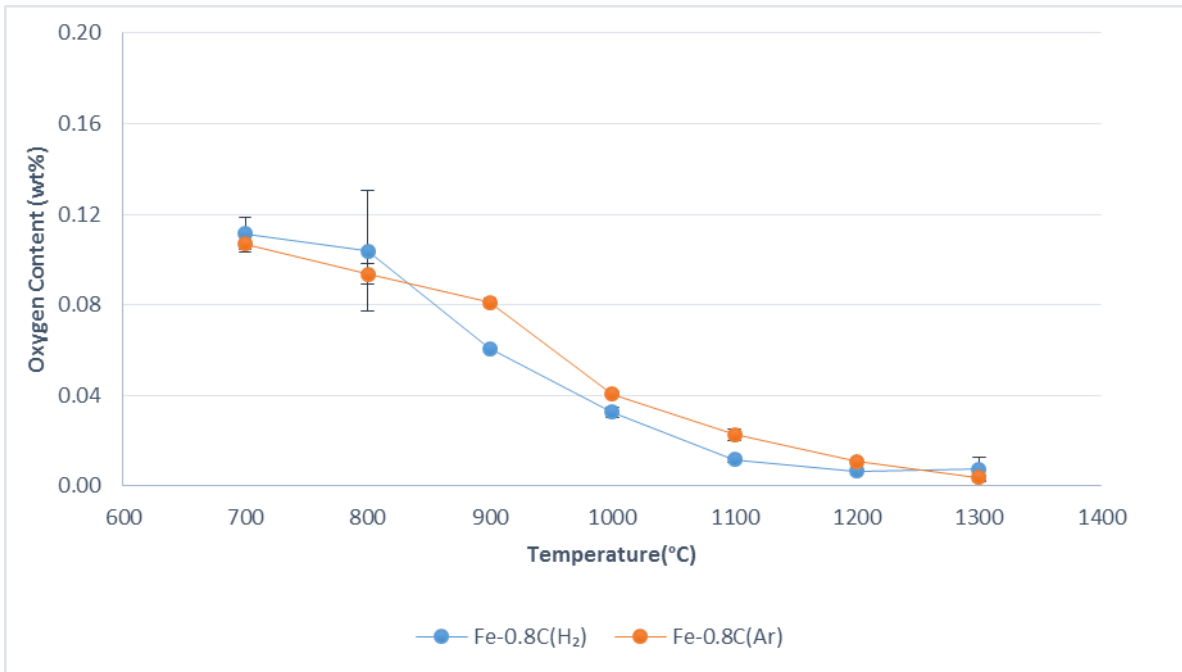


Figure 3.34: Oxygen content versus sintering temperature of carbon steel sintered in argon and hydrogen.

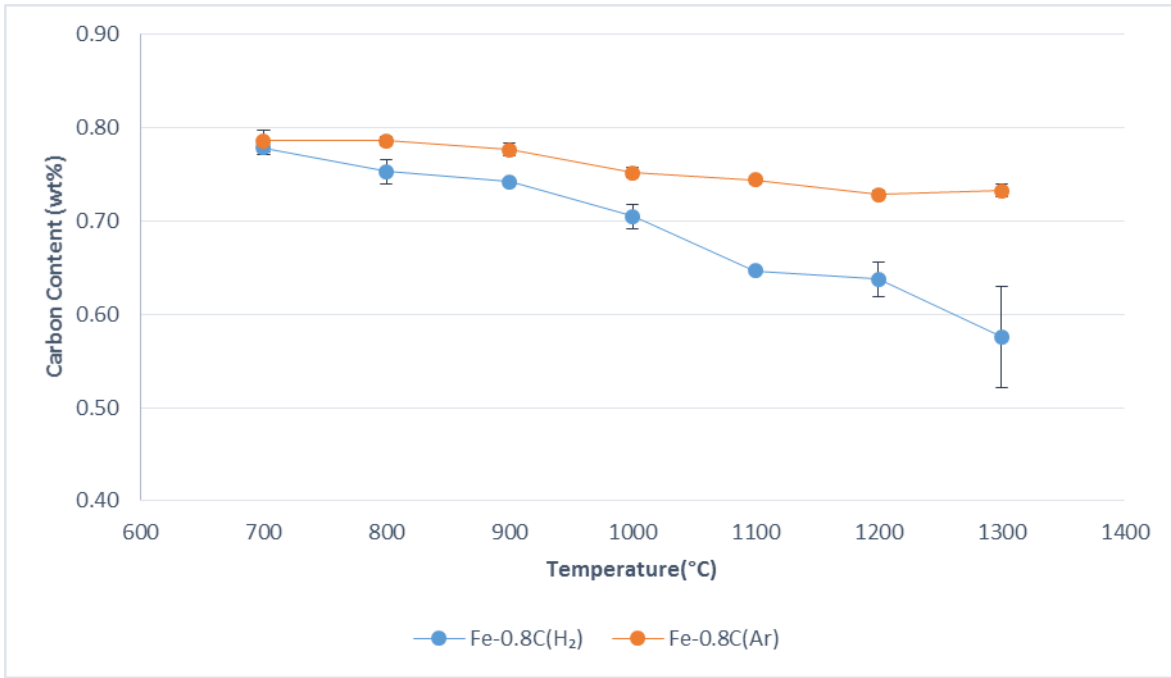


Figure 3.35: As-sintered carbon content versus sintering temperature of carbon steel sintered in argon and hydrogen.

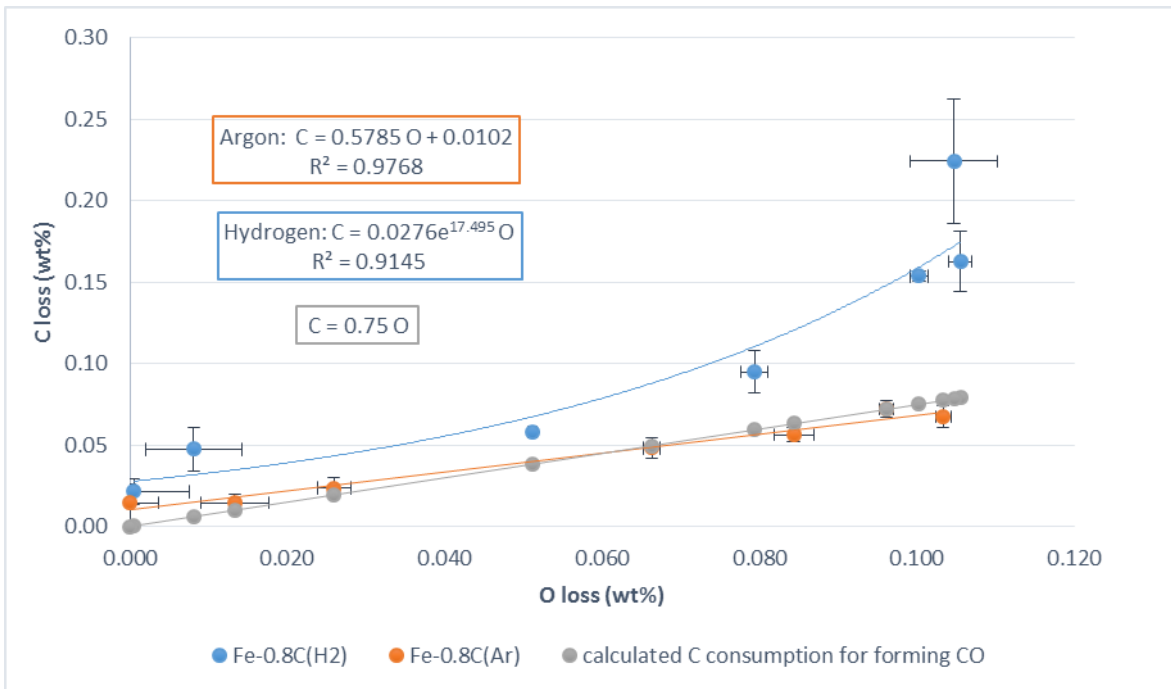


Figure 3.36: Carbon loss as a function of oxygen loss; carbon steel sintered at 700-1300°C in argon and hydrogen.

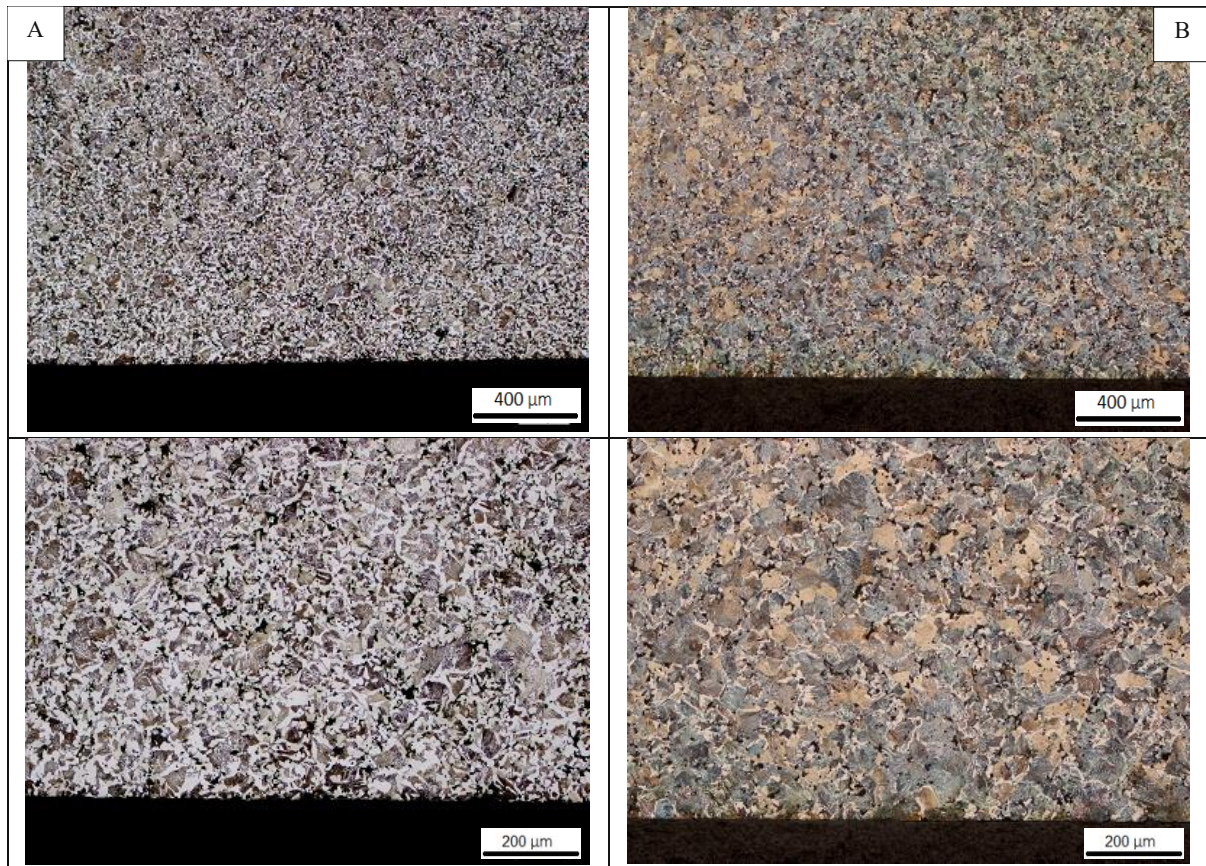


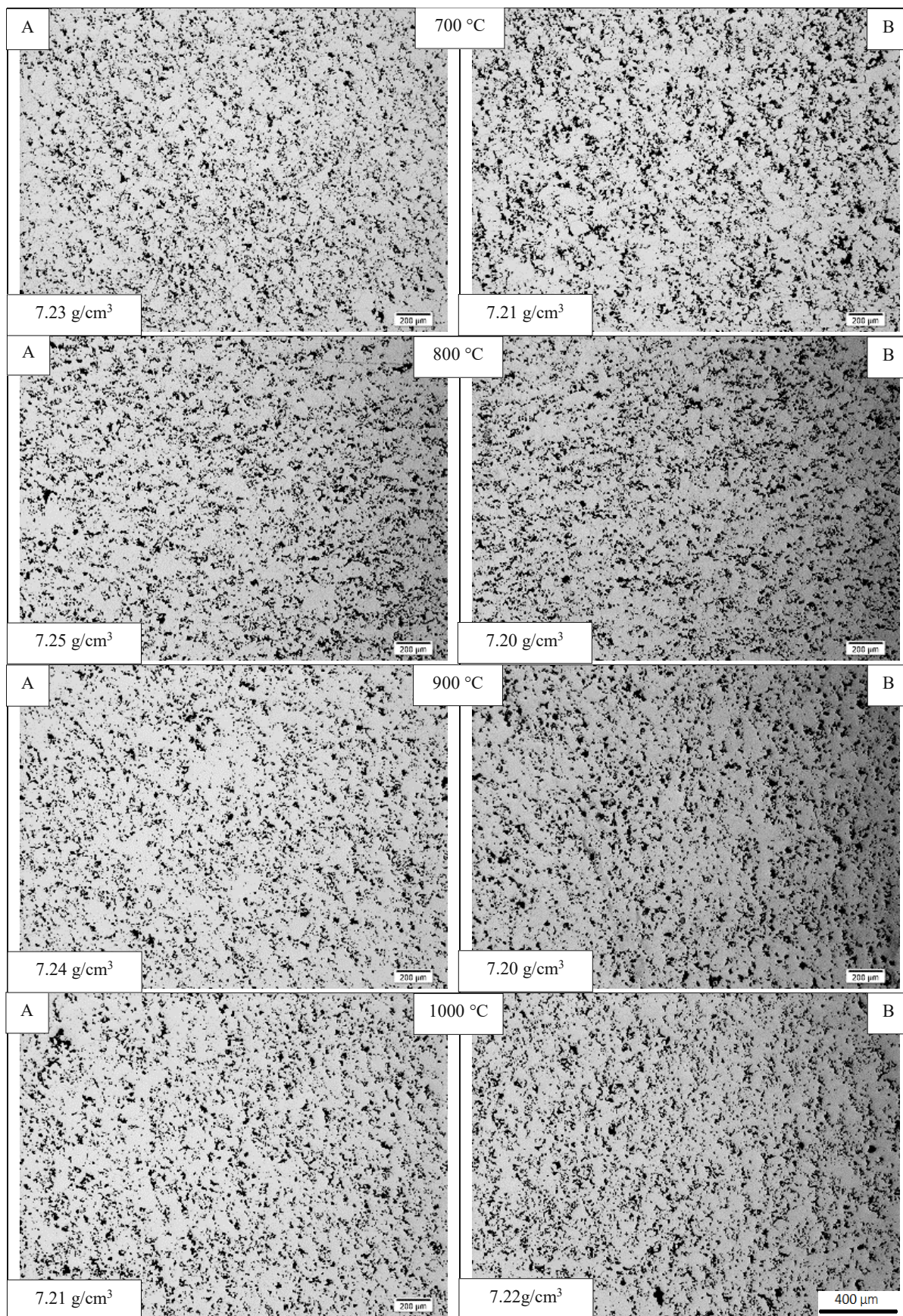
Figure 3.37: Surface microstructures of carbon steels compacted at 600 MPa, sintered 60 min at 1300°C in hydrogen (A) and argon (B), 50x and 100x.

3.2.4. Metallographic investigations (pore morphology and matrix microstructure)

Un-etched optical microscope cross sections of the plain iron specimens sintered under hydrogen and argon at different temperatures are presented in Figure 3.1.38 and 3.1.39. According to the images, in both atmosphere the boundaries between the individual powder particles are visible at 700 and 800°C, which have disappeared at 900°C. Above this temperature, up to 1100°C, the sintering bridges and contacts get larger and stronger with increasing temperature. Above 1100°C, at 1200 and 1300°C, elimination of fine pores and pore rounding are discernible in both atmospheres, however it seems that more rounded pores were formed in hydrogen, which could be the consequence of the higher oxygen removal which resulted in a more active sintering process.

Un-etched optical microscope cross sections of carbon steels sintered in hydrogen and argon at different temperature are presented in Figure 3.1.40 and 3.1.41.

According to the images, at low and moderate sintering temperatures, the pore morphology of the steels in both atmospheres does not show a significant difference. The boundaries between individual powder particles are visible at 700 and 800°C, which then started to disappear from 900°C and above this temperature, up to 1100°C, with higher temperature the sintering bridges and contacts get larger and stronger. Above 1100°C, pore rounding and elimination of fine pores are discernible.



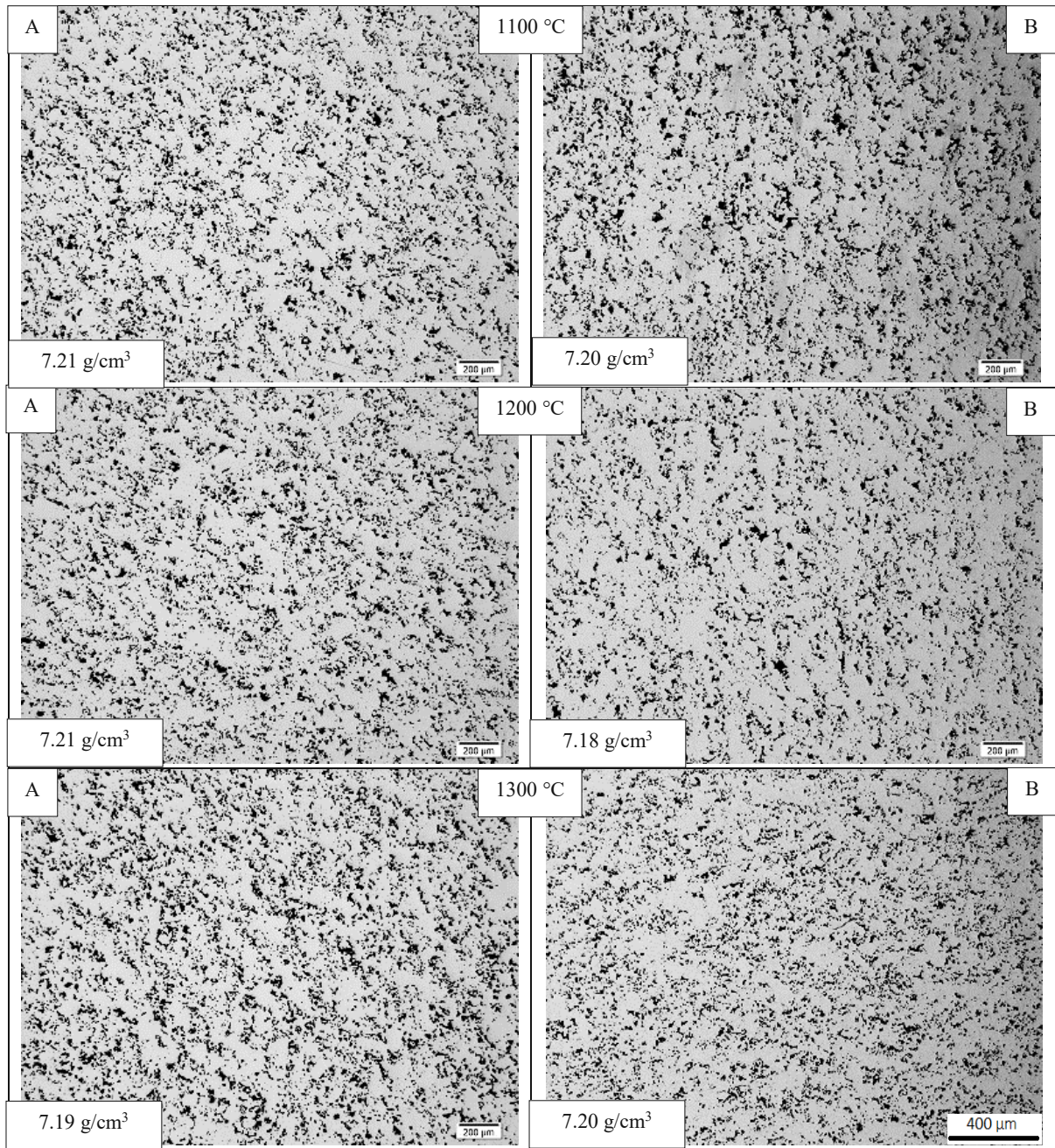
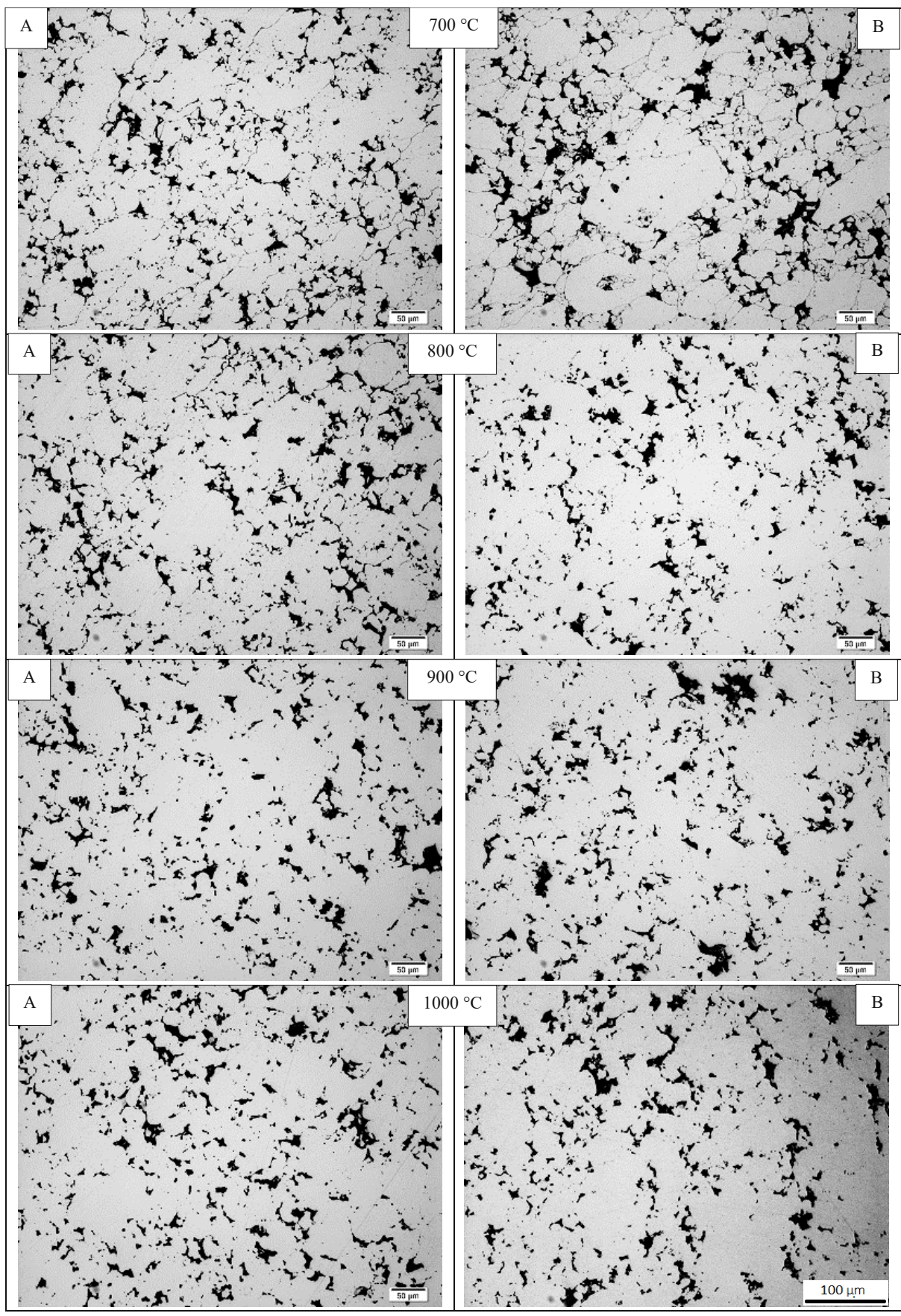


Figure 3.38: Un-etched OM micrographs of plain iron (Fe) compacted at 600 MPa, sintered 60 min in hydrogen (A) and argon (B), 50 x. (scale bar 400μm holds for all images)



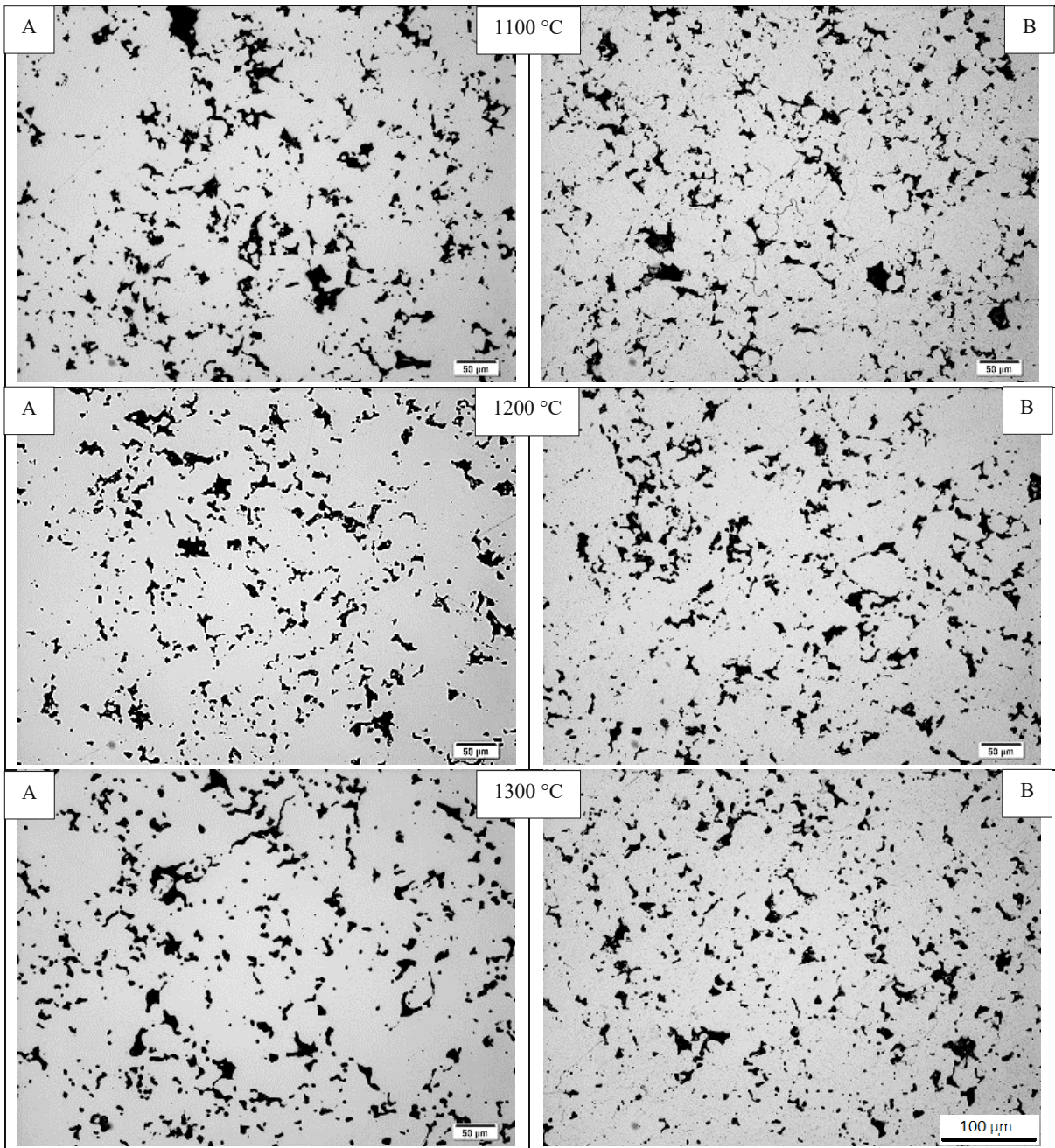
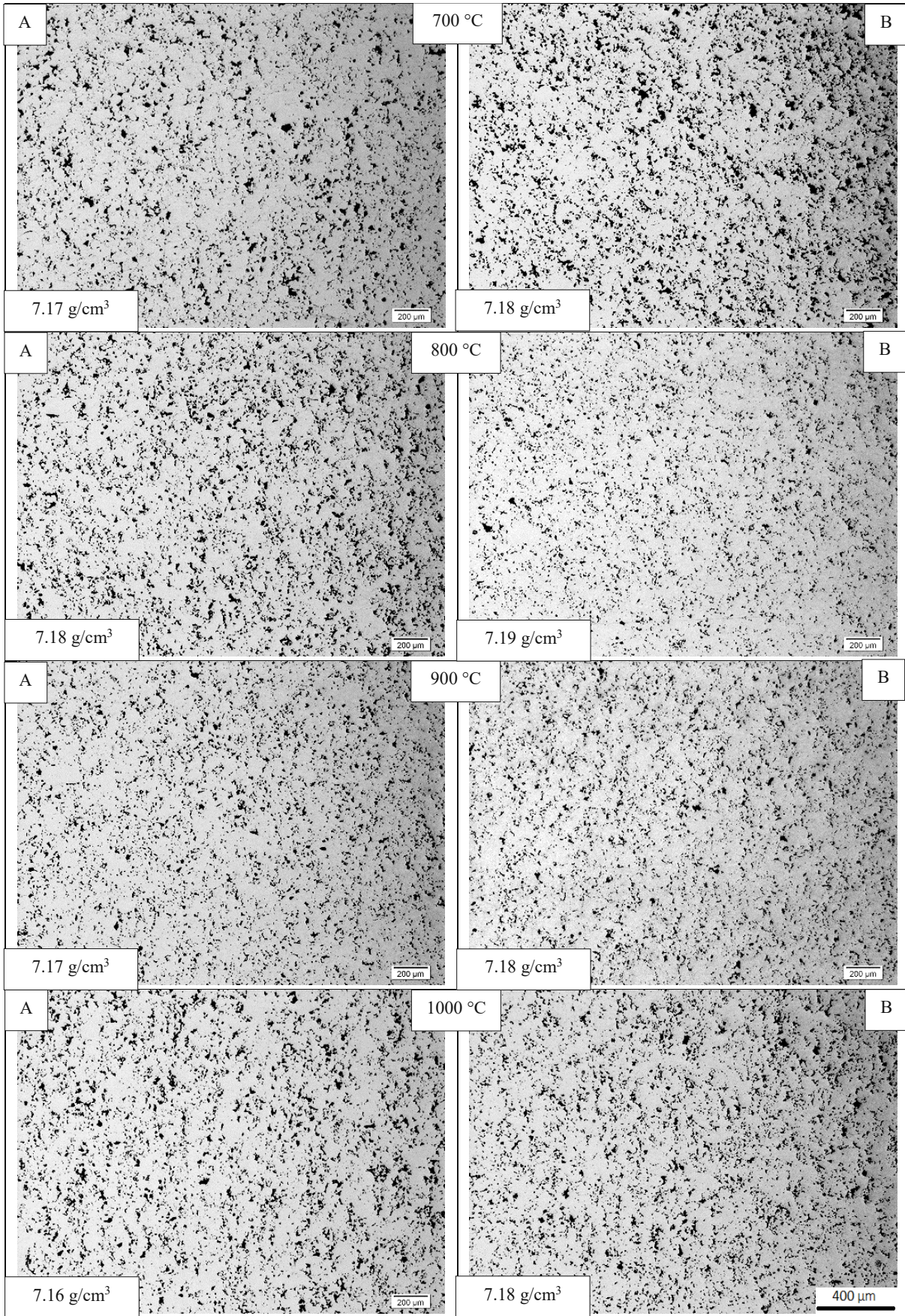


Figure 3.39: Un-etched OM micrographs of plain iron (Fe) compacted at 600 MPa, sintered 60 min in hydrogen (A) and argon (B), 200x. (scale bar 100 μ m holds for all images)



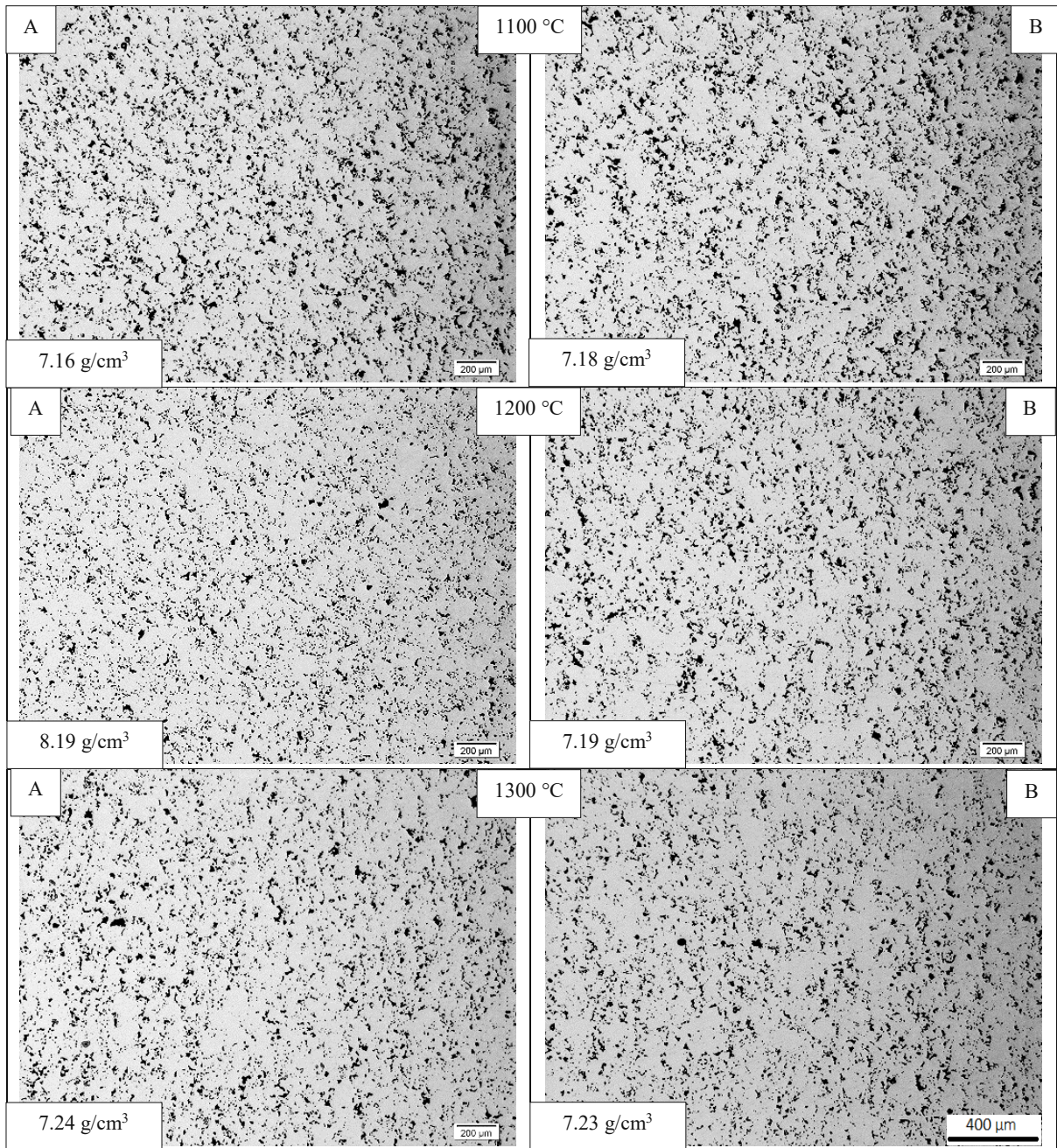
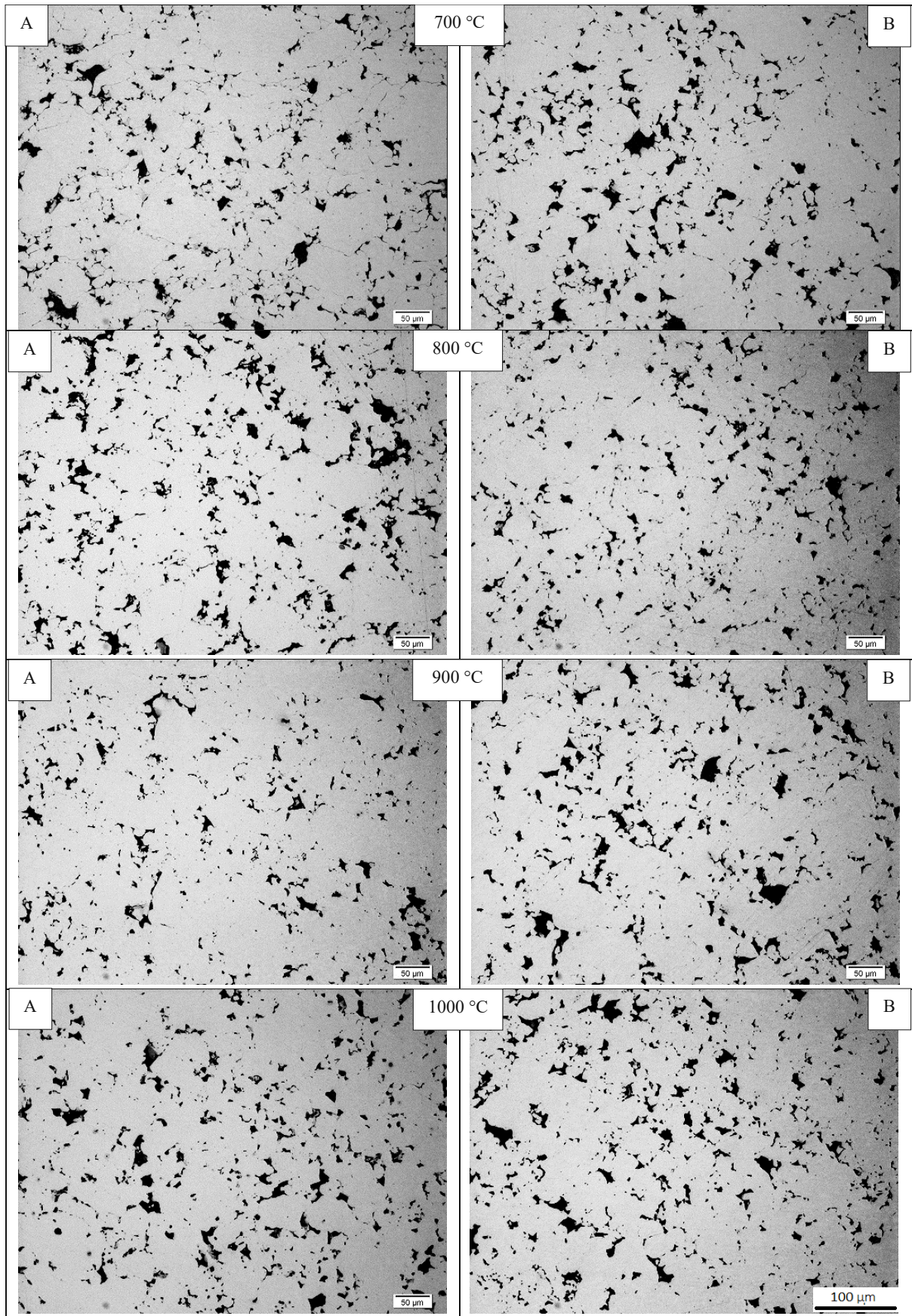


Figure 3.40: Un-etched OM micrographs of carbon steel (Fe-0.8C_{admixed}) compacted at 600 MPa, sintered 60 min in hydrogen (A) and argon (B), 50 x. (scale bar 400μm holds for all images)



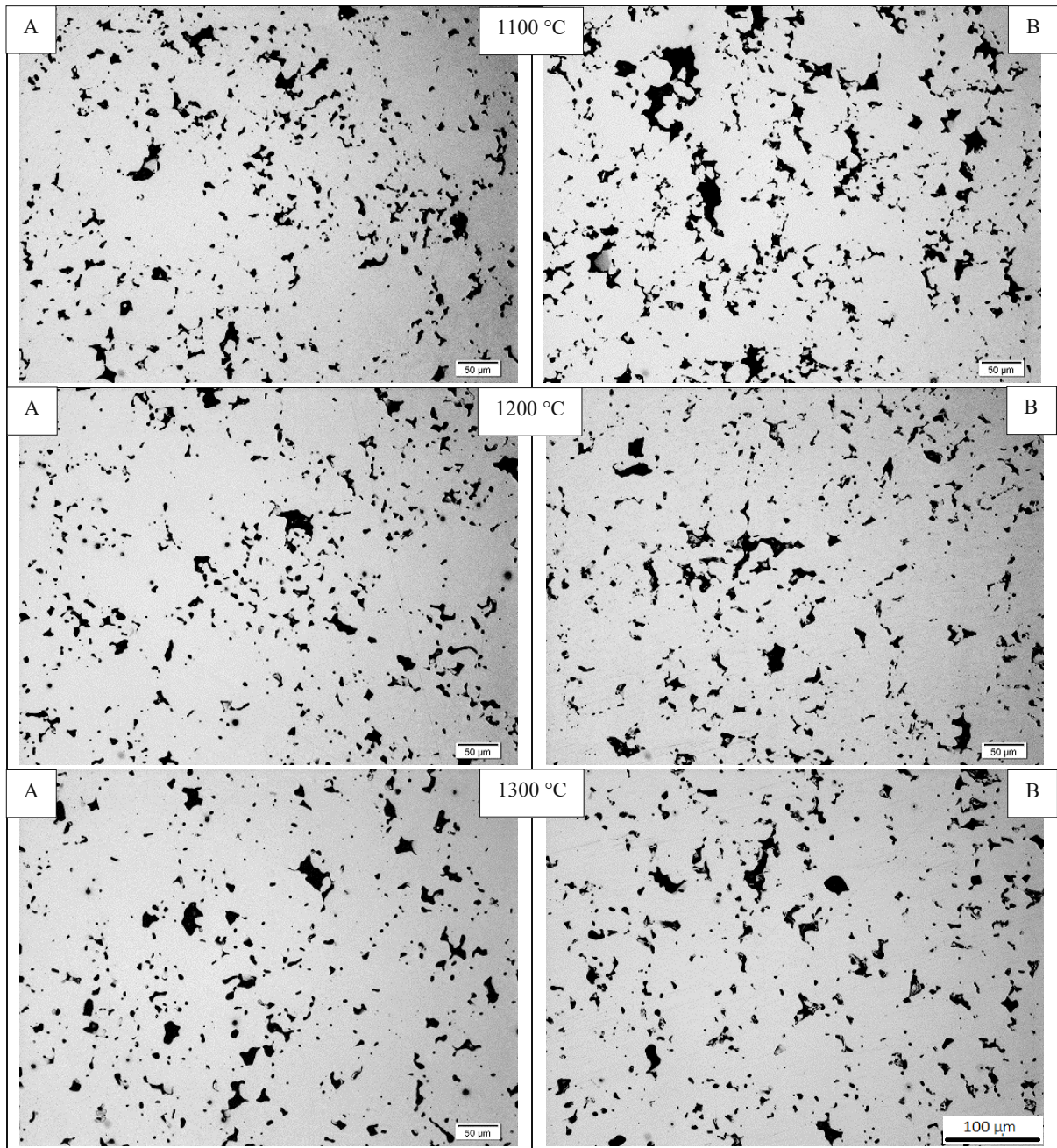
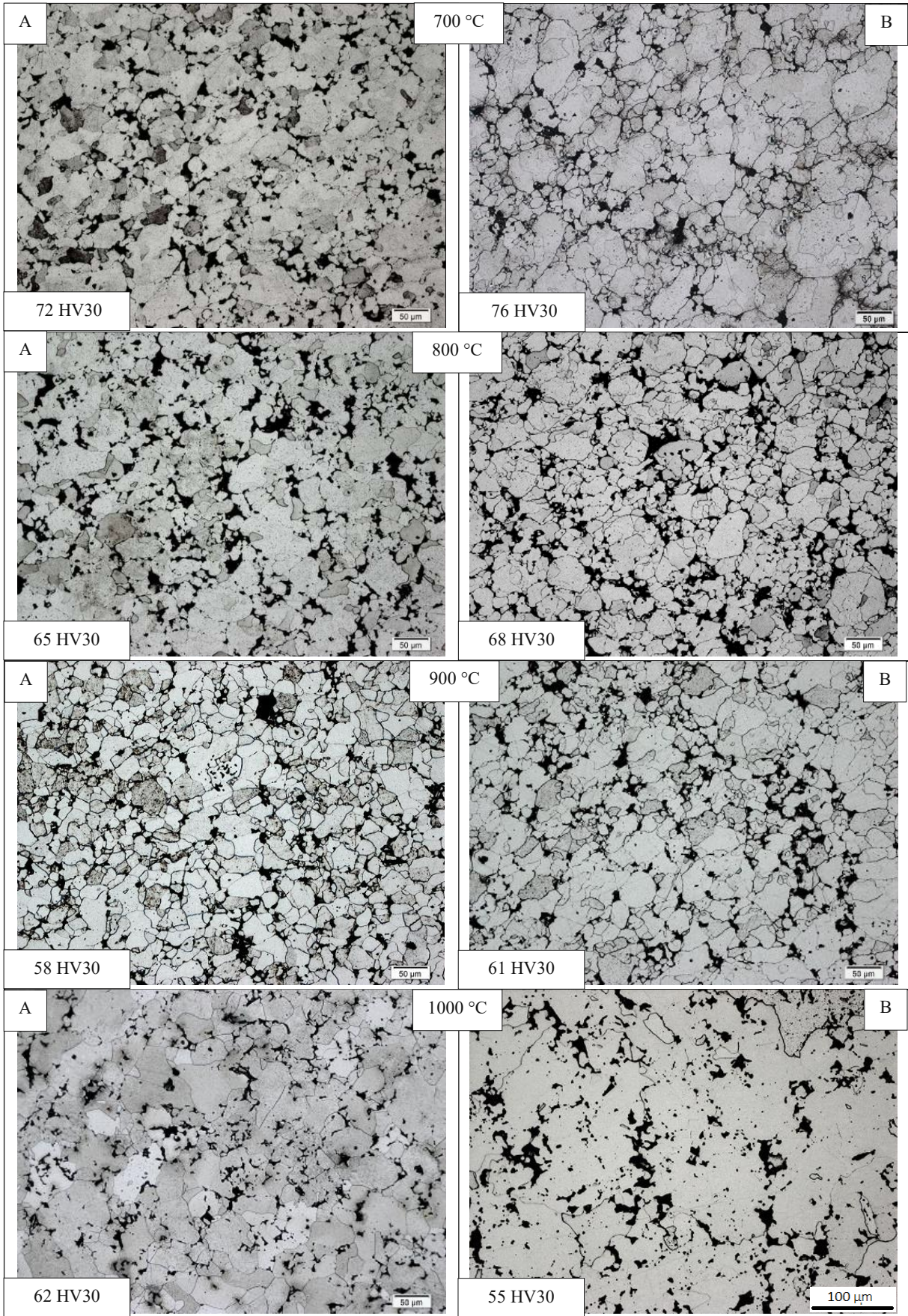


Figure 3.41: Un-etched OM micrographs of carbon steel ($\text{Fe-0.8C}_{\text{admixed}}$) compacted at 600 MPa, sintered 60 min in hydrogen (A) and argon (B), 200x. (scale bar $100\mu\text{m}$ holds for all images)

The etched microstructures of Fe after sintering in hydrogen and argon are presented in Figure 3.42 and 3.43. At 700 and 800°C, the microstructures in both atmospheres show mainly the original iron particles without any sign of sintering, the boundaries between the powder particles and also sub-grain boundaries in the core of ferrite grains are visible in both atmospheres, while at 900 and 1000°C the structures showed more difference. Evidently, sintering in Ar led to an enormous grain coarsening, whereas in hydrogen less grain growth is visible. As stated in Chapter 3.2.2., Danninger [147] claimed that this grain coarsening occurs during the γ to α transformation and is a consequence of transformation within a very narrow temperature interval, under which condition only few ferrite nuclei are created, which results in such large grains. Kuroki et al [150, 151] also showed that in the pure iron materials, coarse ferrite crystals are attributed to the absence of interstitial elements such as carbon and nitrogen. In fact, in the presence of these elements this coarsening does not occur due to enrichment of expelled atoms from the growing ferrite at the phase boundary between austenite and ferrite, which leads to nucleation of new ferrite crystals ahead of the growing ferrite and thus suppresses more grain growth. However, the results of our study show that sintering in hydrogen also can prevent such grain coarsening during the γ to α transformation.

Metallographic sections of the carbon steels sintered at different temperatures in hydrogen and argon are presented in figure 3.44 and 3.45. The nucleation of the pearlite seems to be started at 800°C in both atmospheres; increasing the sintering temperature to 900 and 1000°C enhanced carbon dissolution. Microstructures at these temperatures show that the carbon dissolution in H_2 occurred faster than in Ar. The fraction of pearlite in hydrogen atmosphere indicates that carbon dissolution at 1000°C is almost finished, while in case of argon only about 50-60% of the microstructure is covered by pearlite. It seems that presence of H_2 in addition to CO resulted in faster carburizing, which agrees with results of some previous investigation on effect of hydrogen on the rate of the carburizing process of steels [152, 153]. This is a further indication that carbon dissolution occurs via the gas phase. Another point that should not be ignored here is the faster heating of the specimens in H_2 compared to Ar, which might also play a role here.

At 1200°C, the fraction of pearlite is similar for both atmospheres, and sintering also resulted in microstructural homogenizing and pore rounding. Although 0.8% carbon had been admixed, the microstructures after sintering at 1200°C do not show 100 % pearlite, and some proeutectoid ferrite is discernible for both atmospheres. The reason is once more the carbon loss during sintering caused by carbothermal reduction of surface oxides on the powders which implies that a sintered steel with nominally 0.8%C (admixed) after sintering rather contains less than this amount and thus is no more fully pearlitic unless cooled fairly fast. Micrographs for 1300°C show slightly more ferrite in hydrogen atmosphere compared to argon, which shows that after sintering in hydrogen, in addition to the surface decarburization, the carbon loss occurred in the core of the samples as well, which is not surprising regarding the very fast diffusion of C at these temperatures.



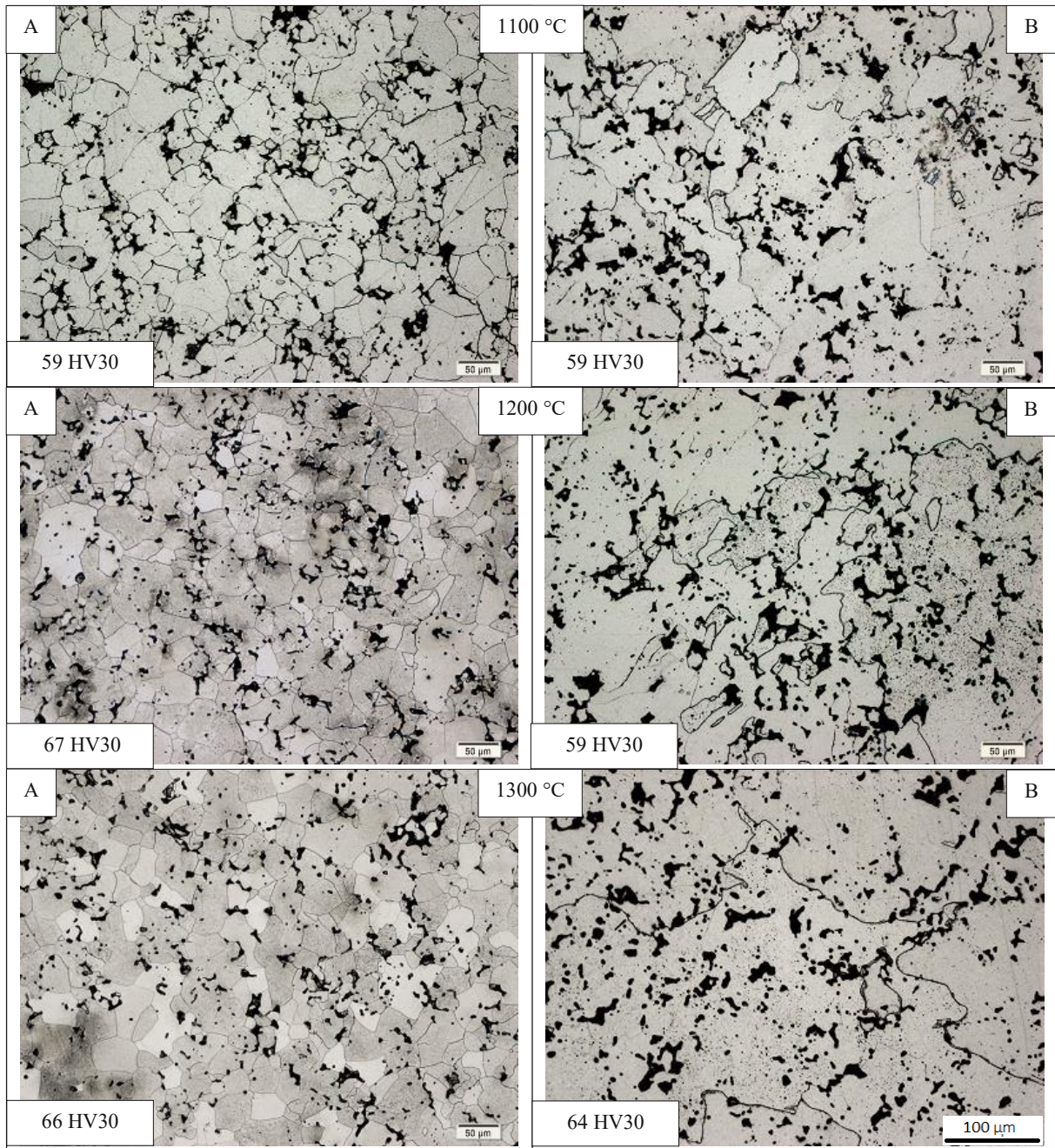
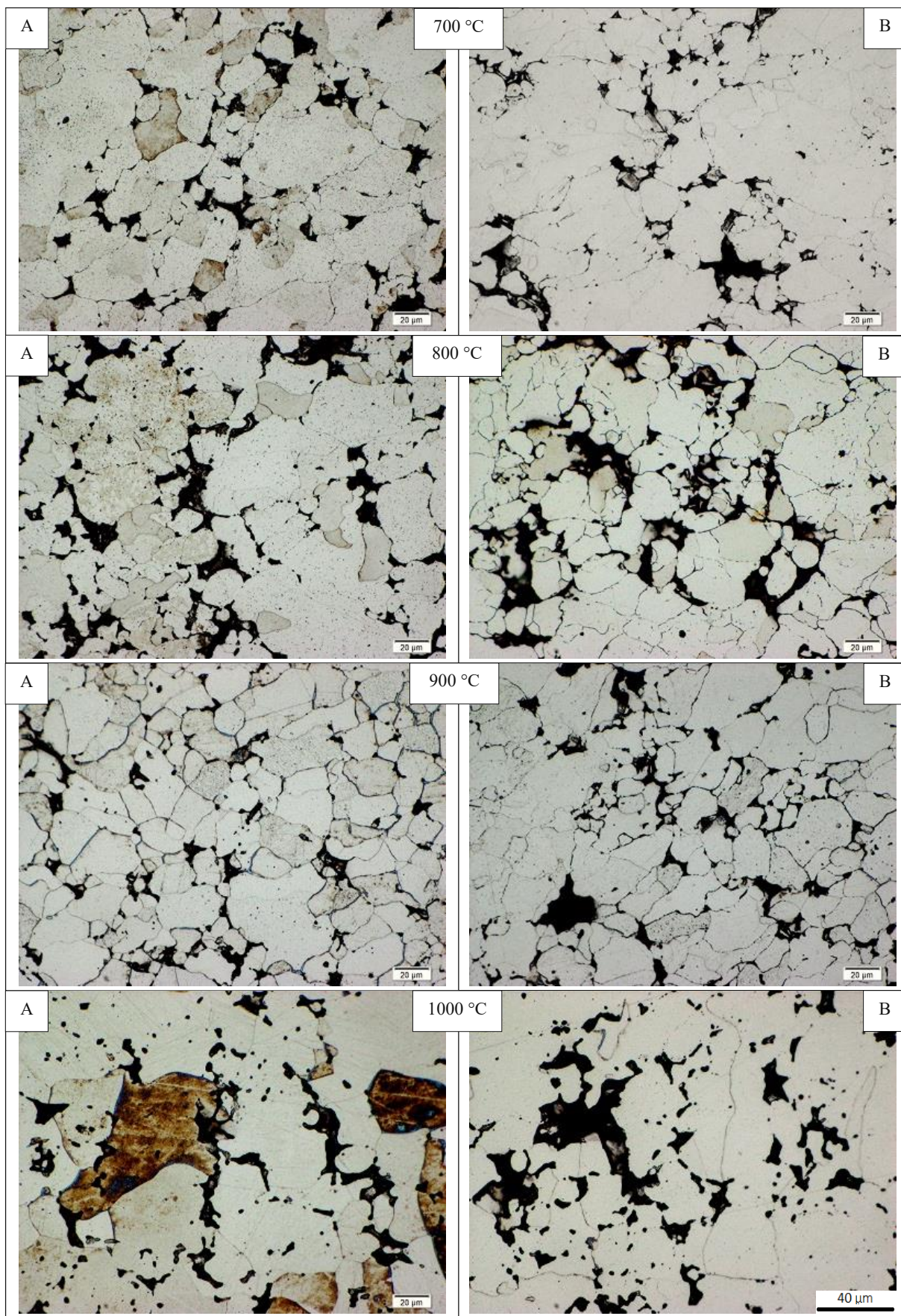


Figure 3.42: Etched microstructures of plain iron (Fe) compacted at 600 MPa, sintered 60 min in hydrogen (A) and argon (B), Nital, 200x. (scale bar 100 μ m holds for all images)



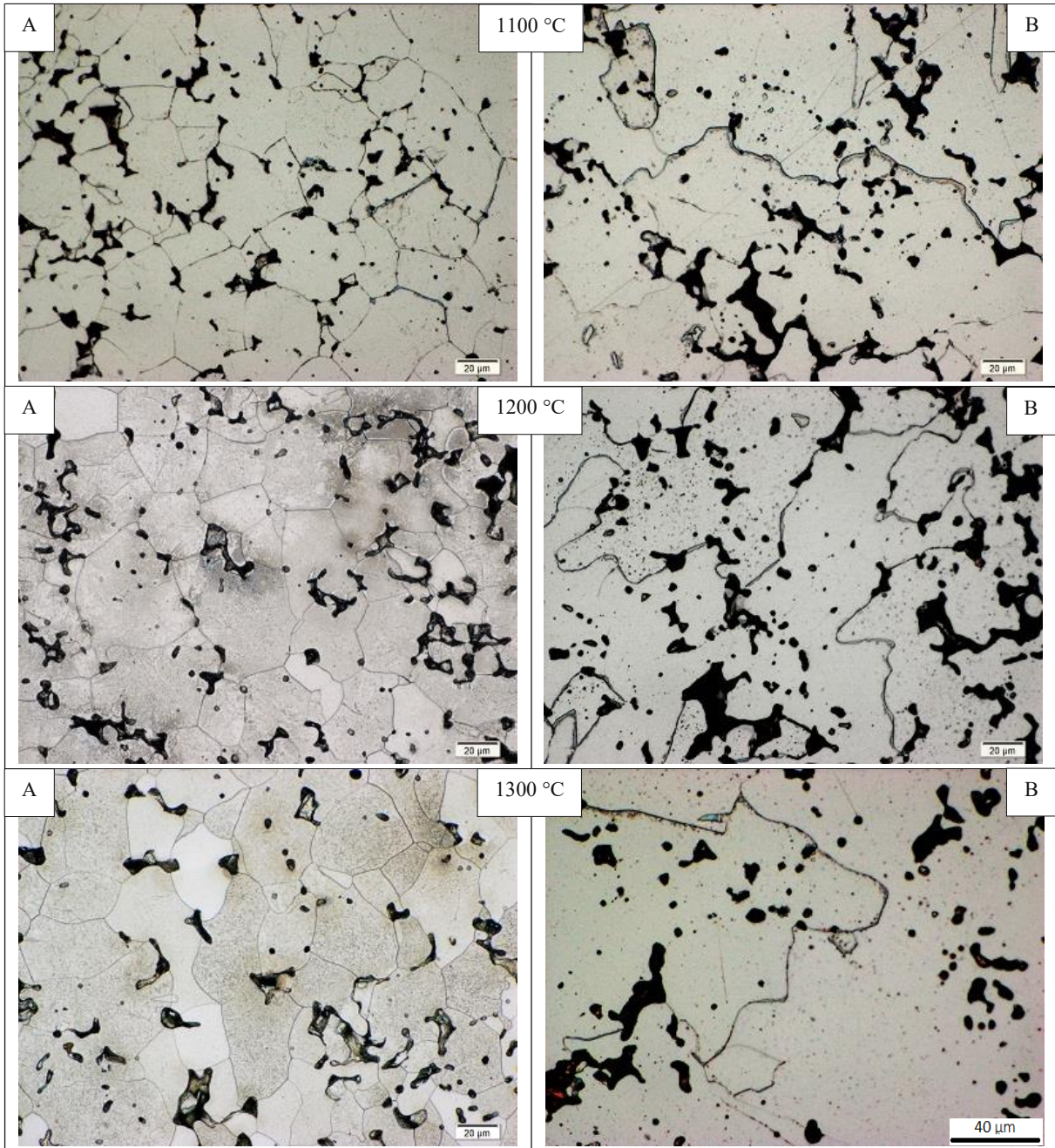
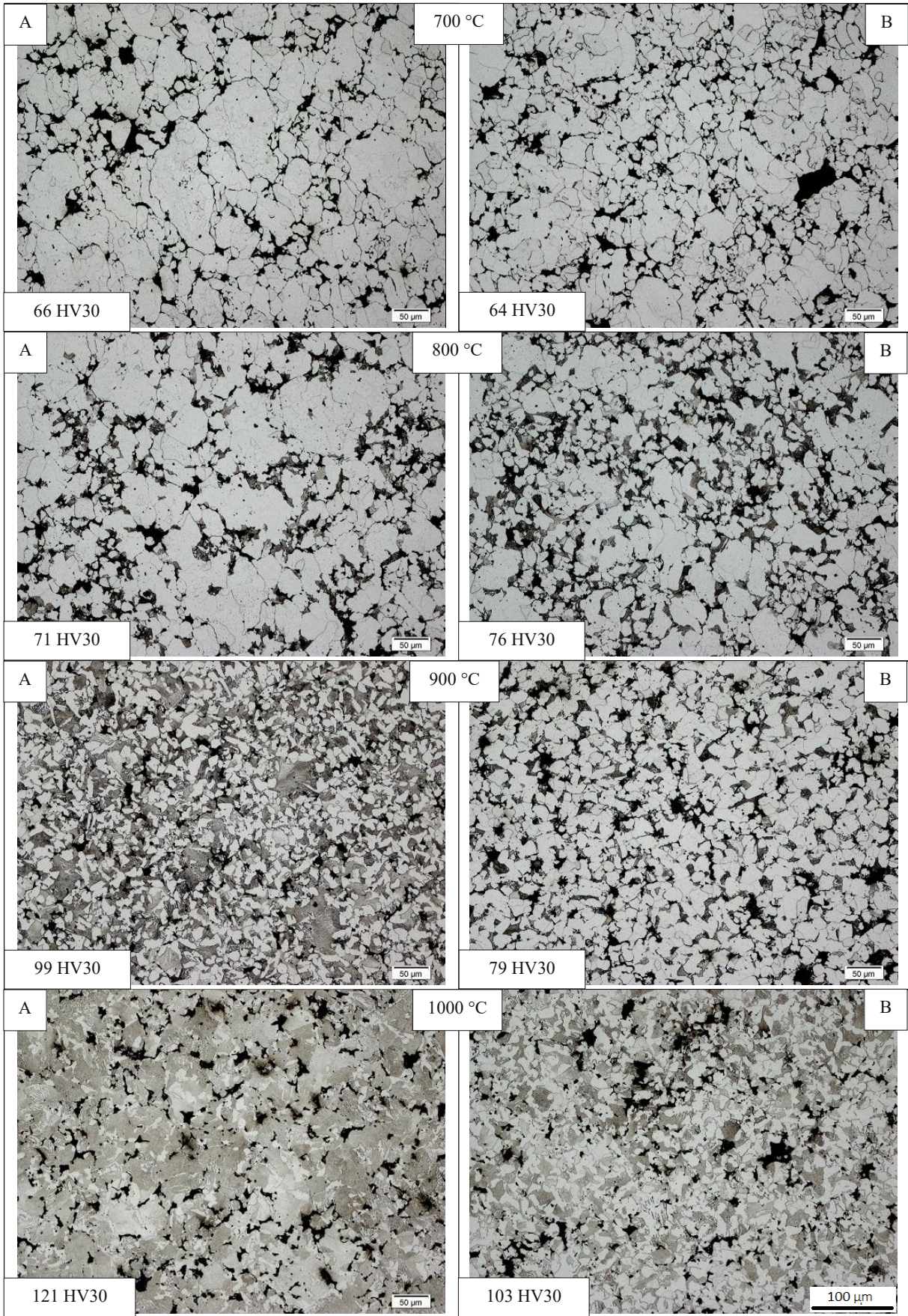


Figure 3.43: Etched microstructures of plain iron (Fe) compacted at 600 MPa, sintered 60 min in hydrogen (A) and argon (B), Nital, 500x. (scale bar 40 μ m holds for all images)



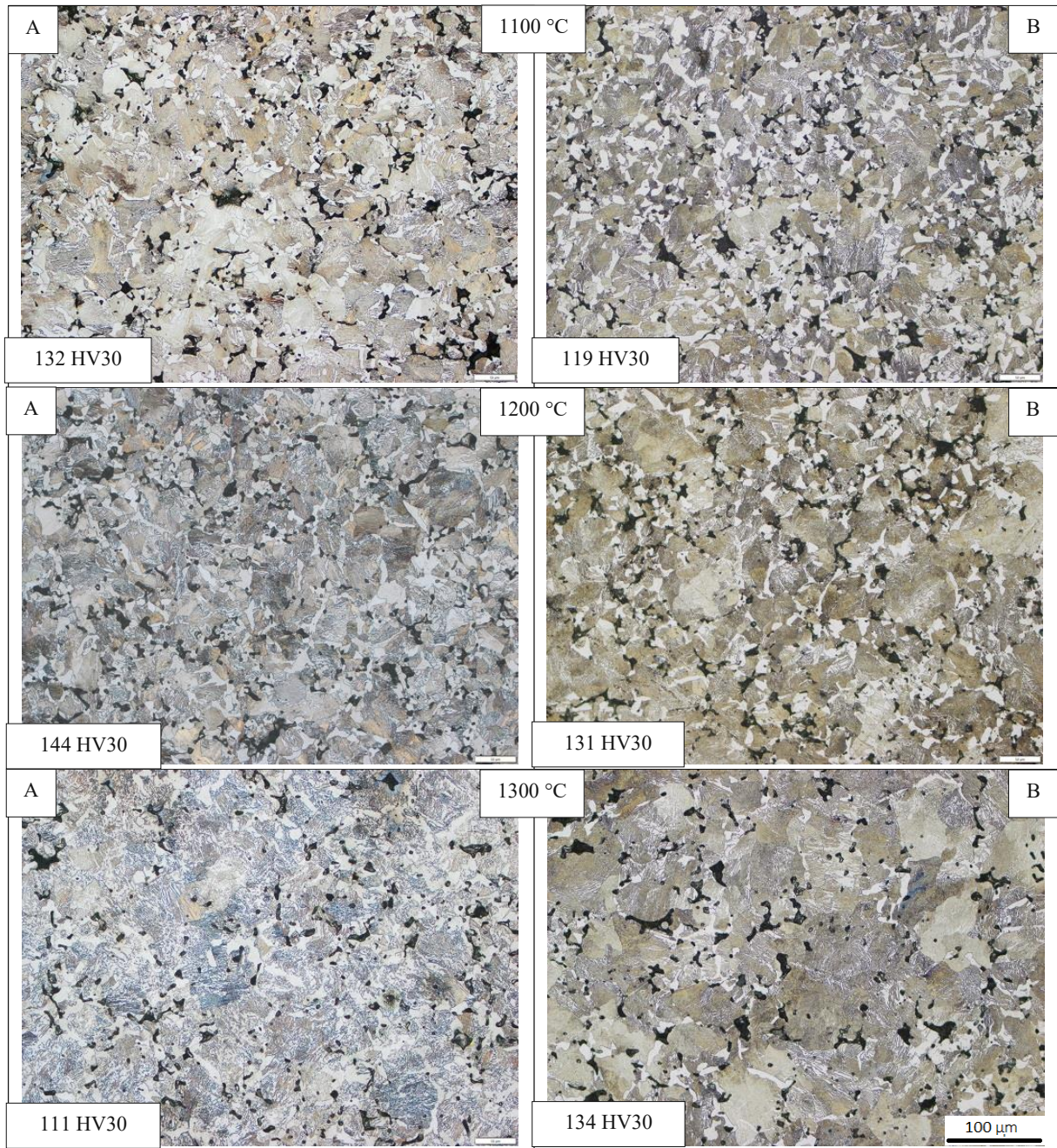
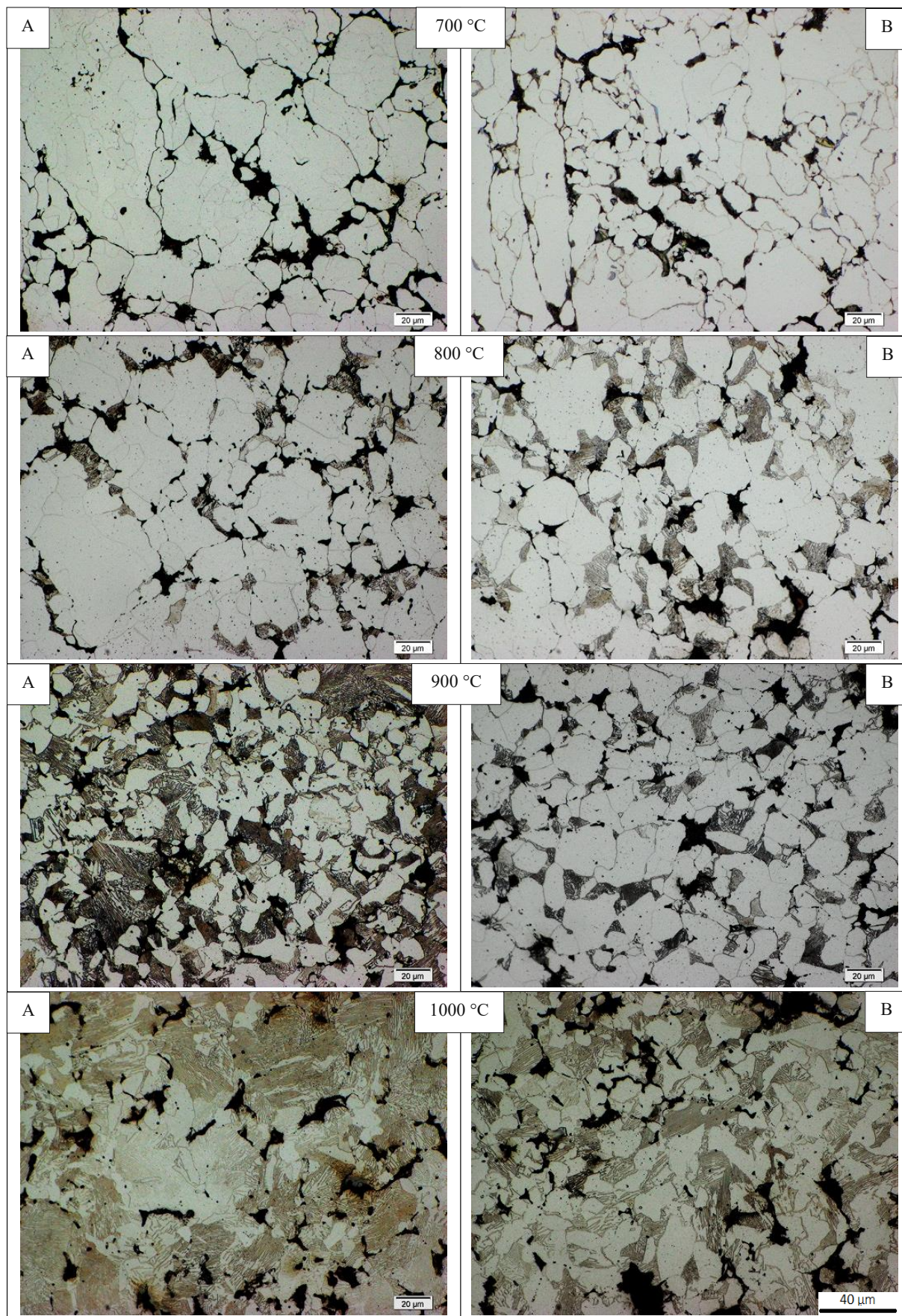


Figure 3.44: Etched microstructures of carbon steel (Fe-0.8% $C_{admixed}$) compacted at 600 MPa, sintered 60 min in hydrogen (A) and argon (B), Nital, 200x. (scale bar 100 μ m holds for all images)



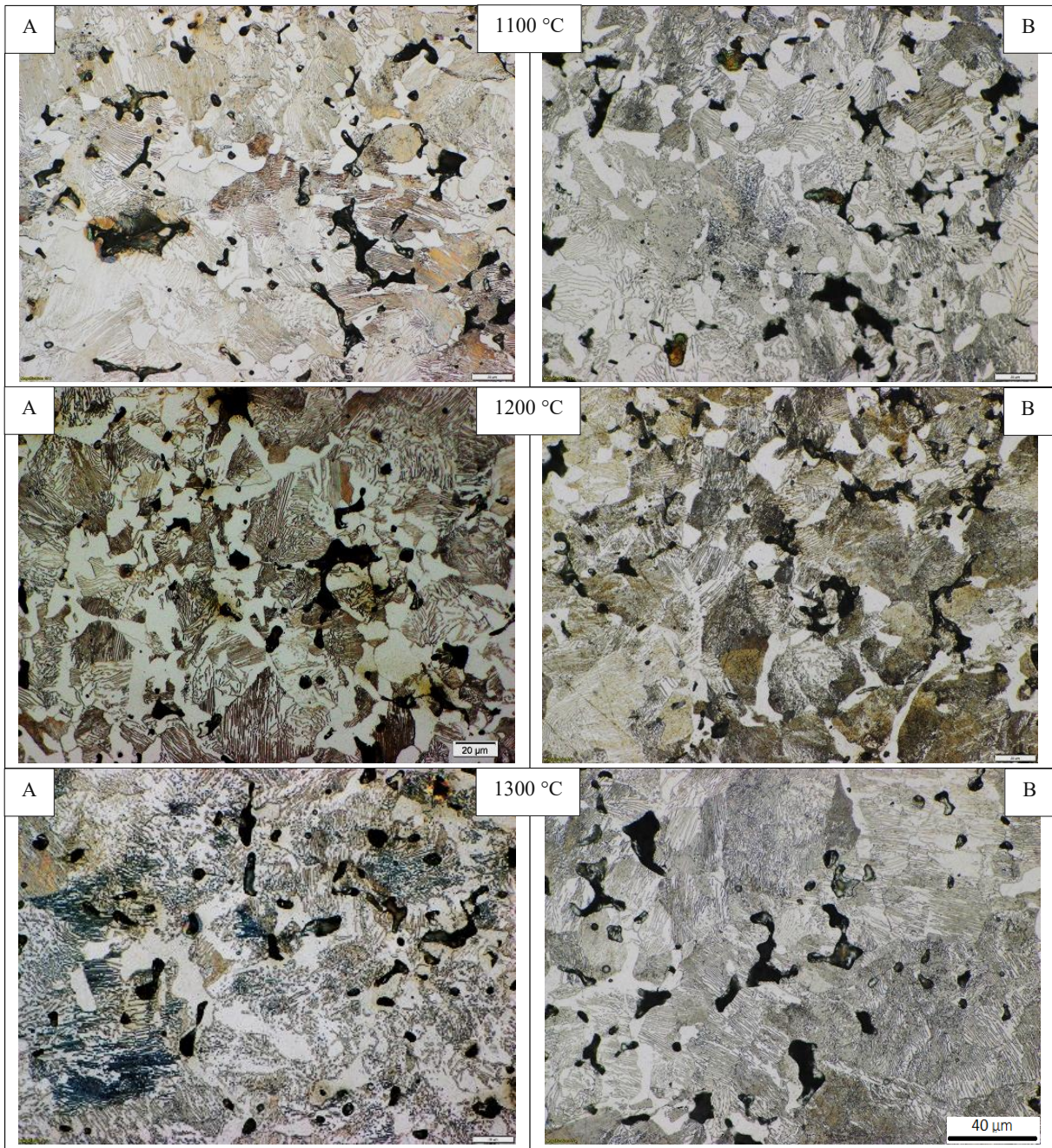
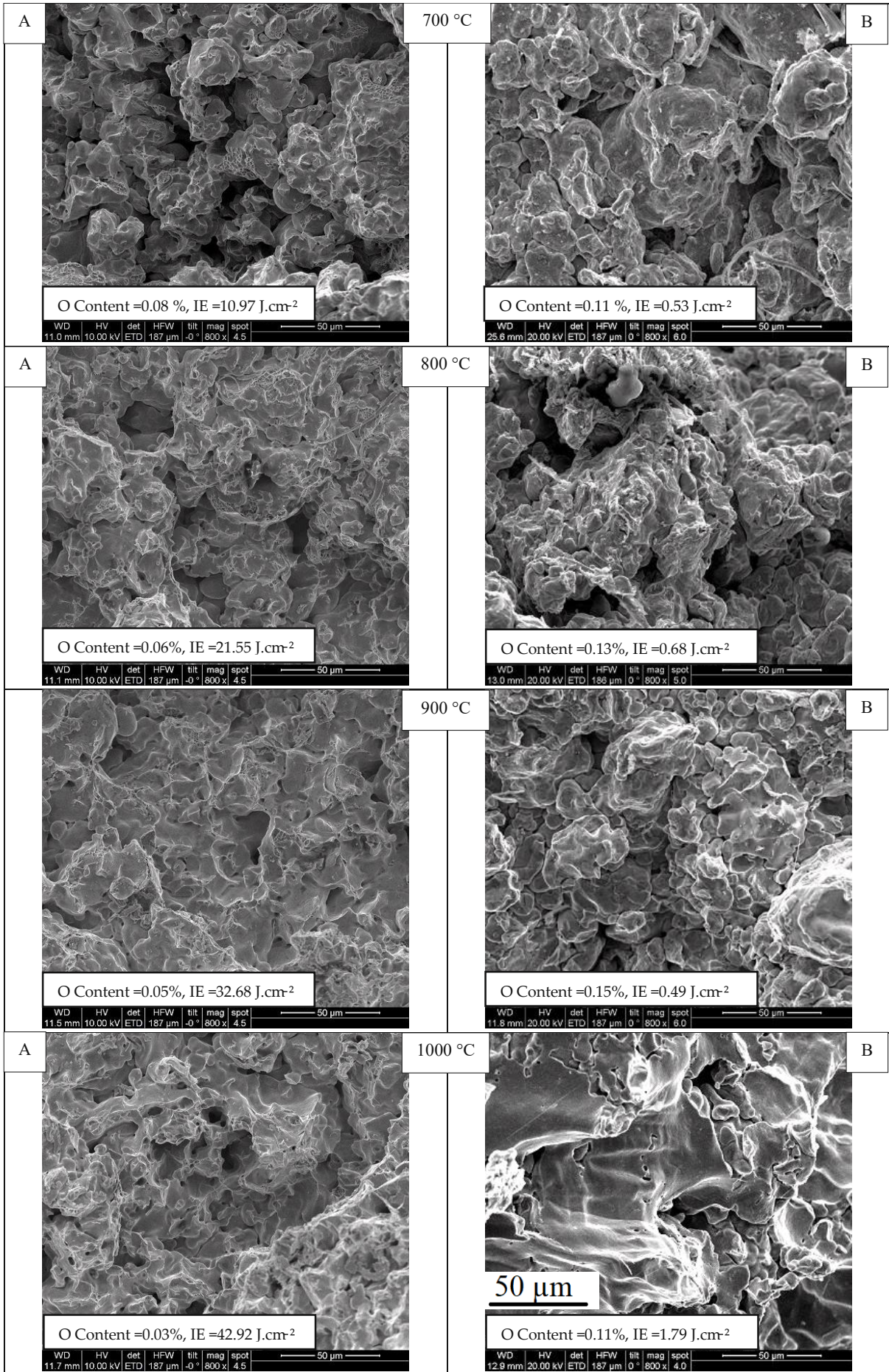


Figure 3.45: Etched microstructure of carbon steel (Fe-0.8% C_{admixed}) compacted at 600 MPa, sintered 60 min in hydrogen (A) and argon (B), 500x. (scale bar 40 μm holds for all images)

3.2.5. Fractography

Fracture surfaces and corresponding impact energies as well as the oxygen content of the plain iron specimens are shown in Figure 3.46 as a function of the sintering temperature. At 700 and 800°C, after sintering in Ar no significant contacts between powder particles are formed, which agrees with the very low obtained impact energies, 0.53 and 0.68 J/cm² respectively, while sintering in hydrogen at the same temperatures led to formation of some initial sintering contacts which resulted in localized ductile fracture and higher impact energies, 10.97 and 21.6 J/cm², respectively. Above 900°C and up to 1300°C, in Ar atmosphere the fracture mode is intergranular failure along the boundaries of very large ferrite grains as observed already in Figure 3.43, while the samples sintered in hydrogen show a completely different fracture mechanism, a classic ductile rupture is observable in this case. In hydrogen atmosphere the values of impact energy show a pronounced increase with higher sintering temperature, while sintering in Ar does not show any significant change in impact energy, even after high temperature sintering at 1300°C, which can be attributed to the grain coarsening and simultaneous oxygen enrichment at the grain boundaries [147].

In figure 3.47, fracture surfaces of the carbon steels are presented with corresponding impact energy data. At 700°C, no sign of sintering and contact formation is visible in both atmospheres, which is in contrast to plain Fe sintered in H₂ and illustrates the inhibiting effect of the graphite lamellae. SEM fractographs at 800°C show formation of the first sintering contacts in both atmospheres, however the higher value of impact energy in H₂ indicates that these initial bridges between particles are stronger in this atmosphere, which can be the result of faster surface oxide reduction. At 1000°C, a very similar mode of fracture and impact energy is observed for both atmospheres, an interparticle ductile dimple failure. The fractographs from 1100°C show that increasing the temperature resulted in formation of stronger sintering bonds which led to formation of transgranular cleavage facets in the fracture surfaces for both atmospheres. It is evident that increasing the sintering temperature to 1200 and 1300°C increased the fraction of the cleavage facets in the fracture surfaces.



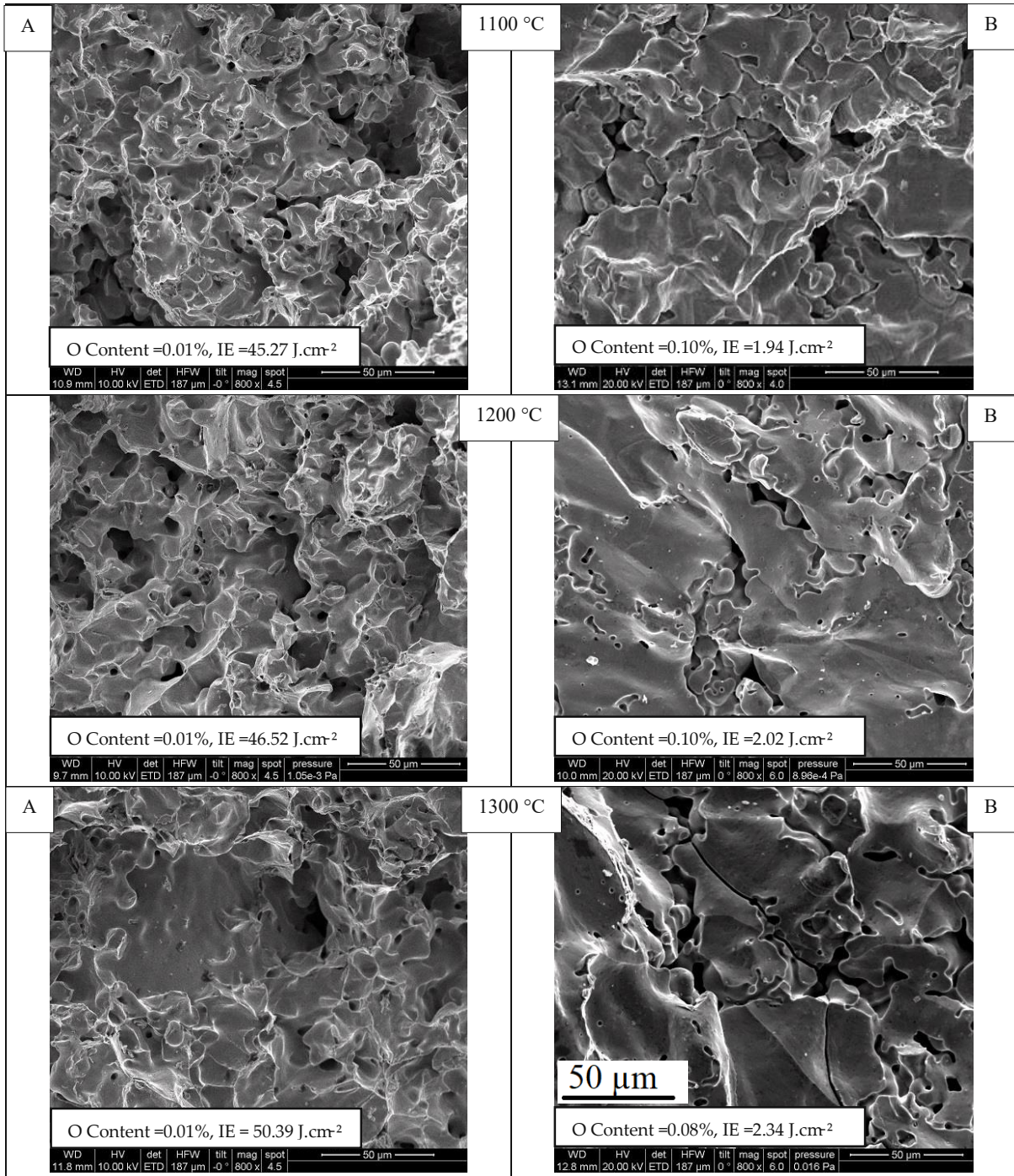
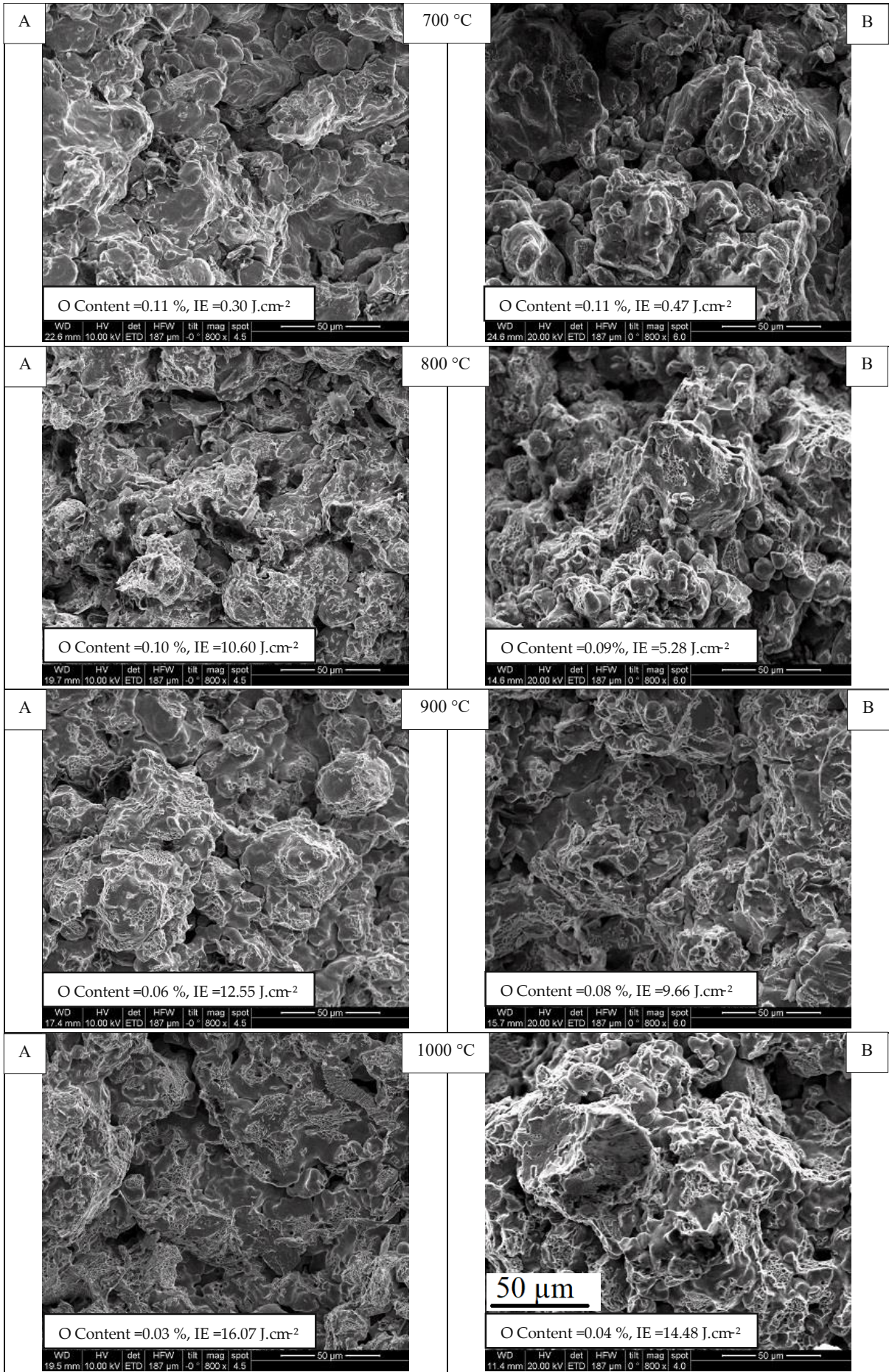


Figure 3.46: Fractographs of plain iron (Fe), compacted at 600 MPa, sintered at different temperatures for 60 min in hydrogen (A) and argon (B), 800 x. (scale bar 50µm holds for all images)



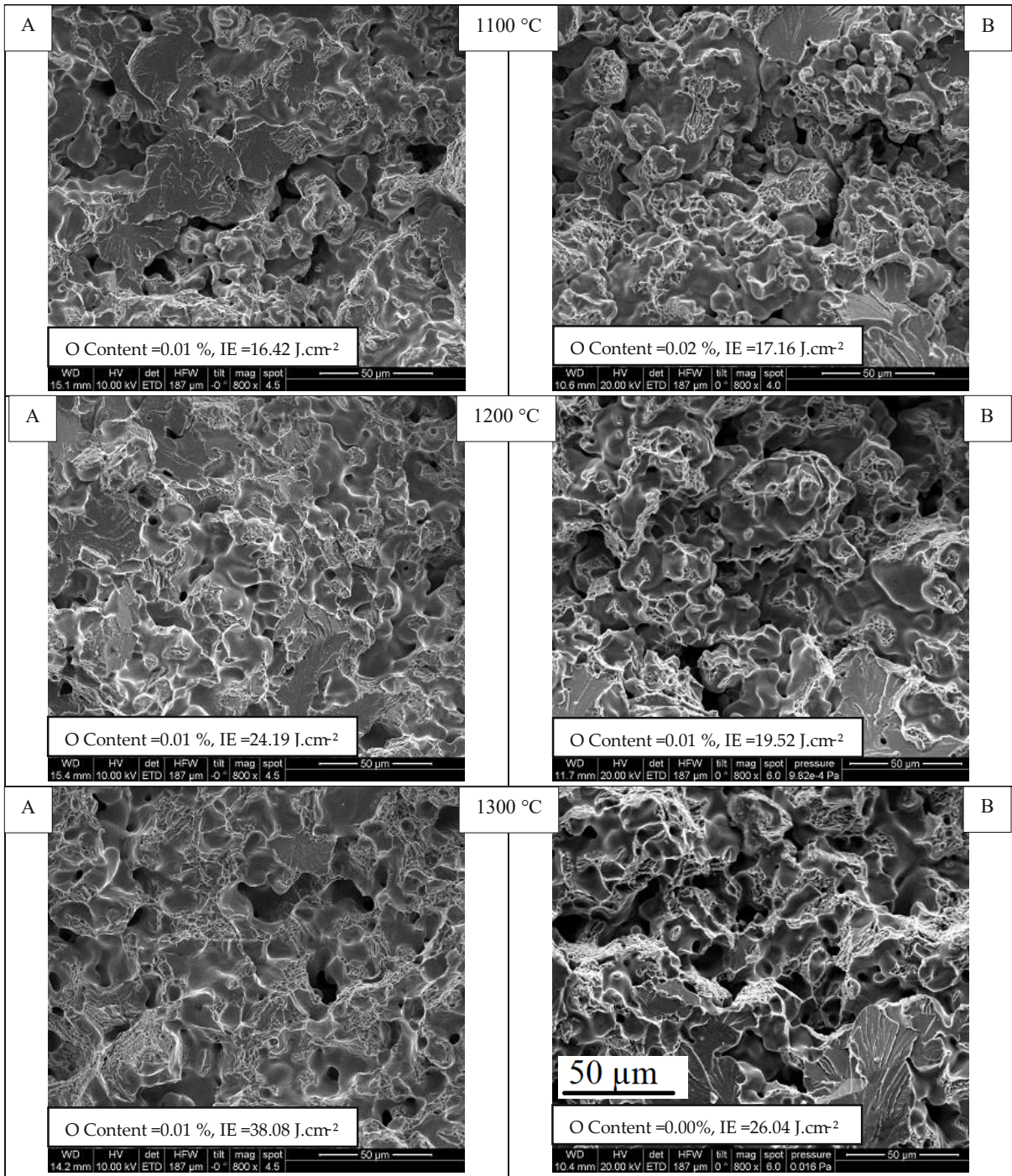


Figure 3.47: Fractographs of carbon steel (Fe-0.8C_{admixed}), compacted at 600 MPa, sintered 60 min at different temperatures in hydrogen (A) and argon (B), 800 x. (scale bar 50μm holds for all images)

3.2.6. Dimensional change and sintered density

Figure 3.48 and 3.49 present the dimensional change and sintered density of the plain iron specimens after sintering in hydrogen and argon. In this case (plain iron), in both atmospheres sintering resulted in a negative dimensional change at all temperatures. The sintered density data show that in the initial stages of sintering, sintering of Fe in hydrogen led to higher density compared to argon which can be attributed to the removal of oxygen from the surface of the iron particles and resulting faster contact formation and sintering shrinkage, which is in good agreement with the results of the fractography presented in Figure 3.46. Above this temperature, from 1000 to 1300°C, sintering is more active due to higher temperature, and sintering in both atmospheres resulted in almost the same sintered density without any significant change in dimension with higher sintering temperature.

The dimensional change and sintered density of the carbon steels as a function of the sintering temperature are presented in Figure 3.50 and 3.51, respectively. It is obvious that sintering in the temperature range of 800 to 1100°C resulted in expansion and lower density, which results from dissolution of carbon atoms into the iron lattice. After this process is completed, shrinkage follows during sintering at the higher temperatures up to 1300°C. Here, the higher shrinkage in the samples sintered in hydrogen at 1200 and 1300°C compared to argon is discernible. In this case it could be supposed that the earlier reduction of the surface oxides in hydrogen supports the shrinkage.

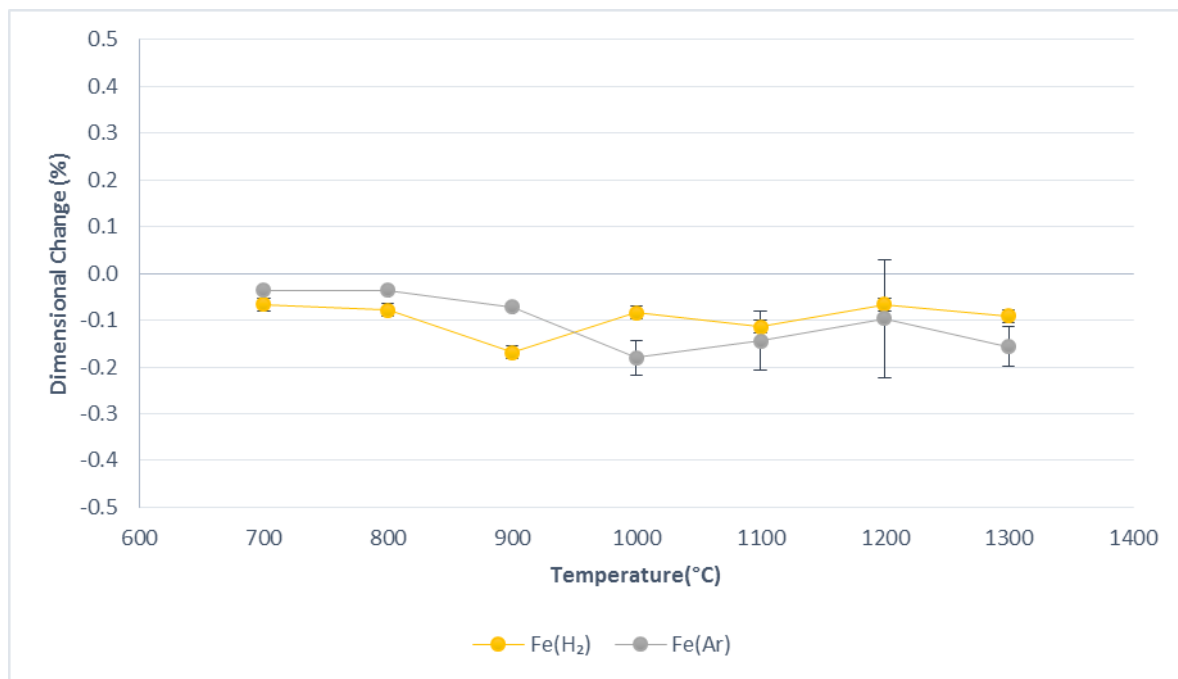


Figure 3.48: Dimensional change of plain iron (Fe) versus sintering temperature, compacted at 600 MPa, sintered in argon and hydrogen.

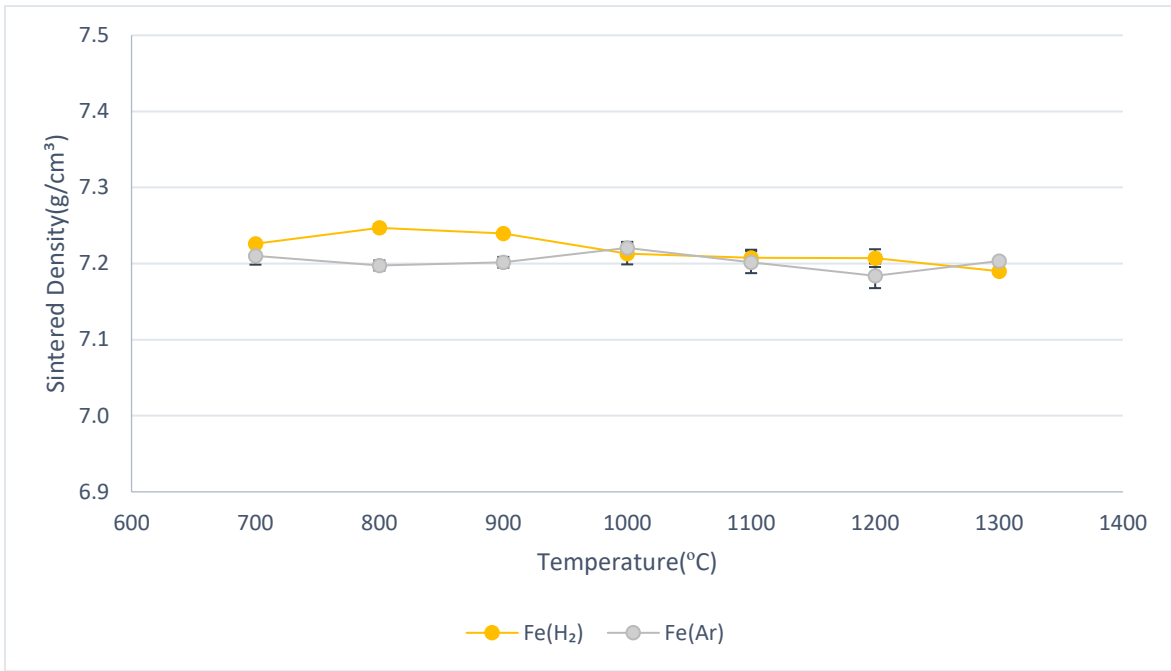


Figure 3.49: Sintered density of plain iron (Fe) versus sintering temperature, compacted at 600 MPa, sintered in argon and hydrogen.

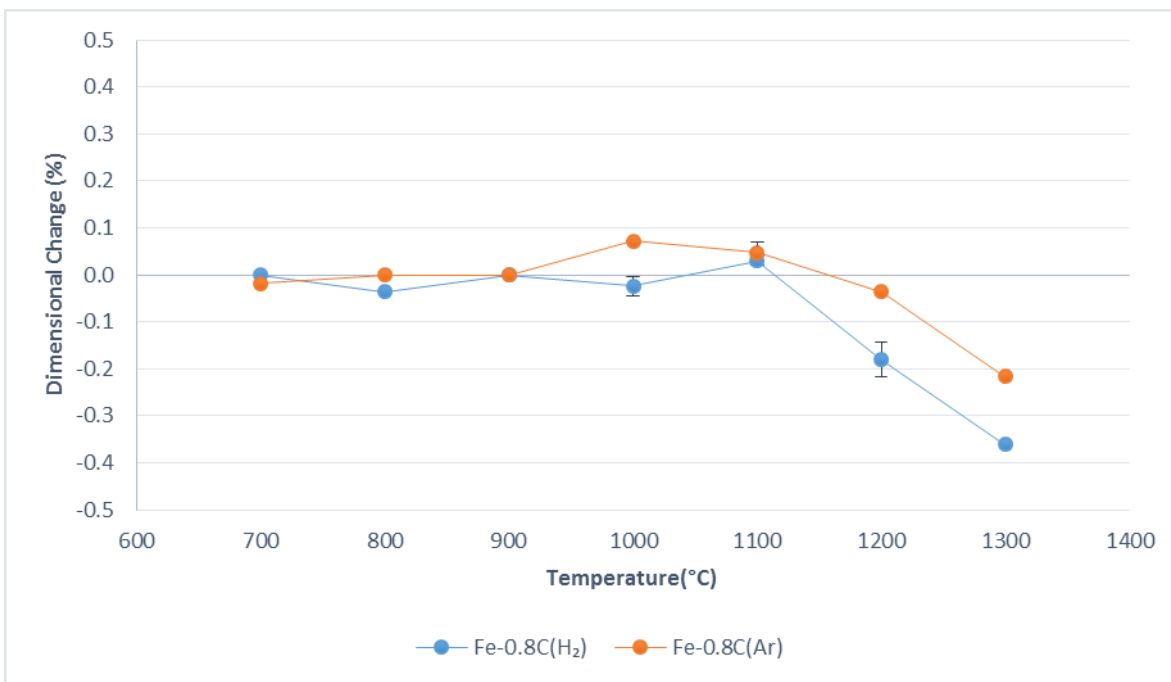


Figure 3.50: Dimensional change of carbon steel (Fe-0.8%C_{admixed}) versus sintering temperature, compacted at 600 MPa, sintered in argon and hydrogen.

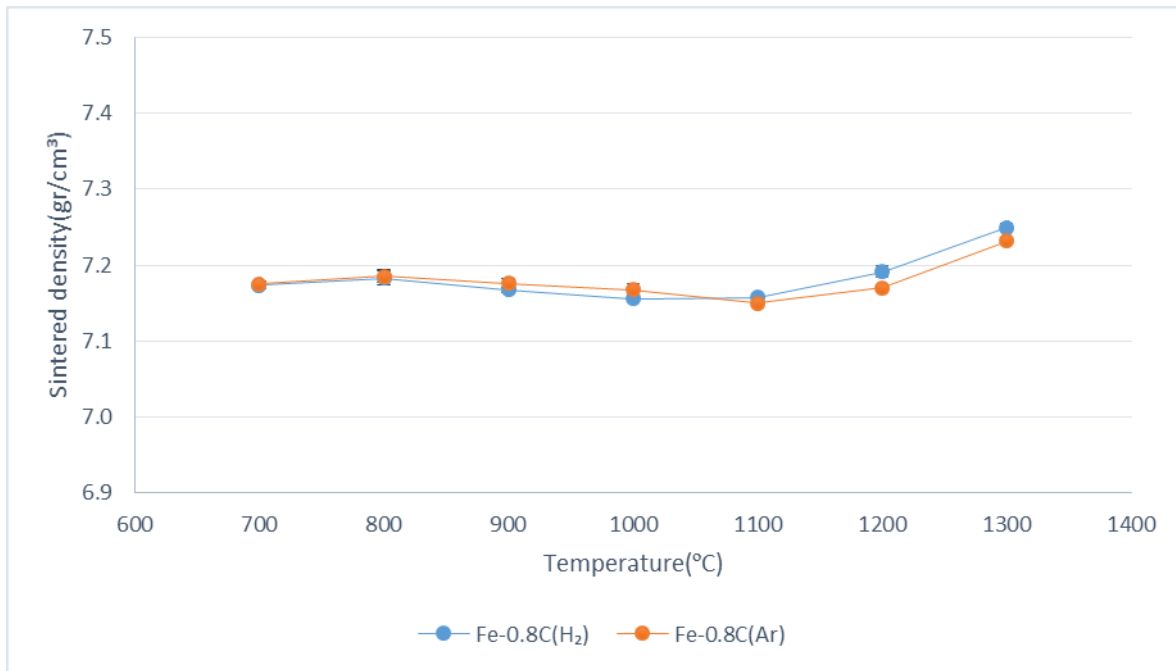


Figure 3.51: Sintered density of carbon steel (Fe-0.8%C_{admixed}) versus sintering temperature, compacted at 600 MPa, sintered in argon and hydrogen.

3.2.7. Mechanical properties

3.2.7.1. Hardness

The hardness of plain iron sintered in hydrogen and argon is shown in Figure 3.52. It is not surprising for ASC100.29 without carbon to have hardness levels between 60 to 70 HV₃₀. At low sintering temperatures of 700 to 900°C in both atmosphere the hardness of the samples decreased smoothly by around 10 HV. Recrystallization and recovery are two phenomena occurring in the initial stages of sintering of plain iron [118] that can affect and lower the hardness in this temperature window. Above 1000°C there is no pronounced change in hardness for sintering in argon, only a slight increase at 1300°C that might be caused by formation of stronger sintering contacts between particles at higher temperature. Above 1000°C, sintering in hydrogen resulted in more or less higher values of hardness which can be attributed to the smaller ferrite grains formed after sintering in this atmosphere.

Hardness data of the carbon steels are presented in Figure 3.53. At 700 and 800°C the carbon dissolution is negligible in both atmospheres, and the hardness is almost the same. At 900 and 1000°C the higher fraction of pearlite (see Figure 3.44) resulting from higher carbon dissolution is the main reason of higher hardness after sintering in hydrogen. Above this temperature, at 1100 and 1200°C, when carbon dissolution is complete in both atmosphere, higher hardness of the samples sintered in hydrogen might be related to the higher cooling rate of the samples in nitrogen compared to argon. At 1300°C the graph shows a pronounced drop in the hardness of the samples sintered in hydrogen which is attributed to the severe decarburization of the carbon steel at this temperature which affected the pearlite fraction of the surface and the core of the specimens (see Figure 3.45 at 1300°C).

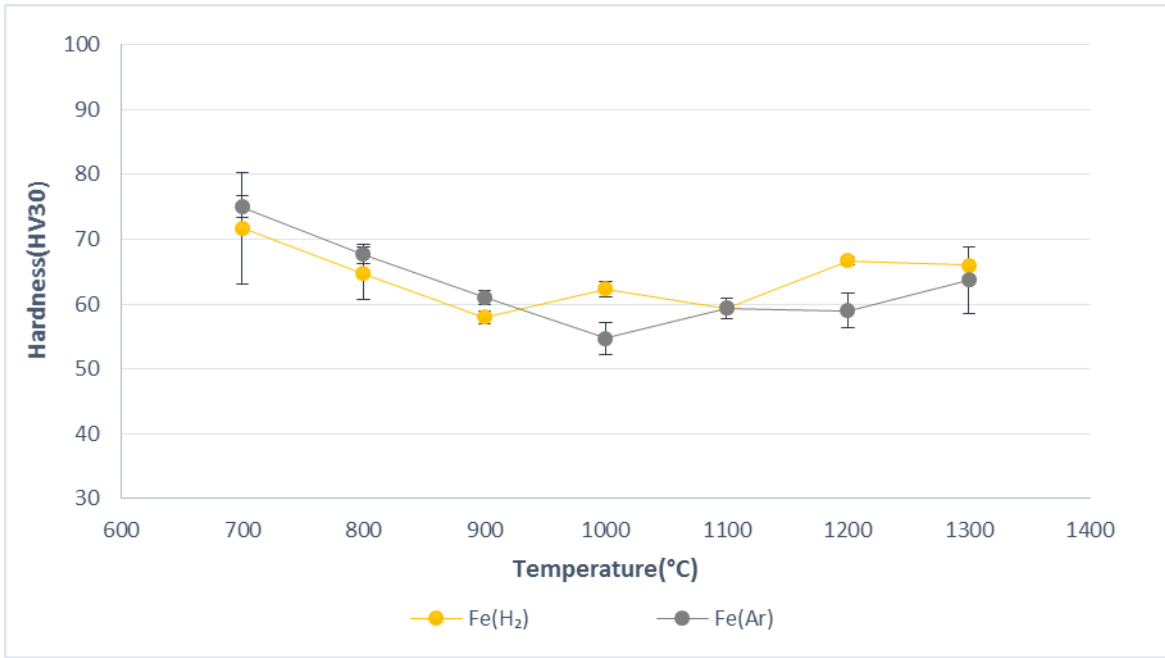


Figure 3.52: Hardness of plain iron (Fe) versus sintering temperature, compacted at 600 MPa, sintered in argon and hydrogen.

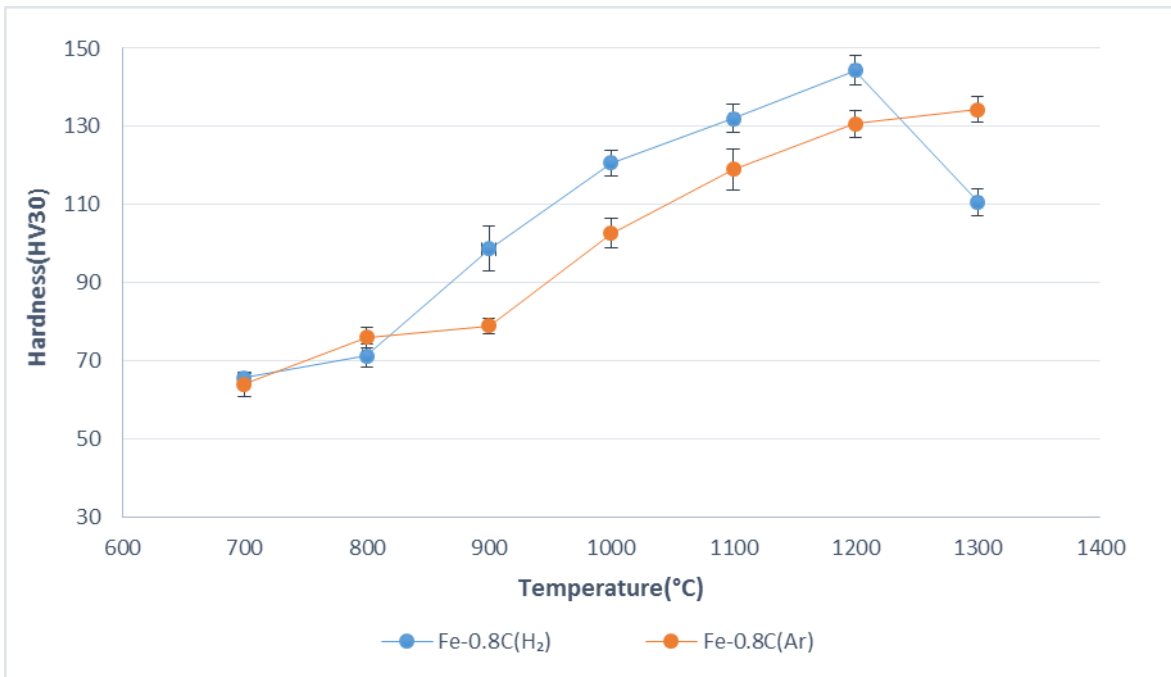


Figure 3.53: Hardness of carbon steel (Fe-0.8%C_{admixed}) versus sintering temperature, compacted at 600 MPa, sintered in argon and hydrogen.

3.2.7.2. Charpy impact energy

The impact energy consumed to break the plain iron Charpy specimen at room temperature is given in Figure 3.54. According to the results the plain iron shows a very brittle fracture with the lowest impact energy after sintering in argon. In fact the values of impact energy for this

material did not exceed 3 J/cm^3 even at the highest sintering temperature of 1300°C , while a considerable progressive trend is discernible for the samples sintered in H_2 . As mentioned before, during sintering in Ar and in the absence of interstitial alloying elements such as carbon and nitrogen, excessive grain coarsening occurs, and as we see in the chemical analysis, the amount of oxide reduction during sintering of this material under argon atmosphere is negligible compared to hydrogen. At this condition one possible reason can be enrichment of oxygen and precipitation of oxides at the grain boundaries during cooling [147] that present sites for the crack initiation and propagation which can be the main reason of this embrittlement of the material.

The Charpy impact energy data at room temperature of the carbon steels are given in Figure 3.55. Generally, mechanical properties are strongly influenced by the sintering temperature. In carbon steels it could be due to the higher densities, more rounded porosity and higher oxygen removal which, as mentioned in Chapter 1, is the precondition to create sintering contacts. According to the results, a continuous upward trend from 700 to 1300°C is indicated in both atmospheres. In order to better explain the behaviour, the graph should be separated into 3 different stages, low, moderate and high sintering temperature. At low temperatures, between 700 to 900°C , sintering of the carbon steels in hydrogen resulted in higher impact energy compared to argon, here a possible reason could be the removal of the surface oxides which occurs faster and at lower temperatures in hydrogen atmosphere. At intermediate temperatures at which the carbothermal reduction is the dominant mechanism for oxide reduction in both atmospheres and carbon dissolution has been already completed, the impact energy values are close to each other for both atmospheres. High temperature sintering, at 1200 and 1300°C resulted in higher impact energy in hydrogen. Higher ferrite fraction resulting from the pronounced decarburization at these temperatures can be the main reason of the higher impact energy of samples at these temperatures after sintering in hydrogen. Another point that should not be neglected here is the better thermal conductivity of hydrogen compared to argon, which leads to faster heating of the specimens in hydrogen, which extends the effective isothermal sintering time and could have a positive effect on the sintering process.

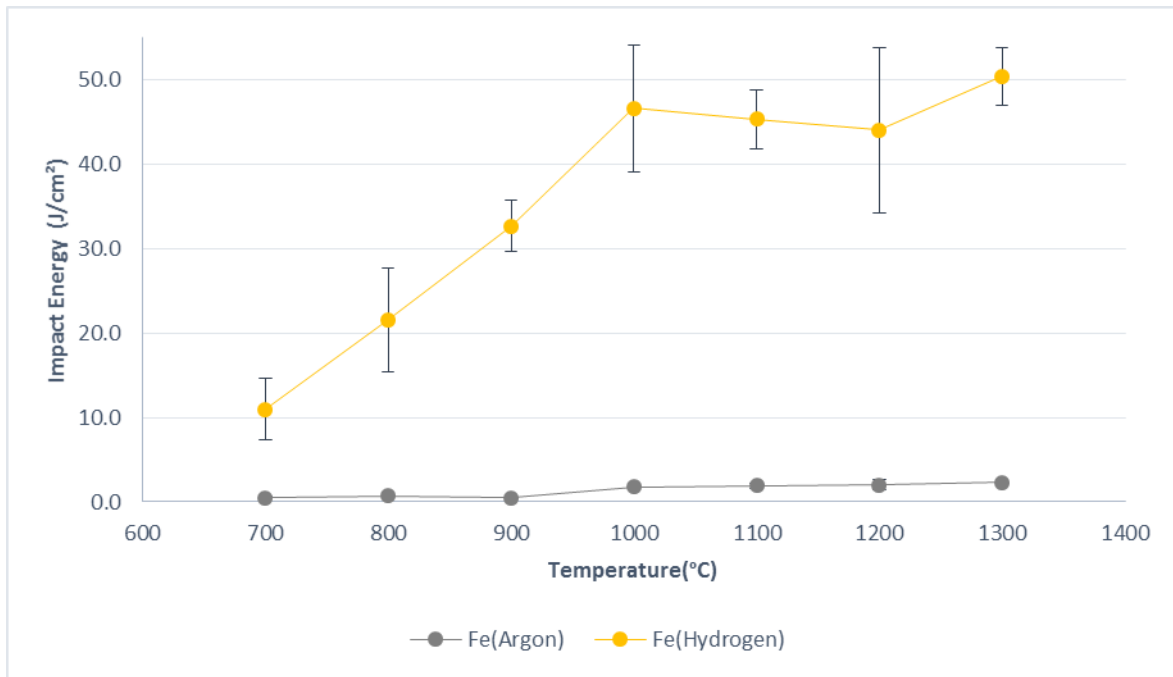


Figure 3.54: Charpy impact energy (at room temperature) of un-notched samples for plain iron (Fe) versus sintering temperature (sintered in hydrogen and argon).

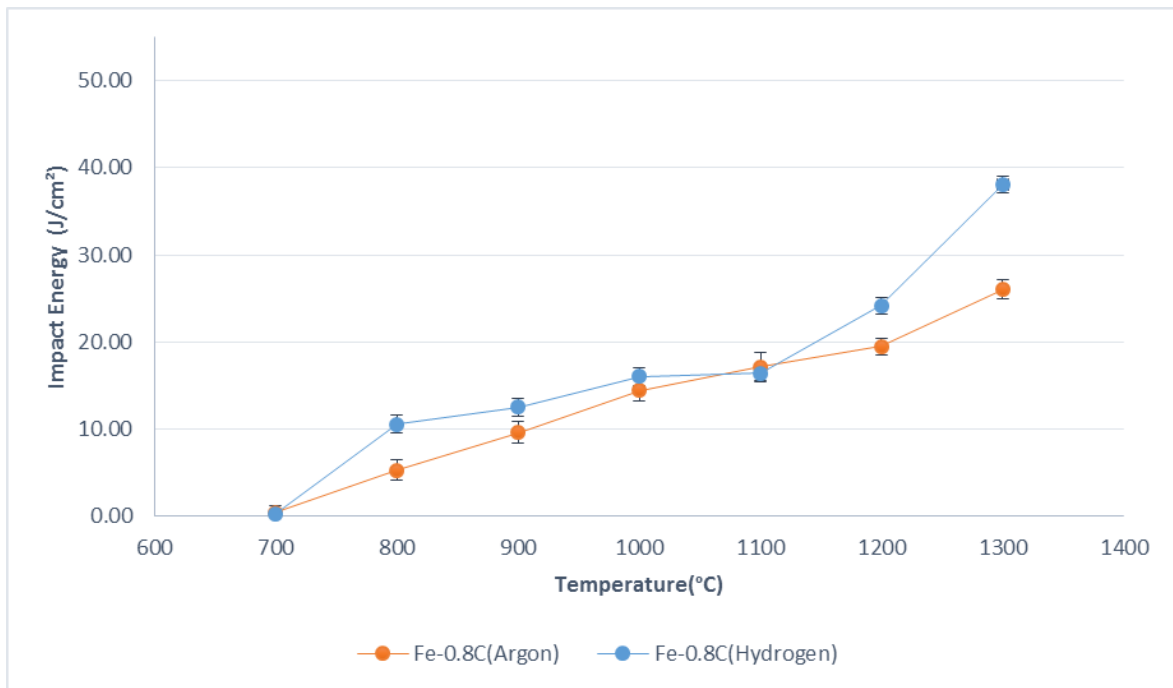


Figure 3.55: Charpy impact energy (at room temperature) of un-notched samples for carbon steel (Fe-0.8C_{admixed}) versus sintering temperature (sintered in hydrogen and argon).

3.2.7.3. Dynamic Young's modulus

Figure 3.1.56 shows the effective dynamic Young's modulus of plain iron sintered in hydrogen and argon, determined by measurement of the frequencies of flexural vibrations. It is well known that the Young's modulus of the material is mainly influenced by the density. According to the results, the dynamic Young's modulus of plain iron shows almost the same results for

both atmospheres, and increasing the sintering temperature does not have a significant effect on this parameter. At 700 °C in argon atmosphere when the surface of the iron particles is covered by iron oxides the reported value is only slightly lower than in hydrogen in which case the surface oxides have been reduced already. It shows that in case of plain iron, the dynamic Young's modulus does not depend markedly on the reduction of surface oxides. The effect of contact formation and neck coarsening also does not seem to be significant. It is evident that, in contrast to the impact energy which increased in hydrogen atmosphere, the dynamic Young's modulus was not affected by increasing the sintering temperature and neck enlargement. The dynamic Young's moduli of the carbon steels are presented in Figure 3.57. At 700°C the carbon steels showed lower values for the Young's modulus compared to plain iron, while sintering at 800°C in both atmospheres resulted in a jump in the parameter and above this temperature, sintering in both atmosphere resulted in almost the same values and the Young's modulus increased continuously with a smooth slope up to 1300°C.

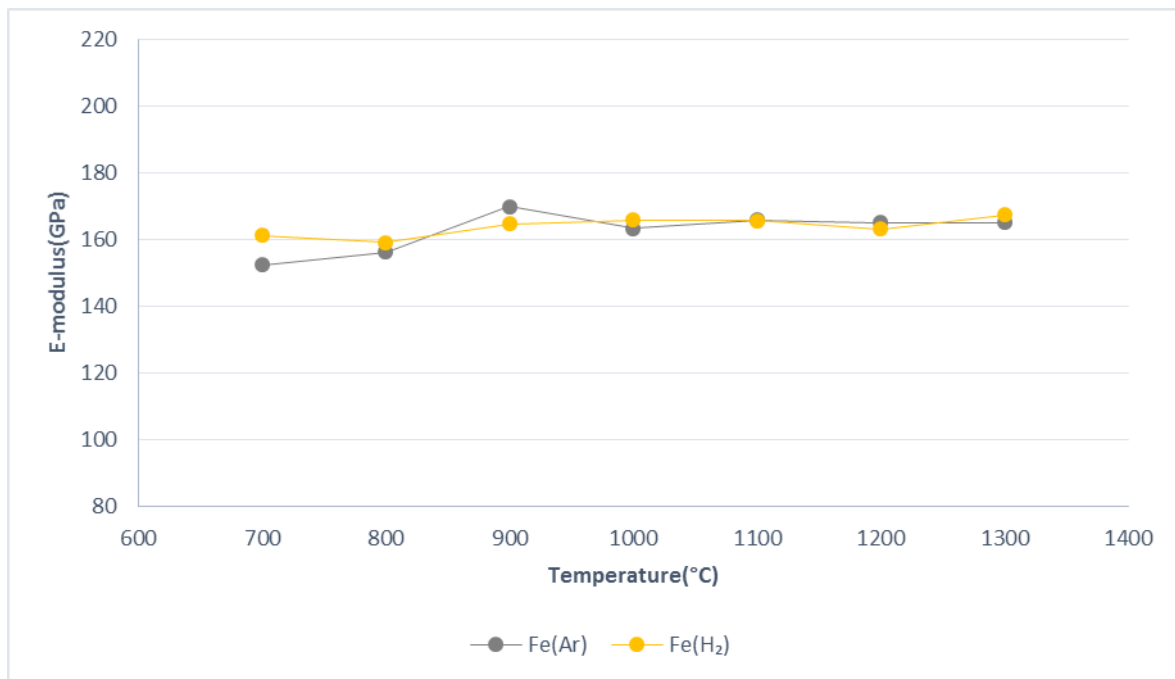


Figure 3.56: Dynamic Young's modulus of plain iron (Fe) as a function of the sintering temperature, compacted at 600 MPa, sintered 60 min in argon and hydrogen.

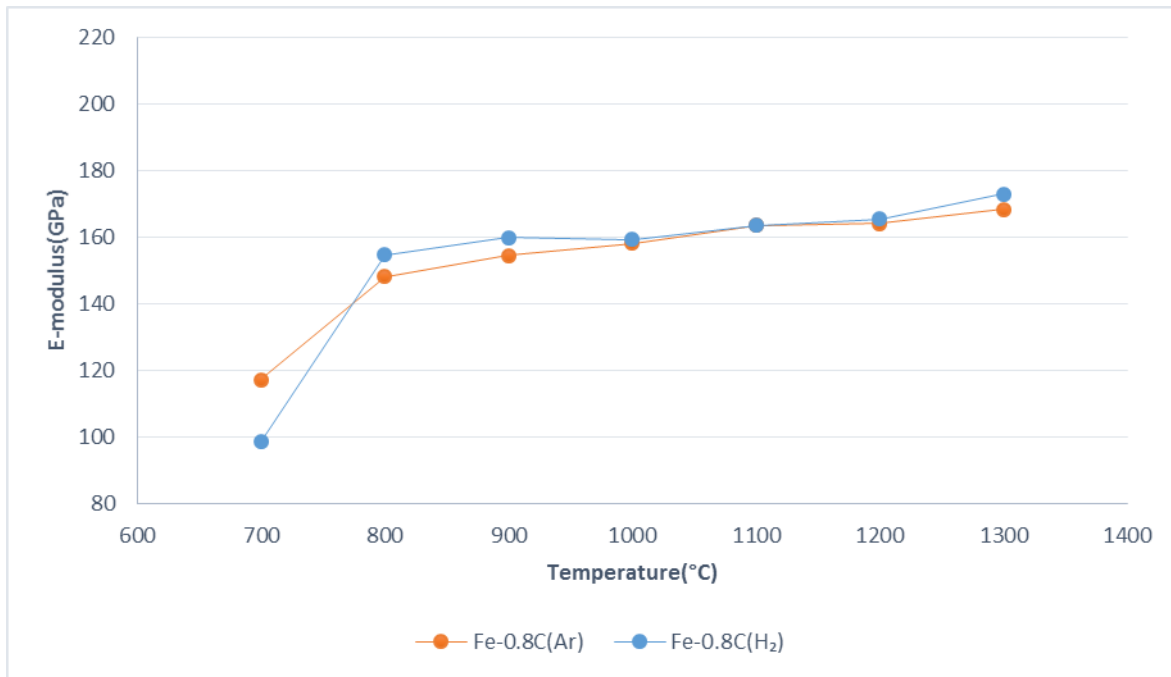


Figure 3.57: Dynamic Young's modulus of carbon steel (Fe-0.8C_{admixed}) as a function of the sintering temperature, compacted at 600 MPa, sintered 60 min in argon and hydrogen.

3.2.8. Physical properties

3.2.8.1. Electrical conductivity

Electrical conductivity data of the plain iron specimens sintered in hydrogen and argon are presented in Figure 3.58. It is obvious that, the specimens sintered in argon showed a smooth upward trend in conductivity with higher sintering temperature up to 1100°C. Two major reasons for this result are stress relaxation and also formation and growth of the sintering contacts. Above 1100°C there is no pronounced change in the parameter which remained almost constant up to 1300°C. On the other hand, sintering of plain iron in hydrogen resulted in lower conductivity with increasing sintering temperature. In this case it might be assumed that the negative effect of dissolution of the hydrogen atoms – which increased by increasing the temperature [154] – in the iron lattice is more dominant and compensates the positive effect of both oxygen removal and neck coarsening on the electrical conductivity; of course this would require that hydrogen did not diffuse out of the specimen during cooling, which is however quite probable, as shown e.g. in [155]. This effect could not be observed in the case of argon, because, in contrast to hydrogen, argon atoms are not soluble in the iron lattice. Alternatively, the difference also might rather be caused by the grain size since grain boundaries are obstacles for electron transport. In the very coarse-grained Ar specimens, this effect might be quite noticeable.

The electrical conductivity data of the carbon steels are presented in Figure 3.59. In both atmospheres, carbon steels showed a rapid increase in the conductivity at 800°C attributed to oxygen removal from the surfaces of powder particles and stress relaxation in the grains [115, 118]. Above 800°C, the electrical conductivity of the carbon steels is affected by several

phenomena, carbon dissolution and resulting pearlite formation in the iron lattice, which reduces the electrical conductivity of the compacts. On the other hand, reduction of surface oxides, neck formation, development of the sintering contacts and changing the shape of pores can increase the conductivity of PM parts during sintering at higher temperatures [115, 118, 120]. As can be seen, between 800 and 1000°C in hydrogen atmosphere a pronounced decrease in the parameter is visible which shows that in this temperature range, the effect of carbon (and possibly hydrogen) dissolution is more dominant than the contact formation and neck growth, which led to decreased electrical conductivity. At 1100 °C, the electrical conductivity is in its minimum and above this temperature and up to 1300 °C, a small increase in the parameter is discernible which can be attributed to the carbon loss as already shown.

In contrast to hydrogen, in argon atmosphere at 900°C, the electrical conductivity did not decrease and showed a slight increase compared to 800°C. It shows that at this temperature, carbon dissolution was not as pronounced as in the case of hydrogen, which is in good agreement with the results of metallography presented already (Figure 3.45). Above 900°C and up to 1100°C, a decline in the parameter is visible, which is the result of carbon dissolution in this temperature range. Above 1100°C and up to 1300°C, the electrical conductivity remained without significant change, which shows again that growth of the sintering contacts at higher temperature does not have a significant effect on electrical conductivity. Generally, according to these results it can be concluded that in sintering of PM carbon steels, dissolution of carbon into the iron lattice plays a more significant role compared with development and coarsening of the sintering contacts, at least at medium to high temperatures, which agrees with Simchi's results.

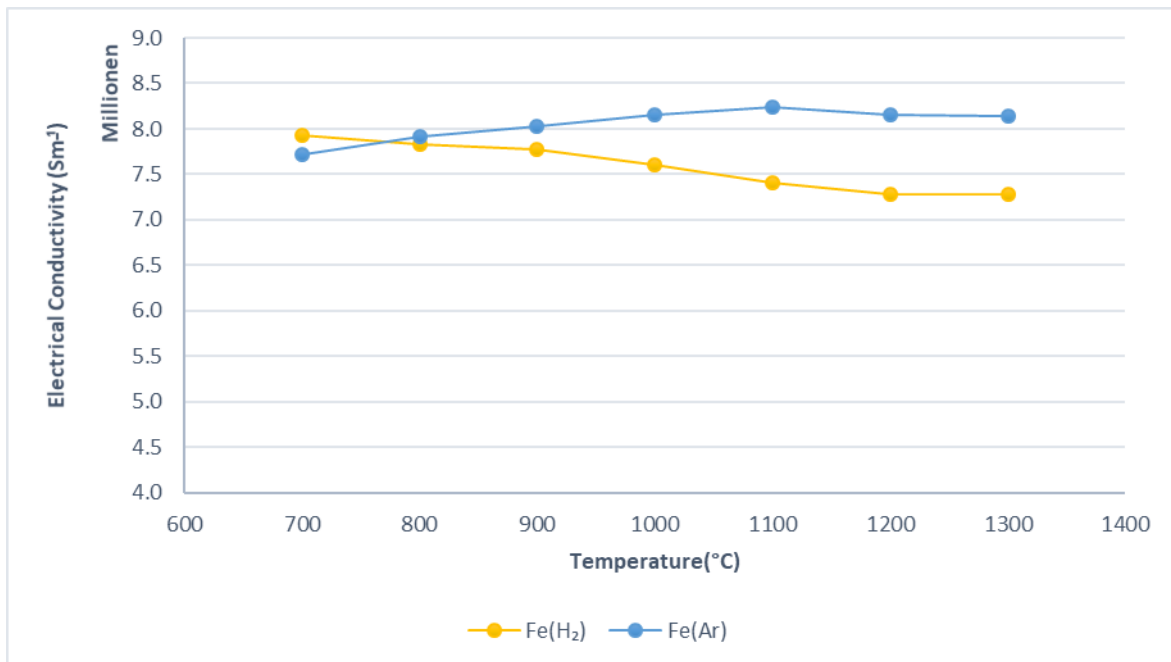


Figure 3.58: Electrical conductivity of plain iron (Fe) as a function of the sintering temperature, compacted at 600 MPa, sintered 60 min in argon and hydrogen.

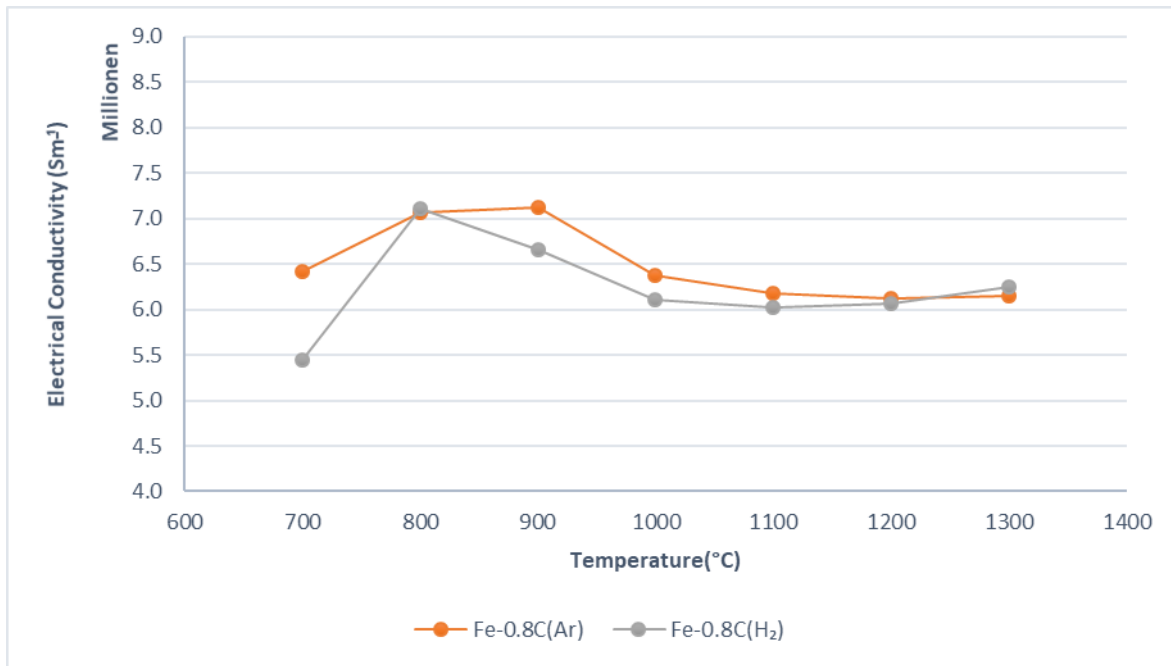


Figure 3.59: Electrical conductivity of carbon steel (Fe-0.8C_{admixed}) as a function of the sintering temperature, compacted at 600 MPa, sintered 60 min in argon and hydrogen.

3.2.8.2. Coercivity

It is well known that the coercive force is influenced by numerous parameters. The most important ones are mechanical strain (dislocations), grain size of the iron matrix and the purity of the material. Imperfections such as strain and dislocations cause considerable increase of H_c but they can be eliminated completely by annealing, which includes also sintering (which furthermore involves a double phase transformation, at least if done at $T > 900^\circ\text{C}$). Analysing the influence of various parameters on the coercive force of sintered Fe-parts showed that the density is rather insignificant while size and shape of the pores are much more important than their total volume (density) [121]. For instance it is shown that intense sintering lowers the specific pore surface by pore rounding and pore coarsening and thus also lowers the effect of the pores towards H_c [124].

The relationship between coercivity and sintering temperature of plain iron is shown in Figure 3.60. In both atmospheres a smooth decline from 700 to 1300°C is visible. However, it is well known that grain growth during sintering is the reason for this reduction of the coercivity [156], however in this case the coarser ferrite grains in the argon atmosphere did not lead to lower coercivity. An explanation for this could be the lower oxygen content in hydrogen atmosphere which led to more active sintering and resulting rounded and coarser pores as shown in the pore morphology, see the metallography sections (Figure 3.39).

The coercive force data of the carbon steels sintered at different atmospheres are shown in Figure 3.61. As stated above, it has been shown that the presence of non-magnetic inclusions, principally carbides, in ferromagnetic materials such as steels inhibit the motion of domain walls and result in degradation of the magnetic properties [122]. The samples sintered in argon

showed a slight upward trend from 700 to 900°C. At 1000°C the graph shows a pronounced raise which is attributed to carbon diffusion and pearlite formation as shown already in the metallography sections. After completion of carbon dissolution above 1000°C and up to 1300°C, this property is reduced only slightly as a consequence of phenomena such as pore rounding and coarsening of the grains.

The coercivity of the samples sintered in hydrogen showed a significant raise at 900°C which is 100 K lower than in argon atmosphere and confirms the results of metallography which indicated faster carbon dissolution in hydrogen atmosphere at this temperature. Similar to argon atmosphere, in this case the coercivity does not show significant changes after completion of the carbon dissolution. At 1300°C a drop in the coercivity is visible which is attributed to the pronounced decarburization showed already in Figure 3.35.

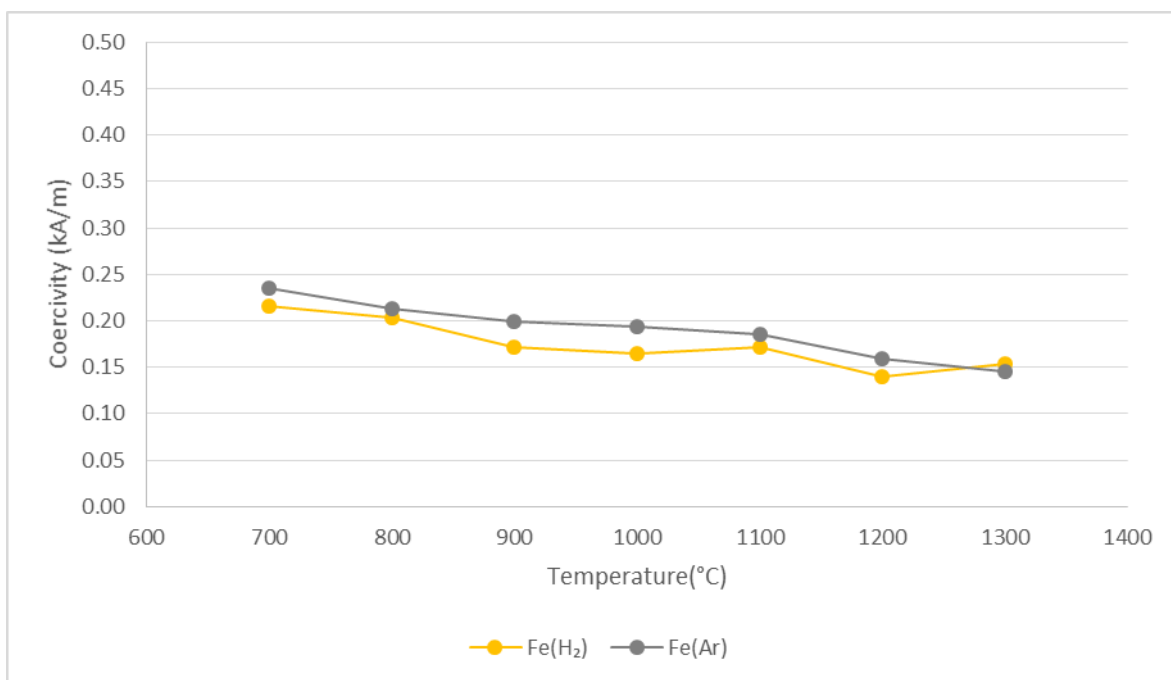


Figure 3.60: Coercivity of plain iron (Fe) as a function of the sintering temperature, compacted at 600 MPa, sintered 60 min in argon and hydrogen.

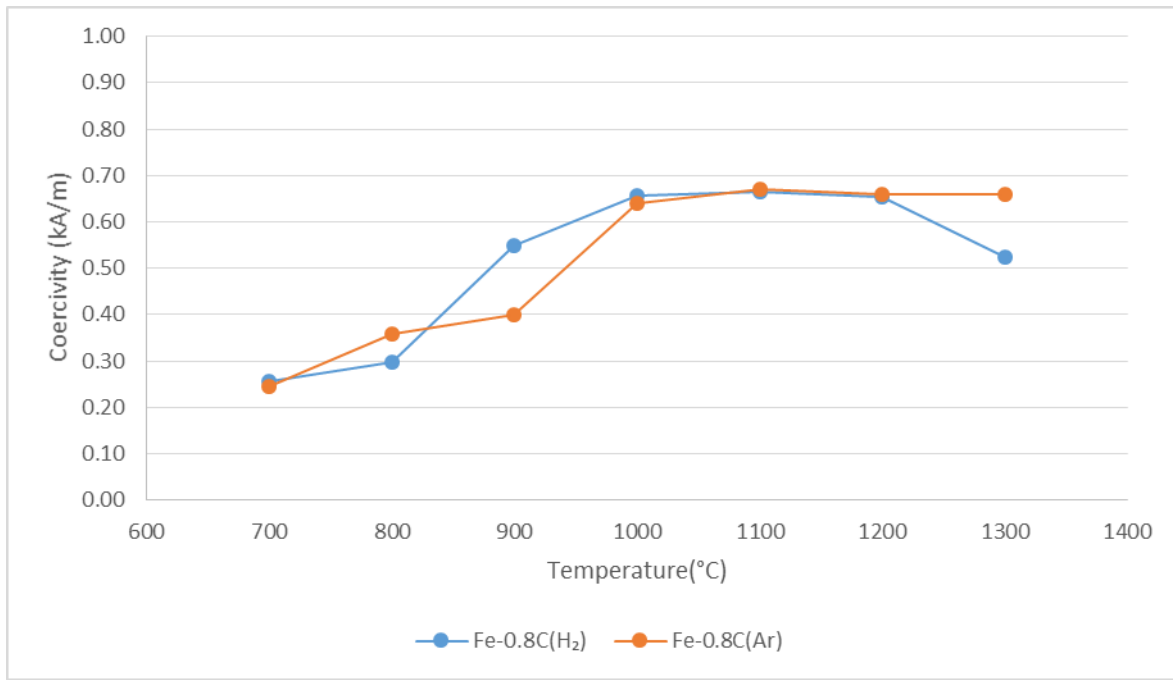


Figure 3.61: Coercivity of carbon steel (Fe-0.8% C_{admixed}) as a function of the sintering temperature, compacted at 600 MPa, sintered 60 min in argon and hydrogen.

3.3. Part 1c: Sintering process and properties of PM steels alloyed with atomized Fe-C Masteralloy

In production of many ferrous PM precision parts, carbon plays a major role as the most important alloy element, in particular components with higher strength and hardness contain carbon in their matrix. As mentioned in Chapter 1.4.2, introducing carbon within prealloyed powder particles increases the hardness and thus severely reduces the compactibility. Therefore, addition of this element is usually done through admixing fine graphite grades that are completely dissolved during sintering [11].

The dissolution of graphite in the iron matrix requires temperatures well above the eutectoid. Some previous studies [11, 42] have shown that even for the most reactive graphite grades temperatures $>900^{\circ}\text{C}$ are required to attain significant carbon dissolution, which temperature is however still well below the standard sintering temperatures for ferrous PM parts. As stated in Chapter 1, carbon also acts as a reducing agent for the oxides on metal powders, resulting in formation of CO_2 but mainly of CO . According to the gasification theory of carburizing, this CO (in presence of free carbon or graphite) can subsequently act as carburizing gas through Boudouard's equilibrium or through the water gas reaction.

As mentioned before, one of the most attractive features of powder metallurgy processing is its flexibility in chemical composition. There are many studies on the effect of alloy elements and processing conditions on physical and mechanical properties of PM components to increase the chance of using PM steels and developing the application of them in the different industries. For low alloy PM steels that have great potential for use e.g. in powertrain parts, chromium and molybdenum have been used to boost the mechanical and wear properties [49, 74, 157-159]. Molybdenum increases the tensile strength as well as the hardness by enhancing bainitic phase transformation and, moreover, minimizes dimensional changes of the final specimen after sintering [70, 158]. Chromium also can provide good hardenability at low cost, which makes it an attractive alloying element for sinter hardening steel grades. Chromium is an element with high oxygen affinity and sensitive to oxidation, and therefore sintering of steels containing Cr in industrial condition is a major challenge. Presence/Formation of the stable chromium oxides which weaken the sintering contacts is the main problem if these are not reduced properly. Reducing these oxides is only possible at high sintering temperatures, with carbon acting as the main reducing agent even if sintering in H_2 containing atmospheres. There are several studies that have investigated this issue [83, 160].

In the present work the effect of using an Fe_3C -containing masteralloy as carbon carrier and sintering enhancer on sintering of a carbon steel as well as a Cr-Mo prealloyed steel in inert atmosphere (Ar) has been investigated. Furthermore, introducing carbon through a high density compound – $7.69 \text{ g}\cdot\text{cm}^{-3}$ for Fe_3C compared to $2.24 \text{ g}\cdot\text{cm}^{-3}$ for graphite – increases the theoretical density and should enable attaining higher green density levels [161, 162], at least if compacting to very high density. The investigation presented here focuses on the sintering process including deoxidation, carbon dissolution and formation of sintering contacts from the initial stages of sintering up to high sintering temperature as well as the physical and mechanical properties of sintered components.

In this part of the work, the starting base powders used were ASC100.29 and the prealloyed grade Fe-3%Cr-0.5%Mo (AstaloyCrM). Natural graphite UF4 was added as carbon carrier. The iron-carbon masteralloy (H49, about 4.5%C) was used as an additive. To attain 0.8% total carbon content in the starting powder mix, the steel and masteralloy powders were dry mixed in a laboratory mixer. Table 3.7 shows the designation and composition of the prepared mixtures. Charpy bars (ISO 5754) have been produced for this study in the tool with floating lubricated die at 600 MPa. Sintering of the samples was performed in the push-type laboratory furnace at different temperatures (700 -1300°C) for 1 hr under plain Ar (99.999% quality). After the holding period at the target temperature, the steels were cooled in the water-jacketed exit zone under the same protective atmosphere that was used for the sintering. The results of the measurements are listed in Tables 3.8 and 3.9. (remark: the values of the reference materials Fe-0.8%C(graphite) presented here have been taken from the previously described test series in Chapter 3.2 with the same composition)

Table 3.7: Composition of powder mixes.

	Designation	Mix composition
1	Fe-0.8C	ASC100.29+ 0.8% C (only graphite)
2	Fe-0.8C(MA)	ASC100.29+ 0.8% C (0.62% graphite + 4% Fe-C masteralloy)
3	CrM-0.8C	Ast CrM + 0.8% C (only graphite)
4	CrM-0.8C(MA)	Ast CrM + 0.8% C (0.62% graphite + 4% Fe-C masteralloy)

Table 3.8: Sintered properties of carbon steels; compacted at 600 MPa, sintered 60 min at 700-1300°C in argon

<i>Sintering Temp.</i> (°C)	<i>Material</i>	<i>Sintered density</i> (g/cm ³)	<i>Dimensional Change</i> (%)	<i>Impact energy</i> (J/cm ²)	<i>Hardness (HV30)</i>	<i>Dyn. Young's modulus</i> (GPa)	<i>Oxygen content</i> (wt %)	<i>Combined carbon content</i> (wt %)	<i>Electrical conductivity</i> (S.m ⁻¹)10 ⁴	<i>Coercivity</i> (kA/m)
700	Fe-0.8C	7.18 ± 0.00	-0.02 ± 0.00	0.5 ± 0.3	64.0 ± 3.0	117.2	0.107 ± 0.004	0.786 ± 0.012	641	0.25
	Fe-0.8C(MA)	7.10 ± 0.00	-0.01 ± 0.01	1.0 ± 0.1	57.0 ± 1.0	70.1	0.130 ± 0.011	0.782 ± 0.014	400	0.27
800	Fe-0.8C	7.19 ± 0.01	0.00 ± 0.00	5.3 ± 1.2	76.0 ± 2.6	148.1	0.094 ± 0.004	0.786 ± 0.005	706	0.36
	Fe-0.8C(MA)	7.11 ± 0.01	0.02 ± 0.00	2.6 ± 0.4	80.7 ± 1.5	132.3	0.145 ± 0.005	0.780 ± 0.010	618	0.50
900	Fe-0.8C	7.18 ± 0.01	0.00 ± 0.00	9.7 ± 1.2	79.0 ± 2.0	154.6	0.081 ± 0.002	0.776 ± 0.006	712	0.40
	Fe-0.8C(MA)	7.10 ± 0.01	0.03 ± 0.01	7.8 ± 0.1	90.0 ± 2.0	147.8	0.108 ± 0.030	0.761 ± 0.004	626	0.67
1000	Fe-0.8C	7.17 ± 0.01	0.07 ± 0.00	14.5 ± 1.3	102.7 ± 3.8	158.2	0.041 ± 0.001	0.752 ± 0.006	638	0.64
	Fe-0.8C(MA)	7.11 ± 0.01	0.01 ± 0.01	13.2 ± 1.0	120.3 ± 3.8	154.0	0.042 ± 0.006	0.745 ± 0.004	607	0.73
1100	Fe-0.8C	7.18 ± 0.00	0.05 ± 0.00	17.2 ± 1.6	119.0 ± 5.2	163.5	0.023 ± 0.003	0.744 ± 0.004	618	0.67
	Fe-0.8C(MA)	7.16 ± 0.01	-0.16 ± 0.02	18.6 ± 1.5	120.3 ± 3.8	160.5	0.015 ± 0.004	0.726 ± 0.005	590	0.77
1200	Fe-0.8C	7.19 ± 0.00	-0.04 ± 0.00	19.5 ± 1.0	130.7 ± 3.5	164.1	0.011 ± 0.001	0.728 ± 0.005	612	0.66
	Fe-0.8C(MA)	7.19 ± 0.01	-0.28 ± 0.03	21.9 ± 2.5	140.3 ± 2.9	164.6	0.009 ± 0.001	0.715 ± 0.004	593	0.80
1300	Fe-0.8C	7.23 ± 0.00	-0.22 ± 0.00	26.0 ± 1.1	134.3 ± 3.2	168.3	0.004 ± 0.001	0.733 ± 0.006	615	0.66
	Fe-0.8C(MA)	7.22 ± 0.01	-0.50 ± 0.00	30.0 ± 1.5	145.0 ± 4.4	169.5	0.011 ± 0.005	0.718 ± 0.002	608	0.81

Table 3.9: Sintered properties of Cr-Mo prealloyed steels; compacted at 600 MPa, sintered 60 min at 700-1300°C in argon

<i>Sintering Temp.</i> (°C)	<i>Material</i>	<i>Sintered density</i> (g/cm ³)	<i>Dimensional Change</i> (%)	<i>Impact energy</i> (J/cm ²)	<i>Hardness (HV30)</i>	<i>Dyn. Young's modulus</i> (GPa)	<i>Oxygen content</i> (wt %)	<i>Combined carbon content</i> (wt %)	<i>Electrical conductivity</i> (S.m ⁻¹)10 ⁴	<i>Coercivity</i> (kA/m)
700	CrM-0.8C	6.95 ± 0.01	0.04 ± 0.00	0.1 ± 0.0	81.0 ± 2.0	45.3	0.224 ± 0.020	0.801 ± 0.033	89	0.52
	CrM-0.8C(MA)	6.88 ± 0.01	0.10 ± 0.01	1.0 ± 0.1	94.7 ± 6.4	31.1	0.244 ± 0.012	0.808 ± 0.008	116	1.00
800	CrM-0.8C	6.95 ± 0.00	0.05 ± 0.02	0.2 ± 0.0	51.3 ± 4.2	75.9	0.230 ± 0.014	0.794 ± 0.018	145	0.41
	CrM-0.8C(MA)	6.89 ± 0.00	0.09 ± 0.00	0.9 ± 0.2	77.7 ± 2.1	52.4	0.260 ± 0.006	0.809 ± 0.010	175	0.93
900	CrM-0.8C	6.93 ± 0.01	0.02 ± 0.02	0.5 ± 0.1	71.7 ± 3.2	100.2	0.225 ± 0.004	0.794 ± 0.016	244	0.54
	CrM-0.8C(MA)	6.89 ± 0.00	0.08 ± 0.01	1.6 ± 0.2	150.7 ± 8.1	99.6	0.239 ± 0.007	0.809 ± 0.013	232	2.31
1000	CrM-0.8C	6.96 ± 0.01	-0.01 ± 0.02	3.4 ± 1.7	200.3 ± 9.7	136.2	0.166 ± 0.030	0.783 ± 0.036	276	2.30
	CrM-0.8C(MA)	6.91 ± 0.00	-0.01 ± 0.02	7.3 ± 0.4	240.0 ± 2.6	142.0	0.179 ± 0.024	0.762 ± 0.012	272	2.68
1100	CrM-0.8C	6.98 ± 0.01	-0.02 ± 0.02	8.9 ± 0.6	226.7 ± 4.9	145.6	0.122 ± 0.008	0.757 ± 0.049	281	2.47
	CrM-0.8C(MA)	6.95 ± 0.01	-0.13 ± 0.01	11.5 ± 1.6	258.7 ± 8.5	150.7	0.082 ± 0.006	0.722 ± 0.008	268	2.54
1200	CrM-0.8C	7.01 ± 0.00	-0.22 ± 0.00	16.7 ± 0.9	269.7 ± 7.6	157.4	0.027 ± 0.013	0.680 ± 0.014	266	2.47
	CrM-0.8C(MA)	7.01 ± 0.01	-0.45 ± 0.03	18.3 ± 0.8	283.7 ± 5.7	155.9	0.017 ± 0.002	0.662 ± 0.004	252	2.47
1300	CrM-0.8C	7.04 ± 0.01	-0.41 ± 0.02	20.1 ± 1.5	330.7 ± 2.0	161.2	0.008 ± 0.004	0.678 ± 0.013	262	2.58
	CrM-0.8C(MA)	7.08 ± 0.00	-0.83 ± 0.02	23.3 ± 3.6	310.0 ± 8.1	162.4	0.008 ± 0.002	0.656 ± 0.008	253	2.5

3.3.1. Green density

The green density of the steels is shown in Figure 3.62. The figure shows that addition of the MA to the mixtures has a slightly negative effect on the compactibility. The maximum attained green densities after using MA are reduced by 0.06 and 0.03 g/cm³ for carbon steel and Cr-Mo prealloyed steel, respectively.

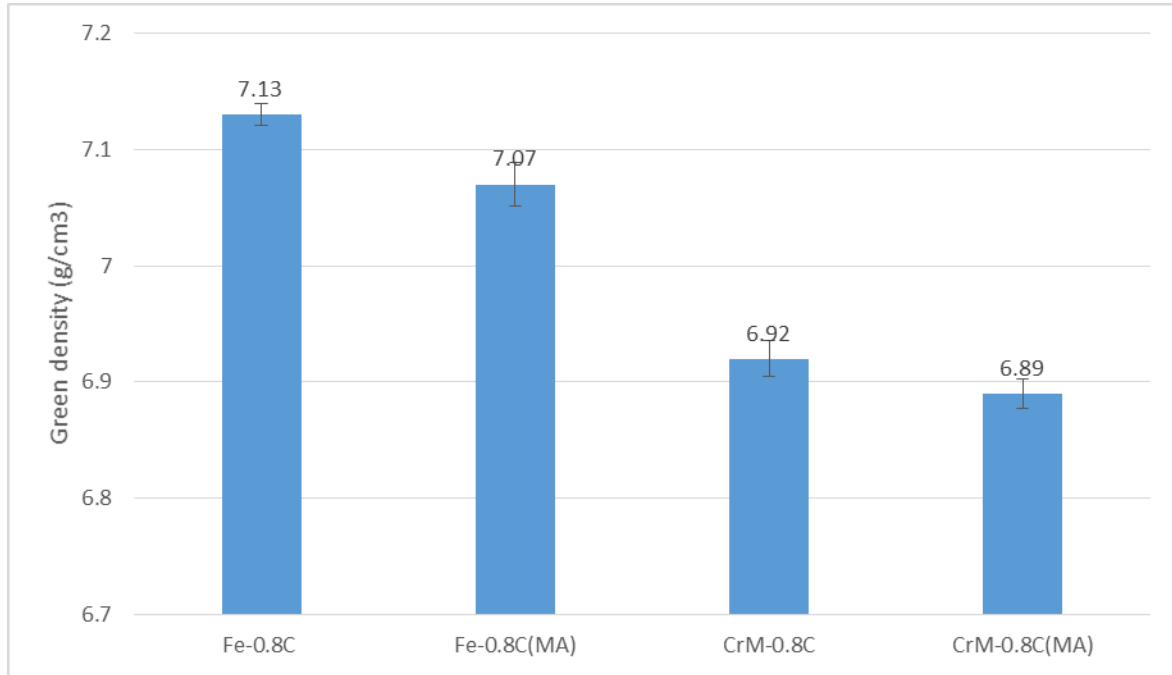


Figure 3.62: Green density of steels, compacted at 600 MPa in lubricated die (Charpy impact bars ISO 5754).

3.3.2. Thermal analysis and degassing behaviour

Dilatometric/MS runs in the heating period are shown with MS signals for gas intensities in Figure 3.63 through Figure 3.66, accompanied by four separate graphs for mass 12 (C), mass 18 (water), mass 28 (CO) and mass 44 (CO₂). Isothermal sintering was done at 1300°C for 60 min in Ar atmosphere. By using argon as sintering atmosphere and in the absence of other reduction gases like hydrogen, the effect of carbon as a reducing agent is well defined [159].

In the carbon steels, Figures 3.63 and 3.64, degassing peaks m28 show two pronounced reduction processes. The first peak, which, as mentioned in Chapter 3.2.2, is related to the reduction of the surface oxides of iron, occurred at 680°C and 600°C (peak maximum each) for only graphite containing and MA containing steel, respectively. With increasing temperature, the second peak with maximum at around 1070°C, which is associated with reduction of internal oxides, shows similar reduction behaviour for both steels. The figures also show the dilatometry graphs of the carbon steels. It is obvious that in MA containing steel (section B of Figures) the α to γ transformation during heating occurred at almost 30 K lower temperature and within a much smaller temperature interval than the only graphite containing steel, which can be the result of faster carbon dissolution. The graphs also show that the transformation during cooling occurred at almost the same temperature at 700°C. Focusing on the isothermal

part of the dilatogram shows that adding the MA resulted in higher shrinkage during isothermal sintering at 1300°C, which then led to higher total shrinkage after the complete sintering cycle.

Figures 3.65 and 3.66 show the dilatometry/MS graphs of Cr-Mo prealloyed steels (The intensities of m12 should not be overestimated here). In the steel containing only graphite (section A), the results show an m28 signal with the peak at 1160°C. In the chromium-molybdenum prealloyed steel no pronounced m28 peak is observed up to 1000°C. Karamchedu et al. [163] already showed that the surface of chromium prealloyed powder is covered by a heterogeneous oxide layer, a mix of thin iron oxide layer and some more stable oxide (Cr rich) islands [164]. Therefore, in this case a reduction peak at medium temperature was expected to indicate the reduction of iron oxide, which however was not observed. In that context, Danninger et al. [53] have shown that a transformation of the surface iron oxides towards more stable types can occur at temperatures of 600-700°C when sintering is done in inert atmosphere (Ar). This changes the surface chemistry of the particles, the particles then being covered with more stable oxides. Therefore, according to these findings, effective oxide reduction and sintering would not be expected in inert atmosphere below 1000°C, which is also supported by the results given in [58]. Addition of the MA to the system (section B) however resulted in formation of two peaks, the first at 580°C and the second one, which is a double peak, at 1090 and 1220°C. Visual comparison of the area under the m28 graphs in the temperature range of 800 to 1000°C shows that the CO emitted in the steel containing MA is more pronounced compared to the only graphite-admixed steel, and this shows that not only the reduction of the surface oxide but also the internal oxides started earlier in the mix with the masteralloy. Here it seems that presence of Fe-C masteralloy led to reduction of the surface iron oxides mentioned above before formation of the more stable oxides could occur. The DIL graphs in these figures show that addition of the MA to the mixture of the Cr-Mo steel lowered the α to γ temperature by about 65°C, which is an indicator for faster carbon dissolution in the system containing the masteralloy. Results of DIL also show that in the steel containing MA, shrinkage started earlier and before the isothermal sintering stage at about 1200°C, which could be an indicator for more active sintering in this steel by addition of MA.

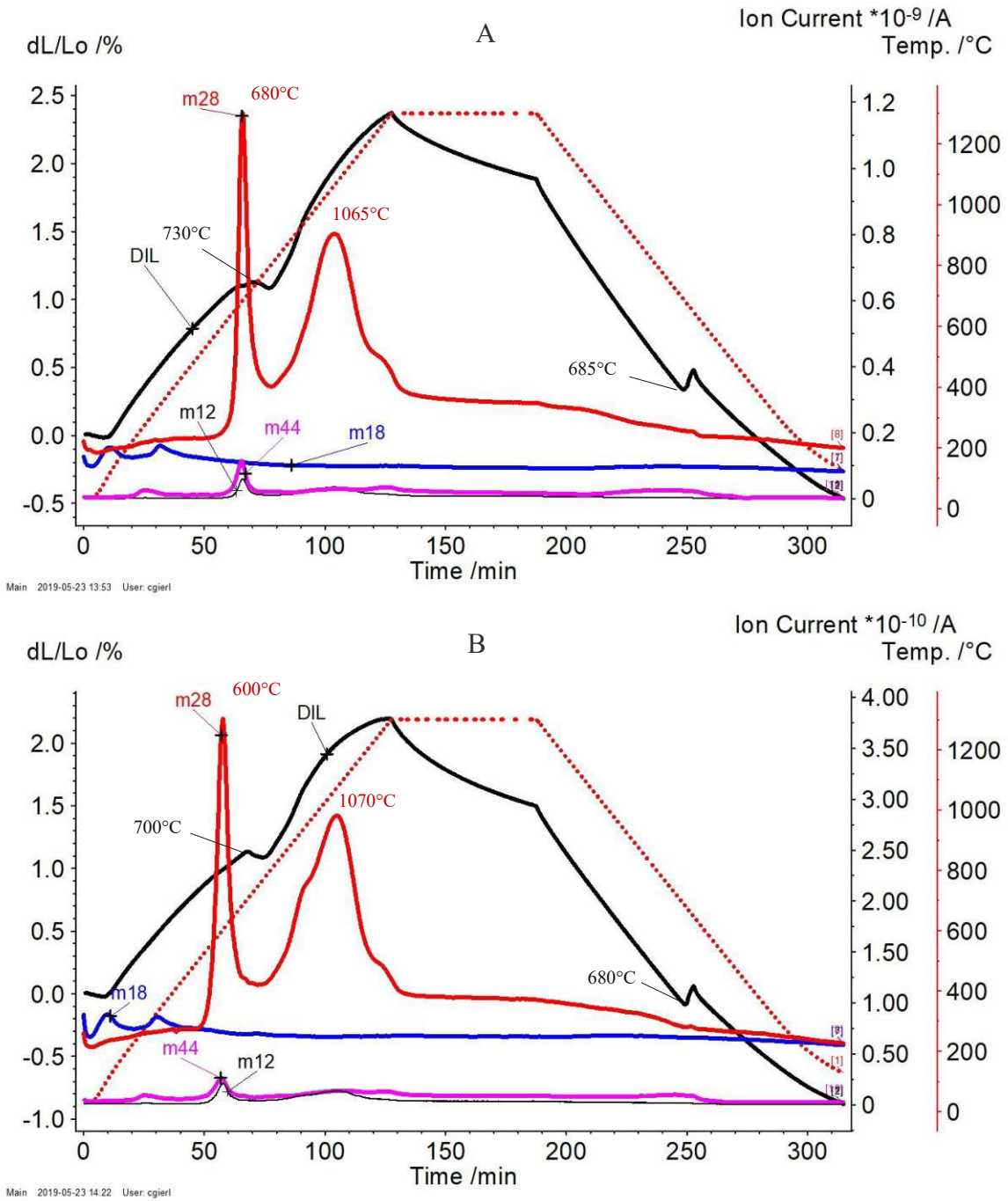


Figure 3.63: Dilatometry/MS graphs of carbon steels versus time, compacted at 600 MPa, sintered 60 min at 1300°C in Ar, heating-cooling rate ± 10 K/min; A: Fe-0.8C, B: Fe-0.8C (MA).

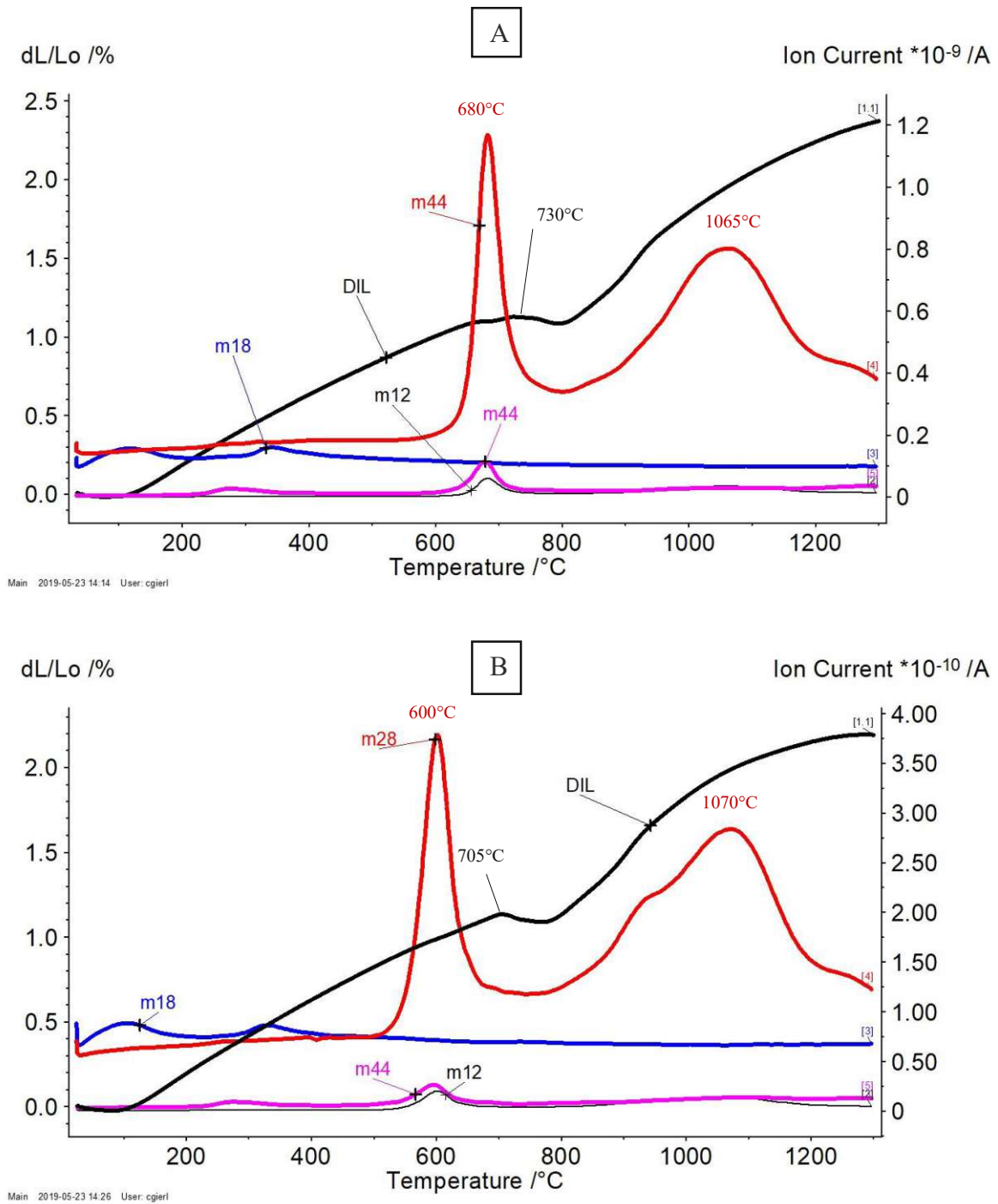


Figure 3.64: Dilatometry/MS graphs (heating section) of carbon steels versus temperature, compacted at 600 MPa, sintered 60 min at 1300°C in Ar, heating-cooling rate ± 10 K/min; A: Fe-0.8C, B: Fe-0.8C(MA).

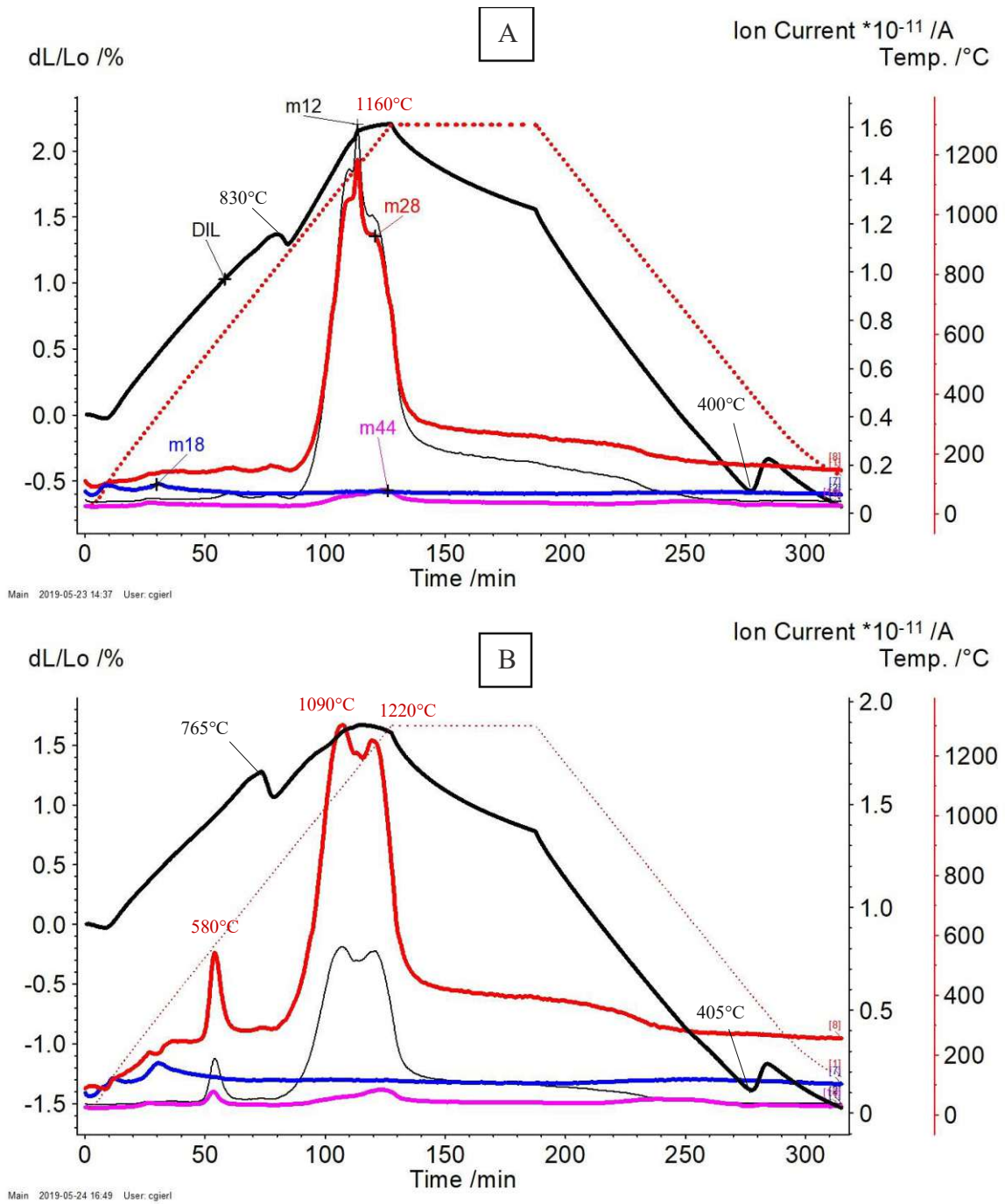
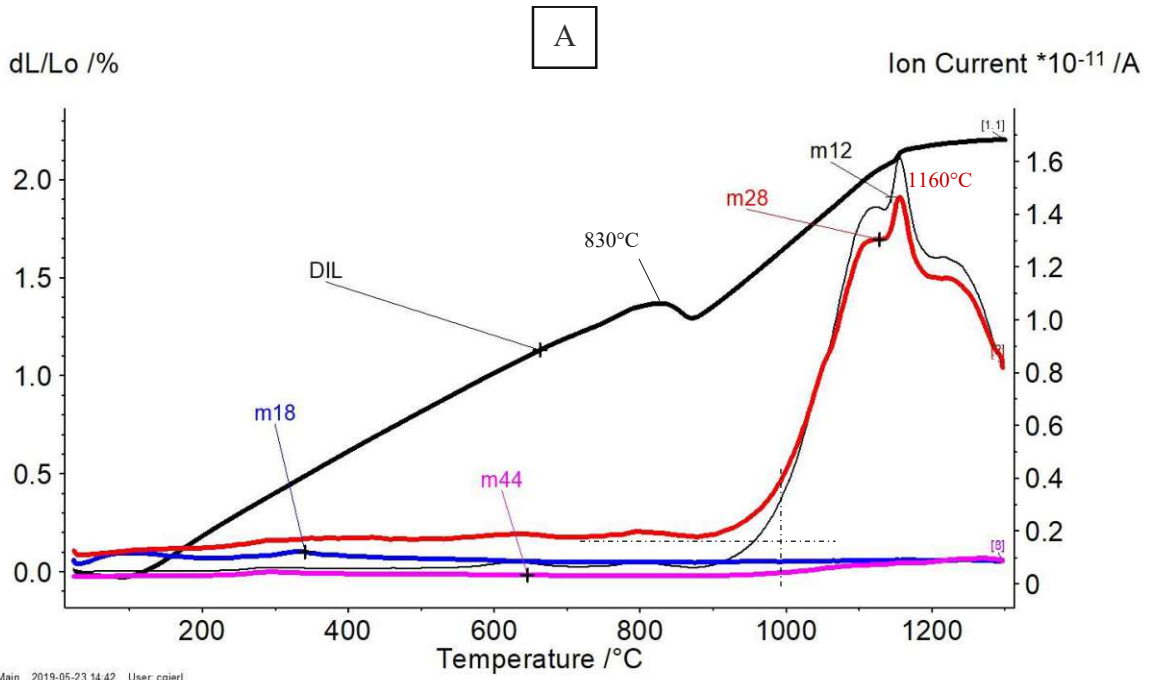
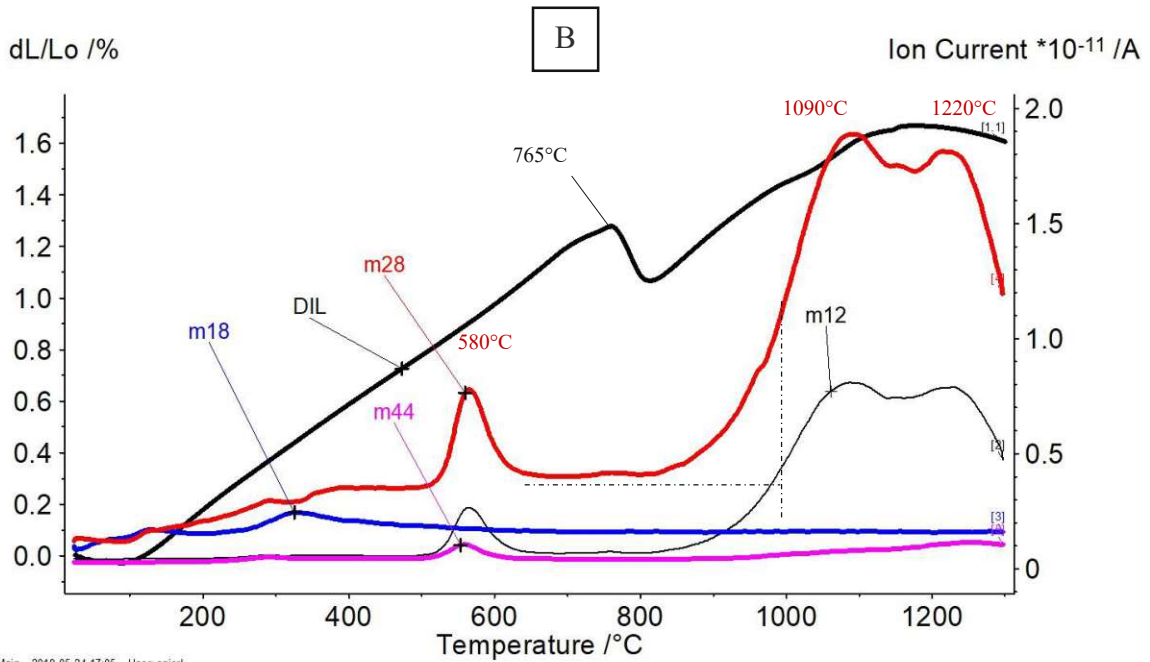


Figure 3.65: Dilatometry/MS graphs of Cr-Mo alloyed steels versus time, compacted at 600 MPa, sintered 60 min at 1300°C in Ar, heating-cooling rate ± 10 K/min; A: CrM-0.8%C, B: CrM-0.8C(MA).



Main 2019-05-23 14:42 User: cgierl



Main 2019-05-24 17:05 User: cgierl

Figure 3.66: Dilatometry/MS graphs (heating section) of Cr-Mo steel versus temperature, compacted at 600 MPa, sintered 60 min at 1300°C in Ar, heating-cooling rate ± 10 K/min; A: CrM-0.8%C, B: CrM-0.8C(MA).

3.3.3. Chemical analysis (carbon and oxygen content)

The oxygen and carbon contents of the steels are presented in Figures 3.67 and 3.68. The oxygen content of the carbon steels presented in Fig.3.1.67-A, shows a continuous downward trend for both steels with increasing sintering temperature. The main oxygen removal in both steels occurred in the temperature range of 900 to 1100°C, which is in good agreement with the results of MS (Fig. 3.64). Above 1100°C and up to 1300°C the graph shows less carbon removal and almost the same values for both steels. Figure 3.67-B shows the oxygen content for the two Cr-Mo alloyed steels. Between 700 and 900°C the oxygen content remained almost constant and without a significant change, while above 900°C both steels showed a reduction of the oxygen content with increasing sintering temperature. The graph also shows that at 1100°C, the steel with MA had better oxygen removal, however sintering at higher temperatures, 1200 and 1300°C, resulted in almost the same values for the oxygen content.

Results of the carbon measurement of the carbon steels (Fig. 3.68-A) show continuous downward trend in the carbon content of the steels with increasing temperature. The lower amount of carbon content in the temperature range of 800 to 1100°C in the steel containing MA shows that the carbon consumption (consequence of carbothermal reduction) is higher than in the steel containing only graphite, which is in good agreement with the results of oxygen measurement, which showed higher oxygen removal in this temperature range.

In the section B of Figure 3.68, the carbon contents of Cr-Mo steels are presented. It is evident that in both steels the carbon consumption occurred above 900°C, which confirms the results of the oxygen measurement. In the range of 900 to 1200°C, higher carbon loss is discernible in the MA containing steel, which is the consequence of higher oxygen removal in this steel. Figure 3.68-1 shows the linear relationship between carbon loss and oxygen removal from the alloys during the sintering process.

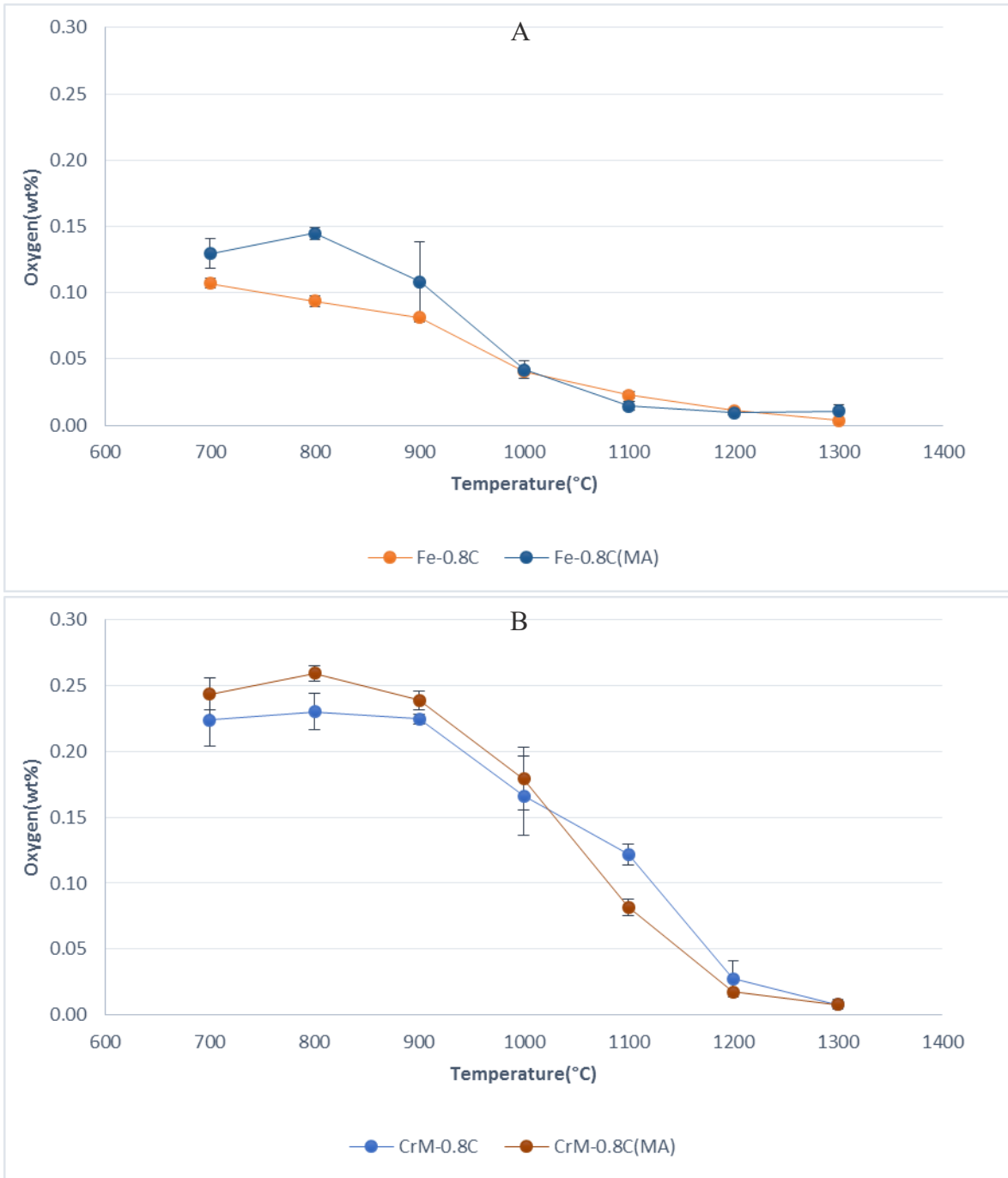


Figure 3.67: Oxygen content of steels versus sintering temperature, compacted at 600 MPa, sintered 60 min in argon; A: carbon steels, B: Cr-Mo prealloyed steels.

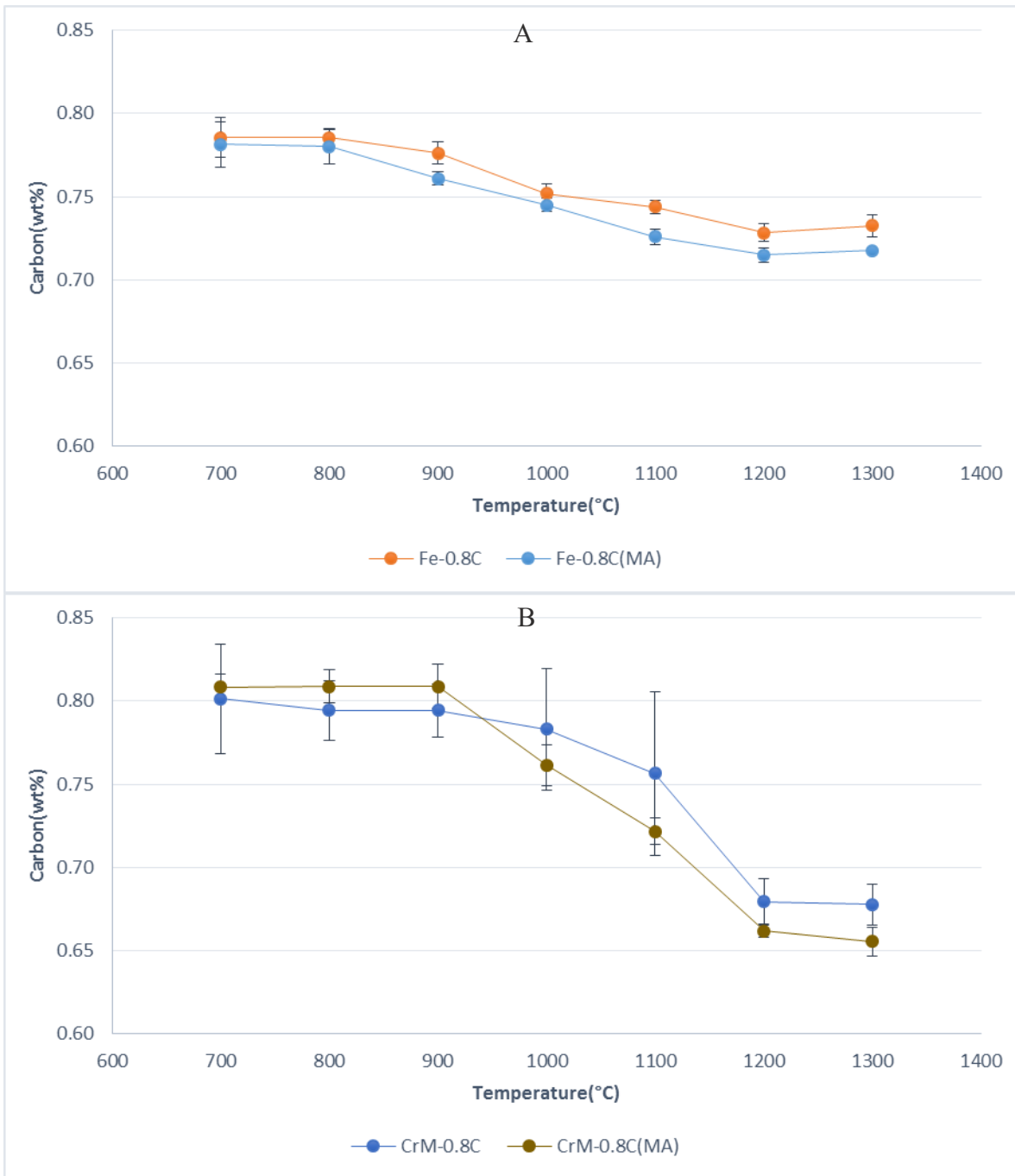


Figure 3.68: Carbon content of steels versus sintering temperature, compacted at 600 MPa, sintered 60 min in argon; A: carbon steels, B: Cr-Mo prealloyed steels.

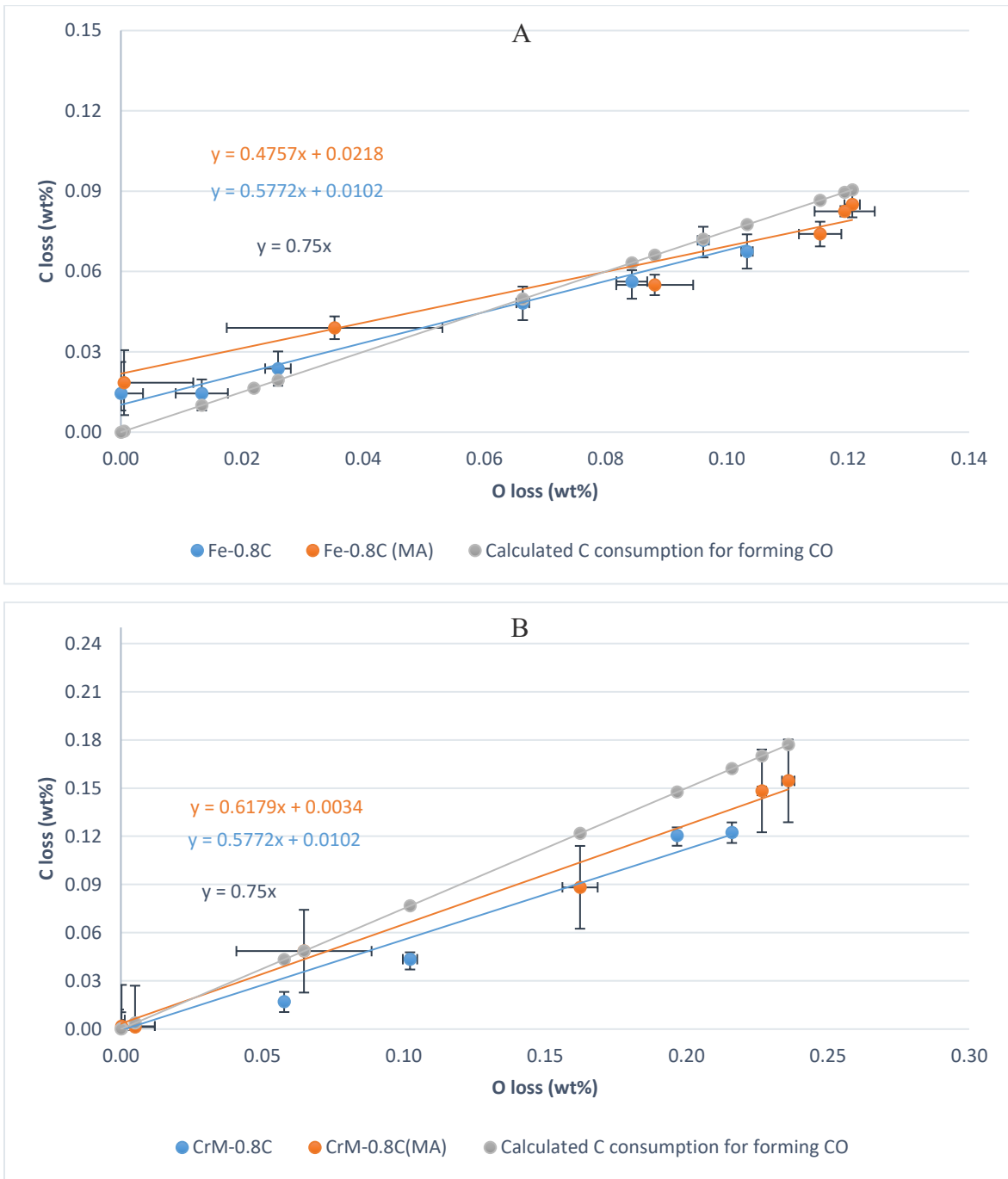


Figure 3.68-1: Carbon loss of steels as a function of oxygen loss, steels compacted at 600 MPa, sintered 60 min in argon at 700-1300°C; A: carbon steels, B: Cr-Mo prealloyed steels.

3.3.4. Metallographic investigations (pore morphology and matrix microstructure)

In order to investigate the pore morphology of the steels, un-etched optical microscope cross sections are presented in Figures 3.69 and 3.70. Pore morphology of the carbon steels (Fig. 3.69) at 800°C shows the boundaries between the individual iron particles in the steel containing MA, while these boundaries are less discernible in the steel with only graphite. The borders between the iron particles could be related to the very fine MA particles which are located between the main iron powder particles. In both steels these boundaries disappeared at 1000°C, which shows the formation of stronger sintering contacts at this temperature. The results also show that sintering at 1200°C resulted in pore coarsening and rounding in both steels.

Figure 3.70 shows the pore morphology of the Cr-Mo alloyed steels. At 800°C, the boundaries between the individual powder particles are visible in both steels. When the sintering temperature is increased to 1000°C these boundaries disappear, which is the result of surface oxide reduction and the resulting contact formation. The micrographs also show that increasing the temperature to 1200°C resulted in pore rounding and enlargement, however it seems that this effect is more pronounced in the steel containing MA.

Etched microstructures of the steels are presented in Figures 3.71 and 3.72. Figure 3.71 shows etched cross sections of the carbon steels. At 800 and 1000°C the fraction of the pearlite and resulting hardness are higher in the MA containing steel compared to the steel with only graphite. It is evident that addition of the Fe-C masteralloy to the mixture of the carbon steel enhanced the carbon dissolution process. At 1200°C, the fraction of pearlite is almost the same, and sintering caused microstructural homogenization and pore rounding at higher temperatures.

Etched micrographs for Cr-Mo prealloyed steels are shown in Figure 3.72. At 800°C, the boundaries between the individual powder particles are clearly visible in both steels. At 1000°C, the carbon dissolution resulted in a fine bainitic microstructure in both steels, however the apparent hardness at this temperature is higher in the MA containing steel, which indicates more carbon dissolution at this temperature. At 1200°C, both steels show a bainitic microstructure with some martensitic regions. For showing the influence of Fe-C masteralloy on carbon dissolution at low sintering temperature, the microstructures of Cr-Mo steels at 900°C are presented in Figure 3.73. Here it seems that addition of the MA to the mixture of Cr-Mo alloyed steel resulted in faster carbon dissolution and resulting higher hardness.

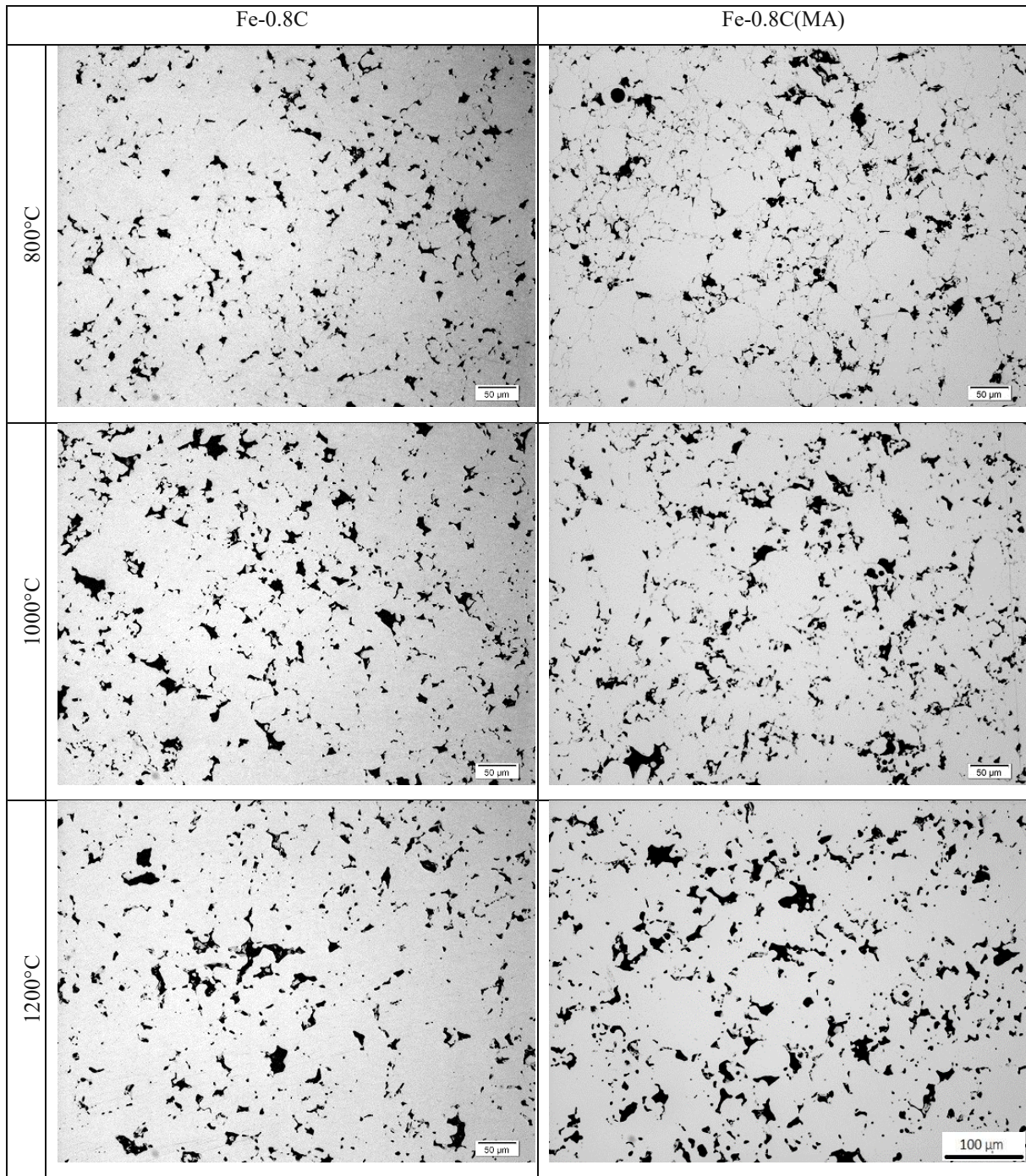


Figure 3.69: Un-etched OM micrographs of carbon steels compacted at 600 MPa, sintered 60 min in Ar, 200x. (scale bar 100µm holds for all images)

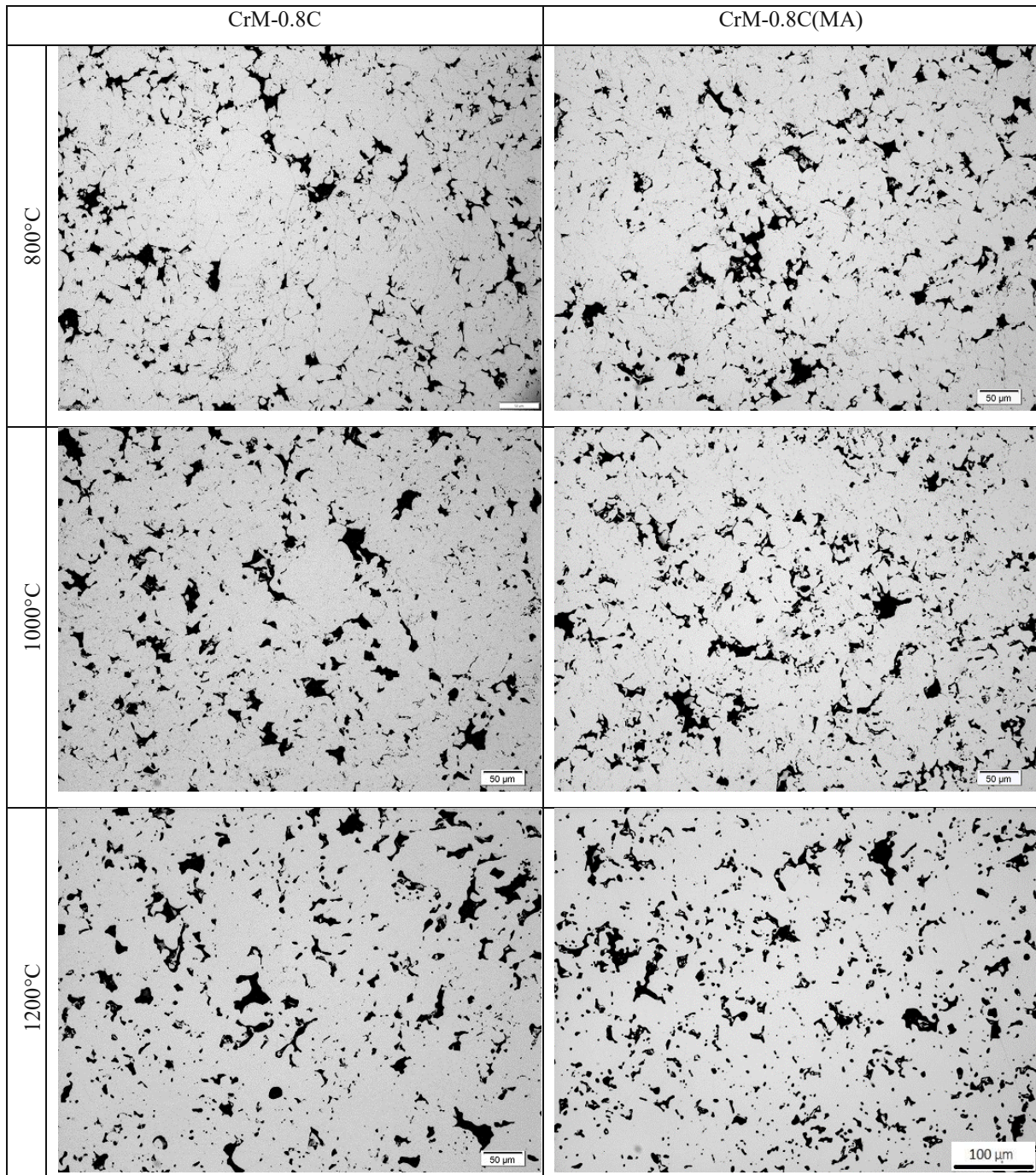


Figure 3.70: Un-etched OM micrographs of Cr-Mo prealloyed steels compacted at 600 MPa, sintered 60 min in Ar, 200x. (scale bar 100μm holds for all images)

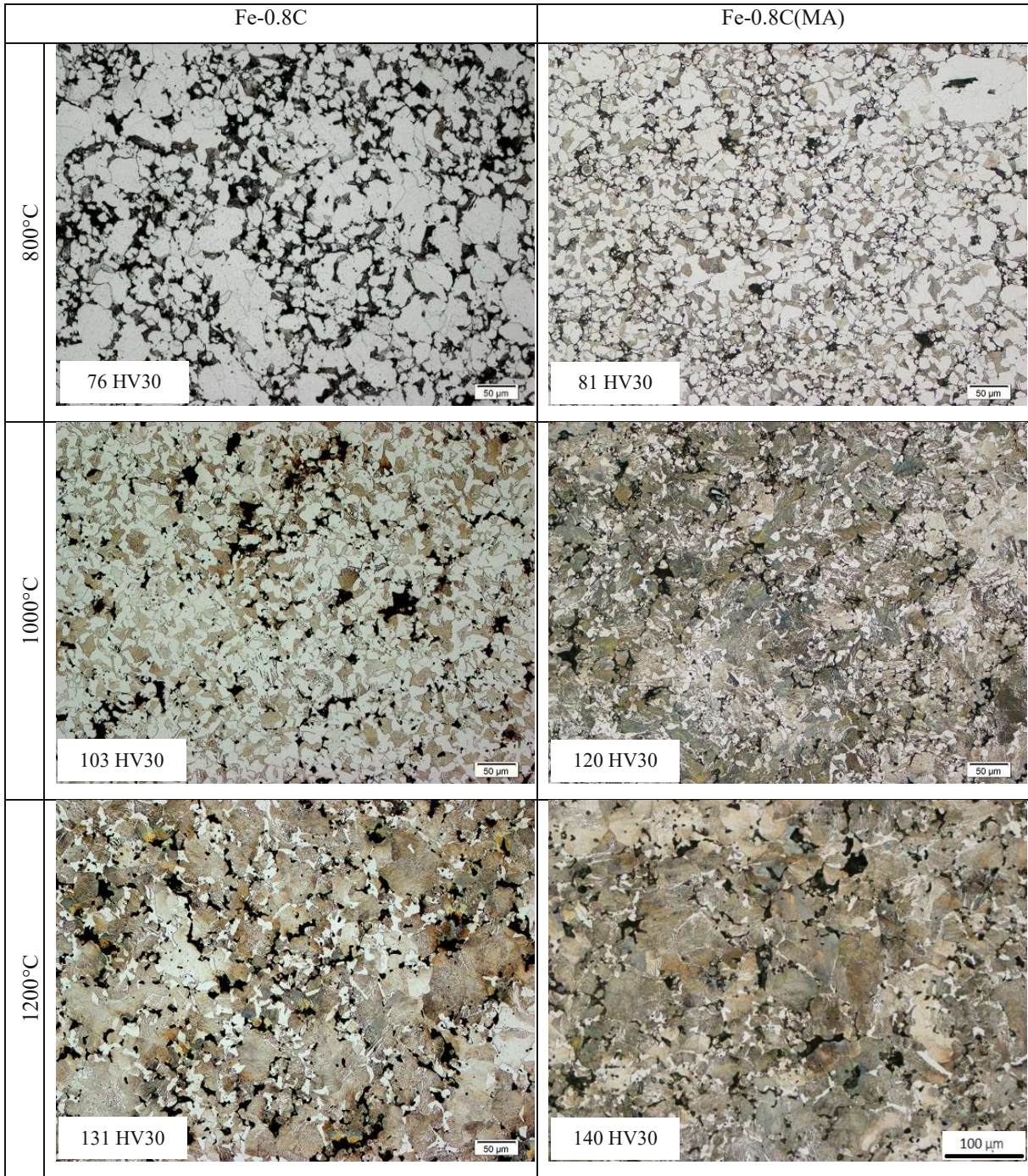


Figure 3.71: Etched OM micrographs of carbon steels compacted at 600 MPa, sintered 60 minute in Ar, Nital, 200x. (scale bar 100 μ m holds for all images)

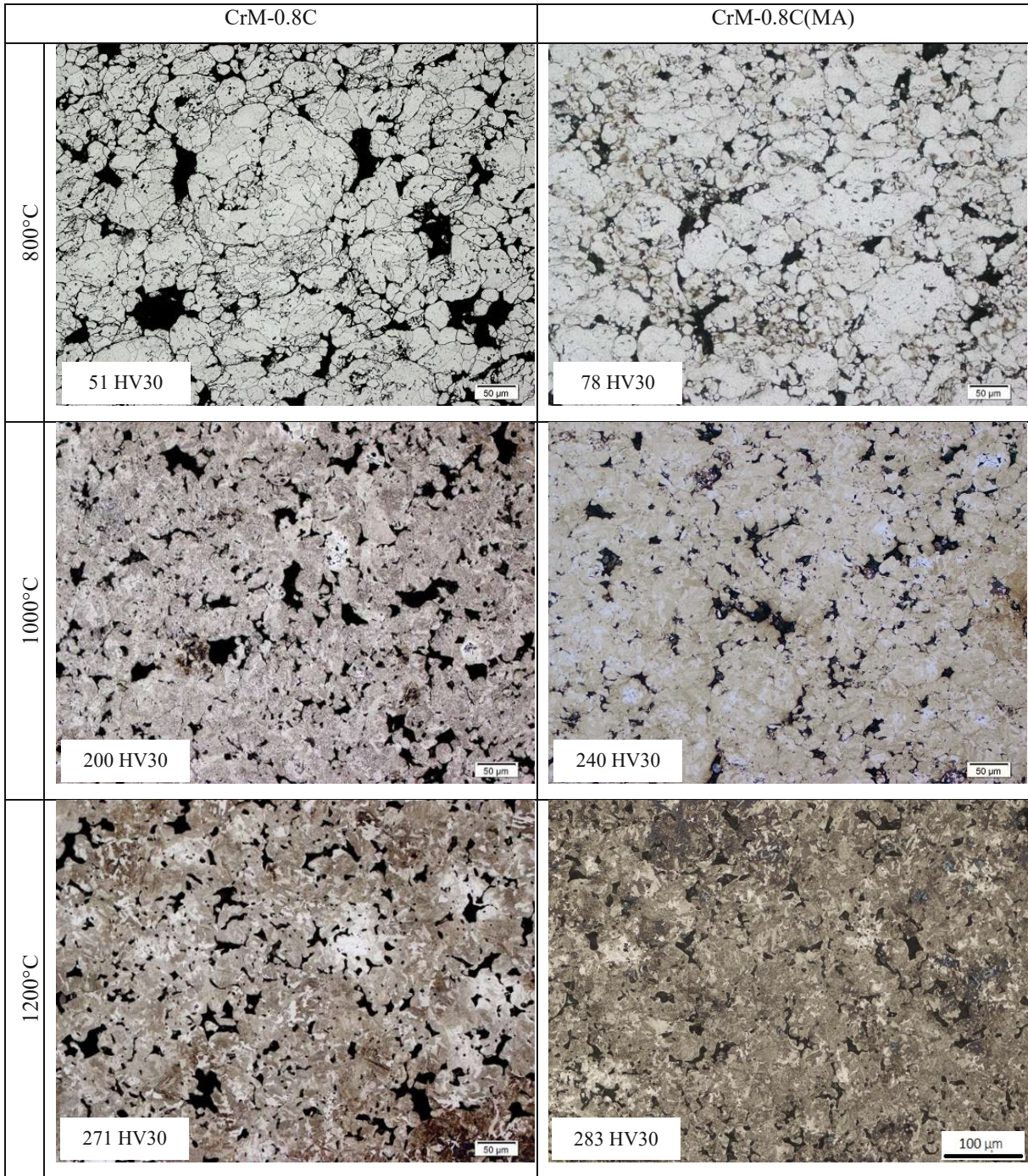


Figure 3.72: Etched OM micrographs of Cr-Mo prealloyed steels compacted at 600 MPa, sintered 60 min in Ar, Nital, 200x. (scale bar 100μm holds for all images)

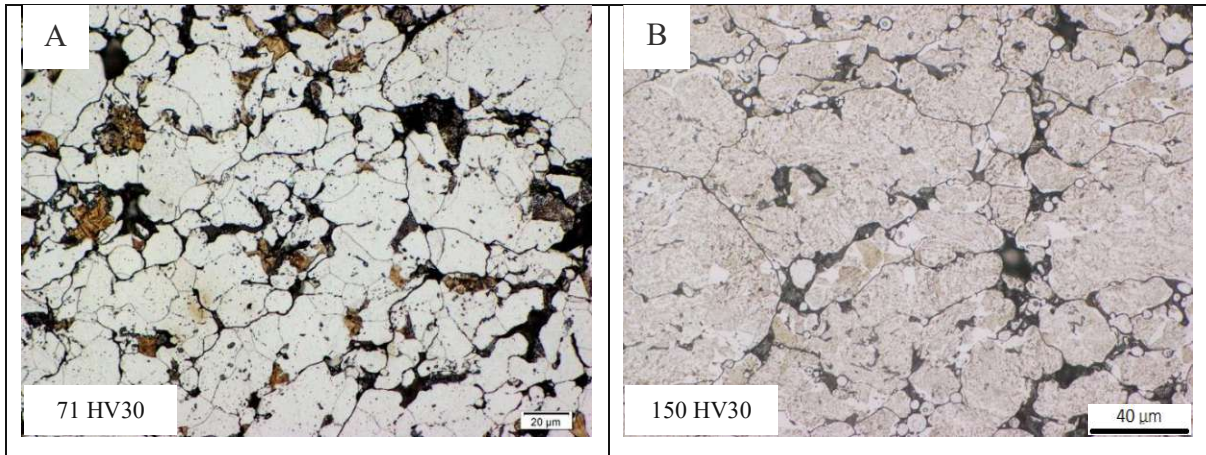


Figure 3.73: Microstructure of Cr-Mo prealloyed steels compacted at 600 MPa, sintered at 900°C 60 min in Ar, 500 x; A: only graphite added, B: graphite and masteralloy added. (scale bar 40µm holds for both images)

3.3.5. Fractography

Fracture surfaces of the carbon steels, broken at room temperature by Charpy impact testing, are presented in Figure 3.74. At 800°C the first signs of formation of the sintering contacts in both steels are discernible. At this temperature the spherical MA particles are still visible in the fracture surface of the MA containing steel. At 1000°C, both steels showed dimple intergranular fracture mechanism as well as almost the same impact energy. The fractographs at 1200°C show that higher sintering temperature resulted in formation of stronger bonds between particles which led to some cleavage facets in the fracture surfaces of both steels.

Fracture surfaces of the Cr-Mo alloyed steels are presented in Figure 3.75. At 800°C - due to stability of chromium oxide - no sign of sintering contacts between the powder particles is visible. Fracture surfaces at 1000°C show that addition of the MA to the mixture resulted in formation of more sintering contacts which also led to higher impact energy compared to the steel with only graphite. Similar to the carbon steels, Cr-Mo alloyed steels at lower temperatures show mainly interparticle dimple fracture mechanism which converted to transgranular cleavage with a river pattern after raising the sintering temperature to 1200°C.

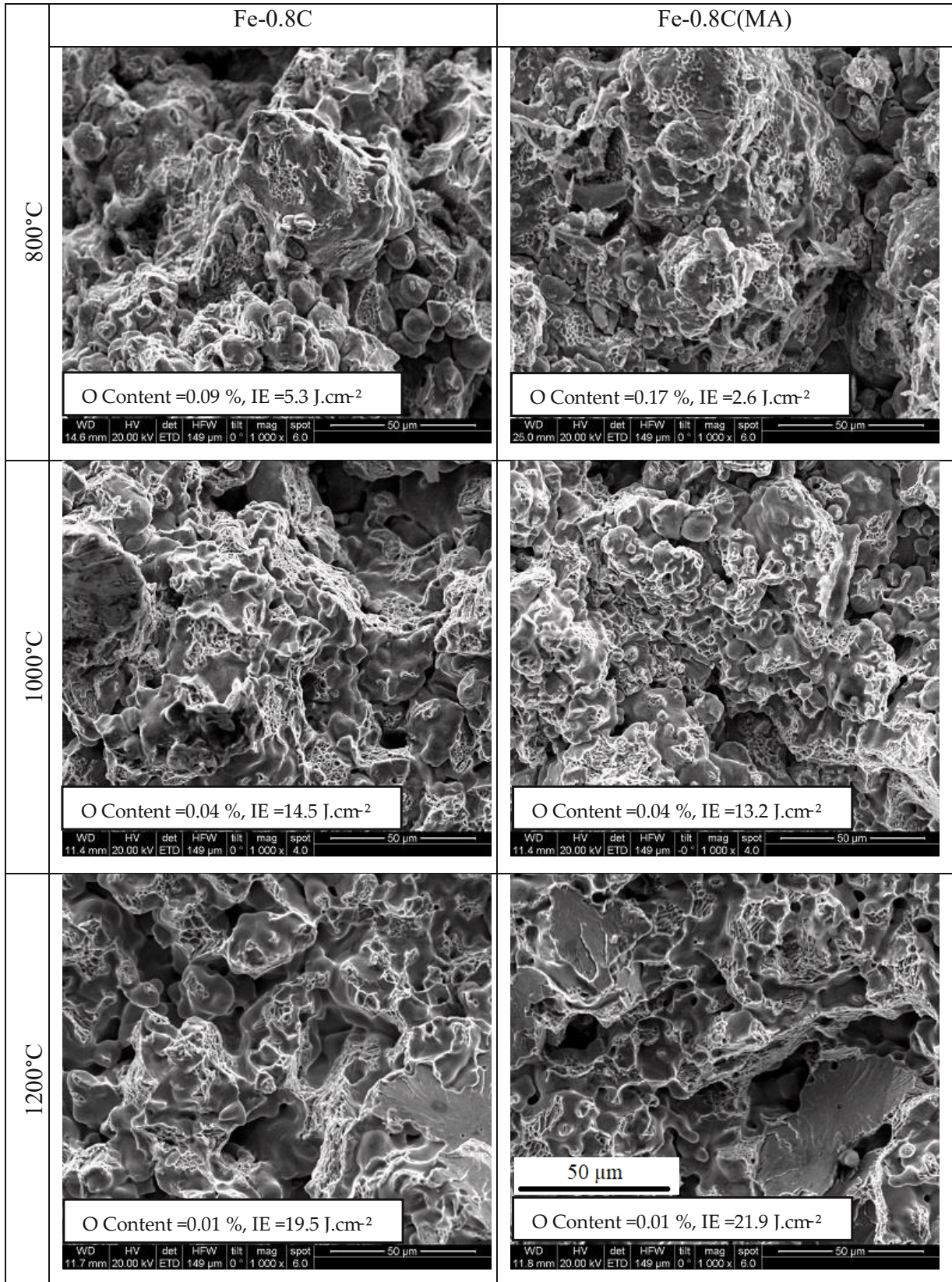


Figure 3.74: Fractographs of carbon steels compacted at 600 MPa, sintered 60 min in argon, broken at RT by Charpy impact test, 1000 x; A: only graphite added, B: graphite and masteralloy added. (scale bar 50µm holds for all images)

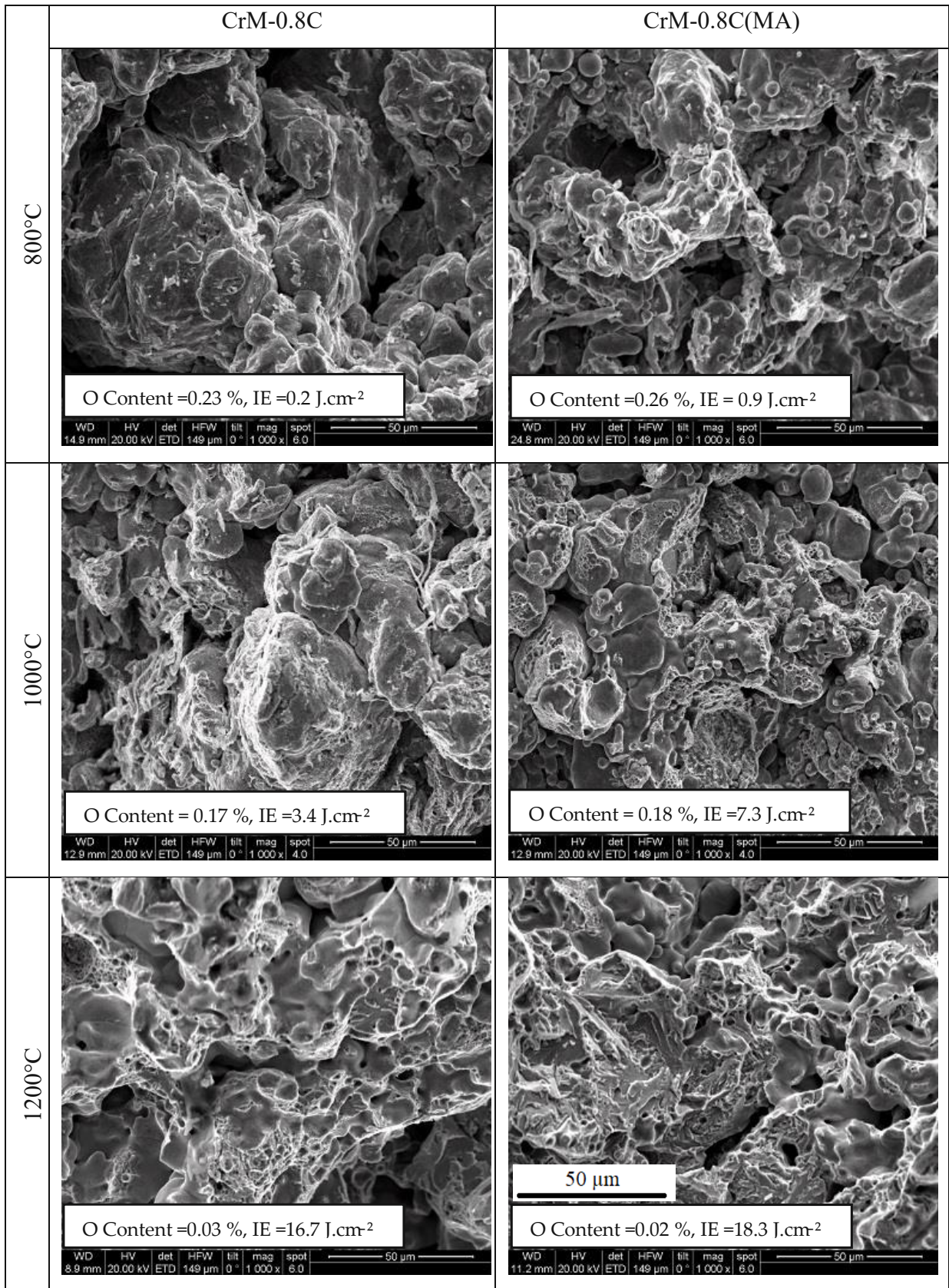


Figure 3.75: Fractographs of Cr-Mo alloyed steels compacted at 600 MPa, sintered 60 min in argon, broken at RT by Charpy impact test, 1000 x; A: only graphite added, B: graphite and MA added. (scale bar 50μm holds for all images)

3.3.6. Dimensional change and sintered density

Results of the dimensional change of the steels are presented in Figure 3.76. In the section A of the figure, the two grades of the carbon steels showed different dimensional behaviour. Between 700 and 900°C, both steels do not show significant dimensional change. Above 900°C, the dimensional changes are different, the carbon steel with only graphite showed an expansion at 1000 and 1100°C (as a consequence of carbon dissolution) and then shrinkage at 1200 and 1300°C. The MA containing steel, in contrast, stayed almost without dimensional change at this temperature, despite considerable carbon dissolution at 1000°C, and then showed a significant shrinkage above this temperature, which shows higher sintering activity compared to the previously mentioned steel.

The dimensional change of Cr-Mo alloyed steels is presented in part B of Figure 3.76. It is evident that in both steels, the dimensions stayed almost constant in the temperature range of 700-900°C. At 1000°C the dimensional change is zero for both steels, and sintering above 1000°C led to shrinkage. The results also show that in the range of 1100 to 1300°C, the addition of MA to Cr-Mo steel led to more pronounced shrinkage compared to the steel with only graphite. The sintered density of the steels as a function of sintering temperature is presented in Figure 3.77. An opposite and corresponding trend for all groups of material with dimensional change is clearly visible in this figure. These results also show that despite the lower initial green density of the steels with MA, these grades attained almost the same sintered density as the steels containing only graphite in case of sintering above 1100°C.

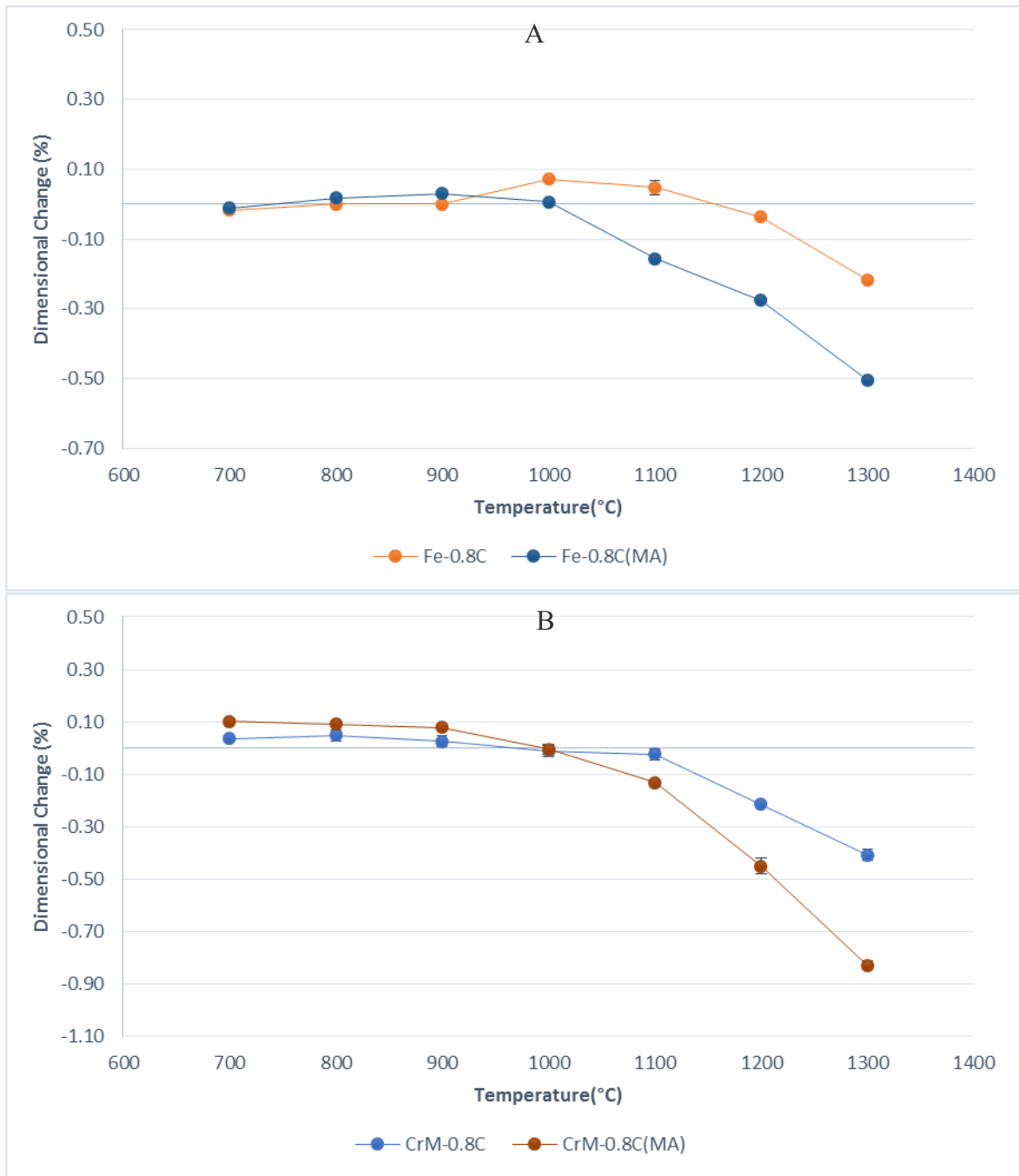


Figure 3.76: Dimensional change of steels versus sintering temperature, compacted at 600 MPa and sintered 60 min in argon; A: carbon steels, B: Cr-Mo prealloyed steels.

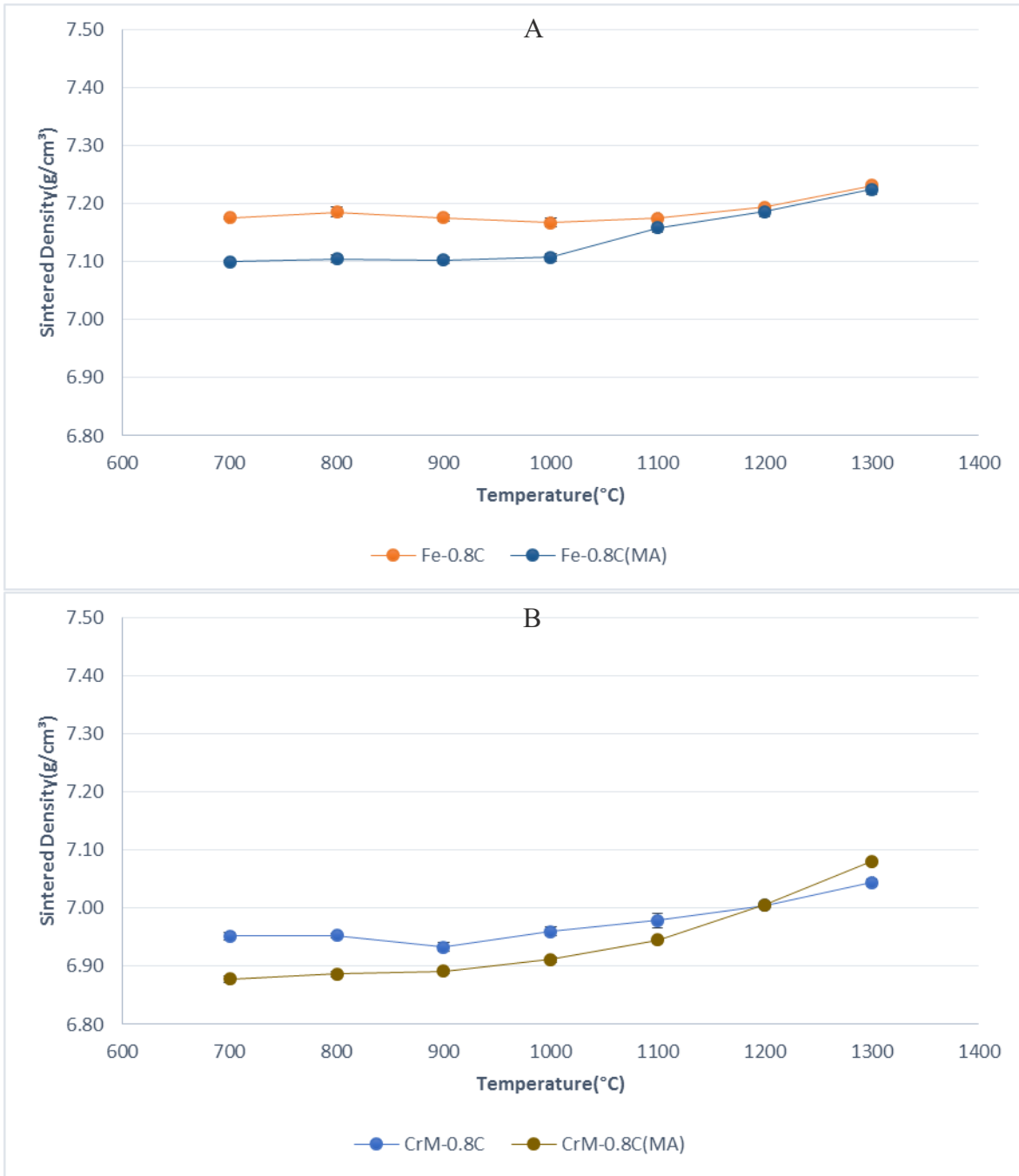


Figure 3.77: Sintered density of steels versus sintering temperature, compacted at 600 MPa and sintered 60 min in argon; A: carbon steels, B: Cr-Mo prealloyed steels.

3.3.7. Mechanical properties

3.3.7.1. Hardness

Apparent hardness data of the steels versus sintering temperature are presented in Figure 3.78. The results of the hardness measurement of the carbon steels (Fig. 3.78-A) show that the hardness of both steels increased continuously with higher sintering temperature. In the temperature range of 700-1000°C the MA containing mix showed higher trend in the increase of the hardness, which could be attributed to faster carbon dissolution and resulting higher fraction of pearlite (see metallographic sections in Figure 3.71). Both steels also showed a slight increase of the hardness above 1100°C, attributed to the neck enlargement which occurred after sintering at higher temperatures.

Section B of Figure 3.78 shows the hardness of the Cr-Mo alloyed steels. The main reason of the increasing hardness for this material during the sintering process is the carbon dissolution and resulting bainite and martensite formation [165]. As can be seen, between 700 and 900°C the steel with only graphite does not show a significant raise in the hardness, while addition of the MA to the mixture led to increased hardness at 900°C, which is the result of carbon dissolution in the alloy (see Figure 3.72). The results also show that above 900°C and up to 1100°C, the hardness of the MA containing mix is higher than that of the steel with only graphite which can once more be attributed to the faster carbon dissolution and oxide reduction and resulting more active alloying process. At 1200 and 1300°C, almost the same values for the hardness are obtained for both steels, which shows that at these temperatures carbon dissolution and the corresponding alloying process are rather similar.

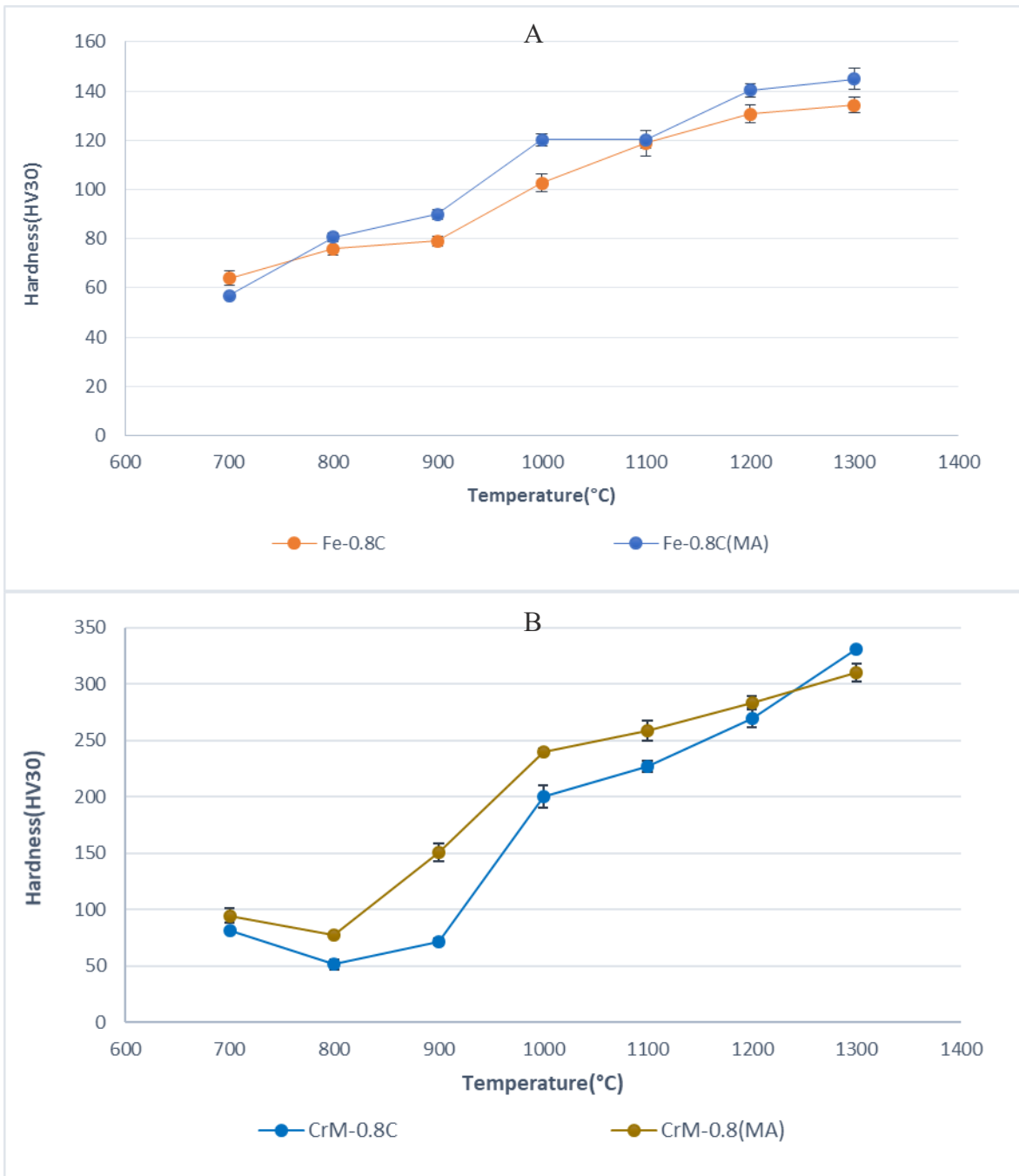


Figure 3.78: Hardness measurement of steels versus sintering temperature, compacted at 600 MPa, and sintered 60 min in argon; A: carbon steels, B: Cr-Mo prealloyed steels, with carbon steels shown as a reference.

3.3.7.2. Charpy impact energy

Results of the room temperature Charpy impact tests are given in Figure 3.79. In section A of the figure, both carbon steels with and without MA showed a continuous upward trend from 700 to 1300°C. From 700 to 1000°C, the higher values of impact energy belong to the carbon steel with only graphite, which can be explained by the higher density, which resulted in stronger sintering bonds. The results also show that in the range of 1100 to 1300°C, the MA alloy containing steel gained higher values of the impact energy, which could be related to the significant densification as well as the lower carbon content in this range of the temperatures.

In Cr-Mo alloyed steels (Fig. 3.79-B), between 700 to 900°C, both steels showed very low values of impact energy. As mentioned earlier, the oxide reduction is the precondition to create sintering contacts, and in this range of the temperature the presence of the surface oxides prevents formation of the sintering contacts. Above 900°C, when sintering contacts started to appear (see results of fractography, Figure 3.75), the impact energy of both groups started to increase steadily while the MA containing mix showed higher values of impact energy. At 1000 and 1100°C, in the MA containing mix - despite having lower density - more effective oxygen removal and resulting stronger sintering contacts could be the reason for this higher impact energy. Above these temperatures, at 1200 and 1300°C, densification and higher sintering activity as well as to some degree maybe the slightly lower carbon content in the steel containing MA can explain the higher impact energy compared to the steel with only graphite.

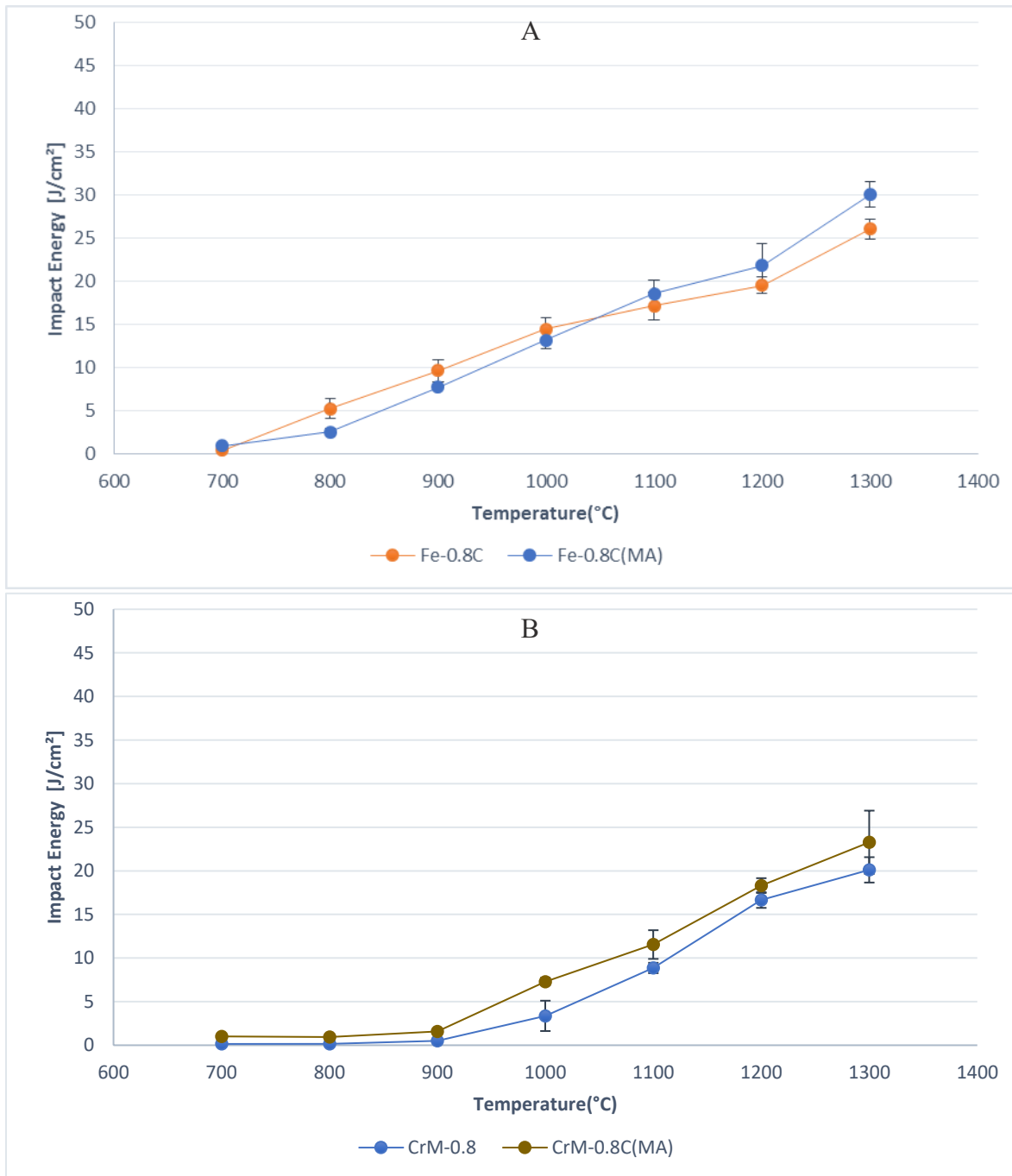


Figure 3.79: Impact energy of steels (broken by Charpy impact test at RT) versus sintering temperature, compacted at 600 MPa, sintered 60 min in argon; A: carbon steels, B: Cr-Mo prealloyed steels.

3.3.7.3. Dynamic Young's modulus

Figure 3.80 shows the effective dynamic Young's modulus of the steels. In Fig 3.80-A, at 800°C, both carbon steels showed a significant raise in the parameter as a consequence of formation of the first sintering bridges which is followed by a smooth upward trend with increasing sintering temperature. According to the result, from 700 to 1000°C, lower values for MA containing steels were obtained which is related to the lower density of this steel in this

temperature range, while in the range of 1100 to 1300°C, in which the steels have the same density, almost identical values were obtained.

In Cr-Mo alloyed steels (Fig 3.80-B), from 900°C both steels showed almost the same values which increased with higher sintering temperature. In the temperature range of 900 to 1100°C, in which the MA containing steel has lower sintered density, formation of stronger sintering contacts could explain the reason of the identical values. The results also show that at 1200 and 1300°C the Young's moduli for both steels are the same.

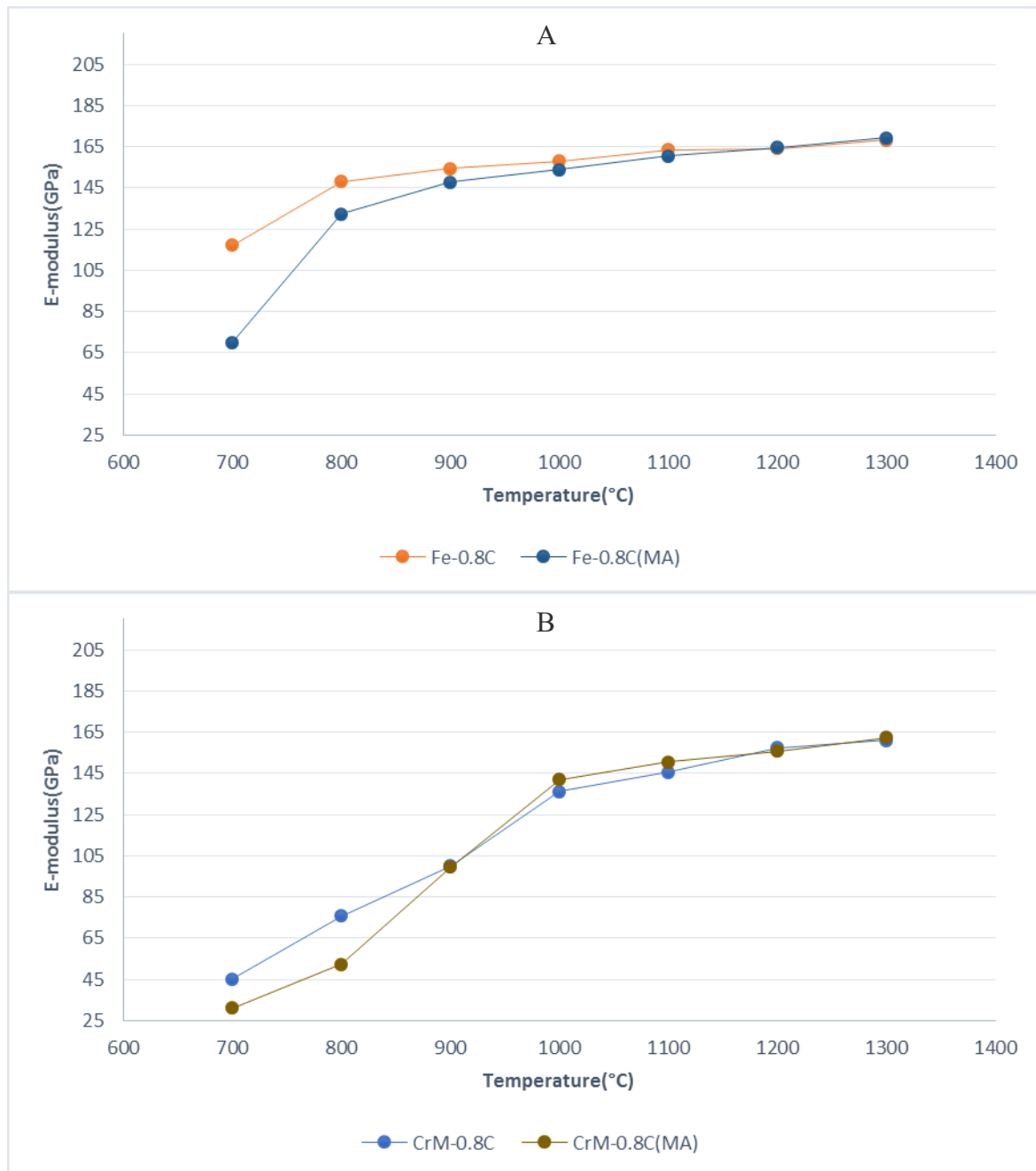


Figure 3.80: Dynamic Young's modulus of steels versus sintering temperature, compacted at 600 MPa, sintered 60 min in argon; A: carbon steels, B: Cr-Mo prealloyed steels.

3.3.8. Physical properties

3.3.8.1. Electrical conductivity

The electrical conductivity of the steels is shown in Figure 3.81. According to the results, in the Fe-C system (Fig. 3.81-A), at 800°C, both carbon steels showed a pronounced raise in the electrical conductivity after formation of the first sintering bonds. In the temperature range of 800 to 1000°C, the MA containing mix showed lower electrical conductivity, as a consequence of faster carbon dissolution in this steel, which is in good agreement with the result of metallography. It is evident that above 1000°C, when carbon dissolution is complete, both carbon steels showed almost the same values and trends in the electrical conductivity.

In Cr-Mo alloyed steels (Fig. 3.81-B), at 700 and 800°C, the MA containing steel showed slightly higher electrical conductivity which shows that presence of MA resulted in formation of stronger metal-metal contacts between the particles of the alloy. The results also indicate that both steels have similar behaviour and trend in the electrical conductivity with increasing sintering temperature.

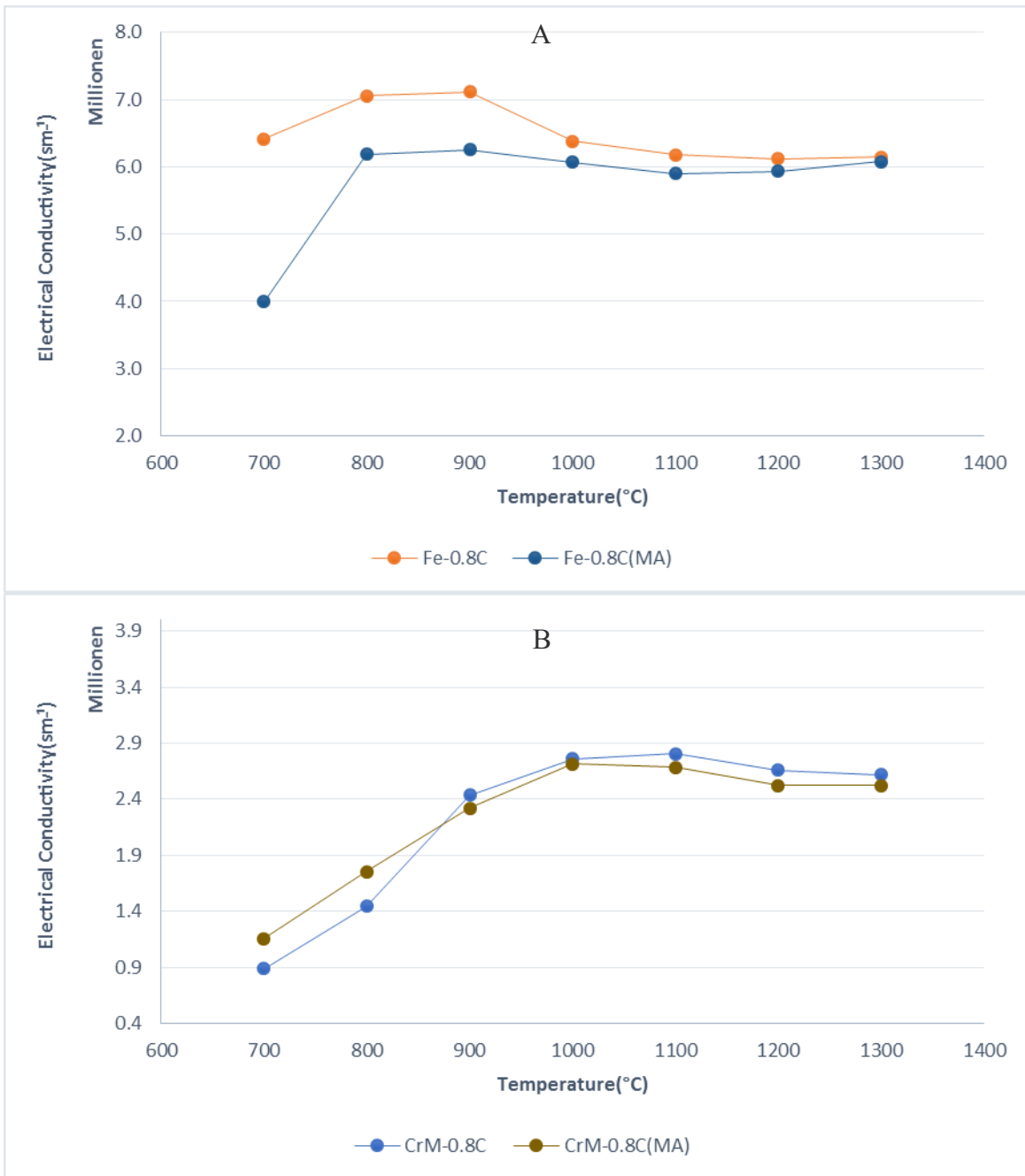


Figure 3.81: Electrical conductivity of steels versus sintering temperature, compacted at 600 MPa, sintered 60 min in argon; A: carbon steels, B: Cr-Mo prealloyed steels.

3.3.8.2. Coercivity

The relationship between the coercivity and the sintering temperature of the steels is shown in Figure 3.82. For the two carbon steels (Fig. 3.82-A), the determining factors at the initial stages of sintering are dissolution of carbon and changes in the microstructure. In the steel containing MA at 800 and 900°C, higher values are obtained which can be the result of the higher carbon dissolution at these temperatures. The results also show that above 1000°C and up to 1300°C, the coercivity remained almost steady and without significant changes for both steels, which

confirms that processes such as neck enlargement or pore rounding have less effect on this property of the carbon steels.

In the Cr-Mo steels (Fig. 3.82-B), the main raise in the coercivity is visible at 900 and 1000°C for the steel with and without MA, respectively. This result can be explained by the carbon dissolution, which occurred at lower temperatures in the MA containing steel, which is also in good agreement with the previous results (see the metallography sections in Fig. 3.73). After these significant jumps both steels showed less change in the parameter up to 1300°C.

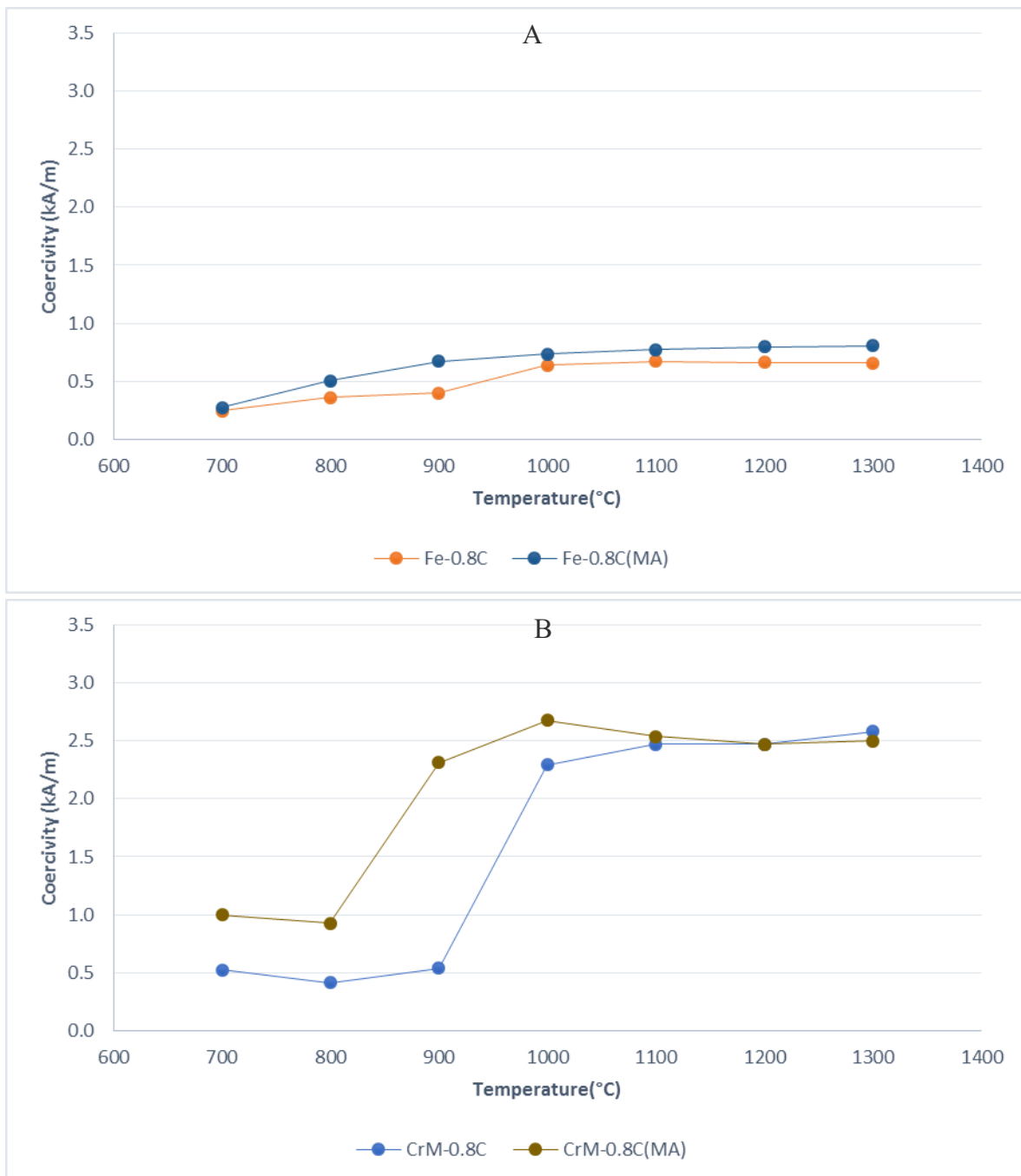


Figure 3.82: Coercivity of steels versus sintering temperature, compacted at 600 MPa, and sintered 60 min in argon; A: carbon steels, B: Cr-Mo prealloyed steels

3.4. Part 1d: Mechanical and physical properties of differently alloyed sintered steels as a function of the sintering temperature

As already stated, the powder metallurgy (PM) route is a well-known manufacturing process for large-scale production of precision parts in a cost-effective manner. The constant demands for improved mechanical properties of the produced structural parts are met by the PM industry through various routes.

One of the main advantages of the powder metallurgy process compared with ingot metallurgy is the larger flexibility in the material usage and the choice of the alloying route. This potential usually can be utilized easily when using conventional alloying elements of powder metallurgy such as carbon, copper, nickel and/or molybdenum, e.g. by adding the elemental powders to the mix or by diffusion bonding them to the base powder. But the alloying by these methods could be more difficult when adding powders with higher sensitivity to oxygen which form more stable oxides. Some of these elements such as chromium, silicon and manganese, which are usually cheaper than Ni, Cu and Mo, are widely used in ingot metallurgy but have found less application in the powder metallurgy. As mentioned above, the main challenge regarding the use of oxygen-sensitive elements is the formation of stable oxides especially on the particle surfaces, which can negatively affect the sintering process and the final properties of the sintered PM steels [58]. Therefore, minimizing oxidation during sintering of PM steels that contain such elements seems to be an important task in order to have a successful sintering process. Furthermore, all powders that have been exposed to air at any time carry “natural” surface oxides which are easily reducible in case of Cu, Ni and Mo but more difficult to reduce for Cr, Mn and Si. One solution for both problems could be to lower the chemical activity of these elements by alloying them with elements of lower oxygen affinity [19]. To achieve this, there are basically two main routes: 1- using conventional prealloyed iron powder, e.g. commercial Astaloy grade powders, 2- by mixing a plain iron base powder with a masteralloy (MA) powder which contains the desired alloy elements in a combined form [166].

The masteralloy route allows the introduction of oxygen-sensitive elements such as Si, Mn and Cr, which can significantly improve the properties of low alloy steels. Compared to prealloying, the masteralloy route suggests some more benefits such as better compressibility, more flexibility in the selection of the final composition of the steel and the potential reduction of the overall cost. As stated in Chapter 1, the development of masteralloys for PM steels has been a topic of research since the early 70's [20-23, 167]. This route was not too attractive for the PM industry until the 1990's [166] because of two main reasons: 1- the masteralloys available required high sintering temperatures (about 1280°C) to dissolve carbide phases present in the masteralloy particles, 2- extreme tool wear caused by the very hard and angular MA powder particles produced by milling of ingots. At the end of the 1990's these problems were solved by using inert gas atomization to produce fine particles with rounded shape and using computational tools to define composition with adequate melting points [168, 169]. “Ultra-High Pressure Water Atomization” (UHPWA) is a new atomization technique developed in recent years to produce fine ($d_{50} < 8 \mu\text{m}$) MA powder with rounded morphologies and low oxygen content ($< 1 \%$) at reasonable production cost [170]. This eliminates the handicap of previous atomized masteralloy types that only a small fraction of the atomized powder batches, typically the fraction $< 45 \mu\text{m}$, could be used for alloying purposes, with resulting cost penalty.

In addition to the selection of the alloying system, sintering conditions such as temperature, time and atmosphere also play a key role on the final properties and microstructure of PM steels, which have been the target of numerous investigations [79, 171, 172]. Basically, the most important sintering processes that can affect the final properties are the following [42]:

- _ Change of particle surface chemistry, in particular, reduction of oxide layers covering the powder particles.
- _ Formation and growth of solid metallic bridges out of pressing contacts.
- _ Dissolution of alloy elements, in particular carbon, and distribution within the metallic matrix.

In this part of research, these three processes are discussed for five different steels which were sintered in the temperature range of 700 to 1300°C, in order to investigate the effect of the sintering temperature on the development of the sintered properties of PM steels. For material preparation, in addition to the traditional method of adding elemental powder to mixes, which was used to produce two steels in the Fe-C and Fe-Cu-C systems, two prealloyed powder (Astaloy CrM and Mo) and a grade admixed with masteralloy were used to prepare steels which contain different alloying elements.

For this purpose, three grades of water atomized ferrous powders were used as base powders, a plain iron powder (ASC100.29), a Cr-Mo pre-alloyed powder (Astaloy CrM) and a Mo pre-alloyed powder (Astaloy Mo), all supplied by Höganäs AB, Sweden. Carbon was introduced as natural graphite (grade UF4, Kropfmühl) and copper was of electrolytical type which was sieved to the dimensional size < 25 µm. The masteralloy used in this research was H46 produced by Ultra High Pressure Water Atomization, sieved below 20 µm. Table 3.11 shows the designations and compositions of the prepared mixes. The powders were dry blended in a tumbling mixer for 60 min. Charpy bars (ISO 5754) were pressed for this study in the tool with floating die at 600 MPa, die wall lubrication being afforded (using Multical sizing fluid). Sintering of the samples was performed in the SiC rod heated electrical laboratory furnace at temperatures varying in the range 700-1300°C (interval 100°C) for 1 hr (isothermal sintering) under plain Ar (99.999 quality). After the isothermal holding period at temperature, the samples were cooled in the water-jacketed exit zone under the same protective atmosphere as was used for the sintering. The results of the measurements are listed in Table 3.11 to 3.15. (remark: the values of the reference materials Fe-0.8%C(graphite) presented here have been taken from Chapter 3.2)

Table 3.10: Material composition of mixes (in brackets: alloy element content in wt %)

	Designation	Mix composition
1	Fe-0.8C (reference)	ASC100.29 + 0.8%C (0%)
2	Fe-2Cu-0.8C	ASC10.29 + 2% Cu + 0.8% C (2%)
3	Fe-4MA-0.8C	ASC100.29 + 4% MA+ 0.8% C (1.94%)
4	Fe-1.5Mo-0.8C	Astaloy Mo + 0.8%C (1.5%)
5	Fe-3Cr-0.5Mo-0.8C	Astaloy CrM + 0.8%C (3.5%)

Table 3.11: Sintered properties of carbon steel (Fe-0.8C_{admixed}); compacted at 600 MPa, sintered 60 min at 700-1300°C in argon.

<i>Sintering Temp.</i> (°C)	<i>Sintered density</i> (g/cm ³)	<i>Dimensional Change</i> (%)	<i>Impact energy</i> (J/cm ²)	<i>Hardness (HV30)</i>	<i>Dyn. Young's modulus</i> (GPa)	<i>Damping (Q⁻¹ 10E-9)</i>	<i>Oxygen content</i> (wt %)	<i>Combined carbon content</i> (wt %)	<i>Electrical conductivity</i> (S.m ⁻¹ 10E4)	<i>Coercivity</i> (kA/m)
700	7.18±0.00	-0.02±0.00	0.5±0.3	64.0±3.0	117.2	23.4	0.107±0.004	0.786±0.012	641	0.25
800	7.18±0.01	0.00±0.00	5.3±1.2	76.0±2.6	148.1	11.5	0.094±0.004	0.786±0.005	706	0.36
900	7.18±0.01	0.00±0.00	9.7±1.2	80.0±2.0	154.6	7.8	0.081±0.002	0.776±0.006	712	0.40
1000	7.17±0.01	0.07±0.00	14.5±1.3	102.7±3.8	158.2	7.0	0.041±0.001	0.752±0.006	638	0.64
1100	7.18±0.00	0.05±0.02	17.2±1.6	119.0±5.2	163.5	4.6	0.023±0.003	0.744±0.004	618	0.67
1200	7.19±0.00	-0.04±0.00	19.5±1.0	130.7±3.5	164.1	4.6	0.011±0.001	0.728±0.005	612	0.66
1300	7.23±0.00	-0.22±0.00	26.0±1.1	134.3±3.2	168.3	5.1	0.004±0.001	0.733±0.006	615	0.66

Table 3.12: Sintered properties of carbon steel (Fe-2Cu-0.8C_{admixed}); compacted at 600 MPa, sintered 60 min at 700-1300°C in argon.

<i>Sintering Temp.</i> (°C)	<i>Sintered density</i> (g/cm ³)	<i>Dimensional Change</i> (%)	<i>Impact energy</i> (J/cm ²)	<i>Hardness (HV30)</i>	<i>Dyn. Young's modulus</i> (GPa)	<i>Damping (Q⁻¹ 10E-9)</i>	<i>Oxygen content</i> (wt %)	<i>Combined carbon content</i> (wt %)	<i>Electrical conductivity</i> (S.m ⁻¹ 10E4)	<i>Coercivity</i> (kA/m)
700	7.25±0.01	-0.05±0.01	0.9±0.5	67.0±2.6	145.0	20.5	0.125±0.009	0.753±0.017	700	0.27
800	7.23±0.00	-0.01±0.01	9.7±0.5	84.0±4.0	152.7	7.2	0.111±0.019	0.749±0.005	713	0.35
900	7.21±0.00	0.05±0.00	12.9±2.1	94.3±1.5	158.4	5.7	0.126±0.016	0.743±0.012	660	0.59
1000	7.22±0.01	0.07±0.02	17.0±1.5	141.3±2.3	158.7	5.7	0.048±0.015	0.746±0.007	572	0.88
1100	7.17±0.00	0.25±0.02	17.5±2.3	196.0±5.6	158.8	5.3	0.016±0.002	0.721±0.010	509	0.95
1200	7.21±0.00	0.03±0.01	23.4±2.3	204.7±8.0	164.6	5.4	0.016±0.019	0.707±0.006	502	0.92
1300	7.24±0.00	-0.07±0.00	25.0±2.5	206.3±2.3	167.6	5.8	0.006±0.001	0.702±0.007	499	0.91

Table 3.13: Sintered properties of masteralloy-containing steel (Fe-4MA-0.8C*); compacted at 600 MPa, sintered 60 min at 700-1300°C in argon.
 *nominal content = admixed graphite + carbon contained by the masteralloy

<i>Sintering Temp. (°C)</i>	<i>Sintered density (g/cm³)</i>	<i>Dimensional Change (%)</i>	<i>Impact energy (J/cm²)</i>	<i>Hardness (HV30)</i>	<i>Dyn. Young's modulus (GPa)</i>	<i>Damping (Q⁻¹ 10E-9)</i>	<i>Oxygen content (wt %)</i>	<i>Combined carbon content (wt %)</i>	<i>Electrical conductivity (S.m⁻¹ 10E4)</i>	<i>Coercivity (kA/m)</i>
700	7.14±0.01	0.05±0.01	0.3±0.1	73.0±1.0	125.1	39.4	0.222±0.013	0.770±0.003	492	0.32
800	7.11±0.00	0.13±0.02	5.4±1.0	95.3±1.5	145.4	7.2	0.201±0.040	0.773±0.004	495	0.58
900	7.08±0.00	0.20±0.02	8.6±0.6	133.7±4.0	151.1	5.7	0.198±0.030	0.779±0.017	456	0.97
1000	7.09±0.01	0.18±0.04	10.6±2.3	174.0±2.0	159.4	5.6	0.189±0.023	0.766±0.022	392	1.29
1100	7.13±0.03	-0.04±0.04	21.5±2.5	190.3±5.5	162.6	6.9	0.074±0.012	0.699±0.004	365	1.35
1200	7.15±0.03	-0.07±0.05	26.4±3.2	188.7±1.2	169.0	6.2	0.015±0.001	0.650±0.005	357	1.27
1300	7.16±0.00	-0.19±0.01	33.7±2.9	196.7±7.2	167.7	6.3	0.013±0.017	0.649±0.005	346	1.23

Table 3.14: Sintered properties of Mo prealloyed steel (Fe-1.5Mo-0.8C_{admixed}); compacted at 600 MPa, sintered 60 min at 700-1300°C in argon.

<i>Sintering Temp.</i> (°C)	<i>Sintered density</i> (g/cm ³)	<i>Dimensional Change</i> (%)	<i>Impact energy</i> (J/cm ²)	<i>Hardness (HV30)</i>	<i>Dyn. Young's modulus</i> (GPa)	<i>Damping (Q⁻¹ 10E-9)</i>	<i>Oxygen content</i> (wt %)	<i>Combined carbon content</i> (wt %)	<i>Electrical conductivity</i> (S.m ⁻¹ 10E4)	<i>Coercivity</i> (kA/m)
700	7.09±0.00	0.00±0.00	0.2±0.0	90.3±3.1	60.3	186.2	0.120±0.005	0.765±0.016	166	0.32
800	7.09±0.01	0.06±0.04	1.1±0.1	103.7±6.7	128.5	11.3	0.104±0.003	0.765±0.016	513	0.60
900	7.08±0.00	0.07±0.02	3.6±0.2	151.0±3.0	142.1	6.6	0.080±0.002	0.760±0.008	467	1.19
1000	7.07±0.01	0.14±0.02	7.0±0.5	181.0±6.9	150.8	6.7	0.036±0.005	0.743±0.009	445	1.70
1100	7.08±0.01	0.11±0.00	10.6±0.1	182.0±5.6	151.1	6.8	0.018±0.005	0.730±0.002	436	1.66
1200	7.10±0.00	0.03±0.01	11.5±0.0	182.0±5.3	153.4	6.0	0.014±0.006	0.718±0.013	439	1.78
1300	7.13±0.00	-0.17±0.02	16.4±1.9	185.3±7.2	159.7	5.7	0.006±0.002	0.713±0.005	446	1.77

Table 3.15: Sintered properties of Cr-Mo prealloyed steel (Fe-3Cr-0.5Mo-0.8C_{admixed}); compacted at 600 MPa, sintered 60 min at 700-1300°C in argon.

<i>Sintering Temp. (°C)</i>	<i>Sintered density (g/cm³)</i>	<i>Dimensional Change (%)</i>	<i>Impact energy (J/cm²)</i>	<i>Hardness (HV30)</i>	<i>Dyn. Young's modulus (GPa)</i>	<i>Damping (Q⁻¹ 10E-9)</i>	<i>Oxygen content (wt %)</i>	<i>Combined carbon content (wt %)</i>	<i>Electrical conductivity (S.m⁻¹ 10E4)</i>	<i>Coercivity (kA/m)</i>
700	6.95±0.01	0.04±0.00	0.1±0.1	81.0±2.0	45.3	349.1	0.224±0.020	0.801±0.033	89	0.52
800	6.95±0.00	0.05±0.02	0.2±0.2	51.3±4.2	75.9	99.3	0.230±0.014	0.794±0.018	145	0.41
900	6.93±0.01	0.02±0.02	0.5±0.5	71.7±3.2	100.2	36.1	0.225±0.004	0.794±0.016	244	0.54
1000	6.96±0.01	-0.01±0.02	3.4±1.7	200.3±9.7	136.2	23.8	0.166±0.030	0.783±0.036	276	2.30
1100	6.98±0.01	-0.02±0.02	8.9±0.6	226.7±4.9	145.6	8.1	0.122±0.008	0.757±0.049	281	2.47
1200	7.01±0.00	-0.22±0.00	16.7±0.9	269.7±7.6	157.4	7.7	0.027±0.013	0.680±0.014	266	2.47
1300	7.04±0.01	-0.41±0.02	20.1±1.5	330.7±10.1	161.2	8.0	0.008±0.004	0.678±0.013	262	2.58

3.4.1. Green density

The green density values of the 5 steels studied here are shown in Figure 3.1.83. This shows that after compacting at 600 MPa, the green density of the carbon steel is 7.13 g/cm³. Adding 2% copper increased the density to 7.17 g/cm³, which is in good agreement with the results of some previous studies that showed a positive effect of copper on the compactibility of powders [66, 173, 174], however, part of this effect can be due to higher theoretical density of Fe-2Cu-0.8C compared with Fe-0.8C as well. The decrease of the green density to 7.08 g/cm³ by adding 4% MA reveals a slightly negative effect of this additive on the compactibility. It seems that the soft and dendritic Cu particles could be pressed quite easily and fill the pores between the iron particles, while the spherical MA particles with higher hardness are more difficult to press. Figure 3.1.83 also shows that the Astaloy Mo and CrM based mixes have the lowest compactibility of 7.05 and 6.92 g/cm³, respectively. This is not surprising because it is well known that introducing alloying elements such as Cr and Mo into the iron lattice, as in the case of prealloying, increases the strength and hardness of steels [139, 140] and leads to lower compactibility of the powder.

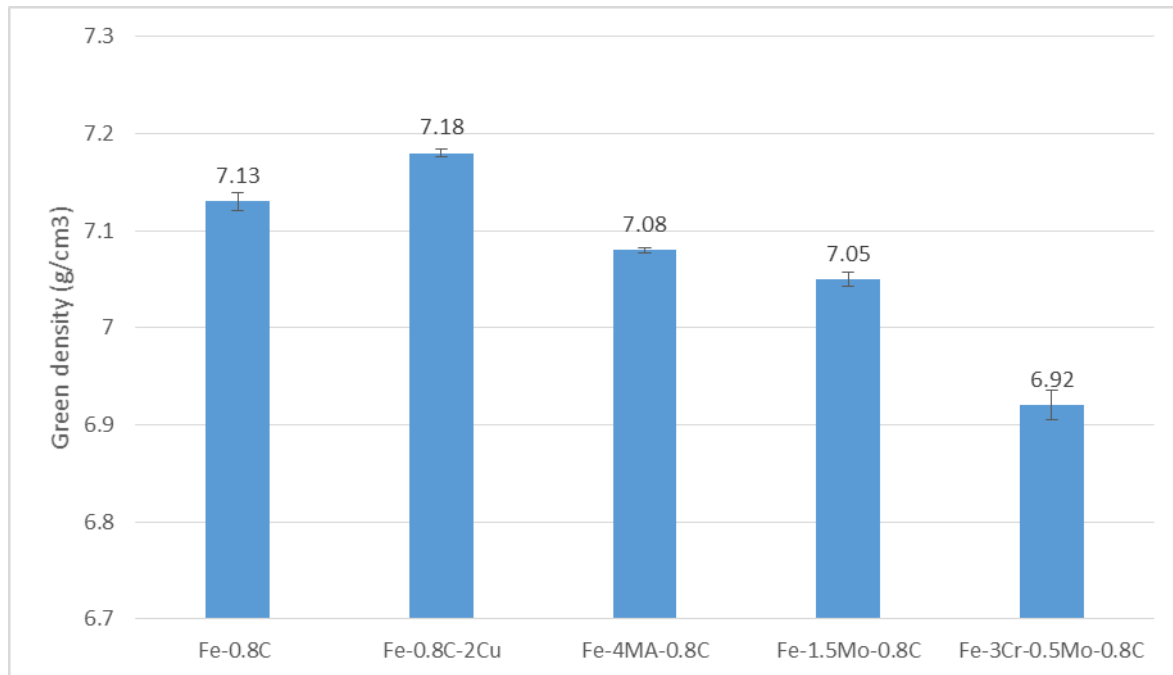


Figure 3.83: Green density of steels, compacted at 600 MPa in lubricated die (Charpy impact test bars ISO 5754).

3.4.2. Thermal analysis and degassing behaviour

For studying the degassing and deoxidation behaviour of the material during the thermal process, Thermogravimetry/Differential thermal analysis (TG/DTA) combined with mass spectrometry (MS), which is a well-known technology for the monitoring the degassing processes [42, 51-53], was used in this part of work. The results of the measurement are given in Figure 3.84 to 3.88. Fe-C is the least oxygen sensitive steel in this study, and the results of thermal analysis are presented here once more as a reference to compare with the carbothermal

reduction of oxides in other alloying systems. It is evident that Fe-0.8C and Fe-2Cu-0.8C (Figures 3.84 and 3.85) show very similar degassing behaviour. The addition of Cu did not cause any change on the typical reduction reactions observed for Fe-0.8C powders. This is because copper forms oxide with thermodynamic stability lower than that of iron, i.e. they are more easily reduced. Similar to Fig.3.31, the most prominent signal in the graphs is mainly related to the release of carbon monoxide (red curve, mass 28 = CO). As expected, two reduction peaks are visible for these systems, one rather narrow peak in the temperature range of 700-800°C, indicating the carbothermal reduction of the surface oxides. The second peak is markedly broader and took longer, with the maximum at around 1100°C, and it has been attributed to the reduction of the internal oxides and those enclosed in the pressing contacts, which are more difficult to remove since the oxygen has to diffuse to the surface before it can be removed as gaseous species [53]. For both reduction processes, the main product is CO (resulting from reactions 3-2 and 3-3) as is evident from the red curve. The characteristic double peak at high temperature in case of Fe-Cu-C is related to the formation of transient liquid phase in this material at about 1080°C.

In Fe-4MA-0.8C (Figure 3.86), despite using the same base powder (ASC100.29) as for the carbon steel, virtually no m28 peak related to reduction of surface iron oxides is evident in the range of 700-800°C, but the carbothermal oxygen removal is shifted to significantly higher temperatures, with the maximum at 1180°C. This process is also confirmed by TG analysis. In this case, elimination of the peak in the range of 700-800°C can be explained by an oxygen transfer process which is called “Internal Getter” effect. This was observed previously in the sintering of steels containing admixed highly oxygen affine elements such as chromium or manganese [50]. The process is an oxygen transfer (or migration) from the element with lower oxygen affinity (Fe) to the other element(s) with higher oxygen affinity such as Mn, Cr or Si, the reason being that the atmosphere that is generated by carbothermal reduction of iron oxides is strongly oxidizing for the alloy elements. In this case therefore, due to the introduction of elements with higher oxygen affinity than Fe (Mn and Si) through the masteralloy, the Internal Getter effect would be expected. Oxygen is transferred through the gas phase from the iron particles (ASC 100.29) to the adjacent MA particles which contain manganese and silicon. The oxides thus formed in the masteralloy require much higher temperatures to be reduced.

The Mo alloyed steel (Figure 3.87) shows similar MS intensities as the Fe-C system, a narrow degassing peak attributed to reduction of surface oxides at low temperature (775 °C) and a wider peak at higher temperature (1100°C) which is the consequence of reduction of internal oxides. This shows that the presence of Mo in the chemical composition of the steels does not affect the degassing behaviour of this steel, which is not surprising regarding the fact that the Mo oxides are chemically no more stable than iron oxides.

In the chromium-molybdenum prealloyed steel (Figure 3.88), similar to the MA steel, no pronounced m28 peak is observed up to 1000°C. As discussed in Chapter 3.3.2, above 700°C the surface iron oxides originally present on chromium prealloyed powder transform into more stable types when sintering is done in inert atmosphere (Ar)[53]. Therefore, effective oxide reduction and sintering would not be expected to occur in inert atmosphere below 1000°C, which is also supported by the results given in [58]. The consequence is that both if oxygen-affine alloy elements are introduced as masteralloys or through prealloying, respectively, high

sintering temperatures, typically $>1200^{\circ}\text{C}$, are required to obtain effective oxygen removal, although the effect of residual oxygen on the mechanical properties can be quite different, as will be shown below.

A point that should be mentioned here is that the small TG signals which are discernible at around 300°C in all graphs of the steels are not related to the reduction process of oxide, these signals are attributed to removal of Multical sizing fluid which was used as a lubricant in compacting could be assumed to be the reason of these signals.

The results of dilatometric runs of the steels are presented in Figure 3.89. The temperatures of the transformation are also presented. In this figure the graph of Fe-C is presented as reference. In the Fe-Cu-C system, the presence of copper in the mixture changed the temperature of the α to γ transformation only by about -20°C compared to Fe-C, which shows that below 1000°C , Cu dissolution during heating up was not significant. The γ to α transformation during cooling, in contrast, occurred at least at 50°C lower than for Fe-C. Another important phenomenon evident in this graph is formation of transient liquid phase by melting of Cu and corresponding copper swelling, which is clearly visible at 1075°C . In Fe-4MA-0.8C, similar to Fe-Cu-C, the temperature of transformation (α to γ) was not changed significantly by adding the MA to the mixture, however in the cooling section of the graph, it is evident that alloying the carbon steel with the masteralloy reduced the temperature of the γ to α transformation to 590°C . The dilatometric graph of the Mo alloyed sintered steels is also presented in Figure 3.89. It is well known that Mo is an α stabilizer, especially when graphite has not yet been dissolved, therefore during the heating process, the starting temperature of the α to γ transformation increases to about 760°C in the 1.5%Mo prealloyed steel, which is 40°C higher than with the Fe-0.8C steel. In Cr-Mo prealloyed steel, the α to γ transformation occurred at 830°C which is the highest temperature among all steel grades investigated here. It shows that carbon dissolution in this steel occurred later compared to the other steels, which led to the higher temperature for α to γ transformation, carbon dissolution also being slowed down by the presence of stable oxide layers. According to the DIL graph, Cr-Mo prealloyed steel showed the lowest temperature (360°C) for the retransformation among all steel grades studied here.

The heating sections of the dilatometric runs and corresponding MS graphs are shown in Figure 3.1.90 the MS graphs agreeing well with the results of the degassing behaviour of steels obtained by DTA/MS as presented in Figures 3.1.84 to 3.1.88. In particular the agreement of the expansion in the dilatogram for Fe-Cu-C with the break in the m28 graph is evident, confirming that this break is caused by liquid phase formation.

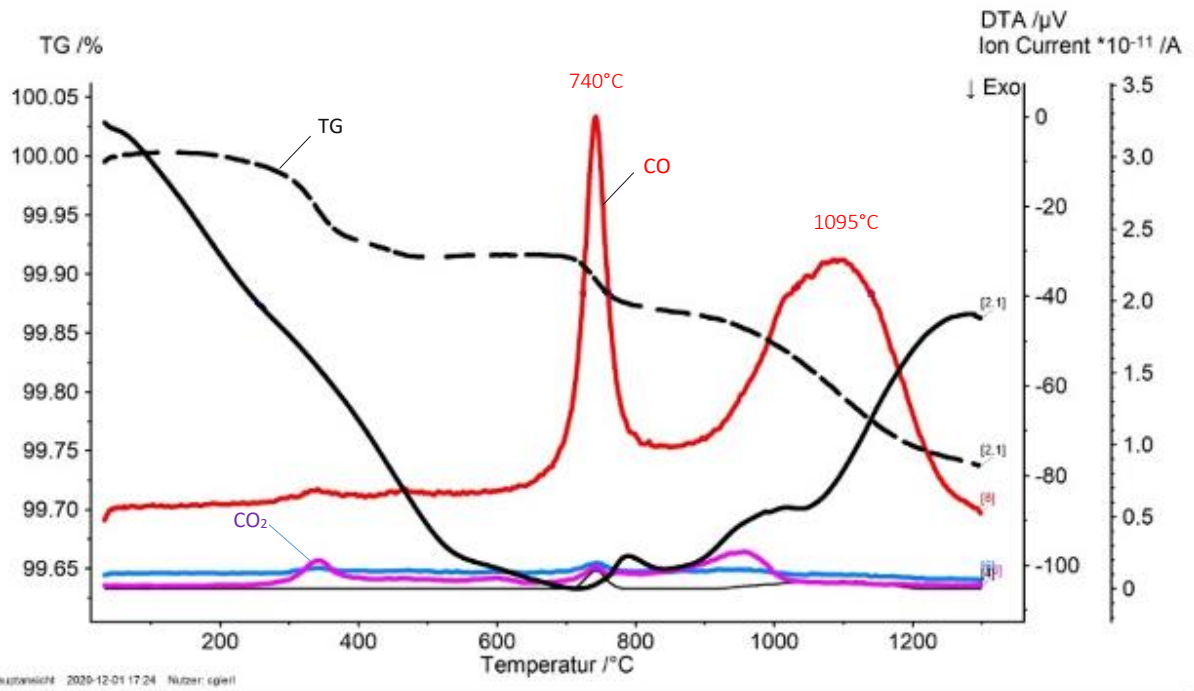


Figure 3.84: DTA/TG graphs with MS (heating section) of carbon steel (Fe-0.8C). Compacted at 600 MPa, sintered at 1300°C, 20 K.min⁻¹, argon.

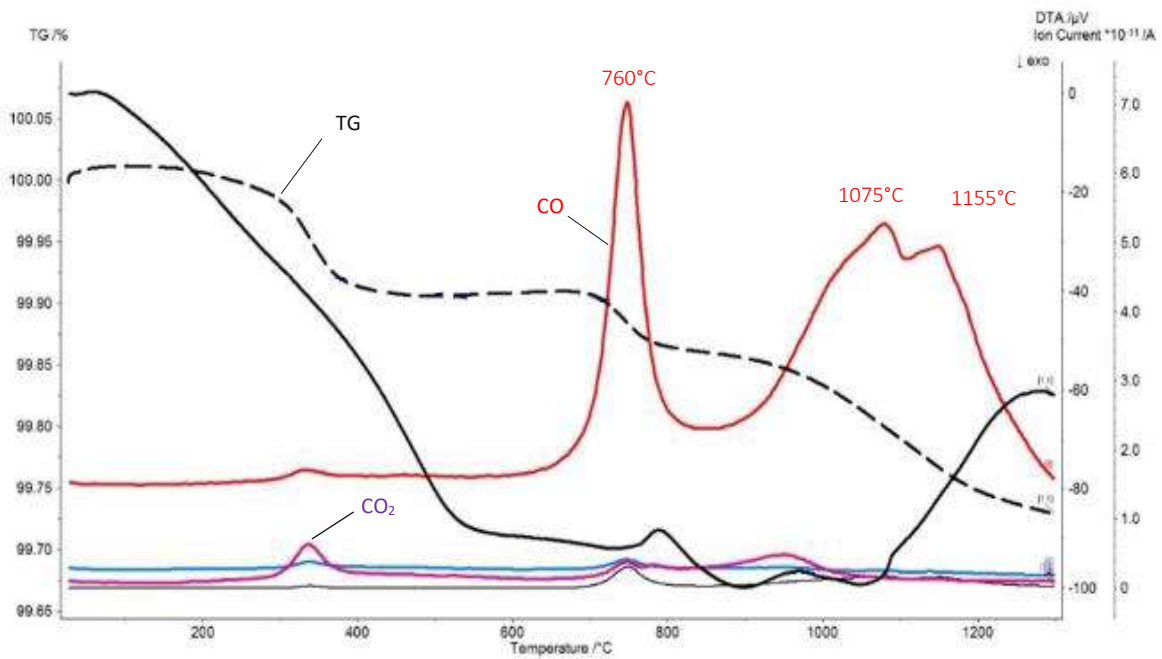


Figure 3.85: DTA/TG graphs with MS (heating section) of Fe-2Cu-0.8C. Compacted at 600 MPa, sintered at 1300°C, 20 K.min⁻¹, argon.

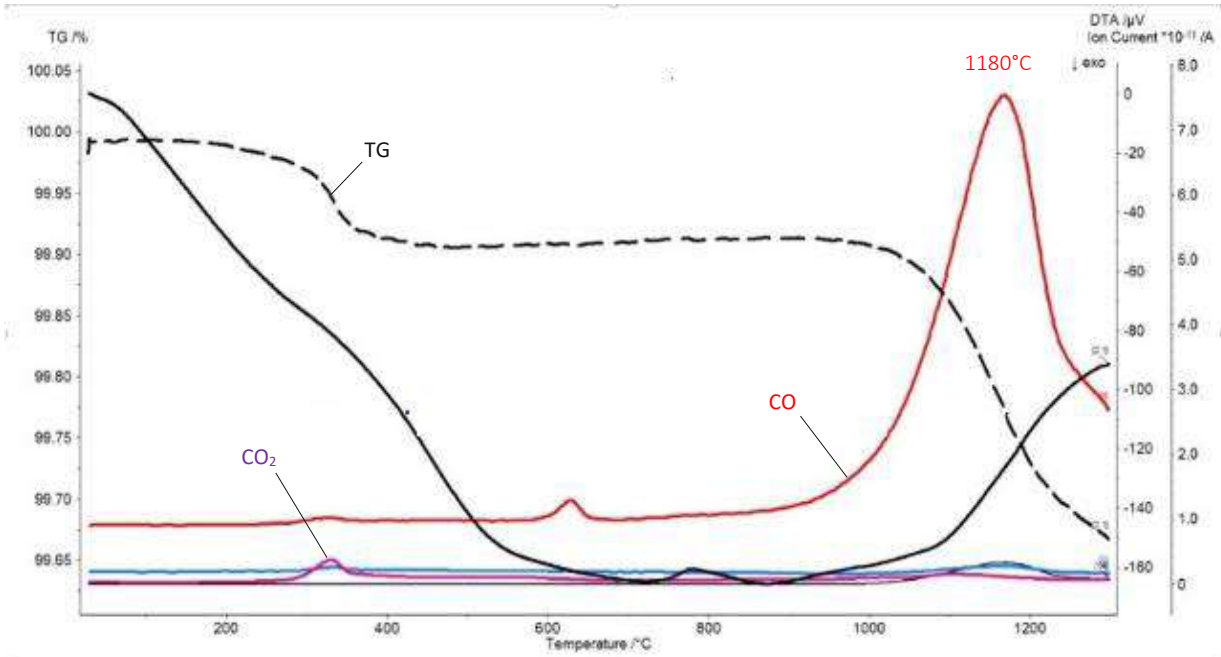


Figure 3.86. DTA/TG graphs with MS (heating section) of Fe-4MA-0.8C. Compacted at 600 MPa, sintered at 1300°C, 20 K.min⁻¹, argon.

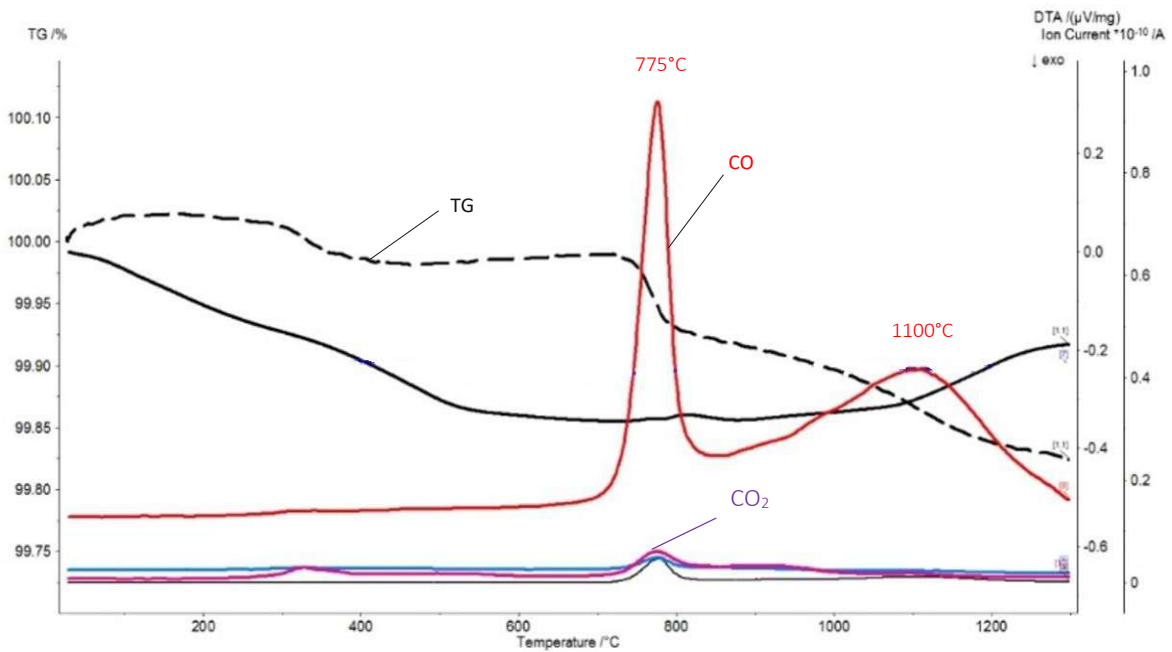


Figure 3.87: DTA/TG graphs with MS (heating section) of Fe-1.5 Mo-0.8C. Compacted at 600 MPa, sintered at 1300°C, 20 K.min⁻¹, argon.

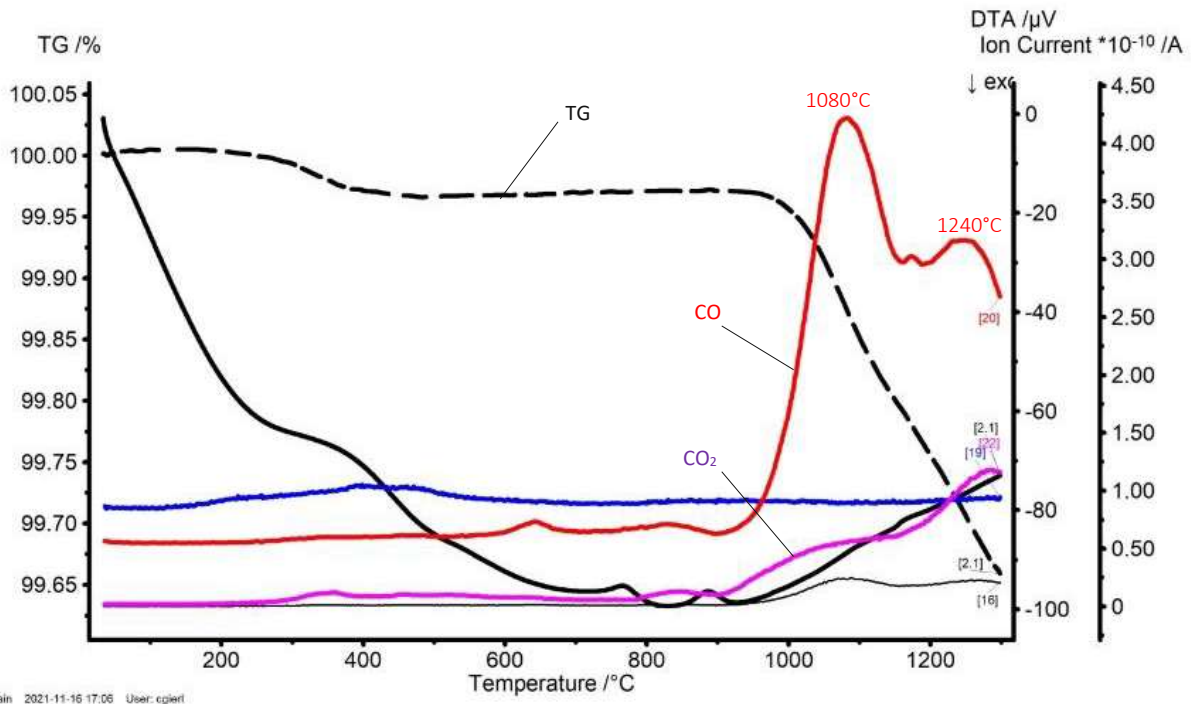


Figure 3.88: DTA/TG graphs with MS (heating section) of Fe-3Cr-0.5Mo-0.8C. Compacted at 600 MPa, sintered at 1300°C, 20 K.min⁻¹, argon.

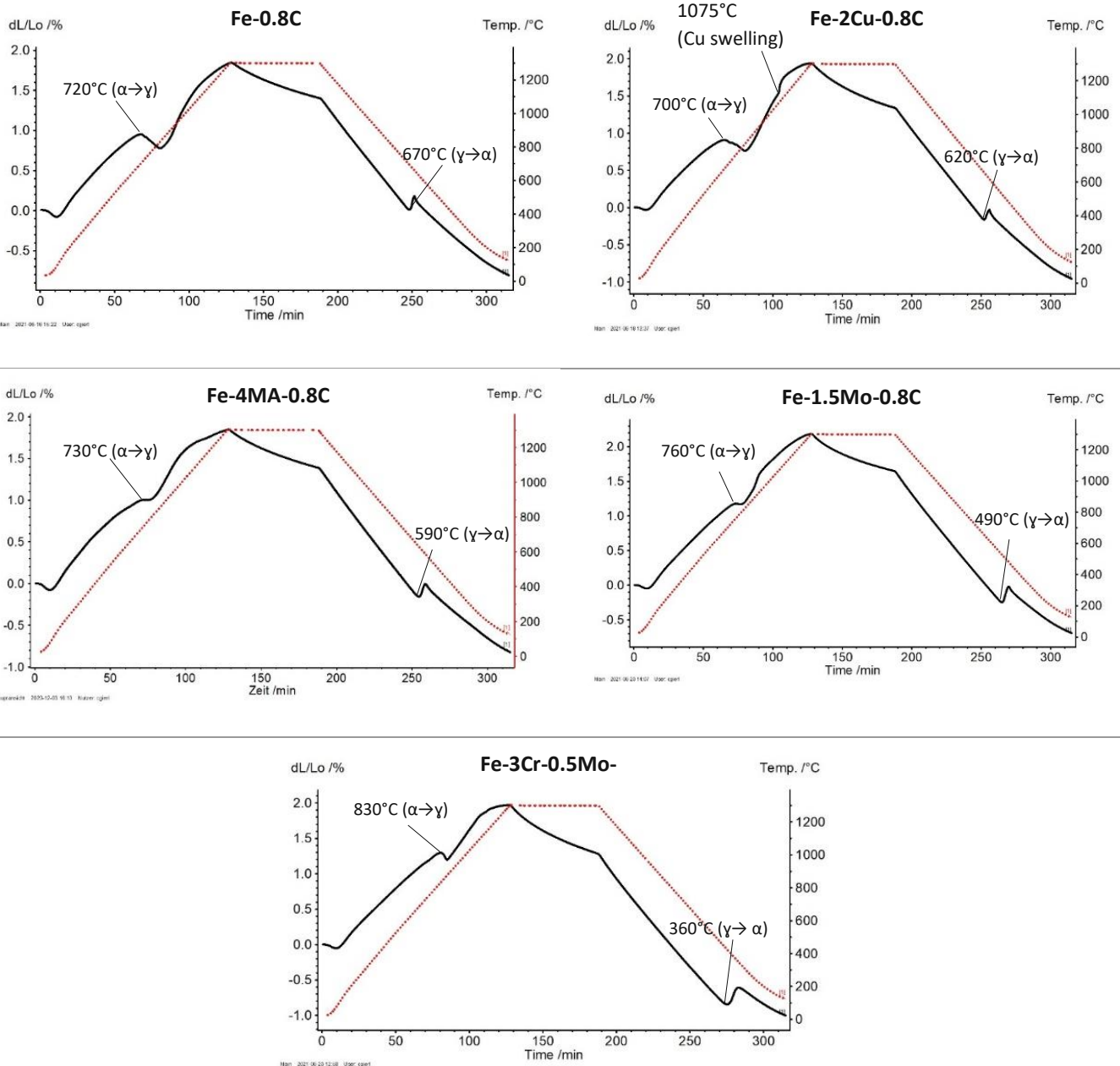


Figure 3.89: Dilatometric graphs for different steels. Compacted at 600 MPa, sintered at 1300°C in argon, heating-cooling rate: 10 K.min⁻¹.

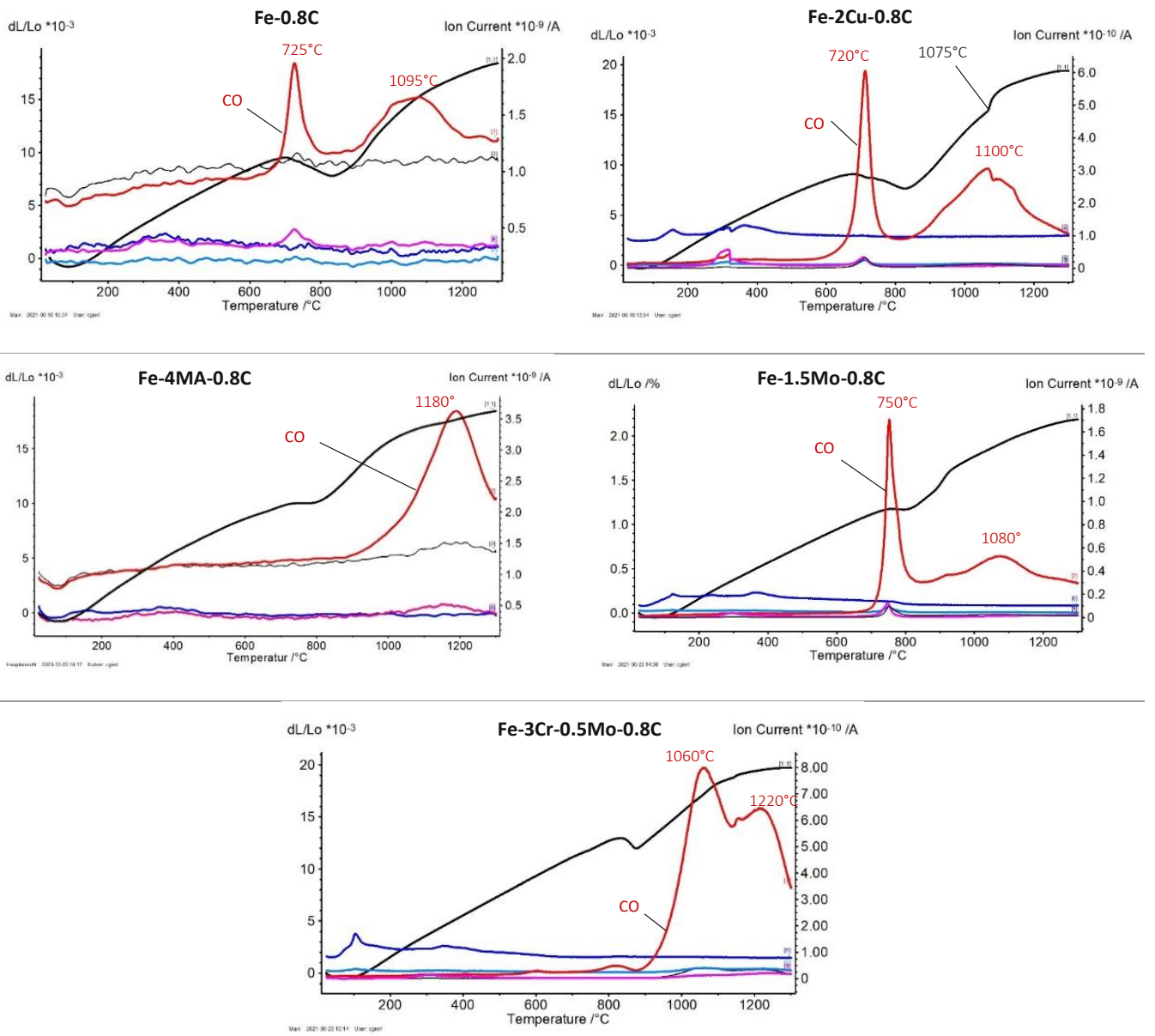


Figure 3.90: DIL/MS graphs for different steels. Compacted at 600 MPa, sintered at 1300°C in argon, heating rate: 10 K.min⁻¹.

3.4.3. Chemical analysis (carbon and oxygen content)

The oxygen and carbon contents of the steels are presented through Figures 3.91 and 3.92, respectively. Oxygen measurement shows that the 3 grades of Fe-0.8C, Fe-2Cu-0.8C and Fe-1.5Mo-0.8C follow almost the same trend in the oxygen removal, which is in good agreement with the results of the MS studies on these steels. The main oxygen removal for these steels occurred at 1000 and 1100°C, which is mainly attributed to the carbothermal reduction of internal oxides (according to the DIL/MS results presented in Figures 3.84, 3.85 and 3.87). It is evident that most of the oxygen in these alloys is removed below 1200°C, and increasing the sintering temperature to 1200 and 1300°C lowered the oxygen content only slightly.

In the MA containing steel the oxygen level remained almost constant and without significant change from 800 to 1000°C, the content being around 0.2%, which is much higher than in the three previously mentioned steels. Here, about half of the oxygen is introduced by the masteralloy (which contains 2.18 % O), the other half by the base powder. It is clearly evident that the main oxygen removal in this steel occurs only after sintering at 1100 and 1200°C which is a higher temperature range than with the three previously mentioned steels, and it is in good agreement with the results of the degassing behaviour of this steel (presented in Figure 3.86). Also in this case, increasing the sintering temperature to 1300°C does not show significant effect on the oxygen content compared to 1200°C.

In Cr-Mo alloyed steel, the oxygen content remained without significant change up to 900°C, and the first sign of oxide reduction is visible after sintering at 1000°C. Increasing the temperature to 1100 and 1200°C improves the oxide reduction, and the steel lost a major amount of oxygen at 1200°C. Further oxygen removal from the steel is not significant at 1300°C.

Results of the carbon measurement are presented in Figure 3.92. As mentioned before (Chapter 1), carbothermal oxide reduction plays the main role in oxygen removal when the sintering atmosphere is an inert gas. There is a good agreement between oxygen removal and carbon consumption. Similar to the oxygen content trend, the main temperature range of carbon consumption for Fe-0.8C, Fe-2Cu-0.8C and Fe-1.5Mo-0.8C is 900 to 1100° while for the masteralloy steel this range is between 1000 and 1200°C, and there is no significant further loss of carbon at 1300°C because almost all the oxides have been reduced effectively below this temperature. In the Cr-Mo alloyed steel the main carbon loss occurs in the range of 900 to 1200°C, which is in good agreement with the results of oxygen measurement. In Figure 3.92-1 the linear relationship between the carbon loss and oxygen removal from the alloys during the sintering process is shown.

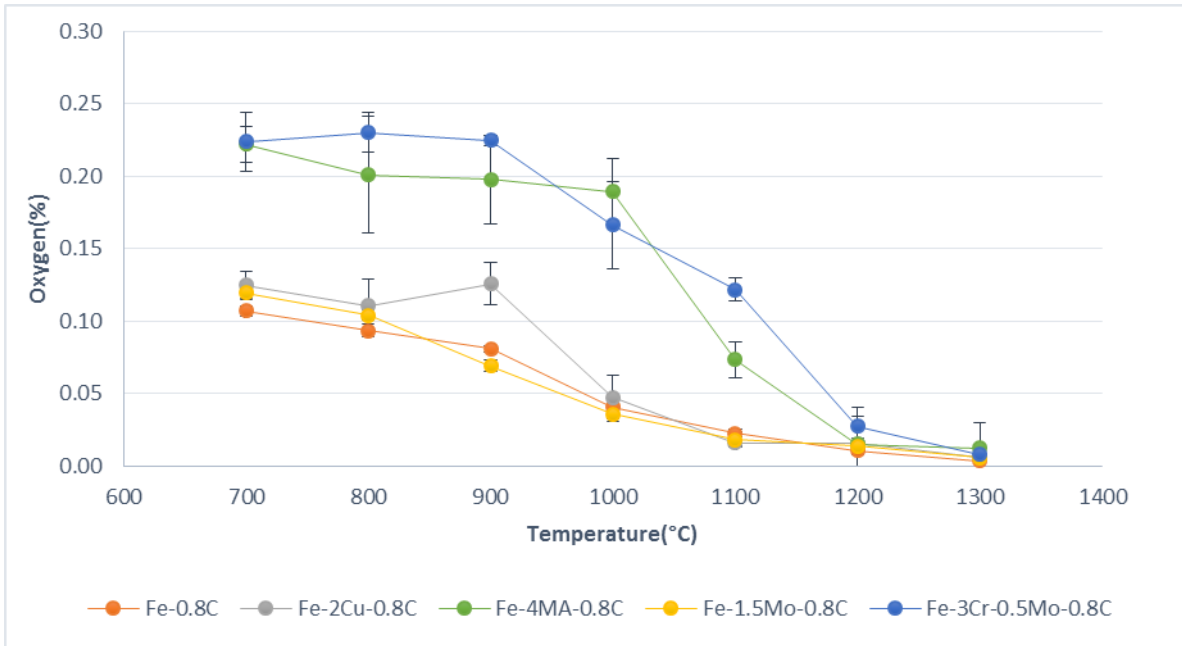


Figure 3.91: Oxygen content of the steels versus sintering temperature, compacted at 600 MPa, sintered 60 min in argon.

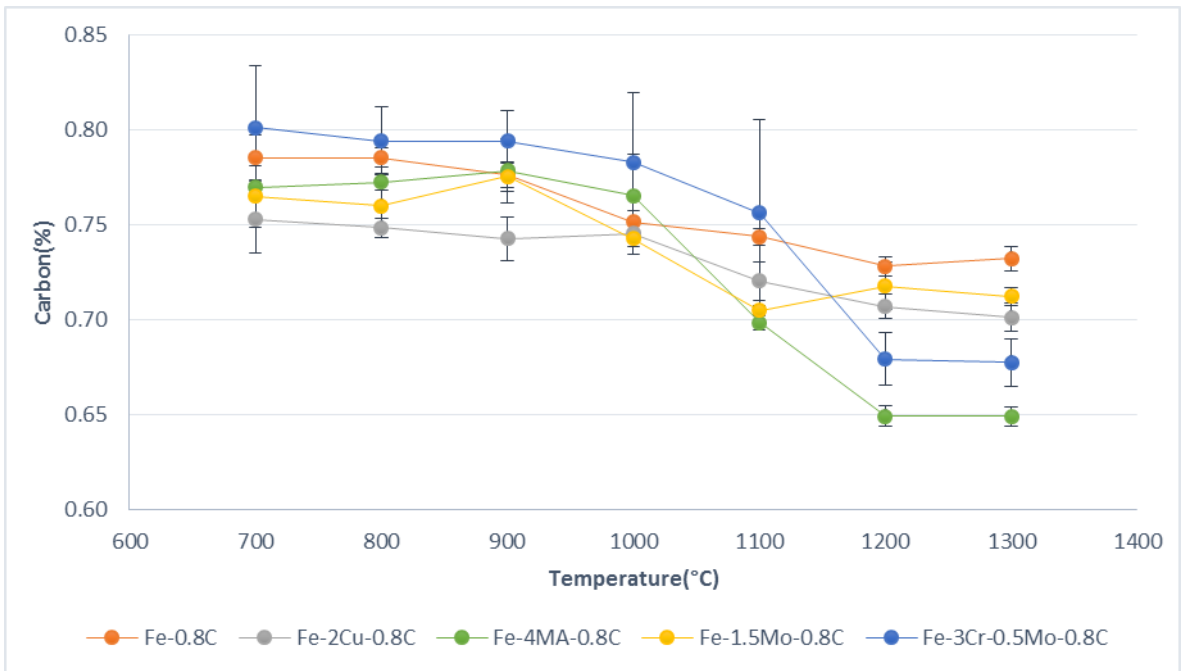


Figure 3.92: Total carbon content of the steels versus sintering temperature, compacted at 600 MPa, sintered 60 min in argon.

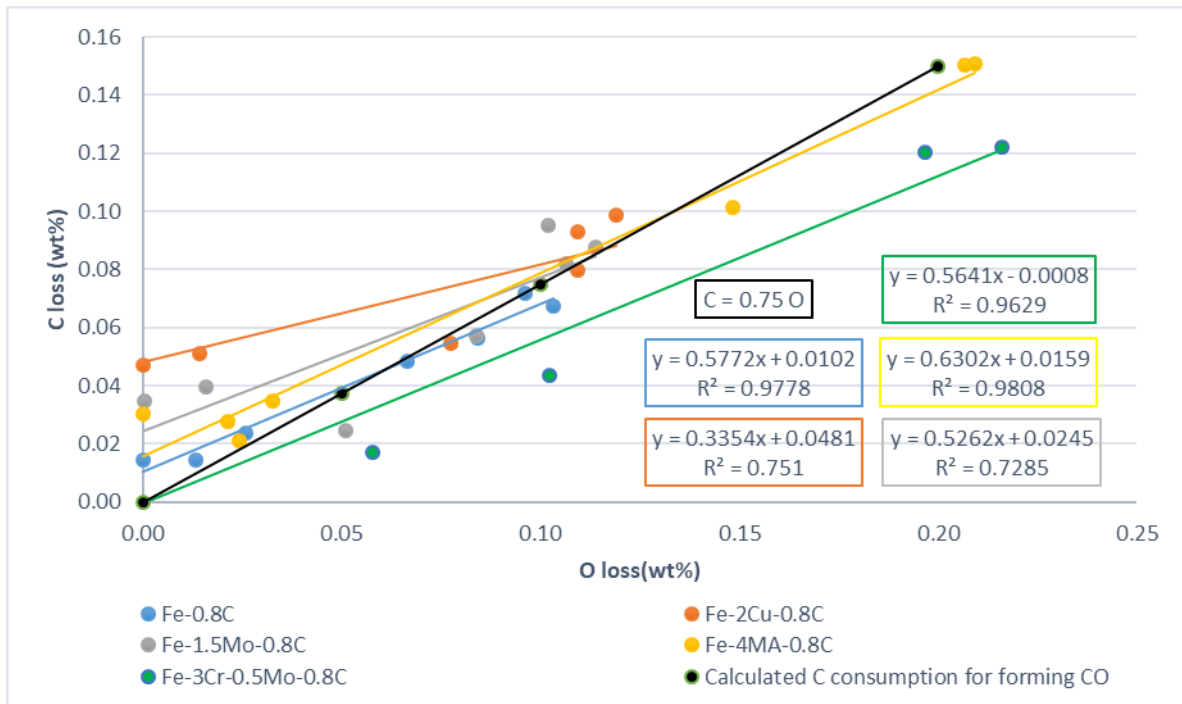


Figure 3.92-1: Carbon loss as a function of oxygen loss; steels sintered at 700-1300°C in argon.

3.4.4. Metallographic investigations (pore morphology and matrix microstructure)

Unetched optical microscopy cross sections of the steels sintered in argon at different temperatures are presented through Figure 3.93 to 3.100 (for Fe-C see Chapter 3.2.4, in argon). The sintered densities are also presented for better comparison. The pore morphology of Fe-2Cu-0.8C at two magnifications of 50 and 200 x is shown in Figures 3.93 and 3.94. Similar to the pore morphology of Fe-C, boundaries between the individual powder particles are visible at 700 and 800°C, which start to disappear from 900°C. The red copper particles, uniformly distributed, are visible in the microstructures below 1100°C, which confirms that the dissolution of this alloying element in the iron lattice through solid state diffusion was not significant below the melting point of Cu (1085°C), while above this threshold no copper particles are visible any more. It is well known that above the Cu melting point, a transient liquid phase mechanism is active [69, 175]. This mechanism resulted in the disappearance of the Cu particles at 1100 °C. Another result of the transient liquid phase in such systems is the presence of secondary pores [42, 47, 176]. Since the melt spreads into the pores and pressing contacts of the matrix, it leaves pores behind, the diameter of which is correlated to the size of the original alloy element particle. However, due the use of fine copper powder (<25 μm) with dendritic shape in the current work, distinguishing such pores from the primary porosity originating from the green compact is hardly possible since there is virtually no difference in size.

Increasing the sintering temperature above 1100°C led to pore rounding and enlargement which is clearly visible in the sections after sintering at 1200 and 1300°C. Fig. 1.95 and 1.96 show the micrographs of Fe-4MA-0.8C. The borders between powder particles are clearly visible at 700 and 800°C, and similar to the previously mentioned steel there is no prominent sintering contact at these temperatures. MA particles are not visible either. In this case, too, increasing the

sintering temperature eliminated the boundaries between the particles, however compared to Fe-Cu-C, in this steel adding 4% MA to the mixture resulted in lower density and higher amount of pores in the system.

The pore morphology of the Mo alloyed steel is presented through Figures 1.97 and 1.98. It is evident that the lower compactibility of this powder compared to Fe-Cu-C resulted in a higher amount of pores. The elimination of the borders between the powder particles in this case also is visible from 900°C, and the most pronouncedly rounded pores were formed in this steel after sintering at the highest temperature of 1300°C.

Figures 1.99 and 1.100 show the pore morphology of Cr-Mo prealloyed steel. Boundaries between the powder particles in this steel started to disappear above 1000°C, which is 100°C higher than in the other previously mentioned steels which is attributed to the presence of stable chromium oxide on the surface of the powder particles. Pore rounding and neck enlargement occur at and above 1200°C.

The characteristic etched matrix microstructures of the investigated steels sintered at different temperatures are presented through Figures 3.101 to 3.108 (for Fe-C see the section 3.2.4, in argon). At 800°C, micrographs of Fe-2Cu-0.8C (Fig. 3.101 and 3.102) show pearlite formation, it indicates partial carbon dissolution at this temperature, which is increased at higher sintering temperature, reaching a maximum at 1100°C and similar to the Fe-C system, remaining almost without significant change up to 1300°C.

In the steel alloyed with the masteralloy (Fig. 3.103 and 3.104), at 900°C, the boundaries between the particles start to disappear and pearlite formation is also visible, as a consequence of carbon dissolution. These observations indicate removal of the oxides from the surface of the plain iron particles at a rather low temperature and confirms the hypothesis of oxygen transfer from the surface of iron particles to the masteralloy particles. At this temperature, in addition to pearlite formation, a darker-etched rim in the surface region of all particles is also visible. Considering the ability of manganese to evaporate and condense on the matrix particles even at moderate sintering temperatures [92], it can be stated that these areas are related to the condensed manganese which has diffused into the iron lattice for some distance as well. The fully pearlitic microstructure at 1100°C indicates that the carbon dissolution process is complete at this temperature. Increasing the sintering temperature to 1300°C has resulted in a more uniform distribution of the alloying elements; the darker rims have disappeared.

Microstructures of Fe-1.5Mo-0.8C are presented through Fig.3.105 and 3.106. At 800°C, the first sign of bainite formation is visible especially at the surface of the powder particles, subgrain boundaries are also discernible at this temperature. Formation of upper bainite is clearly visible at 900°C which got more homogeneous at higher temperatures. With increasing temperature large acicular upper bainite is formed at and above 1100°C.

In the Cr alloy steel (Fig. 3.107 and 3.108), unlike the other grades, at 900°C the boundaries are still clearly visible in the microstructure. This is not surprising since Kremel et al. [1] have shown that at this temperature the Cr-Mo steel is particularly prone to oxygen pickup from the atmosphere. Furthermore, only minor signs of carbon dissolution can be seen, confirming that the stable chromium oxides on the powders prevent both carbon dissolution and formation of

the sintering contacts, which is in good agreement with the results of the fractography and impact test. Formation of a bainitic-ferritic microstructure at 1000°C indicates that some carbon dissolution occurred at this temperature. At 1300°C compared to 1100°C, the microstructure shows a pronounced change, presenting some martensitic regions which suggests that compared with other steels based on ASC100.29 and as well as Astaloy Mo, Astaloy CrM needs higher temperature for completing its carbon homogenization process which depends mainly on reduction of chromium oxide in the system.



Figure 3.93: Un-etched OM micrographs of copper alloyed steel (Fe-2Cu-0.8C_{admixed}) compacted at 600 MPa, sintered 60 min in argon, 50 x. (scale bar 400μm holds for all images)

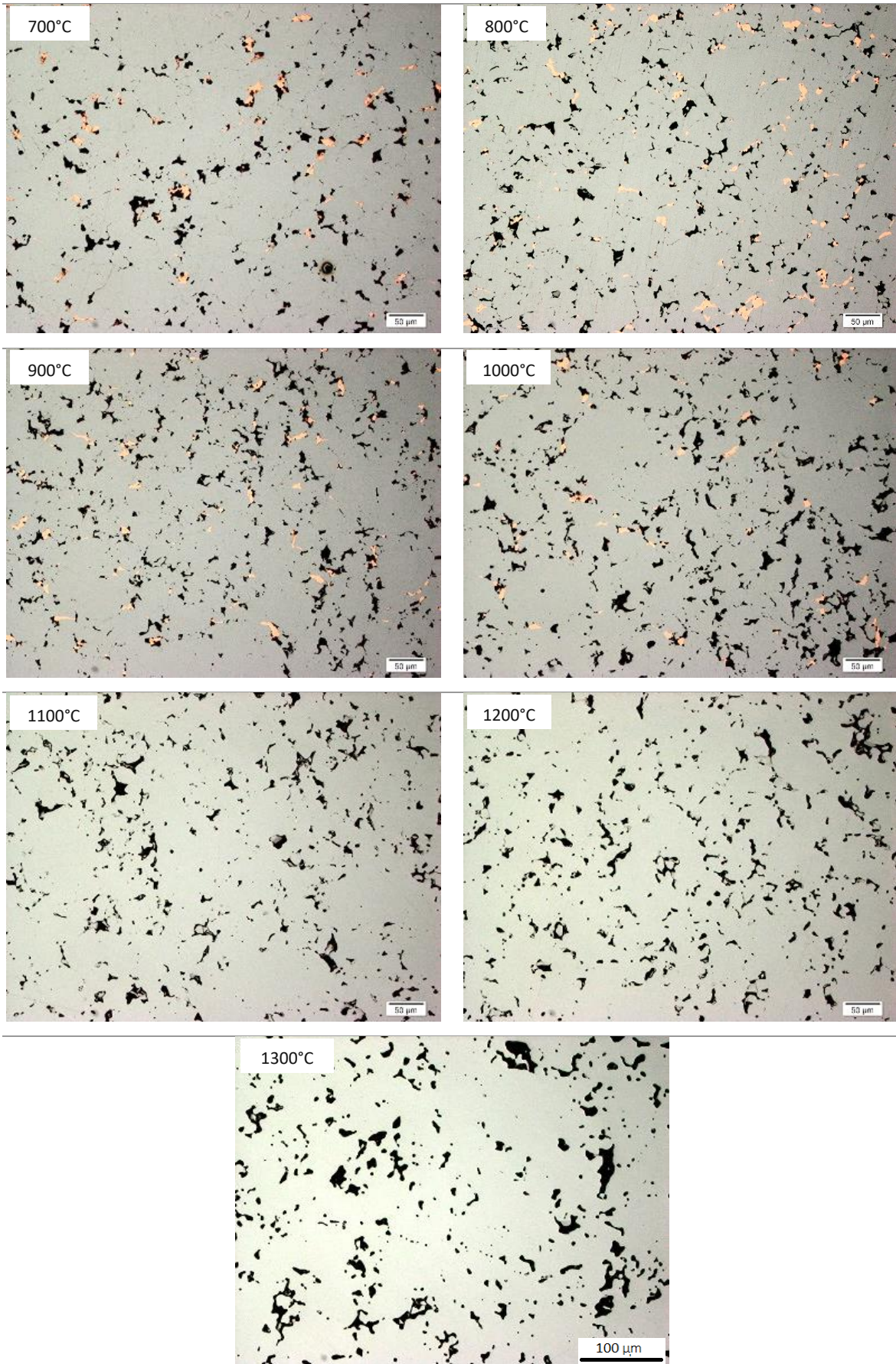


Figure 3.94: Un-etched OM micrographs of copper alloyed steel (Fe-2Cu-0.8C_{admixed}) compacted at 600 MPa, sintered 60 min in argon, 200 x. (scale bar 100μm holds for all images)

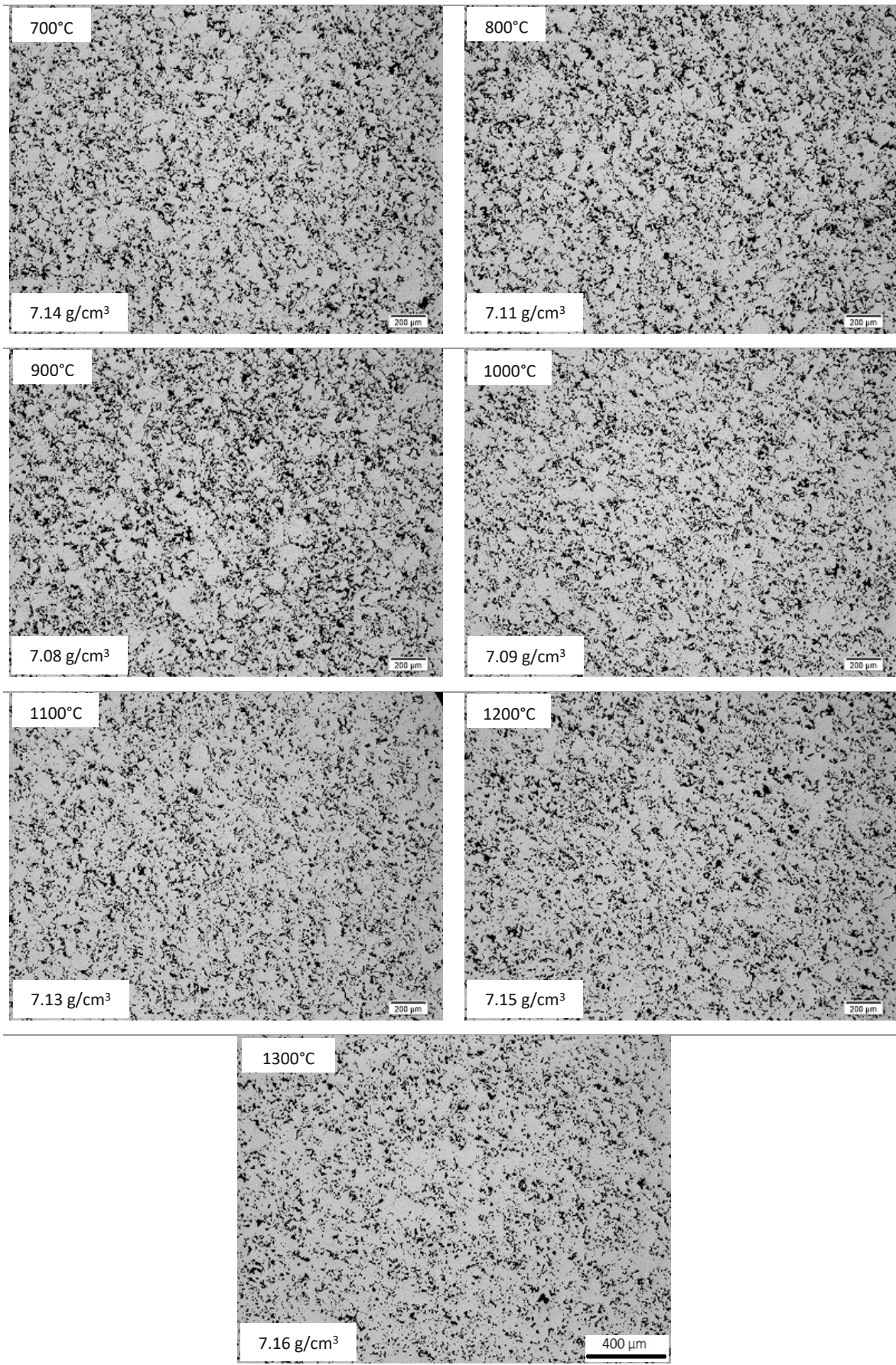


Figure 3.95: Un-etched OM micrographs of masteralloy steel (Fe-4MA-0.8C_{admixed+MA}), compacted at 600 MPa, sintered 60 min in argon, 50 x. (scale bar 400μm holds for all images)

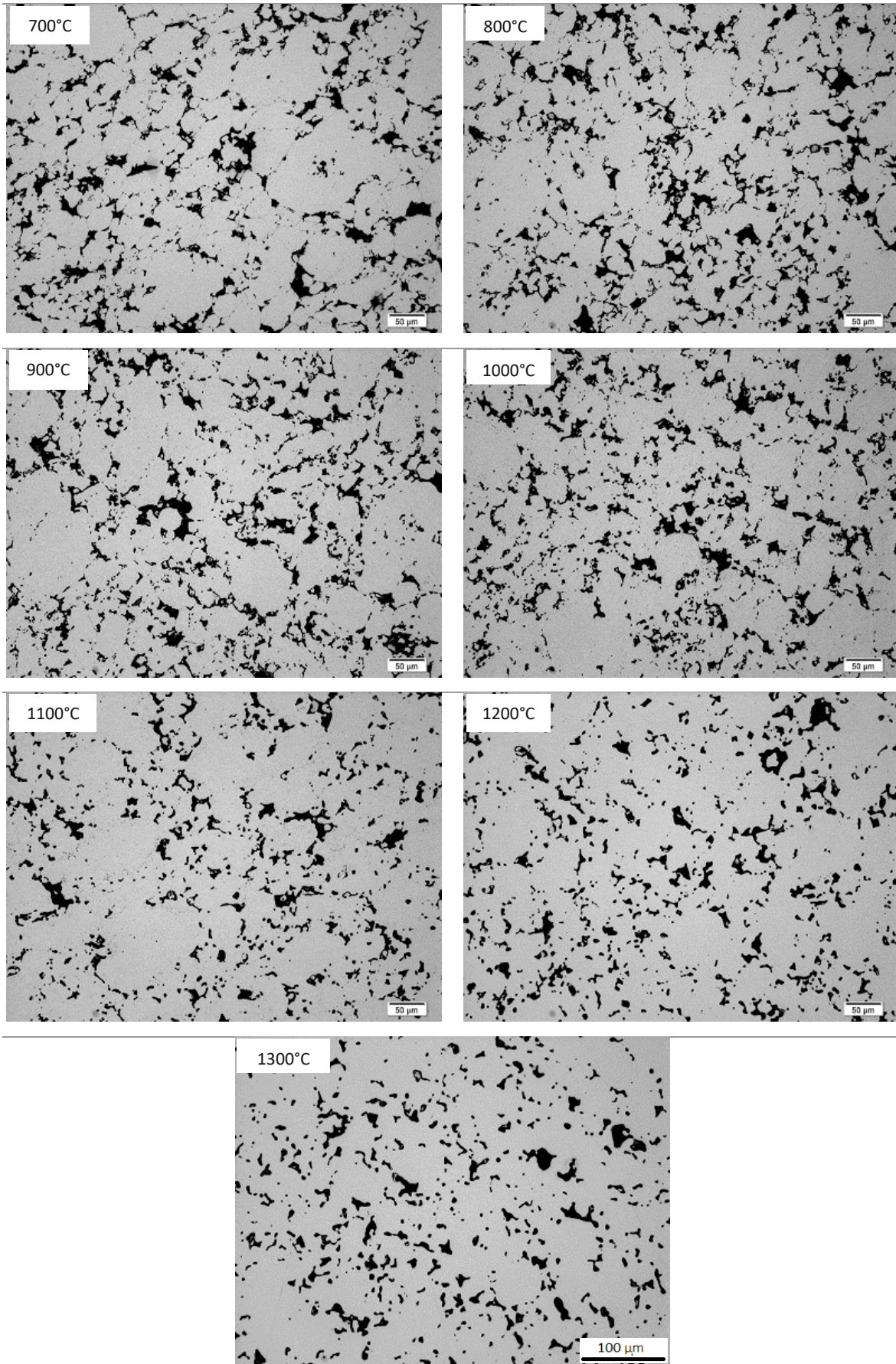


Figure 3.96: Un-etched OM micrographs of masteralloy steel (Fe-4MA-0.8C_{admixed+MA}), compacted at 600 MPa, sintered 60 min in argon, 200 x. (scale bar 100μm holds for all images)

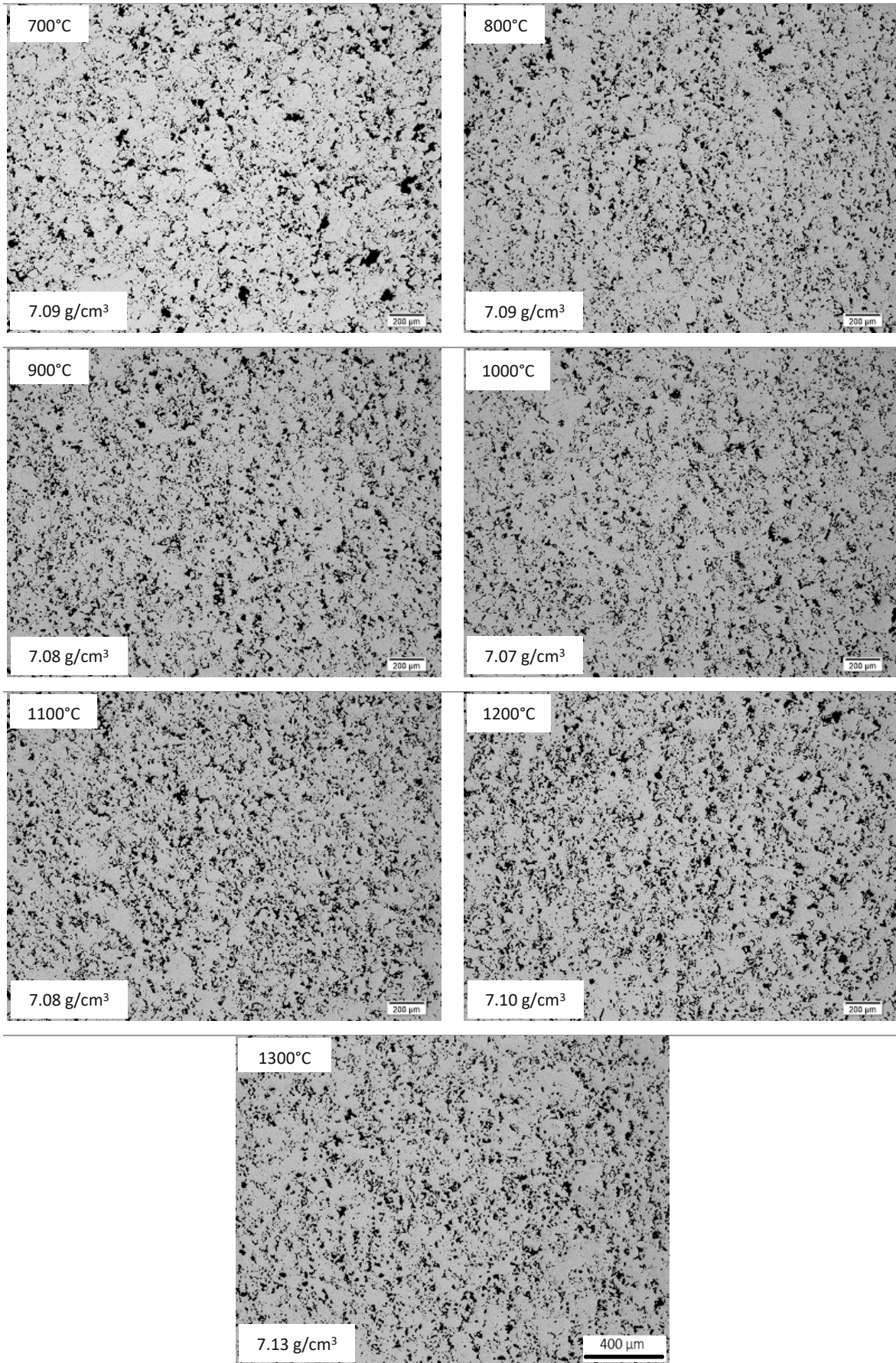


Figure 3.97: Un-etched OM micrographs of Mo pre-alloyed steel (Fe-1.5Mo-0.8Cadmixed), compacted at 600 MPa, sintered 60 min in argon, 50 x. (scale bar 400μm holds for all images)

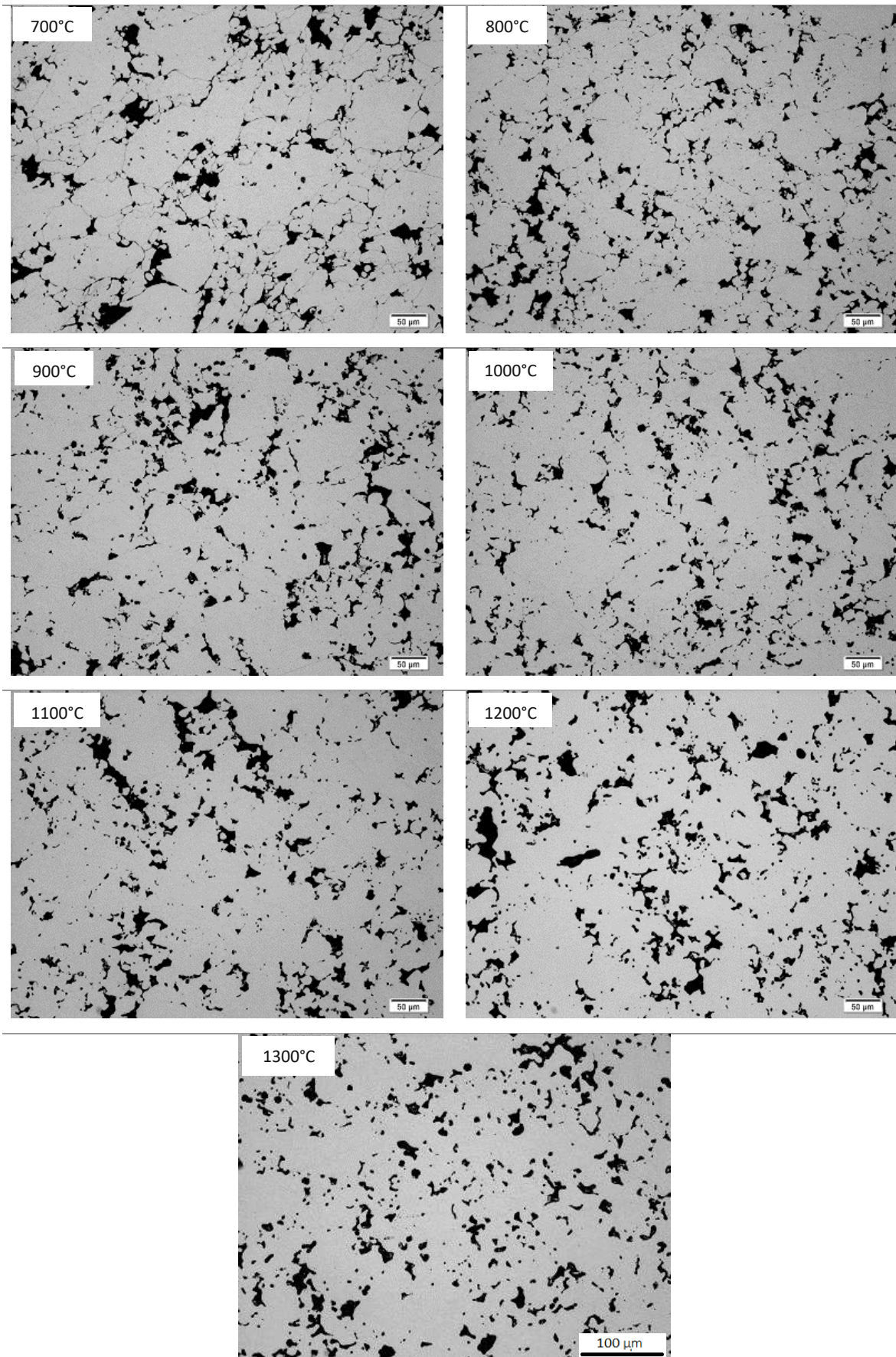


Figure 3.98: Un-etched OM micrographs of Mo pre-alloyed steel (Fe-1.5Mo-0.8C_{admixed}), compacted at 600 MPa, sintered 60 min in argon, 200 x. (scale bar 100μm holds for all images)

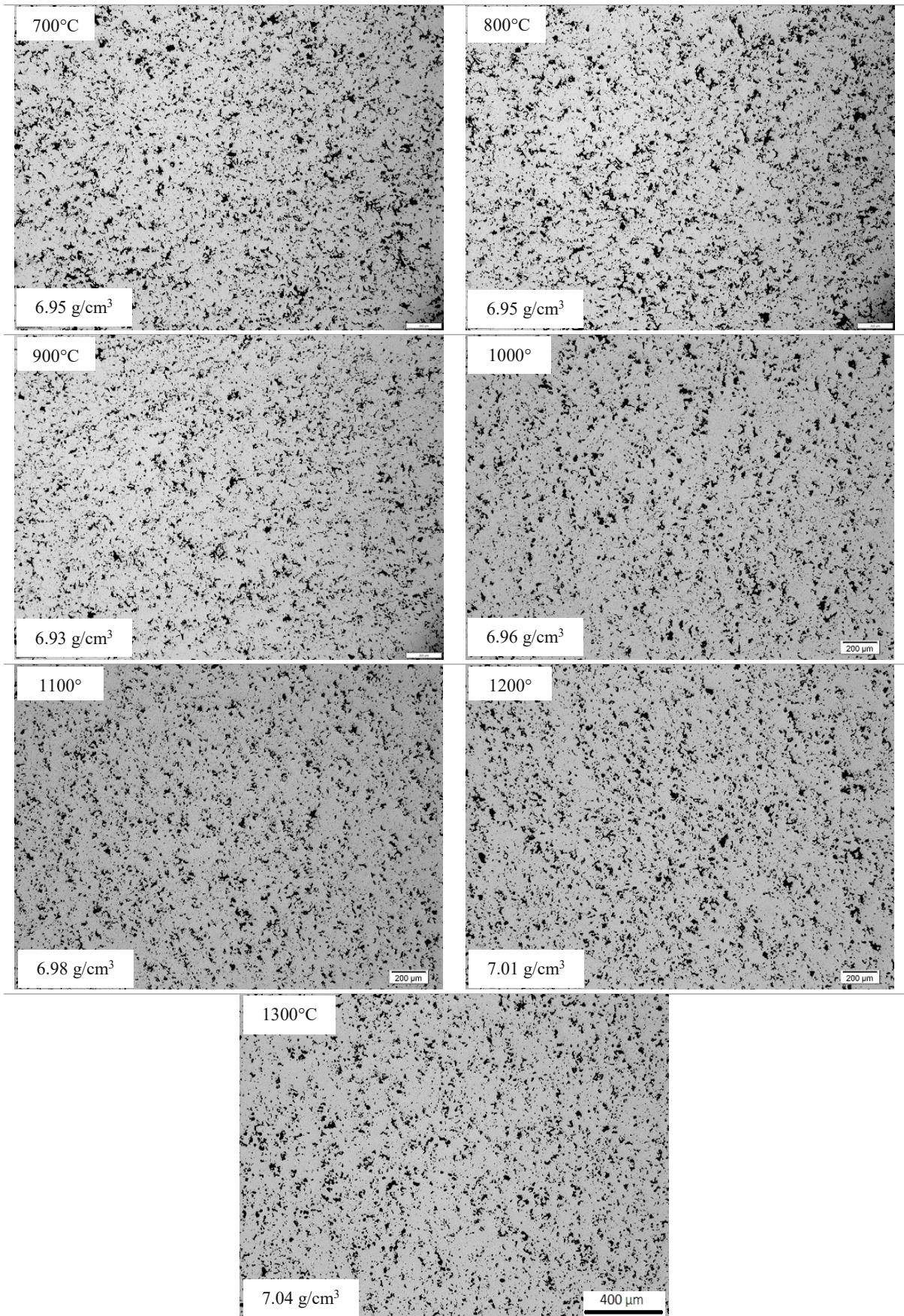


Figure 3.99: Un-etched OM micrographs of Cr-Mo pre-alloyed steel (Fe-3Cr-0.5Mo-0.8C_{admixed}), compacted at 600 MPa, sintered 60 min in argon, 50 x. (scale bar 400μm holds for all images)

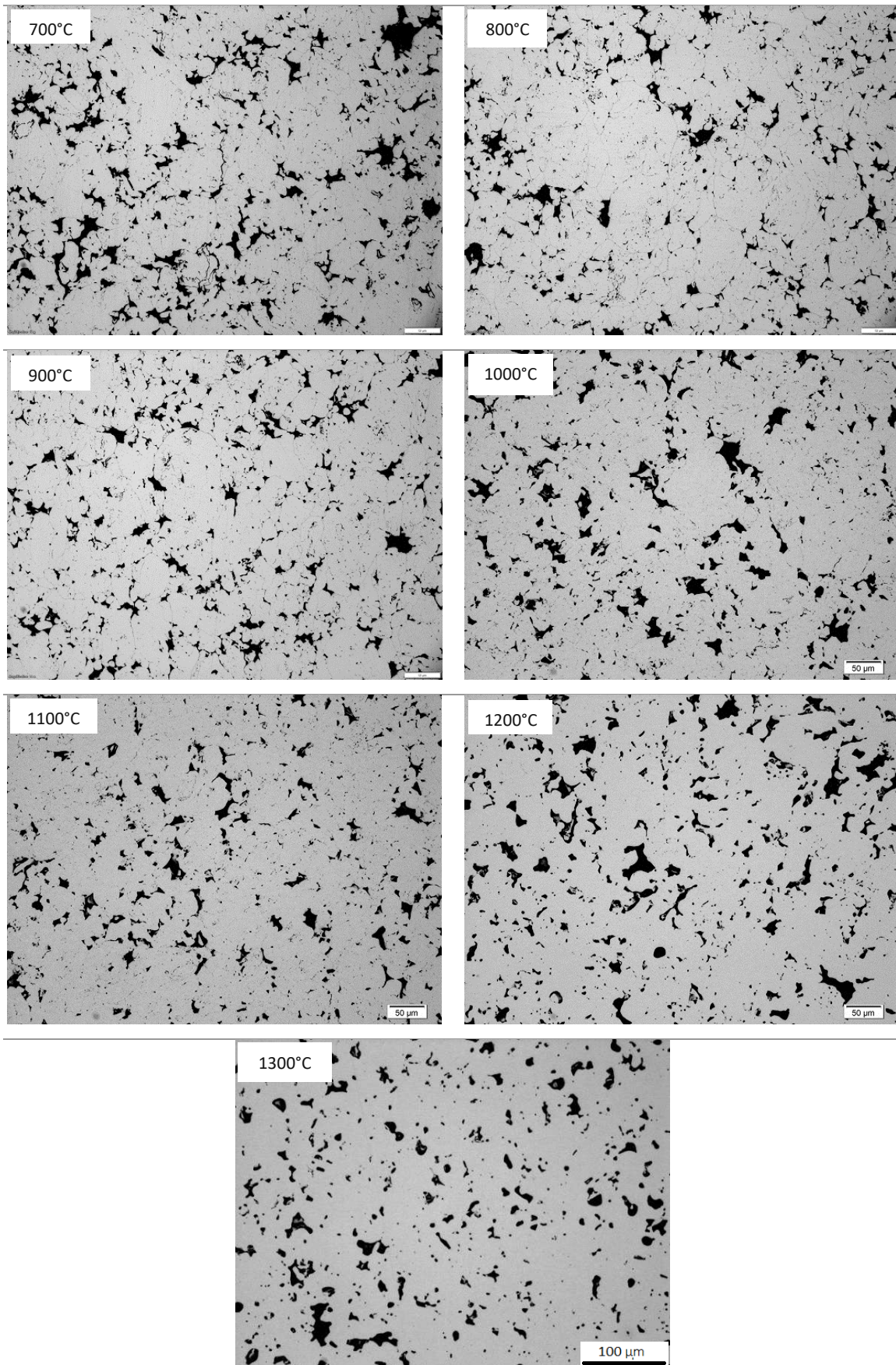


Figure 3.100: Un-etched OM micrographs of Cr-Mo pre-alloyed steel (Fe-3Cr-0.5Mo-0.8C_{admixed}), compacted at 600 MPa, sintered 60 min in argon, 200 x. (scale bar 100 μm holds for all images)

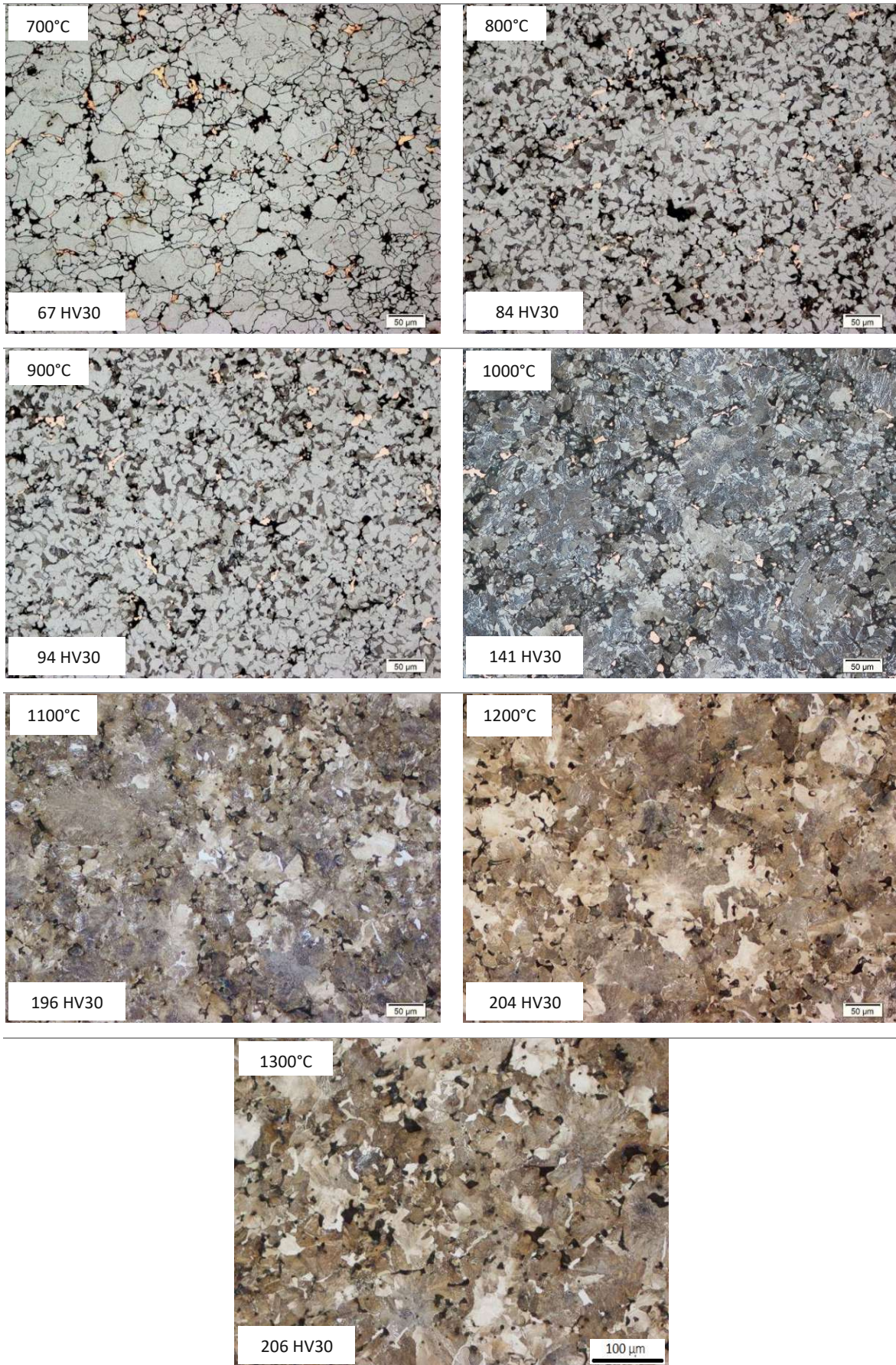


Figure 3.101: Etched OM micrographs of copper alloyed steel (Fe-2Cu-0.8C_{admixed}) compacted at 600 MPa, sintered 60 min in argon, Nital, 200 x. (scale bar 100µm holds for all images)

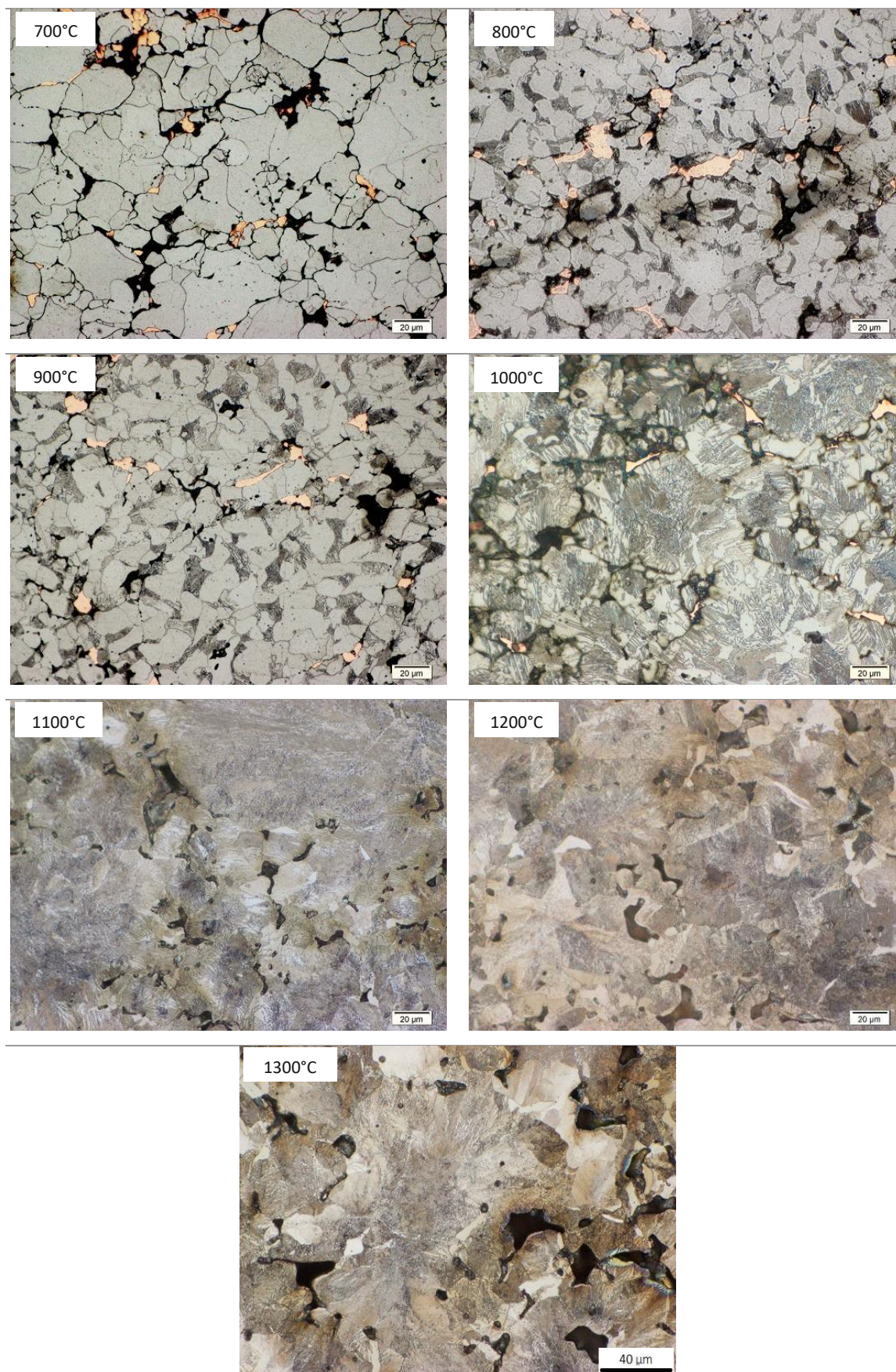


Figure 3.102: Etched OM micrographs of copper alloyed carbon steel ($\text{Fe-2Cu-0.8C}_{\text{admixed}}$) compacted at 600 MPa, sintered 60 min in argon, Nital, 500 x. (scale bar 40 μm holds for all images)

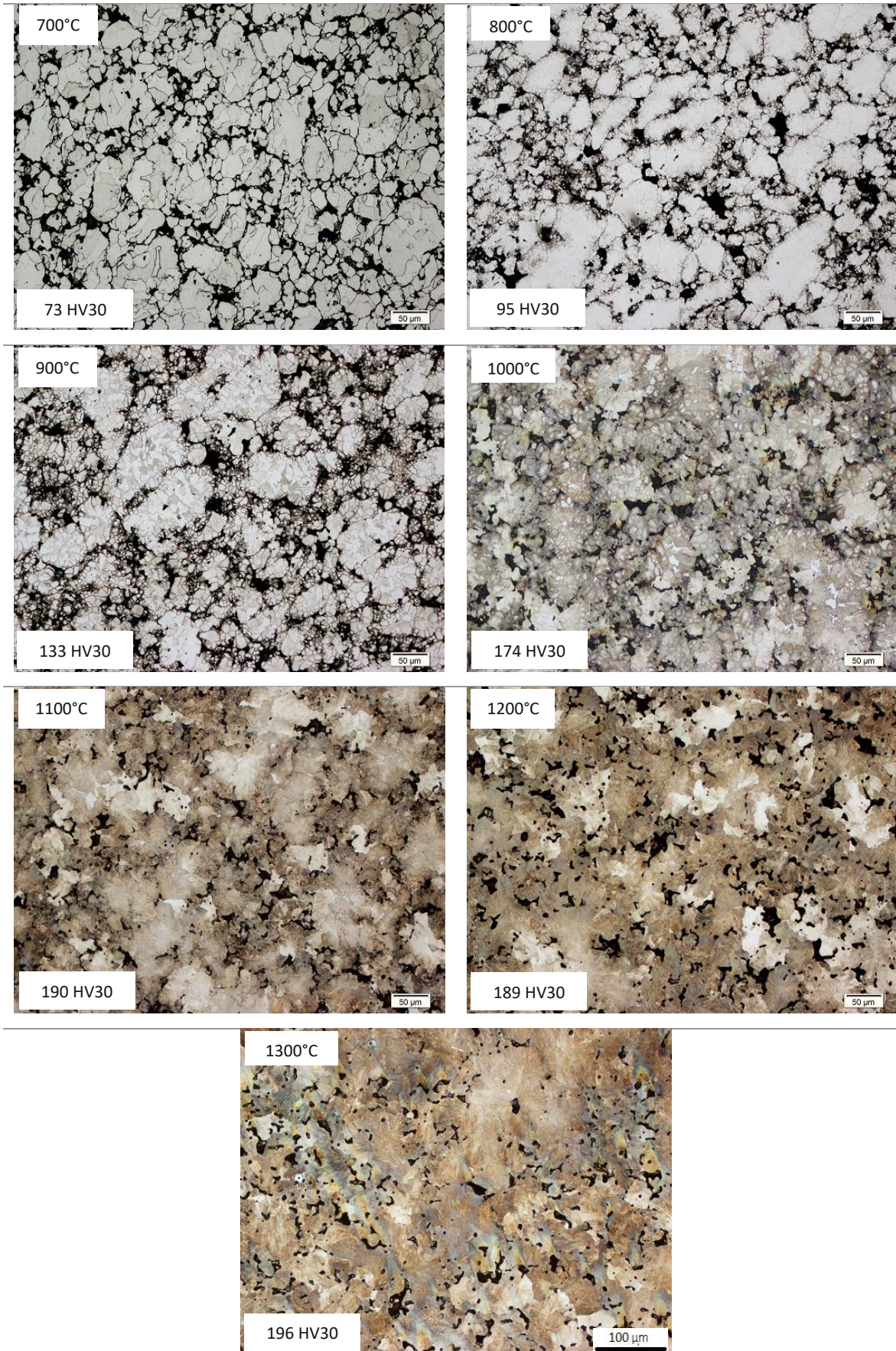


Figure 3.103: Etched OM micrographs of masteralloy steel ($\text{Fe-4MA-0.8C}_{\text{admixed+MA}}$) compacted at 600 MPa, sintered 60 min in argon, Nital, 200 x. (scale bar 100 μm holds for all images)

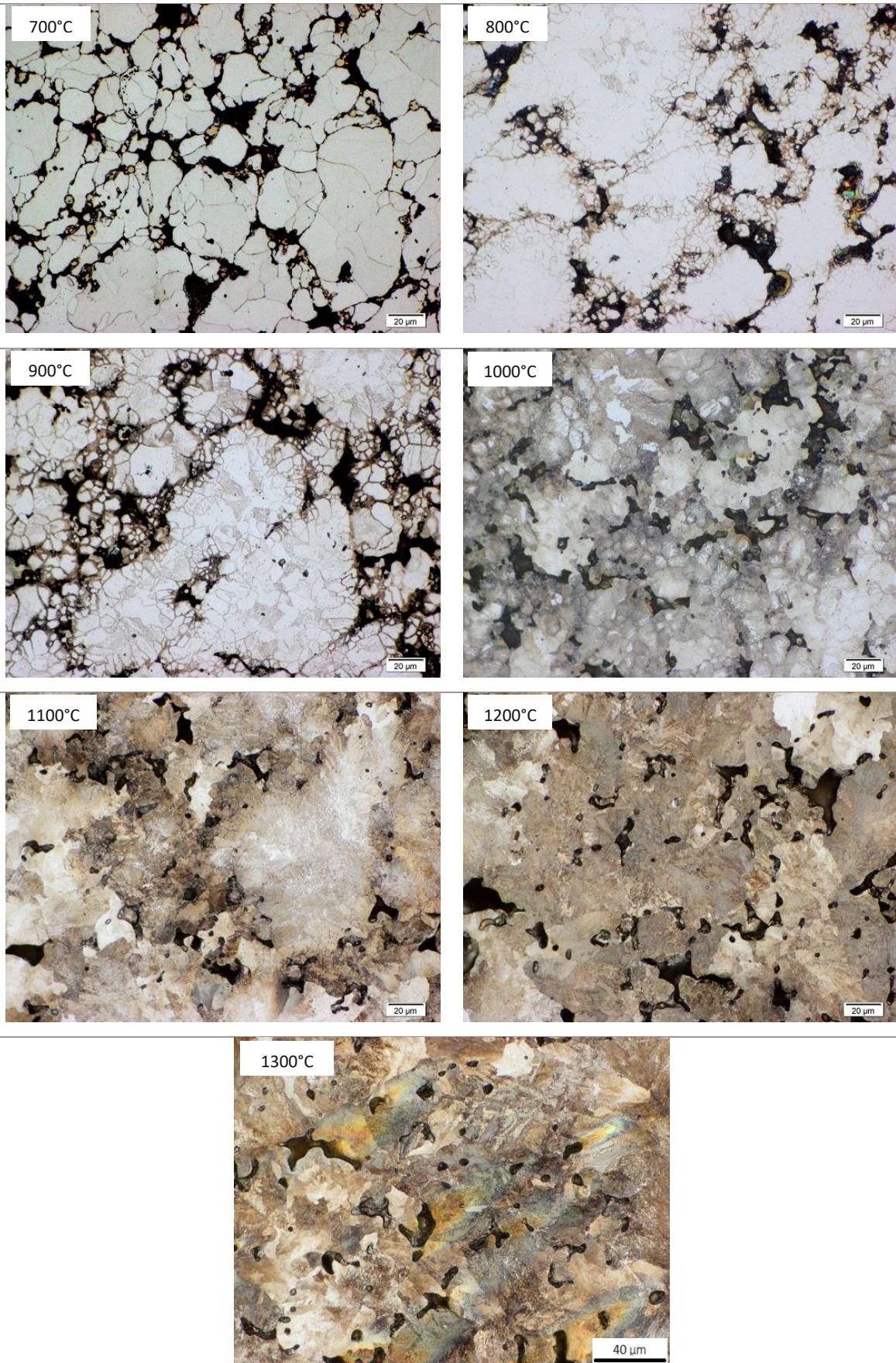


Figure 3.104: Etched OM micrographs of masteralloy steel (Fe-4MA-0.8C_{admixed}+MA) compacted at 600 MPa, sintered 60 min in argon, Nital, 500 x. (scale bar 40µm holds for all images)

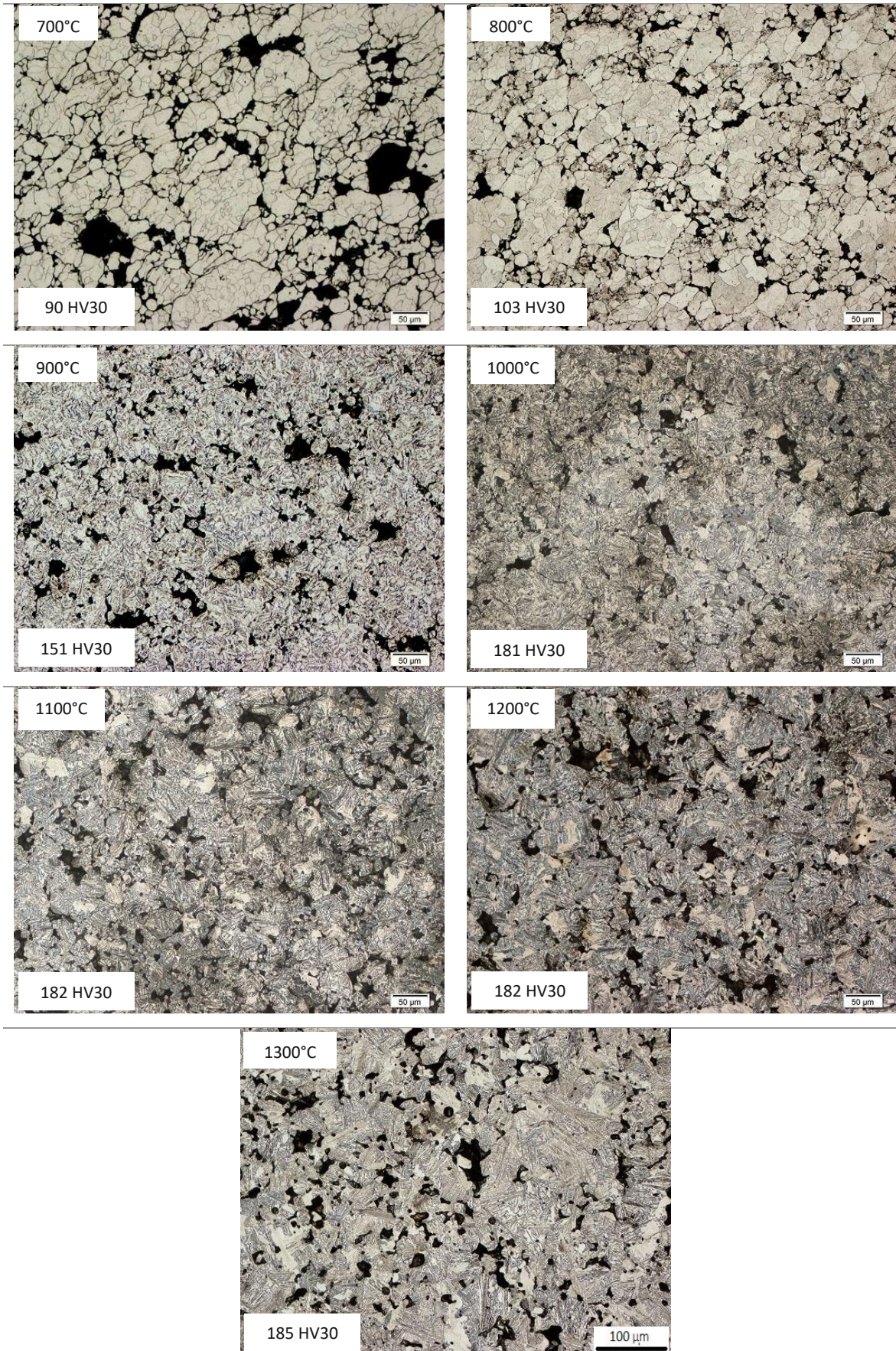


Figure 3.105: Etched OM micrographs of Mo prealloyed steel (Fe-1.5Mo-0.8C_{admixed}) compacted at 600 MPa, sintered 60 min in argon, Nital, 200 x. (scale bar 100μm holds for all images)

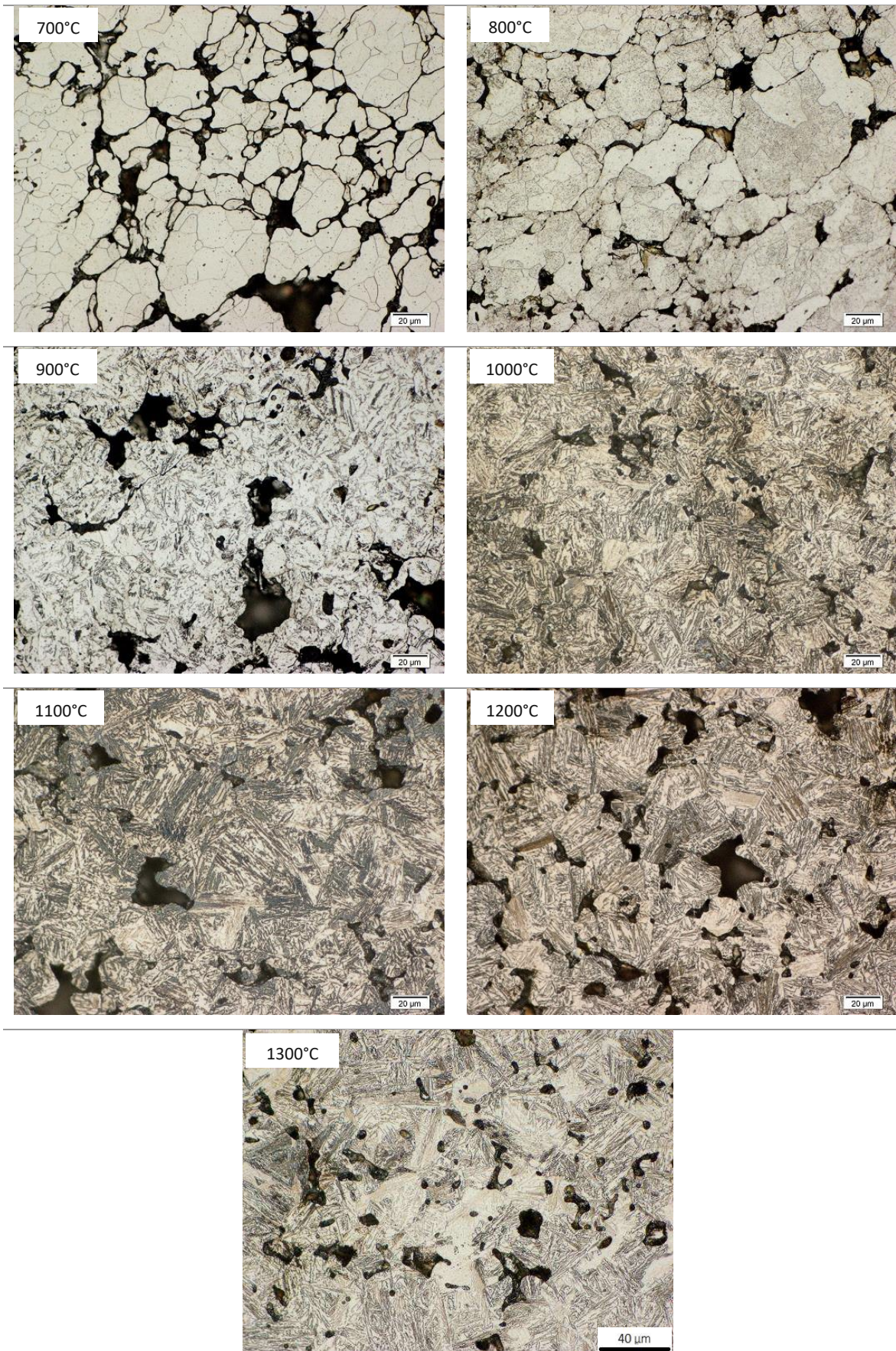


Figure 3.106: Etched OM micrographs of Mo prealloyed steel (Fe-1.5Mo-0.8C_{admixed}) compacted at 600 MPa, sintered 60 min in argon, Nital, 500 x. (scale bar 40μm holds for all images)

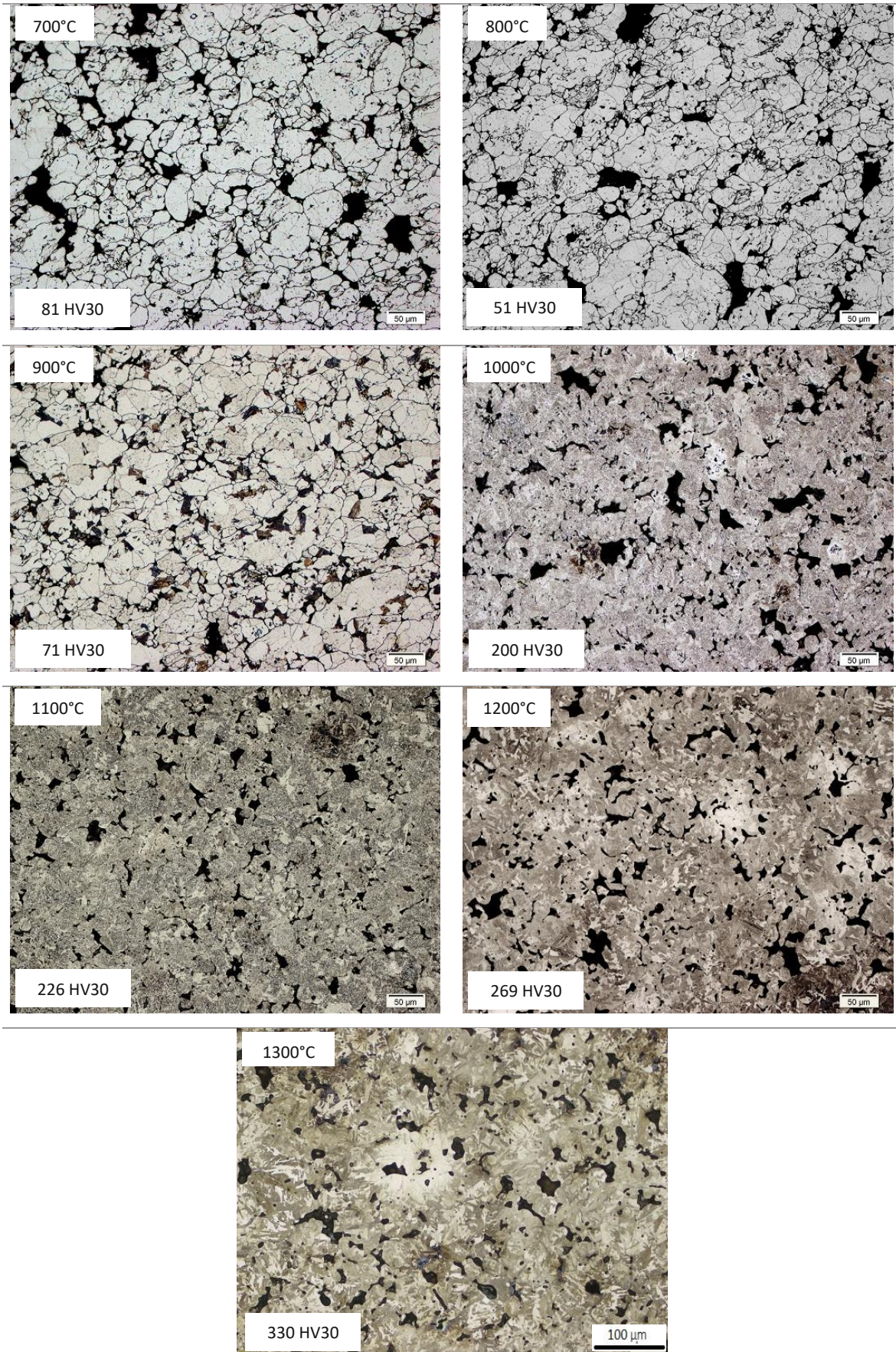


Figure 3.107: Etched OM micrographs of Cr-Mo prealloyed steel (Fe-3Cr-0.5Mo-0.8C_{admixed}) compacted at 600 MPa, sintered 60 min in argon, Nital, 200 x. (scale bar 100μm holds for all images)

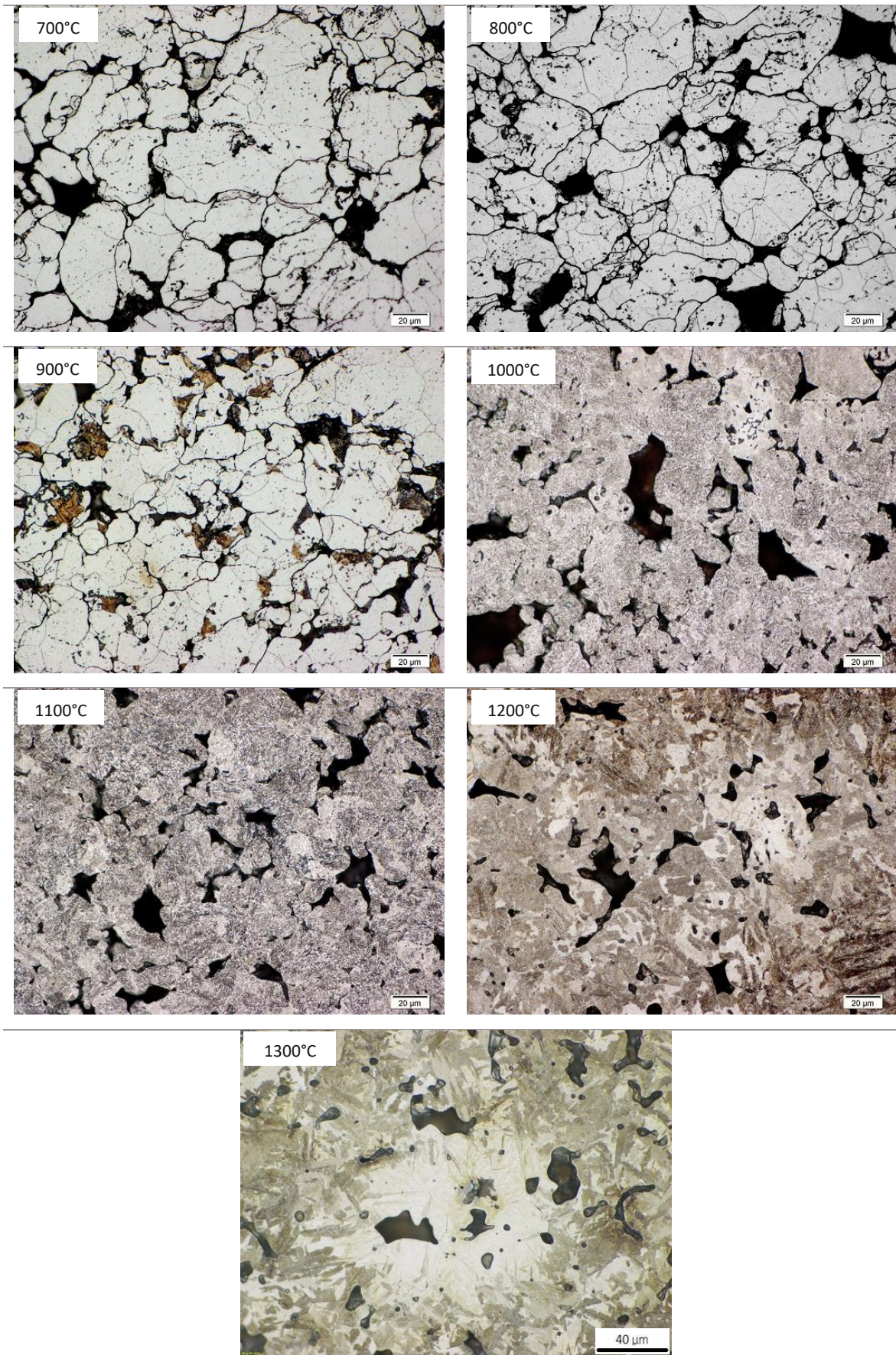


Figure 3.108: Etched OM micrographs of Cr-Mo prealloyed steel (Fe-3Cr-0.5Mo-0.8C_{admixed}) compacted at 600 MPa, sintered 60 min in argon, Nital, 500 x. (scale bar 40μm holds for all images)

3.4.5. Fractography

Fracture surfaces of the steels, broken at room temperature by Charpy impact test, are presented in Figures 3.109 to 3.112 (For Fe-C see Chapter 3.2.5, in argon). The effect of the sintering temperature on the fracture surface of the Fe-2Cu-0.8C is shown in Figure 3.109; here also the impact energy values and the oxygen contents are given. In the fracture surface of the steel sintered at 700°C, the short lines and points on the surfaces of the original powder particles show the first sign of bond formation which occurs as soon as the surface oxides are removed in the range of 700 to 800°C. However, at this temperature range, due to low sintering temperature as well as incomplete reduction of surface oxides, these contacts seem negligible. At 900°C, an interparticle ductile mechanism is evident, rather similar to that in the Fe-C system. It indicates that solid state sintering at this temperature and the resulting fracture surface are not influenced significantly by presence of Cu. However, it is not surprising since, as already shown, almost the same deoxidation processes occur for Fe-C and Fe-Cu-C. At 1100°C, transient liquid phase sintering is a consequence of the melting of copper [47]. The fracture surface for this temperature shows transgranular cleavage facets which are the results of stronger sintering contacts between the particles. Generally, in liquid phase sintering, high diffusion rates are associated with liquids, resulting in fast sintering due to higher mobility of the atoms, which usually leads to form stronger contacts [4]. In this case, however, the fracture surfaces as well as the shape of the pores do not show any significant difference to Fe-C, and the impact energy of Fe-C and Fe-Cu-C is almost identical (see also Fig 3.47, at 1100°C in Ar). One possible reason for this could be related to the copper swelling phenomenon, a process by which molten copper penetrates the boundaries between the individual iron particles and pushes them away, which leads to lower density. As a result, despite formation of liquid phase and thus accelerated sintering process, the sintering contacts are not as large as expected. At 1200 and 1300°C, in addition to the dimple ductile pattern, more transgranular cleavage facets with a river pattern are also visible which resulted in higher values of the impact energy.

As mentioned before, in the sintering of metallic components not only sufficient temperature but also removal of surface oxides are essential conditions for atomic diffusion and formation of sintering bridges. This issue would be even more important when we use alloying systems that contain elements with higher oxygen affinity (such as Cr, Mn and Si), which form more stable oxides that can affect the sintering process.

Figure 3.110 and 3.111 shows the fracture surfaces of two steels containing elements with higher oxygen affinity, Fe-4MA-0.8C (mixed) and Fe-3Cr-0.5Mo-0.8C (prealloyed), both after sintering in the temperature range of 700 to 1300°C. At 900°C, in Fe-4MA-0.8C the formation of sintering contacts is quite noticeable, while the fractograph of Astaloy CrM shows hardly any sign of sintering between the particles. This could be a good explanation for the low impact energy of Astaloy CrM ($0.5 \text{ J}\cdot\text{cm}^{-2}$) at this temperature, while the masteralloy steel, despite having almost the same amount of oxygen, shows better sintering behaviour with the impact energy of $8.6 \text{ J}\cdot\text{cm}^{-2}$, which is fairly close to that of Fe-0.8%C. This indicates that presence (or formation) of the oxide layers on the chromium prealloyed particles prevented contact formation, while in the masteralloy system, despite having rather high oxygen content, transferring (removing) oxygen from the ASC100.29 particles to the masteralloy particles (“internal getter” effect, see [177]) provided a favourable condition for formation of sintering

contacts between the iron particles. This underlines that not only the total oxygen content but also the distribution plays a major role for the mechanical properties. At 1100°C, more developed bonds are visible for both steels. At this temperature the MA steel shows rather higher sintering activity, with transgranular dimple fracture and stronger sintering contacts, while in the case of Astaloy CrM sintering has proceeded less, and the particles retained more or less their original shapes with a fracture mechanism of mostly dimple pattern of the interparticle necks. The presented values for the oxygen content at 1100°C indicate that oxygen removal is more pronounced in the MA steel, which could be a reason for its higher sintering activity and higher impact energy, together with the concentration of oxygen on the MA particles. At 1300°C, growth of the sintering contacts and lowering of the oxygen content resulted in the maximum impact toughness for both steels. However, this progress in the properties at 1300°C was more pronounced for Astaloy CrM than for the masteralloy steel. In other words, sintering at higher temperature is more effective for achieving the full capability of the prealloyed Cr-Mo steel, which confirms the findings of Kremel et al. [1].

Figure 3.112 shows the fractography of Fe-1.5Mo-0.8C. Similar to carbon steel, no sintering bridges are visible at 700°C. According to the fractographs, formation of the initial sintering contacts has started from 800°C, however compared to the Fe-C system, weaker sintering bonds are visible in Mo alloyed steel at this sintering temperature. Visual evaluating of the images shows that sintering at higher temperatures leads to enlargement of the sintering contacts, which resulted in a higher fraction of cleavage facets for the steel.

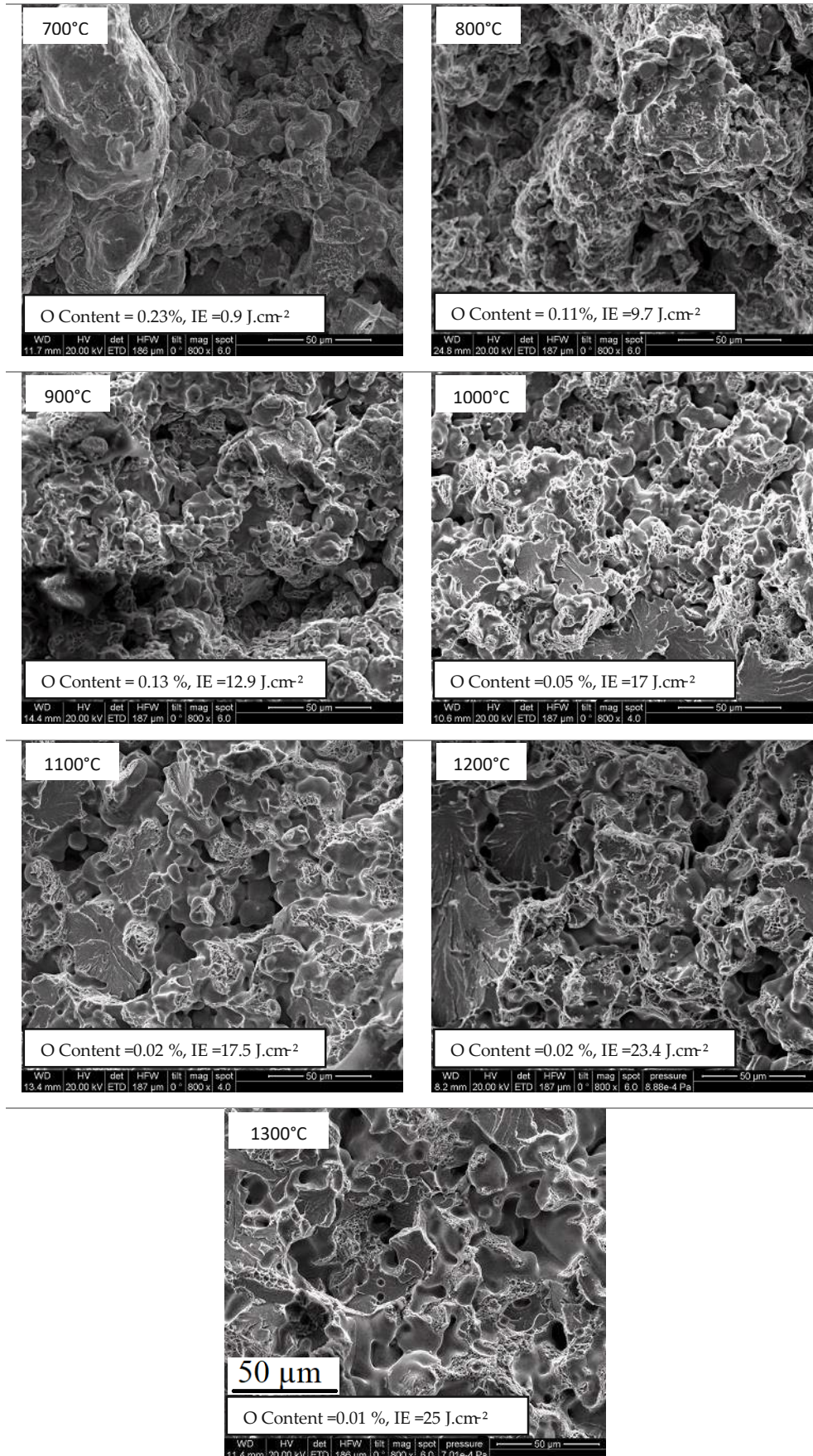


Figure 3.109: Fractographs of copper alloyed steel (Fe-2Cu-0.8C) compacted at 600 MPa, sintered 60 min in argon, broken at RT by Charpy impact test, 800 x. (scale bar 50μm holds for all images)

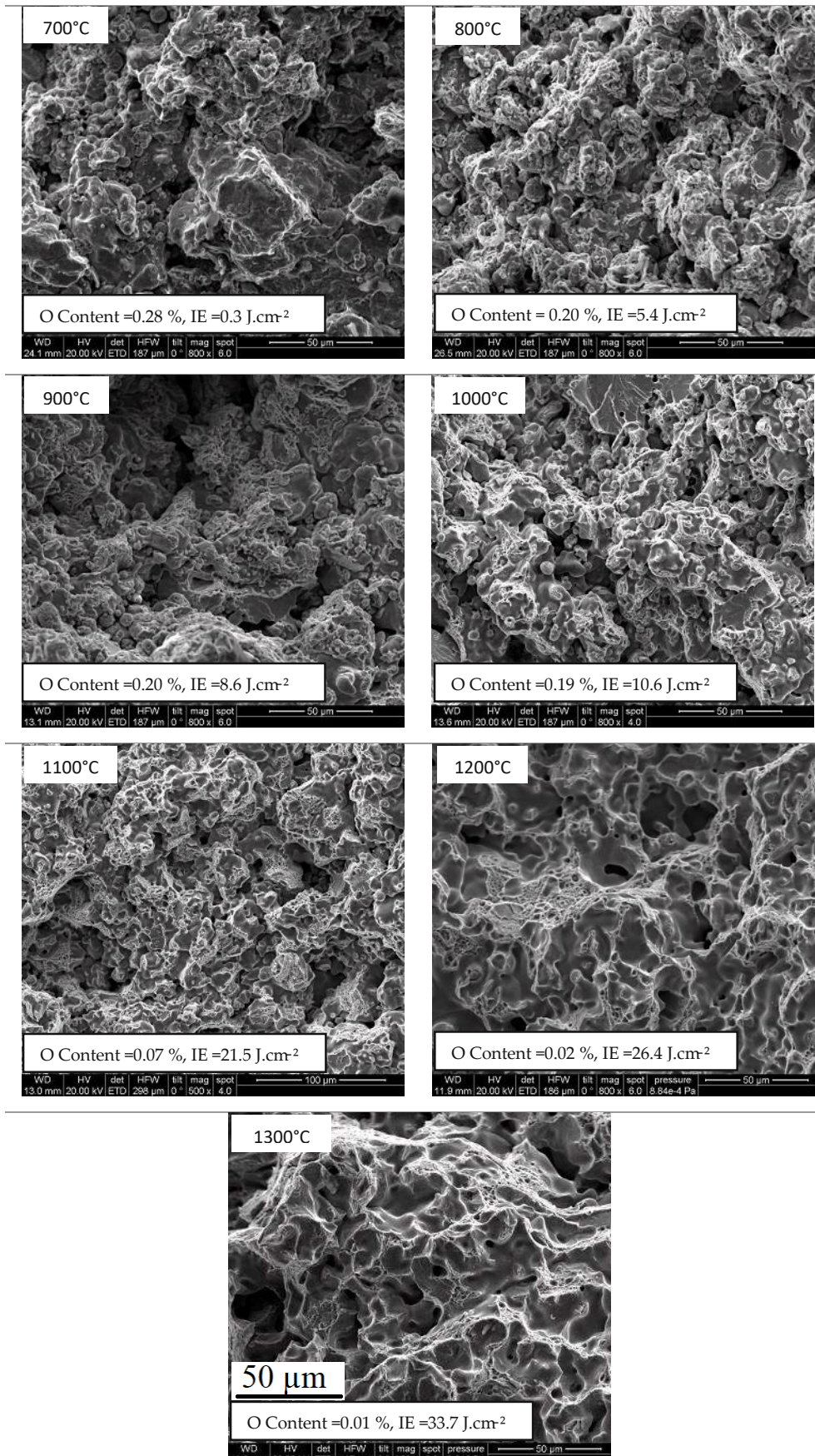


Figure 3.110: Fractographs of masteralloy steel (Fe-4MA-0.8C), compacted at 600 MPa, sintered 60 min in argon, broken at RT by Charpy impact test, 800 x. (scale bar 50µm holds for all images)

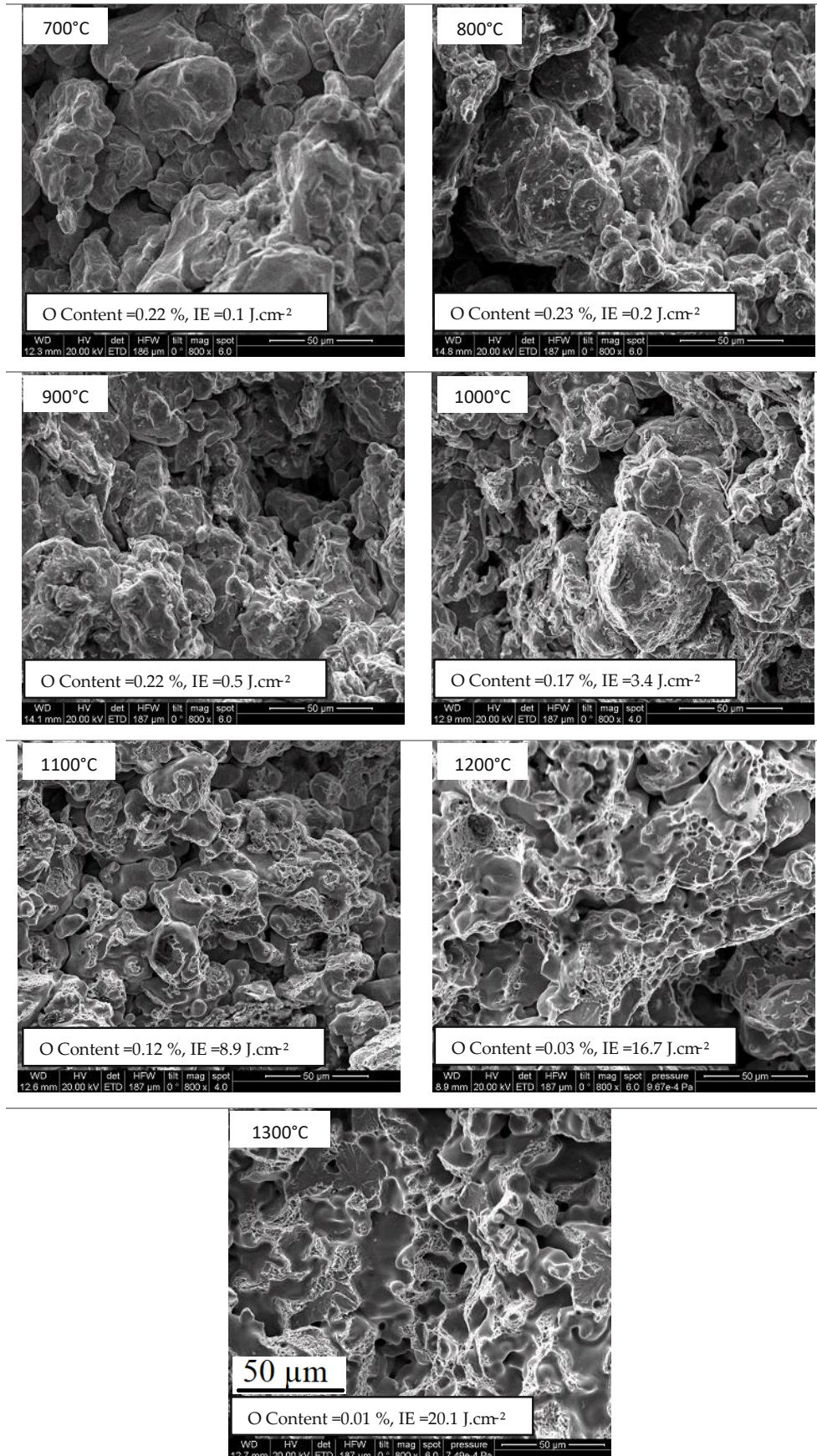


Figure 3.111: Fractographs of Cr-Mo alloyed steel (Fe-3Cr-0.5Mo-0.8C) compacted at 600 MPa, sintered 60 min in argon, broken at RT by Charpy impact test, 800 x. (scale bar 50µm holds for all images)

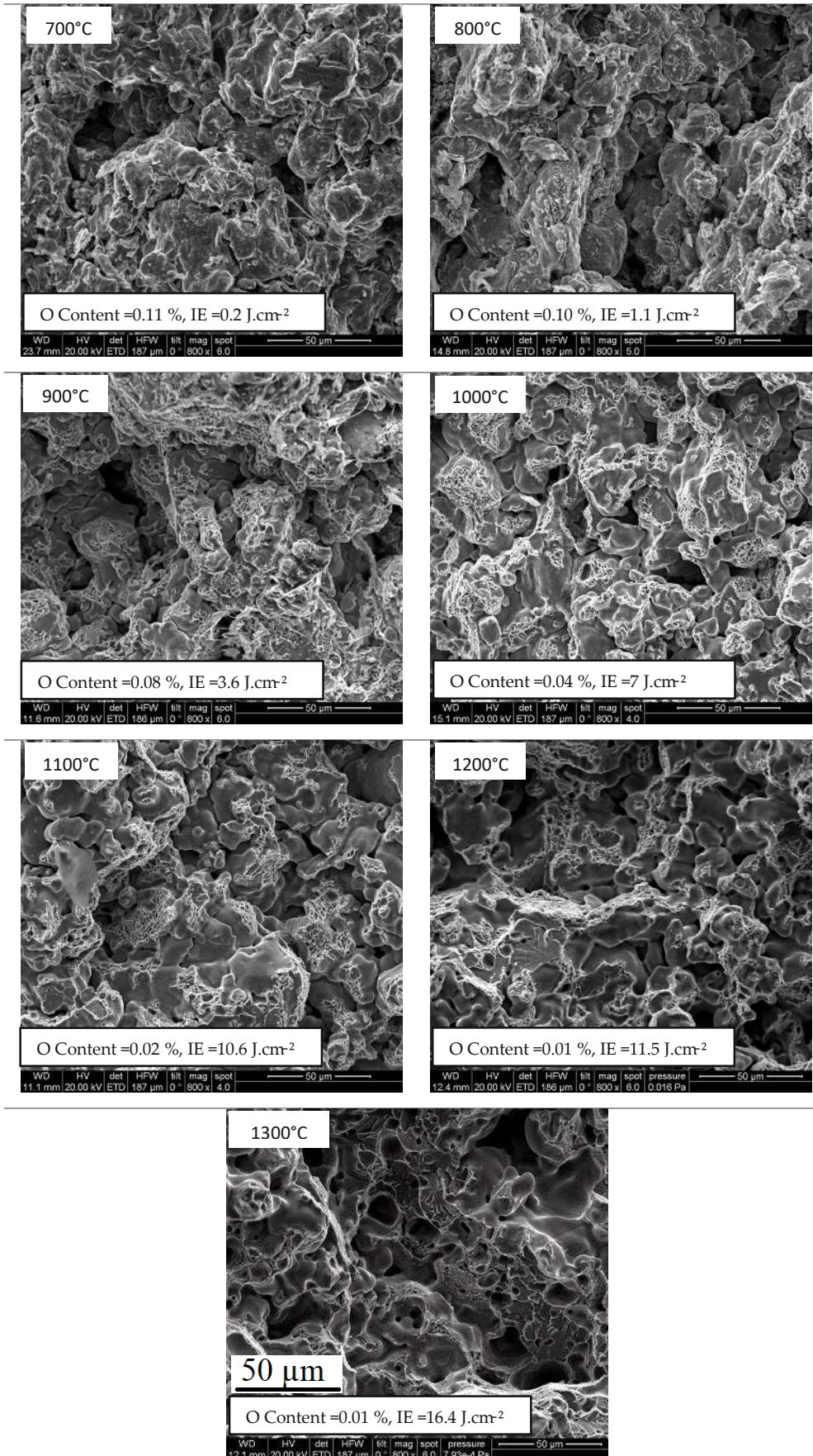


Figure 3.112: Fractographs of Mo alloyed steel (Fe-1.5Mo-0.8C) compacted at 600 MPa, sintered 60 min in argon, broken at RT by Charpy impact test, 800 x. (scale bar 50μm holds for all images)

3.4.6. Dimensional change and sintered density

The dimensional change and sintered density of the steels are presented in Figure 3.113 and 3.114 as a function of the sintering temperature. Fe-0.8C shows a gradual expansion from 700 to 1000°C, caused by carbon dissolution, and after this process is complete, shrinkage follows during sintering at the higher temperatures up to 1300°C. The graph also shows that the dimensional behaviour of the Mo alloyed steel is similar to the Fe-C system at all sintering temperature ranges while in Fe-2Cu-0.8C from 700 to 1000°C the behaviour is more or less similar to Fe-C, with an upward trend resulting from dissolution of carbon and probably of a small amount of Cu in the solid state, but at 1100°C the Cu containing steel revealed a different behaviour to Fe-C, it showed a significant expansion, which resulted in lower sintered density. This also might be a reason why the impact energy at 1100°C was not higher compared to 1000°C, although also the higher hardness due to solid solution strengthening of the Fe matrix by Cu might play a role here, (see results of impact energy and hardness below). This major expansion in the Fe-Cu-C systems is linked to copper melt formation and is well known as “copper swelling” effect [38, 42, 68, 178]. The accepted mechanism of this phenomenon is progressive penetration of liquid copper into iron interparticle boundaries which solidifies there and causes swelling. Another point that should be mentioned in the Fe-Cu-C system is the role of carbon, which is controlling and limiting the copper swelling by increasing the dihedral angle between the Cu melt and the iron particles [41, 69, 143, 179]. Above 1100°C, after completion of carbon and copper dissolution, there follows the usual shrinkage of sintering.

In the steel alloyed with the masteralloy, from 700 to 1000°C a more pronounced expansion than with Fe-C and Fe-Cu-C is visible. As mentioned already and shown in [89, 92], alloying of PM steels with (admixed) Mn can occur through the gas phase even at low sintering temperature. Therefore, also in this case the higher expansion can be explained by the diffusion of manganese into the iron lattice in particular at the sintering contacts, causing “Mn swelling” in a similar way as the Cu swelling, however through the gas phase. At 1100°C, the masteralloy steel showed pronounced shrinkage and densification as well as improved impact energy (see Fig. 3.116), which is followed by less dimensional effects at 1200 and 1300°C. Elemental analysis also showed a significant oxygen removal from the system. All these results obtained at 1100°C revealed that 1100°C is apparently a critical sintering temperature for this steel. Above 1100 and up to 1300°C, sintering results in higher shrinkage and impact energy as well as in more complete oxygen removal.

In contrast to the mentioned steels, the prealloyed Astaloy CrM does not show any trend towards expansion. In the temperature range of 700 to 900°C, the dimension is almost constant due to the presence of the stable surface oxides which prevent both carbon dissolution and sintering. At 1000°C and 1100°C no expansion is visible despite carbon dissolution (metallography, Figure 3.108). It means that at these temperatures the expansion caused by carbon dissolution is compensated by sintering shrinkage. After sintering at 1200 and 1300°C, the Cr alloy steel shows pronounced shrinkage and densification which is highest compared to the other steel grades. The other properties such as O/C contents and impact energy (Figure 3.91 and 3.116) show a significant improvement at this temperature. This indicates that in order to exploit the full potential of this Cr alloy steel, sintering should be performed at least at 1200°C.

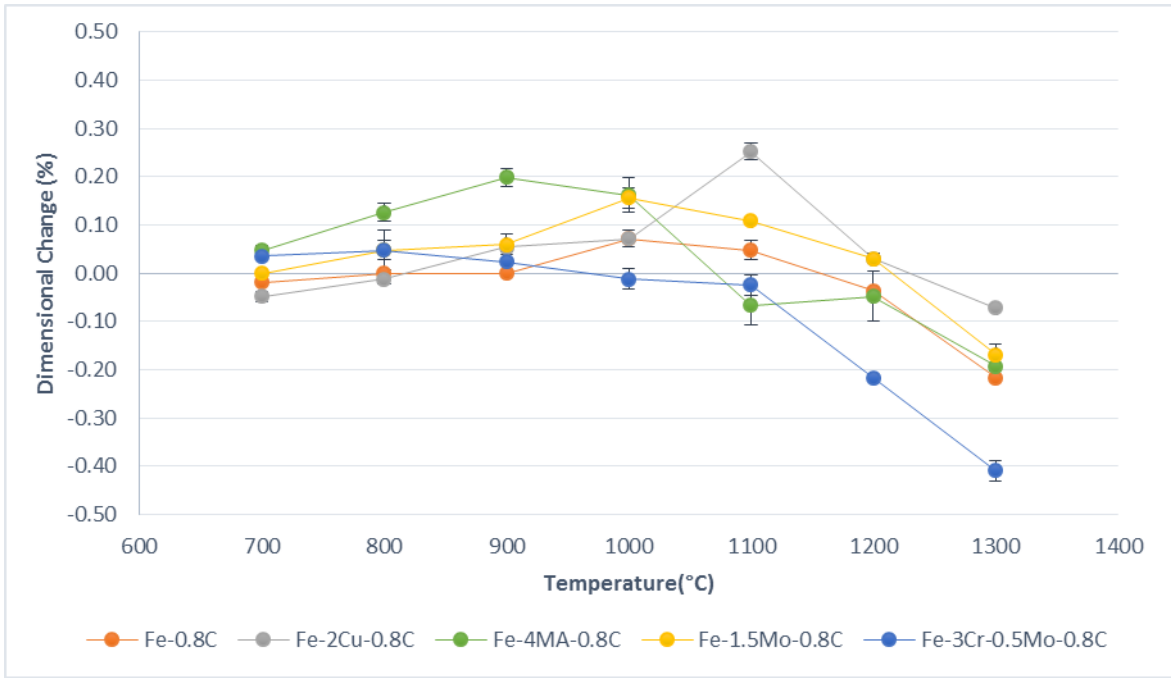


Figure 3.113: Dimensional change of the steels versus sintering temperature, compacted at 600 MPa, sintered 60 min in argon.

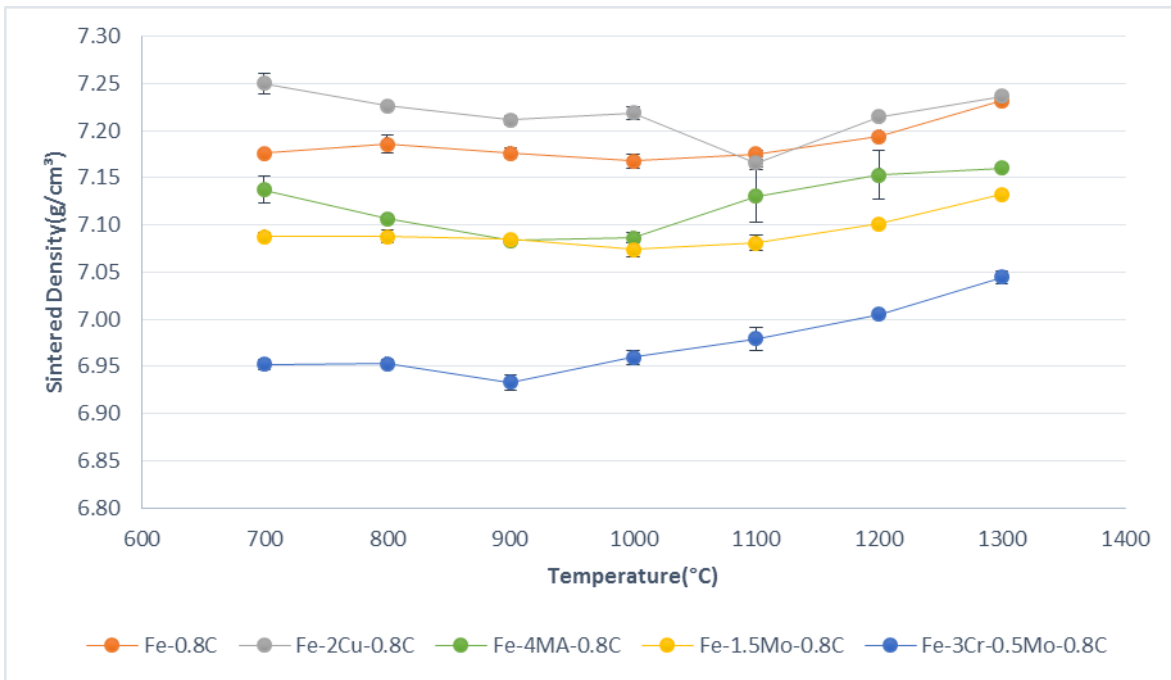


Figure 3.114: Sintered density of the steels versus sintering temperature, compacted at 600 MPa, sintered 60 min in argon.

3.4.7. Mechanical properties

3.4.7.1. Hardness

The hardness data are presented in Figure 3.115 as a function of the sintering temperature. In general, for four steels, Fe-0.8C, Fe-2Cu-0.8C, Fe-4MA-0.8C and Fe-1.5Mo-0.8C, the respective graphs show an upward trend in the hardness from 700 to 1100°C. The hardness at 1100°C reaches almost the maximum value, and further increase of the sintering temperature does not have any significant effect on the hardness. As mentioned previously for Fe-0.8C (see Chapter 3.1.5), the carbon dissolution and pearlite formation are the main reasons for the increase of the hardness between 700 and 1100°C.

In Fe-2Cu-0.8C, in addition to the carbon dissolution, the effect of Cu must be considered which can increase the hardness by solid solution strengthening as well as precipitation hardening. Below 1100°C Cu remains solid, and the diffusion into the iron lattice is not significant. The hardness increase is thus more or less similar to Fe-C, i.e. due to carbon dissolution, while after sintering at 1100°C, Cu melting accelerates the alloying process, resulting in a significant raise in the hardness as a consequence of solid solution hardening.

The masteralloy steel shows a more pronounced upward trend of the hardness in the range 700 to 1100°C compared to Fe-0.8C. Once more these results confirm the hypothesis of gas phase transport of manganese to Fe and subsequent diffusion into the iron lattice during the sintering process, which agrees well with the dimensional change. Constant hardness at the temperatures above 1100°C suggests that the diffusion of manganese and the alloying process at this temperature are virtually complete.

The hardness measurement of the Mo alloyed steel in the temperature range of 700 to 1300°C, showed almost identical values with the masteralloy steel. Presence of molybdenum in solid solution of Fe-Mo-C steel, which resulted in bainitic microstructure, is the main reason of higher hardness compared with the Fe-C steel.

In the Cr-Mo prealloyed steel, no significant change of the hardness is observed at temperatures below 1000°C, while for sintering above 1000°C, a significant increase of this property is observed which trend continues up to 1300°C. Similar to the other steels, the reason of increasing hardness for this material with higher sintering temperature is carbon dissolution and resulting formation of bainite and martensite [165]. However, it seems that in this material the process is delayed until the stable surface chromium oxides have been reduced and thus removed. In contrast to the other steels, which do not show significant hardness changes above 1100°C, Astaloy CrM show a continuous upward trend up to 1300°C. A possible reason for this could be the reduction of the surface chromium oxides which occurred at higher sintering temperature and to some degree also densification, as can be seen in Figure 3.114. This hardness increase is observed despite the considerably lower C content after sintering at high temperatures (Fig.3.92), caused by C consumption for carbothermal reduction processes, the high oxygen content of this prealloyed powders consuming more C than with Fe-C or Fe-Cu-C. The high hardness despite fairly low C content underlines the effect of the high alloy element content in this material, as indicated in Table 3.15.

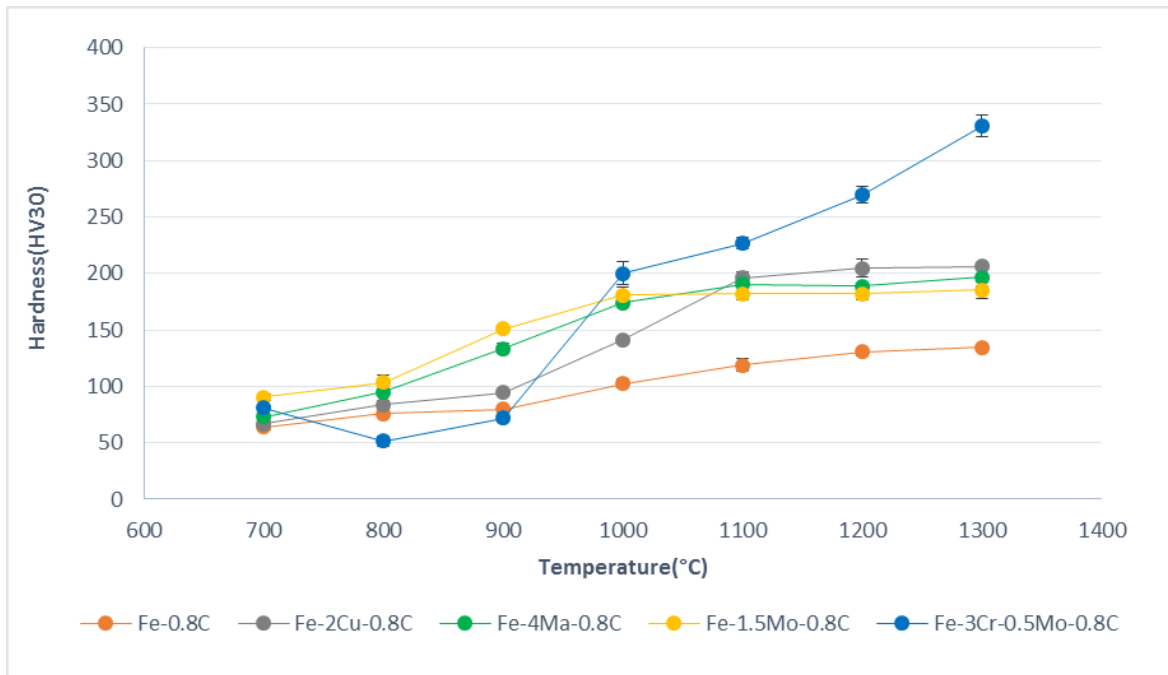


Figure 3.115: Hardness of the steels versus sintering temperature, compacted at 600 MPa, sintered 60 min in argon.

3.4.7.2. Charpy impact energy

The data for the impact energy required to break the Charpy specimens at room temperature are given in Figure 3.116. The figure shows a continuous upward trend from 700 to 1300°C for all steels. Generally, steels based on plain iron showed better impact energy than the prealloyed steels. In the temperature range of 700 to 1000°C Fe-Cu-C showed the highest values for this parameter, which could be attributed to the higher green density and resulting better physical contacts between the iron and copper powder particles. At 1100°C, the masteralloy steel showed a significant improvement in the impact energy which resulted in the highest values compared to the other grades up to 1300°C. Increasing density, oxygen removal and resulting accelerated sintering in this temperature range can be assumed to be the reasons of this effect. Another point that should not be neglected here is the carbon content, which is lower than for the two other steels, which can have a positive effect on the impact energy of the steel.

Among the two other grades (prealloyed grades), from 700 to 1100°C the Mo prealloyed steel showed better impact energy compared to the Cr-Mo steel. The reason is oxygen removal which occurred at lower temperature in Mo steel, while the presence of the stable oxide on the surface of Astaloy CrM particles in this temperature range prevents formation of the sintering bonds. Above 1100°C, after activation of the oxygen removal process in Cr-Mo steel, this steel showed better impact behaviour which is an indicator for a more active sintering process in this steel compared to the Mo steel. In this case, too, the role of the lower carbon content in Cr-Mo steel should be considered which can improve the impact behaviour of this steel.

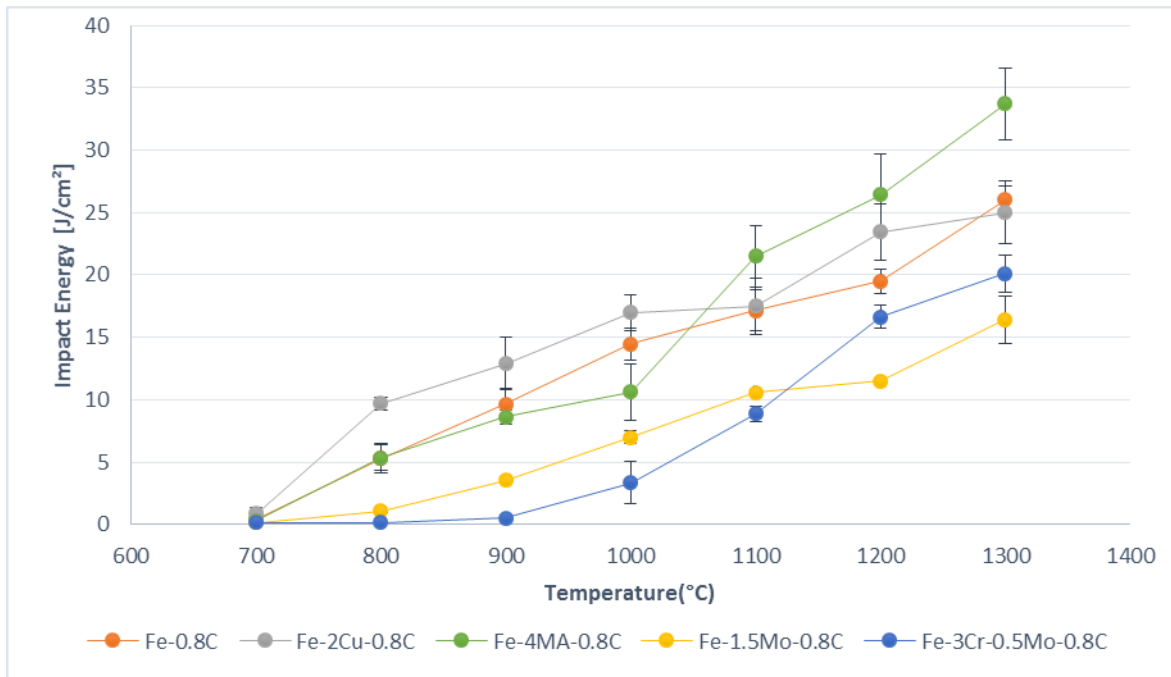


Figure 3.116: Impact energy of the steels versus sintering temperature, compacted at 600 MPa, sintered 60 min in argon, and broken at room temperature by Charpy impact test.

3.4.7.3. Dynamic Young's modulus

Figure 3.117 shows the effective dynamic Young's modulus of the steels. As already shown (see 3.1.5.3) the dynamic Young's modulus of PM steels is influenced mainly by the sintered density.

In the temperature range of 700-1300°C, Fe-Cu-C started from about 145 GPa at 700°C and increased smoothly to about 165 GPa at 1300°C. While the two grades Fe-C and Fe-MA-C showed lower values compared to the Cu alloyed steel at 700°C, a rather pronounced raise at 800°C resulted in values above 145 GPa, reaching almost identical values as Fe-Cu-C at 1300°C.

The Mo alloyed steel generally showed lower values compared to the three previously mentioned steels which might be a consequence of its lower density. It showed a significant jump from 60 GPa to 130 GPa after sintering at 800°C, and then follows an upward trend with increasing temperature, reaching 160 GPa at 1300°C. The Cr-Mo steel showed much lower values in the temperature range of 700 to 1000°C compared to the other steels, which could be the result of the surface chromium oxides. Young's modulus increased from 45 to 135 GPa in this temperature range. In the range of 1000 to 1300°C, the Young's modulus increased from about 135 to 160 GPa, which is in good agreement with the findings by Azadbeh et al. [130] and is a value identical with Mo alloyed steel, however the sintered density of CrM is lower in this temperature range.

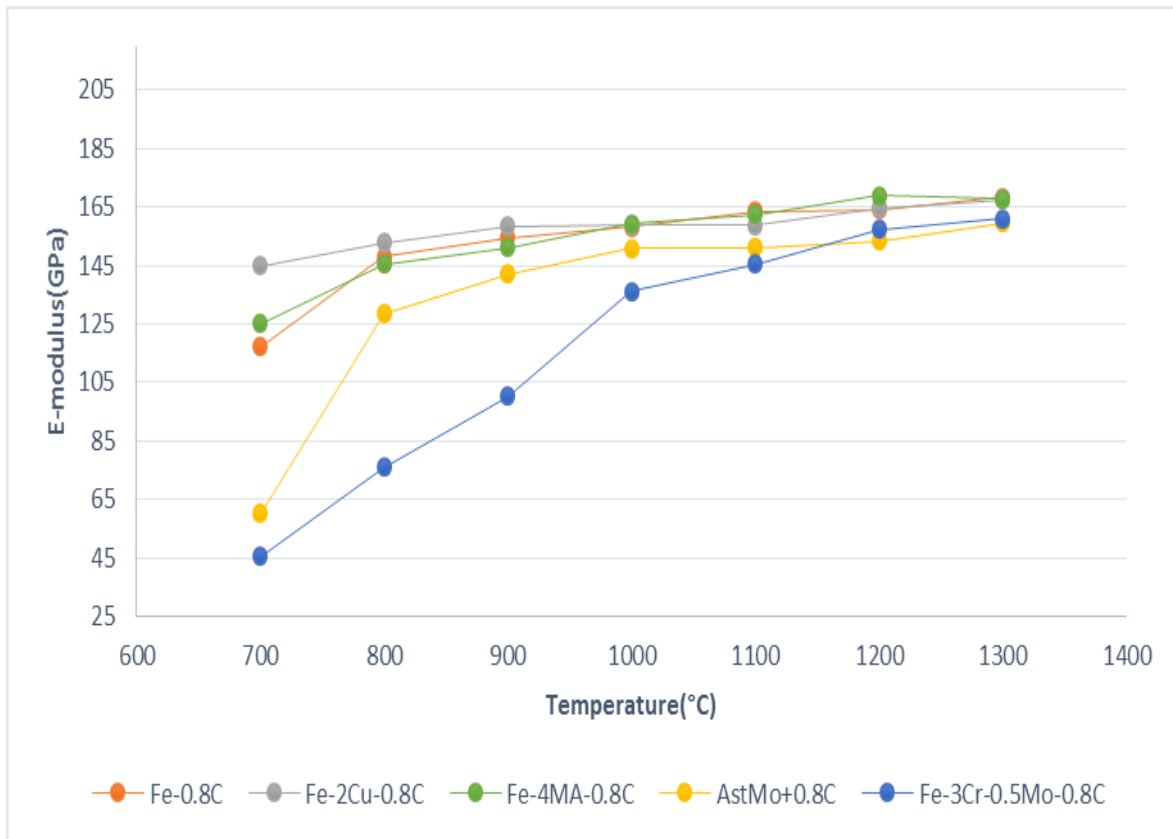


Figure 3.117: Dynamic Young's moduli of the steels versus sintering temperature, compacted at 600 MPa, sintered 60 min in argon.

3.4.7.4. Damping

The damping parameter of the materials as a function of the sintering temperature is presented in Figure 3.118. In the temperature range of 700 to 1000°C, the presence of the surface chromium oxides in the Cr-Mo steel resulted in pronounced damping compared to the other steels, which was lowered at higher sintering temperature. It is also visible that the other prealloyed steel, Fe-1.5Mo-0.8C at 700°C, showed pronounced damping at 700°C which decreased significantly at 800°C. The other mixes show less change in this temperature range (700-1000°C). Between 1100 and 1300°C the effect of the sintering temperature is not very significant, and it is evident that the highest and lowest values in this range belong to Cr-Mo alloyed steel and carbon steel, respectively. As already shown (see the results of damping in the section 3.1.5.4), lowering the density of PM steels increased the damping ability, therefore here it can be stated that in this case also the density also played a role.

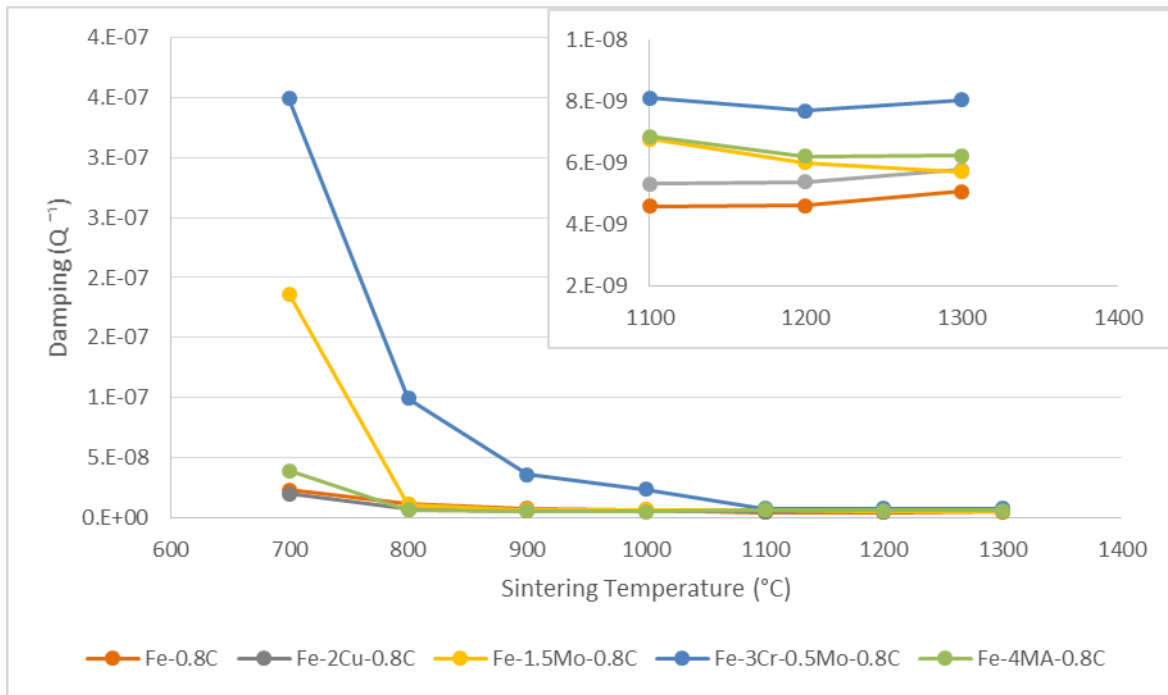


Figure 3.118: Damping of the steels versus sintering temperature, compacted at 600 MPa, sintered 60 min in argon.

3.4.8. Physical properties

3.4.8.1. Electrical conductivity

The electrical conductivity of the steels is presented in Figure 3.119. In the Fe-Cu-C system sintered at 700°C, the presence of Cu particles which fill the free spaces between the iron particles (Figure 3.94, at 700°C), resulted in higher conductivity compared to Fe-C. At 800°C, the results show that the positive and negative factors compensate each other and the conductivity remained constant, but above this temperature, between 800 - 1100°C, the alloying process is accelerated by higher temperature, and the conductivity starts to decrease. Dissolution of copper in addition to that of graphite resulted in lower conductivity compared to Fe-C. The difference to Fe-C at 900 and 1000°C, in which case alloying occurs through solid state for both materials, is small, while at 1100°C, after dissolution of all the copper as a consequence of melt formation, the conductivity of Fe-Cu-C is markedly lower than that of Fe-C. Similar to Fe-C, the electrical conductivity does not show significant changes above 1100°C and up to 1300°C.

In Fe-MA-C, at 700 and 800°C, lower conductivity values are recorded compared to the two previously mentioned steels, although the same base powder was used. Between 800 and 1100°C, a continuous downward trend caused by dissolution of carbon and manganese in the iron matrix is visible in the graph. Above 1100°C, the conductivity showed less change, which indicates that the alloying process is almost complete at this temperature. These results are also in good agreement with the results of dimensional change and hardness measurement (See Figure 3.113 and 3.119).

In Mo alloyed steel, at 800°C a pronounced increase of the electrical conductivity is discernible in the graph which is the result of formation of the initial metal-metal bonds between the powder particles. Above this temperature and up to 1100°C, dissolution of carbon in the steel reduced the electrical conductivity. At 1200 and 1300°C, similar to Fe-C and Fe-Cu-C the electrical conductivity remained almost constant, which shows that carbon dissolution and alloying in this steel have been completed at 1100°C.

In contrast to the other steels which are based on plain iron powder, Astaloy CrM does not show any decrease of the conductivity due to carbon dissolution. An upward trend from 700 to 1100°C is discernible followed by less changes at 1200 and 1300°C. This indicates that in this alloying system, the phenomena which have a positive effect on the conductivity - reduction of the surface oxide or neck formation – play a more significant role which masks the negative effect of the carbon dissolution.

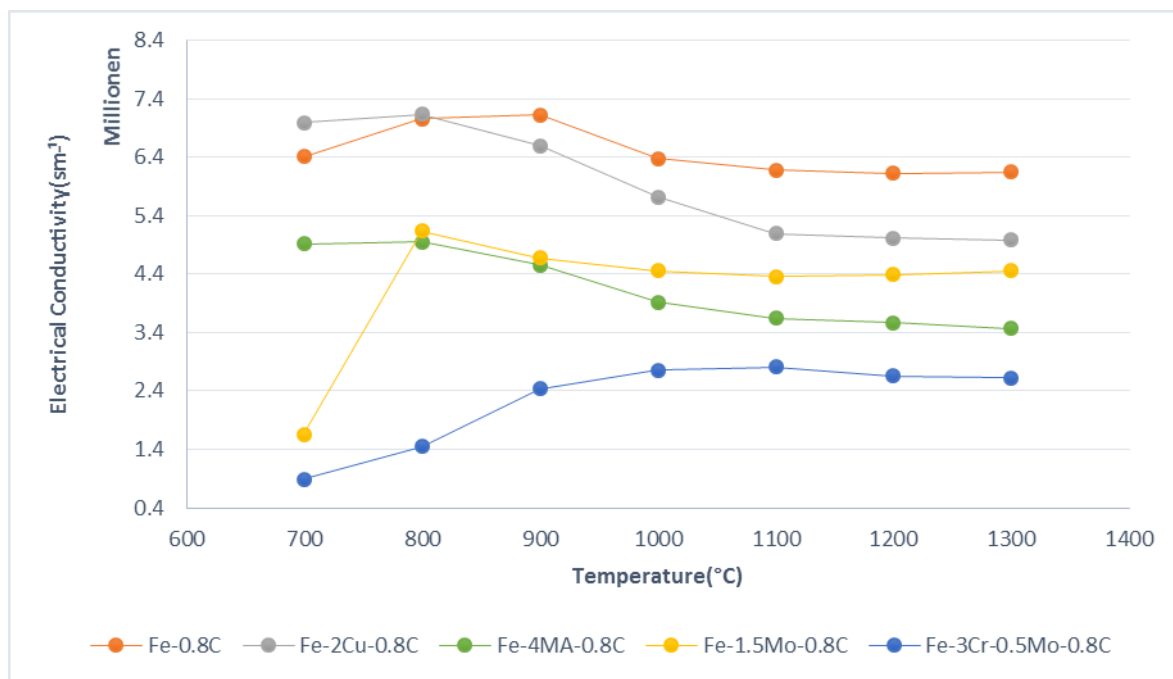


Figure 3.119: Electrical conductivity of the steels, compacted at 600 MPa, sintered 60 min in argon.

3.4.8.2. Coercivity

The coercivity values of the steels are presented in Figure 3.120 as a function of the sintering temperature. The effect of carbon dissolution on the coercivity of Fe-Cu-C is clearly visible between 700 and 1000°C. Above 1000°C and after completion of the alloying process the coercivity showed less changes up to 1300°C. Compared to Fe-C, in Fe-Cu-C, in addition to the carbon, dissolution of Cu affected the coercivity as well and resulted in higher values. In Fe-MA-C, the effect of manganese dissolution in the iron lattice is clearly shown by the increase of coercivity from 800°C up to 1100°C, which is in good agreement with the results of the dimensional change and hardness measurement.

In Fe-Mo-C, the coercivity of the steel increased continuously between 700 and 1000°C with increasing sintering temperature and resulting carbon dissolution, and above this temperature less change in the coercivity of this steel is visible. The results also show that the presence of 1.5 Mo compared to 1.6% Mn and 2% Cu, has more effect on the coercivity of the steels,

In Astaloy CrM, the coercivity does not show any significant change at low temperatures up to 900°C, but at 1000°C, simultaneously with the removal of surface oxides and carbon dissolution, it showed a considerable jump, which indicates that the effect of carbon dissolution on this property is more significant in Cr-Mo alloyed steel than in the other systems. Furthermore, the comparison with Fig. 3.115 clearly shows the distinct, though not perfect, correlation between mechanical and magnetic hardness in particular for this prealloyed steel grade.

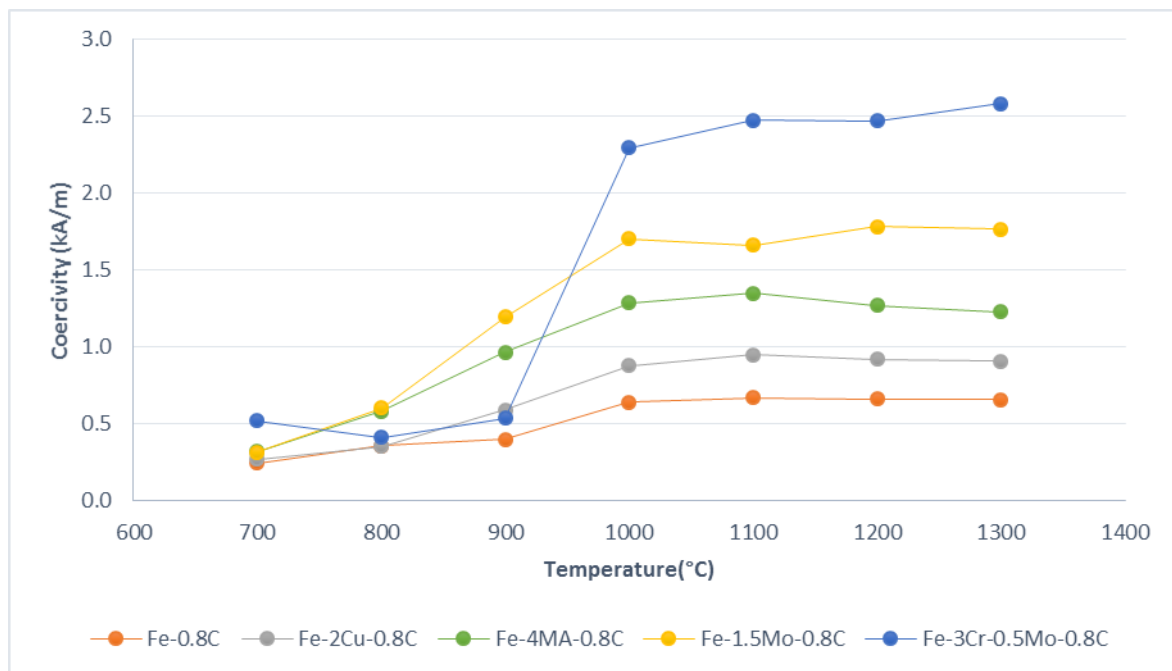


Figure 3.120: Coercivity of the steels, compacted at 600 MPa, sintered 60 min in argon

4. Results and discussion Part 2: Hybrid (Cr-X) alloyed sintered steels for highly loaded PM parts

Development of new PM parts goes towards more complicated shapes and higher performance. The demand is for higher hardness, yield and fatigue strength in combination with high toughness and tight tolerances. All these requirements have to be achieved in a cost-effective way. Sinter hardening, which is a one step process, combines good manufacturing economy with the ability to achieve unique combinations of mechanical properties.

Therefore, tailoring the material composition based on the requirements and the processing condition is of special importance. As already stated above, chromium is a very important alloying element in PM steels. It is a ferrite stabilizer in steels which increases strength, hardness and hardenability and forms hard carbides. Chromium, which has a significantly stronger carbide-forming tendency than iron, can also increase the wear resistance. However, the advantages of using chromium containing PM steels have been offset by the necessity to reduce its oxides at high sintering temperatures [58, 79, 82, 148].

Nickel is another excellent alloying element to work with when targeting a combination of strength and ductility. The addition of Ni is known to improve the mechanical properties of PM steel components by increasing strength, impact resistance, abrasion resistance and fatigue performance [74, 180, 181]. Some previous studies have, however, reported that presence of the soft austenitic phase, i.e. Ni rich areas, can be detrimental to mechanical properties such as the tensile strength [182, 183]. Formation of these areas is due to slower diffusion of Ni into iron as compared to other alloying elements such as C, Cu and Mo [184]. During the last two decades the prices of Ni have been volatile and showed an increasing trend for the time being, especially in the powder form. In addition, Ni allergy and the carcinogenic effect of inorganic Ni compounds are another issue which limited the usage of this alloying element. Therefore, it is of great interest to look at alloying system without or with lower nickel content.

Another alloying element is manganese, which has very common usage in the steel industries (ingot metallurgy) and could be an option for manufacturing the production of highly stressed PM components with high static and dynamic characteristics. It offers increased strength – Mn is strongly hardening ferrite – and hardenability at a much lower price than many other alloy elements such as Cu, Ni and Mo [85]. However, there are some features of Mn that make the industrial production of Mn alloy PM steels through the press-and-sinter route difficult.

One is the high oxygen affinity of Mn, which increases the risk of oxygen pickup from the atmosphere during sintering and makes the removal of the natural oxides present on the powder surfaces more difficult. This exerts stringent requirements on the purity of sintering atmospheres with an extremely low oxygen potential to ensure reduction of oxides covering the surfaces of these powders [46]. However, Šalák showed that Mn evaporation during sintering reduces the risk of oxygen pickup from the atmosphere by the “self-getter effect” [92], though at the expense of Mn loss at the surface.

The second problem is the high vapour pressure of Mn which results in Mn loss during sintering, primarily at the part surfaces where the positive effects of Mn are needed most [93].

As discussed already (see section 3.4), the masteralloy route could be another way for introduction of oxygen-sensitive elements such as Si, Mn and Cr. This route offers some more benefits such as better compressibility, more flexibility in the selection of the final composition of the steel and the potential reduction of the overall cost compared to prealloyed systems. Danninger et al. also showed that introducing Mn not as elemental powder but through suitable masteralloys results in lower final oxygen content and also significantly less Mn evaporation [24, 87].

In the present study, physical, mechanical and sinter hardening properties of a series of hybrid steels prepared on the basis of chromium prealloyed powders with the addition of nickel and manganese was evaluated. The masteralloy route also was investigated as an alternative option to add manganese to the mixtures as well.

For this study, the prealloyed Fe-Cr powder Astaloy CrA was chosen as the base powder and different amounts of Ni, Mn, masteralloy (H46) and graphite were added to the mixtures (all in one step). The mixtures were prepared and investigated in two different groups. Group 1, mixes with different carbon levels added and Group 2, mixes with different alloying element contents and 0.6 % nominal carbon content (see Table 4.1 and 4.2).

Table 4.1: Mixture composition of Group 1 (carbon content: nominal = admixed graphite; for MA: + carbon from the masteralloy).

Alloying system	Mix composition
Fe-Cr (without additives)	Ast CrA
Fe-Cr-C	Ast CrA + (0.4 / 0.5 / 0.6 %) C
Fe-Cr-Ni-C	Ast CrA + 3 %Ni + (0.4 / 0.5 / 0.6 %) C
Fe-Cr-Mn-C	Ast CrA + 3 %Mn + (0.4 / 0.5 / 0.6 %) C
Fe-Cr-MA-C	Ast CrA + 4 %MA + (0.4 / 0.5 / 0.6 %) C

Table 4.2: Mixture composition of Group 2.

Alloying system	Mix composition
Fe-Cr-Ni-C	Ast CrA + (1/2/3 %) Ni + (0.6 %) C
Fe-Cr-Mn-C	Ast CrA + (1/2/3 %) Mn + (0.6 %) C
Fe-Cr-MA-C	Ast CrA + (2/3/4 %) MA + (0.6 %) C

Charpy bars (ISO 5754) were pressed in the tool with floating die at 700 MPa, die wall lubrication being afforded (using Multical sizing fluid). Sintering of the samples was performed in the SiC rod heated electrical laboratory furnace at 1250°C for 1 hr (isothermal sintering, push in-push out method) in N₂-10% H₂ (both in 5.0 grade). The samples were cooled in the water-jacketed exit zone in N₂ atmosphere (5 L/min).

4.1. Green density

The green density data of the steels are presented through Figure 4.1 and 4.2. It is well known that addition of graphite - due to its low theoretical density - could reduce the green density of the PM steels. As can be seen (Fig. 4.1), the addition of graphite has a progressively negative effect on the compactibility of the mixtures and slightly reduces the green densities. The green density of the steels in presence of different amounts of alloying elements is presented in Figure 4.2. It is evident that the addition of Ni, which has higher theoretical density (8.91 g/cm³) than Fe, increased the green density while Mn with the theoretical density of 7.26 (g/cm³) reduced it. Also the addition of MA decreased the green density of the material. This shows that the spherical hard particles of MA play a negative role on the compactibility of the steels.

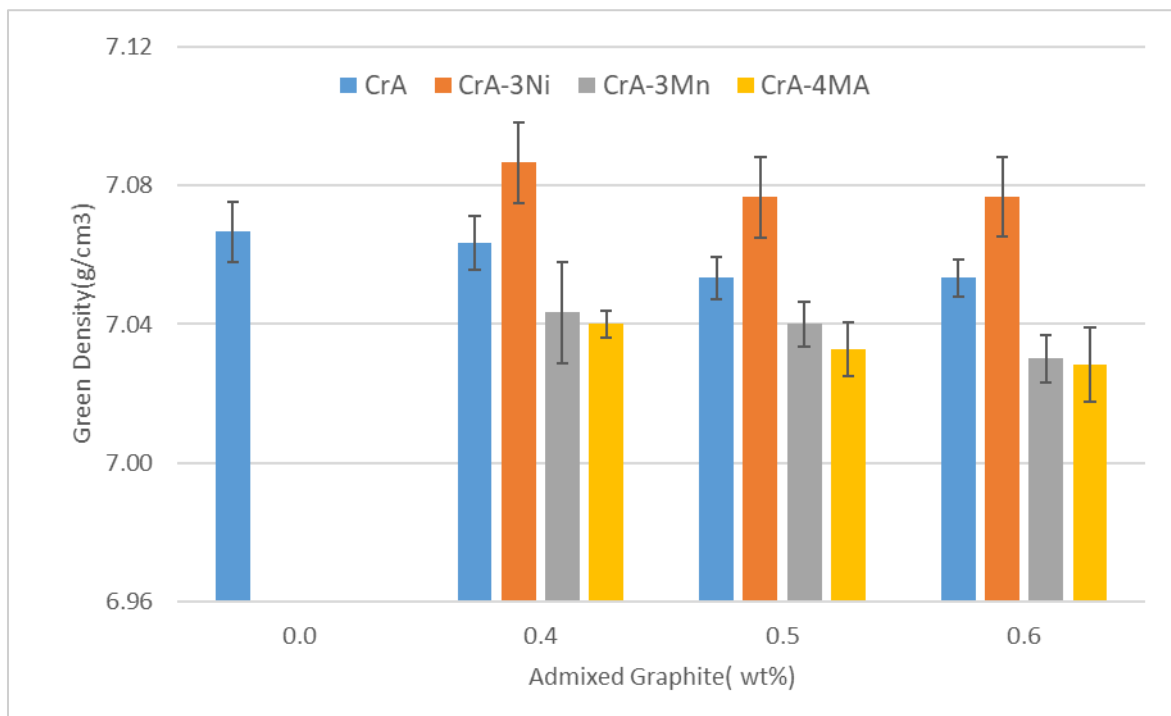


Figure 4.1: Green density of steels with different carbon contents, compacted at 700 MPa. Charpy impact test bars ISO 5754.

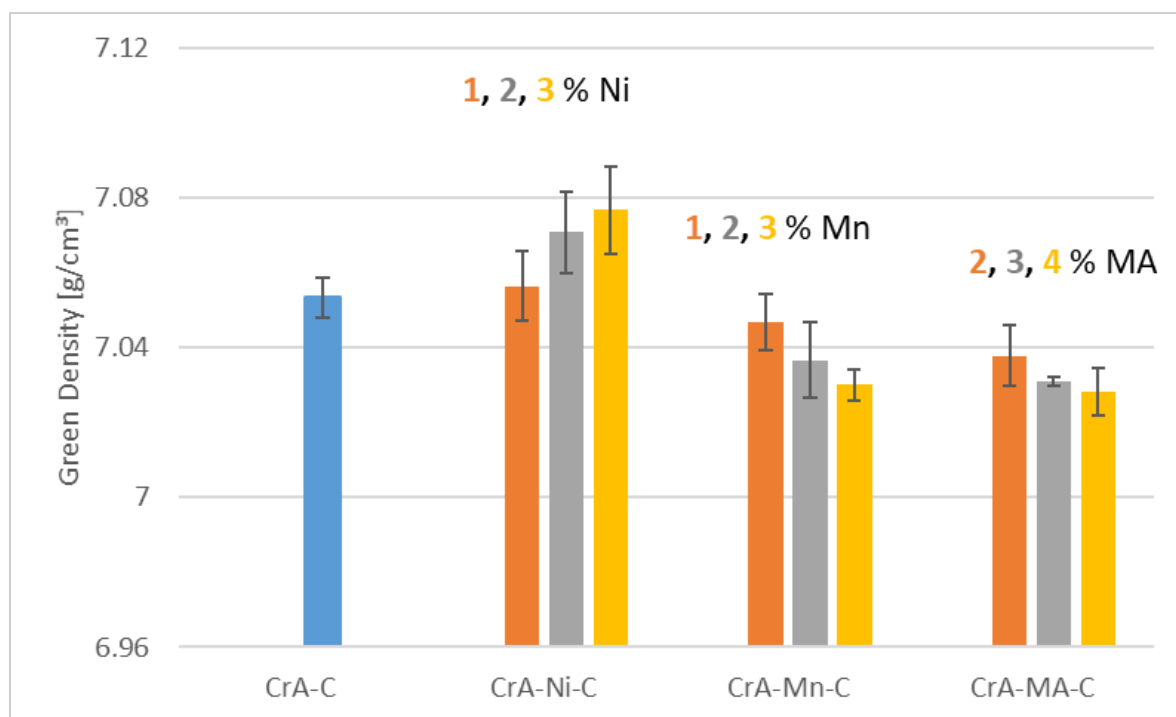


Figure 4.2: Green density of steels with 0.6% admixed carbon, compacted at 700 MPa. Charpy impact test bars ISO 5754

4.2. Chemical analysis

4.2.1. Oxygen and carbon content

Oxygen measurement data of the steels are presented through Figure 4.3 & 4.4. In Figure 4.3, the oxygen content of sintered CrA shows a rather low value (compared to the oxygen in the starting powder of 0.15 mass%) which means that the $N_2-10\%H_2$ atmosphere significantly reduces the stable chromium oxides even in the absence of the carbothermal reducing reactions, however the still lower content of the oxygen after addition of graphite to CrA indicates that the carbothermal reduction further improves the oxide reduction process. In the as-sintered state the highest values for oxygen belong to the MA steels, the oxygen level increasing with higher MA content. A reason for this could be attributed to the presence of the stable silicon oxide in the MA steels which was not reduced even during high temperature sintering. The two other grades, with Ni and Mn, presented lower oxygen contents compared to the MA steels. It is not very surprising in the Ni alloyed steels because Ni increases the C activity [185], which means that also the reducing power is increased, while in the Mn alloyed steels - despite the very high oxygen affinity of the Mn - self-getter properties of the material prevented oxygen pickup from the atmosphere and led to similar values as the reference CrA-C. It is obvious that, in contrast to MA steels, increasing the content of these alloying elements (Mn and Ni) has less effect on the total oxygen content.

Figure 4.5-a & 4.6-a show the combined carbon of the steels after sintering. It is evident that in all steels, the carbon loss is $> 0.1\%$ (compared to the nominal - admixed - C content) which is attributed to the carbothermal reduction of the oxides (See also Fig. 4.5-b and 4.6-b). The

results also show that addition of alloying elements does not have a significant effect on this parameter, which means that most of this carbon loss is related to reduction of the chromium and iron oxide introduced by the base powder (Astaloy CrA). The results of the carbon and oxygen measurement are listed in Table 4.3.

4.2.2. XRF analysis (manganese containing steels)

In table 4.4, the results of the chemical analysis performed through X-Ray Fluorescence (XRF) are presented. The measurement showed different amounts of Mn at different depths in the steels, which was caused by manganese evaporation. At a depth of 0.7 mm beneath the surface, higher Mn loss was observed in the Mn alloyed steel compared to the MA steel; in the latter material Mn loss is discernible only immediately at the surface. However, the results of the measurement at the surface shows higher Mn content (above 2% nominal admixed content), which could be explained by the condensation of the oxidized Mn vapour produced by the Mn steel specimens [93], MnO being deposited.

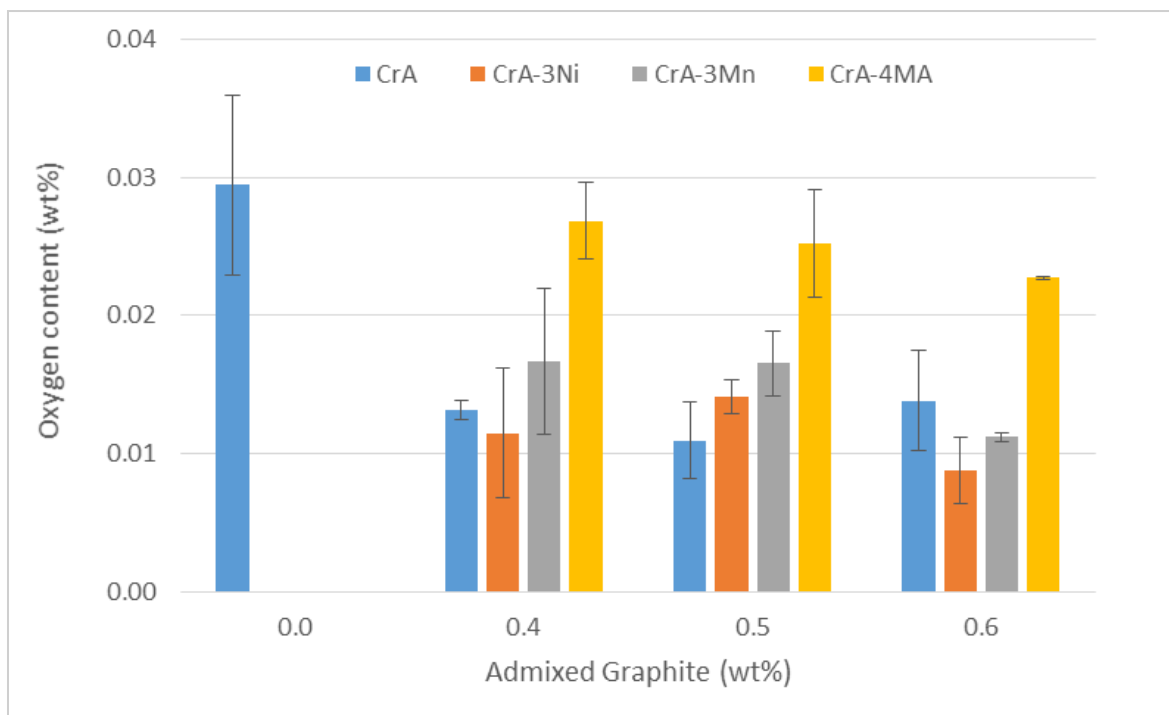


Figure 4.3: Oxygen content of steels (LECO TC-400) with different carbon contents, sintered 60 min at 1250 °C in N₂-10% H₂.

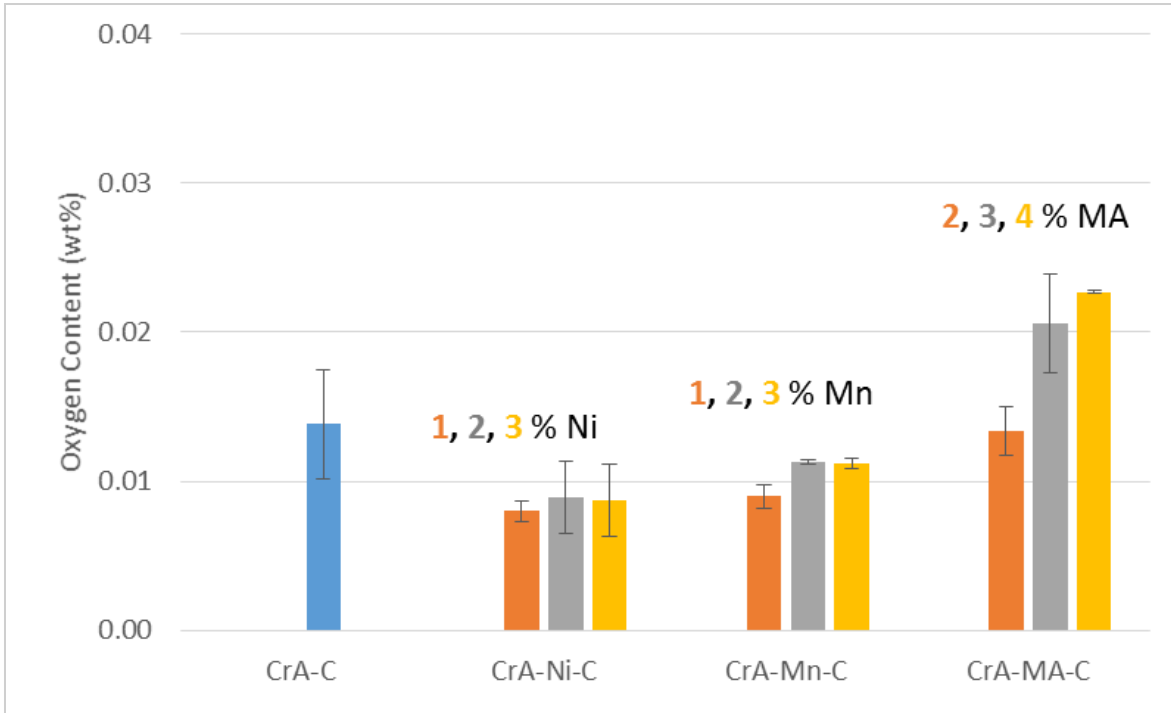


Figure 4.4: Oxygen content of steels (LECO TC-400) with 0.6% carbon, sintered 60 min at 1250 °C in N₂-10% H₂.

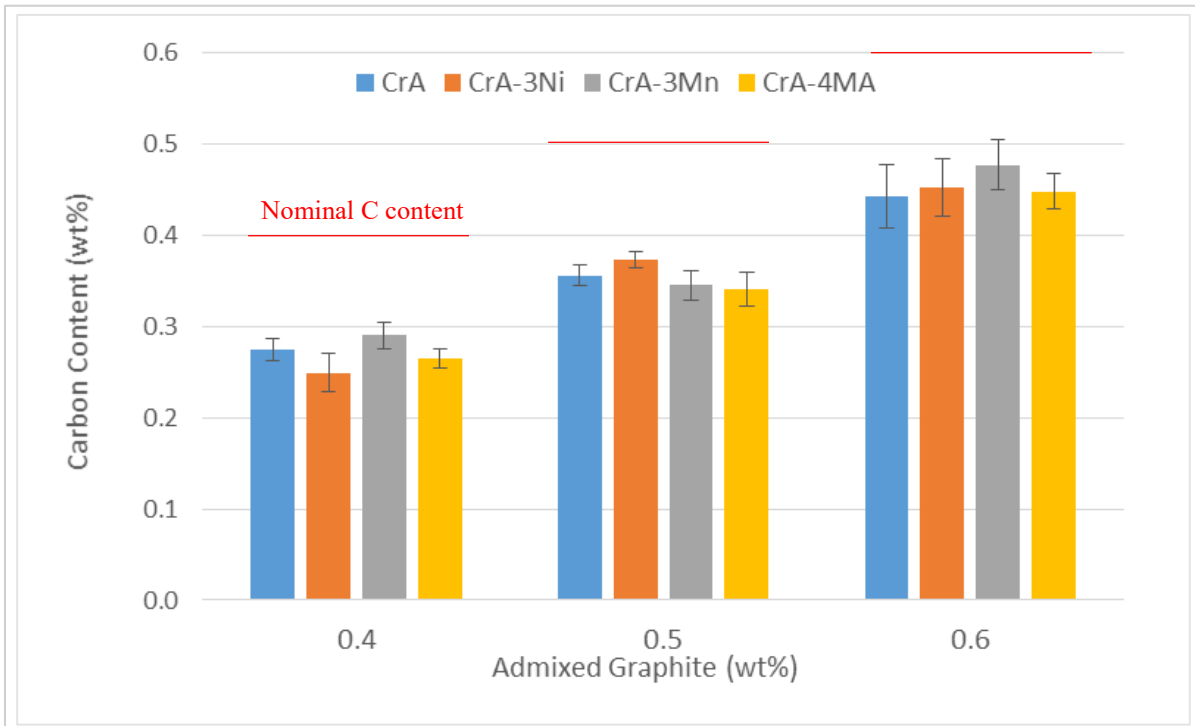


Figure 4.5-a: Carbon content (combined, LECO CS-230) of steels with different carbon contents, sintered 60 min at 1250 °C in N₂-10% H₂.

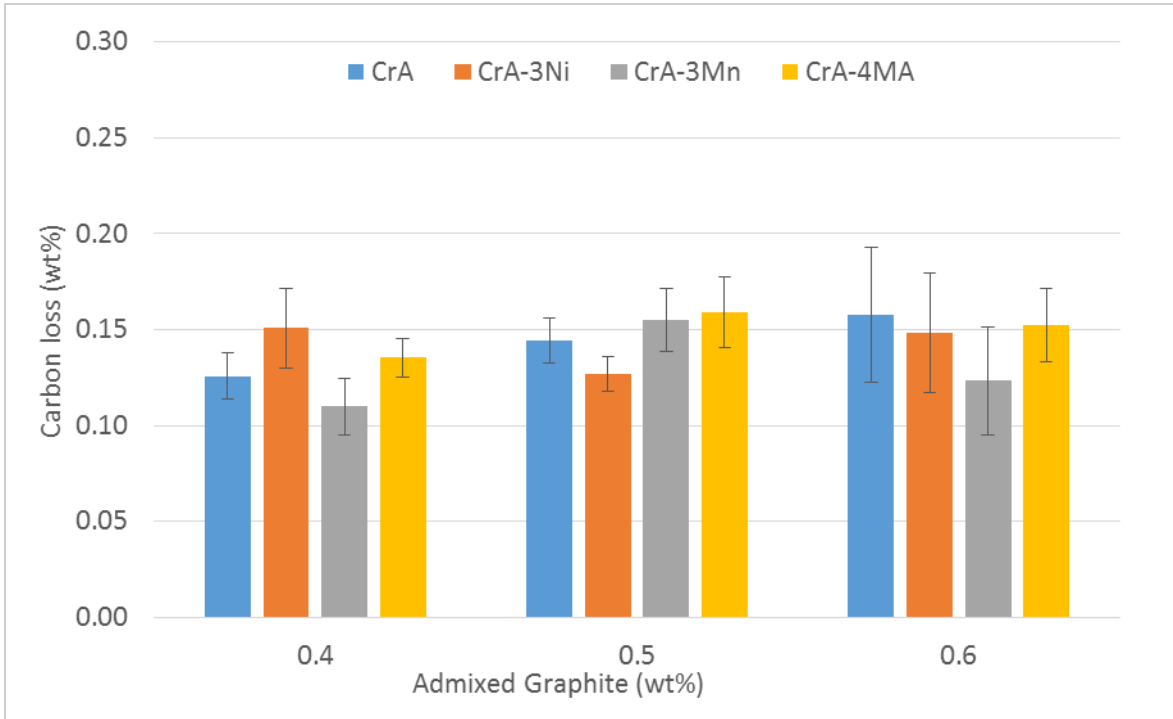


Figure 4.5-b: Carbon loss of steels with different carbon contents, sintered 60 min at 1250 °C in N₂-10% H₂.

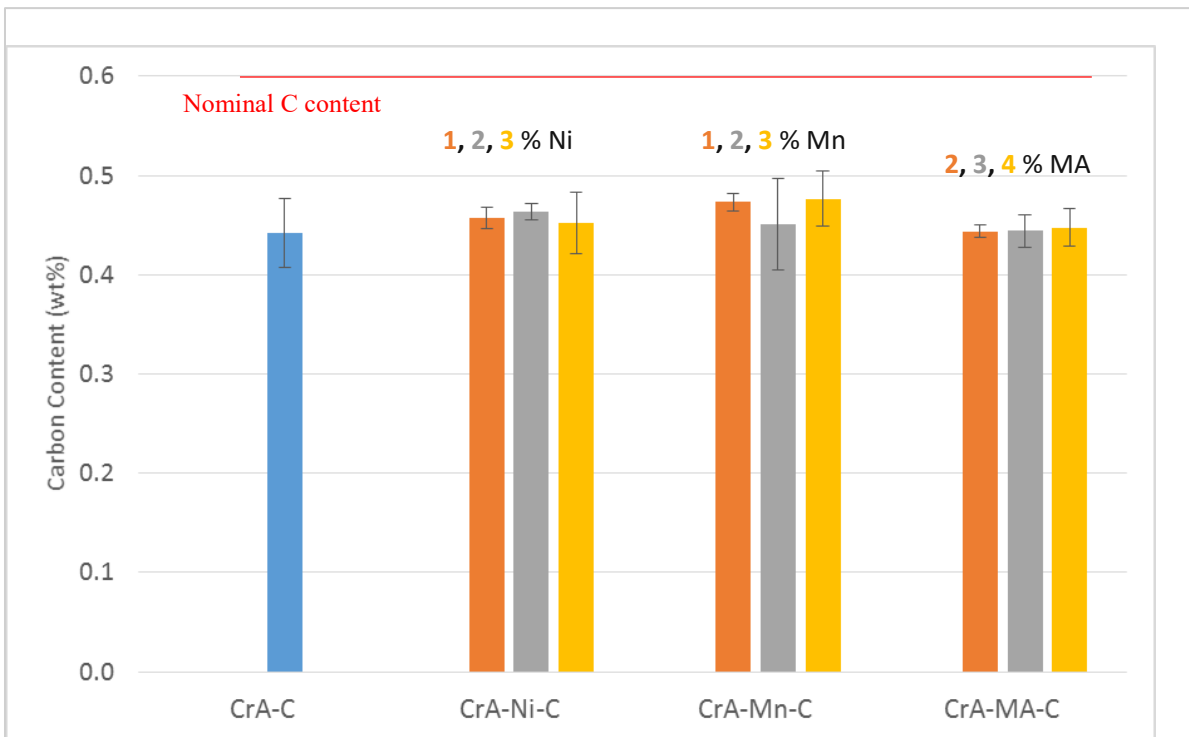


Figure 4.6-a: Carbon content (combined, LECO CS-230) of steels with 0.6% carbon, sintered 60 min at 1250 °C in N₂-10% H₂.

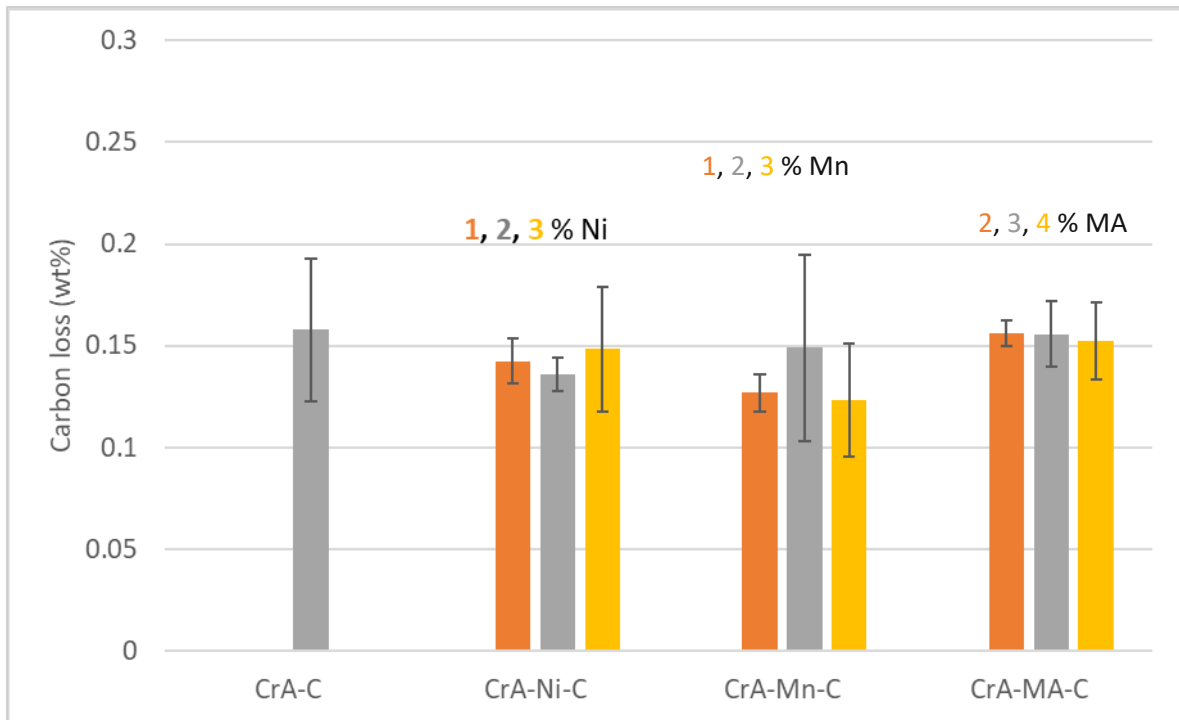


Figure 4.6-b: Carbon loss of steels with 0.6% carbon, sintered 60 min at 1250 °C in N₂-10% H₂.

Table 4.3: Results of oxygen and carbon measurement of the steels, sintered 60 min at 1250 °C in N₂-10% H₂.

	Ni (wt %)*	Mn (wt %)*	MA (wt %)*	C (wt %)*	O content (wt %) **	C content (wt %) **
Fe-Cr-C	0	0.029 ± 0.006	...
	0.4	0.013 ± 0.001	0.274 ± 0.012
	0.5	0.011 ± 0.003	0.356 ± 0.011
	0.6	0.014 ± 0.004	0.442 ± 0.035
Fe-Cr-Ni-C	1	0.6	0.008 ± 0.001	0.458 ± 0.011
	2	0.6	0.009 ± 0.002	0.464 ± 0.008
	3	0.4	0.011 ± 0.005	0.249 ± 0.021
				0.5	0.014 ± 0.001	0.373 ± 0.009
Fe-Cr-Mn-C	...	1	...	0.6	0.009 ± 0.001	0.473 ± 0.009
	...	2	...	0.6	0.011 ± 0.000	0.451 ± 0.046
	...	3	...	0.4	0.017 ± 0.005	0.290 ± 0.015
				0.5	0.017 ± 0.002	0.345 ± 0.016
Fe-Cr-MA-C	2	0.6	0.013 ± 0.002	0.444 ± 0.006
	3	0.6	0.021 ± 0.003	0.444 ± 0.016
	4	0.4	0.027 ± 0.003	0.265 ± 0.010
				0.5	0.025 ± 0.004	0.341 ± 0.019
				0.6	0.023 ± 0.000	0.448 ± 0.019

*Admixed nominal values, ** combined values measured by LECO after sintering.

Table 4.4: Results of XRF chemical analysis of steels at different depths from surface, sintered 60 min at 1250 °C in N₂-10% H₂. (Nominal Mn content in MA steel: 1.20%)

	CrA-2Mn-0.6C		CrA-3MA-0.6C	
	Surface	Surface ground 0.7 mm	Surface	Surface ground 0.7 mm
Mo	0.03 %	0.03%	0.03%	0.03%
Cu	0.06 %	0.04%	0.04%	0.04%
Ni	0.04 %	0.04%	0.04%	0.04%
Fe	95.83 %	96.02%	96.73%	96.50%
Mn	2.05 %	1.89%	0.98%	1.25%
Cr	1.88 %	1.89%	1.90%	1.88 %
S	0.012 %	0.011%	0.009%	0.002%
P	0.008 %	0.005%	0.004%	0.003%
Si	0.07 %	0.06%	0.25%	0.24%

4.3. Metallographic investigations (pore morphology and matrix microstructure)

Un-etched micrographs of the steels are presented through Figure 4.5 to 4.12. For showing the pore distribution and shape, the micrographs are provided in two magnifications of 50 and 200x. In Figure 4.5, the CrA steel without additive showed less pore rounding compared to the other steels, while addition of graphite to the mixtures – which decreases the solidus temperature of the steels and enhances oxygen removal - resulted in more activated sintering and formation of more rounded pores. In the Ni containing steels, Figure 4.9 & 4.10, the pore size and distribution do not show a significant difference compared to CrA-C. Figure 4.11 & 4.12 show the pore morphology of the Mn steels. It is evident that in this steel, addition of Mn to the mixtures led to the formation of larger pores which could be related to the secondary pores left behind by Mn after the evaporation and diffusion of this alloying element into the iron lattice (one-way homogenization). Increasing the content both of Mn and carbon led to formation of larger pores, a possible reason could be agglomeration of Mn with graphite particles which left larger secondary pores.

The pore morphologies of MA containing steels are presented in Figure 4.13 & 4.14. The pore size and distribution in this steel is more or less similar to CrA-C steels, which shows that introducing Mn through the MA route does not lead to formation of such large secondary pores as when elemental Mn is used.

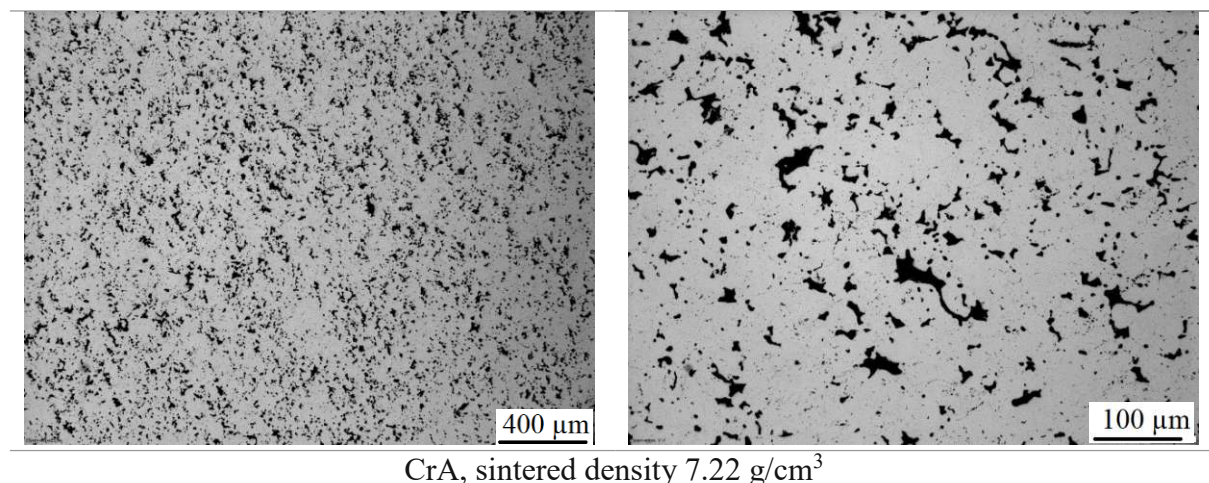
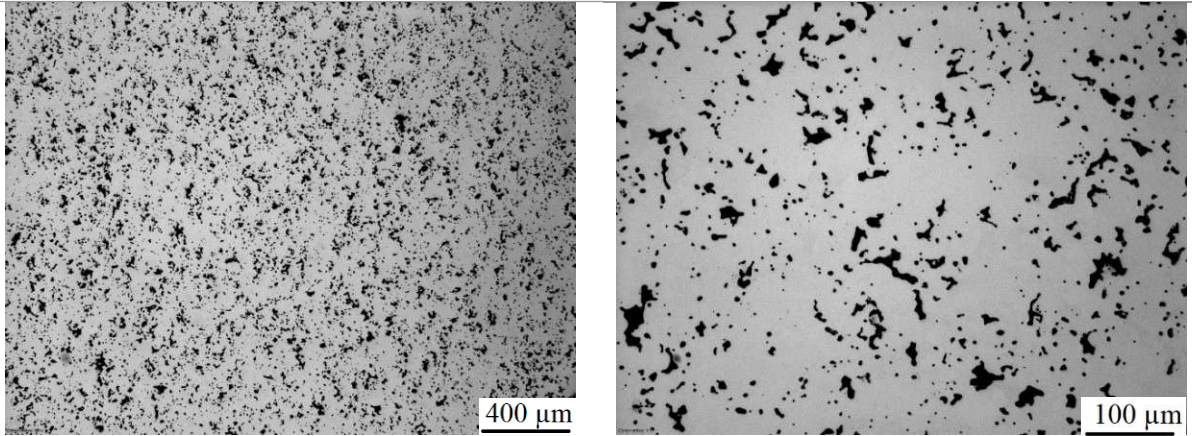
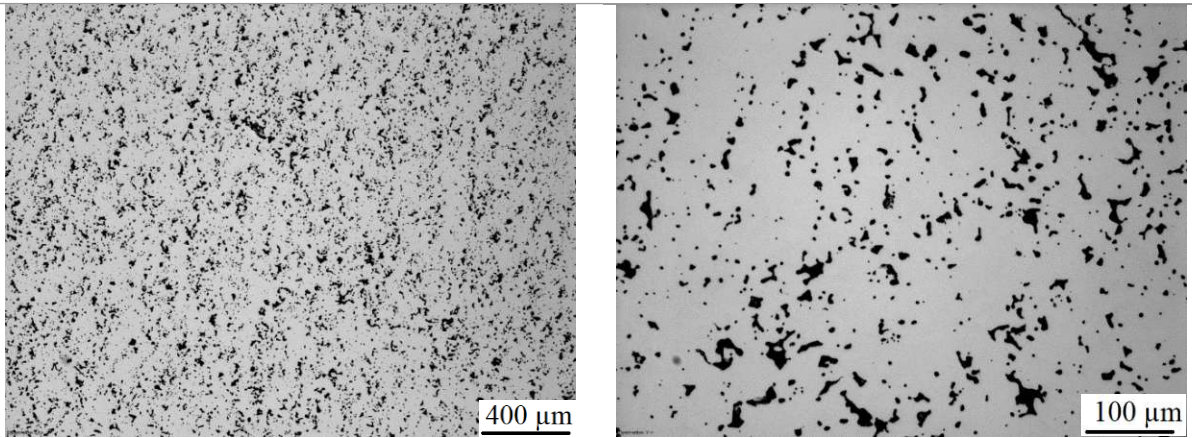


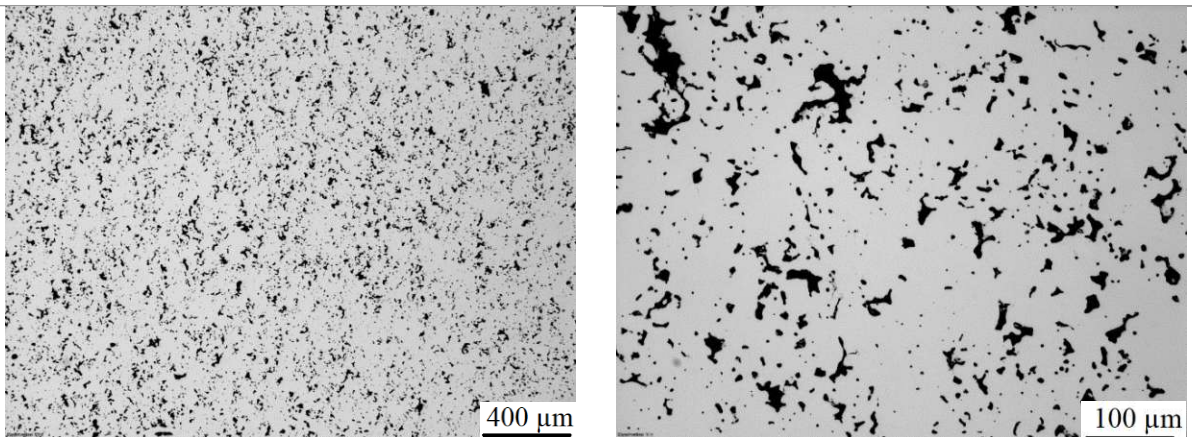
Figure 4.7: OM un-etched microstructures of CrA steel (without carbon), compacted at 700 MPa, sintered 60 min at 1250 °C in N₂-10% H₂, 50 and 200 x.



CrA+0.4C, sintered density 7.25 g/cm³

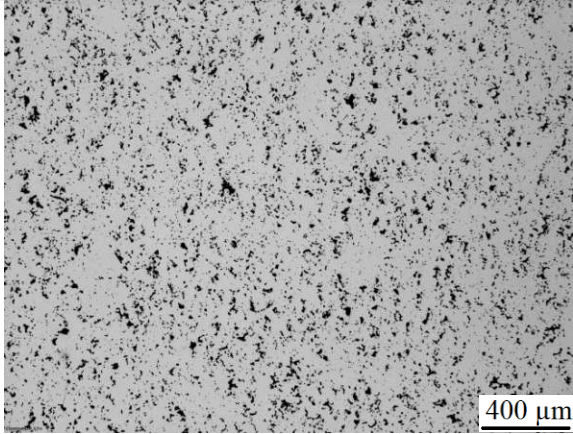


CrA+0.5C, sintered density 7.23 g/cm³



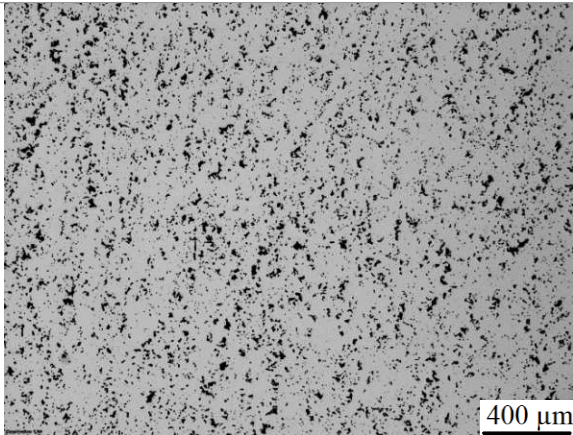
CrA+0.6C, sintered density 7.24 g/cm³

Figure 4.8: OM un-etched microstructures of CrA-C steels, compacted at 700 MPa, sintered 60 min at 1250 °C in N₂-10% H₂, 50 and 200 x.

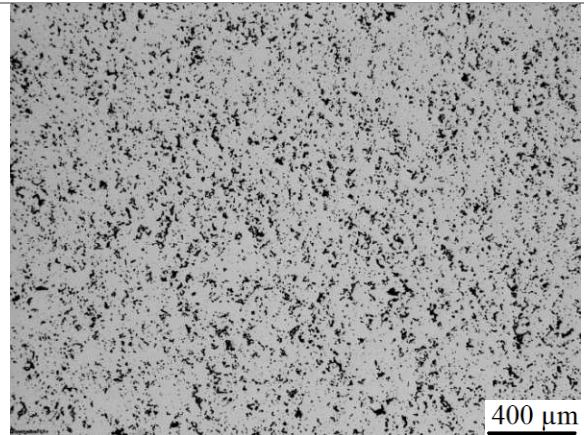


CrA-3Ni-0.4C, sintered density 7.31 g/cm³

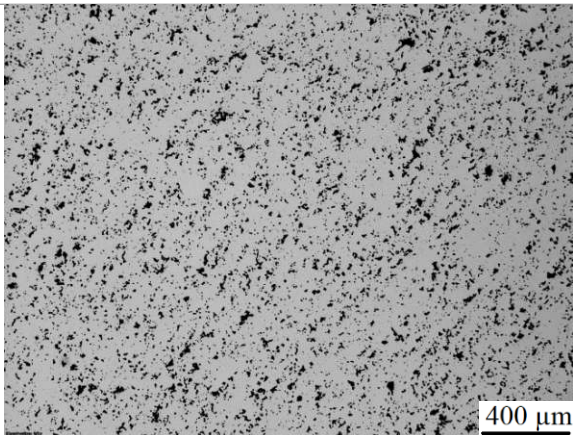
Figure 4.9: OM un-etched microstructures of CrA-Ni-C steels, compacted at 700 MPa, sintered 60 min at 1250 °C in N₂-10% H₂, 50 x.



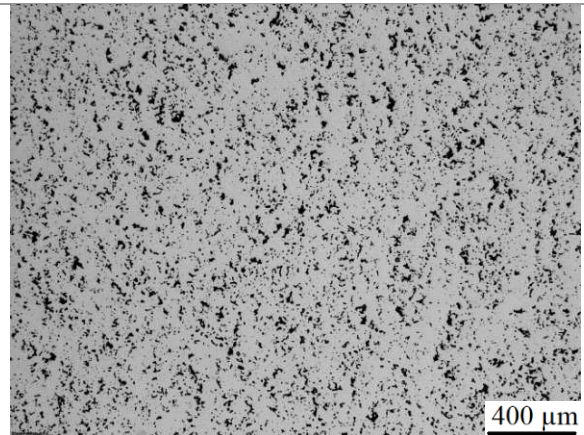
CrA-3Ni-0.5C, sintered density 7.31 g/cm³



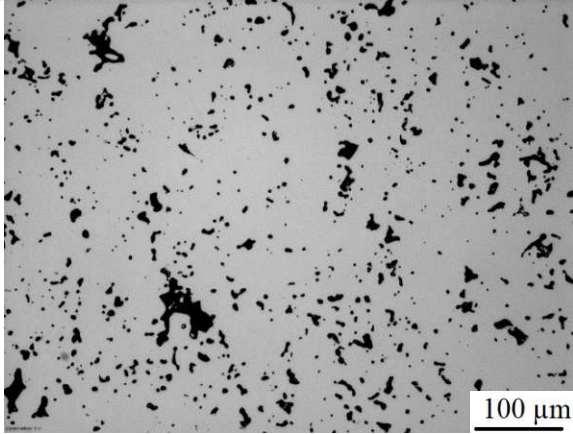
CrA-1Ni-0.6C, sintered density 7.27 g/cm³



CrA-3Ni-0.6C, sintered density 7.31 g/cm³

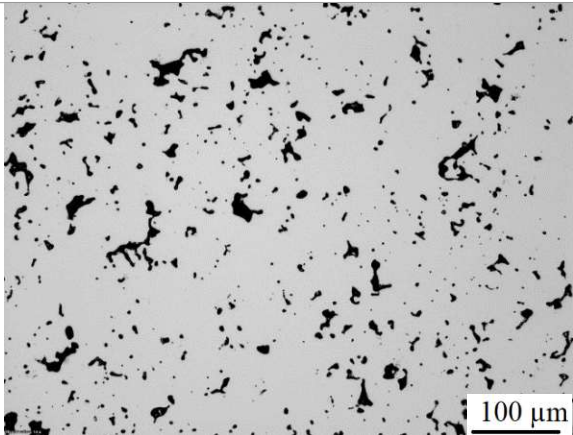


CrA-2Ni-0.6C, sintered density 7.30 g/cm³

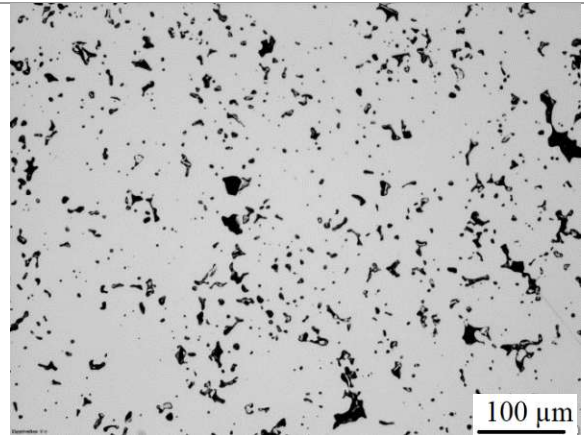


CrA-3Ni-0.4C, sintered density 7.31 g/cm³

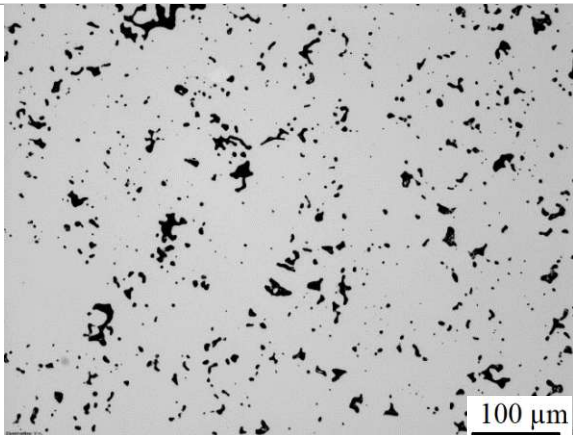
Figure 4.10: OM un-etched microstructures of CrA-Ni-C steels, compacted at 700 MPa, sintered 60 min at 1250 °C in N₂-10% H₂, 200 x.



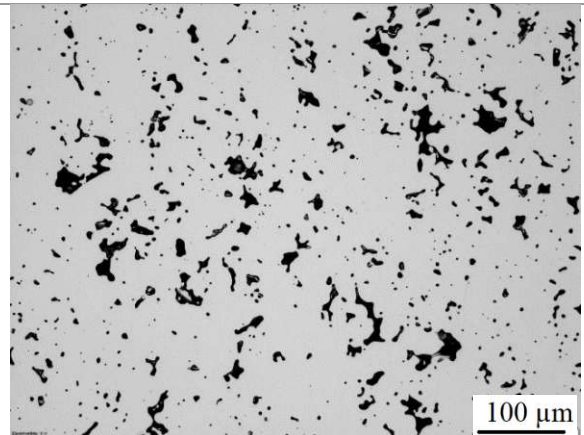
CrA-3Ni-0.5C, sintered density 7.31 g/cm³



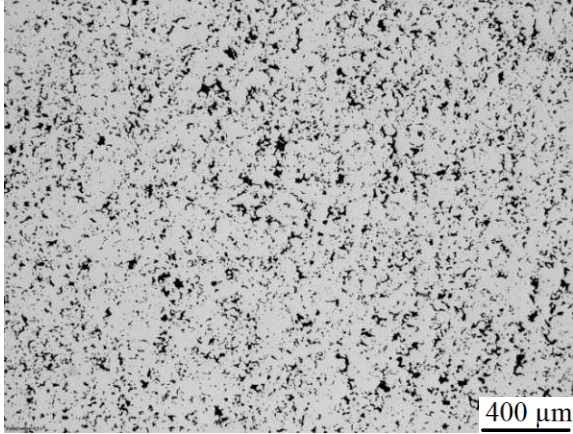
CrA-1Ni-0.6C, sintered density 7.27 g/cm³



CrA-3Ni-0.6C, sintered density 7.31 g/cm³

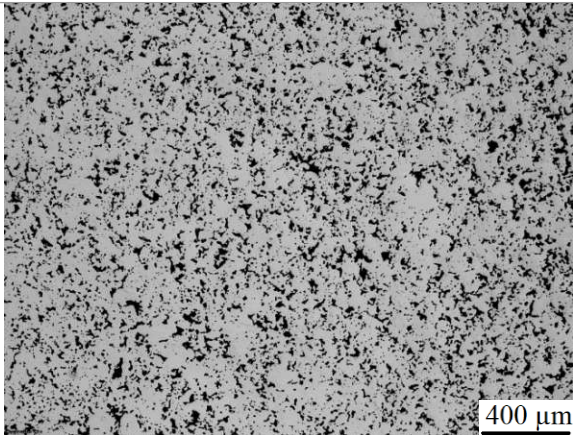


CrA-2Ni-0.6C, sintered density 7.30 g/cm³

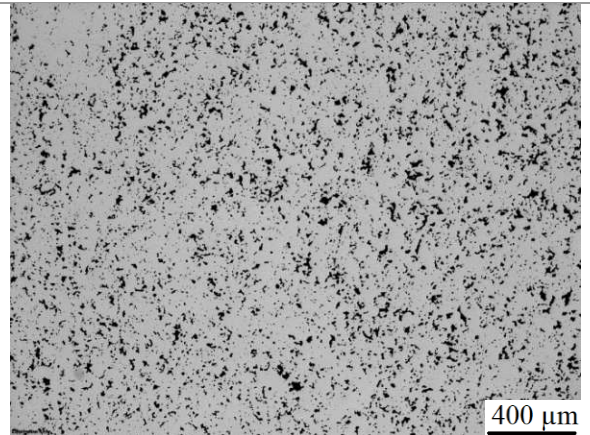


CrA-3Mn-0.4C, sintered density 7.07 g/cm³

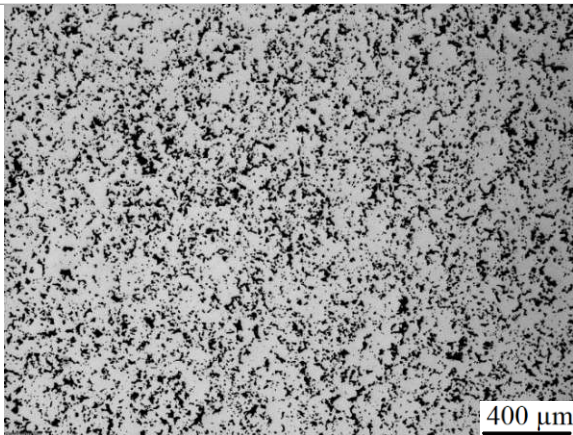
Figure 4.11: OM un-etched microstructures of CrA-Mn-C steels, compacted at 700 MPa, sintered 60 min at 1250 °C in N₂-10% H₂, 50 x.



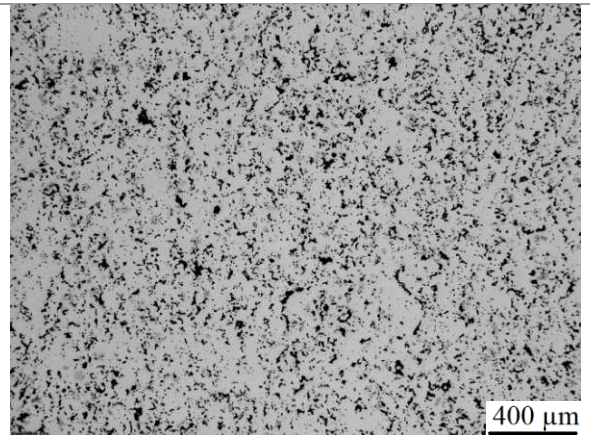
CrA-3Mn-0.5C, sintered density 7.06 g/cm³



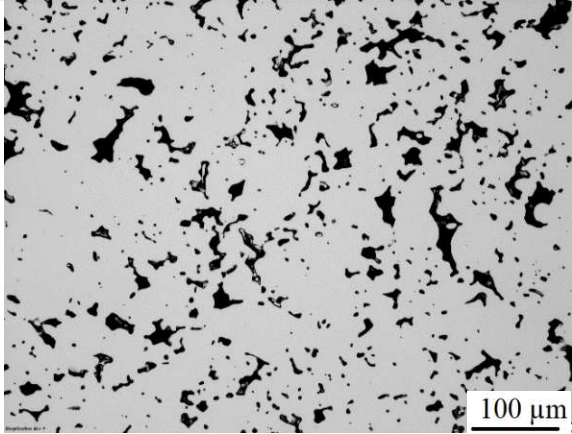
CrA-1Mn-0.6C, sintered density 7.19 g/cm³



CrA-3Mn-0.6C, sintered density 7.04 g/cm³

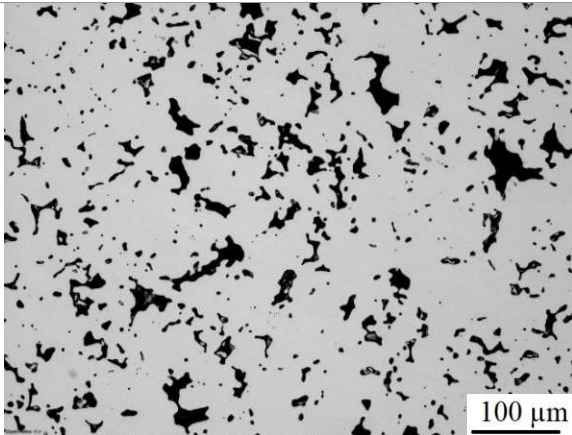


CrA-2Mn-0.6C, sintered density 7.11 g/cm³

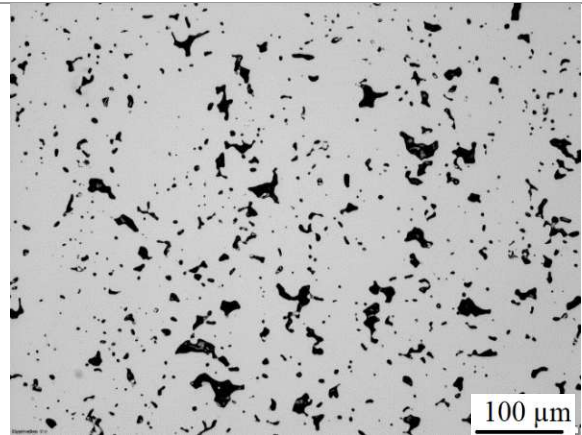


CrA-3Mn-0.4C, sintered density 7.07 g/cm³

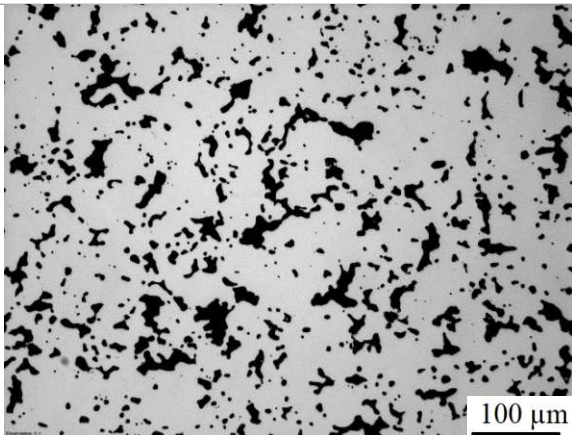
Figure 4.12: OM un-etched microstructures of CrA-Mn-C steels, compacted at 700 MPa, sintered 60 min at 1250 °C in N₂-10% H₂, 200 x.



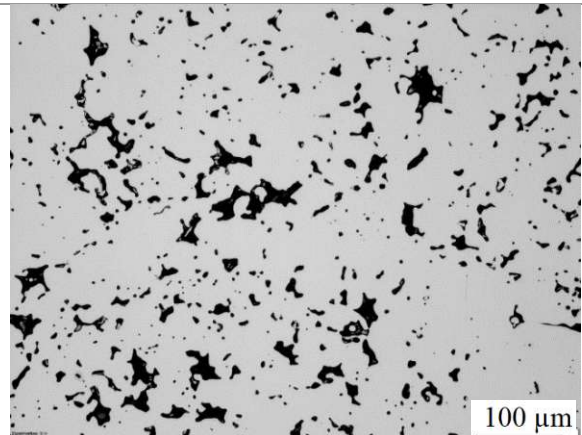
CrA-3Mn-0.5C, sintered density 7.06 g/cm³



CrA-1Mn-0.6C, sintered density 7.19 g/cm³



CrA-3Mn-0.6C, sintered density 7.04 g/cm³



CrA-2Mn-0.6C, sintered density 7.11 g/cm³

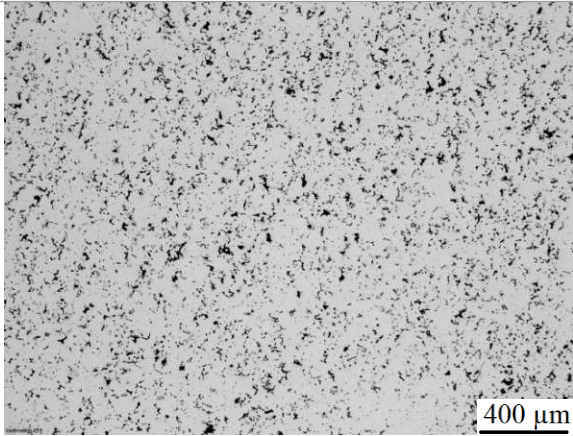
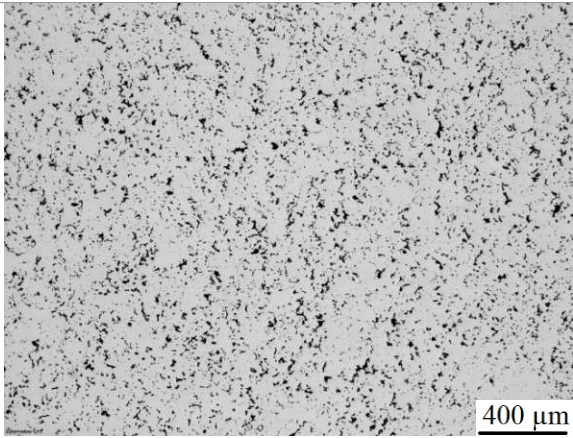
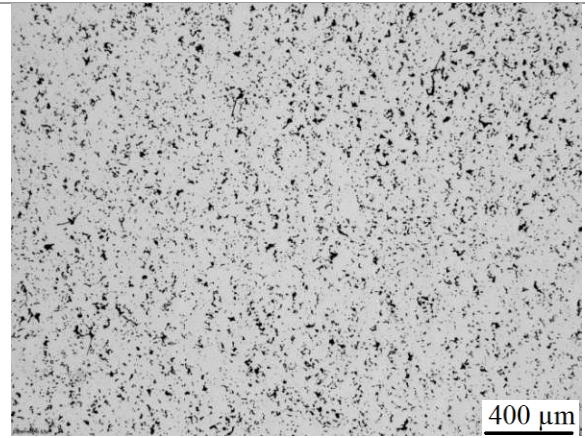


Figure 4.13: OM un-etched microstructures of CrA-MA-C steels, compacted at 700 MPa, sintered 60 min at 1250 °C in N₂-10% H₂, 50 x.

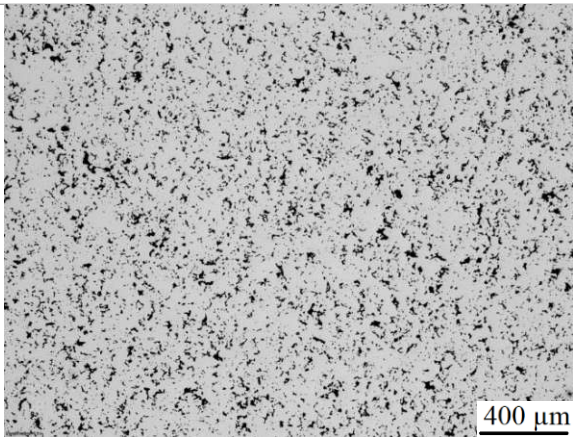
CrA-4MA-0.4C, sintered density 7.19 g/cm³



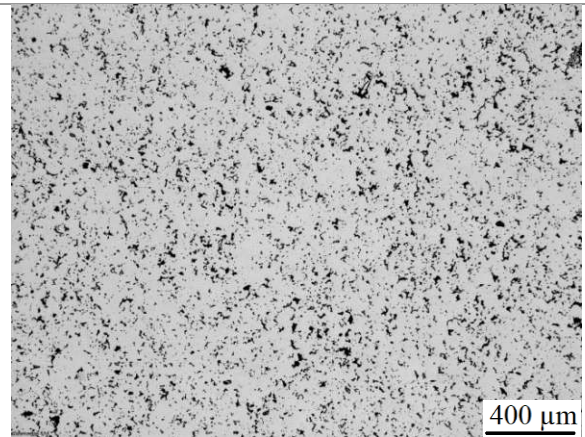
CrA-4MA-0.5C, sintered density 7.17 g/cm³



CrA-2MA-0.6C, sintered density 7.20 g/cm³



CrA-4MA-0.6C, sintered density 7.15 g/cm³



CrA-3MA-0.6C, sintered density 7.18 g/cm³

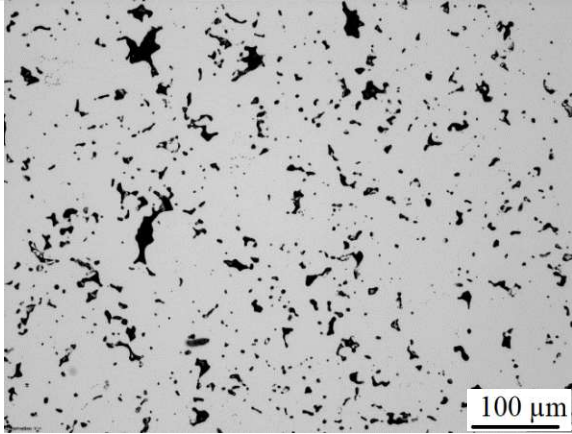
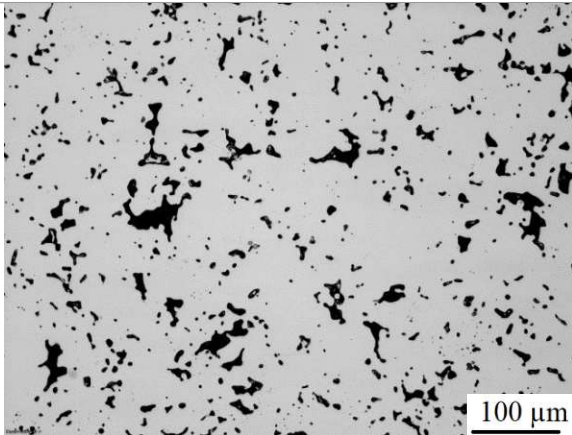
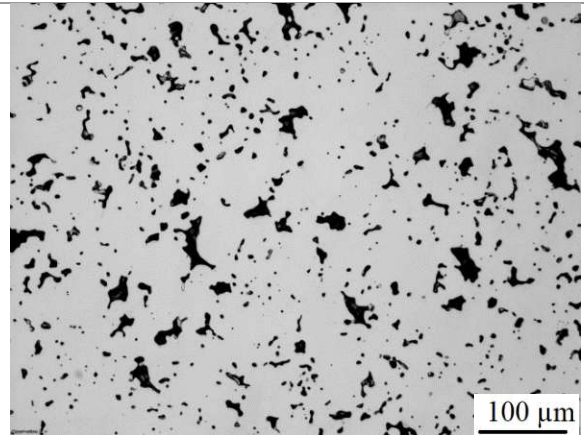


Figure 4.14: OM un-etched microstructures of CrA-MA-C steels, compacted at 700 MPa, sintered 60 min at 1250 °C in N₂-10% H₂, 200 x.

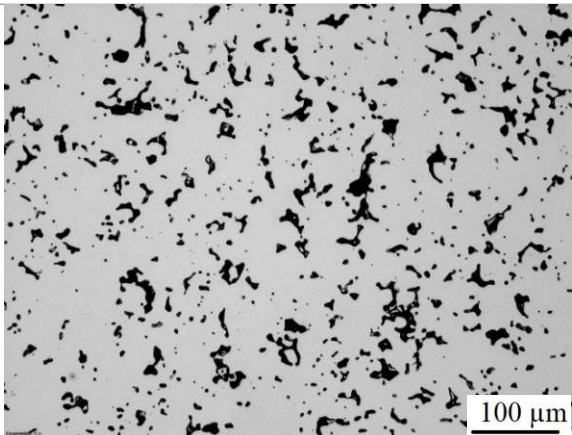
CrA-4MA-0.4C, sintered density 7.19 g/cm³



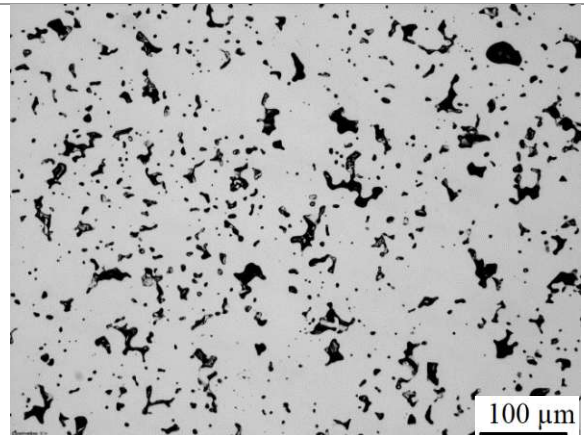
CrA-4MA-0.5C, sintered density 7.17 g/cm³



CrA-2MA-0.6C, sintered density 7.20 g/cm³



CrA-4MA-0.6C, sintered density 7.15 g/cm³



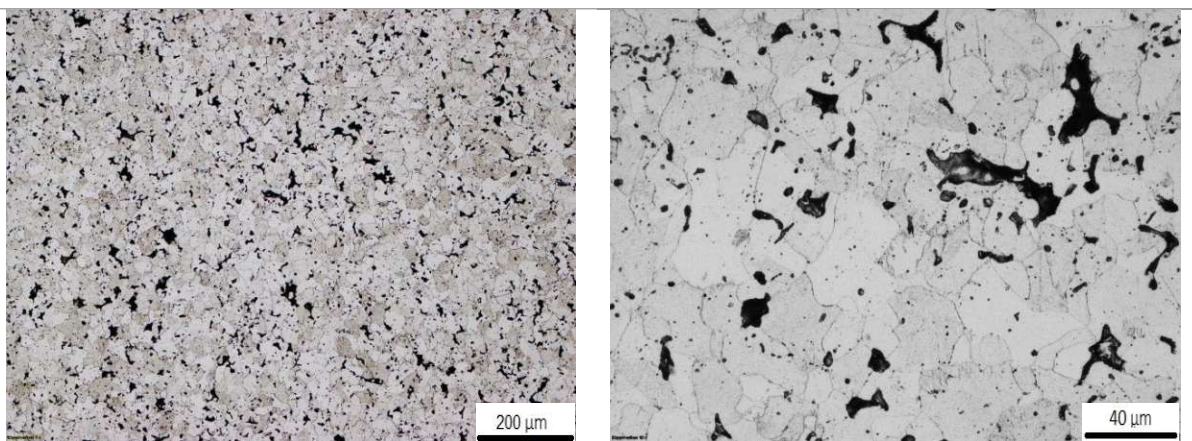
CrA-3MA-0.6C, sintered density 7.18 g/cm³

The etched micrographs of the steels (as-sintered) are presented through Figure 4.15 to 4.25. The microstructure of the CrA steel (Figure 4.15) before addition of carbon is fully ferritic, while addition of 0.4 to 0.6 % of carbon to the system resulted in homogeneous ferrite-pearlite microstructures (Figure 4.16).

The microstructures of the Ni alloyed steels are presented in Figure 4.17 and 4.18. The microstructure of the steel after addition of 1 % nickel is mostly pearlitic and homogeneous, while increasing the Ni content to 2% resulted in bainitic matrix with some martensite and spherical pearlitic regions. In CrA-3Ni-0.4C the microstructure is mostly bainitic and surrounds some pearlitic and martensitic regions. Increasing the carbon content leads to higher fraction of the martensitic regions and higher hardness. In addition to the mentioned phases some Ni-rich austenitic areas caused by aggregation of Ni are also visible (See Figure 4.19).

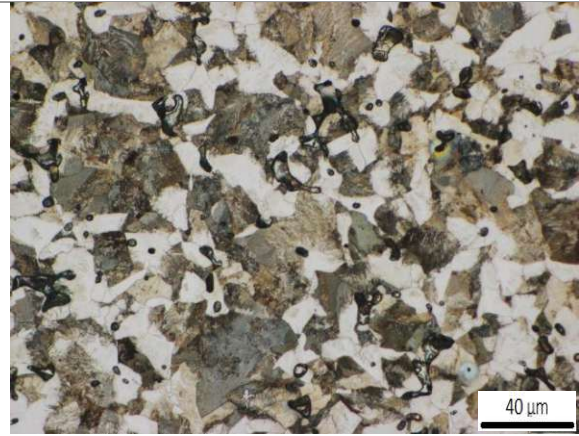
The microstructures of the CrA-Mn-C steels are shown in Figure 4.20 to 4.22. Addition of 1%Mn and 0.6%C resulted in pearlitic microstructure with some bainitic regions which could be Mn-rich zones. Increasing the Mn to 2% led to a martensitic matrix with some bainitic regions and higher hardness, which shows the good potential of this steel for sinter hardening. The steel containing 3% and 0.4%C shows bainitic-martensitic microstructure which turned to mostly martensitic after increasing the carbon to 0.6%, however some pearlitic regions are still visible in the microstructure, which is related to the cores of large powder particles which are alloyed less. In Figure 4.22, the different phases in CrA-3Mn-0.5C in the microstructure are shown.

In the MA containing steels (Figure 4.23 to 4.25), the microstructures after addition of 2 and 3 % MA are mostly pearlitic with some bainitic regions with a rather homogeneous distribution. In CrA-4MA-0.4C the microstructure is mostly bainitic with some small pearlitic regions. Increasing the carbon to 0.5% in this steel led to formation of martensitic areas which extended after increasing the carbon to 0.6%. The microstructure of CrA-4MA-0.5C with the identified phases is shown in Figure 4.25.

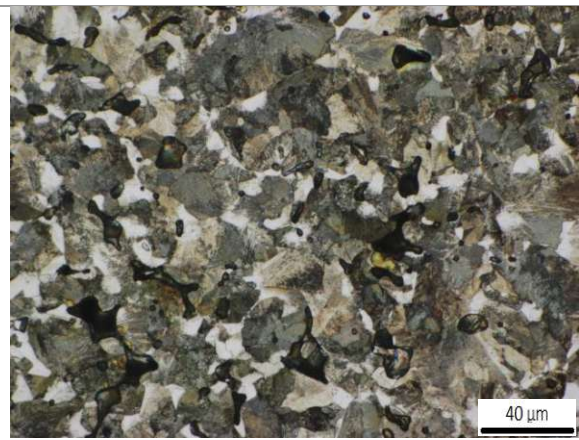
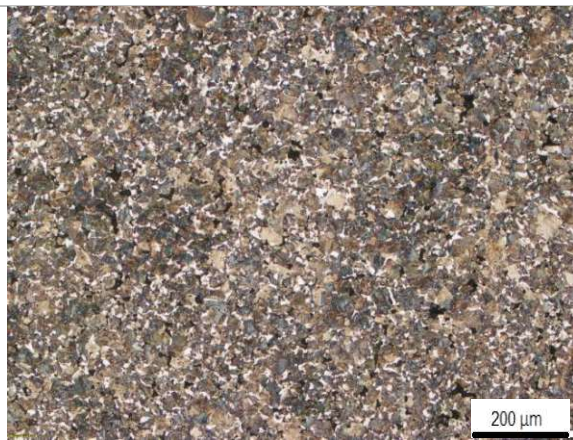


CrA, 71.3 HV30

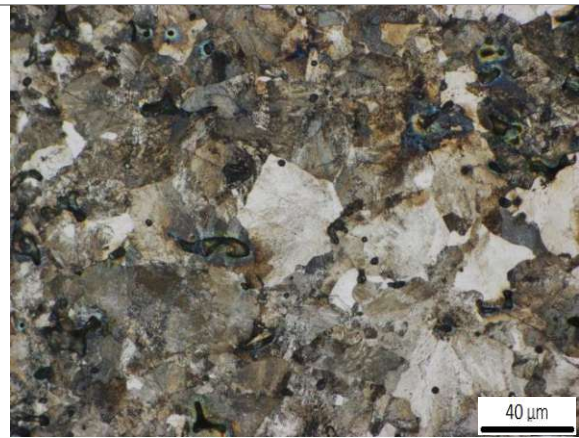
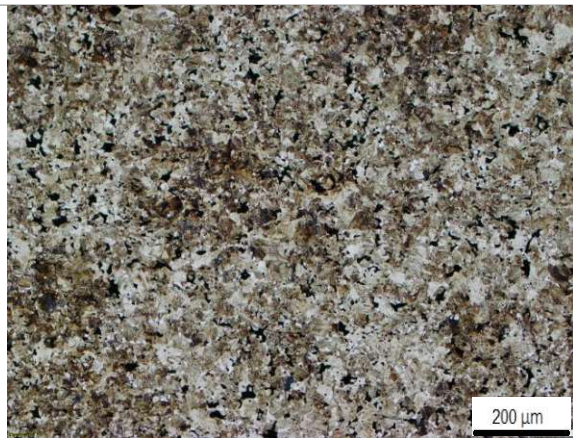
Figure 4.15: OM etched microstructures of plain CrA steel (without carbon), compacted at 700 MPa, sintered 60 min at 1250 °C in N₂-10% H₂, Nital, 100 and 500 x.



CrA-0.4C, 144 HV30



CrA-0.5C, 168 HV30



CrA-0.6C, 172 HV30

Figure 4.16: OM etched microstructures of CrA-C steels, compacted at 700 MPa, sintered 60 min at 1250 °C in N₂-10% H₂, Nital, 100 and 500 x.

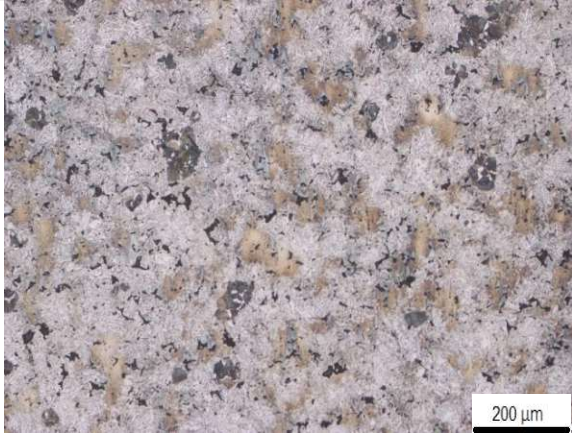
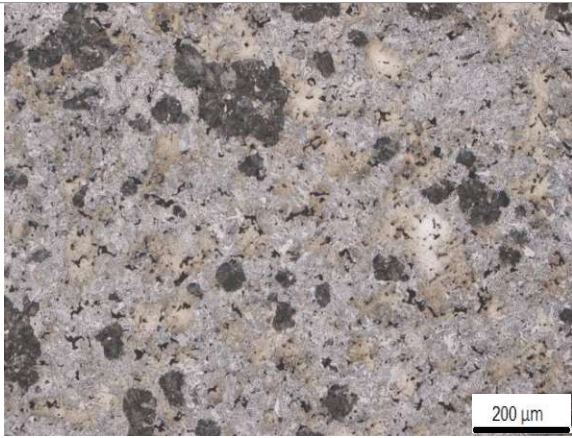
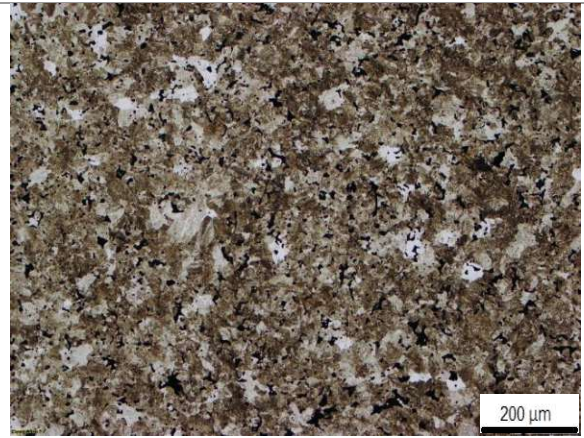


Figure 4.17: OM etched microstructures of CrA-Ni-C steels, compacted at 700 MPa, sintered 60 min at 1250 °C in N₂-10% H₂, Nital, 100 x.

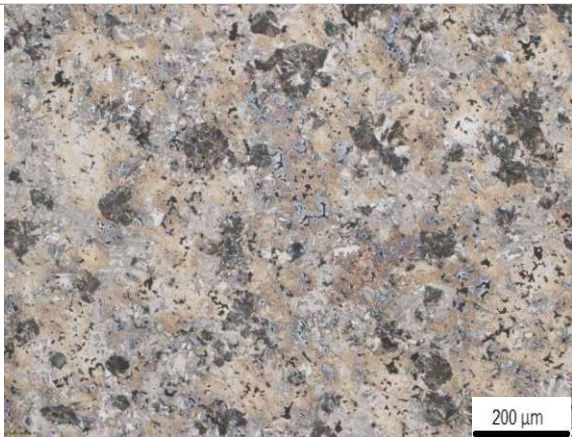
CrA-3Ni-0.4C, 266 HV30



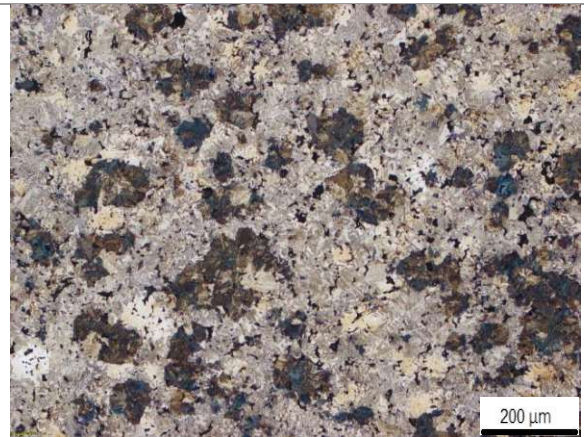
CrA-3Ni-0.5C, 295 HV30



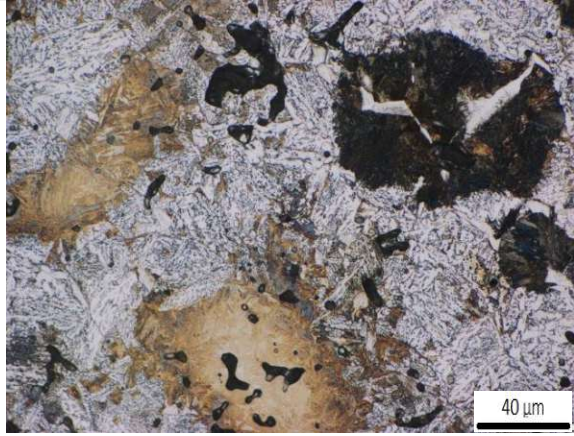
CrA-1Ni-0.6C, 216 HV30



CrA-3Ni-0.6C, 362 HV30

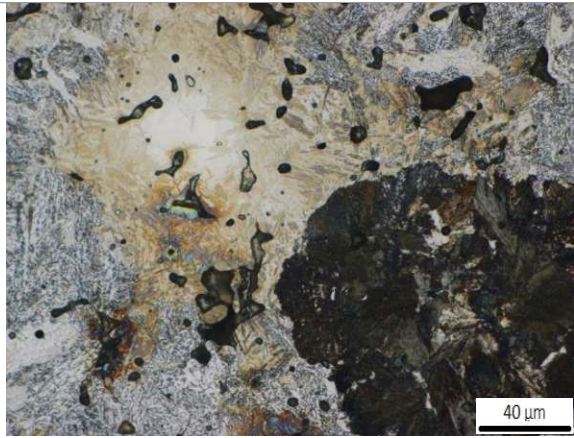


CrA-2Ni-0.6C, 268 HV30

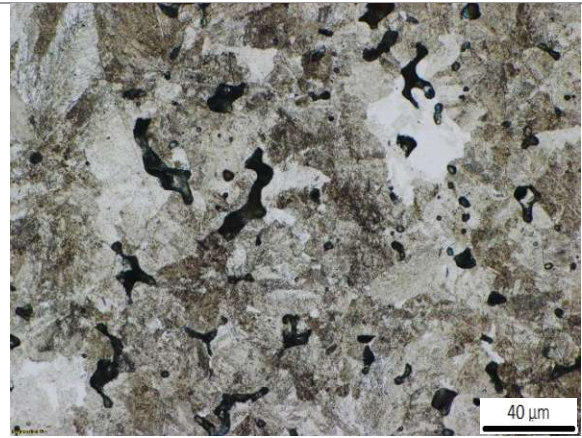


CrA-3Ni-0.4C

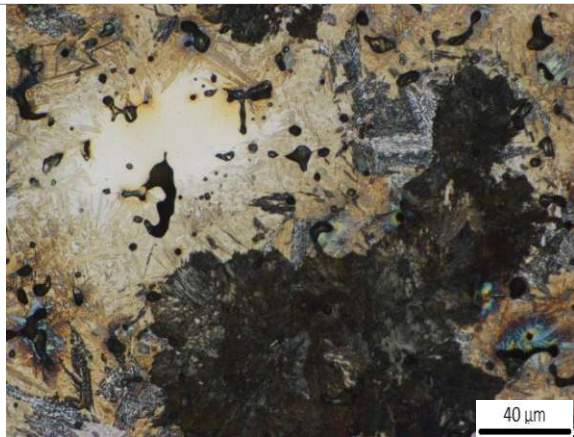
Figure 4.18: OM etched microstructures of CrA-Ni-C, compacted at 700 MPa, sintered 60 min at 1250 °C in N₂-10% H₂, Nital, 500 x.



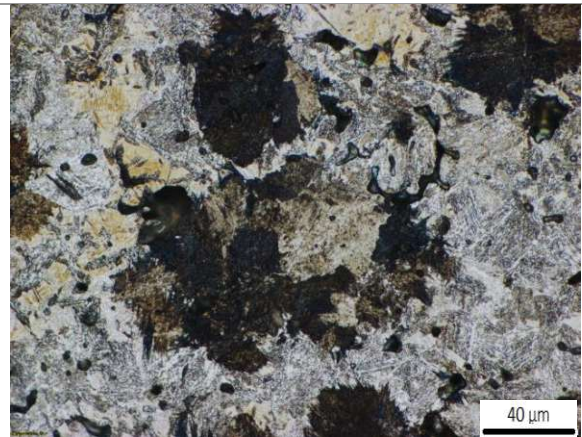
CrA-3Ni-0.5C



CrA-1Ni-0.6C



CrA-3Ni-0.6C



CrA-2Ni-0.6C

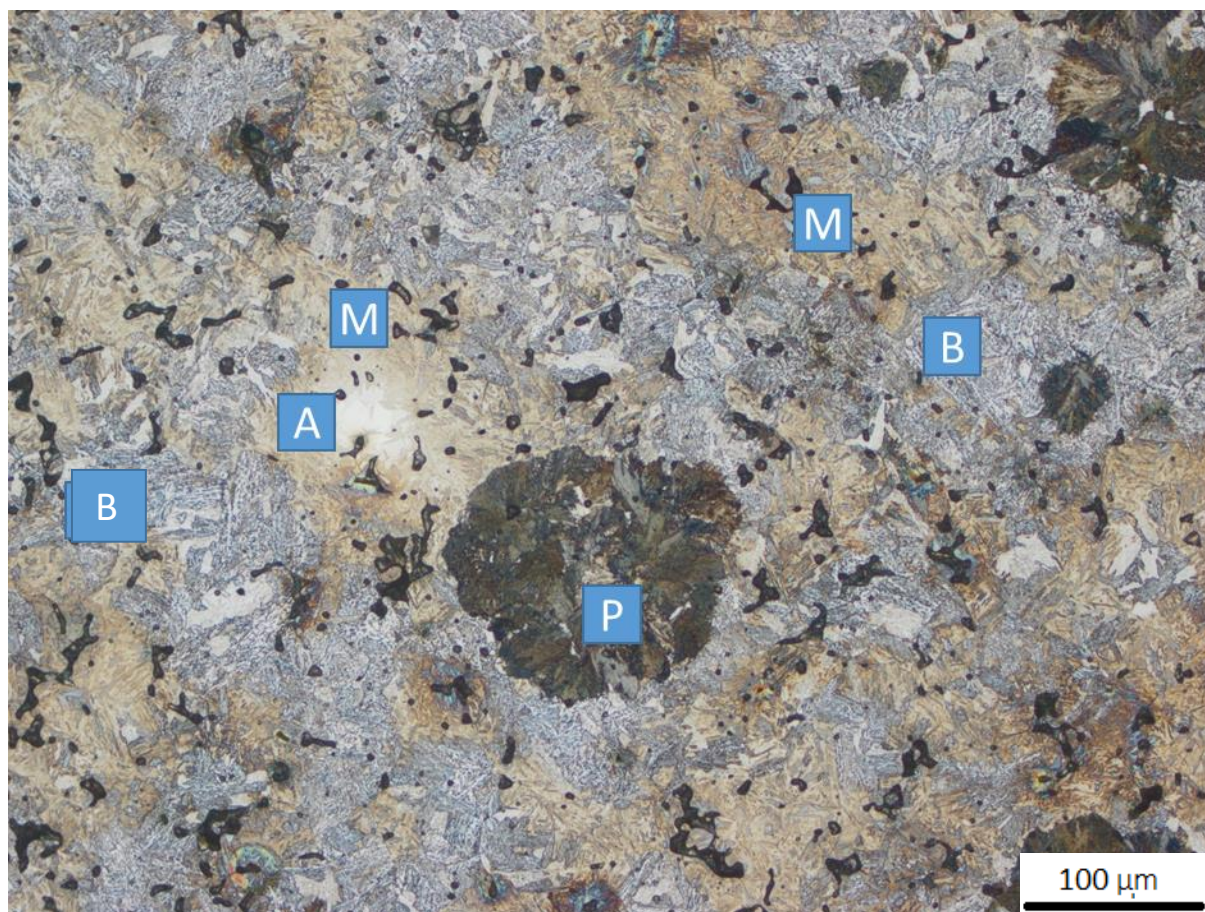


Figure 4.19: OM etched microstructure of CrA-3Ni-0.5C, compacted at 700 MPa, sintered 60 min at 1250°C in N₂-10% H₂, Nital, 500 x (A: Austenite, B: Bainite, P: Pearlite, M: Martensite); apparent hardness: 295 HV₃₀.

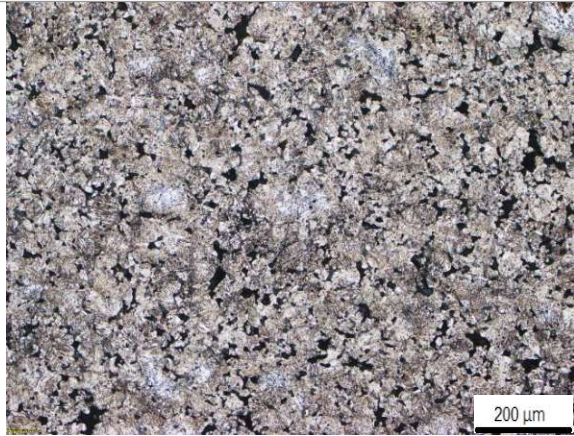
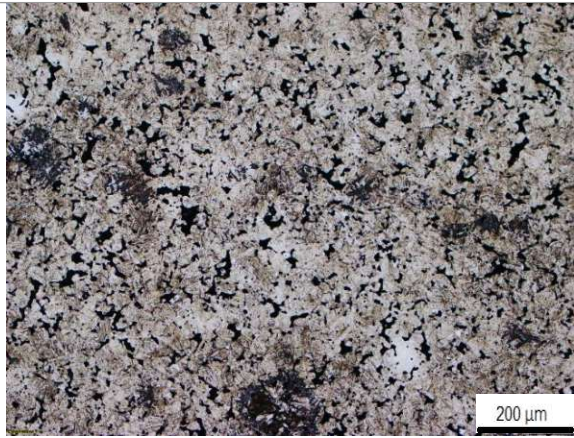
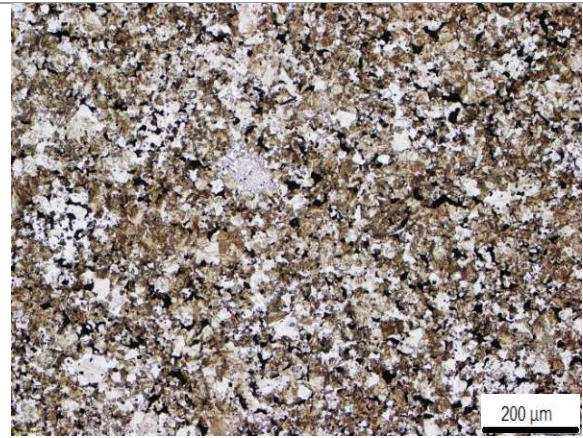


Figure 4.20: OM etched microstructures of CrA-Mn-C, compacted at 700 MPa, sintered 60 min at 1250 °C in N₂-10% H₂, Nital, 100 x.

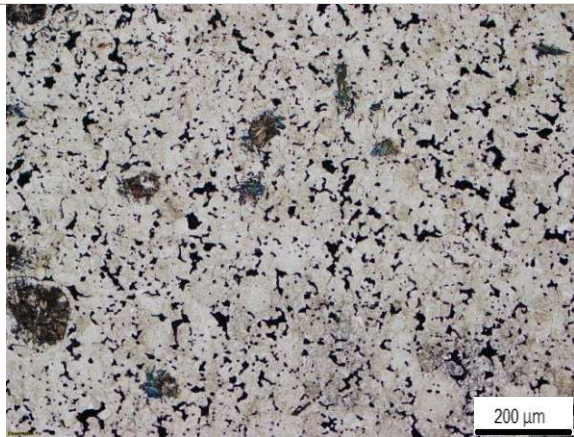
CrA-3Mn-0.4C, 301 HV30



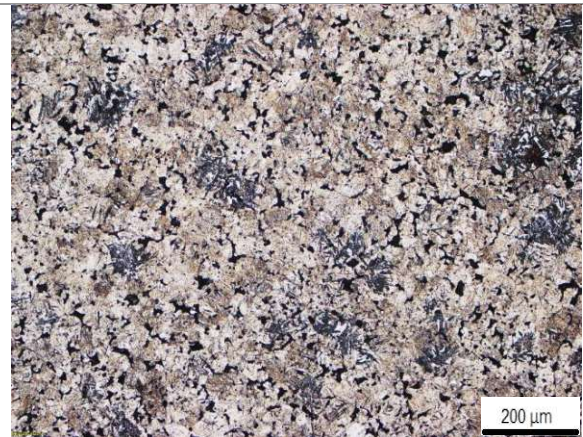
CrA-3Mn-0.5C, 363 HV30



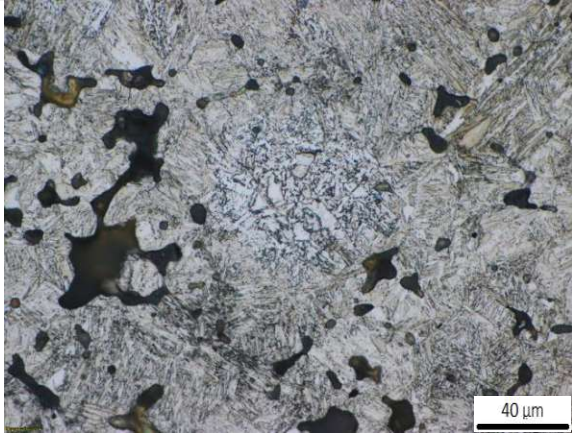
CrA-1Mn-0.6C, 254 HV30



CrA-3Mn-0.6C, 407HV30

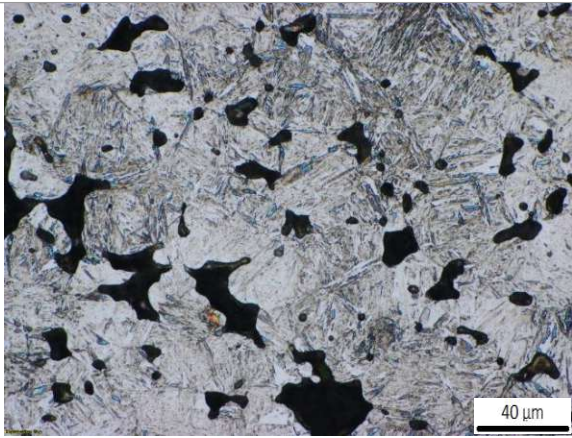


CrA-2Mn-0.6C, 398 HV30

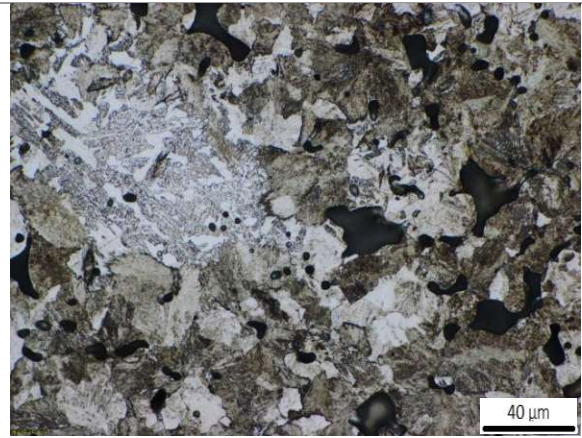


CrA-3Mn-0.4C

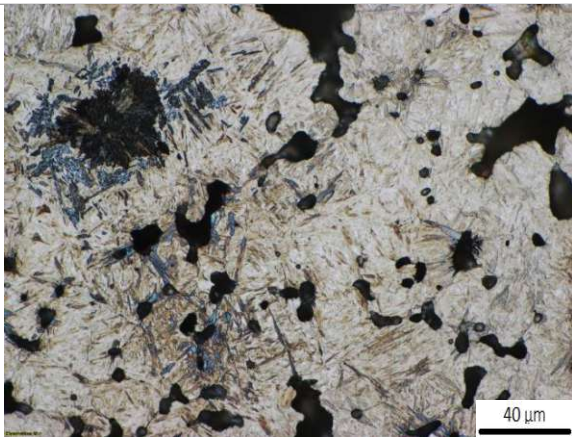
Figure 4.21: OM etched microstructures of CrA-Mn-C, compacted at 700 MPa, sintered 60 min at 1250 °C in N₂-10% H₂, Nital, 500 x.



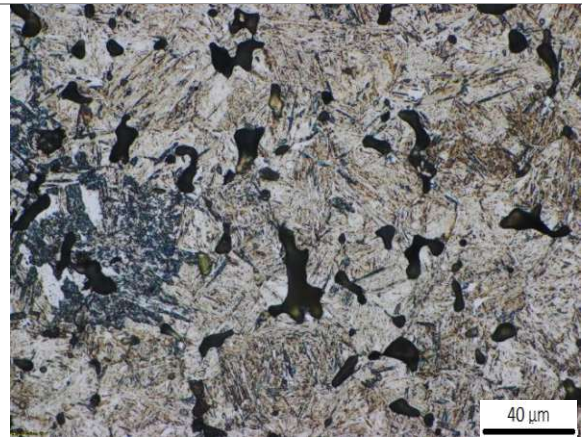
CrA-3Mn-0.5C



CrA-1Mn-0.6C



CrA-3Mn-0.6C



CrA-2Mn-0.6C

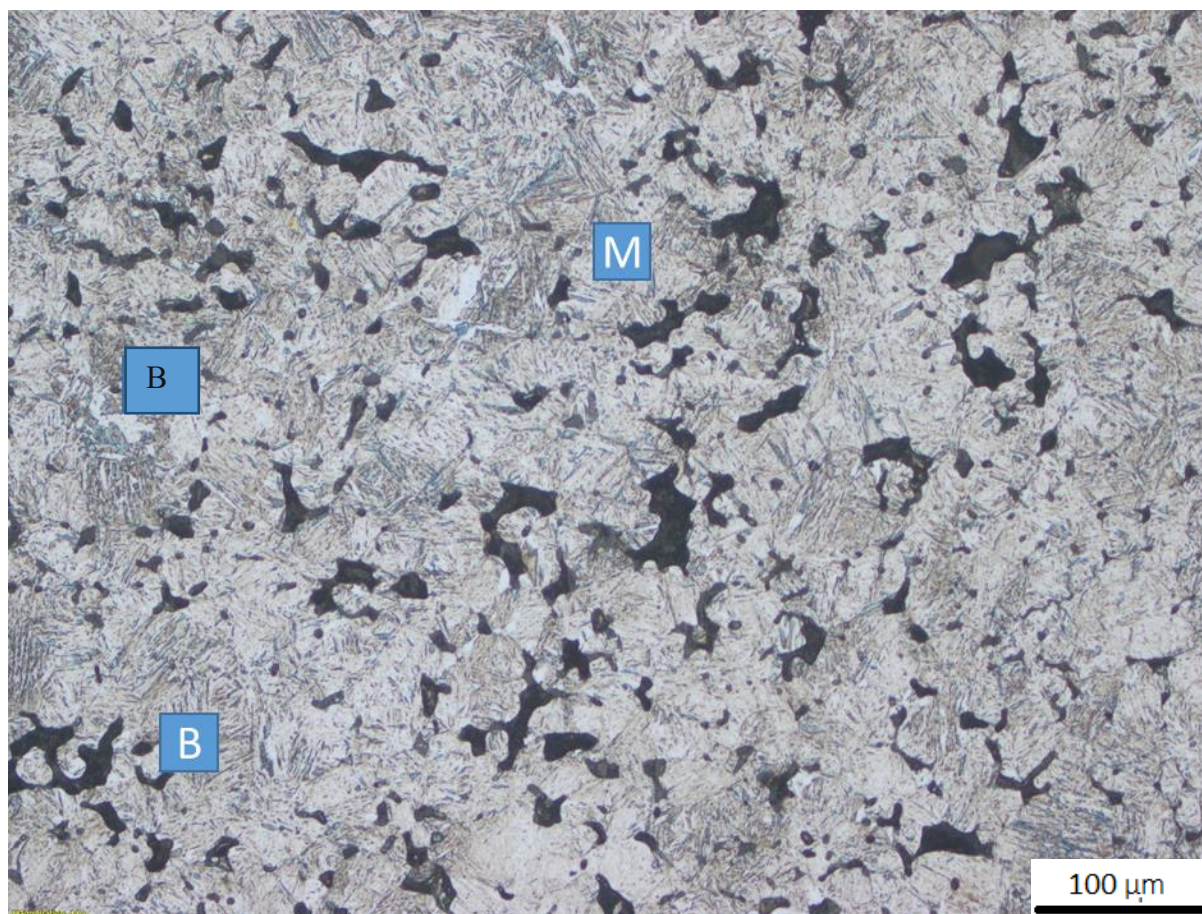
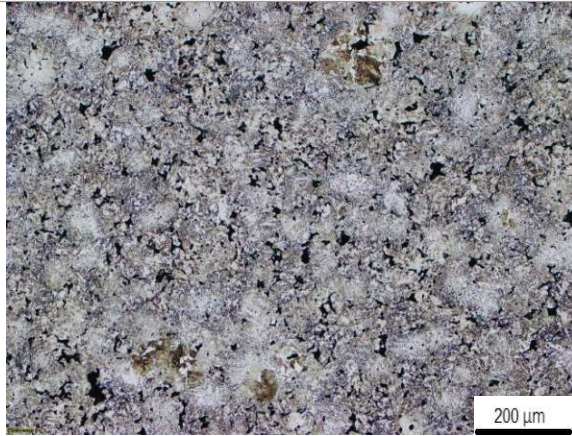
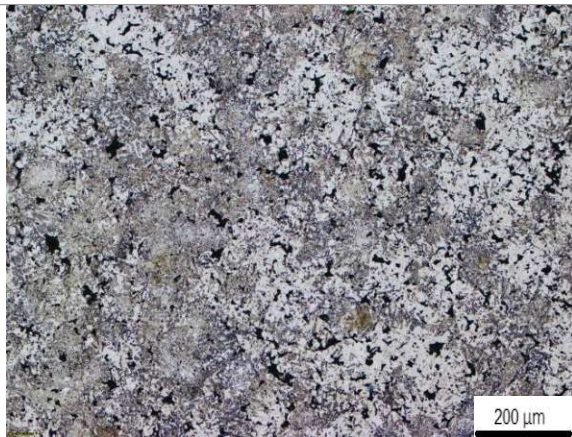


Figure 4.22: OM etched microstructure of CrA-3Mn-0.5C, sintered 60 min at 1250°C in N₂-10% H₂, Nital, 200 x (B: Bainite, M: Martensite); apparent hardness: 363 HV30.

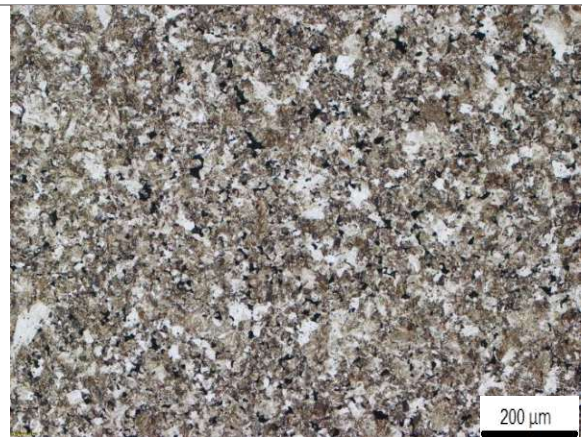


CrA-4MA-0.4C, 276 HV30

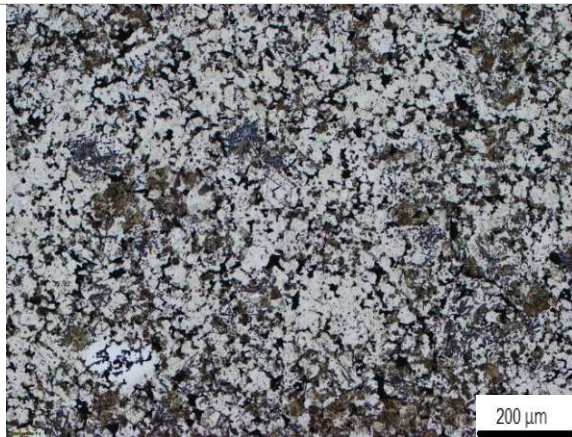
Figure 4.23: OM etched microstructures of CrA-MA-C, compacted at 700 MPa, sintered 60 min at 1250 °C in N₂-10% H₂, Nital, 100 x.



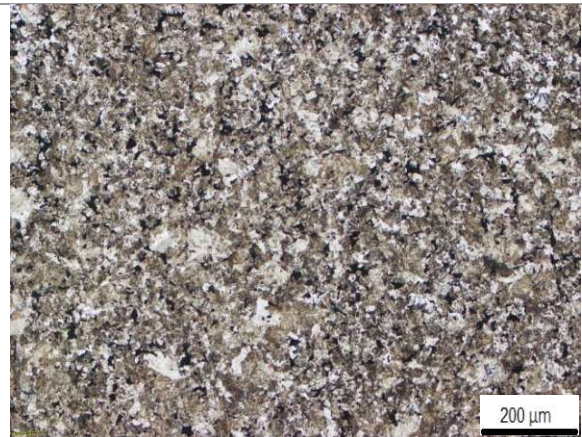
CrA-4MA-0.5C, 337 HV30



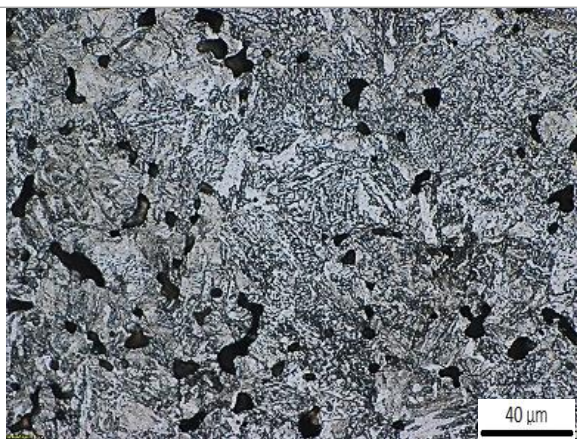
CrA-2MA-0.6C, 217 HV30



CrA-4MA-0.6C, 381 HV30

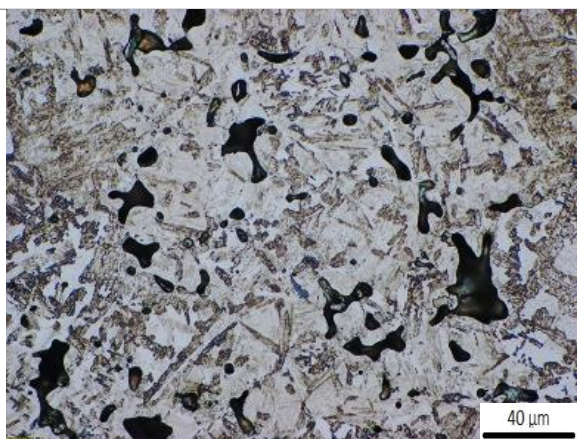


CrA-3MA-0.6C, 228 HV30

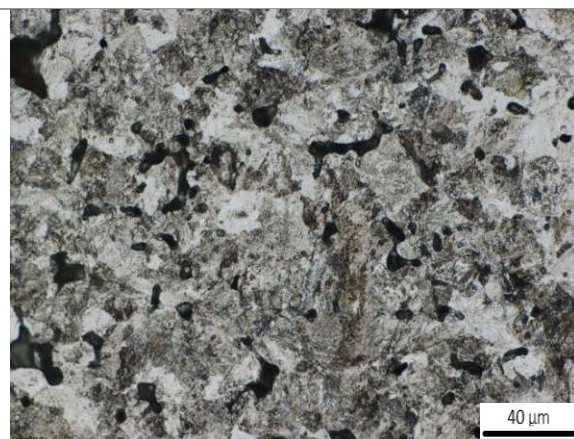


CrA-4MA-0.4C

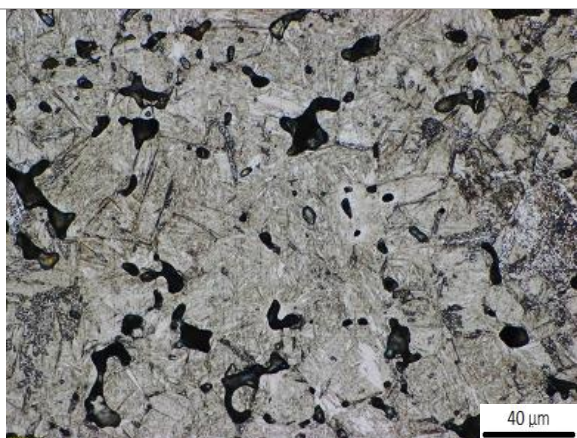
Figure 4.24: OM etched microstructures of CrA-MA-C, compacted at 700 MPa, sintered 60 min at 1250 °C in N₂-10% H₂, Nital, 500 x.



CrA-4MA-0.5C



CrA-2MA-0.6C



CrA-4MA-0.6C



CrA-3MA-0.6C

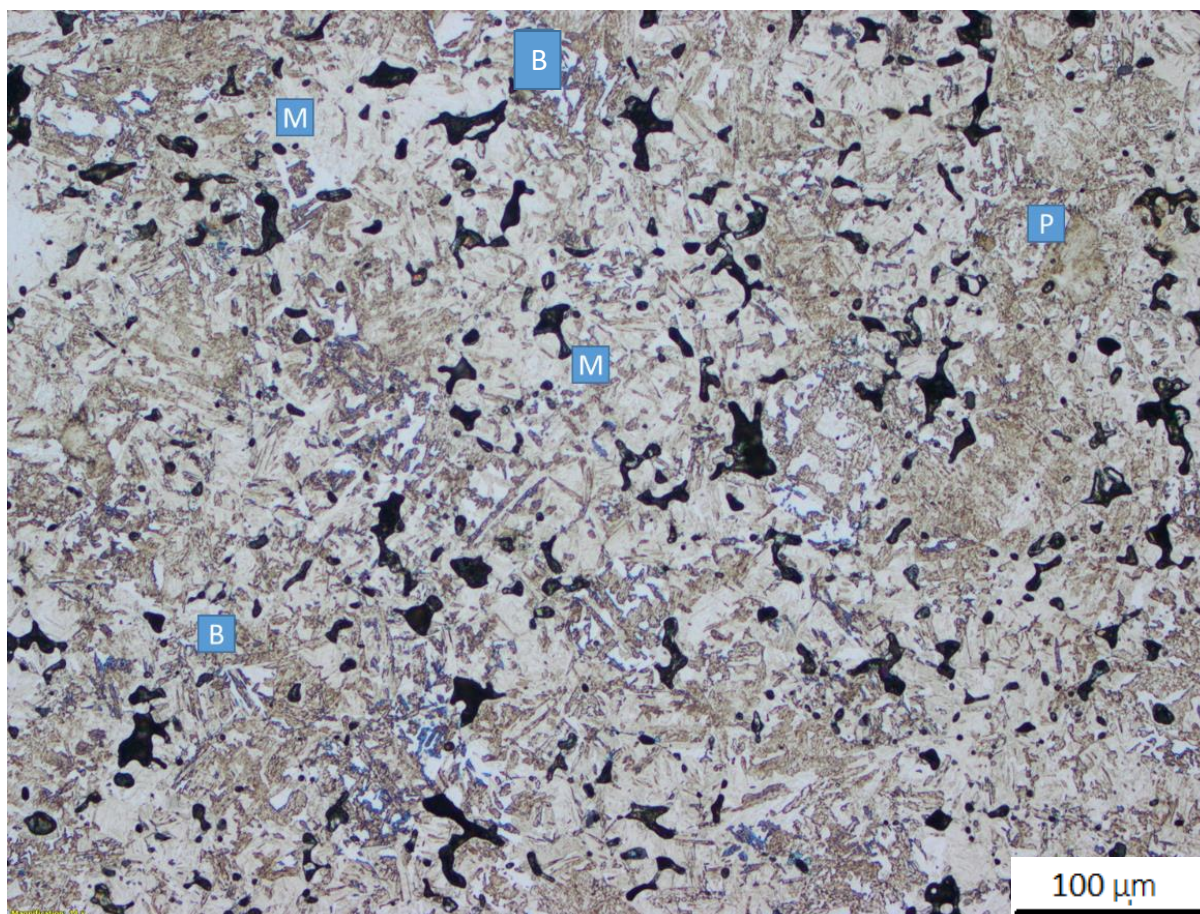


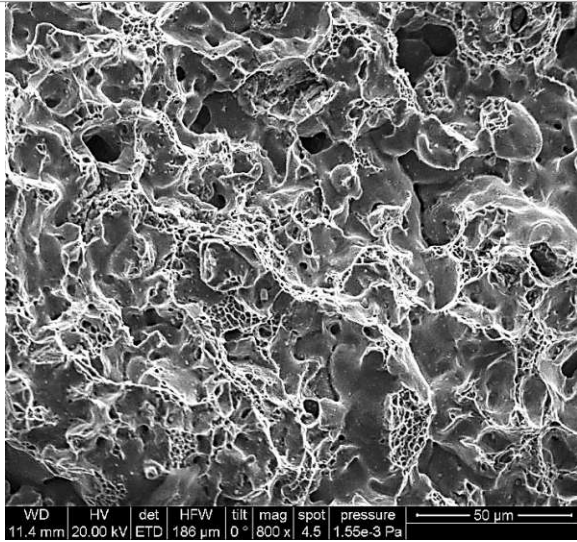
Figure 4.25: OM etched microstructure of CrA-4MA-0.5C, compacted at 700 MPa, sintered 60 min at 1250 °C in N₂-10% H₂, Nital, 200 x (B: Bainite, P: Pearlite, M: Martensite); apparent hardness: 337 HV30.

4.4. Fractography

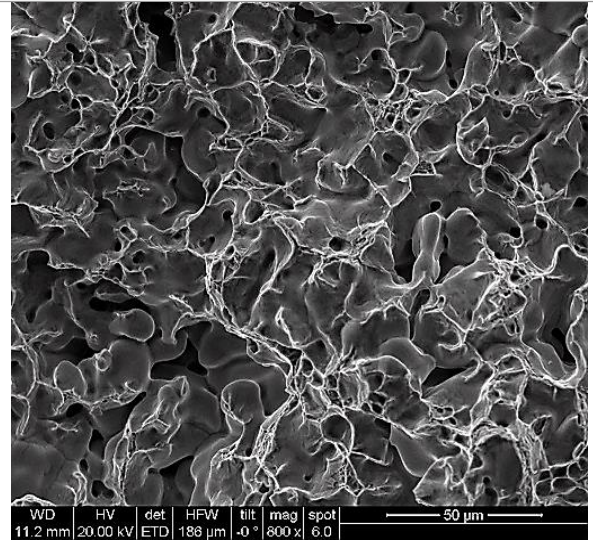
Fractographs of the steels are shown in Figure 4.26 to 4.29. In Figure 4.26, CrA and CrA-C steels are presented, and as can be seen, transgranular ductile dimple fracture is the dominant mechanism in these steels. It is evident that the CrA steel, despite having higher oxygen content compared to the carbon-containing grades, showed higher impact energy, while addition of carbon and the resulting increase in hardness resulted in lower impact energy; however, the fracture mechanism is still ductile. In case of Ni alloying (Figure 4.27), the steel with 1% Ni shows entirely ductile dimple fracture, more or less similar to the CrA-C system, while increasing the Ni content to 2% resulted in some cleavage facets in the fracture surface and also a lower IE. The steels with 3% Ni also show a mix of the dimple and cleavage facets in the fracture surfaces. It is evident that the fraction of cleavage facets increased with higher carbon content. The fracture surfaces of the Mn steels are presented in Figure 4.28. The results indicate that addition of 1% Mn to CrA yielded a mixture of dimple and cleavage transgranular facets which also negatively affected the impact behaviour compared to CrA-C alloys. In the steel containing 2% Mn, the fracture surface is covered mainly by transgranular cleavage facets. In the steels containing 3% Mn, the fracture mode changed from the transgranular to intergranular with increasing carbon content.

A possible reason for this behaviour of the steel could be attributed to the secondary pores which got larger with increasing carbon and Mn contents. Another reason also could be related to the brittleness of the boundaries which are enriched with Mn and oxygen as shown by Eduard Hryha [94], he also explains this such that the high Mn content in the grain boundaries reacts there with the surface oxygen present, forming interfacial oxides, which embrittles steels alloyed with admixed elemental Mn.

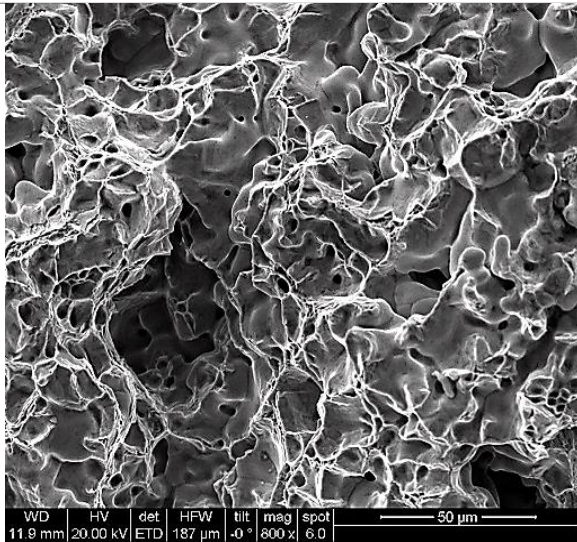
The fracture surfaces of the MA alloyed steels are presented in Figure 4.29. The figure shows that in the steel containing 2 % MA, the fracture mechanism is mostly ductile and dimple transgranular. Increasing the MA to 3% caused a mixture of dimple and cleavage transgranular facets which also reduced the impact energy. Addition of 4% MA to CrA results in cleavage in addition to the dimple structures even at lower carbon content of 0.4%. At higher carbon content the fraction of the cleavage facets increased. The results also show that in 4 % MA alloyed steels, unlike the Mn alloyed ones, the fractures are mostly transgranular which led to higher impact energies. These results are also in good agreement with Hryha's work [94], who showed that even changing from elemental Mn to Ferro-Mn with 80% Mn lowers the tendency to intergranular failure.



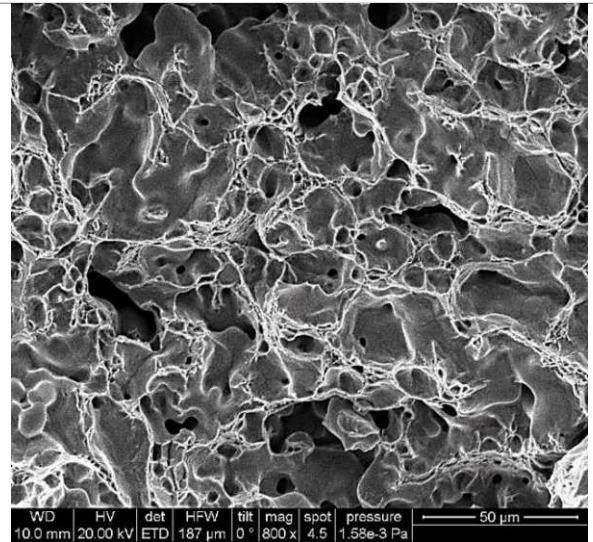
CrA (O Content = 0.029%,
IE = 55.0 J.cm⁻²)



CrA-0.4C (O Content = 0.013%,
IE = 44.7 J.cm⁻²)

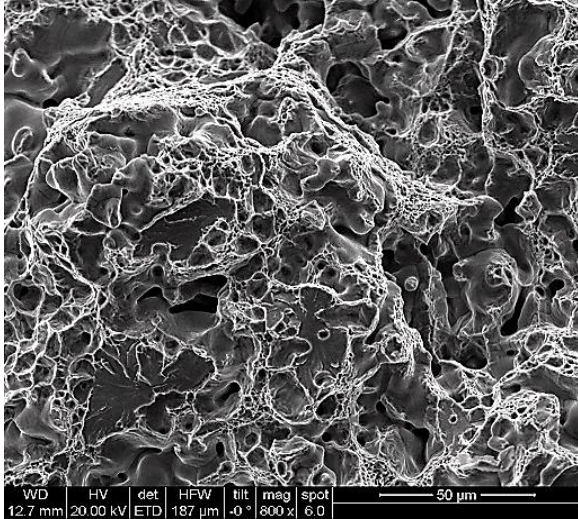


CrA-0.5C (O Content = 0.011%,
IE = 39.9 J.cm⁻²)



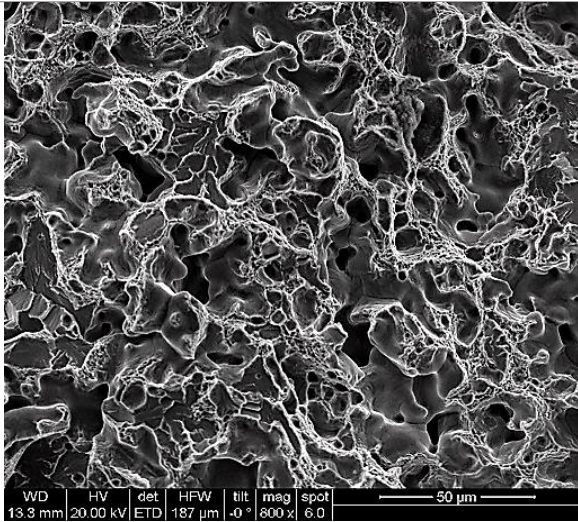
CrA-0.6C (O Content = 0.014%,
IE = 37.6 J.cm⁻²)

Figure 4.26: Fracture surfaces of CrA and CrA-C steels, compacted at 700 MPa, sintered 60 min at 1250 °C in N₂-10 % H₂, broken by Charpy impact test at room temperature, SEM 800x.

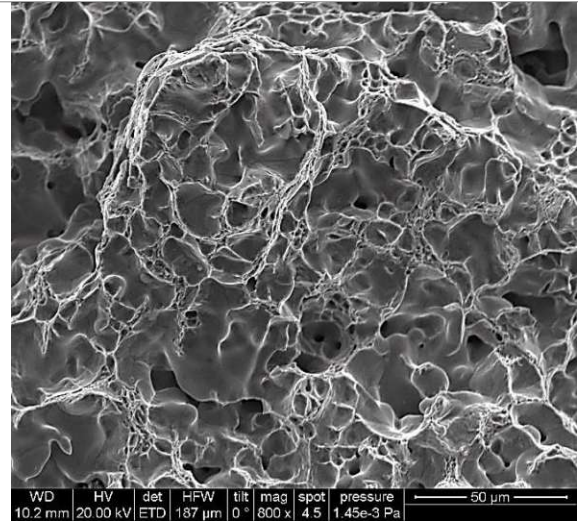


CrA-3Ni-0.4C (O Content = 0.011%,
IE = 42.7 J.cm⁻²)

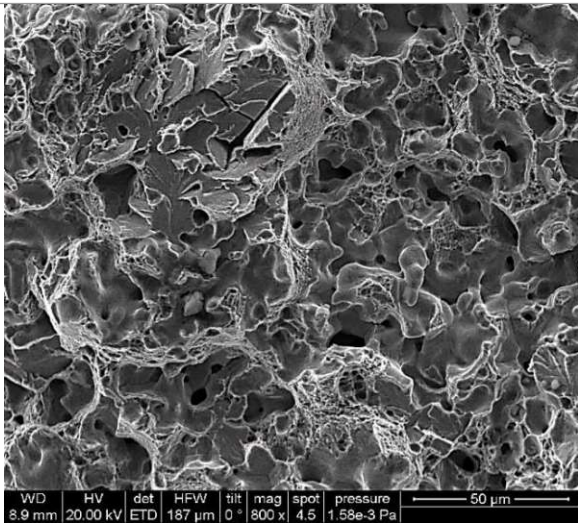
Figure 4.27: Fracture surfaces of CrA-Ni-C, compacted at 700 MPa, sintered 60 min at 1250 °C in N₂-10% H₂, broken by Charpy impact test at room temperature, SEM 800 x.



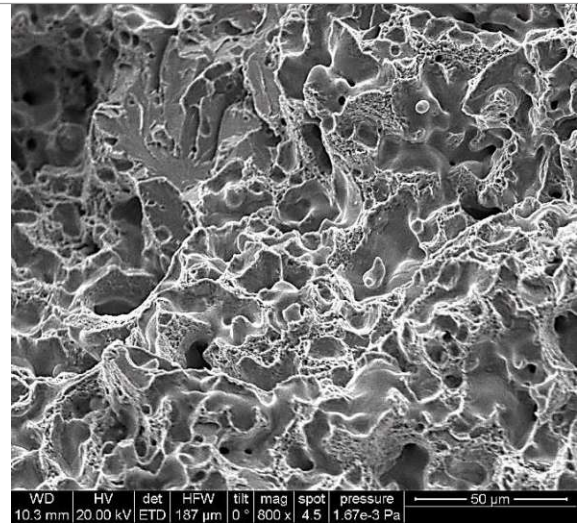
CrA-3Ni-0.5C (O Content = 0.014%,
IE = 42.1 J.cm⁻²)



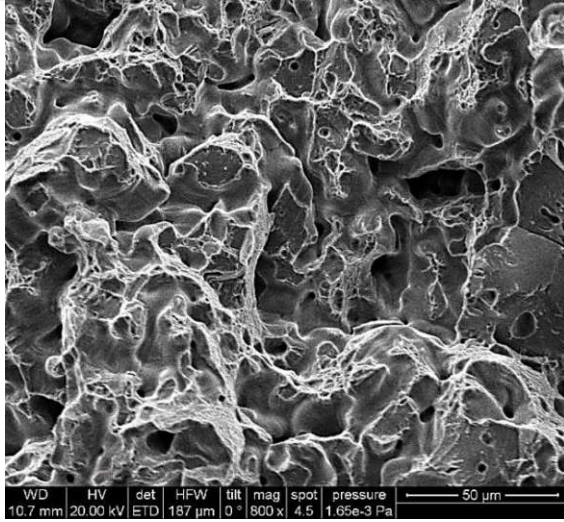
CrA-1Ni-0.6C (O Content = 0.008%,
IE = 42.3 J.cm⁻²)



CrA-3Ni-0.6C (O Content = 0.009%,
IE = 33.3 J.cm⁻²)

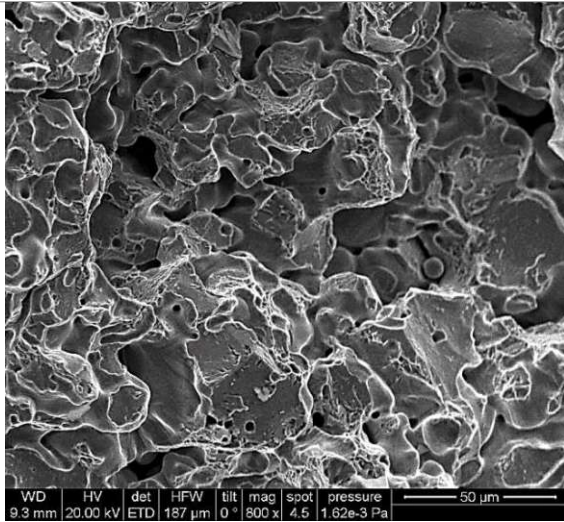


CrA-2Ni-0.6C (O Content = 0.009%,
IE = 34.3 J.cm⁻²)

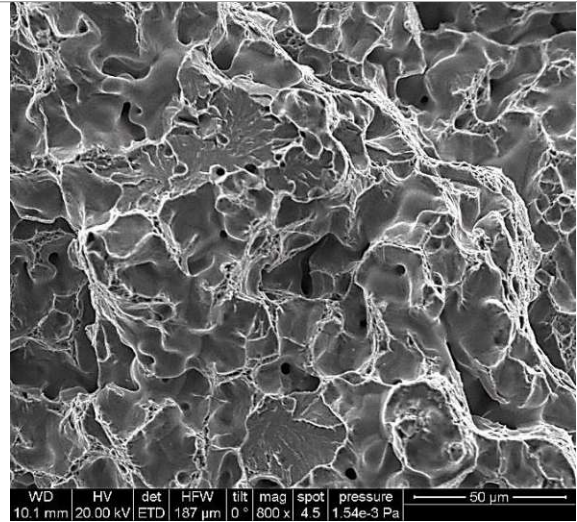


CrA-3Mn-0.4C (O Content = 0.017%,
IE = 17.6 J.cm⁻²)

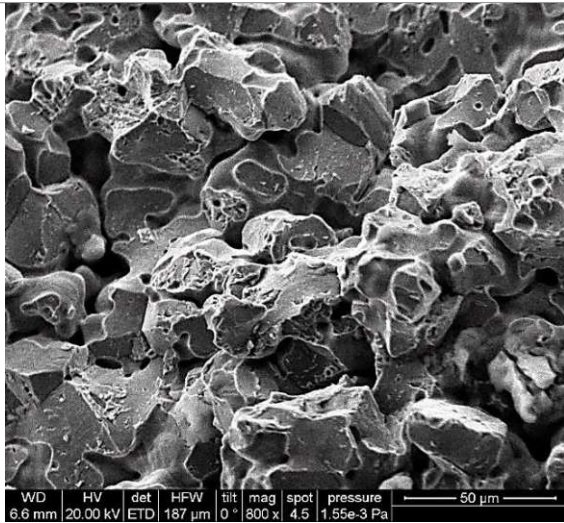
Figure 4.28: Fracture surfaces of CrA-Mn-C, compacted at 700 MPa, sintered 60 min in N₂-10% H₂ at 1250 °C, broken by Charpy impact test at room temperature, SEM 800x.



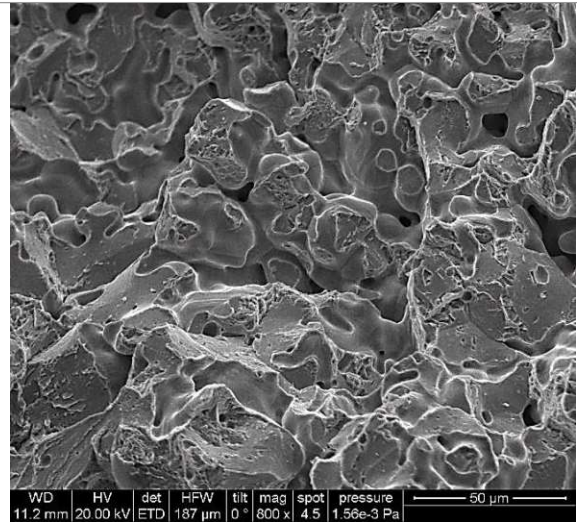
CrA-3Mn-0.5C (O Content = 0.017%,
IE = 13.4 J.cm⁻²)



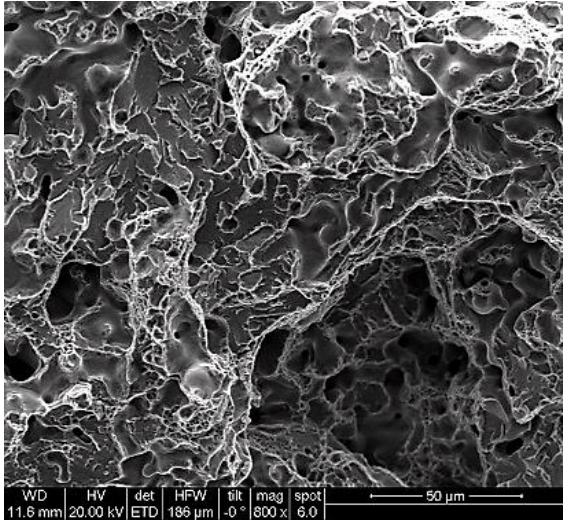
CrA-1Mn-0.6C (O Content = 0.009%,
IE = 25.0 J.cm⁻²)



CrA-3Mn-0.6C (O Content = 0.011%,
IE = 5.8 J.cm⁻²)

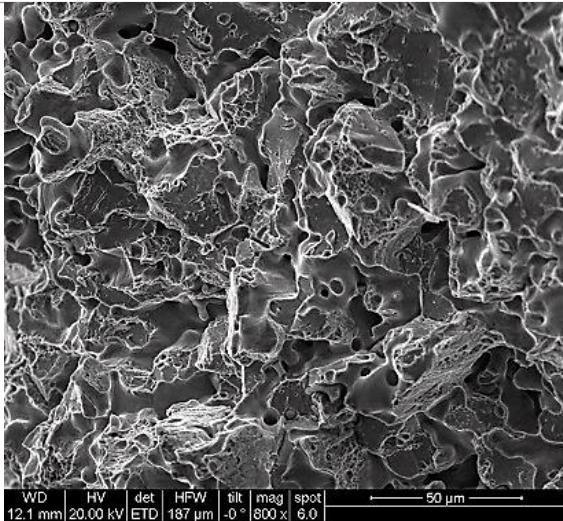


CrA-2Mn-0.6C (O Content = 0.011%, IE =
13.2 J.cm⁻²)

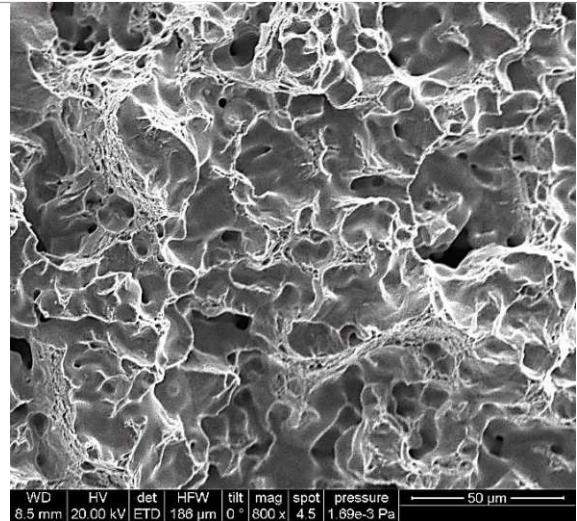


CrA-4MA-0.4C (O Content = 0.027%,
IE = 32.5 J.cm⁻²)

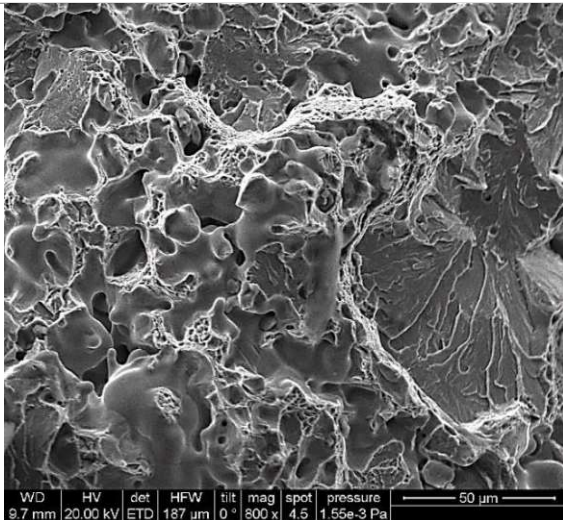
Figure 4.29: Fracture surfaces of CrA-MA-C, compacted at 700 MPa, sintered 60 min at 1250 °C in N₂-10% H₂, broken by Charpy impact test at room temperature, SEM 800x.



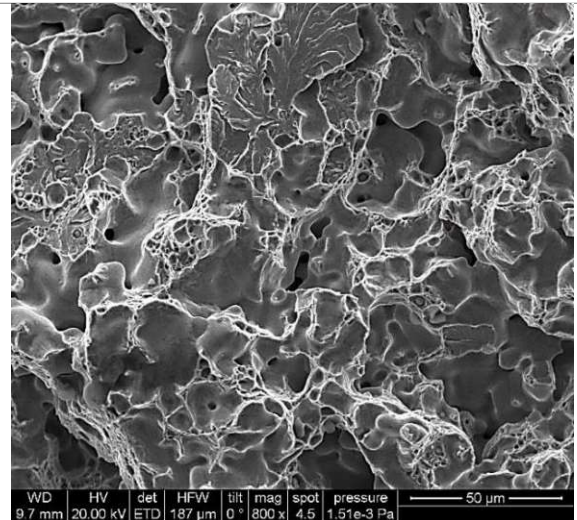
CrA-4MA-0.5C (O Content = 0.025%,
IE = 30.3 J.cm⁻²)



CrA-2MA-0.6C (O Content = 0.013%,
IE = 35.2 J.cm⁻²)



CrA-4MA-0.6C (O Content = 0.023%,
IE = 22.6 J.cm⁻²)



CrA-3MA-0.6C (O Content = 0.021%,
IE = 28.5 J.cm⁻²)

4.5. Dimensional change and sintered density

Data for the dimensional change as well as the sintered density of the steels are presented through Figures 4.30 to 4.33, and the measured values are listed in Table 4.5. The results show that sintering of plain CrA steel at 1250°C led to only slight shrinkage, which indicates a good dimensional stability of the steel. Addition of carbon to the system increased the shrinkage values and dimensional changes, however the sintered densities (presented in Figure 4.32) do not show significant difference compared to CrA steel. Addition of Ni led to significant shrinkage (and resulting densification), which increased with higher Ni content. Increasing the carbon content in this system resulted in higher shrinkage, as shown in Figure 4.30. In contrast to Ni, addition of Mn has a negative effect on the shrinkage and densification process. Even at 1% Mn, the shrinkage of the steel is reduced significantly compared to the CrA-C system, and addition of 3%Mn resulted in about 0.3 % positive dimensional change or swelling, which also lowered the final sintered density. This is the consequence of the “one-way” homogenization of Mn through the gas phase, and it agrees well with previous studies that showed the effect of this alloying element on the swelling behaviour of PM steels [42, 46]. Higher carbon content intensified this effect of manganese. In CrA-MA-C alloys, the results show that addition of MA reduced the shrinkage of the steel, the more, the higher the MA content was. However, in contrast to Mn alloyed steels, MA does not cause swelling even in case of 4% added. In this case, similar to CrA-Mn-C, higher carbon content reduced shrinkage of the steel.

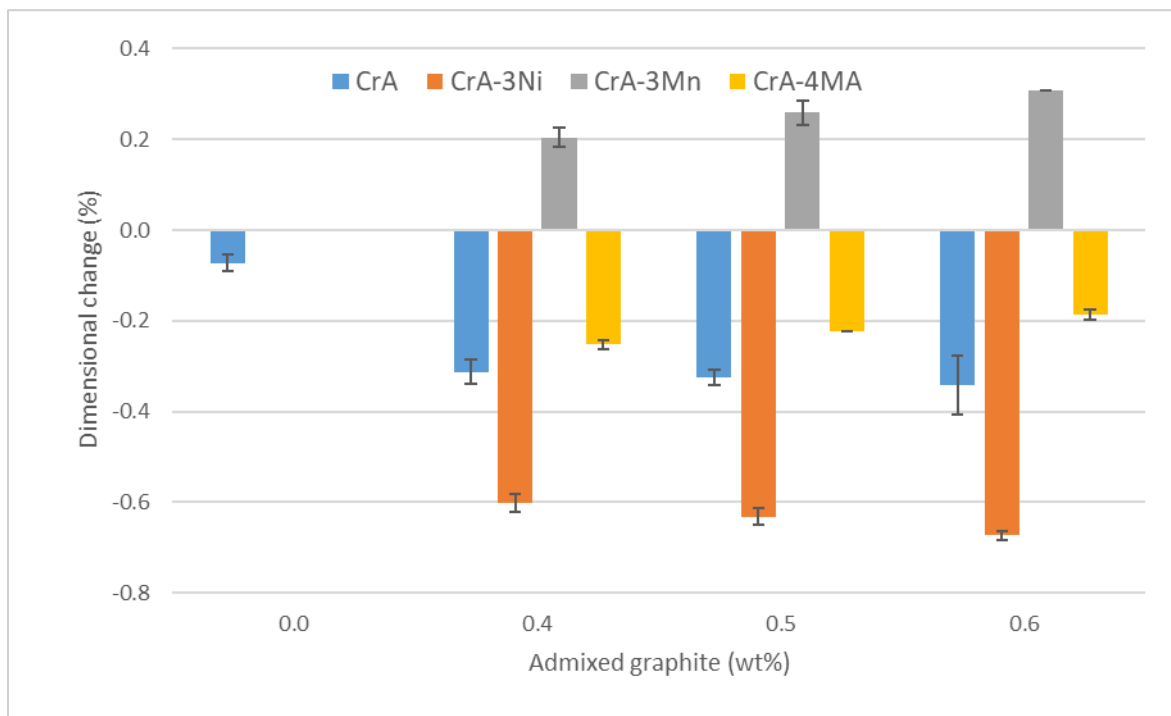


Figure 4.30: Dimensional change of steels with different levels of admixed carbon, compacted at 700 MPa, sintered 60 min at 1250 °C in N₂-10% H₂.

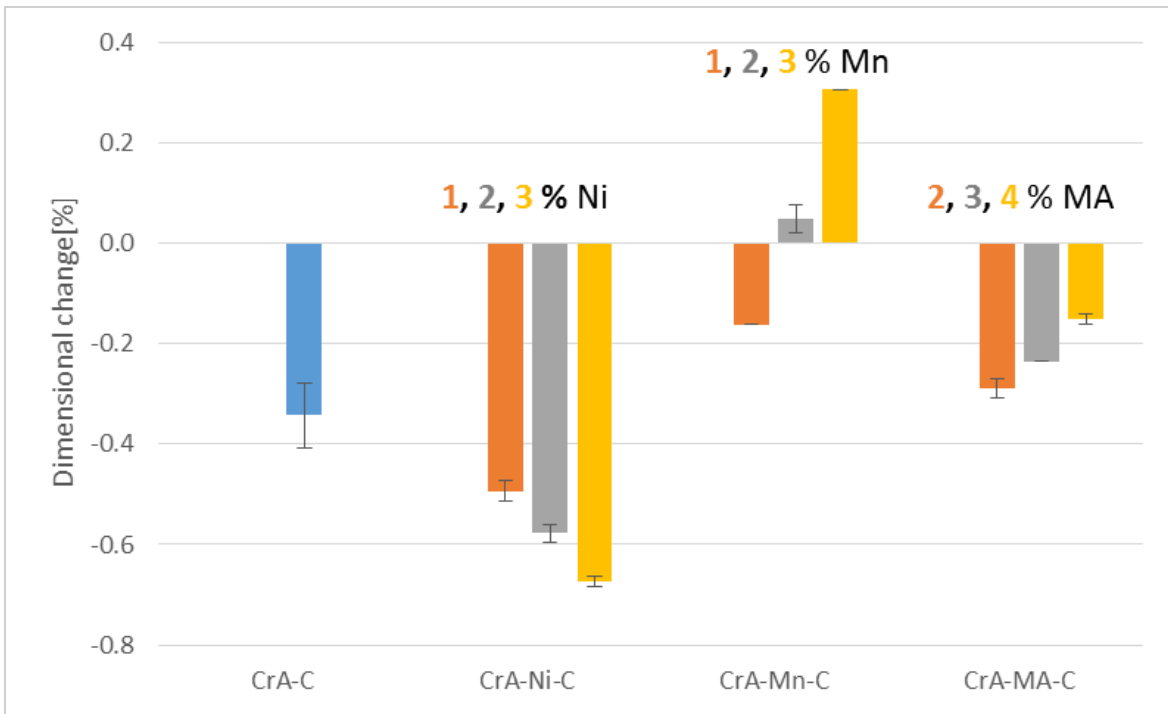


Figure 4.31: Dimensional change of steels with 0.6% admixed carbon, compacted at 700 MPa, sintered 60 min at 1250 °C in N₂-10% H₂.

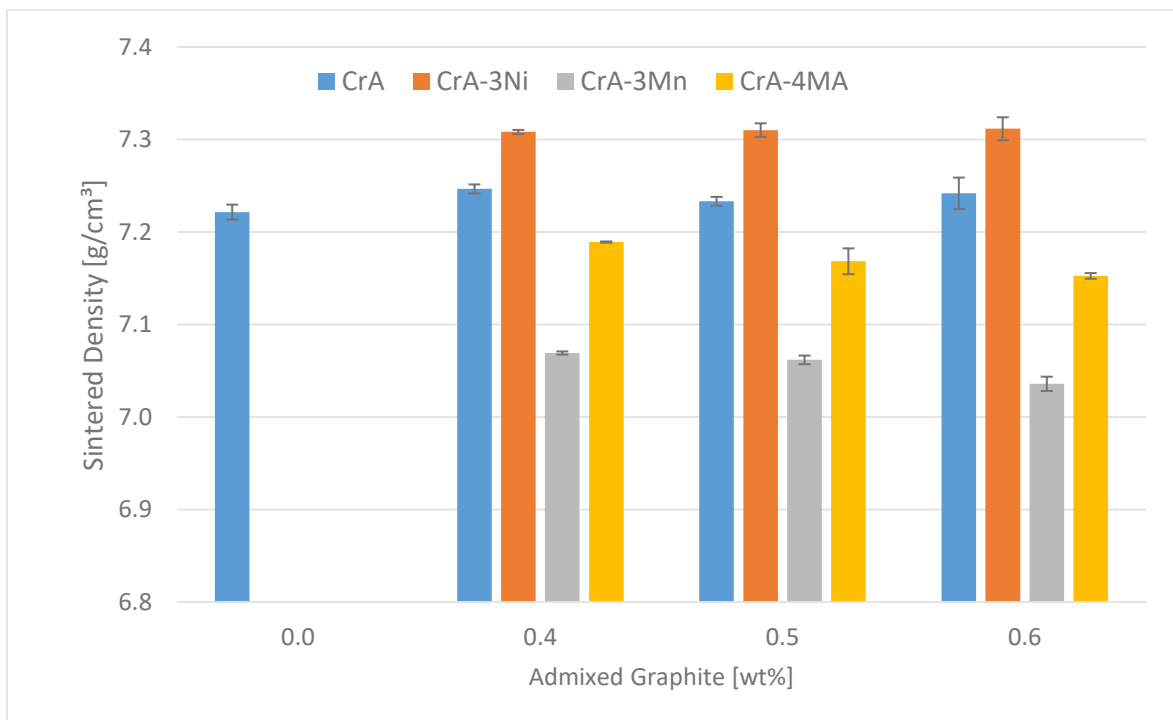


Figure 4.32: Sintered density of steels with different levels of admixed carbon, compacted at 700 MPa, sintered 60 min at 1250 °C in N₂-10% H₂.

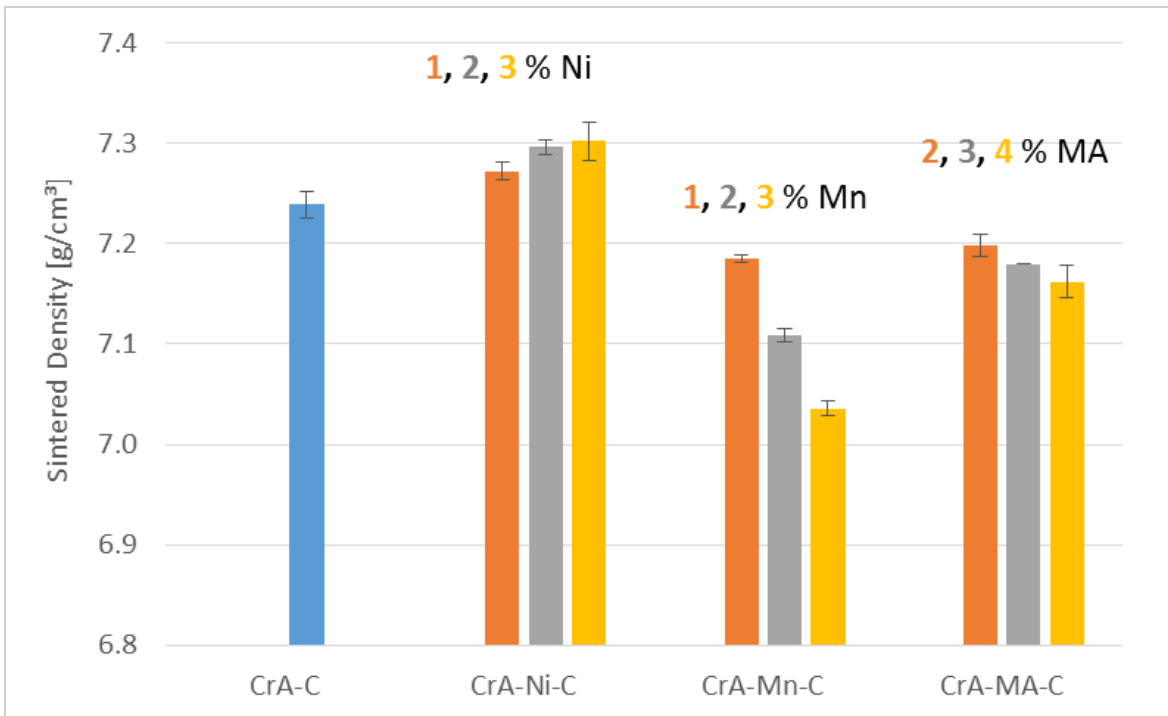


Figure 4.33: Sintered density of steels with 0.6% admixed carbon, compacted at 700 MPa, sintered 60 min at 1250 °C in N₂-10% H₂.

Table 4.5: As-sintered properties of steels, sintered 60 min at 1250 °C in N₂-10% H₂.

	Ni (wt %)	Mn (wt %)	MA (wt %)	C (wt %)	Green density (g/cm ³)	sintered density (g/cm ³)	Dimensional Change (%)
Fe-Cr-C	0	7.07 ± 0.01	7.22 ± 0.01	-0.07 ± 0.02
	0.4	7.06 ± 0.01	7.25 ± 0.00	-0.31 ± 0.03
	0.5	7.05 ± 0.01	7.23 ± 0.00	-0.32 ± 0.02
	0.6	7.05 ± 0.01	7.24 ± 0.01	-0.34 ± 0.07
Fe-Cr-Ni-C	1	0.6	7.06 ± 0.01	7.27 ± 0.01	-0.49 ± 0.02
	2	0.6	7.07 ± 0.01	7.30 ± 0.01	-0.58 ± 0.02
	3	0.4	7.09 ± 0.01	7.31 ± 0.00	-0.60 ± 0.02
				0.5	7.08 ± 0.01	7.31 ± 0.01	-0.63 ± 0.02
			0.6	7.08 ± 0.01	7.31 ± 0.02	-0.67 ± 0.01	
Fe-Cr-Mn-C	...	1	...	0.6	7.05 ± 0.01	7.18 ± 0.00	-0.16 ± 0.00
	...	2	...	0.6	7.04 ± 0.01	7.11 ± 0.01	0.05 ± 0.03
	...	3	...	0.4	7.04 ± 0.01	7.07 ± 0.00	0.20 ± 0.02
				0.5	7.04 ± 0.01	7.06 ± 0.00	0.26 ± 0.03
			0.6	7.03 ± 0.00	7.04 ± 0.01	0.31 ± 0.00	
Fe-Cr-MA-C	2	0.6	7.04 ± 0.01	7.20 ± 0.01	-0.29 ± 0.02
	3	0.6	7.03 ± 0.00	7.18 ± 0.00	-0.23 ± 0.00
	4	0.4	7.04 ± 0.00	7.19 ± 0.00	-0.25 ± 0.03
				0.5	7.03 ± 0.01	7.17 ± 0.01	-0.22 ± 0.02
			0.6	7.03 ± 0.01	7.15 ± 0.00	-0.19 ± 0.01	

4.6. Mechanical properties

4.6.1. Hardness

The effect of the alloying elements on the as-sintered hardness of the steels is shown in Figure 4.34 and 4.35. It is evident that in all systems, increasing the carbon content increased the apparent hardness. In the CrA-C system this increase occurred mainly due to pearlite formation, as indicated by metallography. In the Ni alloyed steels, addition of this element resulted in a raise in hardness due to effect of the densification as well as formation of phases with higher hardness (martensite and bainite) as shown previously. The hardness value in this alloying system reached its maximum (362 HV30) after addition of 3% Ni and 0.6% C. The results also show that increasing the Mn to 2% led to a significant jump in the hardness, up to about 400 HV30, which is mainly due to martensite formation and is in good agreement with metallography. In the MA alloyed steels, the jump in the hardness was achieved in case of 4% MA and 0.6% C, which could be explained by the martensitic microstructure of steel at this

composition. In any case, at a content of 3-4% all alloying additives increased the apparent hardness by 100 to 160 HV compared to the respective CrA-C.

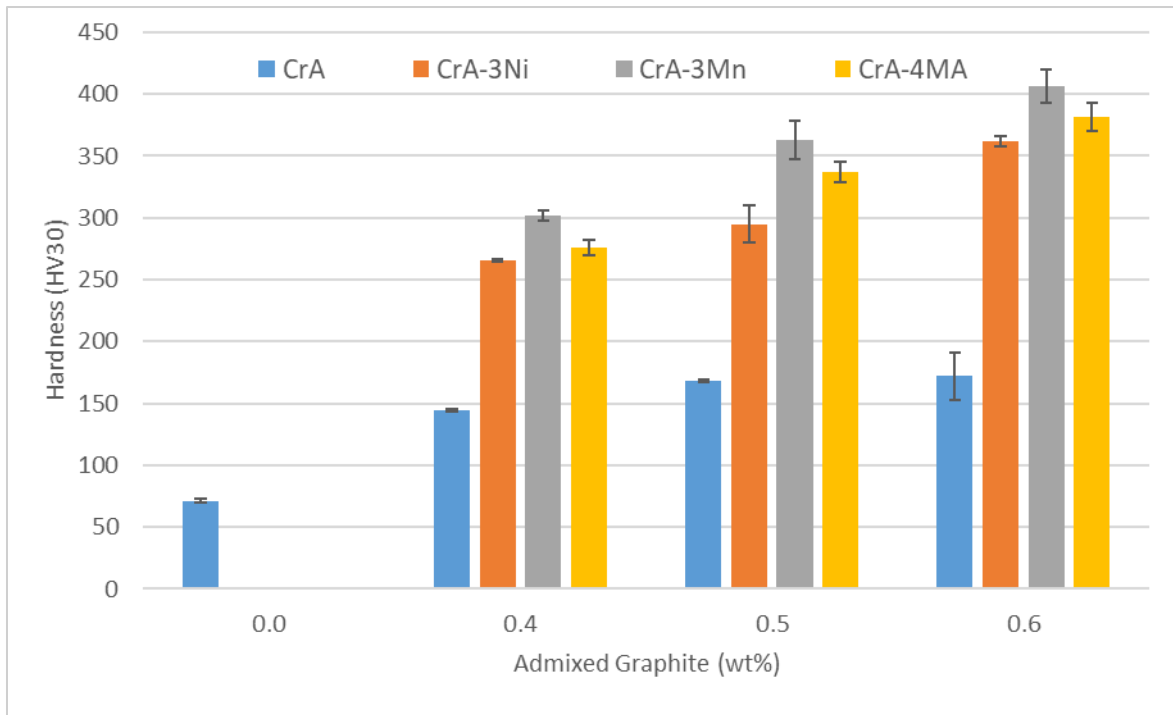


Figure 4.34: As-sintered hardness of steels with different levels of admixed carbon, compacted at 700 MPa, sintered 60 min at 1250 °C in N₂-10% H₂.

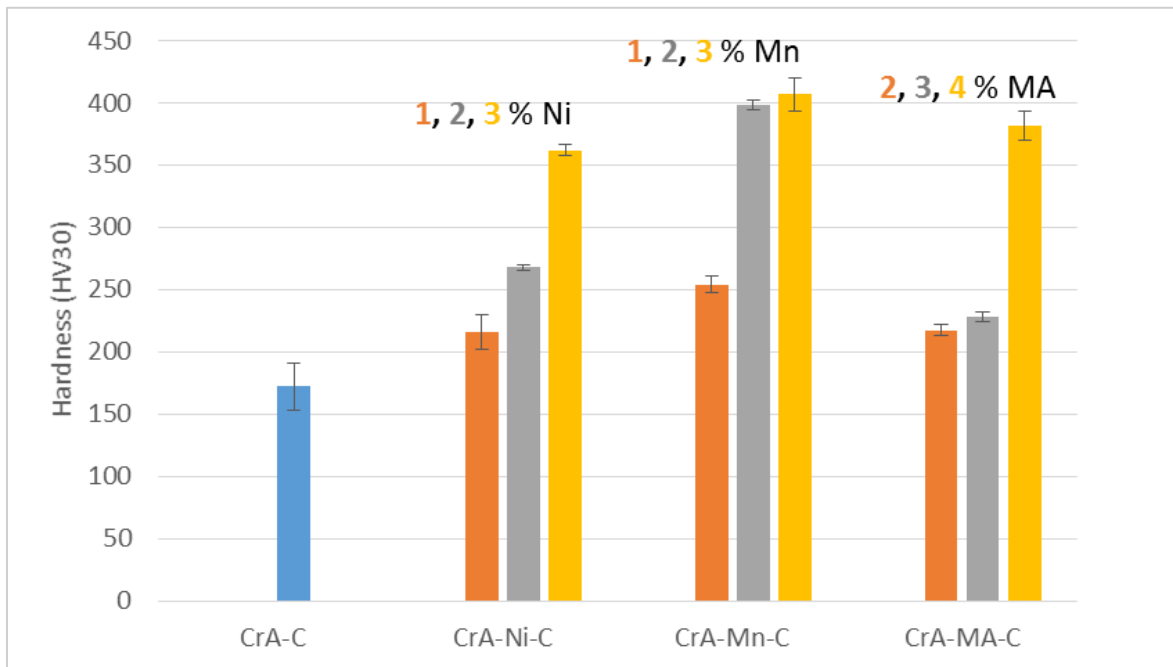


Figure 4.35: As-sintered hardness of steels with 0.6% admixed carbon, compacted at 700 MPa, sintered 60 min at 1250 °C in N₂-10% H₂.

4.6.2. Charpy impact energy

The Charpy impact energy data of the steels measured at room temperature are indicated in Figure 4.36 and 4.37. In Figure 4.36 the negative effect of carbon on the impact energy of the materials is clearly discernible. A reason for the lower impact energy could be the hardness which increased with higher carbon content.

Figure 4.37 shows the impact energy of the steels with different amounts of the alloying elements. Generally it is well known that Ni enhances shrinkage during sintering and improves the ductility without adversely affecting the strength. This effect is discernible in the impact energy of the steels after the addition of 1% Ni. Higher hardness of the steels with higher Ni content (as discussed already) only slightly reduced the impact energy of the material. Generally it is evident that the Ni alloyed steels present higher impact energy compared to the Mn and MA steels. The results also indicate that the introduction of Mn as elemental powder leads to a rather poor toughness, which gets worsened by increasing the Mn and carbon contents. In this case, in addition to the higher hardness of the Mn steels, the large secondary pores as well as brittleness at the Mn-enriched sites, which led to the brittle intergranular fracture, also can be regarded to be responsible for such low impact energies.

The impact energy data of the MA alloyed steel indicate that increasing the MA content lowered the impact energy as well, however these steels showed higher impact energy compared to the Mn alloyed steels, which can be related to the finer pores and also the transgranular fracture mechanism of this steel, which shows the formation of stronger bonds between the powder particles and in particular stronger grain boundaries. The relationships between hardness and impact energy of these steels are presented in Figure 4.38 and 4.39.

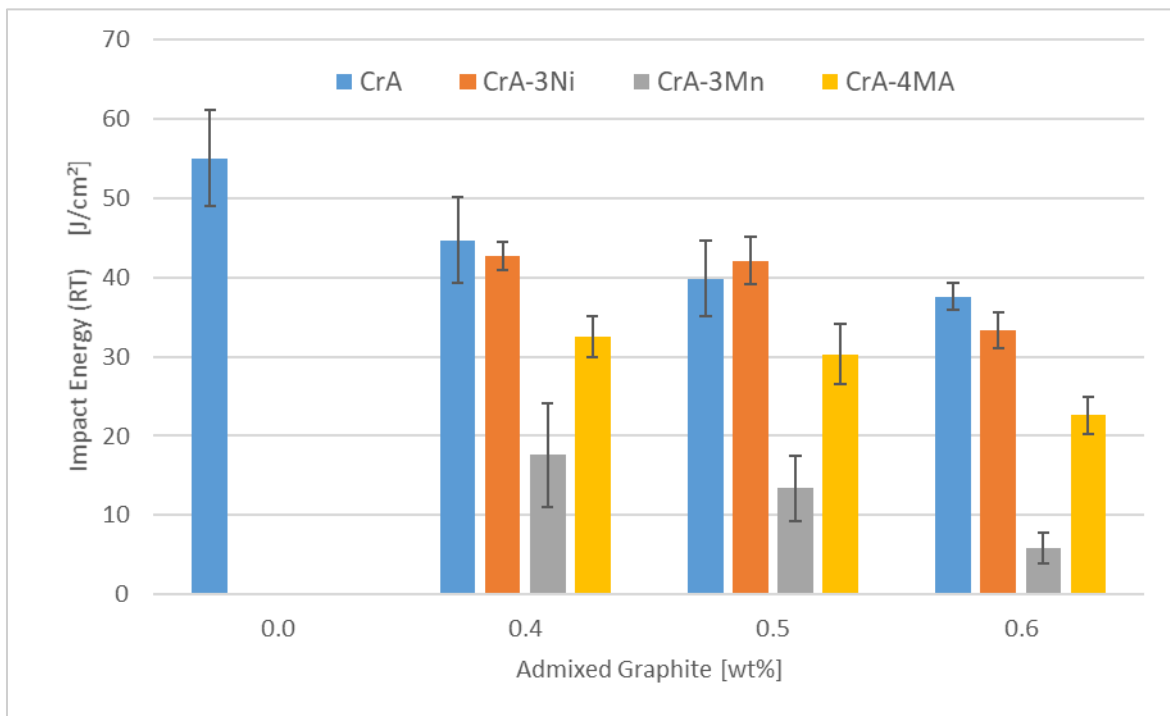


Figure 4.36: Charpy impact energy (RT) of steels with different levels of admixed carbon, compacted at 700 MPa, sintered 60 min at 1250 °C in N₂-10% H₂.

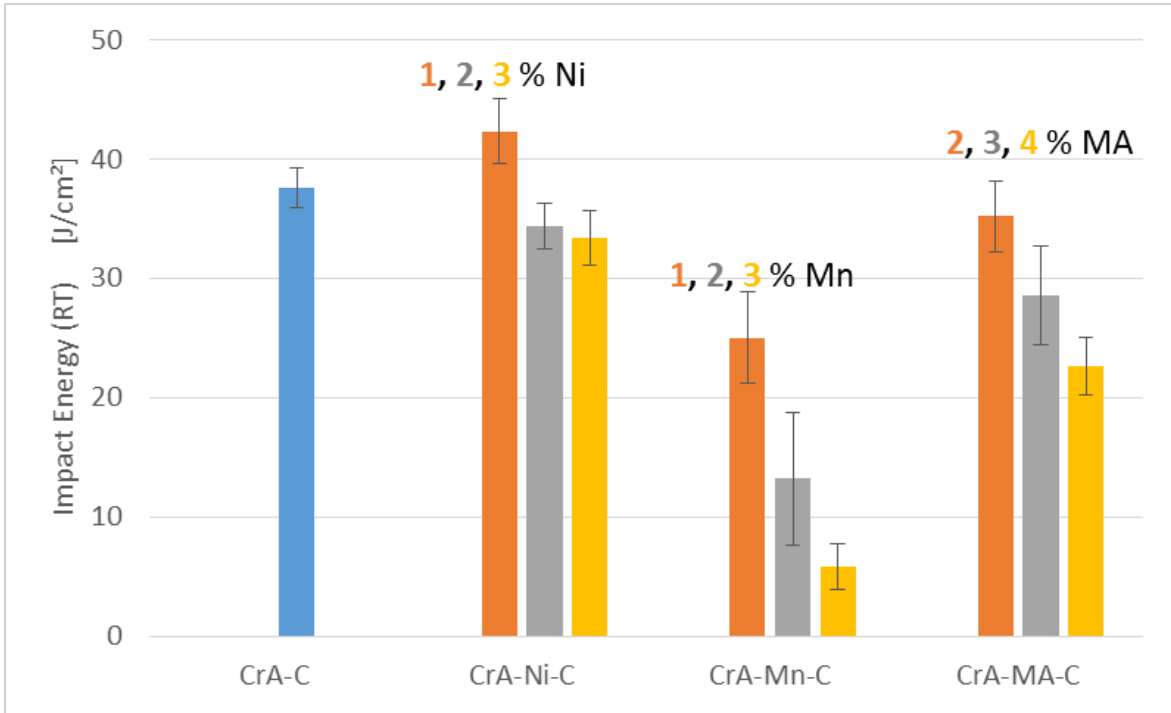


Figure 4.37: Charpy impact energy (RT) of steels with 0.6% admixed carbon, compacted at 700 MPa, sintered 60 min at 1250 °C in N₂-10% H₂.

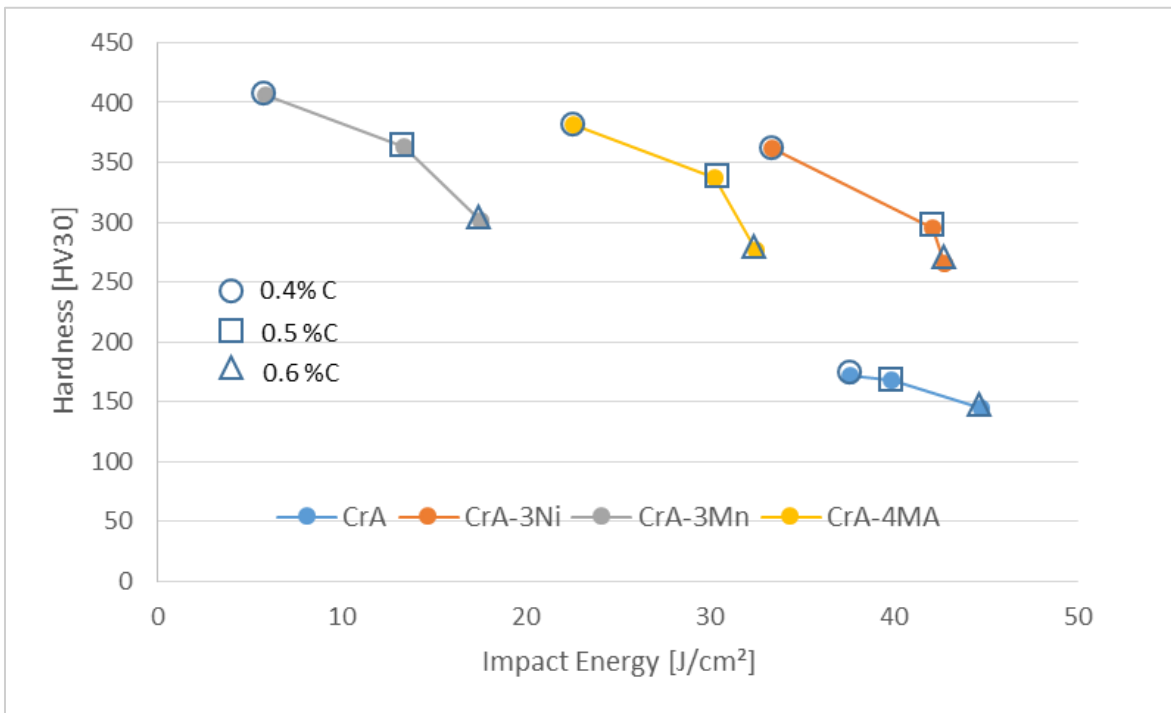


Figure 4.38: Relationship between hardness and impact energy of steels with different levels of admixed carbon, compacted at 700 MPa, sintered 60 min at 1250 °C in N₂-10% H₂.

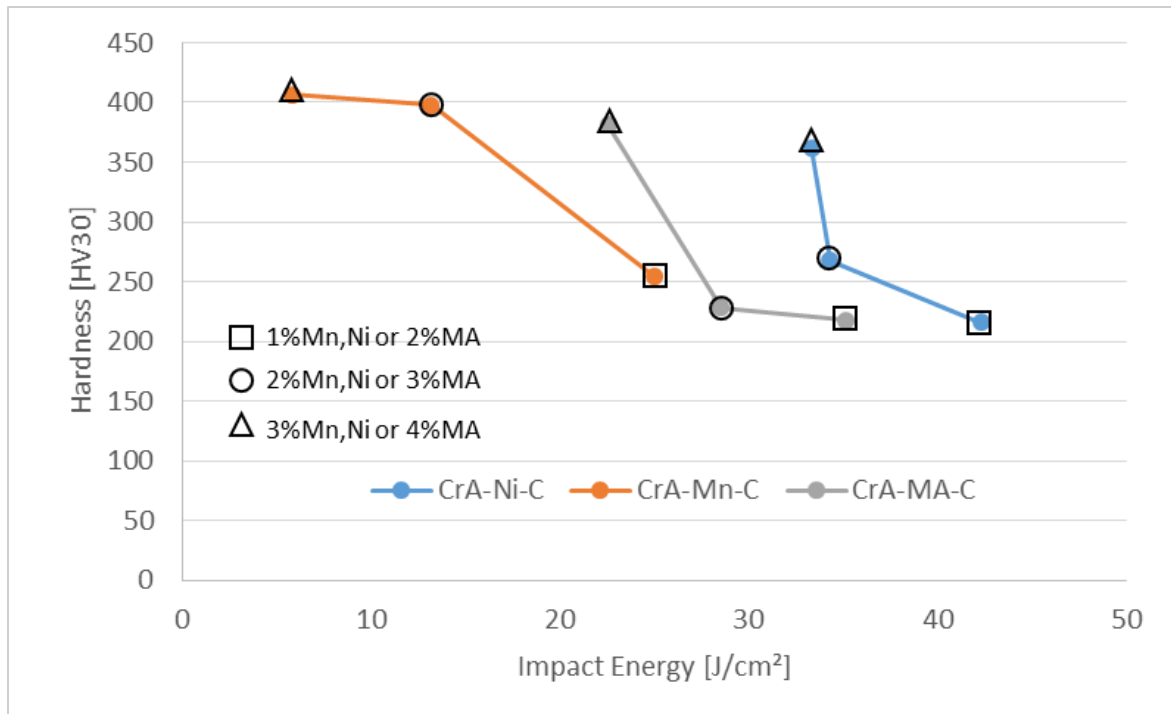


Figure 4.39: Relationship between hardness and impact energy of steels with 0.6% admixed carbon, compacted at 700 MPa, sintered 60 min at 1250 °C in N₂-10% H₂.

4.6.3. Dynamic Young's modulus

In Figures 4.40 and 4.41 the dynamic Young's moduli of the steels are given. It is well known that this property of PM materials is mainly influenced by the density (See the results of dynamic E in section 3.1.1). In Fig. 4.40, the CrA-C steels with higher densities exhibited higher Young's moduli compared to plain CrA. The Ni alloyed steel also showed higher values than the two other steel (Mn and MA steels) which could be explained by the higher density of the Ni steels. In Figure 4.41, the effect of the alloying element content is presented. In all steels, increasing the alloying element content resulted in lower Young's moduli. For the MA and Mn alloyed steels this can be explained by the lower density of the steels at higher alloying content, while in Ni alloyed steels in which the density increased with higher Ni content, the Ni-rich zone and retained austenite could be assumed to be a reason for the lower Young's modulus at the higher Ni content, fcc iron having a lower Young's modulus than the bcc type. The relationship between the density and the dyn. Young's modulus is shown in Figures 4.42 and 4.43. As discussed above and visible here, in all steels except for the Ni alloyed grades, increasing the density resulted in the higher dyn. Young's modulus.

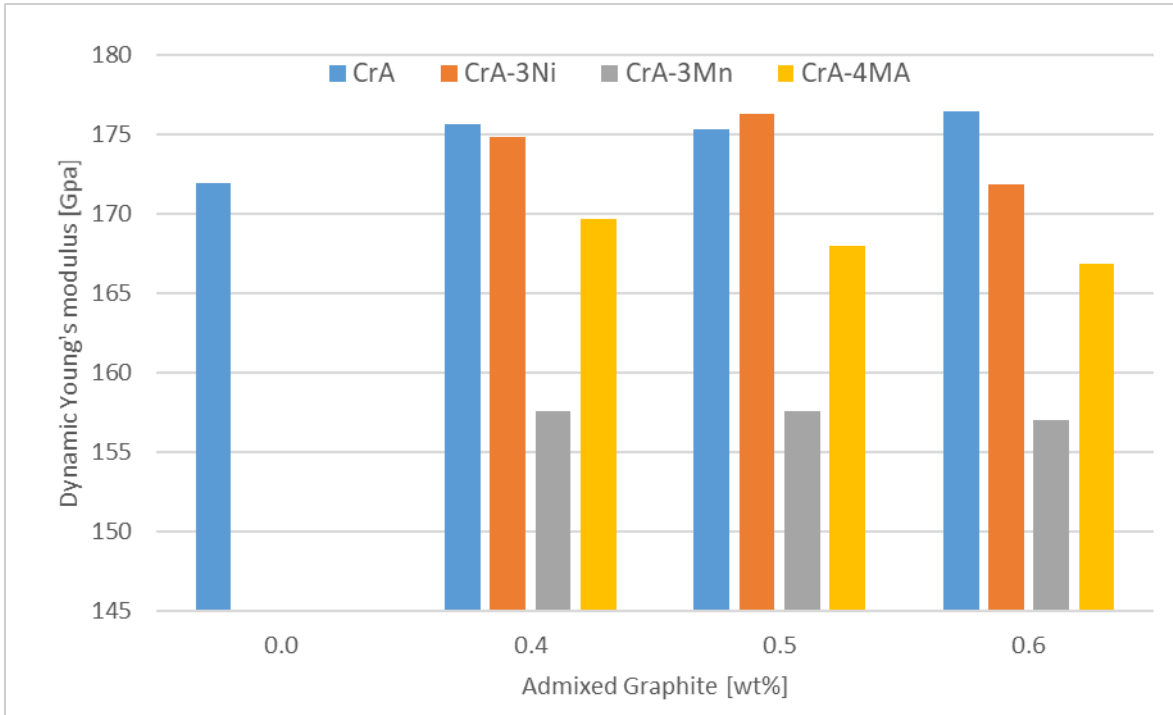


Figure 4.40: Dynamic Young's modulus of steels with different levels of admixed carbon, compacted at 700 MPa, sintered 60 min at 1250 °C in N₂-10% H₂.

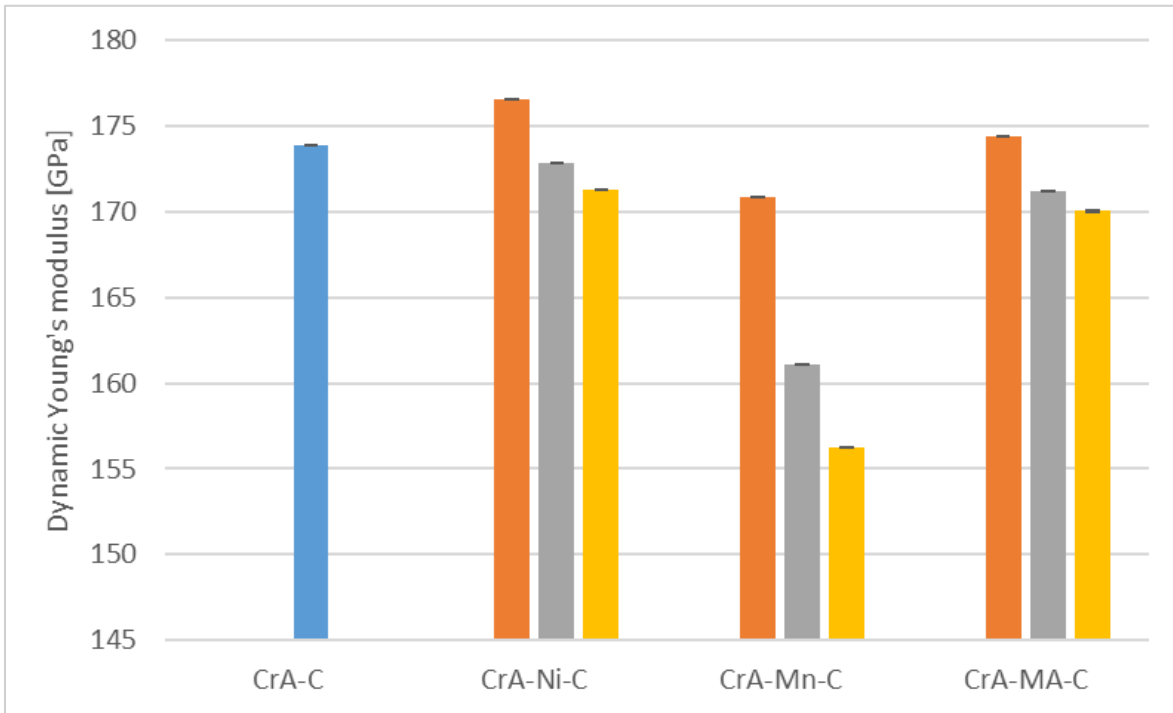


Figure 4.41: Dynamic Young's modulus of steels with 0.6% admixed carbon, compacted at 700 MPa, sintered 60 min at 1250 °C in N₂-10% H₂.

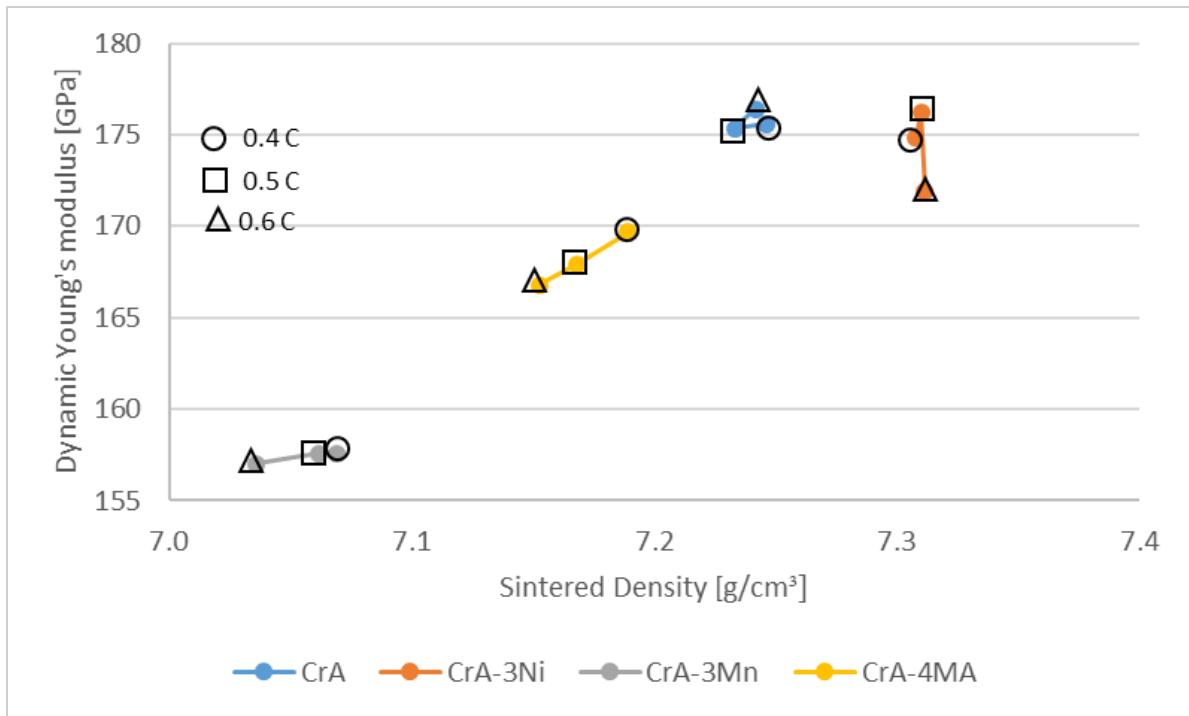


Figure 4.42: Relationship between dynamic Young's modulus and sintered density of steels with different levels of admixed carbon, compacted at 700 MPa, sintered 60 min at 1250 °C in N₂-10% H₂.

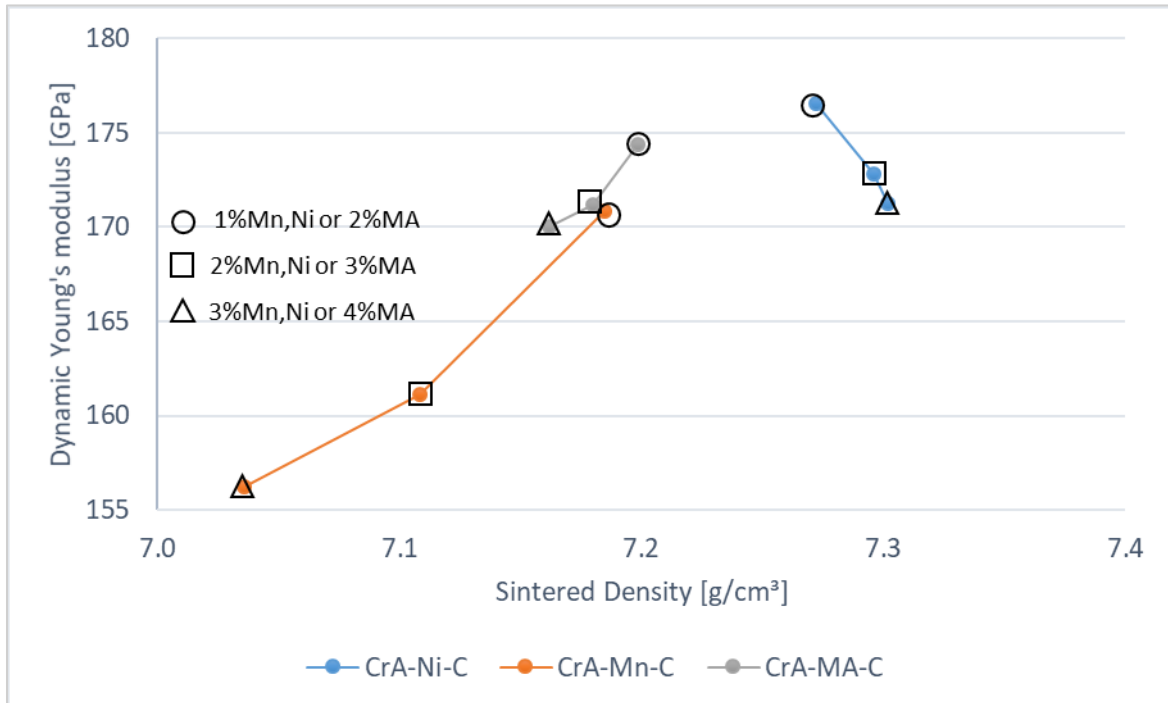


Figure 4.43: Relationship between dynamic Young's modulus and sintered density of steels with 0.6% admixed carbon, compacted at 700 MPa, sintered 60 min at 1250 °C in N₂-10% H₂.

Table 4.6: Mechanical properties of the steels, compacted at 700 MPa, sintered 60 min at 1250 °C in N2-10% H2.

	Ni (wt%)	Mn (wt%)	MA (wt%)	C (wt%)	Hardness (HV30)	Impact energy (J/cm ²)	Dyn. Young's Modulus (GPa)
Fe-Cr-C	0	71.3 ± 1.2	55.0 ± 6.1	171.9
	0.4	144.0 ± 1.0	44.7 ± 5.3	175.6
	0.5	168.0 ± 1.0	39.9 ± 4.7	175.3
	0.6	172.0 ± 19.2	37.6 ± 1.7	176.4
Fe-Cr-Ni-C	1	0.6	215.7 ± 13.7	42.3 ± 2.7	176.5
	2	0.6	267.7 ± 2.1	34.3 ± 1.9	172.9
	3	0.4	266.0 ± 1.0	42.7 ± 1.8	174.8
				0.5	295.0 ± 15.4	42.1 ± 3.0	176.3
				0.6	362.0 ± 4.0	33.3 ± 2.3	171.9
Fe-Cr-Mn-C	...	1	...	0.6	254.0 ± 6.6	25.0 ± 3.9	170.9
	...	2	...	0.6	398.0 ± 3.6	13.2 ± 5.5	161.1
	...	3	...	0.4	301.7 ± 4.0	17.6 ± 6.5	157.6
				0.5	363.0 ± 15.5	13.4 ± 4.1	157.6
				0.6	406.7 ± 13.4	5.8 ± 1.9	157.0
Fe-Cr-MA-C	2	0.6	217.3 ± 4.6	35.2 ± 2.9	174.4
	3	0.6	228.0 ± 4.4	28.5 ± 4.2	171.2
	4	0.4	276.0 ± 6.0	32.5 ± 2.6	169.7
				0.5	337.0 ± 8.2	30.3 ± 3.8	167.9
				0.6	381.3 ± 11.6	22.6 ± 2.4	166.8

4.7. Physical properties

4.7.1. Electrical conductivity

In Figure 44, the effect of the carbon content on the as-sintered electrical conductivity of the steels is shown. Addition of carbon to CrA does not have a significant effect on this property. This is somewhat surprising regarding the observation in the previous chapters that dissolution of carbon during sintering lowers the conductivity. Here it should be considered that in these studies, plain Fe was used as the base powder in most cases. It might be assumed that the effect of Cr in solid solution masks that of carbon, which agrees with the observation in Chapter 3.4. that the effect of C dissolution is least noticeable in the prealloyed Astaloy CrM with fairly high content of metallic alloy elements. The differences in the other grades with different amounts of carbon are not very significant as well, which indicates that the addition of the (substitutional)

metallic alloy elements significantly decreases the conductivity, but this effect is not too different for all carbon levels.

In Figure 45, the effect of the alloying elements on the electrical conductivity is given. It shows that in all grades, increasing the alloying element content lowers the conductivity of the materials. The effect of Mn is higher than that of Ni. In the MA alloyed steel, in addition to Mn, also Si should be considered which affects the electrical conductivity negatively (which is the reason why it is used in transformer cores). At 2% manganese there is a significant drop in the electrical conductivity value which indicates that martensitic material – which is virtually a supersaturated solid solution - exhibits lower conductivity than pearlitic ones, in which carbon is present as precipitate. From comparison of Figs. 4.43 and 4.44 it is clearly evident once more that the metallic alloy elements have a much more pronounced effect on the conductivity than carbon (which is also corroborated by the low conductivity of the steels based on Astaloy CrM, as shown in Fig. 3.119).

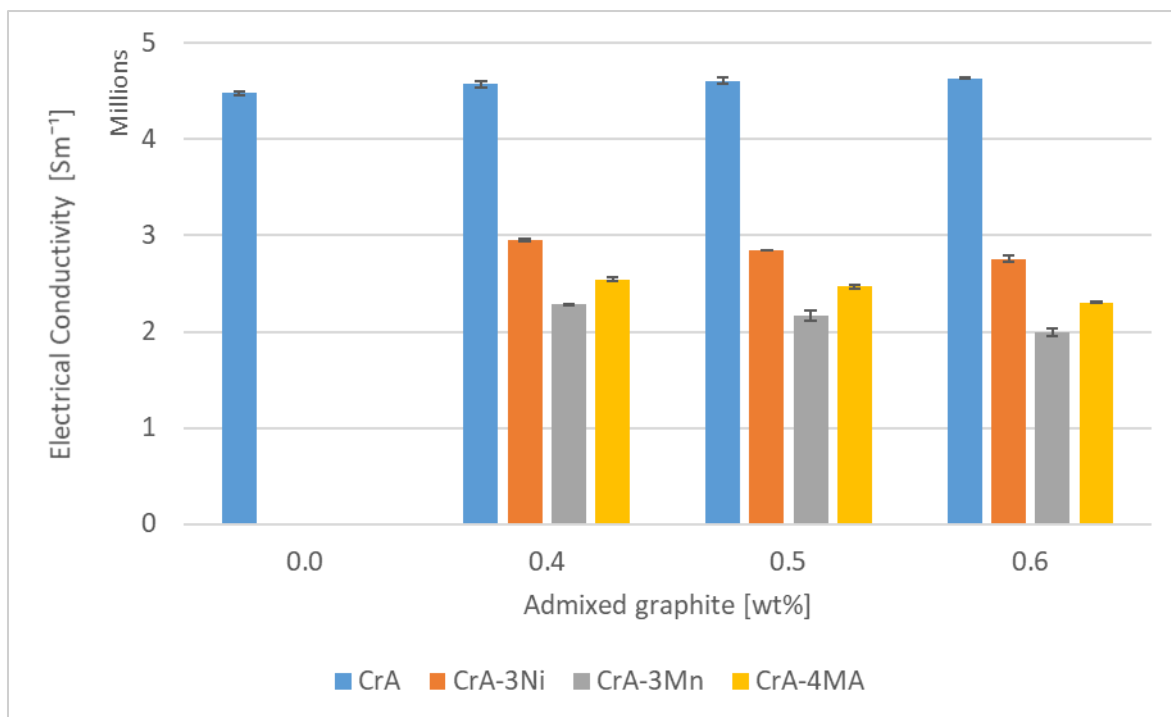


Figure 4.44: Electrical conductivity of steels with different levels of admixed carbon, compacted at 700 MPa, sintered 60 min at 1250 °C in N₂-10% H₂.

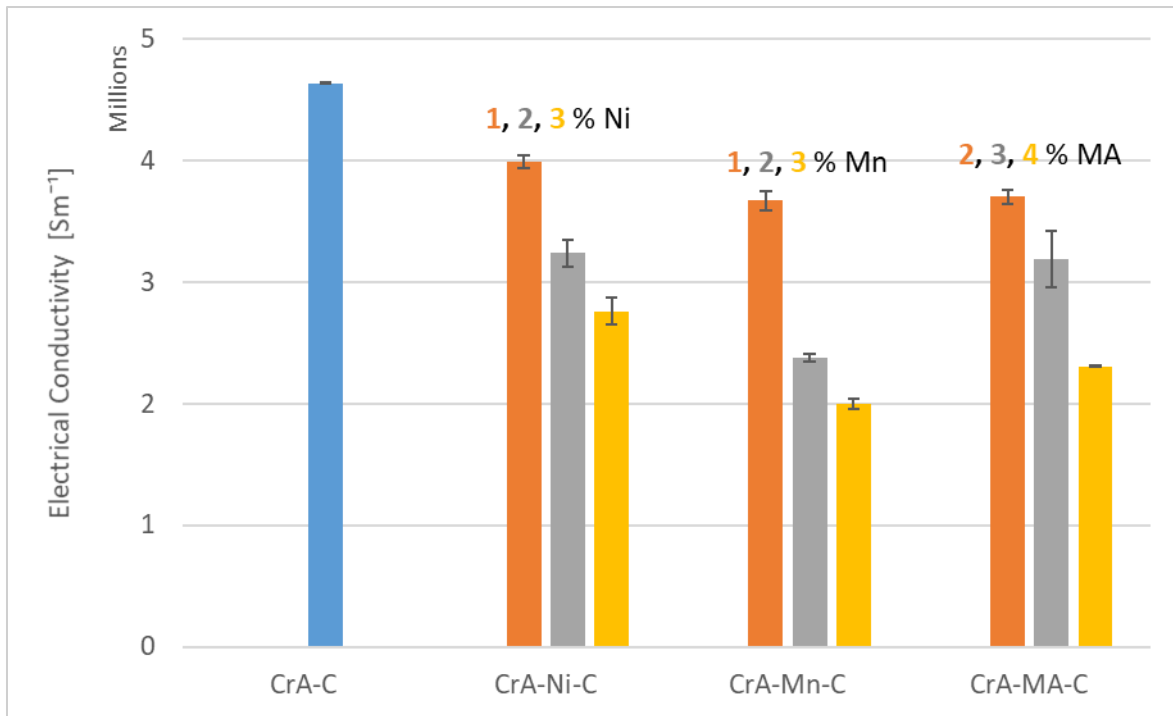


Figure 4.45: Electrical conductivity of steels with 0.6% admixed carbon, compacted at 700 MPa, sintered 60 min at 1250 °C in N₂-10% H₂.

4.7.2. Coercivity

The effect of the carbon content on the coercivity of the steels is exhibited in Figure 46. In all grades, higher carbon content increased the coercivity and the magnetic hardness. In Figure 47, the effect of the alloying elements on this property is presented. It is evident that increasing the alloying element content in all systems increased the coercivity, however this effect is more pronounced in Mn (2&3%) and MA (4%) alloyed steel compared to Ni, which could be related to the presence of martensite in the microstructures. The correlation between the coercivity and the hardness of the steels is shown in Figures 48 and 49.

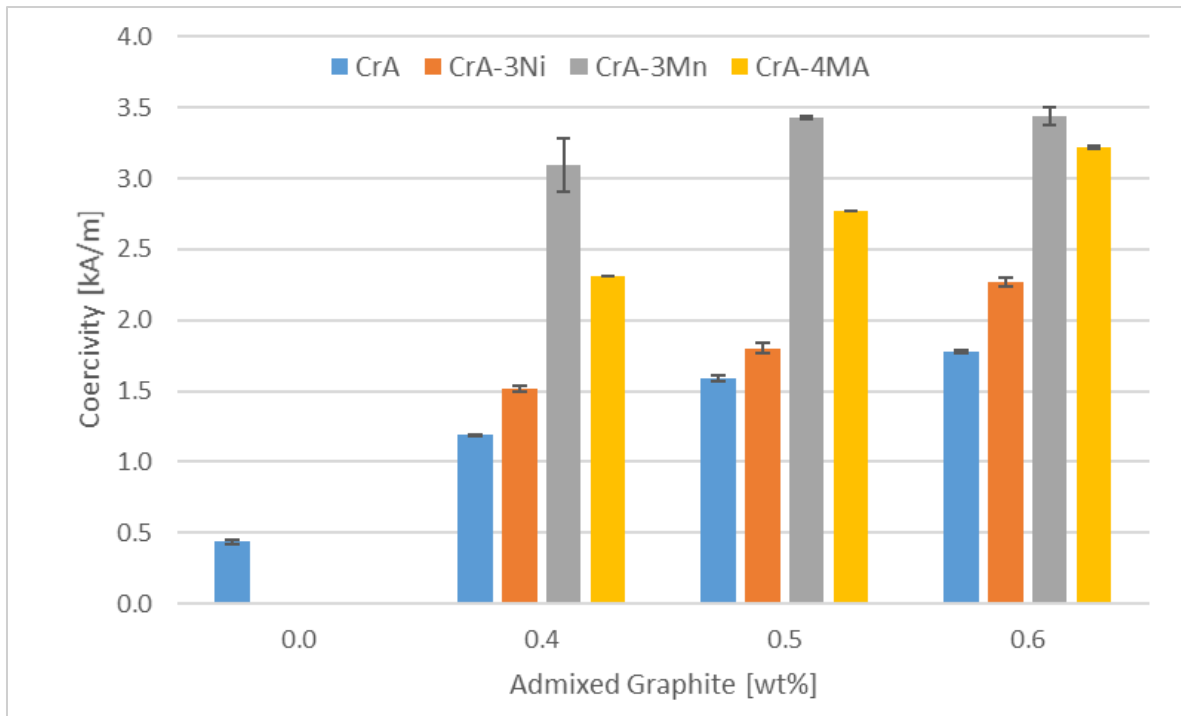


Figure 4.46: Coercivity of steels with different levels of admixed carbon, compacted at 700 MPa, sintered 60 min at 1250 °C in N₂-10% H₂.

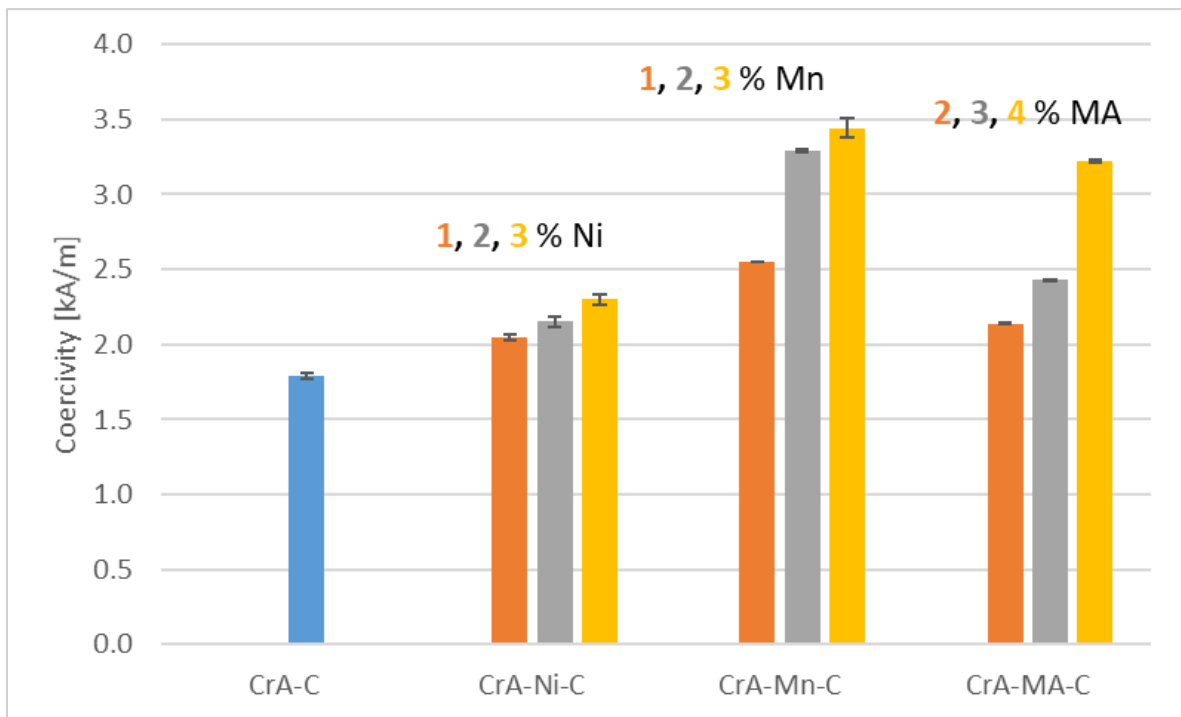


Figure 4.47: Coercivity of steels with 0.6% admixed carbon, compacted at 700 MPa, sintered 60 min at 1250 °C in N₂-10% H₂.

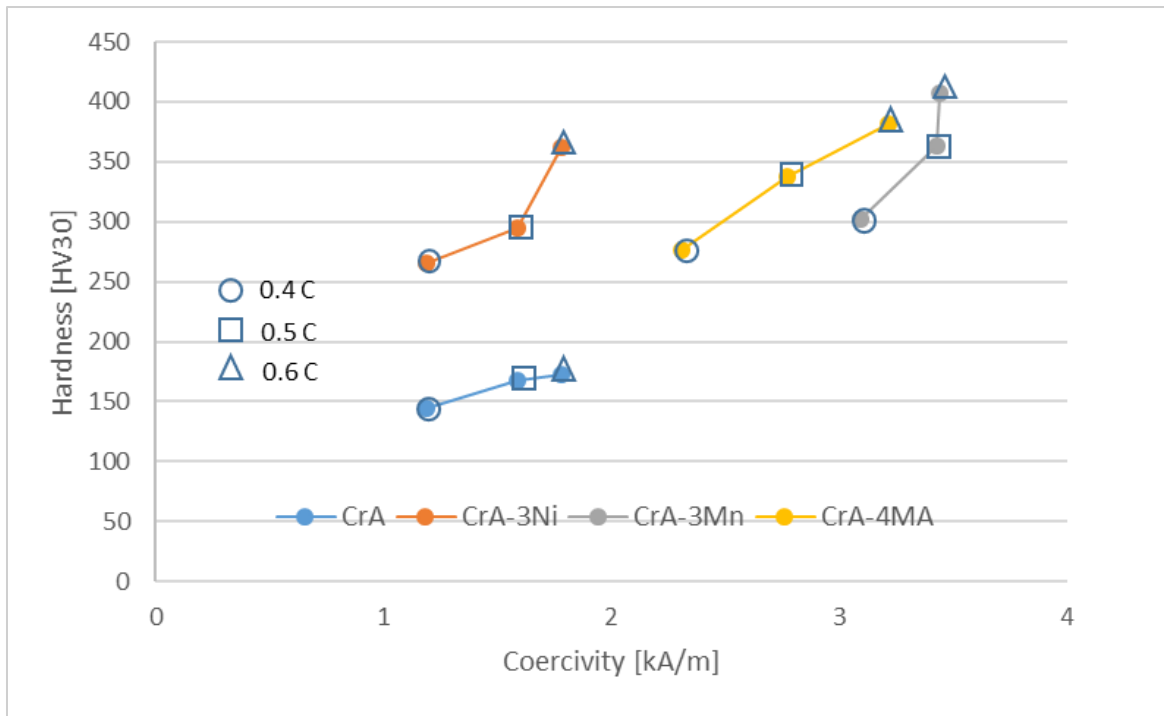


Figure 4.48: Relationship between hardness and coercivity of steels with different admixed carbons, compacted at 700 MPa, sintered 60 min at 1250 °C in N₂-10% H₂.

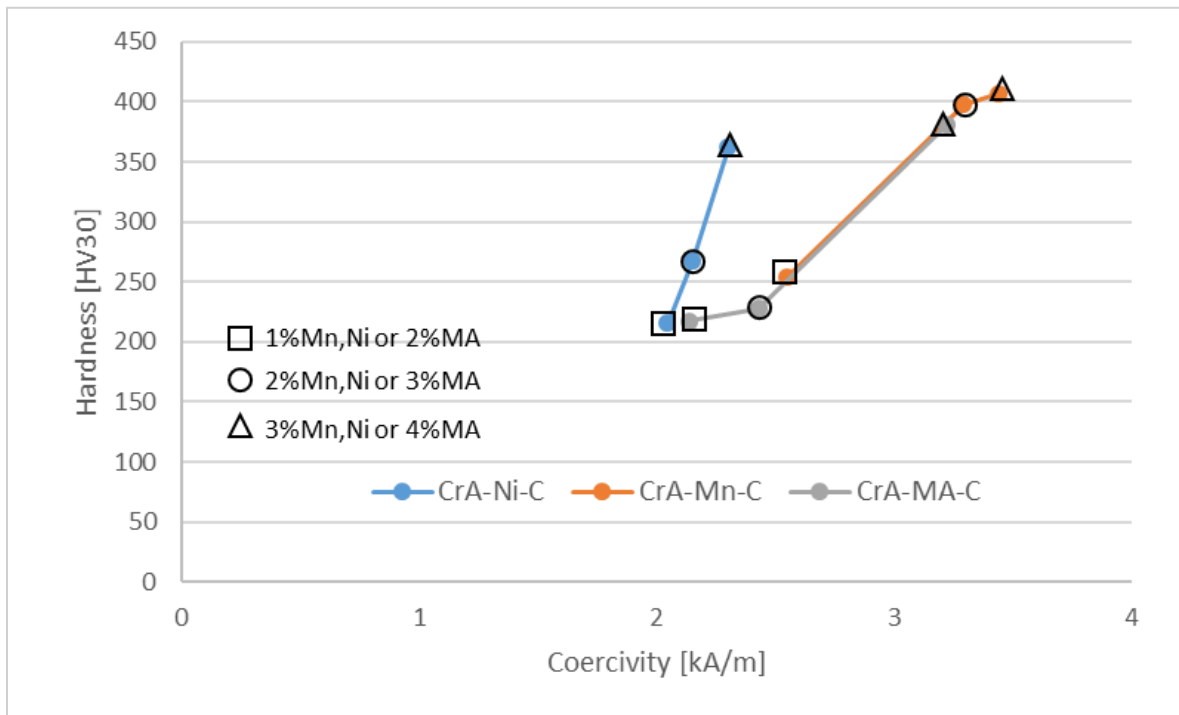


Figure 4.49: Relationship between hardness and coercivity of steels with 0.6% admixed carbon, compacted at 700 MPa, sintered 60 min at 1250 °C in N₂-10% H₂.

4.7.3. Magnetic saturation

It is well known that the sintered density (porosity) as well as the chemical composition can affect the magnetic saturation of PM steels [121, 186]. Fig.4.50 shows the correlation between the saturation values of the magnetic induction (that is, the maximum B values of the B-H hysteresis loop) and the carbon contents of the steels. It is evident that plain CrA has the highest saturation value of the series. The addition of carbon decreased the magnetization, however there is less effect after increasing C from 0.4 to 0.6%. It is also obvious that the addition of the alloying elements to CrA decreased the saturation values. This effect is more pronounced for Mn compared to Ni steels. In all steels, addition of carbon decreased this magnetic property.

In Figure 4.51, the magnetic saturation of the steels with different amounts of alloying elements is presented. The figure shows that addition of alloying elements (Ni, Mn and Si) decreased the values of the saturation and the parameter is reduced by increasing the alloying elements content. However, it is evident that Ni has less effect on the saturation than Mn.

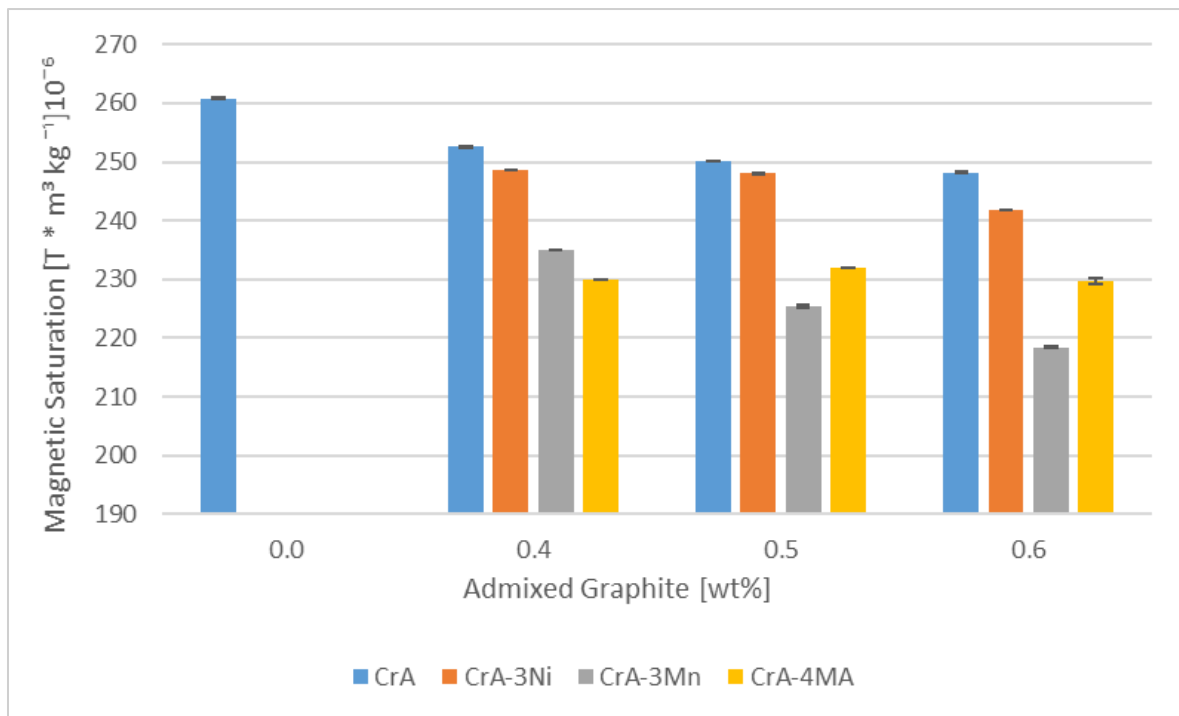


Figure 4.50: Magnetic saturation of steels with different levels of admixed carbon, compacted at 700 MPa, sintered 60 min at 1250 °C in N₂-10% H₂.

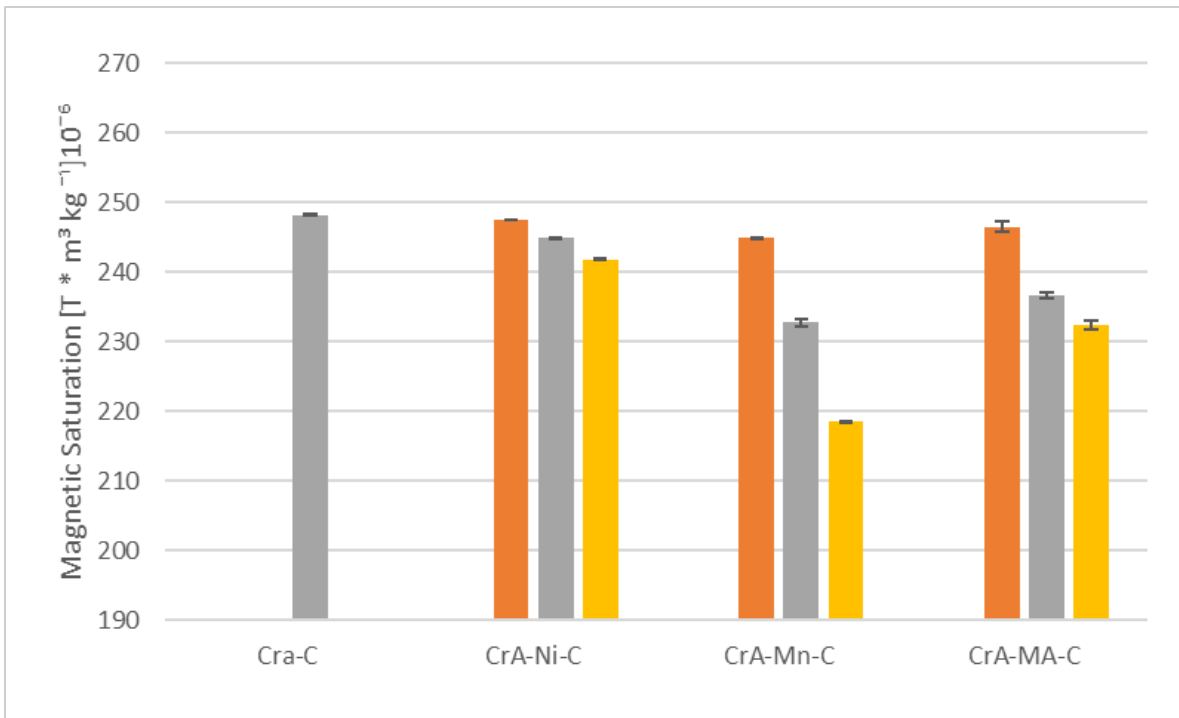


Figure 4.51: Magnetic saturation of steels with 0.6% admixed carbon, compacted at 700 MPa, sintered 60 min at 1250 °C in N₂-10% H₂.

Table 4.7: Electrical and magnetic properties of steels, compacted at 700 MPa, sintered 60 min at 1250 °C in N₂-10% H₂.

	Ni (wt%)	Mn (wt%)	MA (wt%)	C (wt%)	El- conductivity (Sm ⁻¹) 10 ⁴	Coercivity (kA/m)	M-Saturation (T * m ³ kg ⁻¹) 10 ⁻⁶
Fe-Cr-C	0	448	0.44	260.8
	0.4	457	1.19	252.6
	0.5	461	1.59	250.2
	0.6	463	1.78	248.1
Fe-Cr-Ni-C	1	0.6	398	2.05	247.5
	2	0.6	324	2.15	244.8
	3	0.4	295	1.52	248.7
				0.5	285	1.80	248.0
				0.6	276	2.27	241.8
Fe-Cr-Mn-C	...	1	...	0.6	367	2.55	244.8
	...	2	...	0.6	238	3.29	232.7
	...	3	...	0.4	228	3.10	235.0
				0.5	217	3.43	225.4
				0.6	200	3.44	218.4
Fe-Cr-MA-C	2	0.6	370	2.14	246.5
	3	0.6	319	2.43	236.6
	4	0.4	255	2.31	230.0
				0.5	247	2.77	232.0
				0.6	231	3.22	229.7

4.8. Hardenability and CCT diagrams

The stability of the phases during continuous cooling of austenite from 1100 °C as obtained in the quenching dilatometer are shown through the CCT diagrams in Figures 4.52 to 4.55. The results are supplemented by metallography and hardness measurement at the cooling rate of 3 K/s, which is considered as the industrially feasible cooling rate of the sinter hardening process. The CCT diagram of CrA-0.6C is shown in Figure 4.52. It is evident that this steel does not sinter harden at 3 K/s. According to the results, at a cooling rate of 3 K/s bainitic microstructure is expected. The bainitic microstructure and its corresponding hardness also presented in this figure confirms the results of dilatometry. In Figure 4.53, the CCT diagram of the steel after addition of 2% Mn is presented, and it shows that the addition of this alloying element had a significant effect on the hardenability. The CCT diagram of this steel predicted a fully martensitic microstructure and sinter-hardening ability, not only at the cooling rate of 3 K/s but also at lower rates below 1.5 K/s. The metallographic section presented in this figure shows fully martensitic microstructure at 3 K/s, which is in agreement with the CCT data.

The CCT diagram of the hybrid steel alloyed with Ni is presented in Figure 4.54. It is evident that in this steel, at the cooling rate of 3 K/s the microstructure would be martensitic and the sinter-hardening ability is activated by addition of 2% Ni. However, the diagram shows that at lower cooling rates (e.g. 1.5 K/s), the microstructure would be mainly bainitic, which means that the hardenability of this steel is lower than for the Mn alloyed steel. In this steel, Ni homogenization occurs through solid state diffusion, and although at sintering temperature the bulk diffusion coefficients of Ni and Mn in austenite are very similar, the gas phase transport of Mn enhances its distribution in the steel matrix and thus improves the hardenability compared to the Ni steel.

In Figure 4.55, the CCT diagram and etched microstructure of CrA-3MA-0.6C are presented. The results show that alloying the steel with 3% MA gives sinter-hardening behaviour to the steel. Compared to the Ni-alloyed steel, the hardenability is higher. The microstructure of this steel at 3 K/s is mainly martensitic, which is in good agreement with the CCT diagram.

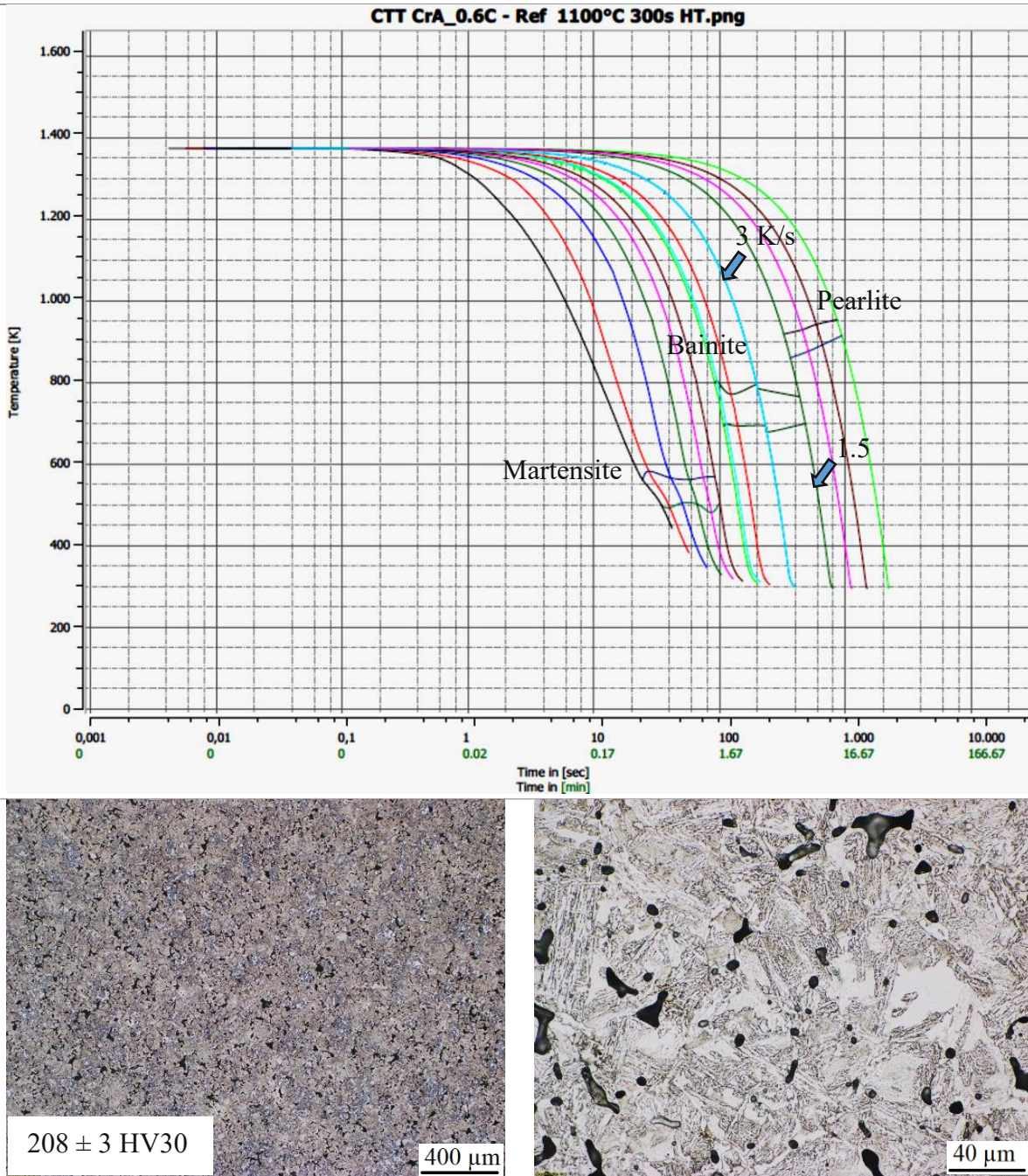


Figure 4.52: CCT diagram of CrA-0.6C. Compacted at 700 MPa, sintered 60 min at 1250 °C in N₂-10% H₂. CCT diagram obtained by quench dilatometry; heated at 11 K/s to 1100 °C and held for 300 s, cooled with different rates; etched microstructure: Cooled at 3 K/s.

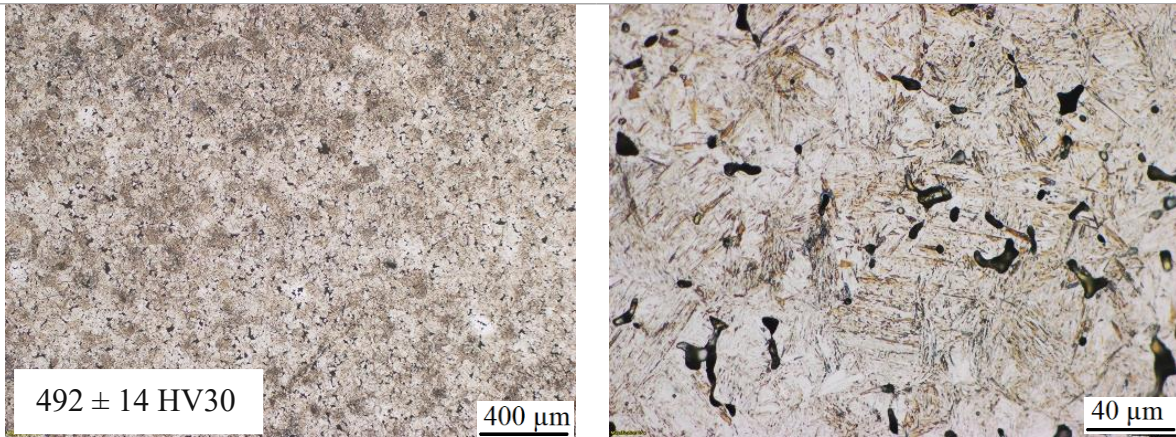
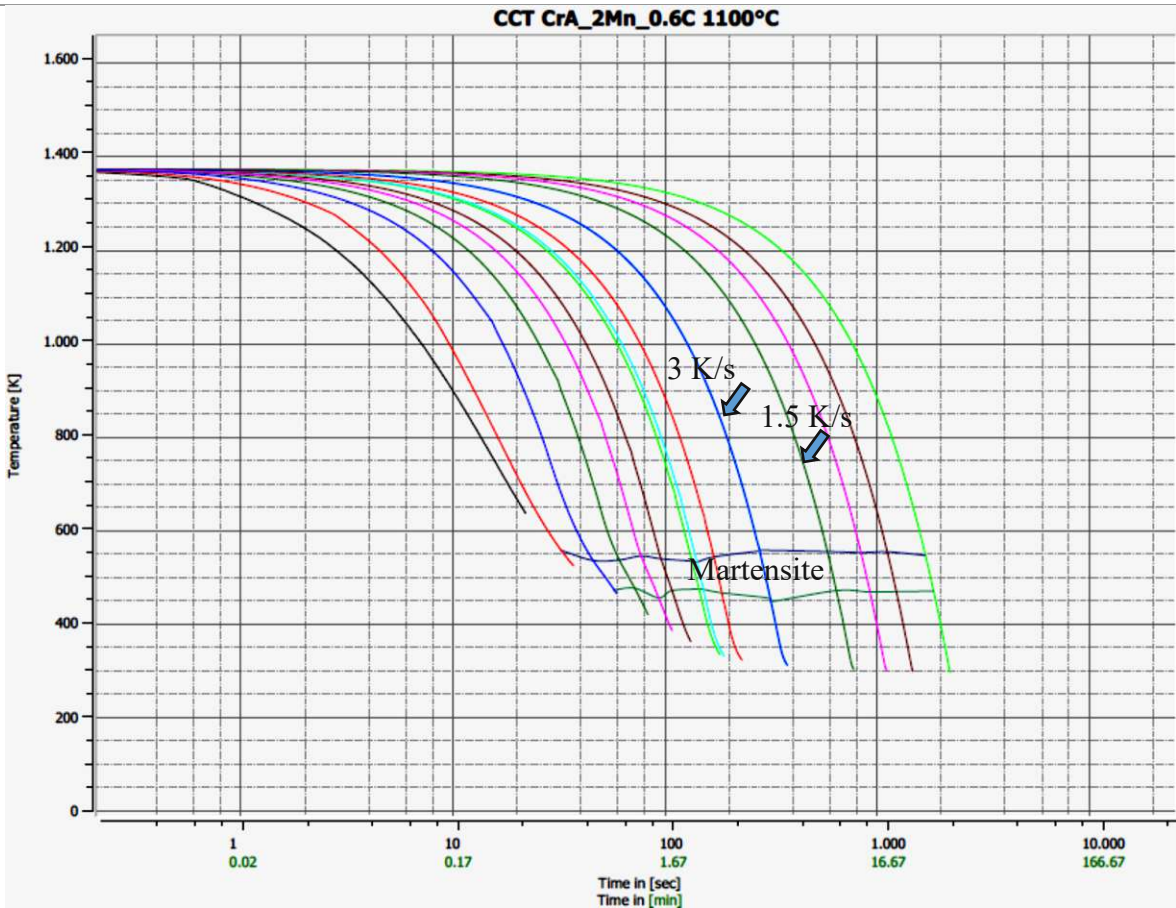


Figure 4.53: CCT diagram of CrA-2Mn-0.6C. Compacted at 700 MPa, sintered 60 min at 1250 °C in N₂-10% H₂. CCT diagram obtained by quench dilatometry; heated at 11 K/s to 1100 °C and held for 300 s, cooled with different rates; etched microstructure: Cooled at 3 K/s.

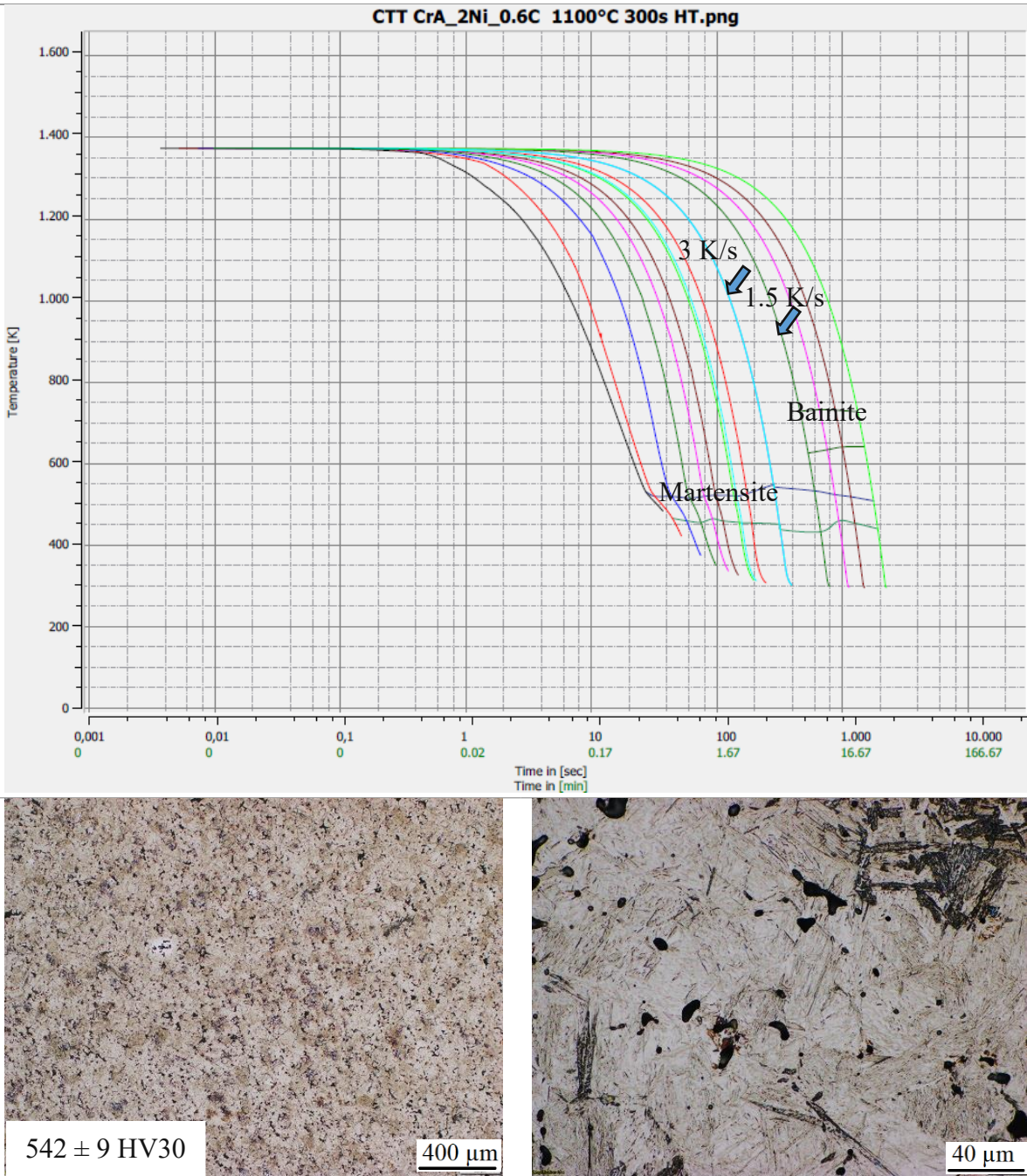


Figure 4.54: CCT diagram of CrA-2Ni-0.6C. Compacted at 700 MPa, sintered 60 min at 1250 °C in N₂-10% H₂. CCT diagram obtained by quench dilatometry; heated at 11 K/s to 1100 °C and held for 300 s, cooled with different rates; etched microstructure: Cooled at 3 K/s.

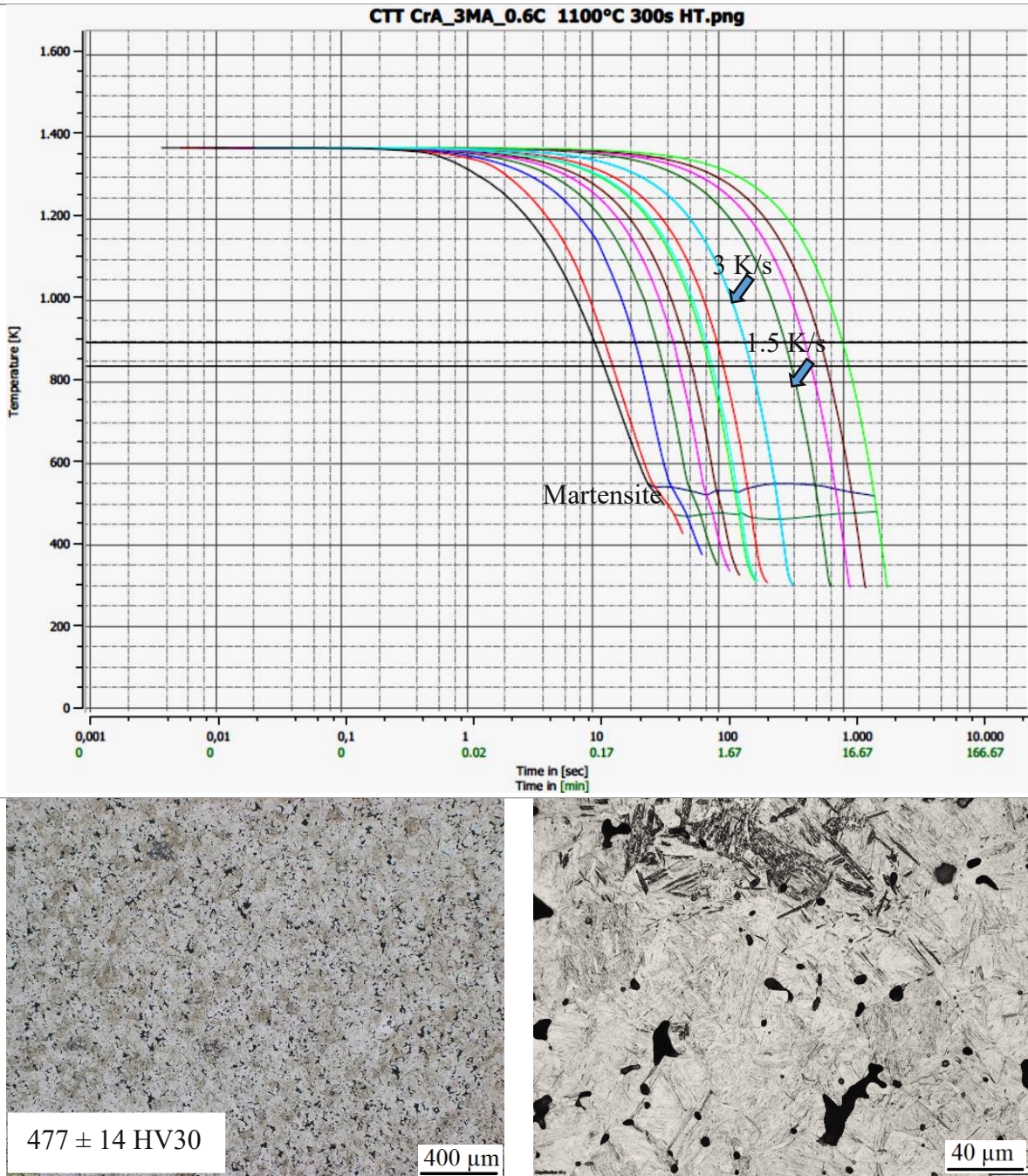


Figure 4.55: CCT diagram of CrA-3MA-0.6C. Compacted at 700 MPa, sintered 60 min at 1250 °C in N₂-10% H₂. CCT diagram obtained by quench dilatometry; heated at 11 K/s to 1100 °C and held for 300 s, cooled with different rates; etched microstructure: Cooled at 3 K/s.

4.9. Gigacycle fatigue of hybrid (Cr-X) alloyed steels

In the last decades the applications for PM precision parts have increased, especially in the automotive industry, where parts used in engines as well as transmission systems are subjected to cyclic stresses with loading cycle numbers frequently $> 10^8$. Therefore, the interest for the high cycle fatigue behaviour of PM steels consistently increased, also because the literature concerning high cycle fatigue is still limited, and most endurance limit data are available for up to $2 \cdot 10^6$ loading cycle numbers or 10^7 maximum.

In this part of the research, the fatigue behaviour of high strength PM steels was investigated. Based on the results of the characterizations in the previous module of this part, three grades of steels with sinter-hardening potential were selected and examined by ultrasonic (US) resonance fatigue testing. These steels are presented in Table 4.8.

Table 4.8: Material composition of the selected mixes for fatigue testing.

	Designation	Mix Composition
1	CrA-2Mn-0.6C	Astaloy CrA+2%Mn+0.6%C
2	CrA-3Ni-0.6C	Astaloy CrA+3%Ni+0.6%C
3	CrA-4MA-0.6C	Astaloy CrA+4%MA+0.6%C

For the high cycle fatigue testing, dumbbell-shaped specimens were prepared as described in Chapter 2.3.10. Rectangular bars were pressed at 700 MPa, sintered at 1250°C in N₂-10% H₂ for 60 min and then soft annealed at 650°C for 1 hr. After turning to shape and surface finishing, which included grinding (2400 mesh grinding paper), the samples were heated to 1000°C in N₂ and held for 30 min, then they were gas quenched with pressurized nitrogen at a cooling rate of 3 K/ sec (linearized between 900 and 300°C [133]). Heat treatment of the samples was completed by tempering at 150°C for 1 hr. Fatigue testing was performed in push-pull mode (R=-1) at 20 kHz in a resonance testing system (see 2.3.10.), liquid cooling being afforded to enable continuous fatigue loading without unwelcome heating effects.

4.9.1. Chemical analysis (carbon and oxygen content)

The oxygen contents of the steels are shown in Fig. 4.56. The lowest oxygen level, 0.009 %, belongs to the Ni alloyed steel, while the steel alloyed with MA showed the highest values of oxygen (0.023%), which is due to the presence of Si in the chemical composition of this steel. The results also show that, despite the high oxygen affinity of Mn, the oxygen content of the Mn alloyed steel is lower than for the MA steel, which is attributed to the self-getter effect of Mn as discussed previously. The carbon content of the steels is presented in Fig. 4.57, as well. Despite the addition of 0.6% carbon in all grades, the carbon content (combined) after sintering is below 0.5%, which shows at least 0.1% carbon loss, due to carbothermal reduction of the oxides.

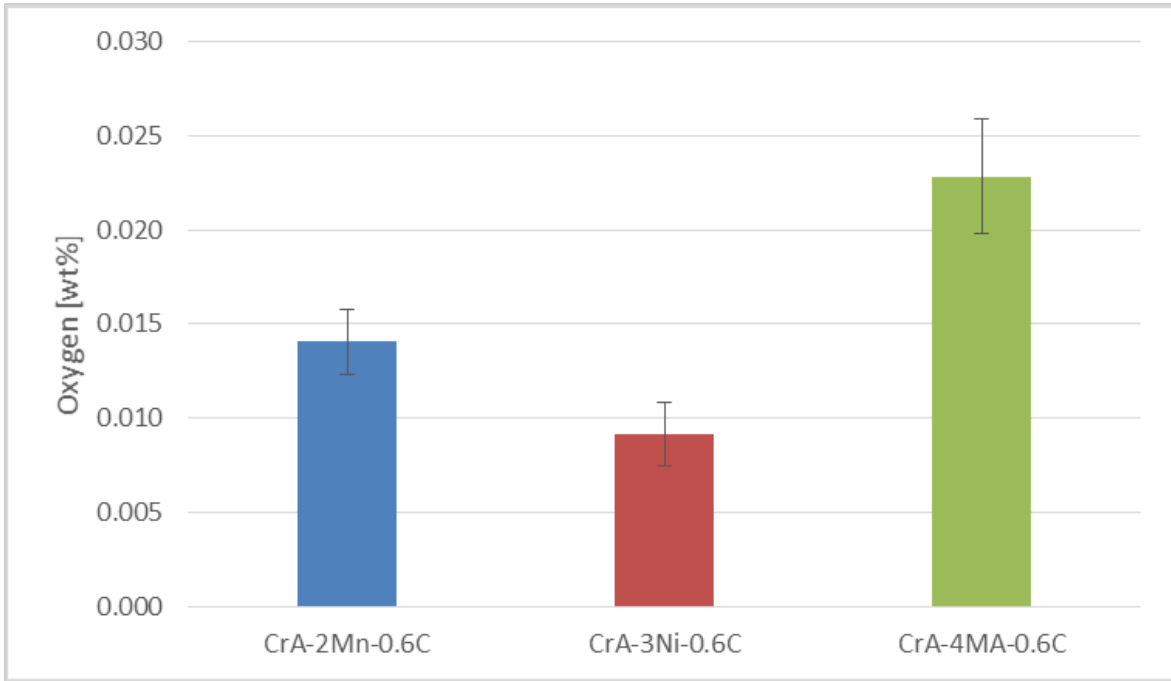


Figure 4.56: Oxygen content of different steels, compacted at 700 MPa, sintered 60 min in N₂-10 %H₂ at 1250 °C (heat treated).

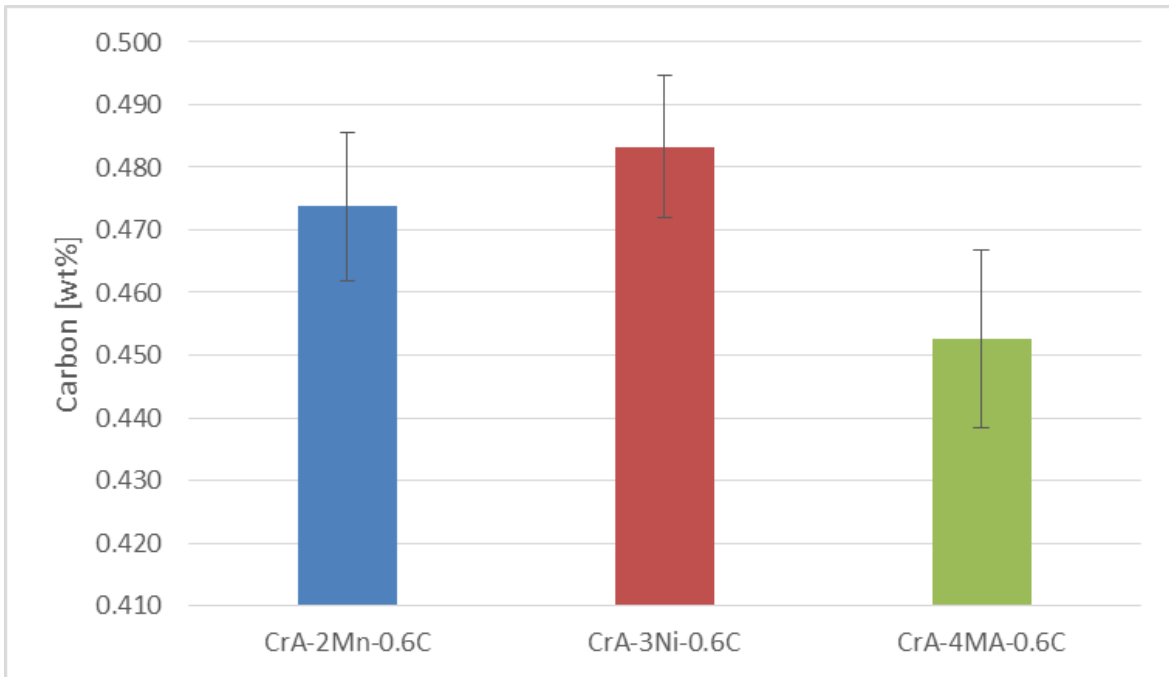


Figure 4.57: Carbon content of different steels, compacted at 700 MPa, sintered 60 min in N₂-10% H₂ at 1250 °C (heat treated).

Table 4.9: Results of oxygen and carbon measurement of the selected mixes for fatigue testing, compacted at 700 MPa, sintered 60 min in N₂-10% H₂ at 1250 °C (heat treated).

	Material	O content (wt %)	C content (wt %)
1	CrA-2Mn-0.6C	0.014 ± 0.002	0.474 ± 0.012
2	CrA-3Ni-0.6C	0.009 ± 0.002	0.483 ± 0.011
3	CrA-4MA-0.6C	0.023 ± 0.003	0.453 ± 0.014

4.9.2. Metallographic investigations (pore morphology and matrix microstructure and singularities)

The correlation between microstructure and mechanical properties of sintered steels is very well known [63, 95]. The pore morphology is depicted on the polished sections of the steels in Figure 4.58. Ni alloyed steel showed finer pores compared to Mn and MA alloyed steels, which can be explained by the higher sintered density of this material. In MA alloyed steel the larger pores can be attributed to the lower green density of the steel, while in Mn alloyed steel, in addition to the lower green density, the formation of secondary pores should be considered as well. Danninger [48, 102] already showed that such pores are comparable to singular inclusions in forged or HIPed material and can influence the monotonic properties decisively. With regard to the pore rounding process, which could be an important issue in fatigue life of the steels, the micrographs presented almost the same condition for all three grades of the steels. In Figure 4.59 a pore cluster in the as-polished microstructure of the Ni alloyed steel is shown, the walls between the fine pores in such clusters are very thin which means that this cluster could behave like a big pore which then could be a probable site for the crack initiation when the material is subjected to fatigue loading.

The etched microstructures of the steels are depicted in Figure 4.60. The matrix of the microstructures of all steels is martensitic which led to hardness levels above 450 HV30. Some dark regions with bainitic microstructure also are visible in the microstructures. These regions - which are mainly related to the cores of the largest original CrA particles where the alloying element (Mn or Ni) content is too low to ensure martensite formation - are more discernible in Ni alloyed steel compared to the other steels, which can be explained by the low diffusion rate of Ni in the iron lattice and homogenization through solid state diffusion. The microstructures also show that MA alloyed steels have more homogeneous microstructure compared to Mn (elemental) alloyed steels.

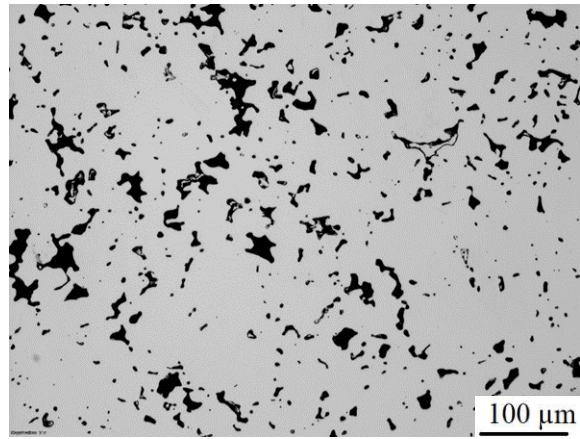
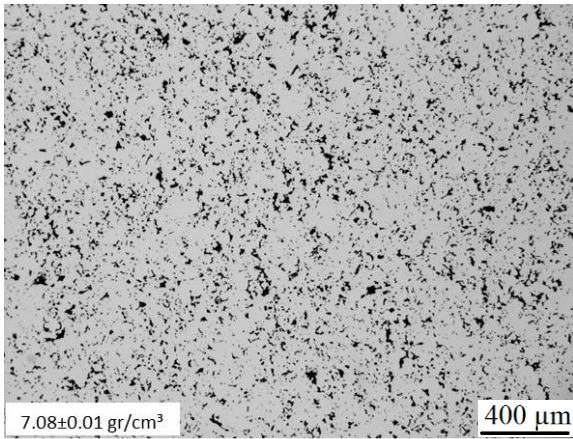
In Figure 4.61, the microstructure of CrA-2Mn-0.8C is shown with the values of microhardness of the different phases. The microhardness of the dark region (bainitic region) is lower compared to the martensitic regions. In Figure 4.62, an inclusion in the microstructure of this steel is shown. The EDS micro-analysis show that this inclusion is a chromium rich particle which might originate from the slags in the base powder (Astaloy CrA).

The microstructure of the Ni alloyed steel with the microhardness values of the phases is depicted in Figure 4.63 and shows the same bainitic regions with lower hardness in the martensitic matrix. In Figure 4.64, a rather large and porous inclusion in this steel is shown.

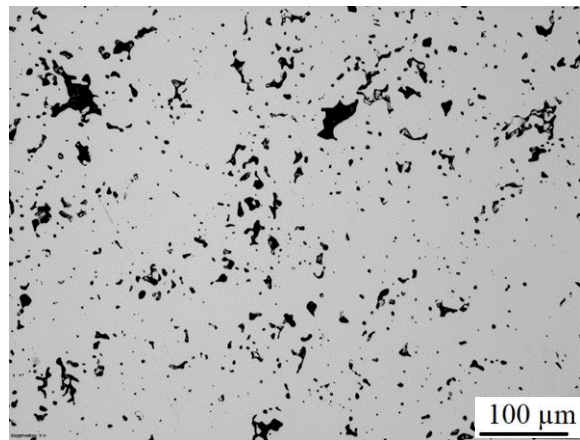
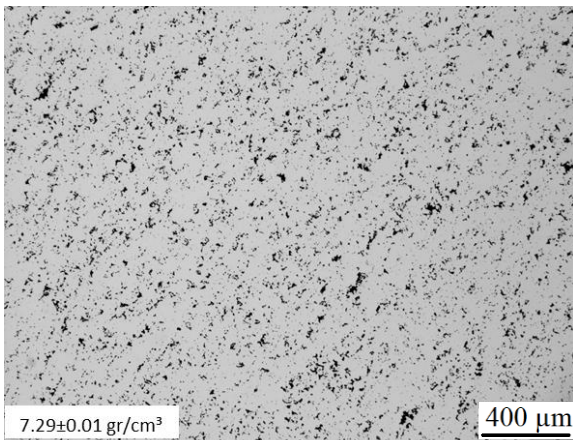
Result of the EDS micro-analysis is also presented in this figure which shows it is a Cr, Ni, Si rich particle. The microhardness of this particle shows the value of 312 HV0.025, which is a rather low value compared to the other martensitic regions. In Figure 4.65, an austenitic Ni-rich (29% Ni) area is shown. The hardness of this area is 110 HV0.025 which is much lower than the surrounding area and indicates the low strength of this area. Therefore, with regard to fatigue endurance of the material, the negative role of such regions should be considered.

A bainitic region, with the hardness of 414 HV0.025, in the microstructure of the Ni alloyed steel is depicted in Figure 4.66. The results of the EDS micro-analysis confirms that this bainitic regions are related to the cores of the large CrA particles with low Ni content.

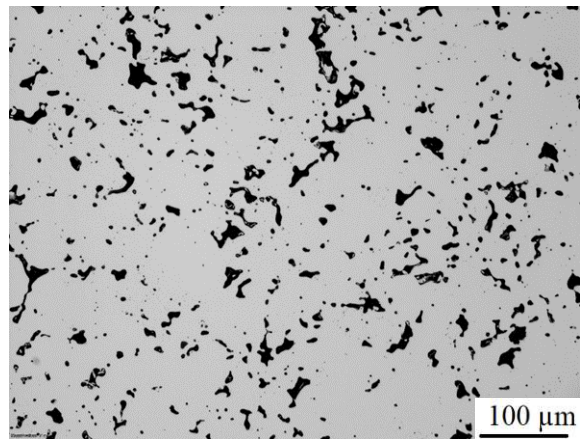
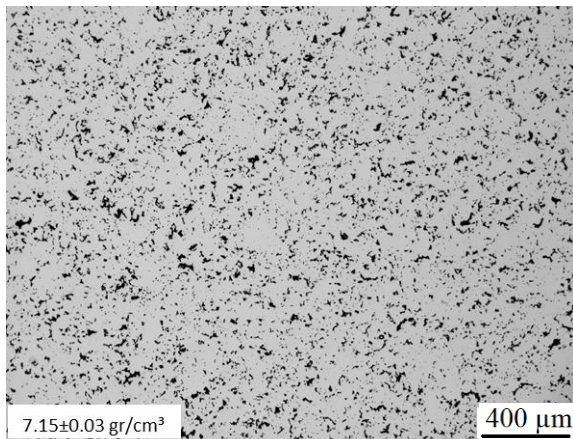
In Figure 4.67 the microstructures and corresponding microhardness data of MA alloyed steel are presented. A Cr-rich inclusion in the microstructure of this steel is also shown in Figure 4.68.



CrA-2Mn-0.6C



CrA-3 Ni-0.6C



CrA-4MA-0.6C

Figure 4.58: Un-etched OM micrographs of different steels, compacted at 700 MPa, sintered 60 min in N₂-10% H₂ at 1250 °C (heat treated).

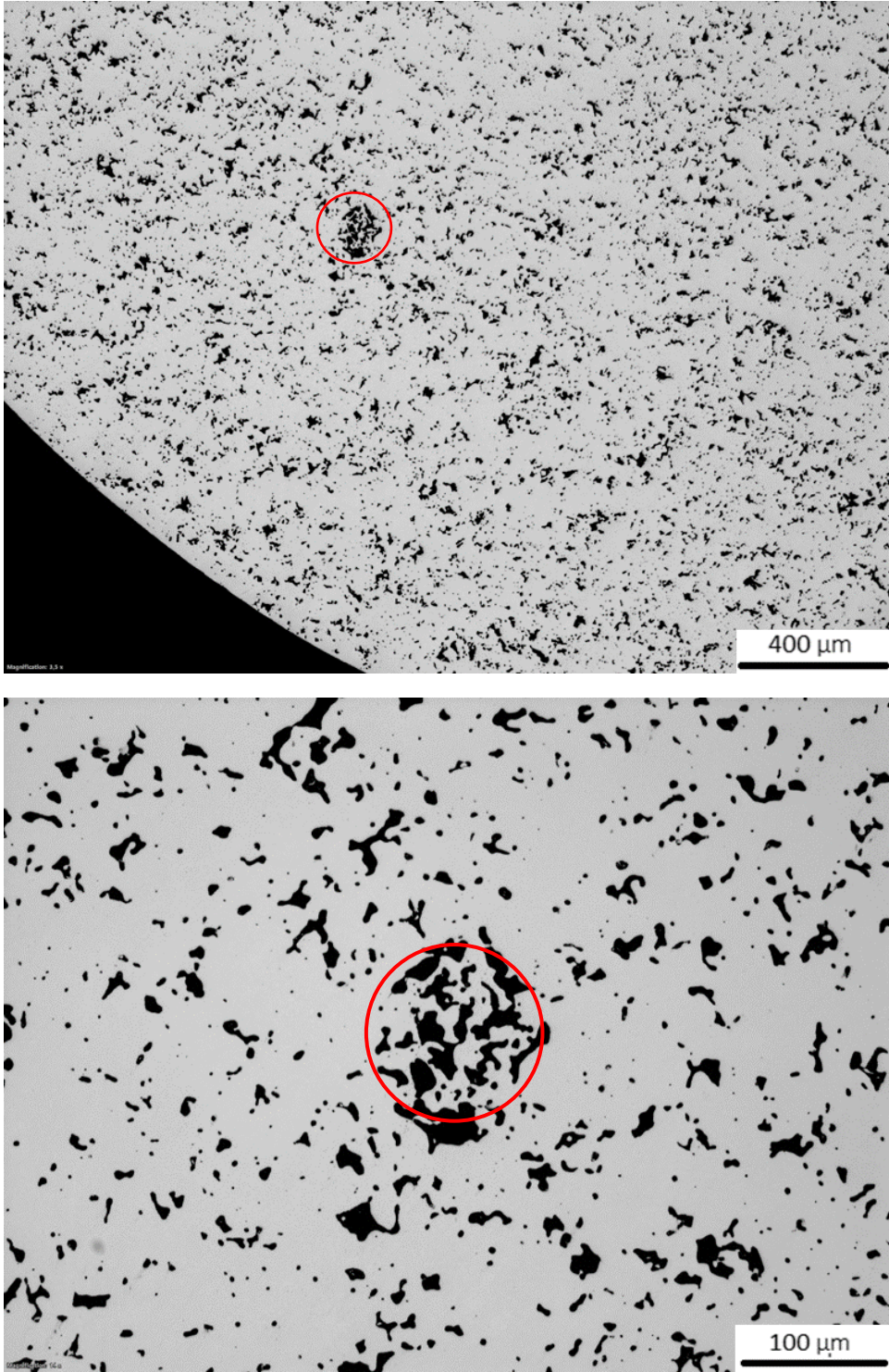
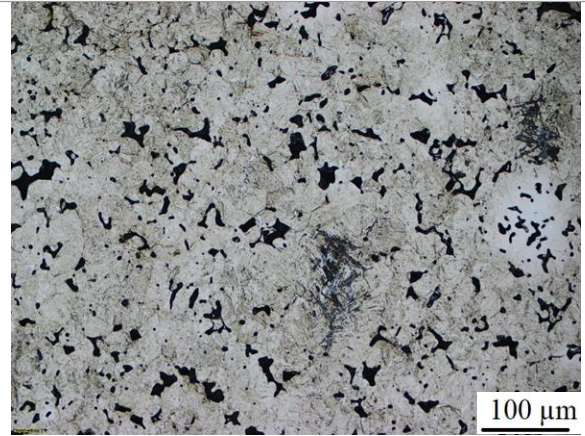
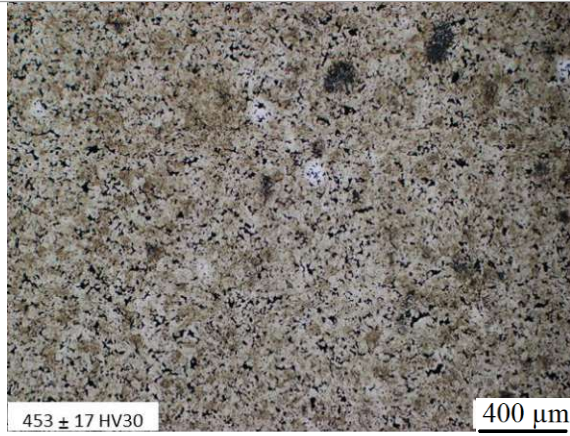
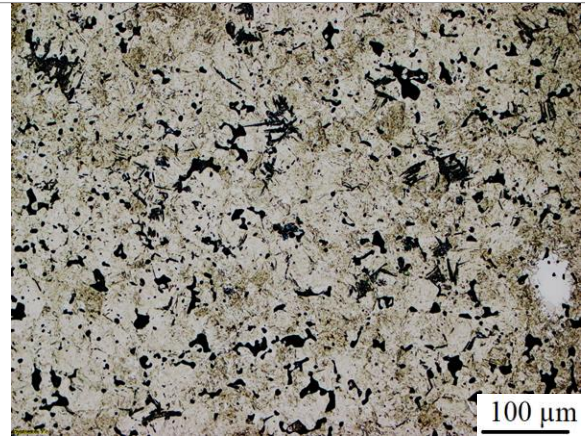
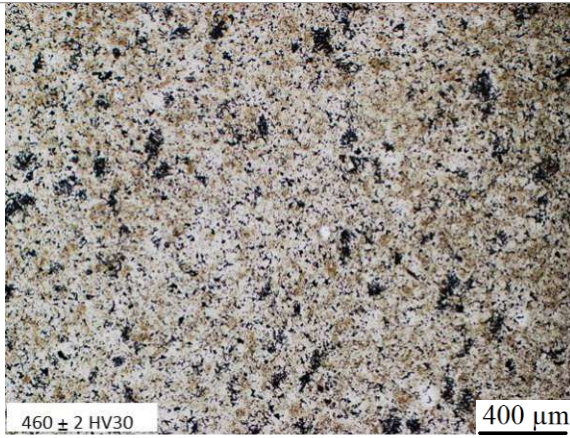


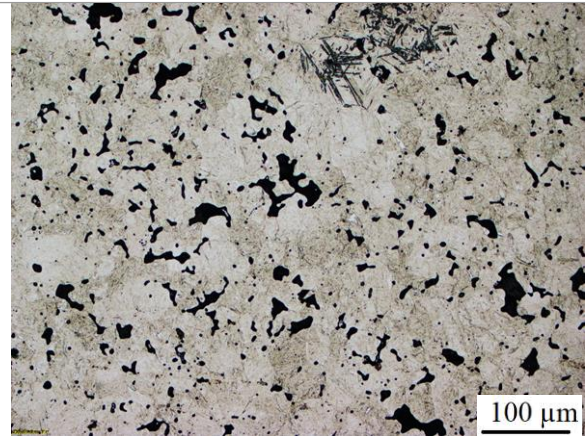
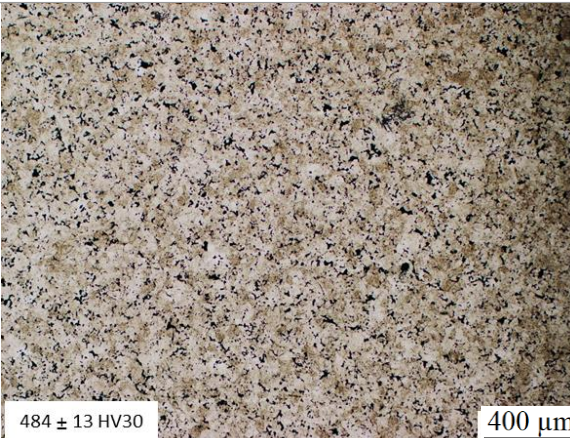
Figure 4.59: a pore cluster in the as-polished microstructure of CrA-3Ni-0.8C, compacted at 700 MPa, sintered 60 min in N₂-10% H₂ at 1250 °C (heat treated).



CrA-2Mn-0.6C



CrA-3Ni-0.6C



CrA-4MA-0.6C

Figure 4.60: Etched OM micrographs of different steels, compacted at 700 MPa, sintered 60 min in N₂-10% H₂ at 1250 °C (heat treated).

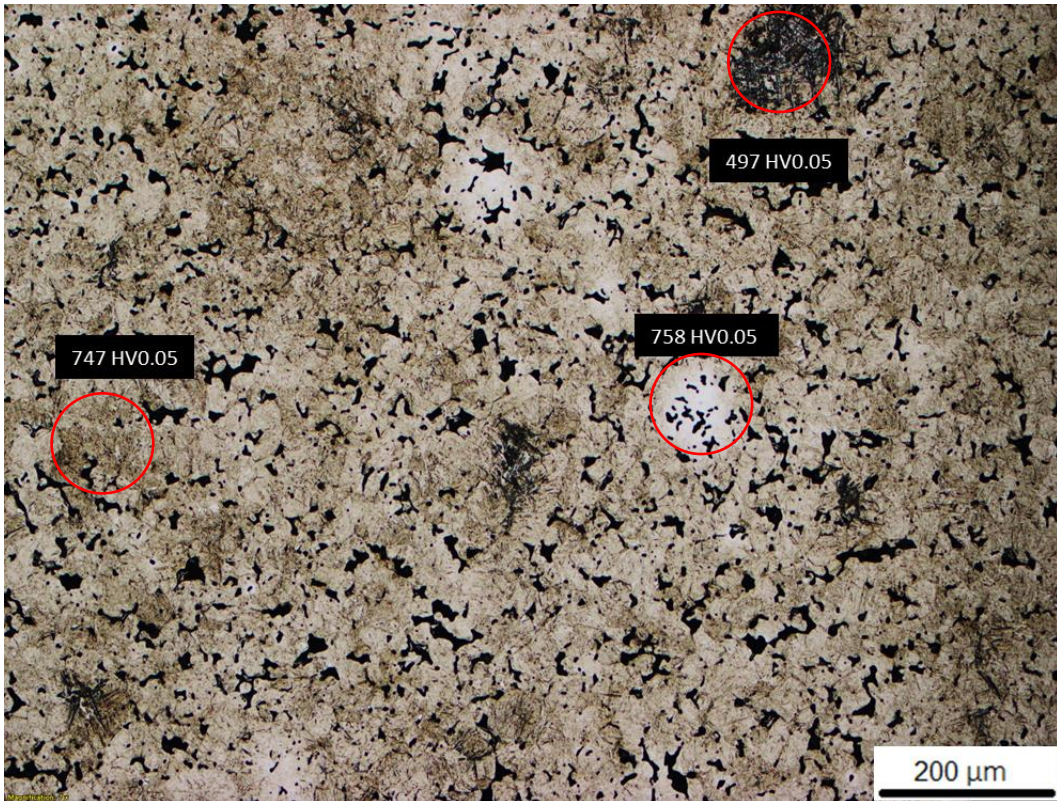


Figure 4.61: Etched OM micrograph and microhardness of CrA-2Mn-0.6C, compacted at 700 MPa, and sintered 60 min in N₂-10% H₂ at 1250 °C (heat treated)

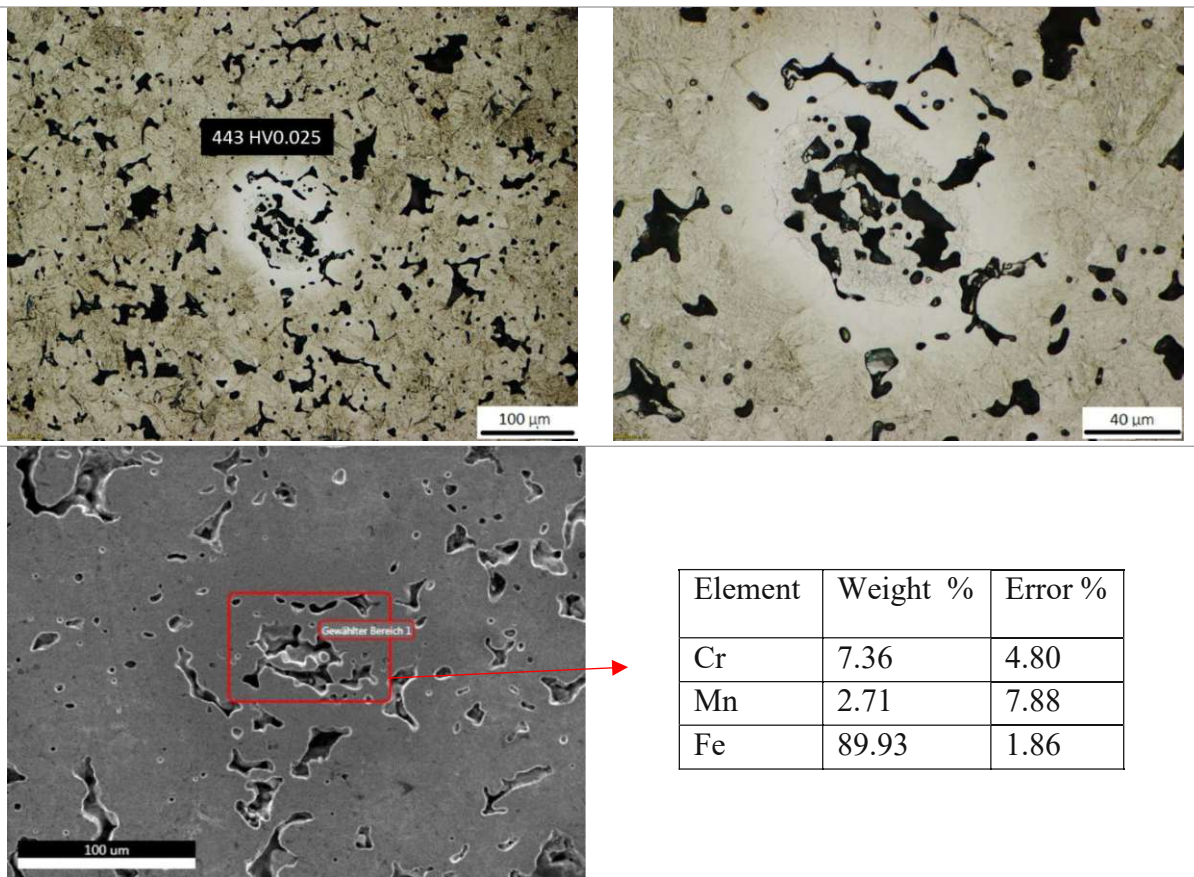


Figure 4.62: Cr-rich inclusion in microstructure of CrA-2Mn-0.6C, compacted at 700 MPa, sintered 60 min in N₂-10% H₂ at 1250 °C (heat treated).

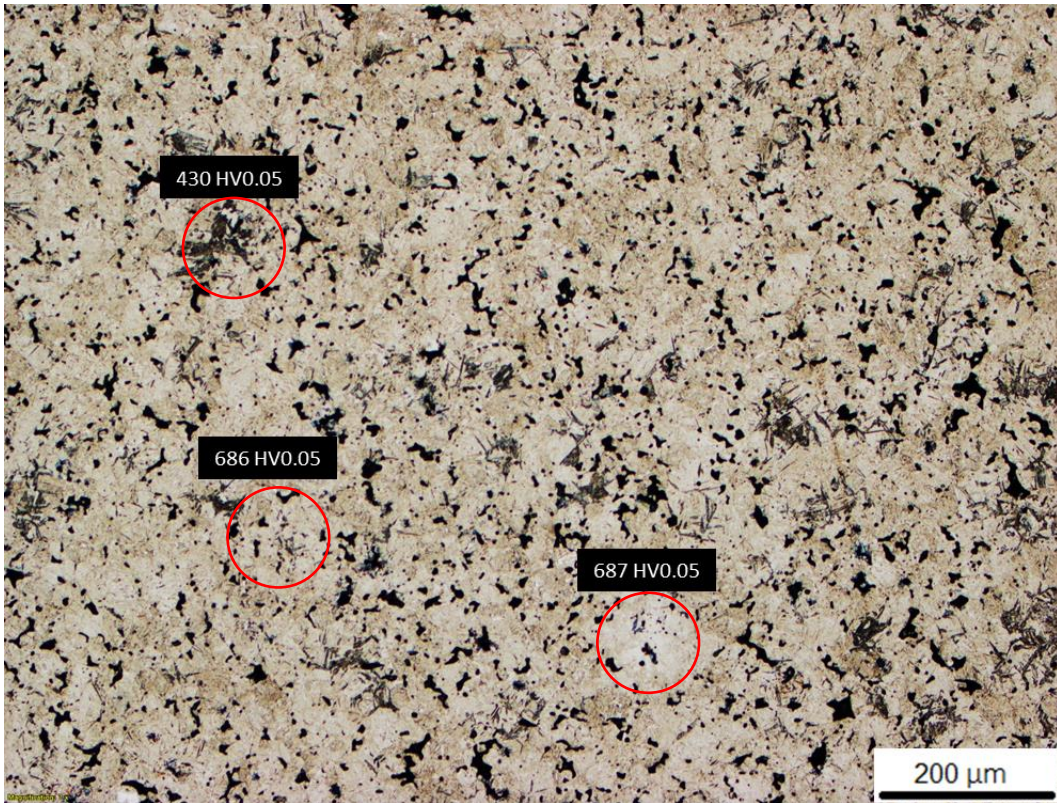


Figure 4.63: Etched OM micrograph and microhardness of CrA-3Ni-0.6C, compacted at 700 MPa, sintered 60 min in N₂-10% H₂ at 1250 °C (heat treated).

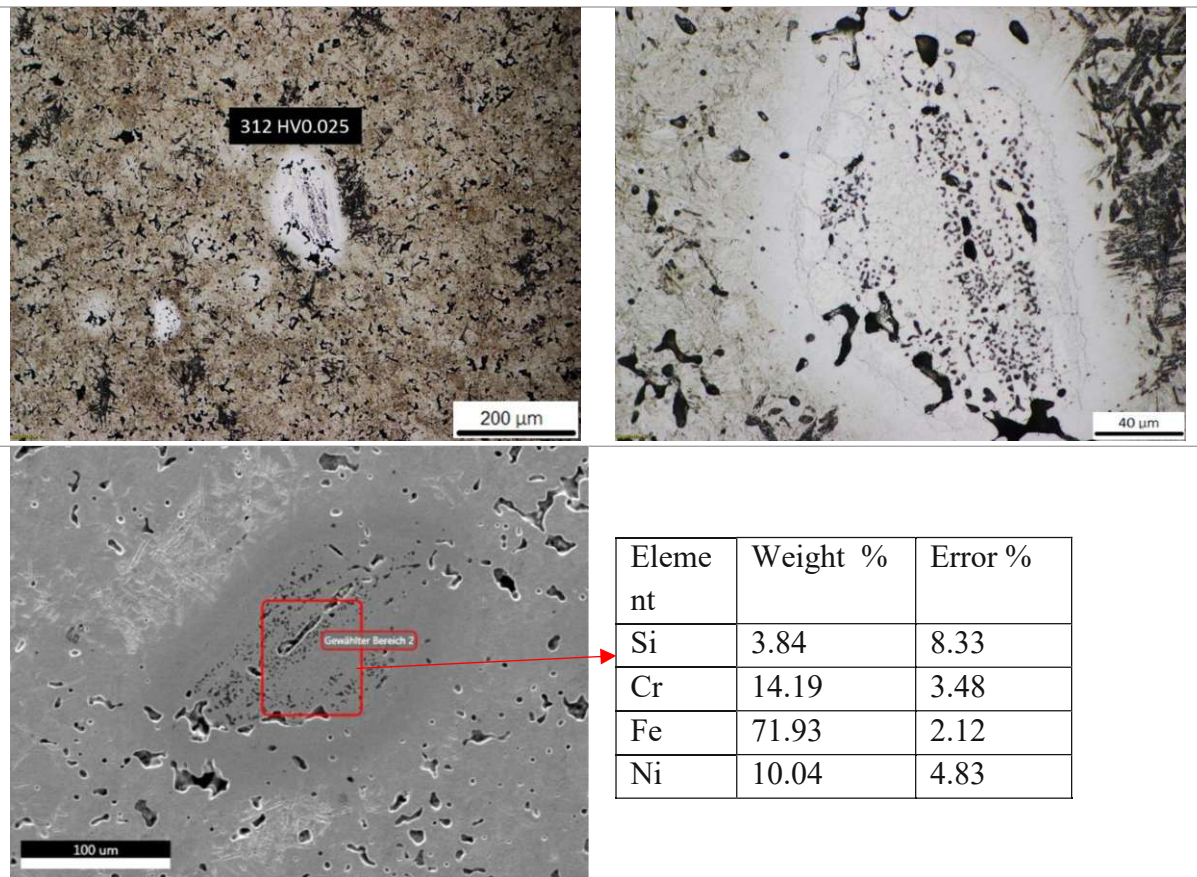


Figure 4.64: Cr, Ni-rich inclusion in the microstructure of CrA-3Ni-0.6C, compacted at 700 MPa, sintered 60 min in N₂-10% H₂ at 1250 °C (heat treated).

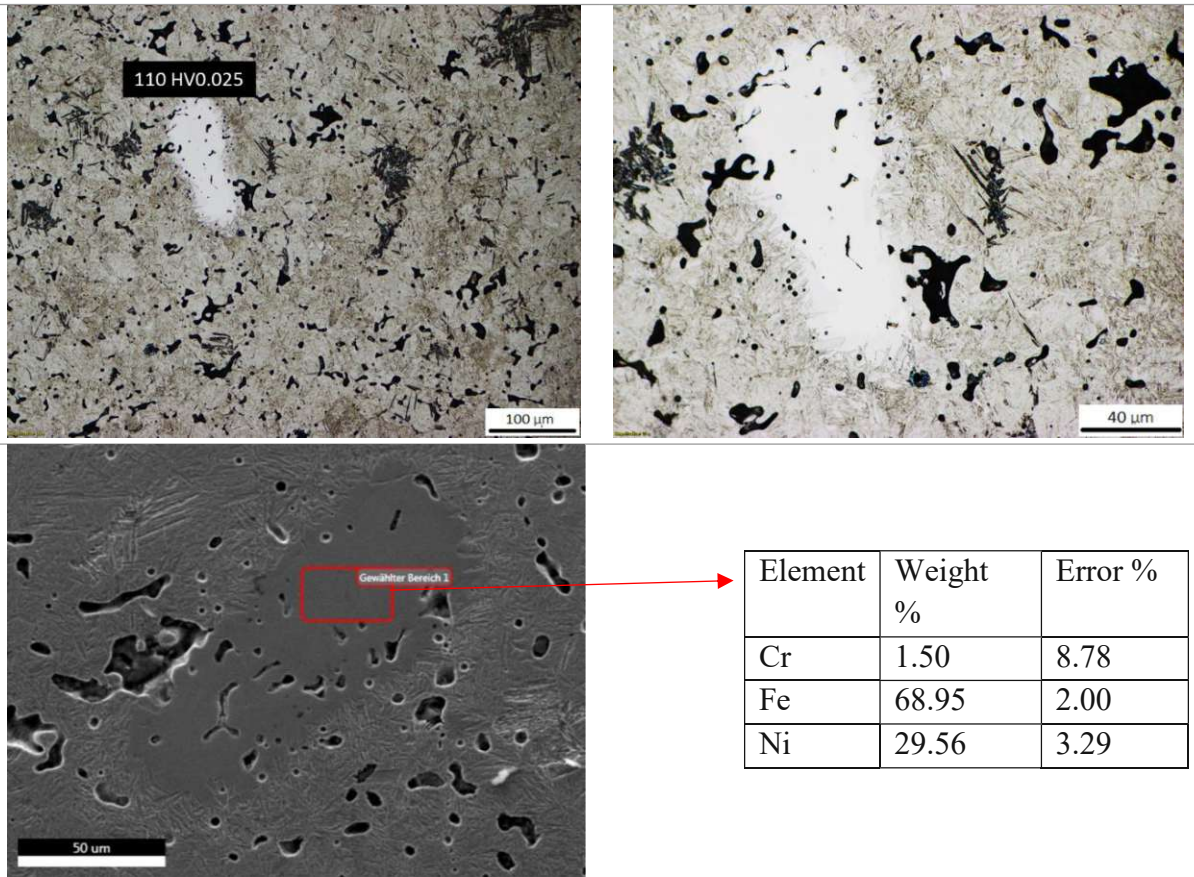


Figure 4.65: Ni-rich austenitic area in the microstructure of CrA-3Ni-0.6C, compacted at 700 MPa, and sintered 60 min in N₂-10% H₂ at 1250 °C (heat treated).

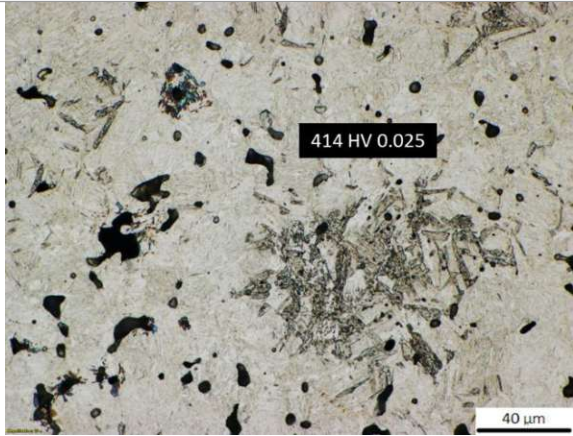
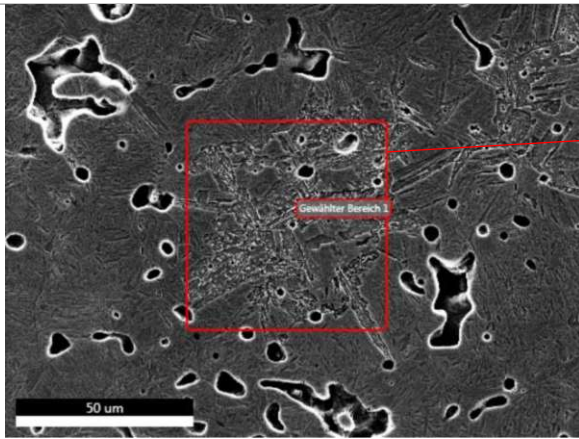


Figure 4.66: bainitic region in microstructure of CrA-3Ni-0.6C, compacted at 700 MPa, and sintered 60 min in N₂-10% H₂ at 1250 °C (heat treated).



Element	weight%	Error %
Cr	2.16	31.87
Fe	96.76	3.28
Ni	1.08	69.88

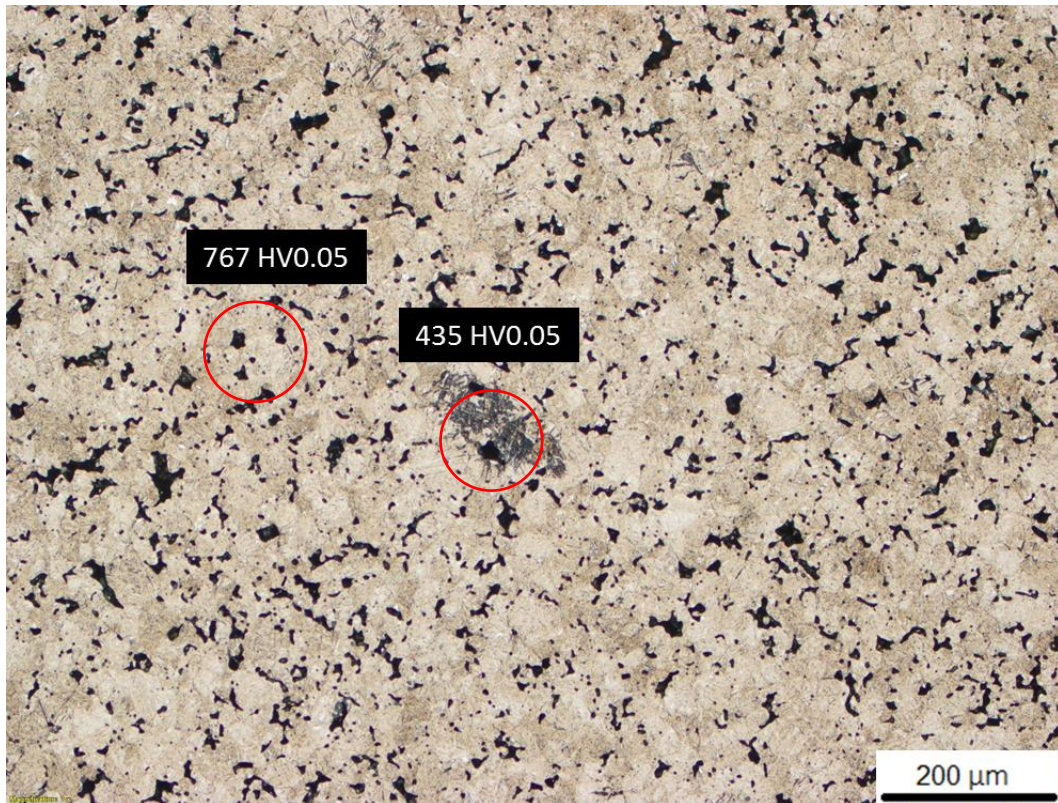


Figure 4.67: Etched OM micrograph and microhardness of CrA-4MA-0.6C, compacted at 700 MPa, sintered 60 min in N₂-10% H₂ at 1250 °C (heat treated).

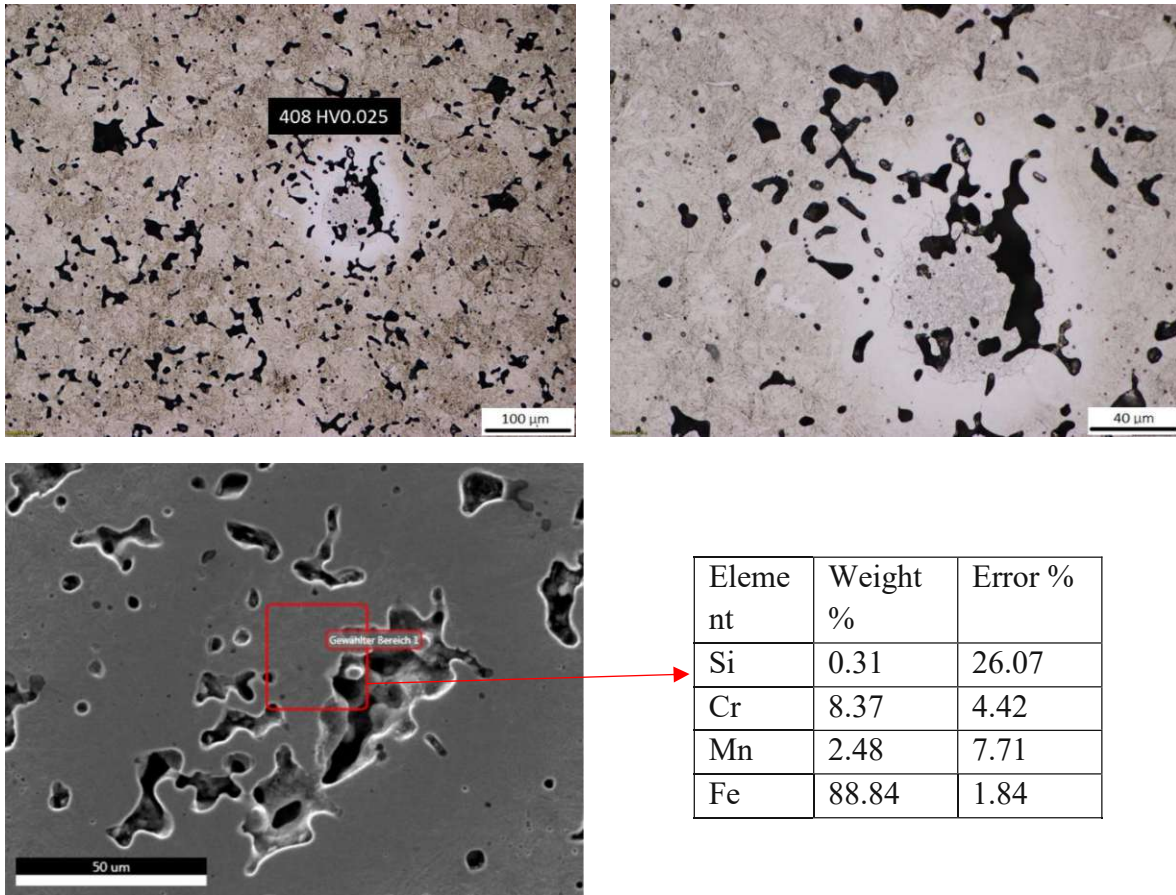
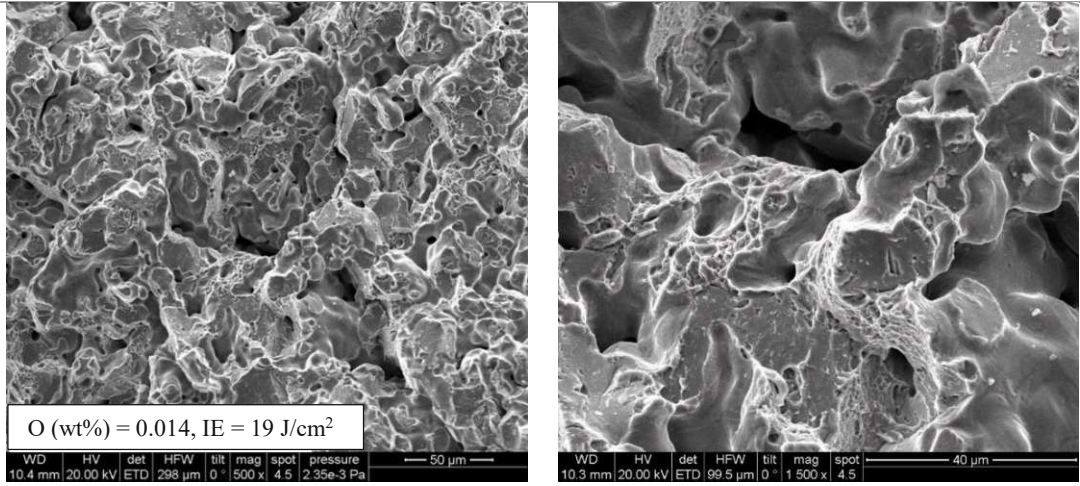


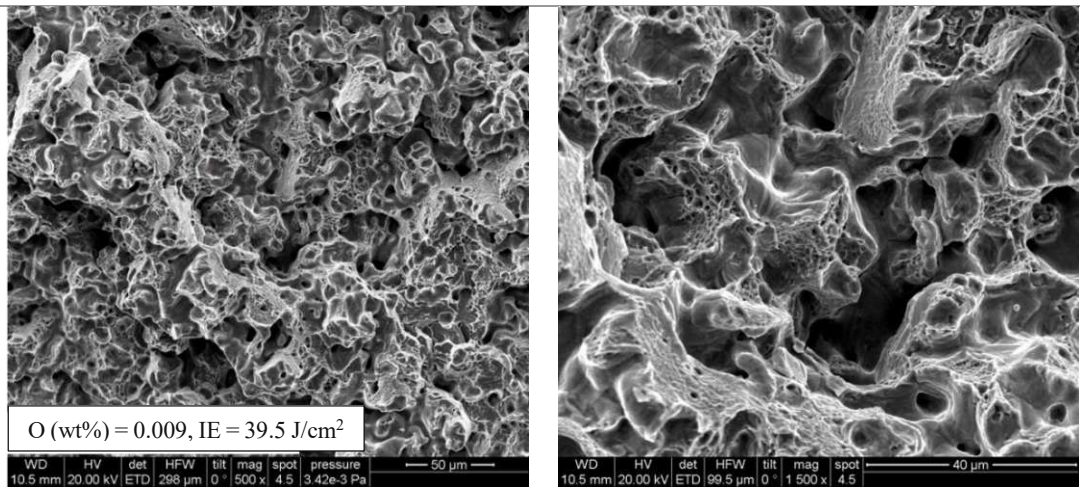
Figure 4.68: Cr-rich inclusion in the microstructure of CrA-4MA-0.6C, compacted at 700 MPa, sintered 60 min in N₂-10% H₂ at 1250 °C (heat treated).

4.9.3. Fractography (broken by Charpy impact test at RT)

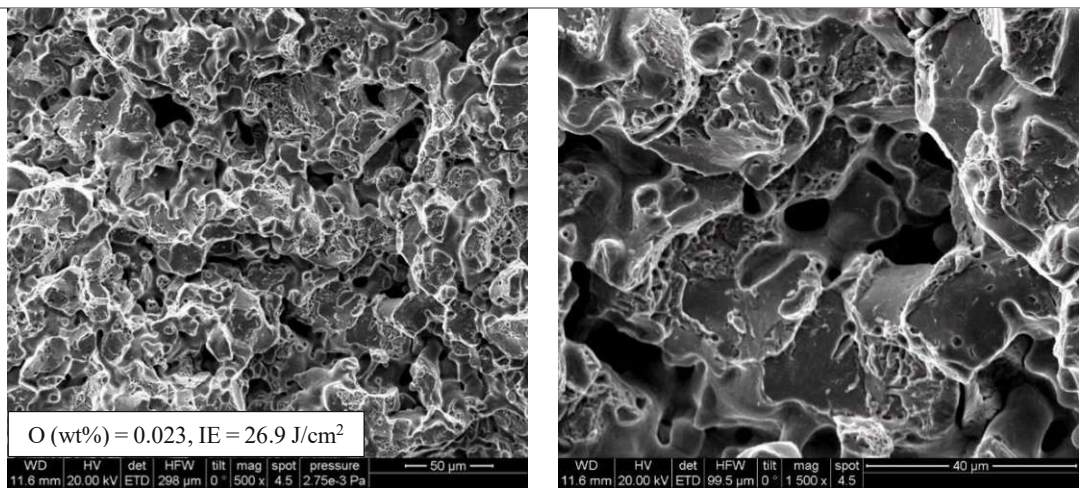
The fracture surfaces of the steels after the Charpy impact test are presented in Figure 4.69 with corresponding impact energy and oxygen content. In the Mn alloyed steel the fracture facets are to a considerable degree intergranular, which – not surprisingly - led to the lowest value of the impact energy (19 J/cm²). In the fracture surfaces of the two other steels (Ni and MA), in addition to transgranular cleavage facets some ductile dimples are also discernible. However, the fraction of ductile rupture in the Ni alloyed steel is much higher than in the MA steel, which led to the highest impact energy of 39.5 J/cm².



CrA-2Mn-0.6C



CrA-3Ni-0.6C



CrA-4MA-0.6C

Figure 4.69: Fracture surfaces of different steels (broken by Charpy impact test at RT), compacted at 700 MPa, sintered 60 min in N₂-10% H₂ at 1250 °C (heat treated).

4.9.4. Mechanical properties

The sintered density data and the mechanical properties of the steels are presented through Figure 4.70 to 4.73. The sintered density of the steels is depicted in Figure 4.70, indicating the highest density for the Ni alloyed steel, at 7.29 g/cm^3 , while the steel alloyed with elemental Mn showed the lowest value of 7.08 g/cm^3 . The results also show that addition of 4% MA leads to higher density (7.15 g/cm^3) compared to the Mn alloyed steel.

The hardness data are shown in Figure 4.71. The apparent hardness of all the steels after the heat treatment attained $>450 \text{ HV}_{30}$, however the MA steel showed slightly higher hardness compared to the other grades, which can be attributed to the presence of 0.3 Si in its chemical composition. In the Ni alloyed steel the hardness value is almost identical to that of the Mn alloyed steel (both about $450\text{-}460 \text{ HV}_{30}$) which indicates that the higher density of the Ni alloyed steel probably compensates the lower hardness of the martensitic matrix (measured by microhardness, see Fig 4.61 and 4.63) in this steel.

Figure 4.72 shows the Charpy impact energy of the steels tested at RT. It is obvious that the Ni alloyed steel exhibits the highest impact energy (39 J/cm^3), thanks to its higher density, lower hardness of martensite and stronger sintering bonds, which resulted in the transgranular and ductile fracture mechanism. The results also show that the Mn alloyed steel has the worst impact behaviour with the impact energy of 19 J/cm^3 , which also is in agreement with its fracture mechanism (in part brittle intergranular), while the steel alloyed with MA showed better results in impact test (28 J/cm^3). The reasons for this poor behaviour of the Mn alloyed steel could be related to the lower density, secondary pores and as well as the lower grain boundary cohesion (compared esp. to the Ni alloyed steel).

The dynamic Young's moduli of the steels are presented in Figure 4.73. As shown already in the previous chapters (section 3.1) this property is mainly influenced by the density. The results show that the Ni alloyed steels has the highest values (167 GPa) which can be explained by its highest sintered density, while the lowest value (160 GPa) is reported for the Mn alloyed steel with the lowest sintered density.

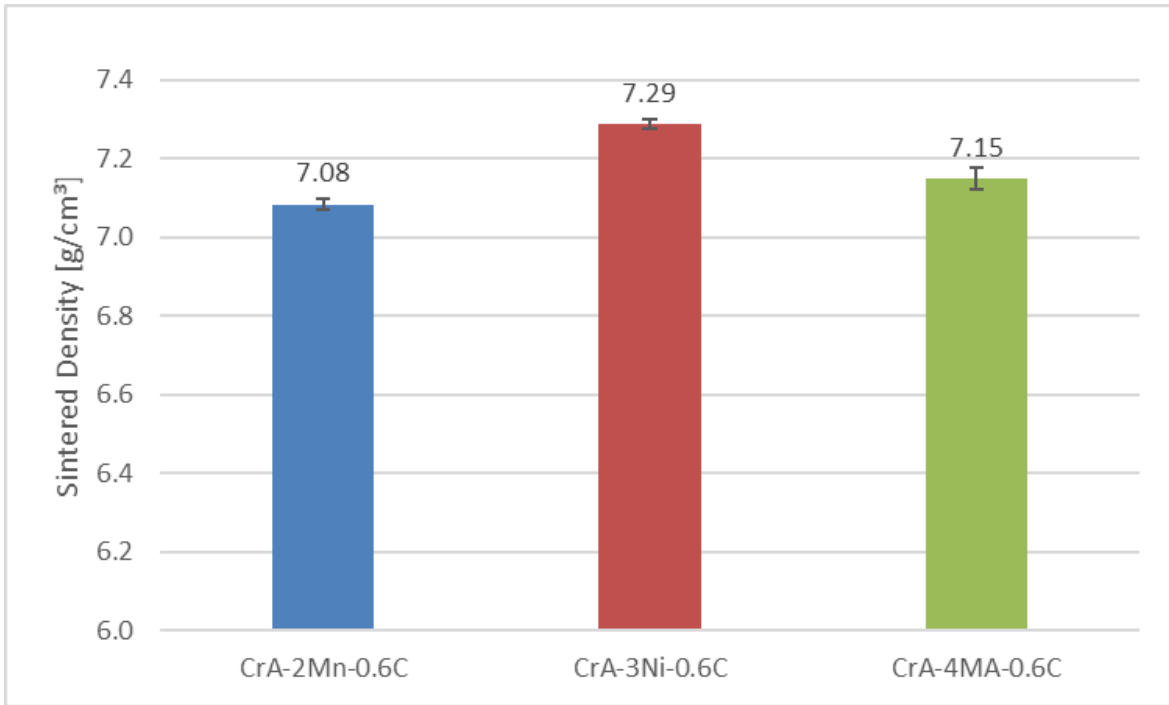


Figure 4.70: Sintered density of different steels, compacted at 700 MPa, sintered 60 min in N₂-10% H₂ at 1250 °C (heat treated).

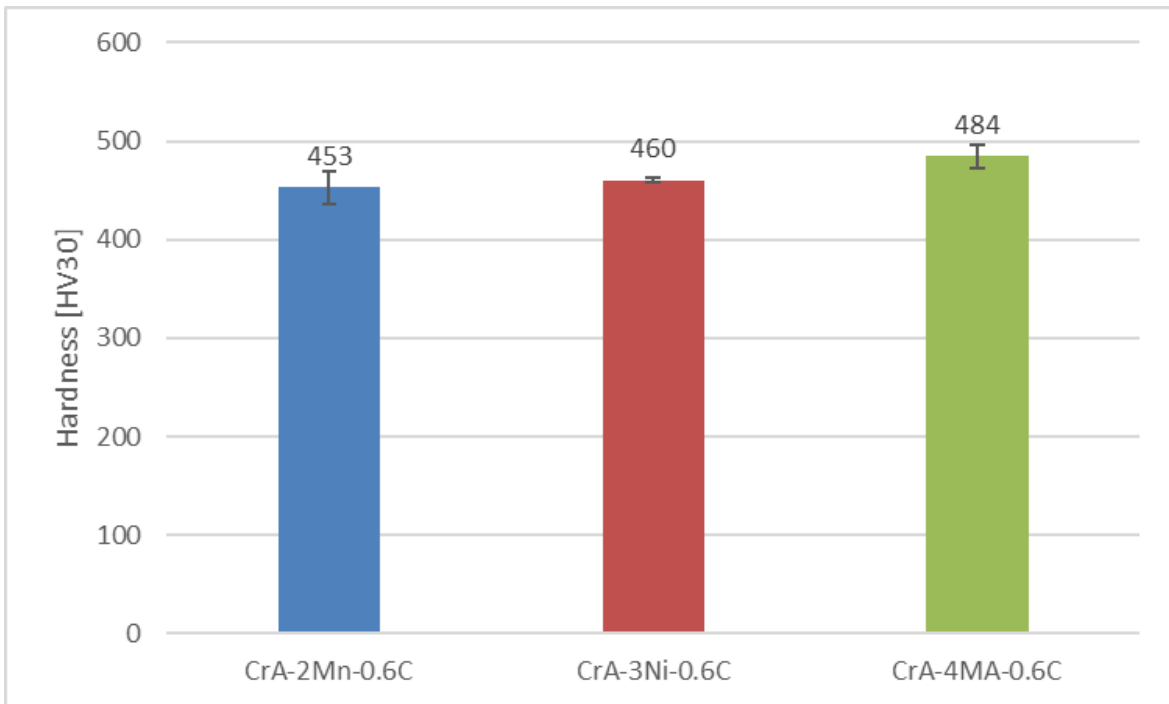


Figure 4.71: Apparent hardness HV30 of different steels, compacted at 700 MPa, sintered 60 min in N₂-10% H₂ at 1250 °C (heat treated)

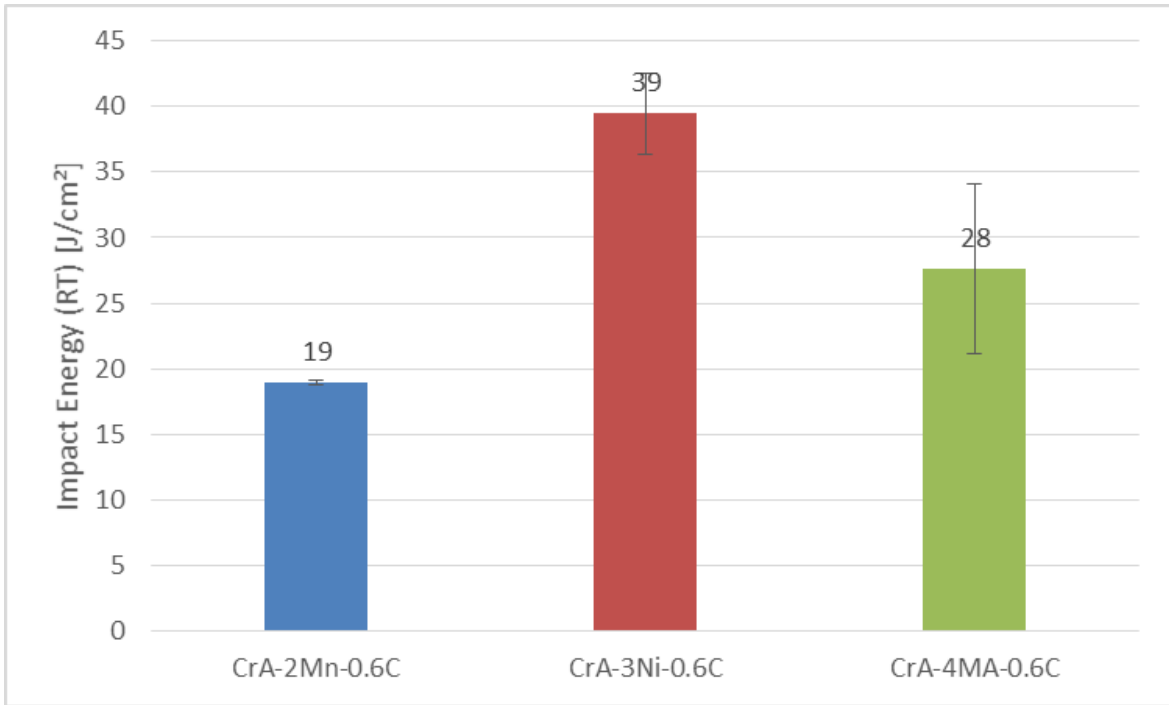


Figure 4.72: Charpy impact energy of different steels at RT, compacted at 700 MPa, sintered 60 min in N₂-10% H₂ at 1250 °C (heat treated).

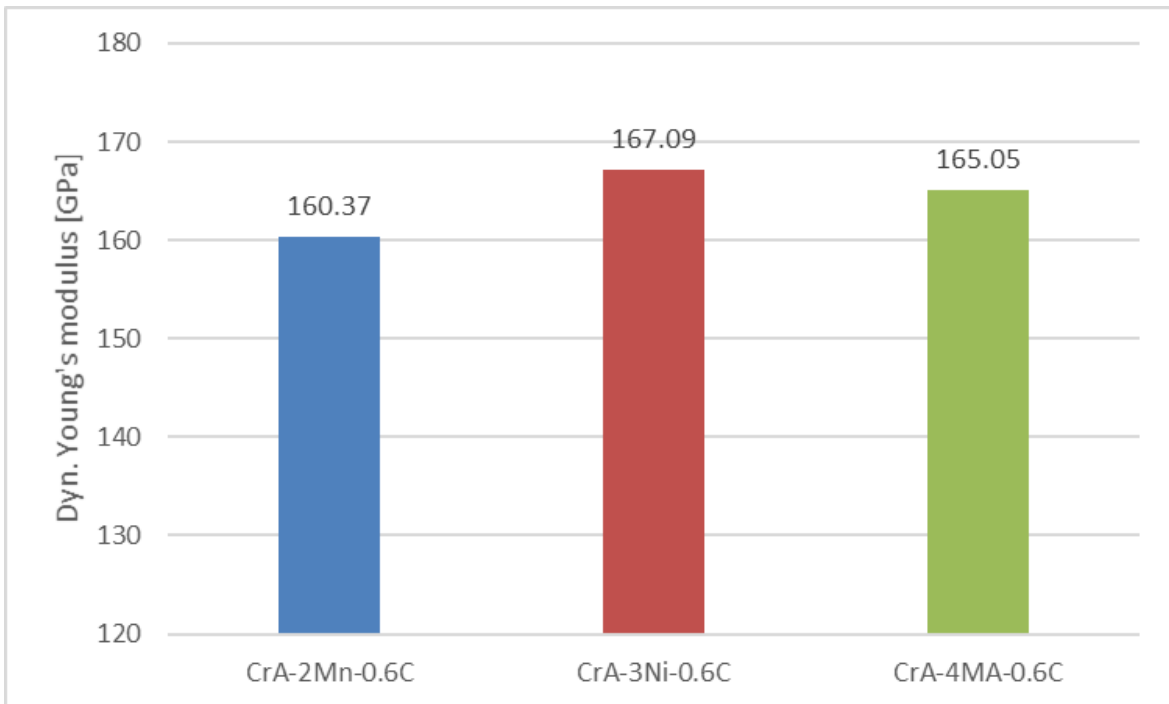


Figure 4.73: Dynamic Young's modulus of different steels, compacted at 700 MPa, sintered 60 min in N₂-10% H₂ at 1250 °C (heat treated).

Table 4.10: Results of mechanical properties of the selected mixes for fatigue testing, compacted at 700 MPa, sintered 60 min in N₂-10% H₂ at 1250 °C (heat treated).

	Material	Sintered density* (g/cm³)	Apparent hardness* (HV30)	impact energy* (J/cm²)	Dyn. Young's Modulus* (GPa)
1	CrA-2Mn-0.6C	7.08 ± 0.01	452.7 ± 17.3	19.0 ± 0.2	160.4
2	CrA-3Ni-0.6C	7.29 ± 0.01	460.2 ± 2.0	39.5 ± 3.1	167.1
3	CrA-4MA-0.6C	7.15 ± 0.03	484.3 ± 12.5	27.6 ± 6.4	165.1

* the measurements were performed on 90*12*12 bars

4.9.5. Fatigue S/N curves

The S/ε/N data for the steels are listed in table 4.11. The S/N and ε/N curves are also plotted in Figures 4.74 and 4.75, respectively. First of all, it is evident that the graphs drop consistently up to the gigacycle range. This means that there is no “fatigue limit” up to 10E10 cycles, which agrees e.g. with the statement of C.M.Sonsino [187]. When comparing the fatigue behaviour of the steels containing different alloying elements it stands out clearly that addition of Ni to the base powder markedly improves the fatigue strength below 10⁸ loading cycles, while at N > 10⁸ the fatigue endurance is similar to that of the MA alloyed steel.

The good fatigue behaviour of the Ni alloyed steel at N < 10⁸ could be explained by its higher density (lower porosity), and stronger sintering bonds of the steel compared to the other grades, while at higher fatigue cycles (N > 10⁸) the Ni alloyed grade, which showed to be quite promising in the high amplitude (lower N) range, does not retain this advantage into the gigacycle range and furthermore showed a very large scatter of the cycles to failure. It has already been shown that the high strength/low ductility metallic materials are sensitive to singular defects in the case of high cycle fatigue [188], therefore in this case as well, the larger austenitic areas (with very low hardness) shown above might well cause crack initiation. The figure also shows that the steel alloyed with 2% Mn has the lowest fatigue strength, however it showed the same trend and a parallel curve with the MA alloyed steel. In this case, the lower density of Mn alloyed steel as well as the lower grain boundary cohesion could be a reason for this low fatigue strength. A point that should not be neglected here is the role of the secondary pores which are formed in Mn alloyed PM steels due to Mn evaporation; this might also lower the fatigue strength. This assumption is supported by the previous results with Mo steels containing secondary pores [43].

As mentioned before, the MA steel in this series showed the same trend and slope as the Mn alloyed steel, however the S/N curves shows that the fatigue strength of this steel is approximately 60 MPa higher than of the steels alloyed with Mn, which could be explained by the higher density as well as stronger sintering bonds and more regular microstructure. In Figure 4.75 the strain amplitudes are plotted against the number of cycles to failure.

Table 4.11: S/N and ϵ/N data for different steels, compacted at 700MPa, and sintered 60 min in N₂-10% H₂ at 1250 °C (heat treated).

CrA-2Mn-0.6C			CrA-3Ni-0.6C			CrA+4MA+0.6C		
σ (MPa)	ϵ	N	σ (MPa)	ϵ	N	σ (MPa)	ϵ	N
201	1.2E-03	4.7E+06	411	2.4E-03	3.9E+05	273	1.6E-03	3.0E+06
201	1.2E-03	3.1E+06	334	1.9E-03	8.5E+06	273	1.6E-03	4.3E+06
183	1.1E-03	8.7E+07	334	1.9E-03	2.0E+06	273	1.6E-03	3.1E+06
183	1.1E-03	2.5E+07	334	1.9E-03	3.0E+06	237	1.4E-03	2.0E+08
183	1.1E-03	6.4E+07	334	1.9E-03	2.6E+06	237	1.4E-03	6.7E+07
166	1.0E-03	2.1E+08	334	1.9E-03	1.8E+07	237	1.4E-03	1.2E+08
166	1.0E-03	2.1E+08	295	1.7E-03	2.0E+07	236	1.4E-03	4.0E+07
166	1.0E-03	1.2E+08	295	1.7E-03	3.7E+07	236	1.4E-03	3.0E+07
166	1.0E-03	1.3E+08	295	1.7E-03	5.7E+07	216	1.3E-03	1.8E+08
148	9.2E-04	7.1E+08	295	1.7E-03	2.0E+07	216	1.3E-03	3.1E+08
148	9.2E-04	7.5E+08	257	1.5E-03	5.4E+08	216	1.3E-03	8.9E+07
148	9.2E-04	2.3E+08	257	1.5E-03	3.8E+08	196	1.2E-03	8.9E+08
131	8.1E-04	4.5E+09	257	1.5E-03	1.2E+08	196	1.2E-03	1.9E+09
131	8.1E-04	2.9E+09	257	1.5E-03	3.6E+08	196	1.2E-03	2.0E+09
131	8.1E-04	2.4E+09	214	1.3E-03	9.6E+08	176	1.0E-03	5.5E+09
113	7.0E-04	1.3E+09	190	1.1E-03	2.9E+08	176	1.0E-03	1.2E+09
113	7.0E-04	3.2E+09	190	1.1E-03	1.0E+08	176	1.0E-03	5.9E+09
113	7.0E-04	>1.2E+10	170	9.9E-04	9.4E+08	156	9.2E-04	>1.0E+10
			170	9.9E-04	1.5E+08			

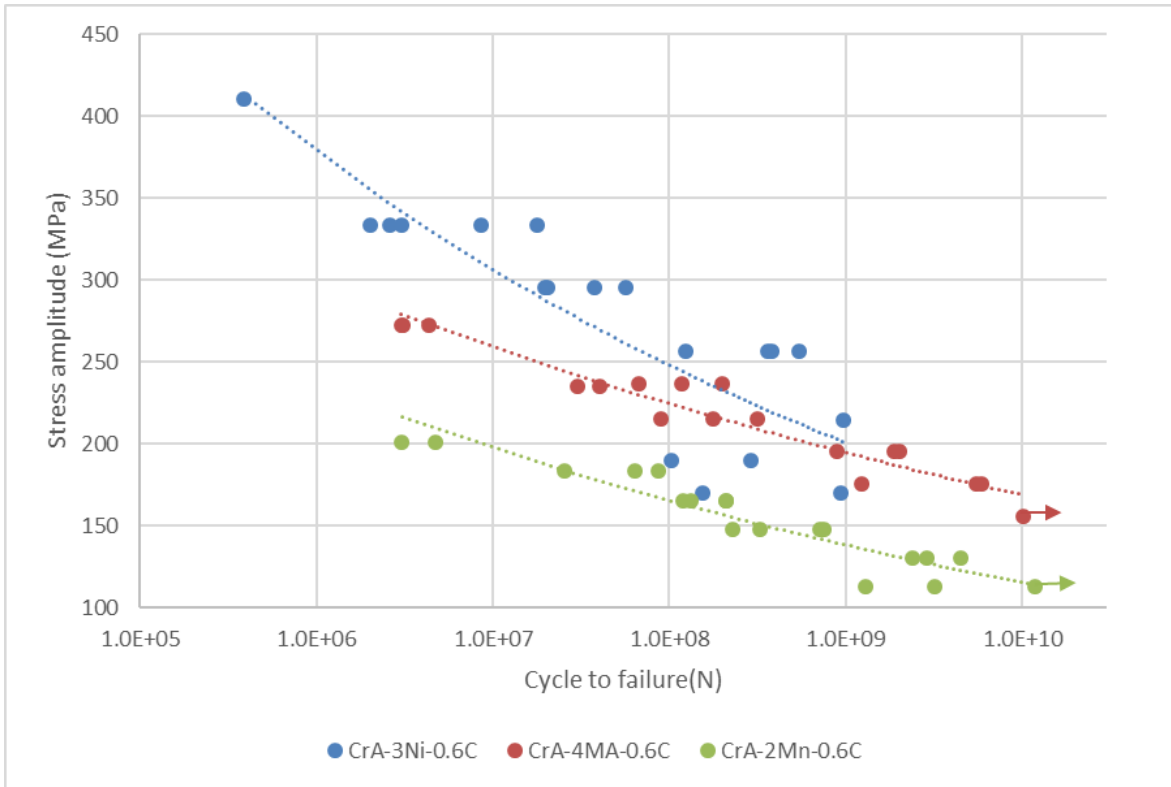


Figure 4.74: S/N curves of different steels, compacted at 700 MPa, sintered 60 min in N₂-10% H₂ at 1250 °C (heat treated). Ultrasonic fatigue testing, 20 kHz, push-pull, R = -1

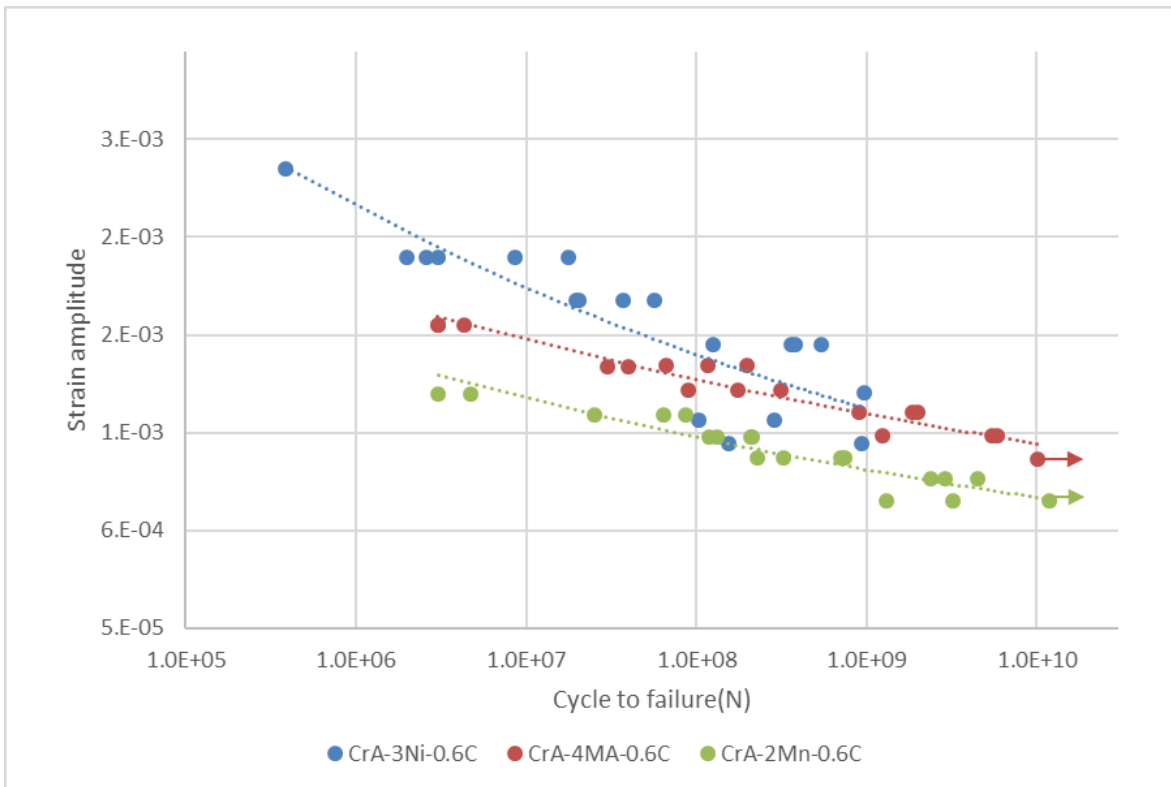


Figure 4.75: ϵ/N curves of different steels, compacted at 700 MPa, sintered 60 min in N₂-10% H₂ at 1250 °C (heat treated). Ultrasonic fatigue testing, 20 kHz, push-pull, R = -1

4.9.6. Fractography of fatigue specimens

In Figure 4.76 to 4.84, the fatigue fracture surfaces of the different steels are shown. The areas related to the stable and unstable growth of the fatigue crack are marked with “fatigue fr.” and “final fr.”, respectively. The topography and appearance of the fatigue fracture area clearly differs from the final fracture area, due to plastic deformation of the surface during final fracture while the fatigue fracture surfaces are very smooth, as a consequence of slow crack growth. The fractographs also show that in all steels, the smooth area related to fatigue fracture increases at lower stress amplitude and resulting higher loading cycle number. The studies on the fracture surface also revealed that crack initiation occurs predominantly at the surface or near the surface; however, identifying the exact position of the crack initiation is rather difficult in PM steels compared to fully dense materials, due to presence of pores. However, in this study it was attempted to identify the probable position of the crack initiation based on the topography of the surface or presence of large pores. In some cases such as Fig. 4.77, 4.80 and 4.83, the crack initiation and propagation from the surface is clearly evident, in such cases singularities such as a large pore (similar to what we see in Fig.4.83), inclusions or soft phases (for instance a Ni-rich austenitic area) could result in crack initiation. In Fig. 4.76, 4.78 and 4.84 it seems that a near-surface point is the site of crack initiation. For instance in Fig 4.81 presence of a pore cluster seems to be the cause of the crack initiation. In Fig. 4.84, formation of a “fisheye” fracture in the fracture surface shows a crack initiation from an interior point as well. The fractographs also indicate that the final fracture is more brittle compared to the mechanisms observed by Charpy impact test (Fig. 4.69). It is evident that in the Mn alloyed steel the mechanism is mostly intergranular while the MA alloyed steel shows a mix of inter- and transgranular fracture. In the Ni alloyed steel, in addition to the trans-granular cleavage facets, some dimple facets related to more ductile fracture are also discernible.

CrA-2Mn-0.6C
 $\sigma=201$ MPa, $N = 3.06E+06$

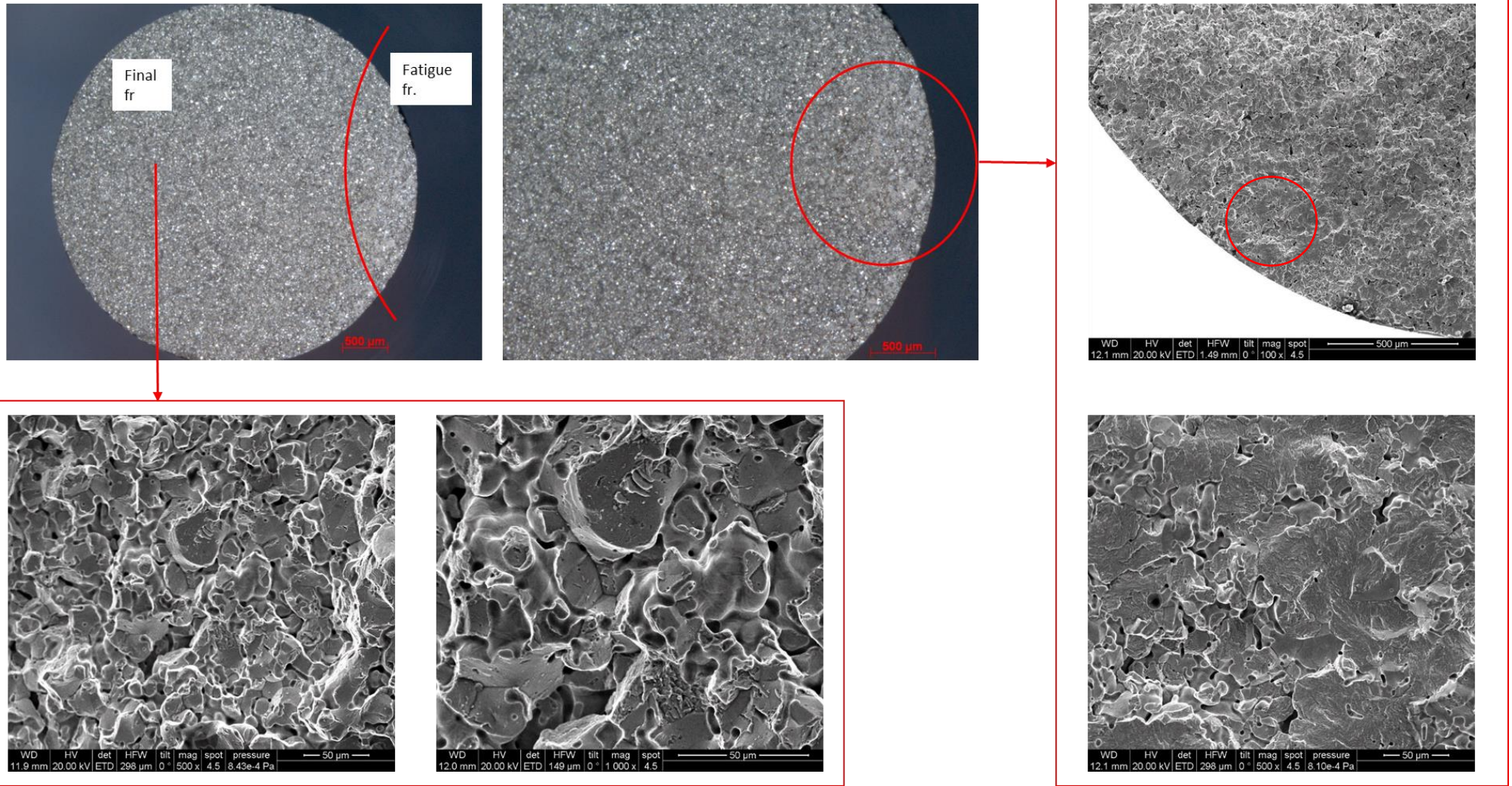


Figure 4.76: Fatigue fracture surface of CrA-2Mn-0.6C, compacted at 700 MPa, sintered 60 min in N₂-10% H₂ at 1250 °C (heat treated).

CrA-2Mn-0.6C
 $\sigma=166$ MPa, $N = 2.08E+08$

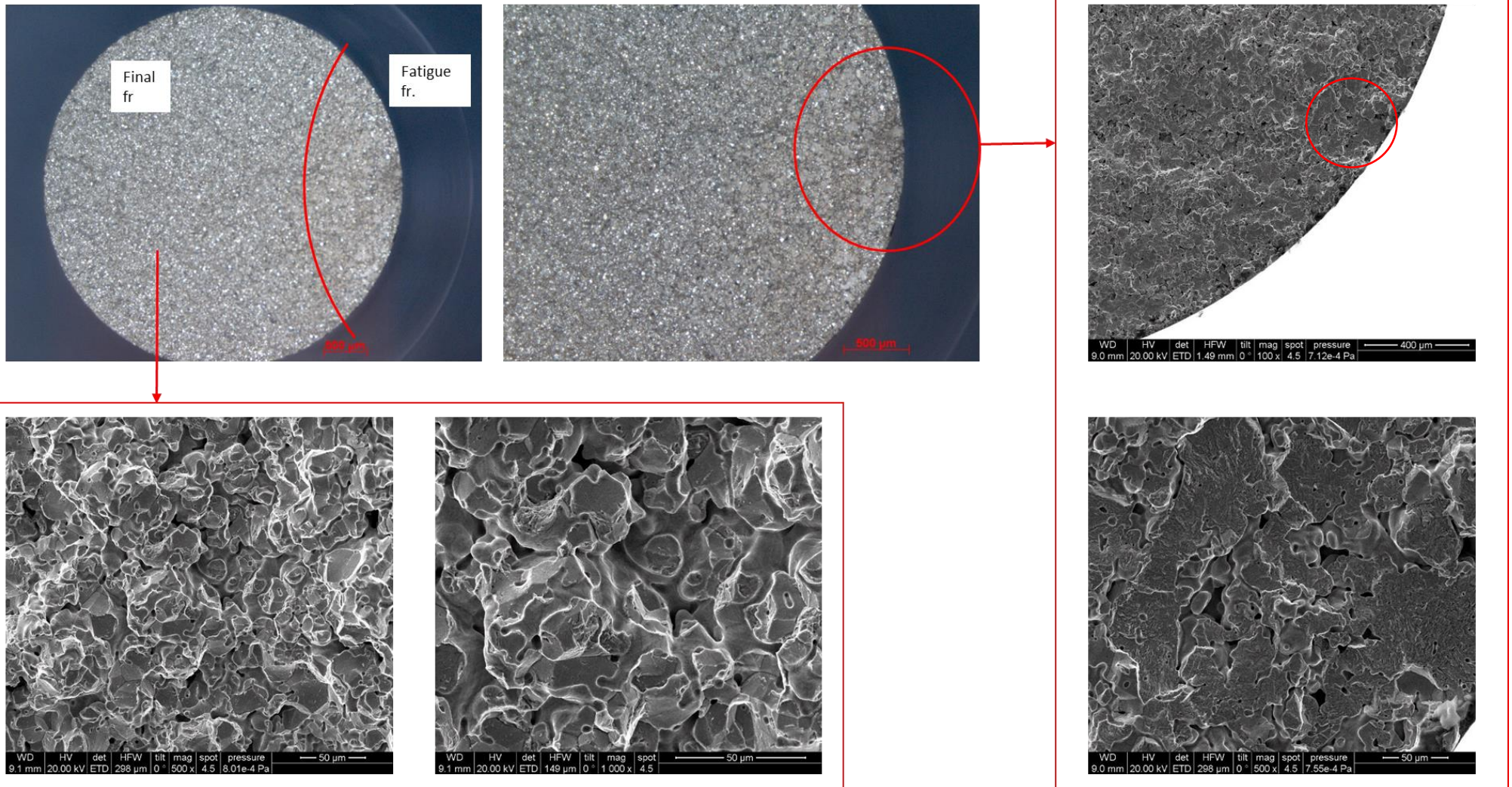


Figure 4.77: Fatigue fracture surface of CrA-2Mn-0.6C, compacted at 700 MPa, sintered 60 min in N₂-10% H₂ at 1250 °C (heat treated).

CrA-2Mn-0.6-C
 $\sigma = 113 \text{ MPa}$, $N = 1.3\text{E}+09$

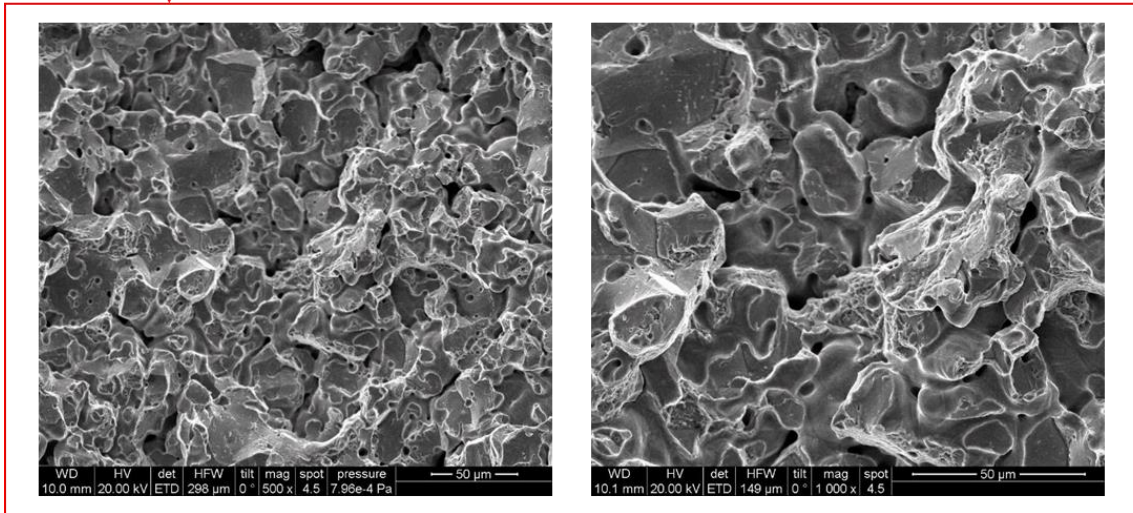
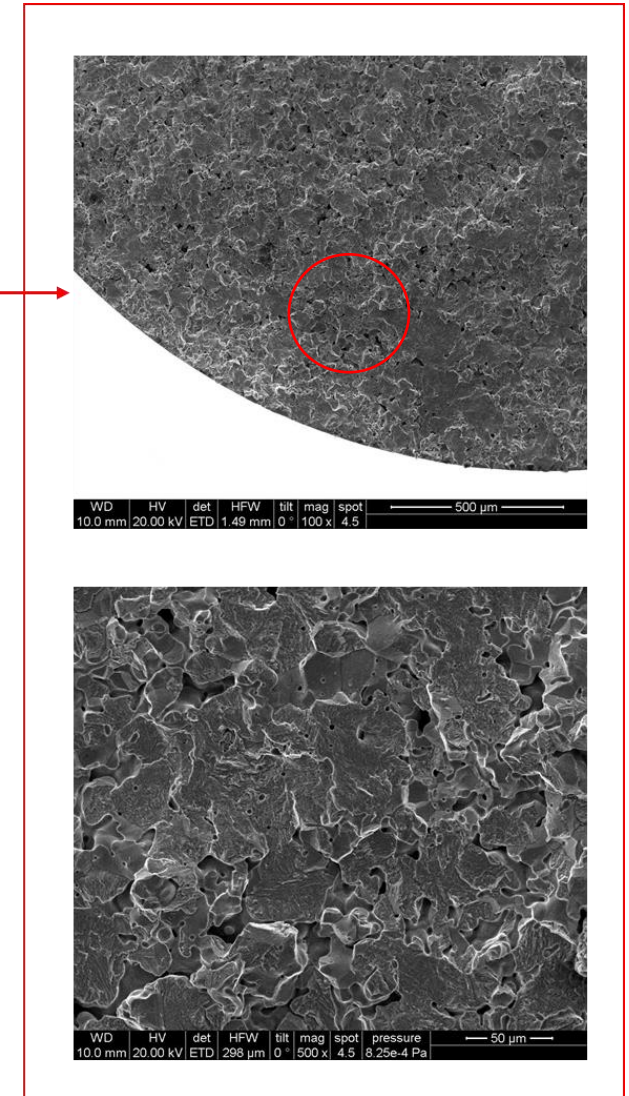
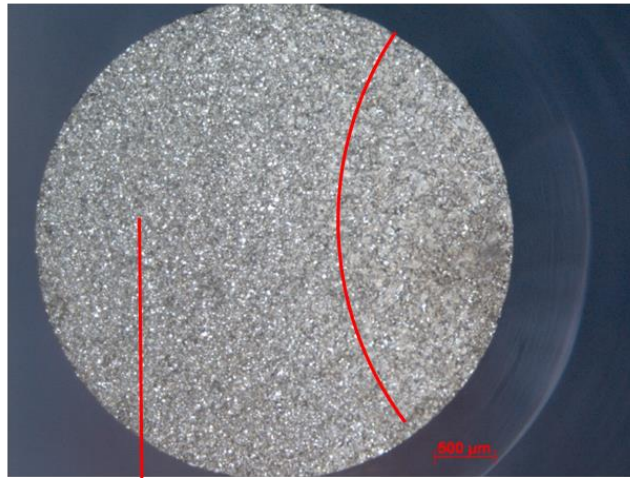


Figure 4.78: Fatigue fracture surface of CrA-2Mn-0.6C, compacted at 700 MPa, sintered 60 min in N₂-10% H₂ at 1250 °C (heat treated).

CrA-3Ni-0.6C
 $\sigma=334$ MPa, $N = 2.00E+06$

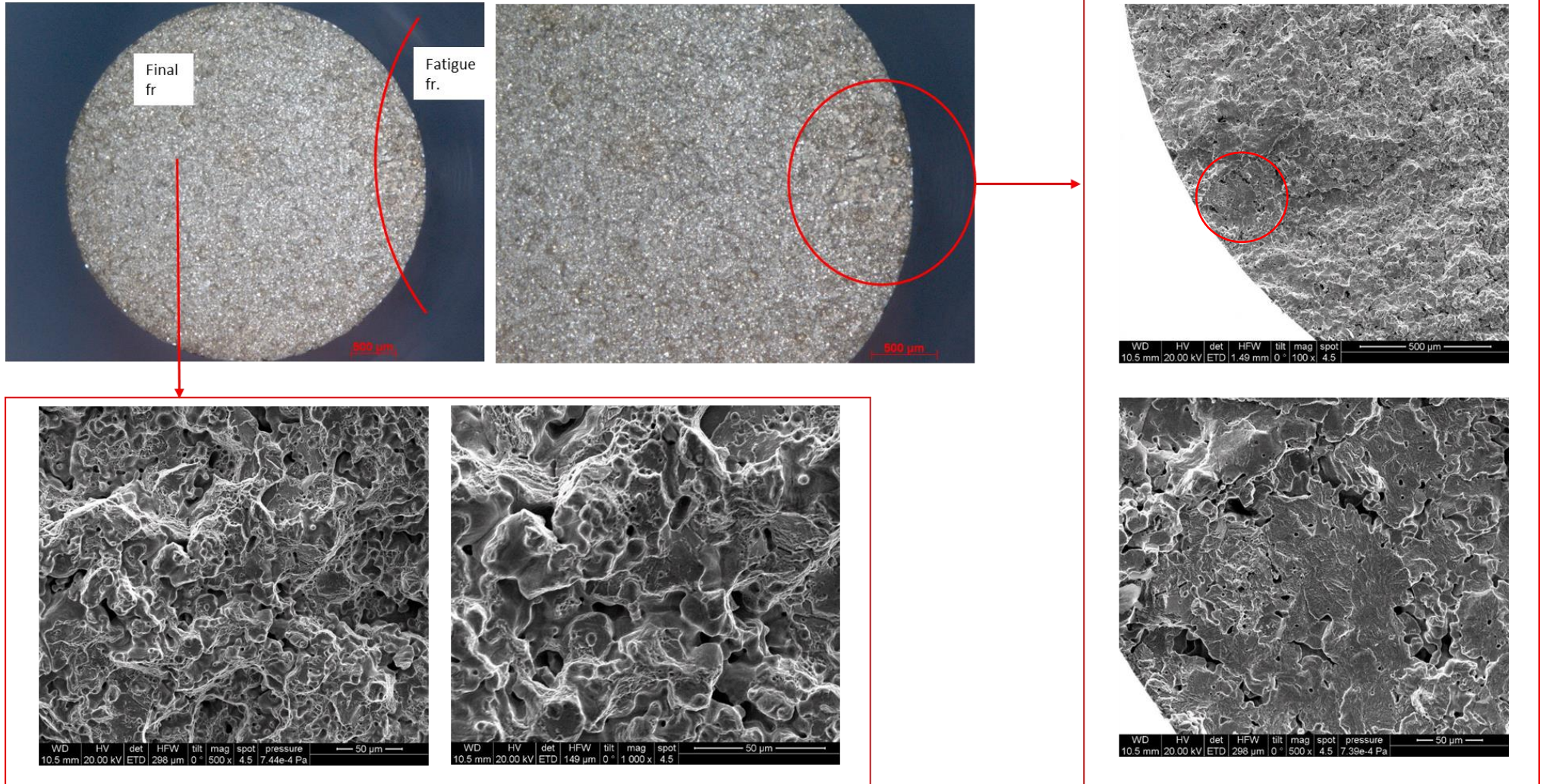


Figure 4.79: Fatigue fracture surface of CrA-3Ni-0.6C, compacted at 700 MPa, sintered 60 min in N₂-10% H₂ at 1250 °C (heat treated).

CrA-3Ni-0.6C
 $\sigma = 295 \text{ MPa}$, $N = 2.03E+07$

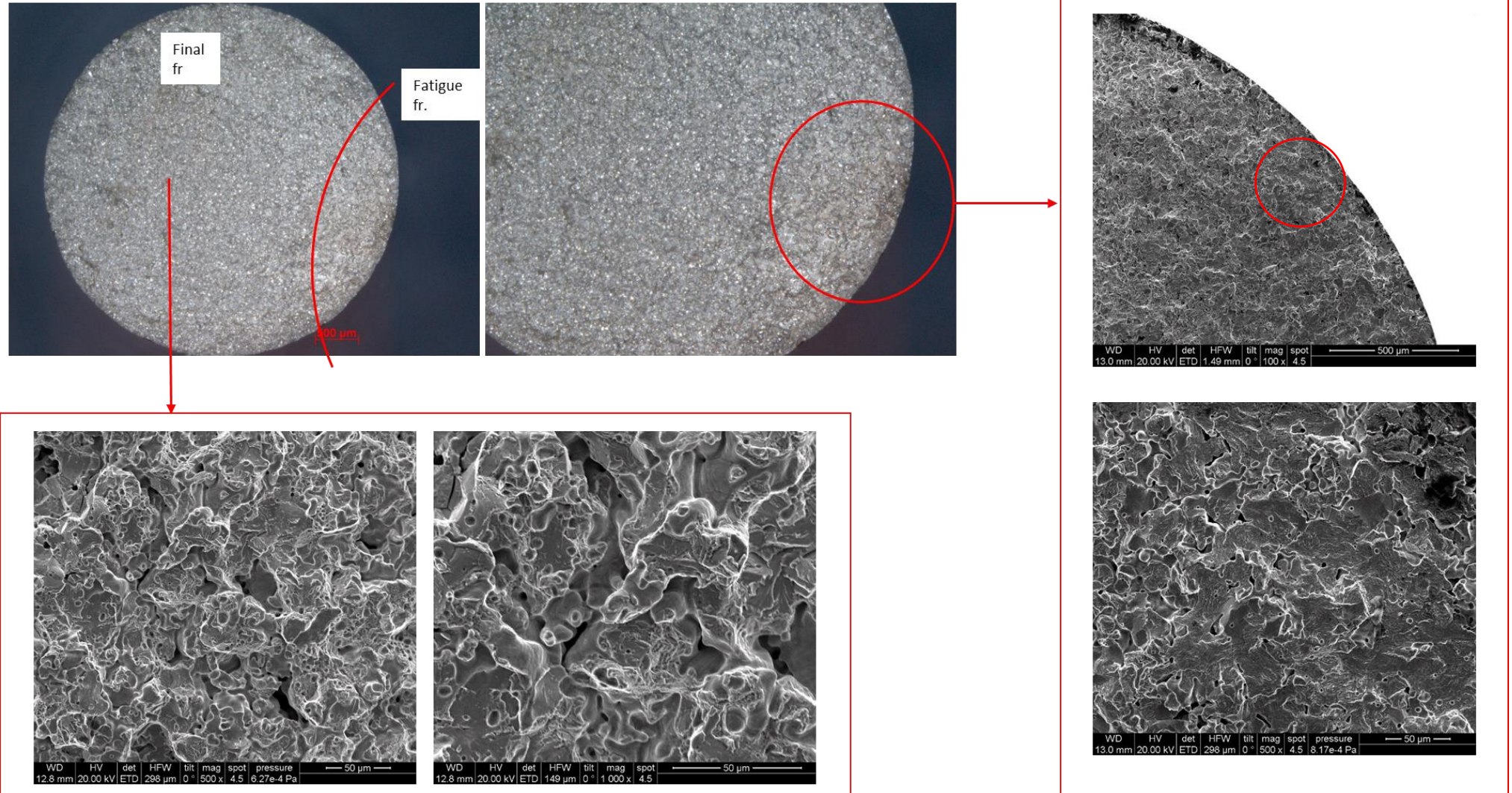


Figure 4.80: Fatigue fracture surface of CrA-3Ni-0.6C, compacted at 700 MPa, sintered 60 min in N₂-10% H₂ at 1250 °C (heat treated).

CrA-3Ni-0.6C
 $\sigma = 257 \text{ MPa}$, $N = 5.40E+08$

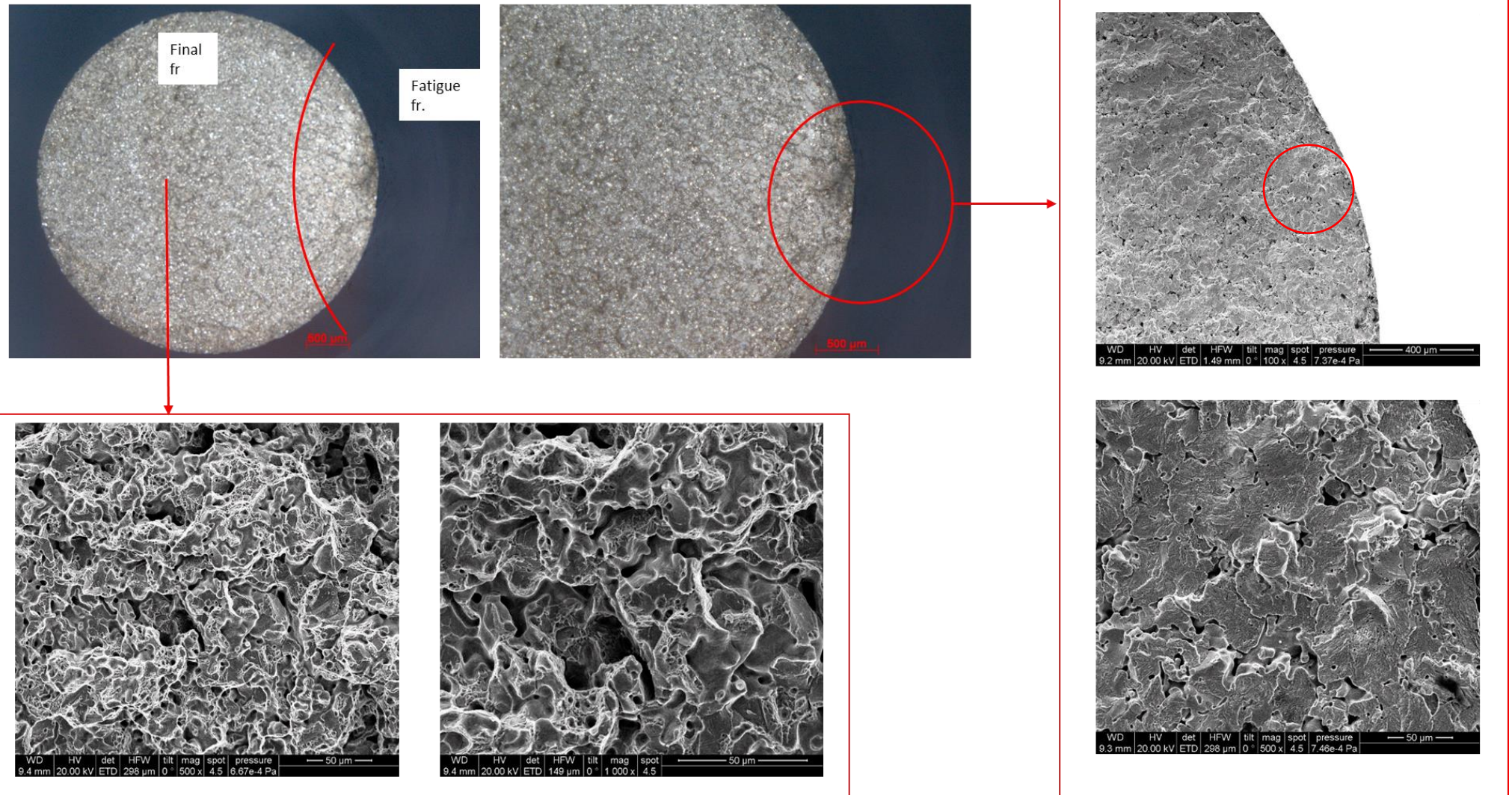


Figure 4.81: Fatigue fracture surface of CrA-3Ni-0.6C, compacted at 700 MPa, sintered 60 min in N₂-10% H₂ at 1250 °C (heat treated).

CrA-4MA-0.6C
 $\sigma = 273$, $N = 4.31E+06$

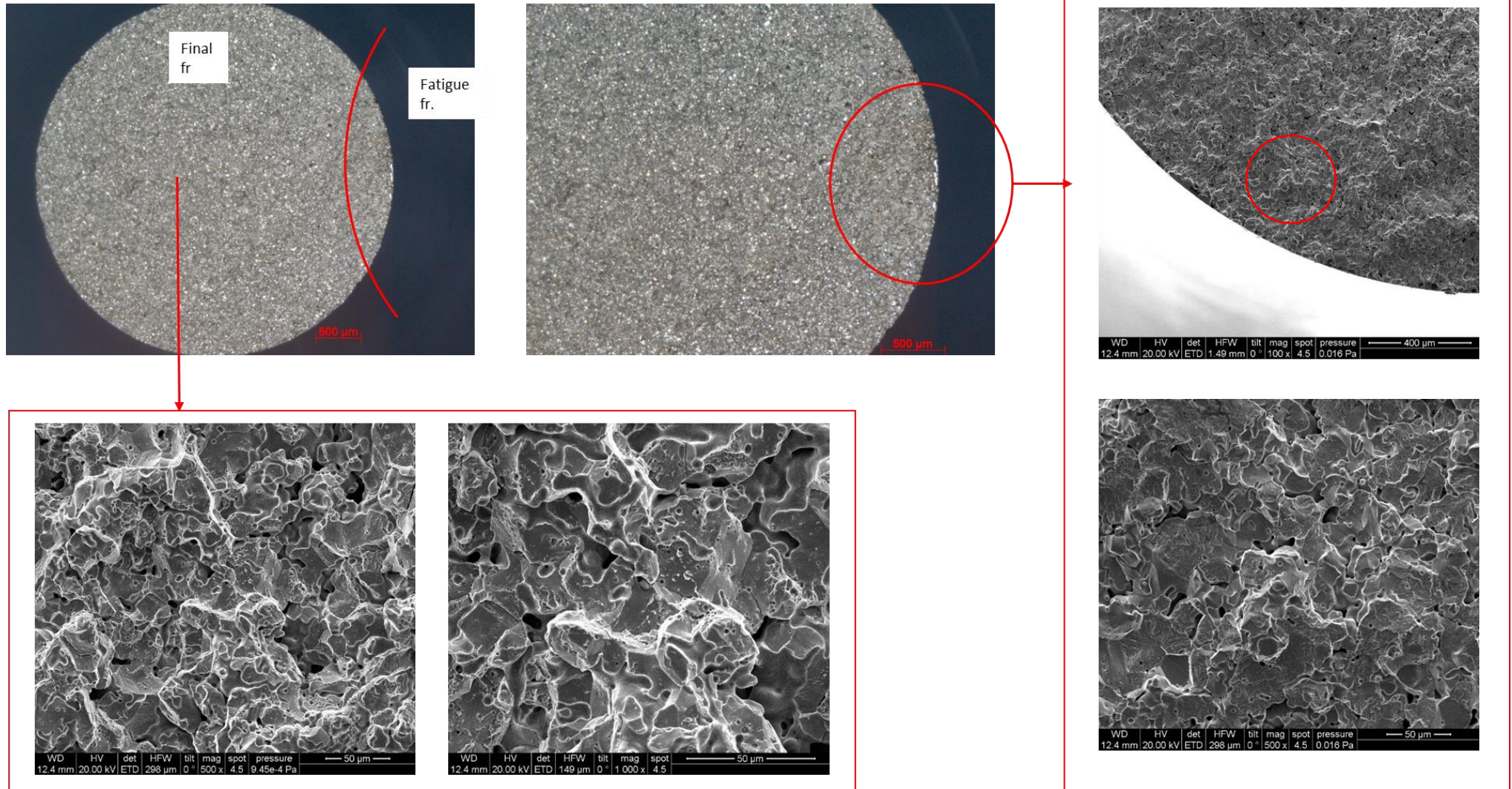


Figure 4.82: Fatigue fracture surface of CrA-4MA-0.6C, compacted at 700 MPa, sintered 60 min in N_2 -10% H_2 at 1250 °C (heat treated).

CrA-4MA-0.6C
 $\sigma = 216 \text{ MPa}$, $N = 1.76E+08$

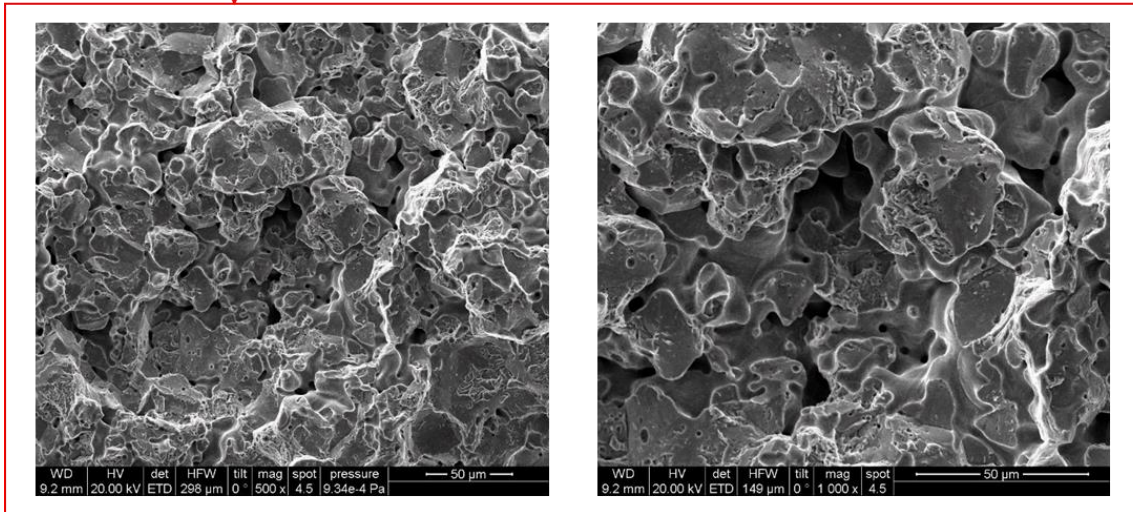
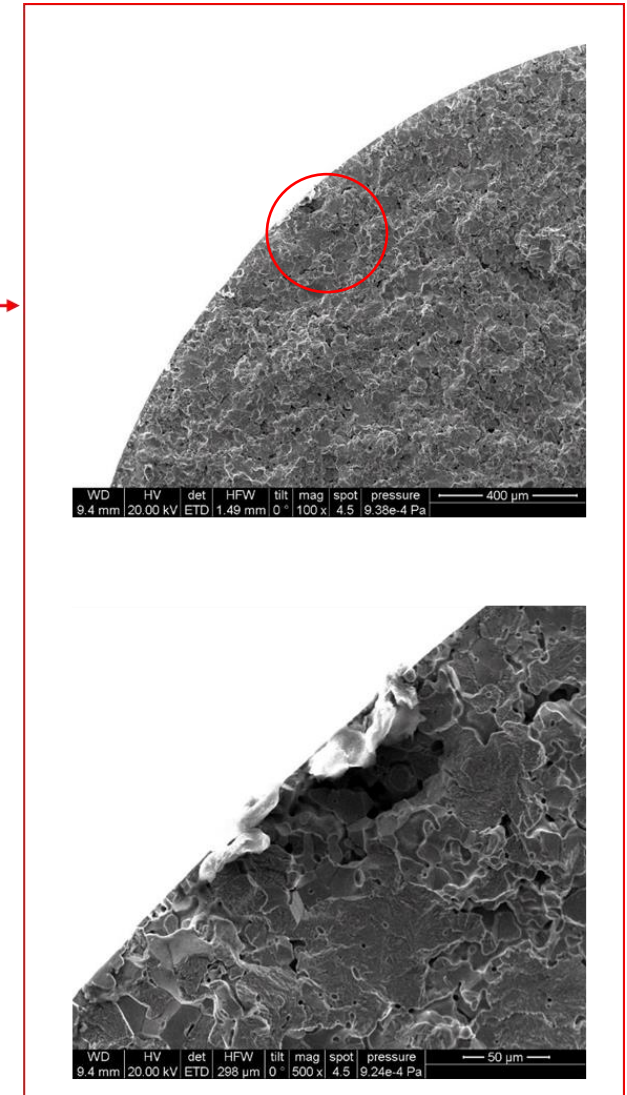
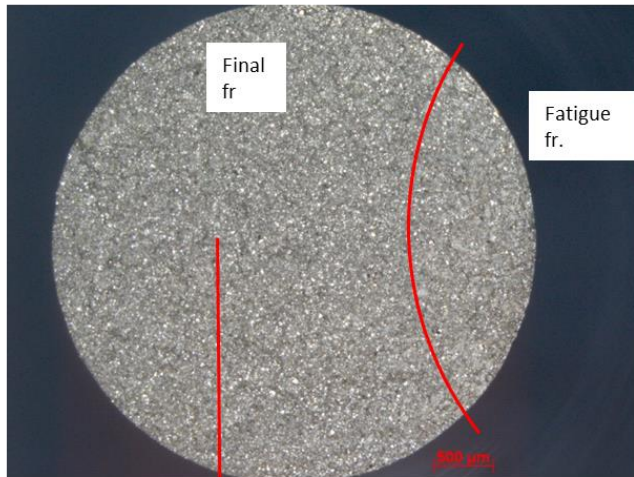


Figure 4.83: Fatigue fracture surface of CrA-4MA-0.6C, compacted at 700 MPa, sintered 60 min in $N_2-10\% H_2$ at 1250 °C (heat treated).

CrA-4MA-0.6C
 $\sigma = 176$, $N = 5.46E+09$

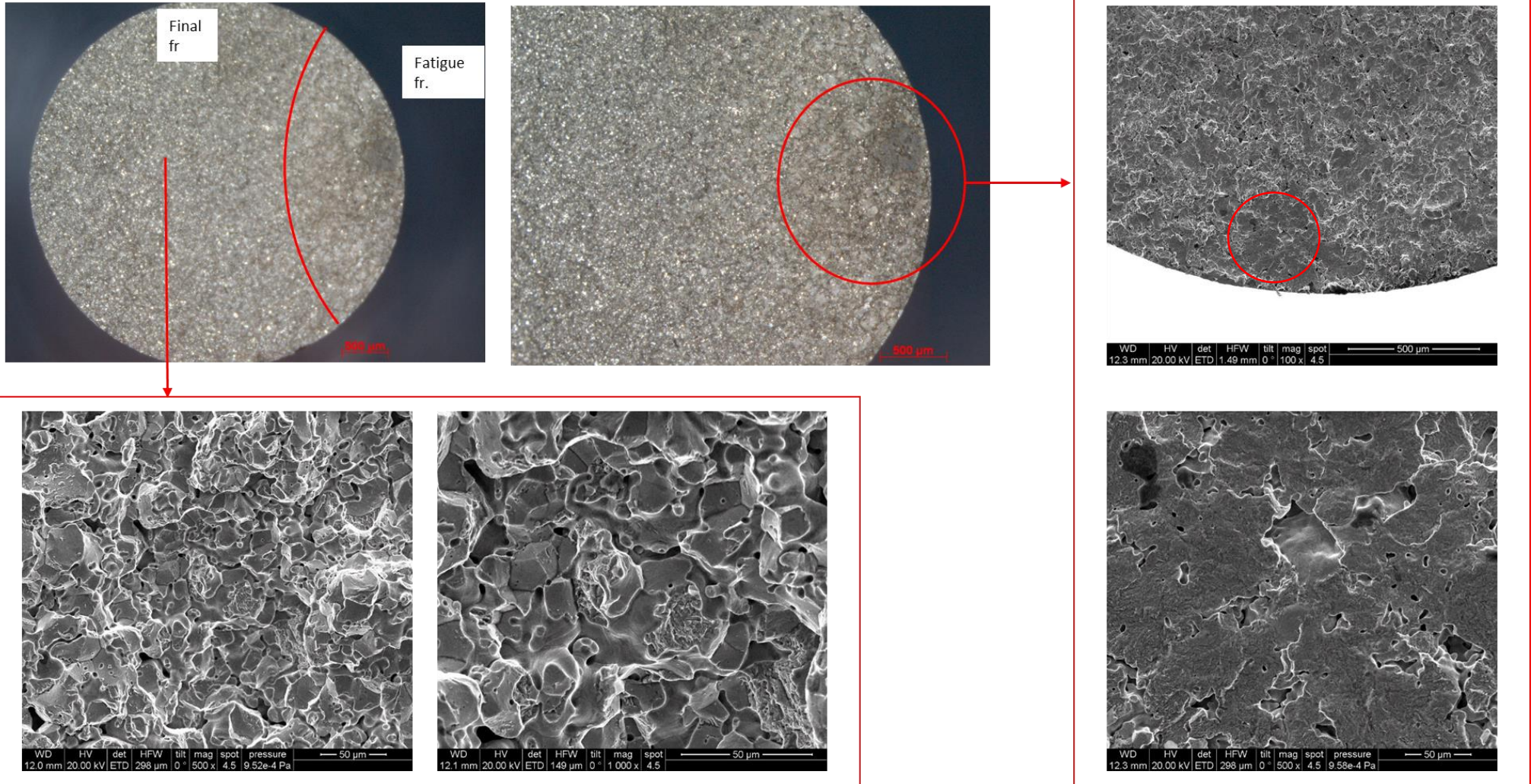


Figure 4.84: Fatigue fracture surface of CrA-4MA-0.6C, compacted at 700 MPa, sintered 60 min in N_2 -10% H_2 at 1250 °C (heat treated).

5. Summary

This thesis focused on investigating the sintering behaviour of PM ferrous materials prepared through the classical press-and-sinter route. The processes occurring in particular in the early stages of sintering were investigated ex situ by sintering studies at widely varying temperature with subsequent characterization of the products and in parallel, in situ, by thermoanalytical studies, using DTA and dilatometry combined with mass spectrometry. Different alloying systems were chosen to obtain a comprehensive pattern for ferrous PM materials. On this basis, high strength steels were prepared, hybrid alloying being chosen, and both monotonic properties as well as the gigacycle fatigue endurance strength were measured. The main findings are systematically summarized in the following.

5.1. Part 1

5.1.1. Part 1a

In this part of the study, the influence of two manufacturing parameters, the compacting pressure and the sintering temperature, on the microstructural changes and mechanical as well as physical properties were assessed. For this purpose, two PM steel grades were prepared, one a carbon steel (Fe-0.8C) and another an Mo prealloyed steel (Fe-1.5Mo-0.8C). The powders were compacted at three different pressures of 300, 500 and 700 MPa. Sintering runs were performed at widely varying temperatures (700 ... 1300°C) to obtain a reasonable comparison between the results.

In general, the results of this section showed almost the same trends for both groups of materials, although in the Mo steels more pronounced changes for the mechanical, electrical and magnetic properties were observed compared to carbon steel.

The effects of the sintering temperature on carbon dissolution and changes in the microstructure during sintering at different temperature were studied by metallography. It showed that in both steel grades the process of C dissolution strongly depended on the sintering temperature. In the Fe-C system, carbon dissolution resulted in pearlite formation, while in the Mo steel, bainitic microstructure was formed. The micrographs of Fe-0.8C for sintering at 1000°C also indicated slightly higher pearlite fraction in the steels compacted at 300 MPa compared to 700 MPa. This suggests that C dissolution occurs rather through gas phase transport than in solid state. However, in the case of Mo alloyed steels, estimating the degree of C dissolution through the bainitic microstructure was not possible. This process was thus observed through the apparent hardness, coercivity and electrical conductivity measurements. Two properties, apparent hardness and coercivity, increased with more complete carbon dissolution, while the electrical conductivity dropped as consequence of the progress in C dissolution. In this context, the effect of change in chemical composition showed to be more pronounced on the coercivity compared to the effects of density and neck enlargement, while for the electrical conductivity, both parameters – chemical composition and density - play major roles. Generally, increasing the density improved the conductivity of the steels, and - after completion of the carbon dissolution

- a linear correlation between electrical conductivity and sintered density was observed for both steels.

Fracture surfaces of the carbon and Mo alloyed steels showed that increasing the compacting pressure leads to more physical contacts. These then form more and stronger sintering bonds between the iron particles, which resulted in higher values of the impact energy and also explains the higher electrical conductivity in the steels compacted at higher pressures. The fracture facets also showed that above 1000°C, transgranular cleavage fracture is more dominant in both grades compacted at 700 MPa compared to those compacted at 500 MPa, while steels compacted at 300 MPa showed dimple fracture of the individual necks even after high temperature sintering, which explains the low impact energy at lower densities. The upward trend of the impact energy versus the sintering temperature revealed a direct relationship between these two parameters. The results also showed that higher compacting pressure improves not only the impact energy but also the rate of the increase when the sintering temperature is raised. In addition to the impact energy, also the hardness of the steels increased with higher compacting pressure.

The other mechanical property, the dynamic Young's modulus of the steels, increased with higher compacting pressure, and thus density, and it also showed an upward trend with higher sintering temperature. Unlike for the impact energy, the rate of increase with higher sintering temperature is almost identical for the different sintered densities. In the temperature range of 800 to 1300 °C there is a linear relationship between the dynamic Young's modulus and the impact energy of the sintered steels. The vibration damping data obtained from the same measurement showed that this property is affected by inter-particle cohesion and to some extent by the density; materials with lower density and especially those sintered at low temperatures have higher ability to absorb energy.

5.1.2. Part 1b

The goal of this part of work was to investigate the effect of two different atmospheres – inert and reducing - on sintering processes like deoxidation, dissolution of carbon in the iron lattice and also formation of sintering contacts during the initial stages of sintering as well as physical and mechanical properties, both in presence and absence of the carbothermal reactions.

Two grades of material were prepared, one plain iron (Fe) and the other an unalloyed carbon steel (Fe-0.8C). Compacting was performed at 600 MPa in a lubricated die and sintering in the temperature range between 700 and 1300°C in H₂ and Ar atmosphere, each of high purity.

Dilatometric/MS runs of the plain iron (Fe) in hydrogen atmosphere proved an active reducing environment by formation of water at rather low temperature. In argon atmosphere, in contrast, there were no chemical reactions related to reduction processes – due to lack of reducing agents - ; these results were also in good agreement with the results of oxygen measurement of the specimens. Dilatometric investigation of plain iron showed that the temperatures of α - γ transformation during heating and cooling are almost the same in the both atmospheres, however in the argon atmosphere a strongly asymmetrical dimensional change during α to γ and γ to α was observed, while the dimensional change in hydrogen showed a rather

symmetrical behaviour. For Fe-C, dilatometric/MS runs in H₂ showed the reduction of the surface oxides at low temperature (at about 370°C) by formation of water, while at higher temperature (above 900°C) carbothermal reduction (formation of CO) was responsible for the oxide reduction in the system. This confirmed that at lower temperatures, H₂ is the stronger reducing agent while at higher temperature the direct carbothermal reduction, which occurs by CO formation, is more dominant. This benefit of H₂ in oxide reduction at lower temperature was observed with the oxygen measurement of the specimens as well. The degassing behaviour of the carbon steel in Ar was different to H₂ and showed the main reduction processes by formation of CO at temperature ranges of about 700-800°C and 900-1150°C, respectively, which showed once more that in the absence of H₂, reduction of surface iron oxides by carbothermal mechanism occurs at higher temperatures. In this context, measuring the carbon content of the carbon steels confirmed that in argon atmosphere the carbon consumption is mainly due to carbothermal reduction of the oxides, while, somewhat surprisingly, sintering in hydrogen led to higher carbon loss compared to Ar, which could be attributed to surface decarburization in addition to carbothermal reduction, as a consequence of atmosphere impurities.

Dilatometry of the carbon steels indicated a marked difference in the dimensional behaviour of the carbon steels in different atmospheres. α to γ transformations started at lower temperature and in a broader interval in Ar compared to H₂, which indicates that carbon dissolution during heating might occur earlier in Ar, which lowers the temperature of the transformation. It was concluded that reduction of surface oxides at low temperature in hydrogen atmosphere prevents formation of CO below 900°C, while, according to the MS results in Ar, CO is produced by carbothermal reduction at about 730°C. It may be supposed that CO gas is formed at lower temperature in argon atmosphere, and then this CO can subsequently act as carburizing gas through Boudouard's equilibrium. This indicates that gas carburizing plays a major role in the dissolution of carbon in the iron matrix, which is in good agreement with the theory of the gas phase transport of carbon during the sintering process and the obtained results in Chapter 3.1.

The microstructures of plain Fe above 900 °C were different for H₂ and Ar. Sintering in Ar led to an enormous grain coarsening which is claimed to be due to the absence of interstitial elements, whereas in hydrogen less grain growth was visible. In the Fe-C system, higher fraction of pearlite at 900 and 1000°C was observed in H₂ atmosphere, showing that the carbon dissolution in H₂ occurred faster than in Ar, although it started slightly later. These results were also in good agreement with the results of the hardness, electrical and coercivity measurements.

Impact tests and fractographic studies on plain iron showed a significant effect of the atmosphere. In the iron specimens sintered in H₂ the formation of initial sintering contacts was observed from 700°C, and higher sintering temperatures resulted in a classic ductile rupture which also increased the impact energy of the material. Sintering of plain iron in Ar, in contrast, resulted in very poor impact behaviour even at high sintering temperature, with intergranular failure along the boundaries of the very large ferrite grains. In contrast to the impact energy, the dynamic Young's moduli of the iron specimens were almost identical in both atmospheres and presented less change by increasing the sintering temperature and neck enlargement.

In the Fe-C system, at low temperatures, in hydrogen atmosphere better oxide reduction led to stronger sintering bonds, higher impact energy and dynamic Young's moduli, while at moderate temperatures (at 1000 and 1100°C), carbothermal reduction plays the main role in oxide reduction, and almost the same mechanical properties were obtained in both atmospheres. However, the results of impact tests after high temperature sintering (1200 and 1300°C) showed higher values of the impact energy for H₂, which could be explained by – undesirable - decarburization of the specimens in this atmosphere.

5.1.3. Part 1c

In this part of the work, the aim was to investigate the effect of an Fe-C masteralloy (MA) as carbon carrier – through Fe₃C -, in addition to natural graphite, on the sintering processes such as deoxidation, carbon dissolution and formation of sintering contacts during the initial stages of sintering up to high sintering temperature. Two types of base powders were used, one plain iron and the other a Cr-Mo pre-alloyed powder. The mixes were prepared both with and without 4% of Fe-4.5%C masteralloy, the mixes containing 0.8% total carbon.

First of all, the results of green density measurement showed that addition of 4% Fe-C masteralloy does not have a significant negative effect on the compactibility of the mixtures.

The effects of the MA on the degassing behaviour and carbon dissolution of the steels were investigated by Dilatometry/MS. The results showed that presence of the MA in the mixture of both steel grades resulted in an onset of the α to γ transformation at lower temperature, which means diffusion of carbon at lower temperature. In the carbon steel this may be explained by formation of CO (by reduction of the surface oxides) which occurred at lower temperature in presence of MA. According to the gasification theory of carbon dissolution this CO then can subsequently act as carburizing gas through Boudouard's equilibrium, therefore reducing the temperature of transformation. Furthermore, it is well known that carbon from cementite is dissolved much faster than C from graphite, and the carbon from the MA may thus trigger faster ferrite-austenite transformation, which in turn promotes graphite dissolution. In the Cr-Mo alloyed steels the effect of MA on the temperature of the transformation was more pronounced than for the Fe-C system. The transformation in the MA containing Cr-Mo steel occurred at least 65°C below the reference steel. This showed that carbon dissolution in this case, as well, is enhanced by the presence of the MA. The MS data of the steel alloyed with MA showed a different pattern of degassing peaks, which could explain this shift in the transformation to the lower temperature. This steel showed a CO peak at low temperature (580°C), probably related to reduction of the surface oxide, which was not visible in the Cr-Mo steel with only graphite. In this case it was concluded that presence of the Fe-C masteralloy in the mixture resulted in reduction of surface iron oxides before they could be converted to more stable oxides (which occurs in the temperature range of 600 to 700°C). This then provided a better condition for dissolution of C and reduced the transformation temperature. Results of the metallographic investigations were in good agreement with the thermal analysis and showed faster carbon dissolution in presence of the masteralloy. The process of carbon dissolution was also observed through hardness, electrical conductivity and coercivity measurements. The results showed a good agreement with the results of metallography.

The data of dimensional change and sintered density showed that in the temperature range of 1100 to 1300°C, the presence of MA in both alloying systems, Fe-C and Fe-Cr-Mo-C, led to higher densification, which compensated the slightly negative effect of the MA on the compactibility. In this temperature range, the carbon steels show higher impact energy for the steel containing MA, which means stronger sintering necks. In the Cr-Mo steels, the impact test showed higher values for the MA containing steel at the moderate and high sintering temperature, which once more indicated that stronger sintering bonds were formed by addition of the Fe-C MA, which acts as sintering activator.

5.1.4. Part 1d

In order to investigate the effect of the sintering temperature on the physical and mechanical properties of PM steels prepared through different alloying routes, five different steel grades were compacted at 600 MPa and then sintered in the temperature range 700 ... 1300°C in an inert atmosphere (Ar). 3 grades were based on plain Fe powder (with Fe-C system as reference), and 2 were prepared from prealloyed powders. The conclusions based on the results of the characterizations are as follows (those for Fe-C have been shown above):

For the **Fe-Cu-C** system, a mixture of iron powder, 0.8% graphite and 2% copper was used. The results show that the presence of Cu in this system hardly affects the reduction reactions and carbon dissolution process compared to **Fe-C**. At temperatures above 1100°C, improvement of hardness was observed due to accelerated homogenization of Cu in the matrix as a consequence of transient liquid phase. However, between 1100 ... 1300°C, impact energy and dynamic Young's modulus of the steel was more or less identical with the Fe-C steel. Dissolution of Cu in iron affected the physical properties as well, the measurements showed a lower electrical conductivity and higher coercive force in this alloy compared to Fe-C.

In case of the variant **Fe-Mn-Si-C**, the oxygen-sensitive alloying elements (Mn and Si) were introduced into the Fe-0.8C mix by adding 4% of a fine masteralloy powder. The experiments showed that in this system, oxygen removal from the surface of the plain iron particles occurs through the "Internal Getter" effect at rather low temperature, transferring oxygen from iron to the masteralloy particles. Therefore the sintering process, including carbon dissolution and contact formation, did not show significant difference to the Fe-C system, the iron particle surface being deoxidized already at moderate temperature, although the total oxygen content does not yet drop. Dimensional change and hardness measurements as well as metallography showed that the alloying process in this system is almost complete at 1100 ° C, assisted by Mn homogenization through the gas phase. This alloying process also was discernible from the beginning at moderate temperatures through both electrical conductivity and coercive force measurements. From 1100°C, the oxygen content is significantly lowered, and the steel showed a pronounced improvement in the impact properties, which placed this variant above all other grades. The dynamic Young's modulus of the steel was also identical with that of Fe-C. Achieving a good combination of the impact and hardness properties at this sintering temperature could present this steel as a suitable option for industrial production, which typically uses continuous mesh belt furnaces with the usual operating temperature of 1120°C.

For the **Fe-Mo-C** system, a mixture of prealloyed Astaloy Mo (Fe-1.5%Mo) and 0.8% graphite was used. The results of the thermal analysis, degassing behaviour and metallography show that the presence of Mo in this system hardly affects the reduction reactions and carbon dissolution process compared to Fe-C. Improvement of hardness was observed from low sintering temperature, due to presence of Mo in the mixture and resulting bainite formation. However, the sintered impact energy and dynamic Young's modulus of the steel were lower than for the Fe-C steel. Presence of Mo in the steel affected the physical properties as well, measurements showed a lower electrical conductivity and higher coercive force in this alloy compared to the Fe-C system.

In the **Fe-Cr-Mo-C** system, the steel was prepared by mixing of prealloyed Astaloy CrM (Fe-3.0%Cr-0.5%Mo) and 0.8% graphite. Up to 1000 °C, no indications for sintering contacts and carbon dissolution were observed. The first signs of these phenomena were visible at the sintering temperature of 1000°C, simultaneous with the onset of carbothermal reduction of surface oxides. At this temperature, the process of carbon dissolution was well noticeable by measuring the coercive force as well. However, measurement of the electrical conductivity showed that, unlike for the other steels, carbon dissolution did not result in lower conductivity. Apparently the effect of this process is compensated by the positive effect of surface oxide reduction and thus enhanced neck formation. The increase of the conductivity between 700 and 1000°C can be attributed to the effect of the tiny metal-metal contacts generated during pressing, which grow even at low temperatures to a degree to improve the conductivity but not so much that also the mechanical properties are increased. The study showed that the desired mechanical properties (hardness and impact energy) could be achieved only at sintering temperatures of 1200° C and above, when the oxides are largely removed from the system. In contrast to the other 4 variants which do not show significant changes of the hardness after sintering above 1100°C, this steel showed an upward trend in hardness up to 1300°C. The dynamic Young's modulus was the lowest up to 1100°C, while sintering at 1200 and 1300°C resulted in identical values with Mo alloyed steel. For the impact energy, in contrast, higher sintering temperatures are beneficial in any of the investigated materials.

5.2. Part 2

In this part of the study, physical, mechanical and sinter hardening properties of a series of hybrid steels prepared on the basis of chromium prealloyed powders with the addition of nickel and manganese were evaluated. The masteralloy route also was investigated as an alternative option to add manganese to the mixtures as well.

For this purpose, Astaloy CrA (Fe-1.8%Cr) was chosen as the base powder, and different amounts of Ni, Mn, masteralloy (H46) and graphite were added to the mixtures. Charpy bars were pressed at 700 MPa. Sintering of the samples was performed at 1250°C for 1 hr in N₂-10%H₂. The samples were cooled in a water-jacketed exit zone in N₂ atmosphere. Then, based on the results obtained from these materials, three compositions, - CrA-2Mn-0.6C, CrA-3Ni-0.6C and CrA-4MA-0.6C – in heat-treated state were selected for ultrasonic resonance fatigue testing.

The chemical analysis of the hybrid alloyed steels showed that addition of graphite to the mixtures and carbothermal reduction could enhance the oxygen removal process of the steels

sintered in N_2 -10% H_2 atmosphere, however in the MA alloyed steels this effect was less pronounced, apparently due to presence of Si. The results also showed that addition of Ni and Mn as elemental powders to the mixtures does not have significant effect on the total oxygen content after sintering. In the case of Mn, which has high oxygen affinity and forms stable oxide, the “self-getter” properties of this element, as described by Šalák, protects the alloy from further oxidation from the atmosphere, however at the expense of evaporation loss. Mn loss was observed in the Mn alloyed steels at the depth 0.7 mm beneath the surface, while the MA alloyed steel did not show such Mn loss at the same depth but just some loss immediately at the surface.

Pore morphology of the Ni alloyed steels showed smaller pores compared to the two other steels (alloyed with Mn and MA), while in Mn alloyed steels larger pores were discernible, which were regarded as mainly secondary pores. The investigation also showed that introducing Mn through the masteralloy route could lead to formation of smaller pores compared to elemental Mn. These results were in good agreement with the dimensional behaviour and sintered density of steels, which showed that increasing the Ni content led to higher shrinkage and density, while addition of Mn and MA to the mixes lowered these parameters. Above 2% Mn admixed, swelling occurred, while the MA alloyed steels did not show any swelling even after addition of 4% MA.

Etched microstructures of the steels showed that in the absence of the alloying elements (Ni and Mn), i.e. with plain AstaloyCrA-C, the as sintered microstructure is mainly pearlitic, while addition of Ni and Mn (elemental or MA) led to formation of bainitic or martensitic microstructure which increased the hardness and indicates increased hardenability of the steels. This latter property was also examined by quenching dilatometry. The CCT diagrams thus obtained did not show any sinter hardenability for CrA-0.6C at a cooling rate of 3 K/s, while this ability could be achieved after addition of certain amounts of alloying elements. The results also showed that Mn has a higher effect on the hardenability of the material compared to Ni, which agrees with the higher Grossmann factor of Mn (4.5) compared to Ni (1.4).

In the case of Ni, the microstructure was less homogeneous compared to the other grades. In this case, although the diffusion rates of manganese ($1.60E-10$ cm^2/s) and nickel ($1.73E-10$ cm^2/s) in austenite are almost the same at sintering temperature, the solid-state homogenization mechanism could be considered as the main reason for the lower homogeneity in Ni steel than in Mn steel, in which case homogenization is supported by gas phase transport.

Fractography of the steels revealed different fracture facets and mechanisms after addition of the alloying elements. In the Ni alloyed steels, stronger sintering necks as well as higher impact energy were observed compared to the other grades with Mn and MA. In Mn alloyed steels, higher Mn content led to local intergranular brittle fracture, which might be the consequence of Mn vapour condensation and oxidation at the grain boundaries, while such effect was not observed when Mn was added to the alloy through the MA. In contrast to admixed elemental Mn, addition of this element through MA resulted in stronger sintered bonds and transgranular fracture facets, which boosted the impact behaviour of the steel as well.

Dynamic Young's modulus as another important mechanical property was investigated as well. Addition of the alloying elements to the system decreases this property compared to CrA-C,

which is mainly due to the lower density in Mn and MA steels, while in Ni alloyed steels, increased austenite content could be responsible for this degradation.

Electrical conductivity of the hybrid steels was less affected by addition of carbon compared to the metallic alloying elements. The results also showed a decrease in this parameter after addition of Ni and Mn, while this drop in the conductivity was more pronounced in the Mn alloyed steels compared to the Ni steels.

Coercivity measurement showed that compared to electrical conductivity measurement, this method is better for tracing the carbon dissolution in these series of steels, because addition of carbon and increasing its content significantly increases H_c . It also showed that addition of Ni and Mn increases the coercivity, the effect of Mn being more pronounced than that of Ni, magnetic hardness thus showing a similar trend as mechanical one.

Measurement of the magnetic saturation of the steels showed that the addition of carbon decreases this property of the material. Also addition of Ni and Mn to the mixture reduces the magnetic saturation. Similar to electrical conductivity and coercivity, also here the effect of Mn was more pronounced compared to Ni.

Based on the results of the characterization above, from these compositions three steel grades were selected for investigating the fatigue behaviour of the hybrid-alloyed steels, and specially prepared specimens were examined by ultrasonic resonance fatigue testing up to the gigacycle range. In all cases the S/N graphs dropped consistently up to $10E10$ cycles i.e., a true “fatigue limit” was not observed with these materials. Addition of Ni to the mixture resulted in higher fatigue strength below 10^8 cycle numbers compared to the two other grades, while at $N > 10^8$ the fatigue endurance was similar to the MA alloyed steel. The good fatigue behaviour of the Ni alloyed steel at $N < 10^8$ was explained by its higher density (lower porosity) and the higher ductility of the material, while at higher fatigue cycle numbers ($N > 10^8$) the Ni alloyed grade showed a very large scatter of the data. The large austenitic areas with very low hardness and strength were supposed to be the main cause of the crack initiation and scattering in the results.

The steel alloyed with 2% Mn showed the lowest fatigue strength. In this case, lower density of the Mn alloyed steel as well as the lower grain boundary cohesion and the large secondary pores were assumed as the main reason for the low fatigue strength.

MA steel in this series showed the same trend and slope in its S/N graphs as the Mn alloyed steel. However, the fatigue strength of this steel is approximately 60 MPa higher than for the steels alloyed with Mn, which was explained by the higher density as well as stronger sintering bonds, which showed that using of MA as a manganese carrier gives better fatigue endurance compared to the addition of elemental Mn powder.

The fractographs of the fatigue test samples showed that crack initiation occurs predominantly at or near the surface. The fractographs also indicate that the final fracture, in the last stage of the fatigue test, is more brittle compared to the mechanisms observed by Charpy impact testing. In the Mn alloyed steel, final fracture is mostly intergranular while the MA alloyed steel shows a mix of inter- and transgranular fracture. In the Ni alloyed steel, in addition to transgranular cleavage facets, some dimple structures, related to more ductile fracture, also were observed.

Summing up all the findings it can be stated that in the process of carbon dissolution, which occurs in the initial stages of sintering of PM steels, gas carburizing seems to play a more important role than solid state reaction. The effect of green density of the steels and sintering atmosphere on the carbon dissolution can be explained by this theory. In the steels containing Fe-C masteralloy, carbothermal reduction of the iron oxides and CO formation occurs at lower temperature compared to the only graphite added ones. The faster carbon dissolution in the MA containing steels also fits in well with the gasification theory of the carburizing. The comparison between the different commercial PM steels and one grade alloyed with Mn-Si masteralloy showed that the masteralloy steel gives a highly attractive compromise between manufacturing requirements, alloy element content, and product properties, and therefore could be considered as an alternative option for production of high performance PM alloyed steels. In the production of hybrid alloyed high-strength steels based on prealloyed Fe-Cr powder Astaloy CrA, the Mn containing steels alloyed through admixed masteralloy also showed advantages in both monotonic and cyclic properties compared to those alloyed with elemental Mn powder. Therefore, hybrid alloying by combining prealloyed powder with suitable masteralloy seems to be an attractive route for flexible production of highly loaded PM precision parts.

6. References

1. *Höganäs Handbook for Sintered Components*. Material and powder properties. 2013: Höganäs AB, Höganäs. 114.
2. *Höganäs Handbook for Sintered Components*. Iron and steel powders for sintered components. 2017: Höganäs AB, Höganäs. 398.
3. Haynes, R., *Development of Sintered Low Alloy Steels*. Powder Metallurgy, 1989. **32**(2): p. 140-146.
4. German, R.M., P. Suri, and S.J. Park, *Review: Liquid Phase Sintering*. Journal of Materials Science, 2009. **44**, no. 1: p. 1-39.
5. Danninger, H., R. De Oro Calderon, and C. Gierl-Mayer, *Powder Metallurgy and Sintered Materials*. Ullmann's Encyclopedia of Industrial Chemistry, Wiley-VCH Verlag GmbH & Co KGaA, Weinheim, 2017: p. 1-57.
6. <https://www.mpif.org/IntrotoPM/Processes/ConventionalPowderMetallurgy.aspx>.
7. <https://www.epma.com/powder-metallurgy-conventional-processing>.
8. Ratzi, R. and P. Orth, *Sinterhardening Reduces Costs for Manual Transmission Synchronizer Parts*. Metal Powder Report, 2000. **55**: p. 22-25.
9. Ratzi, R. and P. Orth, *Cost Effective Manufacture of Synchronizer Hubs and Rings for Manual Transmissions by Sinterhardening*. Proc. Society of Automotive Engineers Detroit, 2000: p. 129-133.
10. <https://mpmiran.com/en/automotive-products/>.
11. Danninger, H., et al., *Dissolution of Different Graphite Grades during Sintering of PM Steels*. Materials Chemistry and Physics, 2001. **67**, no. 1: p. 72-77.
12. Engström, U., C. Lindberg, and J. Tengzelius, *Powders and Processes for High Performance PM Steels*. Powder Metallurgy, 1992. **35**, no. 1: p. 67-73.
13. De Oro Calderon, R., et al., *New Chances for the Masteralloy Approach*. Powder Metallurgy Progress, 2018. **18**: p. 121-127.
14. De Oro Calderon, R., et al., *Master Alloys for Liquid Phase Sintering: Some Key Points for the Design*. Metal Powder Report, 2016. **71**, no. 3: p. 184-192.
15. De Oro Calderon, R., et al., *Masteralloys: a Key to Tailor Hardenability*. Proc. Euro PM2018, 2018. Bilbao, Spain; EPMA, Shrewsbury UK. **Sintering I**: p. 1-6.
16. De Oro Calderon, R., et al., *New Alloying Systems for Sintered Steels: Critical Aspects of Sintering Behavior*. Metallurgical and Materials Transactions A, 2015. **46**: p. 1349-1359.
17. De Oro Calderon, R., et al., *Effect of processing conditions on microstructural features in Mn-Si sintered steels*. Materials Characterization, 2014. **95**: p. 105-117.
18. Marquardt, A., et al., *Improved Mechanical Properties of Low Alloyed Sintered Steels through Fe - Mn - Si Master Alloys*. Proc. Euro PM2011, 2011. Barcelona, Spain; EPMA, Shrewsbury UK. **Sintered Steels: Mn Containing Alloys**: p. 1-6.
19. Zapf, G. and K. Dalal, *Introduction of High Oxygen Affinity Elements Manganese, Chromium and Vanadium in the Powder Metallurgy of P/M Parts*. Modern Developments in Powder Metallurgy, 1977. **10**: p. 129-152.
20. Hoffmann, G. and K. Dalal, *Development and Present Situation of Low Alloyed PM Steels using MCM and MVM Master Alloys*. Powder Metallurgy International, 1979. **11**: p. 177-180.
21. Schlieper, G. and F. Thümmeler, *High Strength Heat-Treatable Sintered Steels Containing Manganese, Chromium, Vanadium and Molybdenum*. Powder Metallurgy International, 1979. **11**: p. 172-176.

22. S. Banerjee, V.G., F. Thümmeler, *Liquid-Phase Formation During Sintering of Low-Alloy Steels with Carbide-Base Master Alloy Additions*. Powder Metallurgy, 1980. **23**, no. 3: p. 126-129.
23. S. Banerjee, G.S., F. Thümmeler, G. Zapf, *New Results in the Master Alloy Concept for High Strength Sintered Steels*. Progress in Powder Metallurgy, 1980. **13**: p. 143-157.
24. Danninger, H., et al., *Sintering of PM Steels with High Mn Content -- Using the Masteralloy Route*. Proc. Euro PM2021, 2021. Virtual conference; EPMA, Chantilly, FR. **Materials for Press & Sinter**: p. 1-6.
25. Danninger, H., et al., *Microstructure and Mechanical Properties of Sintered Iron. Part II: Experimental Study*. Powder Metallurgy International, 1993. **25**, no. 4 & 5: p. 170-173 & 219-223.
26. *Metals Handbook (1984) Powder Metallurgy*, vol. 7, 9th edn, ASM International, Metals Park OH.
27. Danninger, H. and C. Xu, *De-Gassing and Reduction During Sintering of High Density PM Steels*. Proc. Euro PM2003, 2003. Valencia, Spain; EPMA, Shrewsbury UK. **Low alloy steels**: p. 1-7.
28. Danninger, H., C. Xu, and B. Lindqvist, *Oxygen Removal during Sintering of Steels Prepared from Cr-Mo and Mo Prealloyed Powders*. Materials Science Forum 2007. **534**: p. 577-580.
29. Lynn Ferguson, B. and R.M. German, *Powder Shaping and Consolidation Technologies*. ASM Handbook, vol. 7, Powder Metal Technologies and Applications, Metals Park OH, 1998: p. 313-320.
30. ISO 3252:1999(en) (1999) Powder Metallurgy — Vocabulary, I.S.O., Geneva, Switzerland.
31. German, R.M., *History of Sintering: Empirical phase*. Powder Metallurgy, 2013. **56**: p. 117-123.
32. Schatt, W. and K.-P. Wieters, *Powder Metallurgy - Processing and Materials*. 1997: Shrewsbury, UK : EPMA.
33. Christian, J.W., *CHAPTER 9 - Diffusion in the Solid State*, in *The Theory of Transformations in Metals and Alloys*, J.W. Christian, Editor. 2002, Pergamon: Oxford. p. 378-421.
34. Kuczynski, G.C., *Self-Diffusion in Sintering of Metallic Particles*, in *Sintering Key Papers*, S. Sōmiya and Y. Moriyoshi, Editors. 1990, Springer Netherlands: Dordrecht. p. 509-527.
35. Zovas, P.E., et al., *Activated and Liquid-Phase Sintering—Progress and Problems*. JOM, 1983. **35**, no. 1: p. 28-33.
36. De Oro Calderon, R., C. Gierl-Mayer, and H. Danninger, *Fundamentals of Sintering: Liquid Phase Sintering*, in *Encyclopedia of Materials: Metals and Alloys*. 2021, Elsevier Inc. p. 481-492.
37. Danninger, H., *Homogenization and Pore Formation During Sintering with Transient Liquid Phase*. Powder Metallurgy International 1988. **20**, no. 1: p. 21-25.
38. Magee, B.E. and J. Lund, *Mechanisms of Liquid-Phase Sintering in Iron-Copper Powder Compacts*. Zeitschrift für Metallkunde, 1976. **67**, no. 9: p. 596-602.
39. Berner, D., H.E. Exner, and G. Petzow, *Swelling of Iron-Copper Mixture During Sintering and Infiltration*. Modern Dev. in Powder Metall., 1974. **6, Application & Processes**: p. 237-250.
40. Kaysser, W.A., W.J. Huppmann, and G. Petzow, *Analysis of Dimensional Changes During Sintering of Fe-Cu*. Powder Metallurgy, 1980. **23**, no. 2: p. 86-91.
41. Dautzenberg, N. and H.J. Dorweiler, *Dimensional Behaviour of Copper–Carbon Sintered Steels*. Powder Metallurgy International, 1985. **17**, no. 6: p. 279-282.

42. Danninger, H. and C. Gierl-Mayer, *Processes in PM Steel Compacts during the Initial Stages of Sintering*. Materials Chemistry and Physics, 2001. **67**, no. 1: p. 49-55.
43. Danninger, H., et al., *Mo Alloyed PM structural Steels Prepared by Different Alloying Techniques*. Adv. Powder Metall. & Partic. Mater 1996. **Part 13**: p. 229.
44. Danninger, H., *Sintering of Mo Alloyed P/M Steels Prepared from Elemental Powders(II. Mo Homogenization and Dimensional Behaviour)*. Powder Metallurgy International, 1992. **24**, no. 3: p. 163-168.
45. Danninger, H., *Sintering of Mo Alloyed P/M Steels Prepared from Elemental Powders(I. Sintering Temperature and Mechanical Properties)*. Powder Metallurgy International, 1992. **24**, no. 2: p. 73-79.
46. Danninger, H., et al., *Comparison of Mn, Cr and Mo Alloyed Sintered Steels Prepared from Elemental Powders*. Powder Metallurgy, 2005. **48**, no. 1: p. 23-32.
47. Danninger, H., *Pore Formation During Sintering of Fe-Cu and its Effects on Mechanical Properties*. Powder Metallurgy International, 1987. **19**, no.1: p. 19-23.
48. Danninger, H. and B. Weiss, *Ultra High Cycle Fatigue Properties of Sintered Steels*. Powder Metallurgy Progress, 2001. **1**: p. 19-40.
49. Chasoglou, D., E. Hryha, and L. Nyborg, *Effect of Process Parameters on Surface Oxides on Chromium-Alloyed Steel Powder during Sintering*. Materials Chemistry and Physics, 2013. **138**, no. 1: p. 405-415.
50. Gierl-Mayer, C. and H. Danninger, *Dilatometry Coupled with Mass Spectrometry as Instrument for Process Control in Sintering of Powder Metallurgy Steels*. Materials Science Forum, 2016. **835**: p. 106-115.
51. Danninger, H., R. De Oro Calderon, and C. Gierl-Mayer, *Oxygen Transfer Reactions during Sintering of Ferrous Powder Compacts*. Advanced Engineering Forum, 2018. **27**: p. 3-13.
52. Danninger, H., R. De Oro Calderon, and C. Gierl-Mayer, *Surface Chemistry of Metal Powders and Changes during the Sintering Process*. Proc. 2018 World Congress on Powder Metallurgy, 2018. Beijing, China. **Metal Powder Preparation and Processes**: p. 92-97.
53. Danninger, H., R. De Oro Calderon, and C. Gierl-Mayer, *Chemical Reactions during Sintering of PM Steel Compacts as a Function of the Alloying Route*. Powder Metallurgy, 2018. **61**, no. 3: p. 241-250.
54. R.Gaskell, D., *Chapter 12, Reactions Involving Pure Condensed Phases and a Gaseous Phase*, in *Introduction to the Thermodynamics of Materials*. 2003, Taylor & Francis, New York.
55. Dautzenberg, N. and J. Hewing, *Reaction Kinetics during Sintering of Mixed Alloyed Steels of Iron and Graphite Powders*. Powder Metallurgy International, 1977. **9**, no.1: p. 16-19.
56. Y.Tanaka and J.A.Lund, *Alloying and Sintering in Iron-Graphite Compacts at 900°C*. Powder Metallurgy International, 1989. **18**, no. 6: p. 409-411.
57. Y.Tanaka and J.A.Lund, *Catalytic Effect of Carbonates in Iron-Graphite Compacts*. Powder Metallurgy, 1988. **31**, no. 1: p. 45-51.
58. Kremel, S., H. Danninger, and Y. Yu, *Effect of Sintering Conditions on Particle Contacts and Mechanical Properties of PM Steels Prepared from 3% Cr Prealloyed Powder*. Powder Metallurgy Progress, 2002. **2**: p. 211-221.
59. Banerjee, S. and P.G. Mukunda, *Mechanism of Carbon Absorption by Iron During Sintering of Iron-Graphite*. Powder Metallurgy, 1984. **27**, no. 2: p. 93-96.
60. Banerjee, S. and P.G. Mukunda, *Carbon Absorption by Iron During Sintering of Iron-Graphite*. Powder Metallurgy, 1984. **27**(2): p. 89-92.
61. Simchi, A. and H. Danninger, *Microstructural Changes in Mo Steels during Sintering and Effect on Electrical Conductivity*. Powder Metallurgy 2002. **45**, no. 4: p. 307-314.

62. Gierl-Mayer, C. and H. Danninger, *Mechanical Properties of Low Temperature Sintered PMCarbon Steel*. Proc. International Conference DF PM 99, Piestany, 1999, IMR-SAS, Kosice, Slovak Republic: p. 73-80.
63. Šlesár, M., H. Danninger, and K. Sülleiová, *Microstructure Formation and Fracture Processes in Fe-C Systems Sintered in Nitrogen*. Powder Metallurgy Progress, 2002. **2**: p. 199-210.
64. Brian James, W., *High performance ferrous PM materials for automotive applications*. Metal Powder Report, 1991. **46, no.9**: p. 26-32.
65. *Höganäs Handbook for Sintered Components*. 3.Design and Mechanical Properties. 2015: Höganäs AB, Höganäs.
66. Pang Jianming, F.J., Pan Congchao, Song Yaoxin, *Effect of Copper Powder on the Properties of Iron-based Powder Metallurgy Sintered Products*. Proc. 2018 World Congress on Powder Metallurgy, 2018. Beijing, China. **Metal Powder Preparation and Processes**: p. 98-106.
67. Lenel, F.V. and T. Pecanha, *Observations on the Sintering of Compacts from a Mixture of Iron and Copper Powders*. Powder Metallurgy, 1973. **16, no. 32**: p. 351-365.
68. Wanibe, Y., H. Yokoyama, and T. Itoh, *Expansion during Liquid Phase Sintering of Iron-Copper Compacts*. Powder Metallurgy, 1990. **33**: p. 65-69.
69. Jamil, S.J. and G.A. Chadwick, *Investigation and Analysis of Liquid Phase Sintering of Fe-Cu and Fe-Cu-C Compacts*. Powder Metallurgy, 1985. **28, no.2**: p. 65-71.
70. Candela, N., et al., *Influence of Microstructure on Mechanical Properties of Molybdenum Alloyed P/M Steels*. Journal of Materials Processing Technology, 2005. **168, no. 3**: p. 505-510.
71. Junhua, K., et al., *Influence of Mo content on microstructure and mechanical properties of high strength pipeline steel*. Materials & Design, 2004. **25**: p. 723-728.
72. Kong, J. and C. Xie, *Effect of Molybdenum on Continuous Cooling Bainite Transformation of Low-Carbon Microalloyed Steel*. Materials & Design, 2006. **27, no. 10**: p. 1169-1173.
73. Sokolowski, P. and B. Lindsley, *Leaner Alloys for the PM Industry*. Proc. Euro PM2011, 2011. Barcelona, Spain; EPMA, Shrewsbury UK. **Sintered Steels: Mn Containing Alloys**: p. 1-6.
74. Wu, M.W., et al., *The Effects of Alloying Elements and Microstructure on the Impact Toughness of Powder Metal Steels*. Materials Science and Engineering: A, 2012. **538**: p. 135-144.
75. Deng, X., *Microstructure and Mechanical Behavior of Porous Sintered Steels*. Materials Science and Engineering: A, 2005. **390**: p. 98-112.
76. Hojati, M., H. Danninger, and C. Gierl-Mayer, *Mechanical and Physical Properties of Differently Alloyed Sintered Steels as a Function of the Sintering Temperature*. Metals, 2022. **12(1)**.
77. Larsson, C. and U. Engström, *High Performance Sinter Hardening Materials for Synchronizing Hubs*. Proc. Euro PM2011, 2011. Barcelona, Spain; EPMA, Shrewsbury UK. **Sintered Steels: Mechanical Properties**: p. 1-6.
78. Chasoglou, D., *High Performance PM Steels Through Sinter Hardening*. Proc. Euro PM2017, 2017. Milano, Italy; EPMA, Shrewsbury UK. **Sintering**: p. 1-7.
79. Kulecki, P., E. Lichańska, and M. Sułowski, *The Effect of Processing Parameters on Microstructure and Mechanical Properties of Sintered Structural Steels based on Prealloyed Powders*. Metallurgy and Materials, 2015. **60, no. 4**: p. 2543-2549.
80. Dlapka, M., et al., *Fatigue Behavior and Wear Resistance of Sinter-Hardening Steels*. International Journal of Powder Metallurgy, 2012. **48**: p. 49-60.
81. Danninger, H. and C. Gierl-Mayer, *New Alloying Systems for Ferrous Powder Metallurgy Precision Parts*. Science of Sintering, 2008. **40**: p. 33-46.

82. Sulowski, M., P. Kulecki, and A. Radziszewska, *Sintered Structural PM Cr and Cr-Mo Steels/ Spiekane Stale Konstrukcyjne Chromowe I Chromowo-Molibdenowe*. Archives of Metallurgy and Materials, 2014. **59**: p. 1507-1512.
83. Dlapka, M., et al., *Reaction of Unalloyed and Cr-Mo Alloyed Steels with Nitrogen from the Sintering Atmosphere*. Powder Metallurgy Progress, 2016. **16**: p. 86-98.
84. Sulowski, M., *Sintered Structural Steels Containing Mn, Cr And Mo – The Summary of the Investigations*. Powder Metallurgy Progress, 2016. **16**: p. 86-98.
85. *Metals Handbook Vol.1. Properties and Selection: Irons, Steels, and High-Performance Alloys. 10th Ed., ASM, Metals Park OH*. 1990. p. 140.
86. Tasker, J. and M.O.H. Amuda, *Austenitic Steels: Non-Stainless*, in *Reference Module in Materials Science and Materials Engineering*. 2017, Elsevier. p. 1-7.
87. Hryha, E. and E. Dudrová, *The Sintering Behaviour of Fe-Mn-C Powder System, Correlation between Thermodynamics and Sintering Process, Mn Distribution and Microstructure*, in *Application of Thermodynamics to Biological and Materials Science*, M. Tadashi, Editor. 2011, IntechOpen: London. p. 534-536.
88. Šalák, A. and M. Selecká, *Alloying and Sintering of Manganese Steels in terms of High Manganese Vapour Pressure, in Manganese in Powder Metallurgy Steels*. 2012, Cambridge International Science Publishing Ltd. p. 22-37.
89. Šalák, A., M. Selecka, and R. Bures, *Manganese in Ferrous Powder Metallurgy*. Powder Metallurgy Progress, 2001. **1**: p. 41-58.
90. Šalák, A. and M. Selecká, *Adverse Effect of High Purity Atmosphere on Sintering of Manganese Steels*. Powder Metallurgy, 2010. **53**: p. 285-294.
91. Šalák, A., *Manganese Sublimation and Carbon Ferromanganese Liquid Phase Formation during Sintering of Premixed Manganese Steels*. International Journal of Powder Metallurgy and Powder Technology, 1980. **16, no. 4**: p. 369-379.
92. Šalák, A. and M. Selecká, *Alloying and Sintering of Manganese Steels by Manganese Vapour, in Manganese in Powder Metallurgy Steels*. 2012, Cambridge International Science Publishing Ltd. p. 39-72.
93. Jalili Ziyaeian, M., et al., *Manganese Evaporation During Sintering of Fe-Mn-Cr Compacts from Prealloyed Iron Powder*. Proc. Euro PM2008, 2008. Mannheim, Germany; EPMA, Shrewsbury UK. **Sintered Steels**: p. 115-120.
94. Hryha, E., et al., *Sintered Steels Alloyed with Manganese: Effect of Alloying Mode*. Proc. 2010 World Congress on Powder Metallurgy, 2010. Florence, Italy; EPMA, Shrewsbury UK. **Sintered Steels: Mechanical Properties**: p. 1-8.
95. Stoyanova, V., G. Straffellini, and A. Molinari, *Influence of Microstructure and Microhardness in Impact Properties of High Density Cr and Mo Low Alloyed Sintered Steels*. Powder Metallurgy Progress, 2004. **4, no. 4**: p. 243-255.
96. Schmidt, M., P. Thorne, and U. Engström, *Effect of Sintering Time and Cooling Rate on Sinter Hardenable Materials*. Proc. PM2Tec Congress on Powder Metallurgy and Particulate Materials, 2004, Chicago. **MPIF, Princeton NJ, Pressing & Sintering**: p. 1-12.
97. Thakur, S.N., et al., *Mechanical Properties of Sinter-Hardened Steels*. International Journal of Powder Metallurgy, 2004. **40**: p. 45-54.
98. Momeni, M., C. Gierl, and H. Danninger, *Study of the Oxide Reduction and Interstitial Contents during Sintering of Different Plain Carbon Steels by In Situ Mass Spectrometry in Nitrogen Atmosphere*. Materials Chemistry and Physics, 2011. **129, no. 1**: p. 209-216.
99. Sonsino, C.M., *Fatigue Design for Powder Metallurgy*. Metal Powder Report, 1990. **45, no. 11**: p. 754-764.
100. Danninger, H., et al., *Gigacycle Fatigue of Ultra High Density Sintered Alloy Steels*. Powder Metallurgy, 2012. **55**: p. 378-387.

101. Roth, L.D., *Ultrasonic Fatigue Testing*, in *ASM Handbook*, J.R. Newby, et al., Editors. 1992, Volume 8, ASTM: Philadelphia, PA, USA. p. 240-258.
102. Danninger, H., D. Spoljaric, and B. Weiss, *Microstructure Features Limiting the Performance of PM Steels*. International Journal of Powder Metallurgy, 1997. **33**: p. 43-53.
103. Danninger, H., et al., *Microstructure and Mechanical Properties of Sintered Iron. Part I: Basic Considerations and Review of Literature*. Powder Metallurgy International, 1993. **25**, no. 3: p. 111-117.
104. Hadrboletz, A. and B. Weiss, *Fatigue Behaviour of Iron based Sintered Material: a Review*. International Materials Reviews, 1997. **42**, no. 1: p. 1-44.
105. Beiss, P. and M. Dalgic, *Structure Property Relationships in Porous Sintered Steels*. Materials Chemistry and Physics, 2001. **67**: p. 37-42.
106. Spoljaric, D. and H. Danninger, *Secondary Pores and Fatigue Strength of Sintered Fe-3%Cu*. Proc. International Conference on Materials by Powder Technology, 1993. Dresden, Germany: p. 151-157.
107. Danninger, H., et al., *Fatigue Response and Fractography of Sintered Materials*. Powder Metallurgy Progress, 2015. **15**, no. 2: p. 218-233.
108. Bergmark, A. and L. Alzati, *Fatigue Crack Initiation in PM steels*. Fatigue and Fracture of Engineering Materials and Structures, 2005. **28**: p. 1-12.
109. Engdahl, P., B. Lindqvist, and J. Tengzelius, *Fatigue Behaviour of PM Steels*. Proc. PM'90, London, 1990. **2**: p. 144-155.
110. Spoljaric, D., et al., *Influence of the Testing Frequency on the Fracture Properties of PM-Steels*. Proc. DF PM'96 Int. Conf. Deformation and Fracture in Structural PM Materials, Stara Lesna, 1996. IMR-SAS, Kosice, Slovakia: p. 147-158.
111. Danninger, H., et al., *High Cycle Fatigue of Mo alloyed Sintered Steel*. Z. Metallkunde, 1998. **89**: p. 135.
112. Saritaş, S., et al., *Rotating-Bending Fatigue of Pre-Alloyed and Hybrid P/M Steels*. International Journal of Powder Metallurgy, 2005. **41**, no. 3: p. 63-70.
113. Khorsand, H., et al., *Fatigue of Sintered Steels (Fe-1.5 Mo-3 Mn-0.7 C)*. Materials and Structures, 2004. **37**: p. 335-341.
114. Spoljaric, D., H. Danninger, and B. Weiss, *The Influence of the Surface Quality on Rotating Beam Fatigue Testig of PM Steels*. Proc. DF PM'96 Int Conf. Deformation and fracture in structural PM materials, 1996. Kosice, Slovakia: p. 159-169.
115. Simchi, A., H. Danninger, and C. Gierl, *Electrical Conductivity and Microstructure of Sintered Ferrous Materials: Iron-Graphite Compacts*. Powder Metallurgy, 2001. **44**, no. 2: p. 148-156.
116. Lefebvre, L.P., G. Pleizier, and Y. Deslandes, *Electrical Resistivity of Green Powder Compacts*. Powder Metallurgy, 2001. **44**, no. 3: p. 259-268.
117. Momeni, M., H. Danninger, and C. Gierl-Mayer, *Electrical Conductivity and Physical Properties Of Sintered Steels Prepared from Different Base Powders*. Proc. Euro PM2020, 2020. Virtual congress; EPMA, Chantilly, FR. **Sintering of PM Steels**: p. 1-6.
118. Simchi, A. and H. Danninger, *Electrical Conductivity and Microstructure of Sintered Ferrous Materials: Sintered Iron*. Powder Metallurgy, 2000. **43**: p. 209-218.
119. Simchi, A., H. Danninger, and B. Weiss, *Microstructural Modelling of Electrical Conductivity and Mechanical Properties of Sintered Ferrous Materials*. Powder Metallurgy, 2000. **43**: p. 219-227.
120. Momeni, M., C. Gierl, and H. Danninger, *Electrical Conductivity and Microstructural Changes of Sintered Plain Carbon Steels Prepared from Different Base Powders*. Proc. Euro PM2009, 2009. Copenhagen, Denmark; EPMA, Shrewsbury UK. **Sintered Steels** p. 1-6.

121. Jangg, G., et al., *Magnetic Properties of Sintered Iron - The Influence of Porosity on the Magnetic Properties of Sintered Iron*. Powder Metallurgy International, 1983. **15**, no. **4**: p. 173-177.
122. Jiles, D.C., *Magnetic Properties and Microstructure of AISI 1000 Series Carbon Steels*. Journal of Physics D: Applied Physics, 1988. **21**: p. 1186-1195.
123. Ranjan, R., D. Jiles, and P. Rastogi, *Magnetic Properties of Decarburized Steels: An Investigation of the Effects of Grain Size and Carbon Content*. IEEE Transactions on Magnetics, 1987. **23**, no. **3**: p. 1869-1876.
124. Jangg, G., et al., *Magnetic Properties of Sintered Iron - Influence of the Microstructure of Sintered Iron Materials on the Coercive Force*. Powder Metallurgy International, 1984. **16**, no. **2**: p. 60-64.
125. Frayman, L.I., D.R. Ryan, and J.B. Ryan, *Modified P/M Soft Magnetic Materials for Automotive Applications*. SAE Transactions, 1998. **107**: p. 217-224.
126. Ouda, K., H. Danninger, and C. Gierl-Mayer, *Magnetic Measurements Complemented By Thermodynamic Calculations As Tools For Characterizing the Microstructure Of PM Steels*. Proc. Euro PM2018, 2018. Bilbao, Spain; EPMA, Shrewsbury UK. **Post Sintering and Testing**: p. 1-7.
127. *Operating instructions of KOERZIMAT - CS 1.096 V3.09*
128. Hanejko, F.G., H.G. Rutz, and C.G. Oliver, *Effects of Processing and Materials in Soft Magnetic Performance of Powder Metallurgy Parts*. PM World Congress, 1992, San Francisco, CA, MPIF, Princeton NJ: p. 1-27.
129. Gierl-Mayer, C. and H. Danninger, *Dilatometry Coupled with MS as Instrument for Process Control in Sintering of Powder Metallurgy Steels*. Powder Metallurgy Progress, 2015. **15**, no. **1**: p. 3-12.
130. Azadbeh, M., C. Gierl-Mayer, and H. Danninger, *Elastic Properties of Cr-Mo Alloyed Sintered Steels: a Comparison of Dynamic and Static Young's Moduli*. Powder Metallurgy Progress, 2006. **6**, no. **1**: p. 1-10.
131. Zhang, J., R.J. Perez, and E.J. Lavernia, *Documentation of Damping Capacity of Metallic, Ceramic and Metal-Matrix Composite Materials*. Journal of Materials Science, 1993. **28**, no. **9**: p. 2395-2404.
132. *Operation instruction of RFDA professional (Version 2.1)*.
133. Kalss, G., *Sinterhärten von Cr-Mo-legierten PM-Stählen für hochbelastbare Präzisionsteile*. Dissertation; Vienna University of Technology, 2007: p. 34f.
134. Fitzka, M., et al., *Usability of Ultrasonic Frequency Testing for Rapid Generation of High and Very High Cycle Fatigue Data*. Materials (Basel), 2021. **14**, no. **9**.
135. Mayer, H., M. Fitzka, and R. Schuller, *Constant and Variable Amplitude Ultrasonic Fatigue of 2024-T351 Aluminium Alloy at Different Load Ratios*. Ultrasonics, 2013. **53**, no. **8**: p. 1425-1432.
136. Danninger, H., et al., *Thermophysical Properties of Sintered Steels: Effect of Porosity*. International Journal of Powder Metallurgy, 2011. **47**, no. **3**: p. 31-41.
137. Boyer, H.E. and T.L. Gall, *Metals Handbook; desk edition*. 1989, American Society for Metals: United States. p. 219-225.
138. Fleck, N. and R. Smith, *Effect of Density on Tensile Strength, Fracture Toughness, and Fatigue Crack Propagation Behaviour of Sintered Steel*. Powder Metallurgy, 1981. **24**, no. **3**: p. 121-125.
139. Hu, H., et al., *Effect of Mo Content on Microstructure and Property of Low-Carbon Bainitic Steels*. Metals, 2016. **6**, no. **8**: p. 173.
140. Sakuma, Y., D.K. Matlock, and G. Krauss, *Effect of Molybdenum on Microstructure and Mechanical Properties of Intercritically Annealed and Isothermally Transformed Low Carbon Steel*. Materials Science and Technology, 1993. **9**, no. **8**: p. 718-724.

141. Skoglund, P., *High Density PM Parts by High Velocity Compaction*. Powder Metallurgy, 2001. **44**: p. 199-201.
142. Danninger, H., C. Gierl-Mayer, and S. Strobl, *Evolution of Microstructure in Ferrous and Non-Ferrous Materials*, in *Advances in Powder Metallurgy*, I. Chang and Y. Zhao, Editors. 2013, Woodhead Publishing. p. 308-357.
143. Lawcock, R.L. and T.J. Davies, *Effect of Carbon on Dimensional and Microstructural Characteristics of Fe-Cu Compacts during Sintering*. Powder Metallurgy, 1990. **33**, no. **2**: p. 147-149.
144. Dudrova, E. and M. Kabátova, *A Review of Failure of Sintered Steels: Fractography of Static and Dynamic Crack Nucleation, Coalescence, Growth and Propagation*. Powder Metallurgy, 2016. **59**, no. **2**: p. 148-167.
145. Xu, C., et al., *The Effect of the Load Bearing Area on the High Cycle Fatigue Limit in High Density Sintered Low Alloyed Steels* Proc. Euro PM2004, 2004. Vienna, Austria; EPMA, Shrewsbury UK. **3**: p. 35-40.
146. Cytermann, R., *A New Way to Investigate the Dependence of Elastic Moduli on the Microstructure of Porous Materials*. Powder Metallurgy International, 1987. **19**, no. **4**: p. 27-30.
147. Danninger, H., V. Vassileva, and C. Gierl-Mayer, *Atmosphere Effects on Sintering of Carbon-Free Powder Compacts from Different Ferrous Powders*. Proc. Euro PM2009, 2009. Copenhagen, Denmark; EPMA, Shrewsbury UK. **Sintering Atmospheres**: p. 1-6.
148. Danninger, H., et al., *Degassing and Deoxidation Processes During Sintering of Unalloyed and Alloyed PM Steels*. Powder Metallurgy Progress, 2002. **2**, no. **3**: p. 125-140.
149. Jalilizadeh, M., C. Gierl-Mayer, and H. Danninger, *Effect of Sintering Atmosphere and Alloy Elements on the Ferrite-Austenite Transformation of Iron Compacts*. Proc. Euro PM2007, 2007. Toulouse, France; EPMA, Shrewsbury UK. **Sintering – Atmospheres & Dimensional Control**: p. 131-136.
150. Kuroki, H. and H.Y. Suzuki, *Coarse Columnar Structure of Transformation-Grown Ferrite in Pure Iron (On Wrought Iron and Sintered Iron)*. Materials Transactions, 2006. **47**, no. **10**: p. 2449-2456.
151. Kuroki, H. and H. Suzuki, *Coarse Columnar Structure of Transformation-grown Ferrite and Very Low Carbon Content in Pure Iron of Armco Type*. steel research international, 2007. **78**, no. **10**: p. 572.
152. Chen, Y.C., *Effect of H₂O Content in Air on the Carburizing Behavior of Charcoal Gas*. Journal of Materials Engineering and Performance, 1992. **1**, no. **3**: p. 383-392.
153. Kaspersma, J.H. and R.H. Shay, *Carburization of iron by CO-based mixtures in nitrogen at 925 °C*. Metallurgical Transactions B, 1981. **12**: p. 77.
154. Woodtli, J. and R. Kieselbach, *Damage due to Hydrogen Embrittlement and Stress Corrosion Cracking*. Engineering Failure Analysis, 2000. **7**, no. **6**: p. 427-450.
155. Zwettler, F., *Bestimmung von Wasserstoff in Stahl*. PhD Thesis, Vienna University of Technology, 2012.
156. Tajima, S., et al., *Magnetic Properties and Microstructure of High-Density Sintered Iron Formed by Warm Compaction Using Die Wall Lubrication*. Materials Transactions 2005. **46**, no. **6**: p. 1402-1406.
157. Park, J., et al., *Complex Effects of Alloy Composition and Porosity on the Phase Transformations and Mechanical Properties of Powder Metallurgy Steels*. Powder Technology, 2015. **284**: p. 459-466.
158. Shanmugasundaram, D. and R. Chandramouli, *Tensile and Impact Behaviour of Sinter-Forged Cr, Ni and Mo Alloyed Powder Metallurgy Steels*. Materials & Design, 2009. **30**, no. **9**: p. 3444-3449.

159. Campos, M., L. Blanco, and J. Torralba, *Thermal Analysis of Prealloyed Fe–3Cr–0.5Mo Sintered Steel*. Journal of Thermal Analysis and Calorimetry 2006. **84**: p. 483-487.
160. Bergman, O., *Influence of Oxygen Partial Pressure in Sintering Atmosphere on Properties of Cr-Mo Prealloyed Powder Metallurgy Steel*. Powder Metallurgy, 2007. **50**, no. 3: p. 243-249.
161. Gierl, C., et al., *Introduction of Carbon into Sintered Steels through Different Masteralloy Routes*. Proc. 2012 World Congress on Powder Metallurgy, 2012. Yokohama, Japan: p. ISBN: 978-4-9900214-9-8; Paper-Nr. 16C-T1-19.
162. Danninger, H., et al., *Iron-Carbon Masteralloy - a Promising Approach for Introducing Carbon into High Density Sintered Steels*. "Preprints PowderMet2011", I.E. Anderson, T.W. Pelletiers (Hrg.); Metal Powder Industries Federation, Princeton NJ, 2011: p. 11 S.
163. Karamchedu, S., E. Hryha, and L. Nyborg, *Changes in the Surface Chemistry of Chromium-Alloyed Powder Metallurgical Steel During Delubrication and their Impact on Sintering*. Journal of Materials Processing Technology, 2015. **223**: p. 171-185.
164. Karlsson, H., et al., *Surface Product Formation On Chromium Alloyed Steel Powder Particles*. Proc. Euro PM2001, 2001. Nice, France; EPMA, Shrewsbury UK. **1**: p. 22-27.
165. Momeni, M., *Temperature and Interstitial Effect on Physical and Chemical Processes during Sintering of Ferrous Powder Compacts, PhD Thesis*. 2010, Faculty of Technical Chemistry, Technische Universität Wien, Vienna, Austria.
166. De Oro Calderon, R., C. Gierl-Mayer, and H. Danninger, *Sintering Enhancement by the Use of Masteralloys: Important Concepts and New Possibilities*. Proc. 2018 World Congress on Powder Metallurgy, 2018. Beijing, China. **Sintering & Post Processing**: p. 462-472.
167. Bhadeshia, H.K.D.H., *Cementite*. International Materials Reviews, 2020. **65**, no. 1: p. 1-27.
168. Du, H. and J.E. Morral, *Prediction of the Lowest Melting Point Eutectic in the Fe-Cr-Mo-V-C System*. Journal of Alloys and Compounds, 1997. **247**, no. 1(1): p. 122-127.
169. Gómez-Acebo, T., M. Sarasola, and F. Castro, *Systematic Search of Low Melting Point Alloys in the Fe–Cr–Mn–Mo–C System*. Calphad, 2003. **27**, no. 3: p. 325-334.
170. De Oro Calderon, R., et al., *Mechanical Performance of Sintered Steels Containing Fine Masteralloy Powders Produced with a Novel Atomization Technique: "Ultra High Pressure Water Atomization"*. Proc. Euro PM2017, 2017. Milan, Italy; EPMA, Shrewsbury UK. **Tools for Improving PM**: p. 1-6.
171. De Oro Calderon, R., et al., *Effect of Sintering Conditions on the Properties of Lean PM Steels Produced through the Masteralloy Route*. Proc. 2018 World Congress on Powder Metallurgy, 2018. Beijing, China. **Part 3—Sintering & Post Processing**: p. 473-480.
172. Gierl-Mayer, C., W. Molnar, and H. Danninger, *Correlations Between Microstructure, Mechanical Properties and Sintering Parameters for PM Steels*. Proc. Euro PM2011, 2011. Barcelona, Spain; EPMA, Shrewsbury UK. **Sintered Steels: Mechanical Properties**: p. 1-7.
173. Cavdar, U., *Effect of the Copper Amount in Iron-Based Powder Metal Compacts*. Materials and Technologies, 2015. **49**: p. 57-62.
174. Wong-Ángel, W., et al., *Effect of Copper on the Mechanical Properties of Alloys Formed by Powder Metallurgy*. Materials & Design, 2014. **58**: p. 12–18.
175. Fredriksson, H., K. Hansson, and A. Olsson, *On the Mechanism of Liquid Copper Penetration into Iron Grain Boundaries*. Scand. J. Metall., 2001. **30**: p. 41-50.

176. Kleback, B. and W. Schatt, *Anwendung eines kurzzeitigen Flüssigphasensinterns für die Herstellung von Fe-Ti-Sinterlegierungen*. Planseeber. Pulvermet., 1980. **28**: p. 204-215.
177. Gierl-Mayer, C., R. de Oro Calderon, and H. Danninger, *The Role of Oxygen Transfer in Sintering of Low Alloy Steel Powder Compacts: A Review of the "Internal Getter" Effect*. JOM, 2016. **68**, no. 3: p. 920-927.
178. Zhang, Z., R. Sandström, and L. Wang, *Modelling of Swelling of Fe–Cu Compacts Sintered at Temperatures above the Copper Melting Point*. Journal of Materials Processing Technology, 2004. **152**: p. 131-135.
179. Berner, D., H.E. Exner, and G. Petzow, *Swelling of iron-copper mixtures during sintering and infiltration*. Modern Dev. in Powder Metall., 1974. **6**: p. 237-250.
180. Nabeel, M., R. Frykholm, and P. Hedström, *Influence of Alloying Elements on Ni Distribution in PM Steels*. Powder Metallurgy, 2014. **57**: p. 111-118.
181. Behera, D.K., P. Tripathi, and A.K. Chaubey, *Effect of Nickel on Mechanical Properties of Alloy Steel Produced by Powder Metallurgy*. Materials Today: Proceedings, 2018. **5**(1, Part 1): p. 1704-1710.
182. Wu, M., K.-S. Hwang, and H.-S. Huang, *In-Situ Observations on the Fracture Mechanism of Diffusion-Alloyed Ni-Containing Powder Metal Steels and a Proposed Method for Tensile Strength Improvement*. Metallurgical and Materials Transactions A, 2007. **38**: p. 1598-1607.
183. Carabajar, S., C. Verdu, and R. Fougères, *Damage Mechanisms of a Nickel Alloyed Sintered Steel during Tensile Tests*. Materials Science and Engineering 1997. **A 232**: p. 80-87.
184. Bergmark, A. and L. Alzati, *Fatigue crack path in Cu–Ni–Mo alloyed PM steel*. Fatigue & Fracture of Engineering Materials & Structures, 2004. **28**: p. 229-235.
185. Synek, J., *Hartmetall-Stahl-Komposite*. PhD Thesis, Vienna University of Technology, 2014.
186. Jo, S.K., M. Kylan, and H. Fran, *Improved Processing and Handling of Sintered Soft Magnetic Materials*. Proc. 2018 World Congress on Powder Metallurgy, 2018. Beijing, China. **Part 10—Magnetic Materials & Functional Materials**: p. 1384-1389.
187. Sonsino, C.M., *Dauerfestigkeit – eine Fiktion (Endurance limit – A Fiction)*. Konstruktion, 2005. **no.4**: p. 87-92.
188. Danninger, H. and B. Weiss, *The Influence of Defects on High Cycle Fatigue of Metallic Materials*. Journal of Materials Processing Technology, 2003. **143-144**: p. 179-184.

Milad Hojati

Date and place of birth: May 11, 1987, Iran

Education:

Sep. 2010- Sep. 2013: **M.Sc., Materials Engineering - Corrosion and Protection of Materials,** Ferdowsi University of Mashhad, Iran.

Sep. 2005- Sep. 2010: **B.Sc., Industrial Metallurgy Engineering,** Ferdowsi University of Mashhad, Iran.

Thesis:

M.Sc. Thesis, Detection of Corrosion in Austenitic Stainless Steel(304L) by Application of Pulsed Eddy Current Non-Destructive Method, Ferdowsi University of Mashhad, Supervised by Prof. M. Kashefi. Mashhad, 2013

B.Sc. Thesis, Effect of Sintering Atmosphere on Mechanical Properties of Ast-CrM PM Parts, Ferdowsi University of Mashhad, Supervised by Prof. A. Babakhani and Prof. M. Mazinani. Mashhad, 2010

Working Experience in Industry:

Aug. 2009- Jan. 2018: R&D and Heat Treatment division, Mashhad Powder Metallurgy (MPM) Co., Mashhad, Iran

Publications

1. Hojati, M., H. Danninger, and C. Gierl-Mayer, *Mechanical and Physical Properties of Differently Alloyed Sintered Steels as a Function of the Sintering Temperature*. Metals, 2022. **12**(1): p. 13-33.
2. Hojati, M., C. Gierl-Mayer, and H. Danninger, *Iron Carbon Masteralloy as Sintering Activator for Low Alloy Powder Metallurgy Steels*. Materials Science Forum, 2021. **1016**: p. 561-567.
3. Hojati, M., C. Gierl-Mayer, and H. Danninger, *Effect of Sintering Temperature on Microstructure and Physical Properties of Differently Compacted Carbon and Mo Alloyed Steels*. Proc. Euro PM2021, 2021. Virtual congress. **Sintering**: p. 1-7.
4. Hojati, M., C. Gierl-Mayer, and H. Danninger, *Effect of sintering atmosphere on sintering process, microstructure and mechanical properties of compacted plain iron and carbon steel*. Proc. Euro PM2021, 2021, Virtual conference. **Sintering**: p. 1-8.
5. Hojati, M., C. Gierl-Mayer, and H. Danninger, *Monotonic And Cyclic Properties Of Sinter Hardened Sintered Steels Prepared By Hybrid Alloying*. Submitted for 2022 World Congress on Powder Metallurgy, 2022, Lyon, France.
6. Danninger, H., M. Hojati, D. Tokatligil, T. Konegger, C. Gierl-Mayer, *Measurement Of The Pore Diameter In Sintered Steels With Varying Porosity*. Submitted for 2022 World Congress on Powder Metallurgy, 2022. Lyon, france.